Cosmological constraints from standardized non-CMB observations

by

Shulei Cao

M.S., Beijing Normal University, 2016

AN ABSTRACT OF A DISSERTATION

submitted in partial fulfillment of the
requirements for the degree

DOCTOR OF PHILOSOPHY

Department of Physics
College of Arts and Sciences

KANSAS STATE UNIVERSITY
Manhattan, Kansas

2023

Abstract

The current expansion of the Universe has been observed to be accelerating, and the widely accepted spatially-flat concordance model of general relativistic cosmology attributes this phenomenon to a constant dark energy, a cosmological constant, which is measured to comprise about 70% of the total energy budget of the current Universe. However, observational discrepancies and theoretical puzzles have raised questions about this model, suggesting that alternative cosmological models with non-zero spatial curvature and/or dark energy dynamics might provide better explanations.

To explore these possibilities, we have conducted a series of studies using standardized, lower-redshift observations to constrain six different cosmological models with varying degrees of flatness and dark energy dynamics. Through comparing these observations with theoretical predictions, we aim to deepen our understanding of the evolution of the Universe and shed new light on its mysteries. Our data provide consistent cosmological constraints across all six models, with some suggesting the possibility of mild dark energy dynamics and slight spatial curvature. However, these joint constraints do not rule out the possibility of dark energy being a cosmological constant and the spatial hypersurfaces being flat. Overall, our findings contribute to the ongoing efforts to refine our understanding of the Universe and its properties, and suggest that multiple cosmological models remain viable.

In addition, our research demonstrates that certain types of astronomical observations, such as gamma ray bursts and reverberation-mapped quasar measurements, can be standardized and utilized in cosmology. This allows us to gain valuable insights into the properties of the Universe and its evolution by using these observations as distance indicators. By using these new standardized observations to constrain our cosmological models, we can improve our understanding of the nature of dark energy and other fundamental components of the Universe.

Cosmological constraints from standardized non-CMB observations

by

Shulei Cao

M.S., Beijing Normal University, 2016

A DISSERTATION

submitted in partial fulfillment of the
requirements for the degree

DOCTOR OF PHILOSOPHY

Department of Physics
College of Arts and Sciences

KANSAS STATE UNIVERSITY
Manhattan, Kansas

2023

Approved by:

Major Professor
Bharat Ratra

Copyright

© Shulei Cao 2023.

Abstract

The current expansion of the Universe has been observed to be accelerating, and the widely accepted spatially-flat concordance model of general relativistic cosmology attributes this phenomenon to a constant dark energy, a cosmological constant, which is measured to comprise about 70% of the total energy budget of the current Universe. However, observational discrepancies and theoretical puzzles have raised questions about this model, suggesting that alternative cosmological models with non-zero spatial curvature and/or dark energy dynamics might provide better explanations.

To explore these possibilities, we have conducted a series of studies using standardized, lower-redshift observations to constrain six different cosmological models with varying degrees of flatness and dark energy dynamics. Through comparing these observations with theoretical predictions, we aim to deepen our understanding of the evolution of the Universe and shed new light on its mysteries. Our data provide consistent cosmological constraints across all six models, with some suggesting the possibility of mild dark energy dynamics and slight spatial curvature. However, these joint constraints do not rule out the possibility of dark energy being a cosmological constant and the spatial hypersurfaces being flat. Overall, our findings contribute to the ongoing efforts to refine our understanding of the Universe and its properties, and suggest that multiple cosmological models remain viable.

In addition, our research demonstrates that certain types of astronomical observations, such as gamma ray bursts and reverberation-mapped quasar measurements, can be standardized and utilized in cosmology. This allows us to gain valuable insights into the properties of the Universe and its evolution by using these observations as distance indicators. By using these new standardized observations to constrain our cosmological models, we can improve our understanding of the nature of dark energy and other fundamental components of the Universe.

Table of Contents

List of Figures xii

List of Tables xxx

Acknowledgements xxxiv

1 Introduction 1

1.1 General relativity 2

1.1.1 Tensors in differential geometry 2

1.1.2 Metric tensor and curvature 5

1.1.3 Einstein's field equation 10

1.2 Friedmann equations 17

1.3 Distance measures in cosmology 21

2 Dark energy cosmological models 25

2.1 ΛCDM models 25

2.2 XCDM parametrizations 26

2.3 ϕCDM models 27

3 Cosmological constraints from HII starburst galaxy apparent magnitude and other cosmological measurements 32

3.1 Introduction 32

3.2 Data 35

3.3 Data Analysis Methodology 39

3.4 Results 42

3.4.1 H II G constraints . . . 42
3.4.2 $H(z)$, BAO, and H II G (HzBH) constraints . . . 44
3.4.3 $H(z)$, BAO, and QSO (HzBQ) constraints . . . 52
3.4.4 $H(z)$, BAO, QSO, and H II G (HzBQH) constraints . . . 54
3.4.5 Model comparison . . . 55
3.5 Conclusions . . . 56

4 Cosmological constraints from higher-redshift gamma-ray burst, H II starburst galaxy, and quasar (and other) data . . . 58
4.1 Introduction . . . 58
4.2 Data . . . 61
4.3 Data Analysis Methodology . . . 64
4.4 Results . . . 68
4.4.1 H II G, QSO-AS, and GRB constraints, individually . . . 68
4.4.2 H II G, QSO-AS, and GRB (HQASG) joint constraints . . . 69
4.4.3 $H(z)$, BAO, H II G, QSO-AS, and GRB (HzBHQASG) constraints . . . 73
4.4.4 Model comparison . . . 76
4.5 Conclusion . . . 77

5 Using Pantheon and DES supernova, baryon acoustic oscillation, and Hubble parameter data to constrain the Hubble constant, dark energy dynamics, and spatial curvature . . . 84
5.1 Introduction . . . 84
5.2 Data . . . 87
5.3 Data Analysis Methodology . . . 89
5.4 Results . . . 90
5.4.1 $H(z)$ + BAO, HzBSNP, and HzBSND constraints . . . 91
5.4.2 HzBSNPD constraints . . . 93

5.4.3 HzBSNPDQH constraints . . . 99
5.4.4 Model comparison . . . 101
5.5 Conclusion . . . 103

6 Cosmological constraints from H II starburst galaxy, quasar angular size, and other measurements . . . 104
6.1 Introduction . . . 104
6.2 Data . . . 107
6.3 Data Analysis Methodology . . . 109
6.4 Results . . . 109
6.4.1 Constraints from H IIG-2021 versus H IIG-2019 . . . 110
6.4.2 QSO constraints alone and in comparison to those from other probes 113
6.4.3 Joint analyses results . . . 115
6.4.4 Model comparison . . . 122
6.5 Conclusion . . . 122

7 Standardizing Dainotti-correlated gamma-ray bursts, and using them with standardized Amati-correlated gamma-ray bursts to constrain cosmological model parameters . . . 126
7.1 Introduction . . . 126
7.2 Data . . . 129
7.3 Data Analysis Methodology . . . 131
7.4 Results . . . 135
7.4.1 Constraints from ML, MS, and GL data . . . 135
7.4.2 Constraints from A118, A115 (and jointly with ML), and A115′ (and jointly with GL) data . . . 145
7.5 Conclusion . . . 153

8 Standardizing Platinum Dainotti-correlated gamma-ray bursts, and using them with standardized Amati-correlated gamma-ray bursts to constrain cosmological model parameters . . . 155
8.1 Introduction . . . 155
8.2 Data . . . 158
8.3 Data Analysis Methodology . . . 160
8.4 Results . . . 165
8.4.1 Constraints from Platinum, A118, A101, and Platinum + A101 data 165
8.4.2 Constraints from $H(z)$ + BAO data in combination with Platinum (HzBP) and Platinum + A101 (HzBPA101) data . . . 178
8.5 Conclusion . . . 179

9 Using lower-redshift, non-CMB, data to constrain the Hubble constant and other cosmological parameters . . . 181
9.1 Introduction . . . 181
9.2 Data . . . 184
9.3 Data Analysis Methodology . . . 188
9.4 Results . . . 189
9.4.1 Constraints from $H(z)$, BAO, and SN Ia data . . . 191
9.4.2 Constraints from QSO-AS, H II G, Mg II QSO, A118, and Platinum + A101 data . . . 192
9.4.3 Constraints from $H(z)$ + BAO + SN + QSO-AS + H II G + Mg II QSO + A118 (HzBSNQHMA) data . . . 193
9.4.4 Model Comparison . . . 194
9.5 Conclusion . . . 196

10 Gamma-ray burst data strongly favour the three-parameter fundamental plane (Dainotti) correlation over the two-parameter one . . . 205

10.1 Introduction . . . 205
10.2 Data . . . 208
10.3 Data Analysis Methodology . . . 209
10.4 Results . . . 220
10.5 Summary and Conclusion . . . 224

11 Standardizing reverberation-measured C IV time-lag quasars, and using them with standardized Mg II quasars to constrain cosmological parameters . . . 228
11.1 Introduction . . . 228
11.2 Data . . . 231
11.3 Data Analysis Methodology . . . 236
11.4 Results . . . 240
11.4.1 Constraints from C IV, Mg II, and C IV + Mg II QSO data . . . 240
11.4.2 Constraints from $H(z)$ + BAO + C IV + Mg II data . . . 248
11.4.3 Model Comparison . . . 249
11.5 Discussion . . . 251
11.6 Conclusions . . . 259

12 Conclusion . . . 262

Bibliography . . . 264

A QSO-Flux . . . 284
A.1 QSO-Flux constraints . . . 285
A.2 H IIG, QSO-AS, QSO-Flux, and GRB (HQASQFG) constraints . . . 286
A.2.1 $H(z)$, BAO, H IIG, QSO-AS, QSO-Flux, and GRB (HzBHQASQFG) constraints . . . 286
A.3 Model comparison . . . 286

B Corrected GRB data . . . 291

C Golden sample of C IV QSO data 297

List of Figures

3.1 1σ, 2σ, and 3σ confidence contours for flat ΛCDM, where the right panel is the comparison zoomed in. The black dotted line is the zero-acceleration line, which divides the parameter space into regions associated with currently accelerated (below) and currently decelerated (above) cosmological expansion. 44

3.2 Same as Fig. 3.1 but for non-flat ΛCDM. The cyan dash-dot line represents the flat case, with closed spatial hypersurfaces to the upper right. The black dotted line is the zero-acceleration line, which divides the parameter space into regions associated with currently accelerated (above left) and currently decelerated (below right) cosmological expansion. 47

3.3 1σ, 2σ, and 3σ confidence contours for flat XCDM. The black dotted line is the zero-acceleration line, which divides the parameter space into regions associated with currently accelerated (below left) and currently decelerated (above right) cosmological expansion. The magenta lines denote $w_{\rm X} = -1$, i.e. the flat ΛCDM model. 48

3.4 Same as Fig. 3.3 but for non-flat XCDM, where the zero acceleration lines in each of the three subpanels are computed for the third cosmological parameter set to the H II G data only best-fitting values listed in Table 3.2. Currently-accelerated cosmological expansion occurs below these lines. The cyan dash-dot lines represent the flat case, with closed spatial hypersurfaces either below or to the left. The magenta lines indicate $w_{\rm X} = -1$, i.e. the non-flat ΛCDM model. 49

3.5 1σ, 2σ, and 3σ confidence contours for flat ϕCDM. The black dotted zero-acceleration line splits the parameter space into regions of currently accelerated (below left) and currently decelerated (above right) cosmological expansion. The $\alpha = 0$ axis is the flat ΛCDM model. 50

3.6 Same as Fig. 3.5 but for non-flat ϕCDM, where the zero-acceleration lines in each of the subpanels are computed for the third cosmological parameter set to the H II G data only best-fitting values listed in Table 3.2. Currently-accelerating cosmological expansion occurs below these lines. The cyan dash-dot lines represent the flat case, with closed spatial geometry either below or to the left. The $\alpha = 0$ axis is the non-flat ΛCDM model. 51

4.1 1σ, 2σ, and 3σ confidence contours for flat ΛCDM, where the right panel is the cosmological parameters comparison zoomed in. The black dotted lines in the left sub-panels of the left panel are the zero-acceleration lines, which divide the parameter space into regions associated with currently-accelerating (left) and currently-decelerating (right) cosmological expansion. 66

4.2 Same as Fig. 4.1 but for non-flat ΛCDM. The cyan dash-dot line represents the flat ΛCDM case, with closed spatial hypersurfaces to the upper right. The black dotted line is the zero-acceleration line, which divides the parameter space into regions associated with currently-accelerating (above left) and currently-decelerating (below right) cosmological expansion. 67

4.3 1σ, 2σ, and 3σ confidence contours for flat XCDM. The black dotted line is the zero-acceleration line, which divides the parameter space into regions associated with currently-accelerating (below left) and currently-decelerating (above right) cosmological expansion. The magenta lines denote $w_{\rm X} = -1$, i.e. the flat ΛCDM model. 70

4.4 Same as Fig. 4.3 but for non-flat XCDM, where the zero acceleration lines in each of the three subpanels are computed for the third cosmological parameter set to the $H(z)$ + BAO data best-fitting values listed in Table 4.1. Currently-accelerating cosmological expansion occurs below these lines. The cyan dash-dot lines represent the flat XCDM case, with closed spatial hypersurfaces either below or to the left. The magenta lines indicate $w_{\rm X} = -1$, i.e. the non-flat ΛCDM model. 71

4.5 1σ, 2σ, and 3σ confidence contours for flat ϕCDM. The black dotted zero-acceleration line splits the parameter space into regions of currently-accelerating (below left) and currently-decelerating (above right) cosmological expansion. The $\alpha = 0$ axis is the flat ΛCDM model. 75

4.6 Same as Fig. 4.5 but for non-flat ϕCDM, where the zero-acceleration lines in each of the sub-panels are computed for the third cosmological parameter set to the $H(z)$ + BAO data best-fitting values listed in Table 4.1. Currently-accelerating cosmological expansion occurs below these lines. The cyan dash-dot lines represent the flat ϕCDM case, with closed spatial geometry either below or to the left. The $\alpha = 0$ axis is the non-flat ΛCDM model. 78

4.7 Same as Fig. 4.1 (flat ΛCDM) but for different combinations of data. 78

4.8 Same as Fig. 4.2 (non-flat ΛCDM) but for different combinations of data. . . 80

4.9 Same as Fig. 4.3 (flat XCDM) but for different combinations of data. 80

4.10 Same as Fig. 4.4 (non-flat XCDM) but for different combinations of data. . . 81

4.11 Same as Fig. 4.5 (flat ϕCDM) but for different combinations of data. 81

4.12 Same as Fig. 4.6 (non-flat ϕCDM) but for different combinations of data. . . 82

5.1 1σ, 2σ, and 3σ confidence contours for flat ΛCDM, where the right panel is the comparison including derived cosmological matter density parameter Ω_{m0}. In all cases, the favored parameter space is associated with currently-accelerating cosmological expansion. 91

5.2 Same as Fig. 5.1 but for non-flat ΛCDM, where the cyan dash-dot lines represent the flat ΛCDM case, with closed spatial hypersurfaces either below or to the left. The black dotted line in the right subpanel is the zero-acceleration line, which divides the parameter space into regions associated with currently-accelerating (below left) and currently-decelerating (above right) cosmological expansion. In all cases, the favored parameter space is associated with currently-accelerating cosmological expansion. 92

5.3 1σ, 2σ, and 3σ confidence contours for flat XCDM. The black dotted line in the right panel is the zero-acceleration line, which divides the parameter space into regions associated with currently-accelerating (below) and currently-decelerating (above) cosmological expansion. In all cases, almost all of the favored parameter space is associated with currently-accelerating cosmological expansion. The magenta lines denote $w_{\rm X} = -1$, i.e. the flat ΛCDM model. 97

5.4 Same as Fig. 5.3 but for non-flat XCDM, where the zero acceleration lines in each of the three subpanels of the right panel are computed for the third cosmological parameter set to the $H(z)$ + BAO data best-fitting values listed in Table 5.2. Currently-accelerating cosmological expansion occurs below these lines. The cyan dash-dot lines represent the flat XCDM case, with closed spatial hypersurfaces either below or to the left. In all cases, almost all of the favored parameter space is associated with currently-accelerating cosmological expansion. The magenta lines indicate $w_{\rm X} = -1$, i.e. the non-flat ΛCDM model. 98

5.5 1σ, 2σ, and 3σ confidence contours for flat ϕCDM. In all cases, the favored parameter space is associated with currently-accelerating cosmological expansion. The $\alpha = 0$ axis is the flat ΛCDM model. 99

5.6 Same as Fig. 5.5 but for non-flat ϕCDM, where the zero-acceleration lines in each of the sub-panels of the right panel are computed for the third cosmological parameter set to the $H(z)$ + BAO data best-fitting values listed in Table 5.2. Currently-accelerating cosmological expansion occurs below these lines. In all cases, almost all of the favored parameter space is associated with currently-accelerating cosmological expansion. The cyan dash-dot lines represent the flat ϕCDM case, with closed spatial geometry either below or to the left. The $\alpha = 0$ axis is the non-flat ΛCDM model. 100

6.1 One-dimensional likelihoods and 1σ, 2σ, and 3σ two-dimensional likelihood confidence contours for flat ΛCDM. Left panel shows individual data set and $H(z)$ + BAO results and the right panel shows joint data sets constraints. The zero-acceleration lines are shown as black dashed lines in the left panel, which divide the parameter space into regions associated with currently-accelerating (left) and currently-decelerating (right) cosmological expansion, while in the right panel the joint analyses favor currently-accelerating expansion. 117

6.2 Same as Fig. 6.1 but for non-flat ΛCDM. The flat ΛCDM case is shown as the cyan dash-dot lines, with closed spatial hypersurfaces either below or to the left. The black dashed line in the left panel is the zero-acceleration line, which divides the parameter space into regions associated with currently-accelerating (below left) and currently-decelerating (above right) cosmological expansion. In the right panel, the joint analyses favor currently-accelerating expansion. . 118

6.3 One-dimensional likelihoods and 1σ, 2σ, and 3σ two-dimensional likelihood confidence contours for flat XCDM. The black dashed line in the left panel is the zero-acceleration line, which divides the parameter space into regions associated with currently-accelerating (below left) and currently-decelerating (above right) cosmological expansion. In the right panel, the joint analyses favor currently-accelerating expansion. The magenta lines represent $w_{\rm X} = -1$, i.e. the flat ΛCDM model. 119

6.4 Same as Fig. 6.3 but for non-flat XCDM, where the black dashed zero-acceleration lines are computed for the third cosmological parameter set to the $H(z)$ + BAO data best-fitting values listed in Table 6.1, with currently-accelerating cosmological expansion residing below left. The flat XCDM case is denoted as the cyan dash-dot lines, with closed spatial hypersurfaces either below or to the left. The magenta lines represent $w_{\rm X} = -1$, i.e. the non-flat ΛCDM model. In all cases except for the QSO only case, almost all of the favored parameter space is associated with currently-accelerating cosmological expansion. 120

6.5 One-dimensional likelihoods and 1σ, 2σ, and 3σ two-dimensional likelihood confidence contours for flat ϕCDM. The black dashed lines are the zero-acceleration lines, which divides the parameter space into regions associated with currently-accelerating (below left) and currently-decelerating (above right) cosmological expansion. The $\alpha = 0$ axis is the flat ΛCDM model. In all cases except for the QSO only case, almost all of the favored parameter space is associated with currently-accelerating cosmological expansion. 123

6.6 Same as Fig. 6.5 but for non-flat ϕCDM, where the black dashed zero-acceleration lines are computed for the third cosmological parameter set to the $H(z)$ + BAO data best-fitting values listed in Table 6.1. Currently-accelerating cosmological expansion occurs below left of these lines. The cyan dash-dot lines represent the flat ϕCDM case, with closed spatial geometry either below or to the left. The $\alpha = 0$ axis is the non-flat ΛCDM model. In the right panel, the joint analyses favor currently-accelerating expansion. . . 124

7.1 $L_0 - t_b$ correlations for MD-LGRB, MD-SGRB, GW-LGRB, and MD-SGRB + GW-LGRB data using the flat ΛCDM model. The MD-LGRB, MD-SGRB, and GW-LGRB data with error bars are shown in black, dark red, and dark green, respectively. The solid lines are the $L_0 - t_b$ correlations with posterior mean values for the slopes and intercepts listed in Table 7.5, for MD-LGRB (blue), MD-SGRB (red), GW-LGRB (green), and MD-SGRB + GW-LGRB (purple) data. The 1σ and 3σ confidence regions are the dark and light colored shaded regions with the uncertainties propagated from those of k and b (without considering $\sigma_{\rm int}$). 137

7.2 One-dimensional likelihoods and 1σ, 2σ, and 3σ two-dimensional likelihood confidence contours from MD-LGRB (blue), MD-SGRB (gray), MD-LGRB + MD-SGRB (pink), and $H(z)$ + BAO (red) data for all six models. The zero-acceleration lines are shown as black dashed lines, which divide the parameter space into regions associated with currently-accelerating and currently-decelerating cosmological expansion. In the non-flat XCDM and non-flat ϕCDM cases, the zero-acceleration lines are computed for the third cosmological parameter set to the $H(z)$ + BAO data best-fitting values listed in Table 7.4. The crimson dash-dot lines represent flat hypersurfaces, with closed spatial hypersurfaces either below or to the left. The magenta lines represent $w_{\rm X} = -1$, i.e. flat or non-flat ΛCDM models. The $\alpha = 0$ axes correspond to flat and non-flat ΛCDM models in panels (e) and (f), respectively. 142

7.3 One-dimensional likelihoods and 1σ, 2σ, and 3σ two-dimensional likelihood confidence contours from MD-LGRB (blue), GW-LGRB (green), MD-LGRB + GW-LGRB (violet), and $H(z)$ + BAO (red) data for all six models. The zero-acceleration lines are shown as black dashed lines, which divide the parameter space into regions associated with currently-accelerating and currently-decelerating cosmological expansion. In the non-flat XCDM and non-flat ϕCDM cases, the zero-acceleration lines are computed for the third cosmological parameter set to the $H(z)$ + BAO data best-fitting values listed in Table 7.4. The crimson dash-dot lines represent flat hypersurfaces, with closed spatial hypersurfaces either below or to the left. The magenta lines represent $w_{\rm X} = -1$, i.e. flat or non-flat ΛCDM models. The $\alpha = 0$ axes correspond to flat and non-flat ΛCDM models in panels (e) and (f), respectively. 143

7.4 One-dimensional likelihoods and 1σ, 2σ, and 3σ two-dimensional likelihood confidence contours from MD-SGRB (gray), GW-LGRB (green), MD-SGRB + GW-LGRB (orange), and $H(z)$ + BAO (red) data for all six models, without subscripts on $\sigma_{\rm int}$, k, and b. The zero-acceleration lines are shown as black dashed lines, which divide the parameter space into regions associated with currently-accelerating and currently-decelerating cosmological expansion. In the non-flat XCDM and non-flat ϕCDM cases, the zero-acceleration lines are computed for the third cosmological parameter set to the $H(z)$ + BAO data best-fitting values listed in Table 7.4. The crimson dash-dot lines represent flat hypersurfaces, with closed spatial hypersurfaces either below or to the left. The magenta lines represent $w_{\rm X} = -1$, i.e. flat or non-flat ΛCDM models. The $\alpha = 0$ axes correspond to flat and non-flat ΛCDM models in panels (e) and (f), respectively. 144

7.5 One-dimensional likelihoods and 1σ, 2σ, and 3σ two-dimensional likelihood confidence contours from MD-LGRB (green), A118 (gray), A115 (red), and MD-LGRB + A115 (purple) data for all six models. The zero-acceleration lines are shown as black dashed lines, which divide the parameter space into regions associated with currently-accelerating and currently-decelerating cosmological expansion. In the non-flat XCDM and non-flat ϕCDM cases, the zero-acceleration lines are computed for the third cosmological parameter set to the $H(z)$ + BAO data best-fitting values listed in Table 7.7. The crimson dash-dot lines represent flat hypersurfaces, with closed spatial hypersurfaces either below or to the left. The magenta lines represent $w_{\rm X} = -1$, i.e. flat or non-flat ΛCDM models. The $\alpha = 0$ axes correspond to flat and non-flat ΛCDM models in panels (e) and (f), respectively. 150

7.6 One-dimensional likelihoods and 1σ, 2σ, and 3σ two-dimensional likelihood confidence contours from GW-LGRB (green), A118 (gray), A115′ (red), and GW-LGRB + A115′ (purple) data for all six models. The zero-acceleration lines are shown as black dashed lines, which divide the parameter space into regions associated with currently-accelerating and currently-decelerating cosmological expansion. In the non-flat XCDM and non-flat ϕCDM cases, the zero-acceleration lines are computed for the third cosmological parameter set to the $H(z)$ + BAO data best-fitting values listed in Table 7.7. The crimson dash-dot lines represent flat hypersurfaces, with closed spatial hypersurfaces either below or to the left. The magenta lines represent $w_{\rm X} = -1$, i.e. flat or non-flat ΛCDM models. The $\alpha = 0$ axes correspond to flat and non-flat ΛCDM models in panels (e) and (f), respectively. 151

8.1 One-dimensional likelihood distributions and 1σ, 2σ, and 3σ two-dimensional likelihood confidence contours for flat ΛCDM from various combinations of data. The zero-acceleration black dashed lines in panels (a) and (b) divide the parameter space into regions associated with currently-accelerating (left) and currently-decelerating (right) cosmological expansion. 166

8.2 Same as Fig. 8.1 but for non-flat ΛCDM. The zero-acceleration black dashed lines divide the parameter space into regions associated with currently-accelerating (below left) and currently-decelerating (above right) cosmological expansion. 167

8.3 One-dimensional likelihood distributions and 1σ, 2σ, and 3σ two-dimensional likelihood confidence contours for flat XCDM from various combinations of data. The zero-acceleration black dashed lines divide the parameter space into regions associated with currently-accelerating (either below left or below) and currently-decelerating (either above right or above) cosmological expansion. The magenta dashed lines represent $w_{\rm X} = -1$, i.e. flat ΛCDM. 168

8.4 Same as Fig. 8.3 but for non-flat XCDM. The zero-acceleration black dashed lines are computed for the third cosmological parameter set to the $H(z)$ + BAO data best-fitting values listed in Table 8.4, and divide the parameter space into regions associated with currently-accelerating (either below left or below) and currently-decelerating (either above right or above) cosmological expansion. The crimson dash-dot lines represent flat hypersurfaces, with closed spatial hypersurfaces either below or to the left. The magenta dashed lines represent $w_{\rm X} = -1$, i.e. non-flat ΛCDM. 169

8.5 One-dimensional likelihood distributions and 1σ, 2σ, and 3σ two-dimensional likelihood confidence contours for flat ϕCDM from various combinations of data. The zero-acceleration black dashed lines divide the parameter space into regions associated with currently-accelerating (below left) and currently-decelerating (above right) cosmological expansion. The $\alpha = 0$ axes correspond to flat ΛCDM. 170

8.6 Same as Fig. 8.5 but for non-flat ϕCDM. The zero-acceleration black dashed lines are computed for the third cosmological parameter set to the $H(z)$ + BAO data best-fitting values listed in Table 8.4, and divide the parameter space into regions associated with currently-accelerating (below left) and currently-decelerating (above right) cosmological expansion. The crimson dash-dot lines represent flat hypersurfaces, with closed spatial hypersurfaces either below or to the left. The $\alpha = 0$ axes correspond to non-flat ΛCDM. . . 171

8.7 One-dimensional likelihood distributions and 1σ, 2σ, and 3σ two-dimensional likelihood confidence contours for some cosmological parameters of the six cosmological models from Platinum data (gray), A101 data (green), and $H(z)$ + BAO data (red), which more clearly show the cosmological parameter overlaps between Platinum/A101 data and $H(z)$ + BAO data. 172

9.1 One-dimensional likelihood distributions and 1σ, 2σ, and 3σ two-dimensional likelihood confidence contours for flat ΛCDM from various combinations of data. The zero-acceleration black dashed lines in some (a) panels divide the parameter space into regions associated with currently-accelerating (left) and currently-decelerating (right) cosmological expansion. 197

9.2 Same as Fig. 9.1 but for non-flat ΛCDM. The zero-acceleration black dashed lines divide the parameter space into regions associated with currently-accelerating (below left) and currently-decelerating (above right) cosmological expansion. 198

9.3 One-dimensional likelihood distributions and 1σ, 2σ, and 3σ two-dimensional likelihood confidence contours for flat XCDM from various combinations of data. The zero-acceleration black dashed lines divide the parameter space into regions associated with currently-accelerating (either below left or below) and currently-decelerating (either above right or above) cosmological expansion. The magenta dashed lines represent $w_{\rm X} = -1$, i.e. flat ΛCDM. 199

9.4 Same as Fig. 9.3 but for non-flat XCDM. The zero-acceleration black dashed lines are computed for the third cosmological parameter set to the $H(z)$ + BAO data best-fitting values listed in Table 9.4, and divide the parameter space into regions associated with currently-accelerating (either below left or below) and currently-decelerating (either above right or above) cosmological expansion. The crimson dash-dot lines represent flat hypersurfaces, with closed spatial hypersurfaces either below or to the left. The magenta dashed lines represent $w_{\rm X} = -1$, i.e. non-flat ΛCDM. 200

9.5 One-dimensional likelihood distributions and 1σ, 2σ, and 3σ two-dimensional likelihood confidence contours for flat ϕCDM from various combinations of data. The zero-acceleration black dashed lines divide the parameter space into regions associated with currently-accelerating (below left) and currently-decelerating (above right) cosmological expansion. The $\alpha = 0$ axes correspond to flat ΛCDM. 201

9.6 Same as Fig. 9.5 but for non-flat ϕCDM. The zero-acceleration black dashed lines are computed for the third cosmological parameter set to the $H(z)$ + BAO data best-fitting values listed in Table 9.4, and divide the parameter space into regions associated with currently-accelerating (below left) and currently-decelerating (above right) cosmological expansion. The crimson dash-dot lines represent flat hypersurfaces, with closed spatial hypersurfaces either below or to the left. The $\alpha = 0$ axes correspond to non-flat ΛCDM. . . 202

10.1 One-dimensional likelihood distributions and 1σ, 2σ, and 3σ two-dimensional likelihood confidence contours for flat ΛCDM from various combinations of data. The zero-acceleration black dashed lines in panels (a) and (b) divide the parameter space into regions associated with currently-accelerating (left) and currently-decelerating (right) cosmological expansion. 213

10.2 Same as Fig. 10.1 but for non-flat ΛCDM. The zero-acceleration black dashed lines divide the parameter space into regions associated with currently-accelerating (below left) and currently-decelerating (above right) cosmological expansion. 214

10.3 One-dimensional likelihood distributions and 1σ, 2σ, and 3σ two-dimensional likelihood confidence contours for flat XCDM from various combinations of data. The zero-acceleration black dashed lines divide the parameter space into regions associated with currently-accelerating (either below left or below) and currently-decelerating (either above right or above) cosmological expansion. The magenta dashed lines represent $w_{\rm X} = -1$, i.e. flat ΛCDM. 215

10.4 Same as Fig. 10.3 but for non-flat XCDM. The zero-acceleration black dashed lines are computed for the third cosmological parameter set to the $H(z)$ + BAO data best-fitting values listed in table 4 of Cao & Ratra (2022), and divide the parameter space into regions associated with currently-accelerating (either below left or below) and currently-decelerating (either above right or above) cosmological expansion. The crimson dash-dot lines represent flat hypersurfaces, with closed spatial hypersurfaces either below or to the left. The magenta dashed lines represent $w_{\rm X} = -1$, i.e. non-flat ΛCDM. 216

10.5 One-dimensional likelihood distributions and 1σ, 2σ, and 3σ two-dimensional likelihood confidence contours for flat ϕCDM from various combinations of data. The zero-acceleration black dashed lines divide the parameter space into regions associated with currently-accelerating (below left) and currently-decelerating (above right) cosmological expansion. The $\alpha = 0$ axes correspond to flat ΛCDM. 217

10.6 Same as Fig. 10.5 but for non-flat ϕCDM. The zero-acceleration black dashed lines are computed for the third cosmological parameter set to the $H(z)$ + BAO data best-fitting values listed in table 4 of Cao & Ratra (2022), and divide the parameter space into regions associated with currently-accelerating (below left) and currently-decelerating (above right) cosmological expansion. The crimson dash-dot lines represent flat hypersurfaces, with closed spatial hypersurfaces either below or to the left. The $\alpha = 0$ axes correspond to non-flat ΛCDM. 218

10.7 Comparisons between 3D Dainotti correlation parameters of flat ΛCDM and those of non-flat XCDM from LGRB145 data, where their two-dimensional likelihood confidence contours are mutually consistent within 1σ. 219

10.8 Comparisons between 2D Dainotti correlation parameters of different cosmological models. 219

11.1 The redshift distribution for the "golden" sample of 38 C IV QSOs from Kaspi et al. (2021). The dashed line stands for the redshift median at 2.048, while the dotted lines represent 16% and 84% percentiles at 1.244 and 2.647, respectively. The histogram bin size is $\Delta z \simeq 0.2$. 232

11.2 Radius-luminosity relationship for the "golden" sample of 38 C IV QSOs (see also Kaspi et al., 2021). The luminosity at 1350 Å is based on the flat ΛCDM model (with $H_0 = 70\,\mathrm{km\,s^{-1}\,Mpc^{-1}}$, $\Omega_{m0} = 0.3$, and $\Omega_\Lambda = 0.7$). The points are colour-coded with respect to the calculated Eddington ratio $\lambda_{\rm Edd} = L_{\rm bol}/L_{\rm Edd}$ of the source. When we neglect individual time-delay errors, the best-fit relation (black solid line) determined by the Levenberg-Marquardt algorithm has a slope of $\gamma_{\rm C} = 0.42 \pm 0.03$ and a scatter of $\sigma = 0.32$ dex. The dark and light gray areas around the best-fit solid line are one and two sigma confidence regions. Considering individual time-delay errors yields the best-fit relation (dotted line) with a larger slope of $\gamma_{\rm C} = 0.56 \pm 0.04$ and the scatter of data around this relation is $\sigma = 0.41$ dex. 234

11.3 One-dimensional likelihood distributions and 1σ, 2σ, and 3σ two-dimensional likelihood confidence contours for flat ΛCDM from various combinations of data. The zero-acceleration black dashed lines in panels (a) and (b) divide the parameter space into regions associated with currently-accelerating (left) and currently-decelerating (right) cosmological expansion. 241

11.4 Same as Fig. 11.3 but for non-flat ΛCDM. The zero-acceleration black dashed lines divide the parameter space into regions associated with currently-accelerating (below left) and currently-decelerating (above right) cosmological expansion. 242

11.5 One-dimensional likelihood distributions and 1σ, 2σ, and 3σ two-dimensional likelihood confidence contours for flat XCDM from various combinations of data. The zero-acceleration black dashed lines divide the parameter space into regions associated with currently-accelerating (either below left or below) and currently-decelerating (either above right or above) cosmological expansion. The magenta dashed lines represent $w_{\rm X} = -1$, i.e. flat ΛCDM. 243

11.6 Same as Fig. 11.5 but for non-flat XCDM. The zero-acceleration black dashed lines are computed for the third cosmological parameter set to the $H(z)$ + BAO data best-fitting values listed in Table 11.2, and divide the parameter space into regions associated with currently-accelerating (either below left or below) and currently-decelerating (either above right or above) cosmological expansion. The crimson dash-dot lines represent flat hypersurfaces, with closed spatial hypersurfaces either below or to the left. The magenta dashed lines represent $w_{\rm X} = -1$, i.e. non-flat ΛCDM. 244

11.7 One-dimensional likelihood distributions and 1σ, 2σ, and 3σ two-dimensional likelihood confidence contours for flat ϕCDM from various combinations of data. The zero-acceleration black dashed lines divide the parameter space into regions associated with currently-accelerating (below left) and currently-decelerating (above right) cosmological expansion. The $\alpha = 0$ axes correspond to flat ΛCDM. 245

11.8 Same as Fig. 11.7 but for non-flat ϕCDM. The zero-acceleration black dashed lines are computed for the third cosmological parameter set to the $H(z)$ + BAO data best-fitting values listed in Table 11.2, and divide the parameter space into regions associated with currently-accelerating (below left) and currently-decelerating (above right) cosmological expansion. The crimson dash-dot lines represent flat hypersurfaces, with closed spatial hypersurfaces either below or to the left. The $\alpha = 0$ axes correspond to non-flat ΛCDM. . . 246

11.9 Normalized distributions of the Eddington ratio ($\log \lambda_{\rm Edd}$) for the C IV sample (blue histogram) and for the Mg II sample (pink histogram). Vertical dashed lines stand for median values, while the dot-dashed lines represent 16- and 84-% percentiles. The bin size is $\Delta(\log \lambda_{\rm Edd}) \sim 0.205$. 252

11.10 The Eddington ration $\lambda_{\rm Edd} = L_{\rm bol}/L_{\rm Edd}$ as a function of the source redshift (left panel) and as a function of the monochromatic luminosities L_{1350} or L_{3000} (right panel) for C IV (blue points) and Mg II (red points) sources. In both panels, we include the Pearson (r) and the Spearman rank-order correlation coefficients (s), which indicate significant positive correlations between $\lambda_{\rm Edd}$ and z as well as $\lambda_{\rm Edd}$ and L_{1350} (or L_{3000}). The horizontal dashed line stands for the Eddington limit ($\log \lambda_{\rm Edd} = 0$). The solid blue and red lines stand for the best-fitting linear relations for the C IV and Mg II datasets, respectively, see Eqs. (11.11) and Eqs. (11.12) for the best-fitting slopes and intercepts including 1σ uncertainties. 253

11.11 (Anti)correlation between $\Delta\tau \equiv \log(\tau/\tau_{\rm RL})$ and the Eddington ratio $\lambda_{\rm Edd}$ for both C IV sources (blue points) and Mg II sources (red points). The correlation is more signifcant for the Mg II sample with a Spearman rank-order correlation coefficient of -0.53 ($p = 4.76 \times 10^{-7}$) in comparison with -0.50 ($p = 0.0015$) for the C IV sample. The slope of the anticorrelation is steeper for Mg II sources, see Eq. (11.13) for the comparison. 255

A.1 Same as Fig. 4.1 (flat ΛCDM) but for different combinations of data and showing only cosmological parameters. 287

A.2 Same as Fig. 4.2 (non-flat ΛCDM) but for different combinations of data and showing only cosmological parameters. 287

A.3 Same as Fig. 4.3 (flat XCDM) but for different combinations of data and showing only cosmological parameters. 288

A.4 Same as Fig. 4.4 (non-flat XCDM) but for different combinations of data and showing only cosmological parameters. 288

List of Tables

3.1 BAO data. 36

3.2 Unmarginalized best-fitting parameter values for all models from various combinations of data. 45

3.3 One-dimensional marginalized best-fitting parameter values and uncertainties ($\pm1\sigma$ error bars or 2σ limits) for all models from various combinations of data. 46

3.4 $\Delta\chi^2$, ΔAIC, ΔBIC, and $\chi^2_{\rm min}/\nu$ values. 55

4.1 Unmarginalized best-fitting parameter values for all models from various combinations of data. 74

4.2 One-dimensional marginalized best-fitting parameter values and uncertainties ($\pm1\sigma$ error bars or 2σ limits) for all models from various combinations of data. 79

5.1 BAO data. 88

5.2 Unmarginalized best-fitting parameter values for all models from various combinations of data. 94

5.3 One-dimensional marginalized best-fitting parameter values and uncertainties ($\pm1\sigma$ error bars or 2σ limits) for all models from various combinations of data. 96

5.4 $\Delta\chi^2$, ΔAIC, ΔBIC, and $\chi^2_{\rm min}/\nu$ values. 102

6.1 Unmarginalized best-fitting parameter values for all models from various combinations of data. 111

6.2 One-dimensional posterior mean parameter values and uncertainties ($\pm1\sigma$ error bars or 2σ limits) for all models from various combinations of data. . . . 116

7.1 Summary of data sets used. 131

7.2 Flat priors of the constrained parameters. 132
7.3 One-dimensional marginalized posterior means and 68.27% limits of the Dainotti correlation parameters for the ML, GL, and MS data sets using the flat ΛCDM model with $\Omega_{m0} = 0.3$ and $H_0 = 70$ km s^{-1} Mpc^{-1}, and comparison with the results given in Wang et al. (2022) and Hu et al. (2021). 135
7.4 Unmarginalized best-fitting parameter values for all models from various combinations of data. 138
7.5 One-dimensional marginalized posterior mean values and uncertainties ($\pm 1\sigma$ error bars or 2σ limits) of the parameters for all models from various combinations of data. 139
7.6 MD-SGRB and GW-LGRB data $L_0 - t_b$ correlation parameters (and σ_{int}) differences. 145
7.7 Unmarginalized best-fitting parameter values for all models from various combinations of data. 146
7.8 One-dimensional marginalized posterior mean values and uncertainties ($\pm 1\sigma$ error bars or 2σ limits) of the parameters for all models from various combinations of data. 147

8.1 Summary of data sets used. 160
8.2 50 Platinum GRB samples, which are incorrect. The correct ones are listed in Table B.1 of Appendix B. 161
8.3 Flat priors of the constrained parameters. 162
8.4 Unmarginalized best-fitting parameter values for all models from various combinations of data. 173
8.5 One-dimensional marginalized posterior mean values and uncertainties ($\pm 1\sigma$ error bars or 2σ limits) of the parameters for all models from various combinations of data. 174

9.1 Updated $H(z)$ data. 185
9.2 Updated BAO data. 186
9.3 Flat priors of the constrained parameters. 190
9.4 Unmarginalized best-fitting parameter values for all models from various combinations of data. 203
9.5 One-dimensional marginalized posterior mean values and uncertainties ($\pm1\sigma$ error bars or 2σ limits) of the parameters for all models from various combinations of data. 204

10.1 Flat priors of the constrained parameters. 211
10.2 Unmarginalized best-fitting parameter values for all models from different data sets. 226
10.3 One-dimensional marginalized posterior mean values and uncertainties ($\pm1\sigma$ error bars or 2σ limits) of the parameters for all models from different data sets. 227

11.1 Flat priors of the constrained parameters. 238
11.2 Unmarginalized best-fitting parameter values for all models from various combinations of data. 260
11.3 One-dimensional marginalized posterior mean values and uncertainties ($\pm1\sigma$ error bars or 2σ limits) of the parameters for all models from various combinations of data. 261

A.1 Unmarginalized best-fitting parameter values for all models from various combinations of data. 289
A.2 One-dimensional marginalized best-fitting parameter values and uncertainties ($\pm1\sigma$ error bars or 2σ limits) for all models from various combinations of data. 290

B.1 Updated 50 Platinum GRB samples with 1σ errors, where F_X, $F_{\rm peak}$, $\rm FK_{plateau}$ ($\log \rm FK_{plateau} \equiv \log F_X + \log K_{plateau}$), and $FK_{\rm prompt}$ ($\log \rm FK_{prompt} \equiv \log F_{peak} + \log K_{prompt}$) have units of erg cm^{-2} s^{-1}, and T_X^* and $E_{\rm peak}$ have units of s and keV, respectively. The last Ref. column lists the sources of GRBs, with "C" and "B" representing the third *Swift* GRB Catalog (Lien et al., 2016) and *Swift* BAT burst analyser (Evans et al., 2010), respectively. Central values are estimated to three (or four) significant figures with corresponding non-zero errors matching their decimal places and $\Delta\chi^2 = \chi^2_{\rm PL} - \chi^2_{\rm CPL}$. 292

B.2 Same as Table B.1, but for 95 long GRB samples. Note that PL photon indices of GRBs 151215A and 170405A are taken from the time-averaged BAT spectral analysis and PL peak energy flux of the latter is also time-averaged, since their 1 s peak analysis results are either unreasonable or out of range. 293

B.2 – *Continued from previous page* 294

B.2 – *Continued from previous page* 295

B.2 – *Continued from previous page* 296

C.1 Sample of QSOs with a high-quality detection of the C IV time-delay. The sample is based on 38 sources compiled by Kaspi et al. (2021). In the table, we list from the left to the right column: object name, redshift, flux density at 1350 Å, monochromatic luminosity at 1350 Å for the flat ΛCDM model ($H_0 = 70\,\rm km\,s^{-1}\,Mpc^{-1}$, $\Omega_{m0} = 0.3$, $\Omega_\Lambda = 0.7$), the rest-frame C IV time-lag (in days) determined for all the sources using either the ICCF or the zDCF method (or their combination), and the original reference. 297

Acknowledgments

I am deeply grateful to my major professor, Dr. Bharat Ratra, for his unwavering support, exceptional guidance, and invaluable mentorship throughout my doctoral journey. Dr. Ratra's expertise, patience, and constant encouragement have been instrumental in shaping me as a researcher and scholar. I owe a great deal of my academic success to his insightful feedback and constructive criticism.

I would also like to express my gratitude to my committee members, Dr. Glenn Horton-Smith, Dr. Lado Samushia, and Dr. David Auckly, for their unwavering support, including their attendance at my oral exam and defense. Their presence and thoughtful questions helped me to better understand and articulate my research, and their feedback and guidance were invaluable in ensuring its success.

In addition, I would like to thank my co-authors, Joseph Ryan, Maria Dainotti, Michal Zajaček, Swayamtrupta Panda, Narayan Khadka, Mary Loli Martínez-Aldama, and Bożena Czerny, for their valuable contributions to this project. Our collaboration has been an enriching and rewarding experience, and I look forward to continuing to work with them in the future.

Furthermore, I extend my thanks to Javier de Cruz Pérez, Chan-Gyung Park, Ana Luisa González-Morán, Ricardo Chávez, F. Y. Wang, and J. P. Hu for their insightful discussions on data analysis. I am also grateful for the financial support received from the US Department of Energy grant DE-SC0011840 and to the Beocat Research Cluster at Kansas State University, funded in part by NSF grants CNS-1006860, EPS-1006860, EPS-0919443, ACI-1440548, CHE-1726332, and NIH P20GM113109, for providing the computational resources necessary for these projects.

My sincere gratitude also goes to the Department of Physics at Kansas State University, where I conducted the research for this thesis. Throughout my PhD journey, I had the privilege of learning from and working alongside exceptional professors who provided

invaluable guidance and support. My fellow graduate students also deserve special thanks for their camaraderie and encouragement, which made this experience all the more enriching. I am particularly grateful to Dr. Lado Samushia, who supported me and wrote me a recommendation letter to help me find a job, and to Dr. Mick O'Shea and Kim Coy, whose unwavering commitment to the well-being and success of graduate students is truly commendable. They graciously lent an ear to our concerns and provided invaluable assistance whenever needed. Their dedication to fostering a supportive and inclusive academic community is deeply appreciated.

Finally, I wish to express my deep appreciation to my parents, Xing-Hong Cao and Bai-Lian Zhang, and my sister, Rong-Ju Gao. Their unconditional love, encouragement, and support have been my constant source of inspiration throughout this journey. This work is dedicated to them.

Chapter 1

Introduction

Physical cosmology is the branch of physics, astrophysics, and astronomy that studies the structure, origin, evolution, and overall properties of the Universe on large scales. It seeks to answer fundamental questions about the Universe, such as its age, size, shape, composition, and how it has changed over time.

Physical cosmology is based on the principles of general relativity and the other laws of physics, and it uses observations and data from various sources, including telescopes and spacecraft, to test and refine models of the Universe. It also uses theoretical models and computer simulations to understand the behavior of the Universe on a large scale.

Some of the key areas of study in physical cosmology include the Big Bang model, dark matter and dark energy, the cosmic microwave background (CMB) radiation, the formation and evolution of galaxies and galaxy clusters, and the large-scale structure of the Universe. Physical cosmology is a rapidly evolving field, with new discoveries and insights emerging all the time.

Theoretical aspects of physical cosmology are discussed in this chapter, with a focus on the significance of distance measures in establishing links between theory and observation.

1.1 General relativity

1.1.1 Tensors in differential geometry

Differential geometry is a branch of mathematics that studies the geometry of curved spaces and the properties of objects such as curves and surfaces in these spaces. It uses the tools of calculus, linear algebra, and topology to study the properties of curves, surfaces, and other geometric objects in a rigorous and precise way.

At the heart of differential geometry is the study of manifolds, which are spaces that locally look like Euclidean space but may have global properties that are significantly different. Differential geometry is concerned with the geometric properties of manifolds and their relationships with other mathematical objects such as vector fields, differential forms, and connections.

One of the central concepts in differential geometry is the notion of a tangent space, which is a vector space that is tangent to a manifold at a particular point. Tangent spaces allow us to define notions such as tangent vectors and tangent bundles, which are crucial for describing the geometry of curves and surfaces on manifolds.

In differential geometry, a vector is defined as an element of a tangent space at a point on a manifold. A tangent space is a vector space that is tangent to the manifold at that point. A vector in differential geometry is denoted as a directed line segment with a magnitude and a direction. However, unlike in Euclidean geometry where vectors are represented as ordered pairs or triplets of numbers, in differential geometry, a vector is represented as a differential operator acting on smooth functions defined on the manifold.

A manifold is a topological space that is locally homeomorphic to Euclidean space. This means that every point on the manifold has a neighborhood that can be mapped onto an open set in Euclidean space by a continuous function called a chart (coordinate system). Manifolds can be of any dimension, and they can be either finite or infinite in size. For example, a curve in the plane or a surface in three-dimensional space is a two-dimensional manifold, while a sphere is a two-dimensional manifold that is closed (i.e., compact without

boundary).

Given a point on a manifold, a vector at that point can be thought of as a directional derivative of a function defined on the manifold. In other words, a vector at a point specifies the rate and direction of change of a function as one moves in that direction from the point.

In a coordinate basis $\{X_\mu \coloneqq \partial/\partial x^\mu\}$ with dimension of n, an arbitrary tangent vector v can be expressed as

$$v = \sum_{\mu=1}^{n} v^\mu X_\mu \equiv v^\mu X_\mu = v^\mu \frac{\partial}{\partial x^\mu}, \tag{1.1}$$

where v^μ is the μth component of v in $\{X_\mu\}$, $\mu = 1, 2, \ldots, n$, and the equivalent sign implies the Einstein summation convention of implicitly summing over pairs of repeated upper and lower indices that is used throughout the thesis. By choosing a new coordinate basis $\{X'_\nu\}$, X_μ can be expressed as

$$X_\mu = \frac{\partial x'_\nu}{\partial x^\mu} X'_\nu, \tag{1.2}$$

so that the νth component of v in $\{X'_\nu\}$

$$v'^\nu = v^\mu \frac{\partial x'_\nu}{\partial x^\mu}. \tag{1.3}$$

This transformation law allows us to compare vectors at different points on a manifold and to define vector fields, which are collections of vectors defined on a manifold.

A dual vector space V^* (with a dual basis of $v^{1*}, v^{2*}, \ldots, v^{n*} \in V^*$) to a tangent vector space V (with a basis of $v_1, v_2, \ldots, v_n \in V$) is defined as

$$v^{\mu*}(v_\nu) = \delta^\mu_{\ \nu} = \begin{cases} 1, & \text{if } \mu = \nu, \\ 0, & \text{else.} \end{cases} \tag{1.4}$$

A tensor, T, of type (k, l) over V is a multilinear map (Wald, 1984)

$$T : \underbrace{V^* \times \cdots \times V^*}_{k} \times \underbrace{V \times \cdots \times V}_{l} \to \mathbb{R}, \tag{1.5}$$

where $\mathbb{R}$ is the set of real numbers. Thus, a tensor of type $(0,1)$ or $(1,0)$ is a dual (cotangent) vector or an ordinary (tangent) vector. The contraction operation with respect to ith dual vector and jth vector, defined below, is a map $C : \mathscr{T}(k,l) \to \mathscr{T}(k-1,l-1)$, where $\mathscr{T}(k,l)$ is a vector space with a collection of all tensors of type (k,l), and if $T \in \mathscr{T}(k,l)$, then

$$CT = \sum_{\alpha}^{n} T(\ldots, \overbrace{v^{\alpha *}}^{i\text{th}}, \ldots; \ldots, \underbrace{v_{\alpha}}_{j\text{th}}, \ldots), \tag{1.6}$$

where $\{v_\mu\}$ is a basis of V and $\{v^{\nu *}\}$ is its dual basis. The outer product of T and T' is denoted as $S = T \otimes T'$. The n^{k+l} simple tensors $\{v_{\mu_1} \otimes \cdots \otimes v_{\mu_k} \otimes v^{\nu_1 *} \otimes \cdots \otimes v^{\nu_l *}\}$ is a basis of $\mathscr{T}(k,l)$, then for $T \in \mathscr{T}(k,l)$

$$T = T^{\mu_1 \cdots \mu_k}{}_{\nu_1 \cdots \nu_l} v_{\mu_1} \otimes \cdots \otimes v_{\mu_k} \otimes v^{\nu_1 *} \otimes \cdots \otimes v^{\nu_l *}, \tag{1.7}$$

where $T^{\mu_1 \cdots \mu_k}{}_{\nu_1 \cdots \nu_l}$ are called the components of the tensor T with respect to the basis v_μ. Consequently, the components of CT in equation (1.6)

$$(CT)^{\mu_1 \cdots \mu_{k-1}}{}_{\nu_1 \cdots \nu_{l-1}} = T^{\mu_1 \cdots \alpha \cdots \mu_{k-1}}{}_{\nu_1 \cdots \alpha \cdots \nu_{l-1}}, \tag{1.8}$$

and the outer product $S = T \otimes T'$ has components

$$S^{\mu_1 \cdots \mu_{k+k'}}{}_{\nu_1 \cdots \nu_{l+l'}} = T^{\mu_1 \cdots \mu_k}{}_{\nu_1 \cdots \nu_l} T'^{\mu_{k+1} \cdots \mu_{k+k'}}{}_{\nu_{l+1} \cdots \nu_{l+l'}}. \tag{1.9}$$

The dual basis of $\{X_\mu\}$ in equation (1.2) is $\{dx^\mu\}$ since $dx^\mu(\partial/\partial x^\nu) = \delta^\mu{}_\nu$. Therefore, for a dual vector ω with components of ω_μ in $\{dx^\mu\}$, the components in a new basis of $\{dx'^{\mu'}\}$ become

$$\omega'_{\mu'} = \omega_\mu \frac{\partial x^\mu}{\partial x'^{\mu'}}. \tag{1.10}$$

Consequently, in general, the components of a type (k,l) tensor T follow the tensor trans-

formation law

$$T'^{\mu'_1\cdots\mu'_k}{}_{\nu'_1\cdots\nu'_l} = T^{\mu_1\cdots\mu_k}{}_{\nu_1\cdots\nu_l}\frac{\partial x'^{\mu'_1}}{\partial x^{\mu_1}}\cdots\frac{\partial x^{\nu_l}}{\partial x'^{\nu'_l}}. \tag{1.11}$$

A tensor field is defined as an assignment of a tensor over V_p for every point p in the manifold M.

Following Wald (1984), we use the following abstract index notation rules. A type (k, l) tensor is denoted by a letter followed by k contravariant (tangent) and l covariant (cotangent) indices. These indices are represented using lower case Latin letters, and the tensor itself is denoted as $T^{a_1\cdots a_k}{}_{b_1\cdots b_l}$. The contraction of a tensor is indicated by repeating the letters of the contracted slots. For instance, the type $(2, 2)$ tensor $T^{abc}{}_{bef}$ is obtained by contracting the second contravariant slot and the first covariant slot of $T^{abc}{}_{def}$. The outer product of the tensors $T^{abc}{}_{def}$ and $S^{ab}{}_{c}$ is simply $T^{abc}{}_{def}S^{gh}{}_{i}$. The labels of components are indicated by using Greek letters. For example, $T^{\alpha\beta\gamma}{}_{\sigma\mu\nu}$ is a basis component of the tensor $T^{abc}{}_{def}$.

1.1.2 Metric tensor and curvature

A metric g on a manifold M is a type $(0, 2)$ tensor field that is nondegenerate and symmetric. Nondegeneracy means that $g(v, v_2) = 0$ for all $v \in V_p$ if and only if $v_2 = 0$. Symmetry means that $g(v_1, v_2) = g(v_2, v_1)$ for any $v_1, v_2 \in V_p$. Geometrically, the metric g can be interpreted as an "infinitesimal squared distance" or a (not necessarily positive definite) inner product on the tangent space at each point.

In a coordinate basis of $\{dx^\mu\}$, the metric tensor g_{ab} (or equivalently the line element ds^2) is

$$g_{ab} \equiv ds^2 = g_{\mu\nu}dx^\mu dx^\nu. \tag{1.12}$$

One can always find an orthonormal basis $\{v_\mu\}$ so that $g(v_\alpha, v_\beta) = \pm\delta_{\alpha\beta}$. The signature of a metric is determined by counting the number of "+" and "−" signs that appear in this expression. Metrics with all "+" signs are called Euclidean (or Riemannian in the context of general relativity, Wald, 1984), while those with signatures like the spacetime metric $(-, +, +, +)$ are called Lorentzian. Lorentzian metrics are commonly used in general

relativity to describe the geometry of spacetime.

A derivative operator ∇ (or covariant derivative) on a manifold M is a linear map that takes each smooth (or differentiable) type (k, l) tensor field to a smooth type $(k, l+1)$ tensor field. It satisfies the Leibniz rule, commutativity with contraction, consistency with the notation of tangent vectors as directional derivatives on scalar fields, and sometimes the torsion-free condition. Geometrically, the covariant derivative provides a way of differentiating tensor fields on curved manifolds without reference to a specific coordinate system.

The commutator of two vector fields v^a and ω^b in terms of any derivative operator ∇_a is

$$[v, \omega]^b = v^a \nabla_a \omega^b - \omega^a \nabla_a v^b. \tag{1.13}$$

For any two derivative operators $\tilde{\nabla}$ and ∇ defined on a smooth manifold, there exists a tensor field $C^c{}_{ab}$ $(= C^c{}_{ba})$ of type $(1, 2)$ such that, for $T \in \mathscr{T}(k, l)$ the following identity holds

$$\nabla_a T^{b_1 \cdots b_k}{}_{c_1 \cdots c_l} = \tilde{\nabla}_a T^{b_1 \cdots b_k}{}_{c_1 \cdots c_l} + \sum_i C^{b_i}{}_{ad} T^{b_1 \cdots d \cdots b_k}{}_{c_1 \cdots c_l} - \sum_i C^d{}_{ac_j} T^{b_1 \cdots b_k}{}_{c_1 \cdots d \cdots c_l}. \tag{1.14}$$

One significant use of the equation mentioned above arises when the operator $\tilde{\nabla}_a$ is substituted by the conventional derivative operator ∂_a. In this case, the tensor field $C^c{}_{ab}$ is denoted as the Christoffel symbol $\Gamma^c{}_{ab}$. For example, the equation

$$\nabla_a v^b = \partial_a v^b + \Gamma^b{}_{ac} v^c. \tag{1.15}$$

expresses the covariant derivative of the vector field v^b in terms of its partial derivatives and the Christoffel symbol. This equation plays a crucial role in the study of curved spacetimes, as it allows for the generalization of the concept of differentiation to curved manifolds. A Christoffel symbol $\Gamma^c{}_{ab}$ is a tensor field associated with the derivative operator ∇_a and the coordinate system used to define ∂_a. It is important to note that a different coordinate system with a different ordinary derivative operator ∂'_a would have a different Christoffel symbol $\Gamma'^c{}_{ab}$.

Parallel transport of a vector v^a along a curve C with a tangent t^a can be defined by

$$t^a \nabla_a v^b = t^a \partial_a v^b + t^a \Gamma^b{}_{ac} v^c = 0, \tag{1.16}$$

and in terms of components in the coordinate basis and parameter t along the curve, it takes the form

$$\frac{dv^\nu}{dt} + t^\mu \Gamma^\nu{}_{\mu\lambda} v^\lambda = 0, \tag{1.17}$$

where v^ν are the components of the vector v^a in the coordinate basis. More generally, the parallel transport of an arbitrary type (k, l) tensor $T \in \mathscr{T}(k, l)$ can be defined as

$$t^a \nabla_a T^{b_1 \cdots b_k}{}_{c_1 \cdots c_l} = 0. \tag{1.18}$$

Let g_{ab} be a metric on a manifold and let v^a and ω^a be two vectors on the manifold. The inner product of $g_{ab} v^a \omega^b$ is a scalar function on the manifold. If we parallel-transport v^a and ω^a along any curve, the inner product remains unchanged, which means that its covariant derivative with respect to any tangent vector t^a must be zero: $t^a \nabla_a (g_{bc} v^b \omega^c) = 0$. Now, suppose that v^a and ω^a follow the parallel transport equation (1.16). Since t^a is an arbitrary tangent vector and v^a and ω^a are non-zero, we must have $\nabla_a g_{bc} = 0$. Consequently

$$\nabla_a g_{bc} = 0 \Rightarrow \tilde{\nabla}_a g_{bc} - C^d{}_{ab} g_{dc} - C^d{}_{ac} g_{bd} \Rightarrow C^d{}_{ab} = \frac{1}{2} g^{cd} \{ \tilde{\nabla}_a g_{bd} + \tilde{\nabla}_b g_{ad} - \tilde{\nabla}_d g_{ab} \}. \tag{1.19}$$

Therefore, we have shown that if $\nabla_a g_{bc} = 0$, then there exists a unique derivative operator ∇_a satisfying this condition with the above choice of $C^c{}_{ab}$. If we adopt $\tilde{\nabla}_a$ as the coordinate derivative ∂_a, then the corresponding Christoffel symbols can be computed as

$$\Gamma^d{}_{ab} = \frac{1}{2} g^{cd} \{ \partial_a g_{bd} + \partial_b g_{ad} - \partial_d g_{ab} \}, \tag{1.20}$$

which implies that the coordinate components of $\Gamma^{\alpha}{}_{\mu\nu}$ are given by

$$\Gamma^{\alpha}{}_{\mu\nu} = \frac{1}{2}g^{\alpha\lambda}\{\partial_\mu g_{\nu\lambda} + \partial_\nu g_{\mu\lambda} - \partial_\lambda g_{\mu\nu}\} = \frac{1}{2}g^{\alpha\lambda}\left\{\frac{\partial g_{\nu\lambda}}{\partial x^\mu} + \frac{\partial g_{\mu\lambda}}{\partial x^\nu} - \frac{\partial g_{\mu\nu}}{\partial x^\lambda}\right\}. \tag{1.21}$$

Here, x^μ represents the coordinates of a point on the manifold, and the indices α, μ, and ν range over all possible values.

Let ∇_a denote a derivative operator, ω_a a dual vector field, and f a smooth function. The action of two derivative operators onto $f\omega_c$ can be expressed as

$$\nabla_a\nabla_b(f\omega_c) = \nabla_a(\omega_c\nabla_b f + f\nabla_b\omega_c) = (\nabla_a\nabla_b f)\omega_c + \nabla_b f\nabla_a\omega_c + \nabla_a f\nabla_b\omega_c + f\nabla_a\nabla_b\omega_c. \tag{1.22}$$

By subtracting the tensor $\nabla_b\nabla_a(f\omega_c)$ from both sides, we get

$$(\nabla_a\nabla_b - \nabla_b\nabla_a)(f\omega_c) = f(\nabla_a\nabla_b - \nabla_b\nabla_a)\omega_c. \tag{1.23}$$

This implies that the difference of two derivative operators acting on $f\omega_c$ is proportional to $f(\nabla_a\nabla_b - \nabla_b\nabla_a)\omega_c$, which suggests the existence of a tensor field $R_{abc}{}^d$, known as the Riemann curvature tensor, such that

$$\nabla_a\nabla_b\omega_c - \nabla_b\nabla_a\omega_c = R_{abc}{}^d\omega_d, \tag{1.24}$$

for all dual vector fields ω_c.

The Riemann curvature tensor $R_{abc}{}^d$ has four key properties:

1. *Antisymmetry in the first two indices*: $R_{abc}{}^d = -R_{bac}{}^d$.

2. *Total antisymmetry*: The totally antisymmetric part of $R_{abc}{}^d$ is zero, i.e., $R_{[abc]}{}^d = 0$. Here, the squared brackets denote total antisymmetrization, as defined in equation (2.4.4) of Wald (1984).

3. *Skew symmetry*: For the derivative operator ∇_a associated with the metric $\nabla_a g_{bc} = 0$, we have $R_{abcd} = -R_{abdc}$.

4. *First Bianchi identity*: The Bianchi identity holds, which states that the cyclic sum of covariant derivatives of $R_{abc}{}^{d}$ vanishes, i.e.,

$$\nabla_{[a}R_{bc]d}{}^{e} = 0. \tag{1.25}$$

The Ricci tensor $R_{ab} = R_{acb}{}^{c}$ is a rank-2 tensor that encodes important geometric information about a Riemannian manifold. The Ricci tensor is symmetric, i.e., $R_{ab} = R_{ba}$, which follows from the symmetry of the Riemann tensor. The scalar curvature R is obtained by taking the trace of the Ricci tensor, i.e., $R = R_{a}{}^{a}$. It is a scalar function that describes the intrinsic curvature of the manifold at a given point. Contraction of the first Bianchi identity (1.25) leads to

$$\nabla_{a}R_{bcd}{}^{a} + \nabla_{b}R_{cd} - \nabla_{c}R_{bd} = \nabla_{a}R_{c}{}^{a} + \nabla_{b}R_{c}{}^{b} - \nabla_{c}R = 0, \tag{1.26}$$

or

$$\nabla^{a}(R_{ab} - \frac{1}{2}Rg_{ab}) \equiv \nabla^{a}G_{ab} = 0, \tag{1.27}$$

where G_{ab} is called the Einstein tensor.

By choosing a coordinate system, we can express the derivative operator in terms of the ordinary derivative ∂_a and the Christoffel symbol $\Gamma^{c}{}_{ab}$ as discussed above. For a dual vector field ω_a, we have

$$\nabla_{b}\omega_{c} = \partial_{b}\omega_{c} - \Gamma^{d}{}_{bc}\omega_{d}, \tag{1.28}$$

so the equation (1.24) can be expressed as

$$R_{abc}{}^{d}\omega_{d} = \{-2\partial_{[a}\Gamma^{d}{}_{b]c} + 2\Gamma^{e}{}_{c[a}\Gamma^{d}{}_{b]e}\}\omega_{d} \Rightarrow R_{abc}{}^{d} = -2\partial_{[a}\Gamma^{d}{}_{b]c} + 2\Gamma^{e}{}_{c[a}\Gamma^{d}{}_{b]e}. \tag{1.29}$$

The coordinate basis components of Riemann tensor is then

$$R_{\alpha\beta\gamma}{}^{\lambda} = -2\partial_{[\alpha}\Gamma^{\lambda}{}_{\beta]\gamma} + 2\Gamma^{\sigma}{}_{\gamma[\alpha}\Gamma^{\lambda}{}_{\beta]\sigma}, \tag{1.30}$$

or explicitly

$$R_{\alpha\beta\gamma}{}^{\lambda} = \frac{\partial}{\partial x^{\beta}}\Gamma^{\lambda}{}_{\alpha\gamma} - \frac{\partial}{\partial x^{\alpha}}\Gamma^{\lambda}{}_{\beta\gamma} + \Gamma^{\sigma}{}_{\gamma\alpha}\Gamma^{\lambda}{}_{\beta\sigma} - \Gamma^{\sigma}{}_{\gamma\beta}\Gamma^{\lambda}{}_{\alpha\sigma}. \tag{1.31}$$

If we define $\nabla_a \omega_c \equiv \omega_{c;a}$ and $\partial_a \omega_c \equiv \omega_{c,a}$, and for coordinate basis components $\nabla_\alpha \omega_\beta \equiv \omega_{\beta;\alpha}$ and $\partial_\alpha \omega_\beta = \partial \omega_\beta / \partial x^\alpha \equiv \omega_{\beta,\alpha}$, the above equation becomes

$$R_{\alpha\beta\gamma}{}^{\lambda} = \Gamma^{\lambda}{}_{\alpha\gamma,\beta} - \Gamma^{\lambda}{}_{\beta\gamma,\alpha} + \Gamma^{\sigma}{}_{\alpha\gamma}\Gamma^{\lambda}{}_{\beta\sigma} - \Gamma^{\sigma}{}_{\beta\gamma}\Gamma^{\lambda}{}_{\alpha\sigma}. \tag{1.32}$$

A geodesic is a curve on a manifold, associated with a derivative operator ∇_a, whose tangent vector T^a is parallel transported along itself, and satisfies the equation $T^a \nabla_a T^b = 0$. When a coordinate system is introduced, the geodesic is mapped to a curve $x^\mu(t)$ in $\mathbb{R}^n$. Using equation (1.17), the components of T^a, denoted $T^\mu = dx^\mu/dt$, satisfy the geodesic equation

$$\frac{dT^{\nu}}{dt} + \Gamma^{\nu}{}_{\mu\lambda} T^{\mu} T^{\lambda} = \frac{d^2 x^{\nu}}{dt^2} + \Gamma^{\nu}{}_{\mu\lambda} \frac{dx^{\mu}}{dt} \frac{dx^{\lambda}}{dt} = 0. \tag{1.33}$$

1.1.3 Einstein's field equation

The theory of general relativity is built on two fundamental principles: the equivalence principle and the principle of general covariance. The equivalence principle states that the effects of gravity and acceleration are indistinguishable. Specifically, a particle in a gravitational field experiences a force equivalent to the force it would experience if it were uniformly accelerated in the opposite direction. This principle is the foundation of general relativity, which describes gravity as a curvature of spacetime caused by the presence of matter and energy.

The principle of general covariance requires that the laws of physics be formulated independently of the choice of coordinates used to describe physical phenomena. In other words, the laws of physics should be the same in all coordinate systems related by a smooth transformation. This principle allows us to describe the laws of physics in a coordinate-independent manner and is essential for a theory of gravity consistent with general relativity. By imposing the principle of general covariance, we ensure that the laws of physics are consistent with the

equivalence principle and that they hold true in any coordinate system, regardless of how the coordinates are chosen.

In general relativity, spacetime is a manifold M with a Lorentz metric g_{ab} of signature $-+\cdots+$. A curve is considered timelike if the norm of its tangent is everywhere negative, $g_{ab}T^aT^b < 0$. Particle motion is represented by a timelike curve, and perfect fluids are described using a 4-velocity u^a, density ρ, and pressure p. The electromagnetic field is represented by an antisymmetric tensor F_{ab}. A particle with rest mass m and charge q placed in an electromagnetic field F_{ab} satisfies the Lorentz force equation

$$mu^a\nabla_a u^b = qF^b{}_c u^c, \tag{1.34}$$

where $F^b{}_c = g^{bd}F_{dc}$. The 4-velocity u^a of a free particle satisfies the geodesic equation of motion

$$u^a\nabla_a u^b = 0, \tag{1.35}$$

where ∇_a is the derivative operator associated with g_{ab}. If the acceleration $a^b = u^a\nabla_a u^b$ is non-zero, a force $f^b = ma^b$ acts on the particle, where m is its rest mass. The 4-momentum of the particle can be defined as

$$P^a = mu^a. \tag{1.36}$$

The energy of the particle, as measured by an observer with 4-velocity v^a at the event on the particle's world line is given by

$$E = -P_a v^a. \tag{1.37}$$

A stress-energy tensor T_{ab} describes continuous matter distributions and fields. For a perfect fluid the stress-energy tensor is given by

$$T_{ab} = \rho u_a u_b + p(g_{ab} + u_a u_b), \tag{1.38}$$

and it satisfies the equation of motion

$$\nabla^a T_{ab} = 0, \tag{1.39}$$

which yields the following two equations:

$$u^a \nabla_a \rho + (\rho + p)\nabla^a u_a = 0, \tag{1.40}$$

and

$$(p + \rho)u^a \nabla_a u_b + (g_{ab} + u_a u_b)\nabla^a p = m u^a, \tag{1.41}$$

where $u_b = g_{ab}u^a$. Note that in the special case where the fluid is at rest, i.e., $u^\mu = (1, 0, 0, 0)$, the stress-energy tensor reduces to the familiar form $T_{00} = \rho$, $T_{ij} = p\delta_{ij}$, where δ_{ij} is the Kronecker delta. In the context of general relativity, the spacetime manifold M is typically represented using a coordinate system that maps it onto $\mathbb{R}^4$. In this coordinate system, Latin letters are used to represent the spatial coordinates, with $i, j, k, \cdots = 1, 2, 3$, while Greek letters are used to represent the time coordinate plus the spatial coordinates, with $\alpha, \beta, \gamma, \cdots = 0, 1, 2, 3$. Here, the number 0 represents the time coordinate, while 1, 2, and 3 represent the spatial coordinates. This convention is useful for representing the components of tensors in a coordinate basis and for performing calculations involving them.

The Klein-Gordon scalar field ϕ in curved spacetime satisfies the equation

$$\nabla^a \nabla_a \phi - m^2 \phi = 0. \tag{1.42}$$

The stress-energy tensor of this field is

$$T_{ab} = \nabla_a \phi \nabla_b \phi - \frac{1}{2} g_{ab}(\nabla_c \phi \nabla^c \phi + m^2 \phi^2), \tag{1.43}$$

and satisfies the conservation equation (1.39).

Maxwell's equations in curved spacetime govern the behavior of the electromagnetic field.

They consist of two equations:

$$\nabla^a F_{ab} = -4\pi j_b, \tag{1.44}$$

which relates the current density 4-vector j^a to the field strength tensor F_{ab}, and

$$\nabla_{[a} F_{bc]} = 0, \tag{1.45}$$

which expresses the fact that the electromagnetic field is divergence-free. Here $j_b = g_{ab} j^a$ and j^a is the current density 4-vector of electric charge. The electromagnetic stress-energy tensor is a measure of the energy and momentum density of the electromagnetic field. It is given by

$$T_{ab} = \frac{1}{4\pi} \left\{ F_{ac} F_b{}^c - \frac{1}{4} g_{ab} F_{de} F^{de} \right\}. \tag{1.46}$$

The vector potential A_a satisfies the wave equation in curved spacetime,

$$\nabla^a \nabla_a A_b - R^d{}_b A_d = -4\pi j_b, \tag{1.47}$$

in Lorenz gauge where $\nabla_a A^a = 0$. $R^d{}_b = R_{ab} g^{ad}$ is the Ricci curvature tensor. This equation describes the propagation of electromagnetic waves in a curved spacetime.

Einstein's field equation is the cornerstone of general relativity, relating the geometry of spacetime to the distribution of matter and energy within it. It takes the form

$$G_{ab} \equiv R_{ab} - \frac{1}{2} R g_{ab} = 8\pi T_{ab}, \tag{1.48}$$

where G_{ab} is the Einstein tensor, R is the Ricci scalar, and we use units for which the gravitational constant G and the speed of light c are 1. The left-hand side represents the curvature of spacetime, while the right-hand side represents the distribution of matter and energy in spacetime. This equation encodes the fundamental principle that matter tells spacetime how to curve, and through the geodesic equation or other matter equation og motion, spacetime tells matter how to move. Einstein first proposed this equation in 1915,

and it remains a fundamental equation of modern physics.

Einstein's field equation can be derived using the Lagrangian formalism in a coordinate basis $\{dx^\mu\}$, where the Einstein-Hilbert action is given by

$$S_{\text{EH}} = \int \frac{1}{16\pi} R\sqrt{-g} d^4x, \tag{1.49}$$

with g being the determinant of the metric tensor's coordinate basis components $g_{\mu\nu}$ and $G = c = 1$. The complete action is defined as

$$S = S_{\text{EH}} + S_{\text{M}} = \int \left(\frac{1}{16\pi} R + \mathscr{L}_{\text{M}} \right) \sqrt{-g} d^4x, \tag{1.50}$$

where S_{M} and $\mathscr{L}_{\text{M}}$ are the action and Lagrangian of matter.

Using the principle of least action, we vary the action with respect to the inverse metric tensor $g^{\mu\nu}$, which yields

$$\begin{aligned} 0 &= \delta S \\ &= \int \left[\frac{1}{16\pi} \frac{\delta(R\sqrt{-g})}{\delta g^{\mu\nu}} + \frac{\delta(\mathscr{L}_{\text{M}}\sqrt{-g})}{\delta g^{\mu\nu}} \right] \delta g^{\mu\nu} d^4x \\ &= \int \left[\frac{1}{16\pi} \left(\frac{\delta R}{\delta g^{\mu\nu}} + \frac{R}{\sqrt{-g}} \frac{\delta\sqrt{-g}}{\delta g^{\mu\nu}} \right) + \frac{1}{\sqrt{-g}} \frac{\delta(\mathscr{L}_{\text{M}}\sqrt{-g})}{\delta g^{\mu\nu}} \right] \sqrt{-g} \delta g^{\mu\nu} d^4x, \end{aligned} \tag{1.51}$$

where δ is the variation operator. This equation should be hold for any variation $\delta g_{\mu\nu}$, thus it becomes

$$\frac{\delta R}{\delta g^{\mu\nu}} + \frac{R}{\sqrt{-g}} \frac{\delta\sqrt{-g}}{\delta g^{\mu\nu}} = -\frac{16\pi}{\sqrt{-g}} \frac{\delta(\mathscr{L}_{\text{M}}\sqrt{-g})}{\delta g^{\mu\nu}}. \tag{1.52}$$

The first term on the left-hand-side of equation (1.52) requires the variation of the Ricci scalar

$$\delta R = R_{\alpha\beta} \delta g^{\alpha\beta} + g^{\alpha\beta} \delta R_{\alpha\beta}, \tag{1.53}$$

which requires the variation of the Ricci tensor $\delta R_{\alpha\beta}$. From equation (1.32), we get the

variation of the Riemann tensor

$$\begin{aligned}\delta R_{\alpha\beta\gamma}{}^{\lambda} =&\delta\Gamma^{\lambda}{}_{\alpha\gamma,\beta} - \delta\Gamma^{\lambda}{}_{\beta\gamma,\alpha} + \Gamma^{\lambda}{}_{\beta\sigma}\delta\Gamma^{\sigma}{}_{\alpha\gamma} + \Gamma^{\sigma}{}_{\alpha\gamma}\delta\Gamma^{\lambda}{}_{\beta\sigma} - \Gamma^{\lambda}{}_{\alpha\sigma}\delta\Gamma^{\sigma}{}_{\beta\gamma} - \Gamma^{\sigma}{}_{\beta\gamma}\delta\Gamma^{\lambda}{}_{\alpha\sigma}\\ =&\delta\Gamma^{\lambda}{}_{\alpha\gamma;\beta} - \Gamma^{\lambda}{}_{\beta\sigma}\delta\Gamma^{\sigma}{}_{\alpha\gamma} + \Gamma^{\sigma}{}_{\beta\gamma}\delta\Gamma^{\lambda}{}_{\alpha\sigma} + \Gamma^{\sigma}{}_{\beta\alpha}\delta\Gamma^{\lambda}{}_{\sigma\gamma} - \delta\Gamma^{\lambda}{}_{\beta\gamma;\alpha} + \Gamma^{\lambda}{}_{\alpha\sigma}\delta\Gamma^{\sigma}{}_{\beta\gamma} - \Gamma^{\sigma}{}_{\alpha\gamma}\delta\Gamma^{\lambda}{}_{\beta\sigma}\\ &- \Gamma^{\sigma}{}_{\beta\alpha}\delta\Gamma^{\lambda}{}_{\sigma\gamma} + \Gamma^{\lambda}{}_{\beta\sigma}\delta\Gamma^{\sigma}{}_{\alpha\gamma} + \Gamma^{\sigma}{}_{\alpha\gamma}\delta\Gamma^{\lambda}{}_{\beta\sigma} - \Gamma^{\lambda}{}_{\alpha\sigma}\delta\Gamma^{\sigma}{}_{\beta\gamma} - \Gamma^{\sigma}{}_{\beta\gamma}\delta\Gamma^{\lambda}{}_{\alpha\sigma}\\ =&\delta\Gamma^{\lambda}{}_{\alpha\gamma;\beta} - \delta\Gamma^{\lambda}{}_{\beta\gamma;\alpha},\end{aligned} \tag{1.54}$$

so the variation of the Ricci tensor is

$$\delta R_{\alpha\gamma} = \delta R_{\alpha\lambda\gamma}{}^{\lambda} = \delta\Gamma^{\lambda}{}_{\alpha\gamma;\lambda} - \delta\Gamma^{\lambda}{}_{\lambda\gamma;\alpha}. \tag{1.55}$$

Therefore, equation (1.53) becomes

$$\delta R = R_{\alpha\beta}\delta g^{\alpha\beta} + (g^{\alpha\beta}\delta\Gamma^{\lambda}{}_{\alpha\beta} - g^{\lambda\beta}\delta\Gamma^{\gamma}{}_{\gamma\beta})_{;\lambda} \equiv R_{\alpha\beta}\delta g^{\alpha\beta} + \nabla_{\lambda}v^{\lambda}, \tag{1.56}$$

where the second term can be substituted back into equation (1.51) to get a boundary term

$$\frac{1}{16\pi}\int \sqrt{-g}\nabla_{\lambda}v^{\lambda}dx^{4}. \tag{1.57}$$

This boundary term does not contribute to the variation of the action when $\delta g^{\mu\nu}$ vanishes in a neighborhood of the boundary or when there is no boundary. In this case, the first term on the left-hand-side of equation (1.52) becomes

$$\frac{\delta R}{\delta g^{\mu\nu}} = R_{\mu\nu}. \tag{1.58}$$

In the second term on the left-hand-side of equation (1.52)

$$\delta\sqrt{-g} = -\frac{1}{2\sqrt{-g}}\delta g = -\frac{1}{2}\sqrt{-g}g_{\mu\nu}\delta g^{\mu\nu}, \tag{1.59}$$

where $\delta g = g g^{\mu\nu}\delta g_{\mu\nu}$ and $g^{\mu\nu}\delta g_{\mu\nu} = -g_{\mu\nu}\delta g^{\mu\nu}$ are used. Thus the second term of the left-hand-side of equation (1.52) becomes

$$\frac{R}{\sqrt{-g}}\frac{\delta\sqrt{-g}}{\delta g^{\mu\nu}} = -\frac{1}{2}Rg_{\mu\nu}, \tag{1.60}$$

and then equation (1.52) becomes

$$R_{\mu\nu} - \frac{1}{2}Rg_{\mu\nu} = -\frac{16\pi}{\sqrt{-g}}\frac{\delta(\mathscr{L}_{\mathrm{M}}\sqrt{-g})}{\delta g^{\mu\nu}}. \tag{1.61}$$

In the coordinate basis, the stress-energy tensor's components can be defined using the Lagrangian density $\mathscr{L}_{\mathrm{M}}$ for matter as follows:

$$T_{\mu\nu} \coloneqq -\frac{2}{\sqrt{-g}}\frac{\delta(\mathscr{L}_{\mathrm{M}}\sqrt{-g})}{\delta g^{\mu\nu}} = -2\frac{\delta\mathscr{L}_{\mathrm{M}}}{\delta g^{\mu\nu}} + g_{\mu\nu}\mathscr{L}_{\mathrm{M}}. \tag{1.62}$$

With this definition, equation (1.61) becomes Einstein's field equation (1.48) in the coordinate basis

$$R_{\mu\nu} - \frac{1}{2}Rg_{\mu\nu} = 8\pi T_{\mu\nu}. \tag{1.63}$$

We can modify the Einstein-Hilbert action by adding a cosmological constant term:

$$\tilde{S}_{\mathrm{HE}} = \int \frac{1}{16\pi}(R - 2\Lambda)\sqrt{-g}d^4x, \tag{1.64}$$

where Λ is commonly know as a cosmological constant, which is a form of dark energy in the standard ΛCDM model (Peebles, 1984). When we vary this modified action, we obtain a modified version of Einstein's field equation (1.63):

$$R_{\mu\nu} - \frac{1}{2}Rg_{\mu\nu} + \Lambda g_{\mu\nu} = G_{\mu\nu} + \Lambda g_{\mu\nu} = 8\pi T_{\mu\nu}. \tag{1.65}$$

Note that the property of the Einstein tensor, $\nabla^{\mu}G_{\mu\nu} = 0$, allows the addition of the cosmological constant term $\Lambda g_{\mu\nu}$ into Einstein's field equation. We can also interpret Einstein's

field equation (1.48) with the stress-energy tensor defined as:

$$T_{\mu\nu} = T^{\mathrm{M}}_{\mu\nu} + T^{\Lambda}_{\mu\nu}, \tag{1.66}$$

where $T^{\mathrm{M}}_{\mu\nu}$ is the stress-energy tensor defined in equation (1.62), and

$$T^{\Lambda}_{\mu\nu} \coloneqq -\frac{\Lambda}{8\pi} g_{\mu\nu}. \tag{1.67}$$

1.2 Friedmann equations

The cosmological principle asserts that the Universe is spatially homogeneous and isotropic on large spatial scales. This means that the Friedmann-Lemaître-Robertson-Walker (FLRW) metric can be used to describe the Universe, which takes the form:

$$ds^2 = g_{\mu\nu} dx^\mu dx^\nu = -dt^2 + a^2(t) \left[\frac{dr^2}{1 - kr^2} + r^2 (d\theta^2 + \sin^2 \theta d\phi^2) \right], \tag{1.68}$$

where $g_{\mu\nu}$ are the metric tensor components, $c = 1$, t is cosmic time, (r, θ, ϕ) are spherical coordinates, and $a(t)$ is the scale factor. The scale factor is defined as:

$$\mathbf{r}(t) = a(t)\mathbf{x}, \tag{1.69}$$

where $\mathbf{r}(t)$ is the physical distance between two points at a given time, and $\mathbf{x}$ is the comoving distance between those points. The curvature of the spatial hypersurfaces is described by the value of k, which can be positive $(+1)$, zero, or negative (-1). If k is positive, space is positively curved like a sphere. If k is negative, space is negatively curved like a saddle. If k is zero, space is flat like a sheet of paper.

From equation (1.68), we can see that the non-zero components of the metric tensor in

coordinates $(x^0, x^1, x^2, x^3) = (t, r, \theta, \phi)$ are

$$g_{00} = -1,\ g_{11} = \frac{a^2}{1-kr^2},\ g_{22} = a^2 r^2,\ g_{33} = a^2 r^2 \sin^2\theta. \tag{1.70}$$

Therefore by using equation (1.21), we obtain the non-zero components of the Christoffel symbol $\Gamma^{\alpha}_{\ \mu\nu}$

$$\begin{aligned}
&\Gamma^0_{\ 11} = \frac{a\dot{a}}{1-kr^2} = \frac{\dot{a}}{a} g_{11},\ \Gamma^0_{\ 22} = a\dot{a}r^2 = \frac{\dot{a}}{a} g_{22},\ \Gamma^0_{\ 33} = a\dot{a}r^2\sin^2\theta = \frac{\dot{a}}{a} g_{33},\ \Longleftrightarrow\ \Gamma^0_{\ ij} = \frac{\dot{a}}{a} g_{ij},\\
&\Gamma^i_{\ 0j} = \Gamma^i_{\ j0} = \frac{\dot{a}}{a}\delta^i_{\ j},\ \Gamma^1_{\ 11} = \frac{kr}{1-kr^2},\ \Gamma^1_{\ 22} = -r(1-kr^2),\ \Gamma^1_{\ 33} = -r(1-kr^2)\sin^2\theta,\\
&\Gamma^2_{\ 12} = \Gamma^2_{\ 21} = \Gamma^3_{\ 13} = \Gamma^3_{\ 31} = \frac{1}{r},\ \Gamma^2_{\ 33} = -\sin\theta\cos\theta,\ \Gamma^3_{\ 23} = \Gamma^3_{\ 32} = \cot\theta.
\end{aligned} \tag{1.71}$$

The stress-energy tensor of a perfect fluid takes the form of equation (1.38), whose components in the coordinate basis is

$$T_{\mu\nu} = \rho u_\mu u_\nu + p(g_{\mu\nu} + u_\mu u_\nu), \tag{1.72}$$

where the symbols are introduced in Section 1.1.3. Since $g_{0i} = g_{i0} = u_i = u^i = 0$, the non-zero parts of $T_{\mu\nu}$ are

$$T_{00} = \rho,\ T_{ij} = p g_{ij}. \tag{1.73}$$

Thus Einstein's field equations (1.65) become the following two equations

$$R_{00} + \frac{1}{2}R = 8\pi\rho + \Lambda, \tag{1.74}$$

and

$$R_{ij} - \frac{1}{2}R g_{ij} = 8\pi p g_{ij} - \Lambda g_{ij}. \tag{1.75}$$

Note that the gravitational constant $G = 1$ is applied here.

From equation (1.71) we can derive the desired components of the Ricci tensor $R_{\mu\nu}$ and

the Ricci scalar R as follows

$$R_{00} = -3\frac{\ddot{a}}{a},\ R_{ij} = \frac{1}{a^2}(2\dot{a}^2 + a\ddot{a} + 2k)g_{ij},\ R = 6\left(\frac{\ddot{a}}{a} + \frac{\dot{a}^2}{a^2} + \frac{k}{a^2}\right). \tag{1.76}$$

Substituting equation (1.76) into equations (1.74) and (1.75), we get

$$\left(\frac{\dot{a}}{a}\right)^2 = \frac{8\pi}{3}\rho + \frac{\Lambda}{3} - \frac{k}{a^2}, \tag{1.77}$$

and

$$2\frac{\ddot{a}}{a} + \frac{\dot{a}^2}{a^2} + \frac{k}{a^2} = -8\pi p + \Lambda. \tag{1.78}$$

Equation (1.77) is known as the first Friedmann equation. By combining equations (1.77) and (1.78), we can get the second Friedmann equation

$$\frac{\ddot{a}}{a} = -\frac{4\pi}{3}(\rho + 3p) + \frac{\Lambda}{3}. \tag{1.79}$$

Friedmann equations (1.77) and (1.79) can yield

$$\dot{\rho} + 3\frac{\dot{a}}{a}(\rho + p) = 0, \tag{1.80}$$

which expresses the conservation of the stress-energy $T^{\mu\nu}{}_{;\nu} = 0$. If we define an equation of state parameter

$$w := \frac{p}{\rho}, \tag{1.81}$$

then equation (1.80) has a solution

$$\rho = \rho_0 \left(\frac{a_0}{a}\right)^{3(1+w)}, \tag{1.82}$$

where at present time $t = t_0$, $\rho(t_0) = \rho_0$, and $a(t_0) = a_0$. For dust ($p = 0$), we find $\rho \propto a^{-3}$; for radiation ($p = \rho/3$), we find $\rho \propto a^{-4}$; and for the cosmological constant $\rho_\Lambda = \Lambda/8\pi$, $w_\Lambda = -1$.

The Hubble parameter is a measure of the expansion rate of the Universe and is defined as the time derivative of the scale factor a normalized by the scale factor itself, i.e.,

$$H \coloneqq \frac{\dot{a}}{a}. \tag{1.83}$$

Here, an overdot represents a derivative with respect to cosmic time t. At the present time $t = t_0$, the value of the Hubble parameter is denoted as H_0, which is commonly known as the Hubble constant.

The first Friedmann equation (1.77) is a fundamental equation in cosmology that relates the expansion rate of the Universe to its energy density and curvature. It takes the form

$$H^2 = \frac{8\pi}{3}(\rho_m + \rho_r + \rho_\Lambda) - \frac{k}{a^2}, \tag{1.84}$$

where ρ_m, ρ_r, and ρ_Λ represent the matter, radiation, and dark energy density, respectively. The term k/a^2 accounts for the curvature of spatial hypersurfaces, where k takes the values -1, 0, or 1 corresponding to open, flat, or closed spatial geometries, respectively. Equation (1.84) can be rewritten in terms of the Hubble constant H_0 as

$$H^2 = H_0^2 \left[\frac{8\pi}{3H_0^2}(\rho_m + \rho_r + \rho_\Lambda) - \frac{k}{a^2 H_0^2} \right]. \tag{1.85}$$

We can define the cosmological parameters as follows:

- The non-relativistic matter density parameter

$$\Omega_m \coloneqq \frac{8\pi}{3H_0^2}\rho_m = \frac{8\pi}{3H_0^2}\rho_{m0}\left(\frac{a_0}{a}\right)^3 = \Omega_{m0}\left(\frac{a_0}{a}\right)^3, \tag{1.86}$$

  where the subscript "0" denotes the current value of the given quantities.

- The radiation density parameter

$$\Omega_r \coloneqq \frac{8\pi}{3H_0^2}\rho_r = \frac{8\pi}{3H_0^2}\rho_{r0}\left(\frac{a_0}{a}\right)^4 = \Omega_{r0}\left(\frac{a_0}{a}\right)^4. \tag{1.87}$$

- The cosmological constant dark energy density parameter

$$\Omega_\Lambda \coloneqq \frac{8\pi}{3H_0^2}\rho_\Lambda. \tag{1.88}$$

- The curvature density parameter

$$\Omega_k \coloneqq -\frac{k}{a^2H_0^2} = \Omega_{k0}\left(\frac{a_0}{a}\right)^2. \tag{1.89}$$

Using these parameters, equation (1.85) becomes

$$H^2 = H_0^2(\Omega_m + \Omega_r + \Omega_k + \Omega_\Lambda) = H_0^2\left[\Omega_{m0}\left(\frac{a_0}{a}\right)^3 + \Omega_{r0}\left(\frac{a_0}{a}\right)^4 + \Omega_{k0}\left(\frac{a_0}{a}\right)^2 + \Omega_\Lambda\right]. \tag{1.90}$$

1.3 Distance measures in cosmology

Light travels along null geodesics, which can be expressed as $ds^2 = 0$. For an isotropic observer in the FLRW metric, it is always possible to find a new set of (θ, ϕ) coordinates such that the null geodesic is radial, leading to the following line element:

$$ds^2 = -dt^2 + a^2\frac{dr^2}{1-kr^2} = 0, \tag{1.91}$$

or equivalently,

$$\frac{dt}{a} = \frac{dr}{\sqrt{1-kr^2}}. \tag{1.92}$$

Consider a light source located at $r = R$ that emits two light beams separated by a time interval equal to the wavelength of light at the source, λ_S. The light beams are emitted at times t_S and $t_S + \lambda_S$. An observer located at $r = 0$ detects the light beams with a wavelength of light at the observer, λ_O, at two different times: t_O and $t_O + \lambda_O$, respectively. Integrating

the light path (1.92) over t and r, we obtain

$$\int_{t_S}^{t_O} \frac{dt}{a} \equiv \int_{t_S}^{t_S+\lambda_S} \frac{dt}{a} + \int_{t_S+\lambda_S}^{t_O} \frac{dt}{a} = \int_R^0 \frac{dr}{\sqrt{1-kr^2}} = \int_{t_S+\lambda_S}^{t_O+\lambda_O} \frac{dt}{a}, \tag{1.93}$$

which yields

$$\int_{t_S}^{t_S+\lambda_S} \frac{dt}{a} = \int_{t_O}^{t_O+\lambda_O} \frac{dt}{a}. \tag{1.94}$$

For small time intervals λ_S and λ_O, we can consider scale factors at the source (a_S) and at the observer (a_O) to be constants. Therefore, the above equation becomes

$$\frac{\lambda_S}{a_S} = \frac{\lambda_O}{a_O} \quad \text{or} \quad \frac{\lambda_S}{\lambda_O} = \frac{a_S}{a_O}, \tag{1.95}$$

We define the redshift z as

$$z = \frac{\lambda_O - \lambda_S}{\lambda_S} = \frac{\lambda_O}{\lambda_S} - 1, \tag{1.96}$$

which, combined with equation (1.95), gives

$$1 + z = \frac{a_O}{a_S}. \tag{1.97}$$

We can simplify equation (1.97) by considering ourselves as the observer at the present time t_0 when the scale factor is a_0, with the source at time t when the scale factor is a. Then we have

$$1 + z = \frac{a_0}{a}. \tag{1.98}$$

By combining equation (1.98) with equation (1.90), we can express the Hubble parameter as a function of redshift z

$$H(z) = H_0\sqrt{\Omega_{m0}(1+z)^3 + \Omega_{r0}(1+z)^4 + \Omega_{k0}(1+z)^2 + \Omega_\Lambda} \equiv H_0 E(z), \tag{1.99}$$

where $E(z)$ is the expansion rate function.

Several key distance measures are used in cosmology to quantify the expansion of the

Universe. The transverse comoving distance $D_M(z)$, also known as the radial distance along the line of sight, can be calculated from equation (1.93) and is given by

$$D_M(z) = \begin{cases} \frac{1}{H_0\sqrt{\Omega_{k0}}} \sinh\left[H_0\sqrt{\Omega_{k0}} D_C(z)\right] & \text{if } \Omega_{k0} > 0, \\ D_C(z) & \text{if } \Omega_{k0} = 0, \\ \frac{1}{H_0\sqrt{|\Omega_{k0}|}} \sin\left[H_0\sqrt{|\Omega_{k0}|} D_C(z)\right] & \text{if } \Omega_{k0} < 0, \end{cases} \tag{1.100}$$

where $D_C(z)$ is the comoving distance to the source, given by

$$D_C(z) = \int_0^z \frac{dz'}{H(z')}. \tag{1.101}$$

$D_M(z)$ is related to other important distance measures, including the luminosity distance $D_L(z)$ and the angular diameter distance $D_A(z)$, through

$$D_M(z) = \frac{D_L(z)}{1+z} = (1+z)D_A(z). \tag{1.102}$$

In addition, the Hubble distance is defined as

$$D_H(z) = \frac{1}{H(z)}, \tag{1.103}$$

and the volume averaged distance is given by

$$D_V(z) = [zD_H(z)D_M^2(z)]^{1/3}. \tag{1.104}$$

Another important quantity is the sound horizon at the drag epoch z_d, which is defined as

$$r_s = \int_{z_d}^{\infty} \frac{c_s(z)}{H(z)} dz, \tag{1.105}$$

where the sound speed in the photon-baryon fluid is given by

$$c_s(z) = \frac{1}{\sqrt{3\left(1+\frac{3}{4}\frac{\rho_b}{\rho_r}\right)}}, \tag{1.106}$$

with ρ_b being the baryon density. In practice, an approximation for r_s calibrated from numerical simulations is often used:

$$r_s = \frac{55.154\exp\left[-72.3(\Omega_\nu h^2+0.0006)^2\right]}{(\Omega_b h^2)^{0.12807}(\Omega_c h^2+\Omega_b h^2)^{0.25351}}\text{Mpc}, \tag{1.107}$$

where $\Omega_\nu h^2$, $\Omega_b h^2$, $\Omega_c h^2$ are the physical energy density parameters for non-relativistic neutrinos, baryons, and cold dark matter respectively, and h is the Hubble constant in units of 100 km s^{-1} Mpc^{-1}. This approximation is accurate to 0.021% for a standard radiation background with effective number of neutrino species $N_{\rm eff} = 3.046$, total neutrino mass $\sum m_\nu < 0.6$ eV, and values of $\Omega_b h^2$ and $\Omega_c h^2$ within 3σ of values derived using Planck CMB anisotropy data (Aubourg et al., 2015).

Note that the sound horizon r_s can be numerically computed using the Cosmic Linear Anisotropy Solving System (CLASS) code (Blas et al., 2011), without relying on CMB anisotropy data. This is the approach used in our latest analyses, Cao & Ratra (2022); Cao et al. (2022a,b,c,d); Cao et al. (2022e).

The distance modulus is defined as

$$\mu = m - M = 5\log\left(\frac{D_L}{10\text{ pc}}\right) = 5\log D_L + 25, \tag{1.108}$$

where m is the apparent magnitude of the object, M is its absolute magnitude, and D_L is the luminosity distance in units of Mpc. Throughout the thesis, unless otherwise specified, the symbol "log" represents the base-10 logarithm. The distance modulus is commonly used in observational cosmology as a measure of the distance to distant objects, such as type Ia supernovae, and can be inferred from the observed apparent magnitudes and the known absolute magnitudes of such objects.

Chapter 2

Dark energy cosmological models

Various measurements indicate that the Universe is currently expanding at an accelerating rate. If general relativity is valid this acceleration is due to the presence of dark energy, a hypothetical substance that has negative pressure. In the spatially-flat ΛCDM model (Peebles, 1984), dark energy is represented by a cosmological constant and accounts for around 70% of the total energy content of the Universe. However, recent observations might indicate potential discrepancies with this model (Abdalla et al., 2022; Di Valentino et al., 2021a; Hu & Wang, 2023; Moresco et al., 2022; Perivolaropoulos & Skara, 2022), leading to investigations into alternative models that allow for non-zero spatial curvature and/or dynamical dark energy. In our analyses we also explore some of these alternatives, described next, to better understand the underlying physics of the Universe.

2.1 ΛCDM models

The Hubble parameter in flat and non-flat ΛCDM models are already derived in equation (1.99), in which the expansion rate function is

$$E(z) = \sqrt{\Omega_{m0}\,(1+z)^3 + \Omega_{k0}\,(1+z)^2 + \Omega_\Lambda}, \tag{2.1}$$

where Ω_{m0} and Ω_{k0} are the current values of the cosmological non-relativistic matter density parameter and the spatial curvature energy density parameter, respectively, the cosmological constant dark energy density parameter $\Omega_\Lambda = 1 - \Omega_{m0} - \Omega_{k0}$, and z is the redshift. In the flat ΛCDM model, $\Omega_{k0} = 0$. For most of the data sets we used, the cosmological parameters being constrained are $\{H_0, \Omega_b h^2, \Omega_c h^2\}$ (or $\{H_0, \Omega_{m0}\}$) and $\{H_0, \Omega_b h^2, \Omega_c h^2, \Omega_{k0}\}$ (or $\{H_0, \Omega_{m0}, \Omega_{k0}\}$) in the flat and non-flat ΛCDM models, respectively. In some cases, certain data sets may not provide constraints on H_0 and $\Omega_b h^2$, in which case fixed values of Ω_b and H_0 are assumed. For example, a commonly used set is $\Omega_b = 0.05$ and $H_0 = 70$ km s^{-1} Mpc^{-1}. As noted in section 1.2, the equation of state parameter of the cosmological constant dark energy is $w_\Lambda = -1$.

It is worth noting that in equation (2.1) the contribution of radiation to the cosmological energy budget is neglected. This is justified for the low-redshift data sets that we used in our analyses, as the contribution of radiation becomes negligible at late times.

2.2 XCDM parametrizations

In the XCDM parametrizations, dark energy is modeled as an X-fluid with a generalized constant equation of state parameter $w_{\rm X}$, which distinguishes it from the ΛCDM models where $w_\Lambda = -1$. The cosmological X-fluid dynamical dark energy parameter is defined as

$$\Omega_{\rm X} \coloneqq \frac{8\pi}{3H_0^2}\rho_{\rm X} = \frac{8\pi}{3H_0^2}\rho_{\rm X0}\left(\frac{a_0}{a}\right)^{3(1+w_{\rm X})} = \Omega_{\rm X0}(1+z)^{3(1+w_{\rm X})}, \tag{2.2}$$

where $\rho_{\rm X}$ (a) and $\rho_{\rm X0}$ (a_0) are the X-fluid dynamical dark energy density (the scale factor) at a given time and at the present time, respectively. By replacing Ω_Λ in equation (2.1) with $\Omega_{\rm X}$, we obtain the expansion rate

$$E(z) = \sqrt{\Omega_{m0}\,(1+z)^3 + \Omega_{k0}\,(1+z)^2 + \Omega_{\rm X0}\,(1+z)^{3(1+w_{\rm X})}}, \tag{2.3}$$

where the current value of the X-fluid dynamical dark energy density parameter $\Omega_{\rm X0} = 1 - \Omega_{m0} - \Omega_{k0}$. The cosmological parameters being constrained are $\{H_0, \Omega_b h^2, \Omega_c h^2, w_{\rm X}\}$ (or $\{H_0, \Omega_{m0}, w_{\rm X}\}$) and $\{H_0, \Omega_b h^2, \Omega_c h^2, w_{\rm X}, \Omega_{k0}\}$ (or $\{H_0, \Omega_{m0}, w_{\rm X}, \Omega_{k0}\}$) in the flat and non-flat XCDM parametrizations, respectively. Note that when $w_{\rm X} = -1$ XCDM reduces to ΛCDM.

2.3 ϕCDM models

A dynamical scalar field can play an important cosmological role. In particular, scalar fields are often used to model the behavior of the inflaton field, which is thought to have driven the very rapid expansion of the Universe during an early inflationary epoch. During inflation, the scalar field energy dominates the cosmological energy budget. The dynamics of the scalar field during this period determines the rate and duration of inflation, as well as the properties of the resulting density fluctuations that seed the formation of large-scale cosmic structures such as galaxies.

After inflation, scalar fields may also play a role in the late-time acceleration of the expansion of the Universe, and are referred to as dynamical dark energy scalar fields. The study of scalar field dynamics in cosmology involves solving the equations of motion that describe the behavior of the scalar field in the expanding Universe, and determining its effects on the evolution of other cosmological parameters.

In this work we explore a dynamical scalar field dark energy model, also known as Quintessence, where the dynamical dark energy is represented by a scalar field ϕ instead of a cosmological constant. The Lagrangian of the scalar field ϕ is given by

$$\mathscr{L}_\phi = -\frac{1}{16\pi}\left[\frac{1}{2}g^{\mu\nu}\partial_\mu\phi\partial_\nu\phi + V(\phi)\right], \tag{2.4}$$

where $V(\phi)$ is the potential energy density of the scalar field. Following the analogy of the stress-energy tensor of matter, we can define the stress-energy tensor of the scalar field ϕ as

$$T_{\mu\nu} \coloneqq -\frac{2}{\sqrt{-g}}\frac{\delta(\mathscr{L}_\phi\sqrt{-g})}{\delta g^{\mu\nu}} = -2\frac{\delta\mathscr{L}_\phi}{\delta g^{\mu\nu}} + g_{\mu\nu}\mathscr{L}_\phi. \tag{2.5}$$

The first term in the right-hand-side of equation (2.5) can be simplified as

$$-2\frac{\delta\mathscr{L}_\phi}{\delta g^{\mu\nu}} = \frac{1}{8\pi}\frac{\delta}{\delta g^{\mu\nu}}\left[\frac{1}{2}g^{\alpha\beta}\partial_\alpha\phi\partial_\beta\phi + V(\phi)\right] = \frac{1}{16\pi}\partial_\mu\phi\partial_\nu\phi. \tag{2.6}$$

Therefore, the stress-energy tensor of ϕ in equation (2.5) becomes

$$T_{\mu\nu} = \frac{1}{16\pi}\left\{\partial_\mu\phi\partial_\nu\phi - g_{\mu\nu}\left[\frac{1}{2}g^{\alpha\beta}\partial_\alpha\phi\partial_\beta\phi + V(\phi)\right]\right\}. \tag{2.7}$$

Consequently, we can obtain the components of the stress-energy tensor in the FLRW metric as

$$\begin{aligned} T_{00} &= \frac{1}{16\pi}\left\{\partial_0\phi\partial_0\phi - g_{00}\left[\frac{1}{2}g^{00}\partial_0\phi\partial_0\phi + V(\phi)\right]\right\} = \frac{1}{16\pi}\left[\frac{1}{2}\dot{\phi}^2 + V(\phi)\right], \\ T_{ij} &= \frac{1}{16\pi}\left\{\partial_i\phi\partial_j\phi - g_{ij}\left[\frac{1}{2}g^{00}\partial_0\phi\partial_0\phi + V(\phi)\right]\right\} = \frac{1}{16\pi}\left[\frac{1}{2}\dot{\phi}^2 - V(\phi)\right]g_{ij}, \end{aligned} \tag{2.8}$$

where ϕ is only a function of t due to the homogeneous and isotropic properties of the FLRW metric. Similarly, following the same procedure as for the stress-energy tensor in equation (1.73), we can identify the energy density and pressure of the scalar field ϕ as

$$\rho_\phi = \frac{1}{16\pi}\left[\frac{1}{2}\dot{\phi}^2 + V(\phi)\right], \tag{2.9}$$

and

$$p_\phi = \frac{1}{16\pi}\left[\frac{1}{2}\dot{\phi}^2 - V(\phi)\right], \tag{2.10}$$

respectively. Therefore, we can express the equation of state of the scalar field dark energy as follows:

$$w_\phi = \frac{\frac{1}{2}\dot{\phi}^2 - V(\phi)}{\frac{1}{2}\dot{\phi}^2 + V(\phi)}. \tag{2.11}$$

Therefore, the Friedmann equation can be expressed in terms of the Hubble parameter

$$H(z) = H_0\sqrt{\Omega_{m0}(1+z)^3 + \Omega_{k0}(1+z)^2 + \Omega_\phi(z,\alpha)}, \tag{2.12}$$

where the scalar field dynamical dark energy density parameter

$$\Omega_\phi(z,\alpha) \coloneqq \frac{8\pi}{3H_0^2}\rho_\phi. \tag{2.13}$$

The action for the scalar field ϕ is given by

$$S_\phi = \int \mathscr{L}_\phi \sqrt{-g} d^4x = -\frac{1}{16\pi}\int \left[\frac{1}{2}g^{\mu\nu}\partial_\mu\phi\partial_\nu\phi + V(\phi)\right]\sqrt{-g}d^4x. \tag{2.14}$$

The equation of motion for ϕ can be obtained using the principle of least action, which states that the variation of the action with respect to ϕ is zero:

$$\begin{aligned}
0 &= \delta S_\phi \\
&= -\frac{1}{16\pi}\delta\int \left[\frac{1}{2}g^{\mu\nu}\partial_\mu\phi\partial_\nu\phi + V(\phi)\right]\sqrt{-g}d^4x \\
&= -\frac{1}{16\pi}\int \left[\frac{1}{2}g^{\mu\nu}\delta(\partial_\mu\phi\partial_\nu\phi) + V'(\phi)\delta\phi\right]\sqrt{-g}d^4x \\
&= -\frac{1}{16\pi}\int \left[g^{\mu\nu}\partial_\mu\phi\delta(\partial_\nu\phi) + V'(\phi)\delta\phi\right]\sqrt{-g}d^4x \\
&= -\frac{1}{16\pi}\int \left[g^{\mu\nu}\partial_\mu\phi\partial_\nu(\delta\phi) + V'(\phi)\delta\phi\right]\sqrt{-g}d^4x \\
&= -\frac{1}{16\pi}\int \left(\int_{-\infty}^{\infty} g^{\mu\nu}\partial_\mu\phi\delta\phi\sqrt{-g}dx^\nu\right)d^3x - \frac{1}{16\pi}\int \left[\partial_\nu(\sqrt{-g}g^{\mu\nu}\partial_\mu\phi) - \sqrt{-g}V'(\phi)\right]\delta\phi d^4x \\
&= -\frac{1}{16\pi}\int \left[\partial_\nu(\sqrt{-g}g^{\mu\nu}\partial_\mu\phi) - \sqrt{-g}V'(\phi)\right]\delta\phi d^4x.
\end{aligned} \tag{2.15}$$

where we used the fact that $\delta\phi$ vanishes at boundaries and a prime denotes a derivative with respect to ϕ. If equation (2.15) is valid for arbitrary $\delta\phi$, we obtain the equation of motion for ϕ:

$$\partial_\nu(\sqrt{-g}g^{\mu\nu}\partial_\mu\phi) = \partial_\nu(\sqrt{-g})g^{\mu\nu}\partial_\mu\phi + \sqrt{-g}\partial_\nu(g^{\mu\nu}\partial_\mu\phi) = \sqrt{-g}V'(\phi). \tag{2.16}$$

In the FLRW metric, the above equation of motion becomes

$$\begin{aligned}
&\partial_0(\sqrt{-g})g^{00}\partial_0\phi + \sqrt{-g}\partial_0(g^{00}\partial_0\phi) = \sqrt{-g}V'(\phi) \\
\implies \quad &\partial_0(\sqrt{-g})(-\dot{\phi}) + \sqrt{-g}(-\ddot{\phi}) = \sqrt{-g}V'(\phi) \\
\implies \quad &\partial_0(a^3)\frac{\sqrt{-g}}{a^3}(-\dot{\phi}) + \sqrt{-g}(-\ddot{\phi}) = \sqrt{-g}V'(\phi) \\
\implies \quad &-3\frac{\dot{a}}{a}\dot{\phi} - \ddot{\phi} = V'(\phi) \\
\implies \quad &\ddot{\phi} + 3\frac{\dot{a}}{a}\dot{\phi} - V'(\phi) = 0 \Longleftrightarrow \ddot{\phi} + 3H\dot{\phi} - V'(\phi) = 0. \qquad (2.17)
\end{aligned}$$

In this work, we use the ϕCDM models with an inverse power-law scalar field potential energy density (Pavlov et al., 2013; Peebles & Ratra, 1988; Ratra & Peebles, 1988)

$$V(\phi) = \frac{1}{2}\kappa m_p^2 \phi^{-\alpha}, \qquad (2.18)$$

where m_p is the Planck mass, α is a positive constant (with $\alpha = 0$ corresponding to a cosmological constant), and κ is a constant that determines the strength of the coupling between the scalar field and gravity. We obtain κ either by using the shooting method in the Cosmic Linear Anisotropy Solving System (CLASS) code (Blas et al., 2011) or by adopting the matter-dominated initial condition form [1] given by

$$\kappa = \frac{8}{3m_p^2}\left(\frac{\alpha+4}{\alpha+2}\right)\left[\frac{2}{3}\alpha(\alpha+2)\right]^{\alpha/2}. \qquad (2.19)$$

Using the numerical solutions of the Friedmann equation (2.12) and the equation of motion (2.17), we can obtain constraints on the cosmological parameters in the ϕCDM models. Specifically, we can obtain constraints on the cosmological parameters $\{H_0, \Omega_b h^2, \Omega_c h^2, \alpha\}$ (or $\{H_0, \Omega_{m0}, \alpha\}$) and $\{H_0, \Omega_b h^2, \Omega_c h^2, \alpha, \Omega_{k0}\}$ (or $\{H_0, \Omega_{m0}, \alpha, \Omega_{k0}\}$) in the flat and non-flat ϕCDM models, respectively. For recent studies on constraints on ϕCDM see Refs. (Adil et al., 2022; de Cruz Perez et al., 2021; Jesus et al., 2022; Ooba et al., 2018b, 2019; Park &

[1] The detailed derivation of this form can be found in subsection 3.6.3 of Farooq (2013).

Ratra, 2018, 2019b, 2020; Singh et al., 2019; Sinha & Banerjee, 2021; Solà Peracaula et al., 2019; Ureña-López & Roy, 2020; Xu et al., 2022; Zhai et al., 2017) and related references within these papers.

Chapter 3

Cosmological constraints from HII starburst galaxy apparent magnitude and other cosmological measurements

This chapter is based on Cao et al. (2020). Figures and tables by Shulei Cao, from analyses conducted independently by Shulei Cao and Joseph Ryan (Ryan, 2021a).

3.1 Introduction

The accelerated expansion of the current universe is now well-established observationally and is usually credited to a dark energy whose origins remain murky (see e.g. Coley & Ellis, 2020; Martin, 2012; Ratra & Vogeley, 2008). The standard ΛCDM model of cosmology (Peebles, 1984) describes a universe with flat spatial hypersurfaces predominantly filled with dark energy in the form of a cosmological constant Λ and cold dark matter (CDM) together comprising $\sim 95\%$ of the total energy budget. While spatially-flat ΛCDM is mostly consistent with cosmological observations (see e.g. Alam et al., 2017; Farooq et al., 2017; Planck Collaboration, 2020; Scolnic et al., 2018), there are indications of some (mild) discrepances between standard ΛCDM model predictions and cosmological measurements. In addition,

the quality and quantity of cosmological data continue to grow, making it possible to consider and constrain additional cosmological parameters beyond those that characterize the standard ΛCDM model.

Given the uncertainty surrounding the origin of the cosmological constant, many workers have investigated the possibility that the cosmological "constant" is not really constant, but rather evolves in time, either by positing an equation of state parameter $w \neq -1$ (thereby introducing a redshift dependence into the dark energy density) or by replacing the constant Λ in the Einstein-Hilbert action with a dynamical scalar field ϕ (Peebles & Ratra, 1988; Ratra & Peebles, 1988). Non-flat spatial geometry also introduces a time-dependent source term in the Friedmann equations. In this paper we study the standard spatially-flat ΛCDM model as well as dynamical dark energy and spatially non-flat extensions of this model.

One major goal of this paper is to use measurements of the redshift, apparent luminosity, and gas velocity dispersion of HII starburst galaxies to constrain cosmological parameters.[1] An HII starburst galaxy (hereinafter "H II G") is one that contains a large HII region, an emission nebula sourced by the UV radiation from an O- or B-type star. There is a correlation between the measured luminosity (L) and the inferred velocity dispersion (σ) of the ionized gases within these H II G, referred to as the L-σ relation (see Section 3.2) which has been shown to be a useful cosmological tracer (see Chávez et al., 2012, 2014, 2016; González-Morán et al., 2019; Melnick et al., 2000; Plionis et al., 2011; Siegel et al., 2005; Terlevich et al., 2015, and references therein). This relation has been used to constrain the Hubble constant H_0 (Chávez et al., 2012; Fernández Arenas et al., 2018), and it can also be used to put constraints on the dark energy equation of state parameter w (Chávez et al., 2016; González-Morán et al., 2019; Terlevich et al., 2015).

H II G data reach to redshift $z \sim 2.4$, a little beyond that of the highest redshift baryon acoustic oscillation (BAO) data which reach to $z \sim 2.3$. H II G data are among a handful of cosmological observations that probe the largely unexplored part of redshift space from $z \sim 2$ to $z \sim 1100$. Other data that probe this region include quasar angular size measurements

[1] For early attempts see Siegel et al. (2005), Plionis et al. (2009, 2010, 2011) and Mania & Ratra (2012). For more recent discussions see Chávez et al. (2016), Wei et al. (2016), Yennapureddy & Melia (2017), Zheng et al. (2019), Ruan et al. (2019), González-Morán et al. (2019), Wan et al. (2019), and Wu et al. (2020).

that reach to $z \sim 2.7$ (Cao et al., 2017b; Chen & Ratra, 2003; Gurvits et al., 1999; Ryan et al., 2019, and references therein), quasar flux measurements that reach to $z \sim 5$ (Khadka & Ratra, 2020a,b; Risaliti & Lusso, 2015, 2019; Yang et al., 2020; Zheng et al., 2020, and references therein), and gamma ray burst data that reach to $z \sim 8$ (Demianski et al., 2021; Lamb & Reichart, 2000; Samushia & Ratra, 2010, and references therein). In this paper we also use quasar angular size measurements (hereinafter "QSO") to constrain cosmological model parameters.

While H II G and QSO data probe the largely unexplored $z \sim 2.3$–2.7 part of the universe, current H II G and QSO measurements provide relatively weaker constraints on cosmological parameters than those provided by more widely used measurements, such as BAO peak length scale observations or Hubble parameter (hereinafter "$H(z)$") observations (with these latter data being at lower redshift but of better quality than H II G or QSO data). However, we find that the H II G and QSO constraints are consistent with those that follow from BAO and $H(z)$ data, and so we use all four sets of data together to constrain cosmological parameters. We find that the H II G and QSO data tighten parameter constraints relative to the $H(z)$ + BAO only case.

Using six different cosmological models to constrain cosmological parameters allows us to determine which of our results are less model-dependent. In all models, the H II G data favor those parts of cosmological parameter space for which the current cosmological expansion is accelerating.[2] The joint analysis of the H II G QSO, BAO and $H(z)$ data results in relatively model-independent and fairly tight determination of the Hubble constant H_0 and the current non-relativistic matter density parameter Ω_{m0}.[3] Depending on the model, Ω_{m0} ranges from a low of $0.309^{+0.015}_{-0.014}$ to a high of 0.319 ± 0.013, being consistent with most other estimates of this

[2]This result could weaken, however, as the H II G data constraint contours could broaden when H II G data systematic uncertainties are taken into account. We do not incorporate any H II G systematic uncertainties into our analysis; see below.

[3]The BAO and $H(z)$ data play a more significant role than do the H II G and QSO data in setting these and other limits, but the H II G and QSO data tighten the BAO + $H(z)$ constraints. We note, however, that the $H(z)$ and QSO data, by themselves, give lower central values of H_0 but with larger error bars. Also, because we calibrate the distance scale of the BAO measurements listed in Table 3.1 via the sound horizon scale at the drag epoch (r_s, about which see below), a quantity that depends on early-Universe physics, we would expect these measurements to push the best-fitting values H_0 lower when they are combined with late-Universe measurements like H II G (whose distance scale is not set by the physics of the early Universe).

parameter (unless indicated otherwise, uncertainties given in this paper are $\pm 1\sigma$). The best-fitting values of H_0, ranging from $68.18^{+0.97}_{-0.75}$ km s^{-1} Mpc^{-1}to 69.90 ± 1.48 km s^{-1} Mpc^{-1}, are, from the quadrature sum of the error bars, 2.01σ to 3.40σ lower than the local $H_0 = 74.03 \pm 1.42$ km s^{-1} Mpc^{-1}measurement of Riess et al. (2019) and only 0.06σ to 0.60σ higher than the median statistics $H_0 = 68 \pm 2.8$ km s^{-1} Mpc^{-1}estimate of Chen & Ratra (2011). These combined measurements are consistent with the spatially-flat ΛCDM model, but also do not strongly disallow some mild dark energy dynamics, as well as a little non-zero spatial curvature energy density.

This paper is organized as follows. In Section 3.2 we introduce the data we use. The models we analyze are described in Chapter 2, with a description of our analysis method in Section 3.3. Our results are in Section 3.4, and we provide our conclusions in Section 3.5.

3.2 Data

We use a combination of $H(z)$, BAO, QSO, and H II G data to obtain constraints on our cosmological models. The $H(z)$ data, spanning the redshift range $0.070 \leq z \leq 1.965$, are identical to the $H(z)$ data used in Ryan et al. (2018, 2019) and compiled in Table 2 of Ryan et al. (2018); see that paper for description. The QSO data compiled by Cao et al. (2017b) (listed in Table 1 of that paper) and spanning the redshift range $0.462 \leq z \leq 2.73$, are identical to that used in Ryan et al. (2019); see these papers for descriptions. Our BAO data (see Table 3.1) have been updated relative to Ryan et al. (2019) and span the redshift range $0.38 \leq z \leq 2.34$. Our H II G data are new, comprising 107 low redshift ($0.0088 \leq z \leq 0.16417$) H II G measurements, used in Chávez et al. (2014), and 46 high redshift ($0.636427 \leq z \leq 2.42935$) H II G measurements, used in González-Morán et al. (2019).[4] These extinction-corrected measurements (see below for a discussion of extinction correction) were very kindly provided to us by Ana Luisa González-Morán (private communications, 2019 and 2020).

In order to use BAO measurements to constrain cosmological model parameters, knowl-

[4] 15 from González-Morán et al. (2019), 25 from Erb et al. (2006), Masters et al. (2014), and Maseda et al. (2014), and 6 from Terlevich et al. (2015).

Table 3.1: BAO data.

z	Measurement[a]	Value	Ref.
0.38	$D_M\,(r_{s,\mathrm{fid}}/r_s)$	1512.39	Alam et al. (2017)[b]
0.38	$H(z)\,(r_s/r_{s,\mathrm{fid}})$	81.2087	Alam et al. (2017)[b]
0.51	$D_M\,(r_{s,\mathrm{fid}}/r_s)$	1975.22	Alam et al. (2017)[b]
0.51	$H(z)\,(r_s/r_{s,\mathrm{fid}})$	90.9029	Alam et al. (2017)[b]
0.61	$D_M\,(r_{s,\mathrm{fid}}/r_s)$	2306.68	Alam et al. (2017)[b]
0.61	$H(z)\,(r_s/r_{s,\mathrm{fid}})$	98.9647	Alam et al. (2017)[b]
0.122	$D_V\,(r_{s,\mathrm{fid}}/r_s)$	539 ± 17	Carter et al. (2018)
0.81	D_A/r_s	10.75 ± 0.43	DES Collaboration (2019b)
1.52	$D_V\,(r_{s,\mathrm{fid}}/r_s)$	3843 ± 147	Ata et al. (2018)
2.34	D_H/r_s	8.86	de Sainte Agathe et al. (2019)[c]
2.34	D_M/r_s	37.41	de Sainte Agathe et al. (2019)[c]

[a] $D_M\,(r_{s,\mathrm{fid}}/r_s)$, $D_V\,(r_{s,\mathrm{fid}}/r_s)$, r_s, and $r_{s,\mathrm{fid}}$ have units of Mpc, while $H(z)\,(r_s/r_{s,\mathrm{fid}})$ has units of km s^{-1} Mpc^{-1}, and D_A/r_s is dimensionless.

[b] The six measurements from Alam et al. (2017) are correlated; see eq. (20) of Ryan et al. (2019) for their correlation matrix.

[c] The two measurements from de Sainte Agathe et al. (2019) are correlated; see eq. (3.15) below for their correlation matrix.

edge of the sound horizon scale at the drag epoch (r_s) is required. We compute this scale more accurately than in Ryan et al. (2019) by using the approximate formula (1.107) (Aubourg et al., 2015). Here $\Omega_{\mathrm{cb}_0} = \Omega_{\mathrm{c}_0} + \Omega_{\mathrm{b}_0} = \Omega_{\mathrm{m}_0} - \Omega_{\nu_0}$ with Ω_{cb_0}, Ω_{c_0}, Ω_{b_0}, and $\Omega_{\nu_0} = 0.0014$ (following Carter et al., 2018) being the current values of the CDM + baryonic matter, CDM, baryonic matter, and neutrino energy density parameters, respectively, and the Hubble constant $H_0 = 100\ h$ km s^{-1} Mpc^{-1}. Here and in what follows, a subscript of '0' on a given quantity denotes the current value of that quantity. Additionally, $\Omega_{\mathrm{b}_0}h^2$ is slightly model-dependent; the values of this parameter that we use in this paper are the same as those originally computed in Park & Ratra (2018, 2019a,c) and listed in Table 2 of Ryan et al. (2019).

As mentioned in Section 3.1, H IIG can be used as cosmological probes because they exhibit a tight correlation between the observed luminosity (L) of their Balmer emission lines and the velocity dispersion (σ) of their ionized gas (as measured from the widths of the

emission lines). That correlation can be expressed in the form

$$\log L = \beta \log \sigma + \gamma, \tag{3.1}$$

where γ and β are the intercept and slope, respectively, and $\log = \log_{10}$ here and in what follows. In order to determine the values of β and γ, it is necessary to establish the extent to which light from an H II G is extinguished as it propagates through space. A correction must be made to the observed flux so as to account for the effect of this extinction. As mentioned above, the data we received from Ana Luisa González-Morán have been corrected for extinction. In González-Morán et al. (2019), the authors used the Gordon et al. (2003) extinction law, and in so doing found

$$\beta = 5.022 \pm 0.058, \tag{3.2}$$

and

$$\gamma = 33.268 \pm 0.083, \tag{3.3}$$

respectively. These are the values of β and γ that we use in the L-σ relation, eq. (3.1).

Once the luminosity of an H II G has been established through eq. (3.1), this luminosity can be used, in conjunction with a measurement of the flux (f) emitted by the H II G, to determine the distance modulus of the H II G via

$$\mu_{\rm obs} = 2.5 \log L - 2.5 \log f - 100.2 \tag{3.4}$$

(see e.g. Terlevich et al., 2015, González-Morán et al., 2019, and references therein).[5] This quantity can then be compared to the value of the distance modulus predicted within a given cosmological model

$$\mu_{\rm th}\left(\mathbf{p}, z\right) = 5 \log D_{\rm L}\left(\mathbf{p}, z\right) + 25, \tag{3.5}$$

[5]For each H II G in our sample we have the measured values and uncertainties of $\log f$, $\log \sigma$, and z.

where the luminosity distance $D_L(\mathbf{p}, z)$ is related to the transverse comoving distance $D_M(\mathbf{p}, z)$ and the angular size distance $D_A(\mathbf{p}, z)$ through equation (1.102). These are functions of the redshift z and the parameters $\mathbf{p}$ of the model in question, and D_M is defined in equation (1.100).

As the precision of cosmological observations has grown over the last few years, a tension between measurements of the Hubble constant made with early-Universe probes and measurements made with late-Universe probes has revealed itself (for a review, see Riess, 2019). Whether a given cosmological observation supports a lower value of H_0 (i.e. one that is closer to the early-Universe *Planck* measurement) or a higher value of H_0 (i.e. one that is closer to the late-Universe value measured by Riess et al., 2019) may depend on whether the distance scale associated with this observation has been set by early- or late-Universe physics. It is therefore important to know what distance scale cosmological observations have been calibrated to, so that the extent to which measurements of H_0 are pushed higher or lower by these different distance calibrations can be clearly identified.

The H_0 values we measure from the combined $H(z)$, BAO, QSO, and H IIG data are based on a combination of both early- and late-Universe distance calibrations. As mentioned above, the distance scale of our BAO measurements is set by the size of the sound horizon at the drag epoch r_s. The sound horizon, in turn, depends on $\Omega_{\mathrm{b}_0} h^2$, which was computed by Park & Ratra (2018, 2019a,c) using early-Universe data. Our H IIG measurements, on the other hand, have been calibrated using cosmological model independent distance ladder measurements of the distances to nearby giant HII regions (see González-Morán et al., 2019 and references therein), so these data qualify as late-Universe probes. The distance scale of our QSO measurements is set by the intrinsic linear size (l_m) of the QSOs themselves, which is a late-Universe measurement (see Cao et al., 2017b). Finally, our $H(z)$ data depend on late-Universe astrophysics through the modeling of the star formation histories of the galaxies whose ages are measured to obtain the Hubble parameter (although the differences between different models are not thought to have a significant effect on measurements of $H(z)$ from these galaxies; see Moresco et al., 2018, 2020).

3.3 Data Analysis Methodology

We perform a Markov chain Monte Carlo (MCMC) analysis with the Python module emcee (Foreman-Mackey et al., 2013) and maximize the likelihood function, $\mathscr{L}$, to determine the best-fitting values of the parameters $\mathbf{p}$ of the models. We use flat priors for all parameters $\mathbf{p}$. For all models, the priors on Ω_{m_0} and h are non-zero over the ranges $0.1 \leq \Omega_{\mathrm{m}_0} \leq 0.7$ and $0.50 \leq h \leq 0.85$. In the non-flat ΛCDM model the Ω_Λ prior is non-zero over $0.2 \leq \Omega_\Lambda \leq 1$. In the flat and non-flat XCDM parametrizations the prior range on w_{X} is $-2 \leq w_{\mathrm{X}} \leq 0$, and the prior range on Ω_{k_0} in the non-flat XCDM parametrization is $-0.7 \leq \Omega_{\mathrm{k}_0} \leq 0.7$. In the flat and non-flat ϕCDM models the prior range on α is $0.01 \leq \alpha \leq 3$ and $0.01 \leq \alpha \leq 5$, respectively, and the prior range on Ω_{k_0} is also $-0.7 \leq \Omega_{\mathrm{k}_0} \leq 0.7$.

For H II G, the likelihood function is

$$\mathscr{L}_{\mathrm{H\,II\,G}} = e^{-\chi^2_{\mathrm{H\,II\,G}}/2}, \tag{3.6}$$

where

$$\chi^2_{\mathrm{H\,II\,G}}(\mathbf{p}) = \sum_{i=1}^{153} \frac{[\mu_{\mathrm{th}}(\mathbf{p}, z_i) - \mu_{\mathrm{obs}}(z_i)]^2}{\epsilon_i^2}, \tag{3.7}$$

and ϵ_i is the uncertainty of the i_{th} measurement. Following González-Morán et al. (2019), ϵ has the form

$$\epsilon = \sqrt{\epsilon^2_{\mathrm{stat}} + \epsilon^2_{\mathrm{sys}}}, \tag{3.8}$$

where the statistical uncertainties are

$$\epsilon^2_{\mathrm{stat}} = 6.25\left[\epsilon^2_{\log f} + \beta^2\epsilon^2_{\log \sigma} + \epsilon^2_\beta(\log\sigma)^2 + \epsilon^2_\gamma\right] + \left(\frac{\partial \mu_{\mathrm{th}}}{\partial z}\right)^2 \epsilon_z^2. \tag{3.9}$$

Following González-Morán et al. (2019) we do not account for systematic uncertainties in our analysis, so the uncertainty on the H II G measurements consists entirely of the statistical uncertainty (so that $\epsilon = \epsilon_{\mathrm{stat}}$).[6] The reader should also note here that although the theoretical statistical uncertainty depends our cosmological model parameters (through the theoretical

[6] A systematic error budget for H II G data is available in the literature, however; see Chávez et al. (2016).

distance modulus $\mu_{\rm th} = \mu_{\rm th}(\mathbf{p}, z)$), the effect of this model-dependence on the parameter constraints is negligible for the current data.[7]

For $H(z)$, the likelihood function is

$$\mathscr{L}_{\rm H} = e^{-\chi^2_{\rm H}/2}, \tag{3.10}$$

where

$$\chi^2_{\rm H}(\mathbf{p}) = \sum_{i=1}^{31} \frac{[H_{\rm th}(\mathbf{p}, z_i) - H_{\rm obs}(z_i)]^2}{\epsilon_i^2}, \tag{3.11}$$

and ϵ_i is the uncertainty of $H_{\rm obs}(z_i)$.

For the BAO data, the likelihood function is

$$\mathscr{L}_{\rm BAO} = e^{-\chi^2_{\rm BAO}/2}, \tag{3.12}$$

and for the uncorrelated BAO data (lines 7-9 in Table 3.1) the χ^2 function takes the form

$$\chi^2_{\rm BAO}(\mathbf{p}) = \sum_{i=1}^{3} \frac{[A_{\rm th}(\mathbf{p}, z_i) - A_{\rm obs}(z_i)]^2}{\epsilon_i^2}, \tag{3.13}$$

where $A_{\rm th}$ and $A_{\rm obs}$ are, respectively, the theoretical and observational quantities as listed in Table 3.1, and ϵ_i corresponds to the uncertainty of $A_{\rm obs}(z_i)$. For the correlated BAO data, the χ^2 function takes the form

$$\chi^2_{\rm BAO}(\mathbf{p}) = [A_{\rm th}(\mathbf{p}) - A_{\rm obs}(z_i)]^T \mathbf{C}^{-1} [A_{\rm th}(\mathbf{p}) - A_{\rm obs}(z_i)], \tag{3.14}$$

where superscripts T and -1 denote the transpose and inverse of the matrices, respectively.

[7] In contrast to our definition of χ^2 in eq. (3.7), González-Morán et al. (2019) defined an H_0-independent χ^2 function in their eq. (27) and weighted this χ^2 function by $1/\epsilon^2_{\rm stat}$ (where $\epsilon^2_{\rm stat}$ is given by their eq. (15)) which we do not do. This procedure is discussed in the literature (Fernández Arenas et al., 2018; Melnick et al., 2017), and when we use it we find that it leads to a reduced χ^2 identical to that given in González-Morán et al. (2019) (being less than 2 but greater than 1) without having a noticeable effect on the shapes or peak locations of our posterior likelihoods (hence providing very similar best-fitting values and error bars of the cosmological model parameters). As discussed below, with our χ^2 definition we find reduced χ^2 values ~ 2.75. González-Morán et al. (2019) note that an accounting of systematic uncertainties could decrease the reduced χ^2 values towards unity.

The covariance matrix $\mathbf{C}$ for the BAO data, taken from Alam et al. (2017), is given in eq. (20) of Ryan et al. (2019), while for the BAO data from de Sainte Agathe et al. (2019),

$$\mathbf{C} = \begin{bmatrix} 0.0841 & -0.183396 \\ -0.183396 & 3.4596 \end{bmatrix}. \tag{3.15}$$

For QSO, the likelihood function is

$$\mathscr{L}_{\rm QSO} = e^{-\chi^2_{\rm QSO}/2}, \tag{3.16}$$

and the χ^2 function takes the form

$$\chi^2_{\rm QSO}(\mathbf{p}) = \sum_{i=1}^{120} \left[\frac{\theta_{\rm th}(\mathbf{p}, z_i) - \theta_{\rm obs}(z_i)}{\epsilon_i + 0.1\theta_{\rm obs}(z_i)} \right]^2, \tag{3.17}$$

where $\theta_{\rm th}(\mathbf{p}, z_i)$ and $\theta_{\rm obs}(z_i)$ are theoretical and observed values of the angular size at redshift z_i, respectively, and ϵ_i is the uncertainty of $\theta_{\rm obs}(z_i)$ (see Ryan et al., 2019 for more details).

For the joint analysis of these data, the total likelihood function is obtained by multiplying the individual likelihood functions (that is, eqs. (3.6), (3.10), (3.12), and (3.16)) together in various combinations. For example, for $H(z)$, BAO, and QSO data, we have

$$\mathscr{L} = \mathscr{L}_{\rm H}\mathscr{L}_{\rm BAO}\mathscr{L}_{\rm QSO}. \tag{3.18}$$

We also use the Akaike Information Criterion (AIC) and Bayesian Information Criterion (BIC) to compare the goodness of fit of models with different numbers of parameters, where

$$AIC = -2\ln\mathscr{L}_{\rm max} + 2n \equiv \chi^2_{\rm min} + 2n, \tag{3.19}$$

and

$$BIC = -2\ln\mathscr{L}_{\rm max} + n\ln N \equiv \chi^2_{\rm min} + n\ln N. \tag{3.20}$$

In these two equations, $\mathscr{L}_{\rm max}$ refers to the maximum value of the given likelihood function, $\chi^2_{\rm min}$ refers to the corresponding minimum χ^2 value, n is the number of parameters of the given model, and N is the number of data points (for example for H II G we have $N = 153$, etc.).

3.4 Results

3.4.1 H II G constraints

We present the posterior one-dimensional (1D) probability distributions and two-dimensional (2D) confidence regions of the cosmological parameters for the six flat and non-flat models in Figs. 3.1–3.6, in gray. The unmarginalized best-fitting parameter values are listed in Table 3.2, along with the corresponding χ^2, AIC, BIC, and degrees of freedom ν (where $\nu \equiv N - n$). The marginalized best-fitting parameter values and uncertainties ($\pm 1\sigma$ error bars or 2σ limits) are given in Table 3.3.[8]

From the fit to the H II G data, we see that most of the probability lies in the part of the parameter space corresponding to currently-accelerating cosmological expansion (see the gray contours in Figs. 3.1–3.6). This means that the H II G data favor currently-accelerating cosmological expansion,[9] in agreement with supernova Type Ia, BAO, $H(z)$, and other cosmological data.

From the H II G data, we find that the constraints on the non-relativistic matter density parameter Ω_{m0} are consistent with other estimates, ranging between a high of $0.300^{+0.106}_{-0.083}$ (flat XCDM) and a low of $\Omega_{\rm m_0} = 0.210^{+0.043}_{-0.092}$ (flat ϕCDM).

The H II G data constraints on H_0 in Table 3.3 are consistent with the estimate of $H_0 = 71.0 \pm 2.8({\rm stat.}) \pm 2.1({\rm sys.})$ km s^{-1} Mpc^{-1}made by Fernández Arenas et al. (2018) based on a compilation of H II G measurements that differs from what we have used here. The H II G H_0 constraints listed in Table 3.3 are also consistent with other recent measurements of H_0, being

[8] We plot these figures by using the Python package GetDist (Lewis, 2019), which we also use to compute the central values (posterior means) and uncertainties of the cosmological parameters listed in Table 3.3.

[9] Although a full accounting of the systematic uncertainties in the H II G data could weaken this conclusion.

between 0.90σ (flat XCDM) and 1.56σ (non-flat ϕCDM) lower than the recent local expansion rate measurement of $H_0 = 74.03 \pm 1.42$ km s^{-1} Mpc^{-1}(Riess et al., 2019),[10] and between 0.78σ (non-flat ϕCDM) and 1.13σ (flat XCDM) higher than the median statistics estimate of $H_0 = 68 \pm 2.8$ km s^{-1} Mpc^{-1}(Chen & Ratra, 2011),[11] with our measurements ranging from a low of $H_0 = 70.60^{+1.68}_{-1.84}$ km s^{-1} Mpc^{-1}(non-flat ϕCDM) to a high of $H_0 = 71.85 \pm 1.96$ km s^{-1} Mpc^{-1}(flat XCDM).

As for spatial curvature, from the marginalized 1D likelihoods in Table 3.3, for non-flat ΛCDM, non-flat XCDM, and non-flat ϕCDM, we measure $\Omega_{k_0} = 0.094^{+0.237}_{-0.363}$,[12] $\Omega_{k_0} = 0.011^{+0.457}_{-0.460}$, and $\Omega_{k_0} = 0.291^{+0.348}_{-0.113}$, respectively. From the marginalized likelihoods, we see that non-flat ΛCDM and XCDM models are consistent with all three spatial geometries, while non-flat ϕCDM favors the open case at 2.58σ. However, this seems to be a little odd, especially for non-flat ϕCDM, considering their unmarginalized best-fitting Ω_{k_0}'s are all negative (see Table 3.2).

The fits to the H II G data are consistent with dark energy being a cosmological constant but don't rule out dark energy dynamics. For flat (non-flat) XCDM, $w_X = -1.180^{+0.560}_{-0.330}$ ($w_X = -1.125^{+0.537}_{-0.321}$), which are both within 1σ of $w_X = -1$. For flat (non-flat) ϕCDM, 2σ upper limits of α are $\alpha < 2.784$ ($\alpha < 4.590$), with the 1D likelihood functions, in both cases, peaking at $\alpha = 0$.

Current H II G data do not provide very restrictive constraints on cosmological model parameters, but when used in conjunction with other cosmological data they can help tighten the constraints.

[10] Note that other local expansion rate measurements are slightly lower with slightly larger error bars (Dhawan et al., 2018; Fernández Arenas et al., 2018; Freedman et al., 2019, 2020; Rameez & Sarkar, 2021; Rigault et al., 2015; Zhang et al., 2017).

[11] This is consistent with earlier median statistics estimates (Chen et al., 2003; Gott et al., 2001) and also with a number of recent H_0 measurements (Chen et al., 2017; Cuceu et al., 2019; DES Collaboration, 2018; Domínguez et al., 2019; Gómez-Valent & Amendola, 2018; Haridasu et al., 2018; Lin & Ishak, 2021; Martinelli & Tutusaus, 2019; Planck Collaboration, 2020; Schöneberg et al., 2019; Zeng & Yan, 2019; Zhang, 2018; Zhang & Huang, 2019).

[12] Since $\Omega_{k_0} = 1 - \Omega_{m_0} - \Omega_\Lambda$, in the non-flat ΛCDM model analysis we replace Ω_Λ with Ω_{k_0} in the MCMC chains of $\{H_0, \Omega_{m_0}, \Omega_\Lambda\}$ to obtain new chains of $\{H_0, \Omega_{m_0}, \Omega_{k_0}\}$ and so measure Ω_{k_0} central values and uncertainties. A similar procedure, based on $\Omega_\Lambda = 1 - \Omega_{m_0}$, is used to measure Ω_Λ in the flat ΛCDM model.

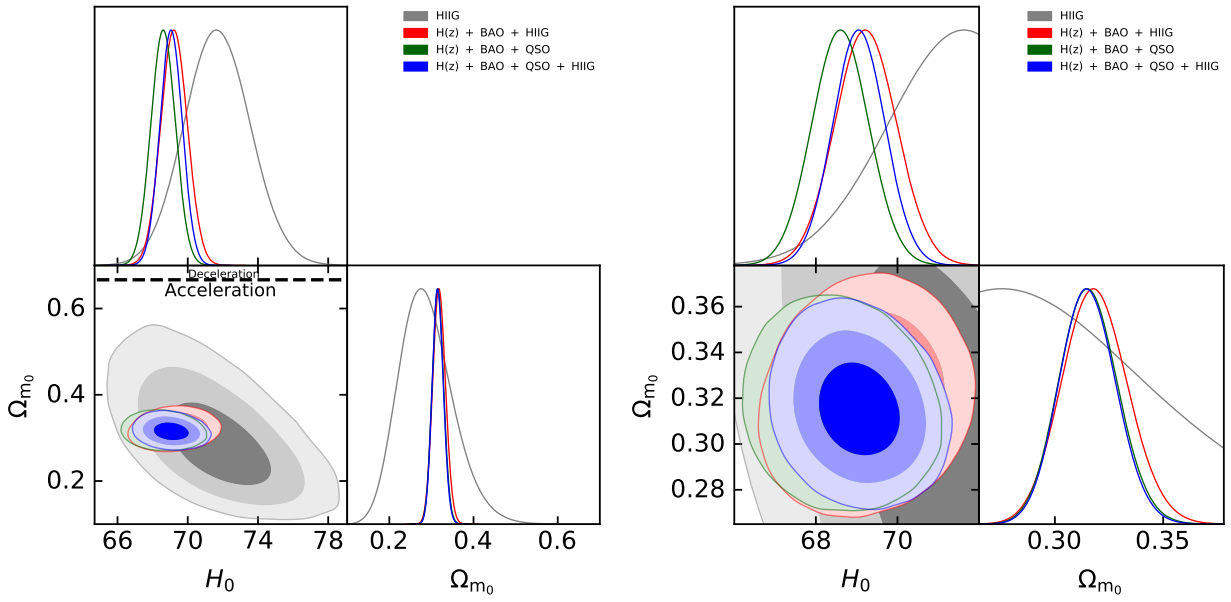

(a) Full parameter range

(b) Zoom in

Figure 3.1: 1σ, 2σ, and 3σ confidence contours for flat ΛCDM, where the right panel is the comparison zoomed in. The black dotted line is the zero-acceleration line, which divides the parameter space into regions associated with currently accelerated (below) and currently decelerated (above) cosmological expansion.

3.4.2 $H(z)$, BAO, and H II G (HzBH) constraints

The H II G constraints discussed in the previous subsection are consistent with constraints from most other cosmological data, so it is appropriate to use the H II G data in conjunction with other data to constrain parameters. In this subsection we perform a full analysis of $H(z)$, BAO, and H II G (HzBH) data and derive tighter constraints on cosmological parameters.

The 1D probability distributions and 2D confidence regions of the cosmological parameters for the six flat and non-flat models are shown in Figs. 3.1–3.6, in red. The best-fitting results and uncertainties are listed in Tables 3.2 and 3.3.

When we fit our cosmological models to the HzBH data we find that the measured values of the matter density parameter Ω_{m0} fall within a narrower range in comparison to the H II G only case, being between 0.314 ± 0.015 (non-flat ΛCDM) and $0.323^{+0.014}_{-0.016}$ (flat ϕCDM).

Similarly, the measured values of H_0 also fall within a narrower range when our models are fit to the HzBH data combination (and are in better agreement with the median statistics

Table 3.2: Unmarginalized best-fitting parameter values for all models from various combinations of data.

Model	Data set	Ω_{m_0}	Ω_Λ	Ω_{k_0}	w_X	α	H_0[a]	χ^2	AIC	BIC	ν
Flat ΛCDM	H II G	0.276	0.724	—	—	—	71.81	410.75	414.75	420.81	151
	$H(z)$ + BAO + H II G	0.318	0.682	—	—	—	69.22	434.29	438.29	444.84	193
	$H(z)$ + BAO + QSO	0.315	0.685	—	—	—	68.61	372.88	376.88	383.06	160
	$H(z)$ + BAO + QSO + H II G	0.315	0.685	—	—	—	69.06	786.50	790.50	798.01	313
Non-flat ΛCDM	H II G	0.312	0.998	−0.310	—	—	72.35	410.44	416.44	425.53	150
	$H(z)$ + BAO + H II G	0.313	0.718	−0.031	—	—	70.24	433.38	439.38	449.19	192
	$H(z)$ + BAO + QSO	0.311	0.665	0.024	—	—	68.37	372.82	378.82	388.08	159
	$H(z)$ + BAO + QSO + H II G	0.309	0.716	−0.025	—	—	69.82	785.79	791.79	803.05	312
Flat XCDM	H II G	0.249	—	—	−0.892	—	71.65	410.72	416.72	425.82	150
	$H(z)$ + BAO + H II G	0.314	—	—	−1.044	—	69.94	433.99	439.99	449.81	192
	$H(z)$ + BAO + QSO	0.322	—	—	−0.890	—	66.62	371.95	377.95	387.21	159
	$H(z)$ + BAO + QSO + H II G	0.311	—	—	−1.045	—	69.80	786.19	792.19	803.45	312
Non-flat XCDM	H II G	0.104	—	−0.646	−0.712	—	72.61	407.69	415.69	427.81	149
	$H(z)$ + BAO + H II G	0.322	—	−0.117	−0.878	—	66.67	432.85	440.85	453.94	191
	$H(z)$ + BAO + QSO	0.322	—	−0.112	−0.759	—	65.80	370.68	378.68	391.03	158
	$H(z)$ + BAO + QSO + H II G	0.310	—	−0.048	−0.957	—	69.53	785.70	793.70	808.71	311
Flat ϕCDM	H II G	0.255	—	—	—	0.261	71.70	410.70	416.70	425.80	150
	$H(z)$ + BAO + H II G	0.318	—	—	—	0.011	69.09	434.36	440.36	450.18	192
	$H(z)$ + BAO + QSO	0.321	—	—	—	0.281	66.82	372.05	378.05	387.31	159
	$H(z)$ + BAO + QSO + H II G	0.315	—	—	—	0.012	68.95	786.58	792.58	803.84	312
Non-flat ϕCDM	H II G	0.114	—	−0.437	—	2.680	72.14	409.91	417.91	430.03	149
	$H(z)$ + BAO + H II G	0.321	—	−0.132	—	0.412	69.69	432.75	440.75	453.84	191
	$H(z)$ + BAO + QSO	0.317	—	−0.106	—	0.778	66.27	370.83	378.83	391.18	158
	$H(z)$ + BAO + QSO + H II G	0.310	—	−0.054	—	0.150	69.40	785.65	793.65	808.66	311

[a] km s^{-1} Mpc^{-1}.

Table 3.3: One-dimensional marginalized best-fitting parameter values and uncertainties ($\pm 1\sigma$ error bars or 2σ limits) for all models from various combinations of data.

Model	Data set	Ω_{m_0}	Ω_Λ	Ω_{k_0}	w_X	α	H_0[a]
Flat ΛCDM	HIIG	$0.289^{+0.053}_{-0.071}$	—	—	—	—	71.70 ± 1.83
	$H(z)$ + BAO + HIIG	$0.319^{+0.014}_{-0.015}$	—	—	—	—	69.23 ± 0.74
	$H(z)$ + BAO + QSO	$0.316^{+0.013}_{-0.014}$	—	—	—	—	68.60 ± 0.68
	$H(z)$ + BAO + QSO + HIIG	$0.315^{+0.013}_{-0.012}$	—	—	—	—	$69.06^{+0.63}_{-0.62}$
Non-flat ΛCDM	HIIG	$0.275^{+0.081}_{-0.078}$	> 0.501[b]	$0.094^{+0.237}_{-0.363}$	—	—	$71.50^{+1.80}_{-1.81}$
	$H(z)$ + BAO + HIIG	0.314 ± 0.015	$0.714^{+0.054}_{-0.049}$	$-0.029^{+0.049}_{-0.048}$	—	—	70.21 ± 1.33
	$H(z)$ + BAO + QSO	$0.313^{+0.013}_{-0.015}$	$0.658^{+0.069}_{-0.060}$	$0.029^{+0.056}_{-0.063}$	—	—	68.29 ± 1.47
	$H(z)$ + BAO + QSO + HIIG	0.310 ± 0.013	$0.711^{+0.053}_{-0.048}$	$-0.021^{+0.044}_{-0.048}$	—	—	$69.76^{+1.12}_{-1.11}$
Flat XCDM	HIIG	$0.300^{+0.106}_{-0.083}$	—	—	$-1.180^{+0.560}_{-0.330}$	—	71.85 ± 1.96
	$H(z)$ + BAO + HIIG	$0.315^{+0.016}_{-0.017}$	—	—	$-1.052^{+0.092}_{-0.082}$	—	70.05 ± 1.54
	$H(z)$ + BAO + QSO	$0.322^{+0.015}_{-0.016}$	—	—	$-0.911^{+0.122}_{-0.098}$	—	$66.98^{+1.95}_{-2.30}$
	$H(z)$ + BAO + QSO + HIIG	0.312 ± 0.014	—	—	$-1.053^{+0.091}_{-0.082}$	—	69.90 ± 1.48
Non-flat XCDM	HIIG	$0.275^{+0.084}_{-0.125}$	—	$0.011^{+0.457}_{-0.460}$	$-1.125^{+0.537}_{-0.321}$	—	$71.71^{+2.07}_{-2.08}$
	$H(z)$ + BAO + HIIG	0.318 ± 0.019	—	$-0.082^{+0.135}_{-0.119}$	$-0.958^{+0.219}_{-0.098}$	—	$69.83^{+1.50}_{-1.62}$
	$H(z)$ + BAO + QSO	0.320 ± 0.015	—	$-0.078^{+0.124}_{-0.112}$	$-0.826^{+0.185}_{-0.088}$	—	$66.29^{+1.90}_{-2.35}$
	$H(z)$ + BAO + QSO + HIIG	$0.309^{+0.015}_{-0.014}$	—	-0.025 ± 0.092	$-1.022^{+0.208}_{-0.104}$	—	$69.68^{+1.49}_{-1.64}$
Flat ϕCDM	HIIG	$0.210^{+0.043}_{-0.092}$	—	—	—	< 2.784	$71.23^{+1.79}_{-1.80}$
	$H(z)$ + BAO + HIIG	$0.323^{+0.014}_{-0.016}$	—	—	—	< 0.411	$68.36^{+1.05}_{-0.86}$
	$H(z)$ + BAO + QSO	$0.324^{+0.014}_{-0.015}$	—	—	—	$0.460^{+0.116}_{-0.440}$	$66.03^{+1.79}_{-1.42}$
	$H(z)$ + BAO + QSO + HIIG	0.319 ± 0.013	—	—	—	< 0.411	$68.18^{+0.97}_{-0.75}$
Non-flat ϕCDM	HIIG	< 0.321	—	$0.291^{+0.348}_{-0.113}$	—	< 4.590	$70.60^{+1.68}_{-1.84}$
	$H(z)$ + BAO + HIIG	$0.322^{+0.015}_{-0.016}$	—	$-0.153^{+0.114}_{-0.079}$	—	$0.538^{+0.151}_{-0.519}$	69.39 ± 1.37
	$H(z)$ + BAO + QSO	$0.319^{+0.013}_{-0.015}$	—	$-0.103^{+0.111}_{-0.091}$	—	$0.854^{+0.379}_{-0.594}$	$65.94^{+1.75}_{-1.73}$
	$H(z)$ + BAO + QSO + HIIG	$0.313^{+0.012}_{-0.014}$	—	$-0.098^{+0.082}_{-0.061}$	—	< 0.926	68.83 ± 1.23

[a] km s^{-1} Mpc^{-1}.

[b] This is the 1σ lower limit. The 2σ lower limit is set by the prior, and is not shown here.

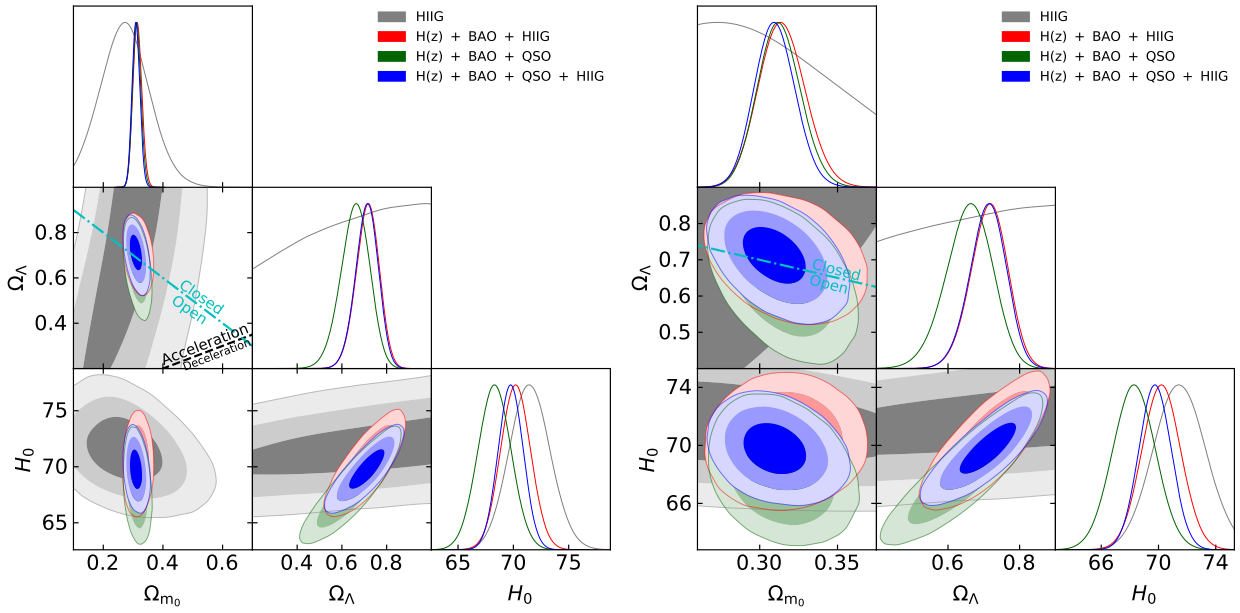

(a) Full parameter range

(b) Zoom in

Figure 3.2: Same as Fig. 3.1 but for non-flat ΛCDM. The cyan dash-dot line represents the flat case, with closed spatial hypersurfaces to the upper right. The black dotted line is the zero-acceleration line, which divides the parameter space into regions associated with currently accelerated (above left) and currently decelerated (below right) cosmological expansion.

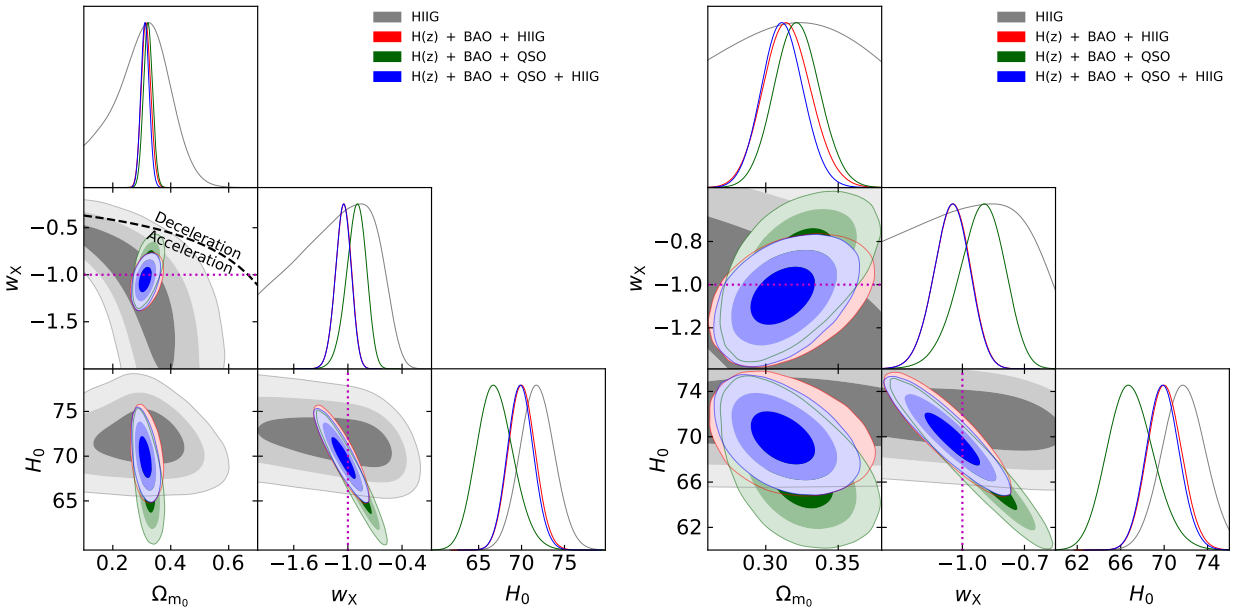

(a) Full parameter range

(b) Zoom in

Figure 3.3: 1σ, 2σ, and 3σ confidence contours for flat XCDM. The black dotted line is the zero-acceleration line, which divides the parameter space into regions associated with currently accelerated (below left) and currently decelerated (above right) cosmological expansion. The magenta lines denote $w_X = -1$, i.e. the flat ΛCDM model.

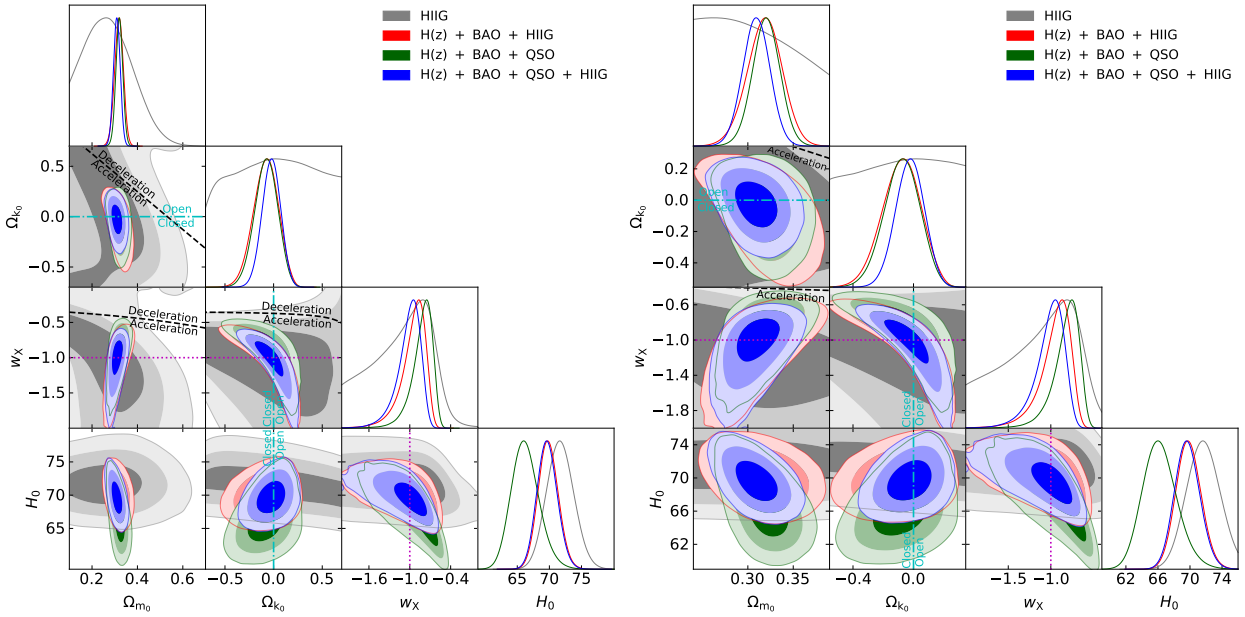

(a) Full parameter range

(b) Zoom in

Figure 3.4: Same as Fig. 3.3 but for non-flat XCDM, where the zero acceleration lines in each of the three subpanels are computed for the third cosmological parameter set to the H IIG data only best-fitting values listed in Table 3.2. Currently-accelerated cosmological expansion occurs below these lines. The cyan dash-dot lines represent the flat case, with closed spatial hypersurfaces either below or to the left. The magenta lines indicate $w_X = -1$, i.e. the non-flat ΛCDM model.

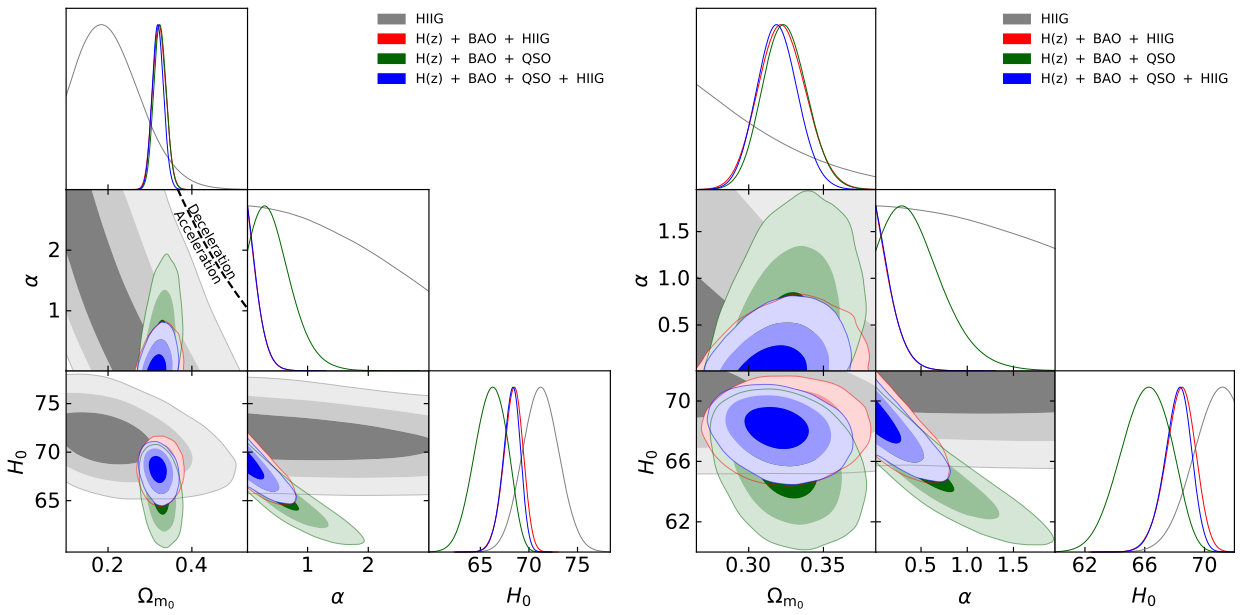

(a) Full parameter range

(b) Zoom in

Figure 3.5: 1σ, 2σ, and 3σ confidence contours for flat ϕCDM. The black dotted zero-acceleration line splits the parameter space into regions of currently accelerated (below left) and currently decelerated (above right) cosmological expansion. The $\alpha = 0$ axis is the flat ΛCDM model.

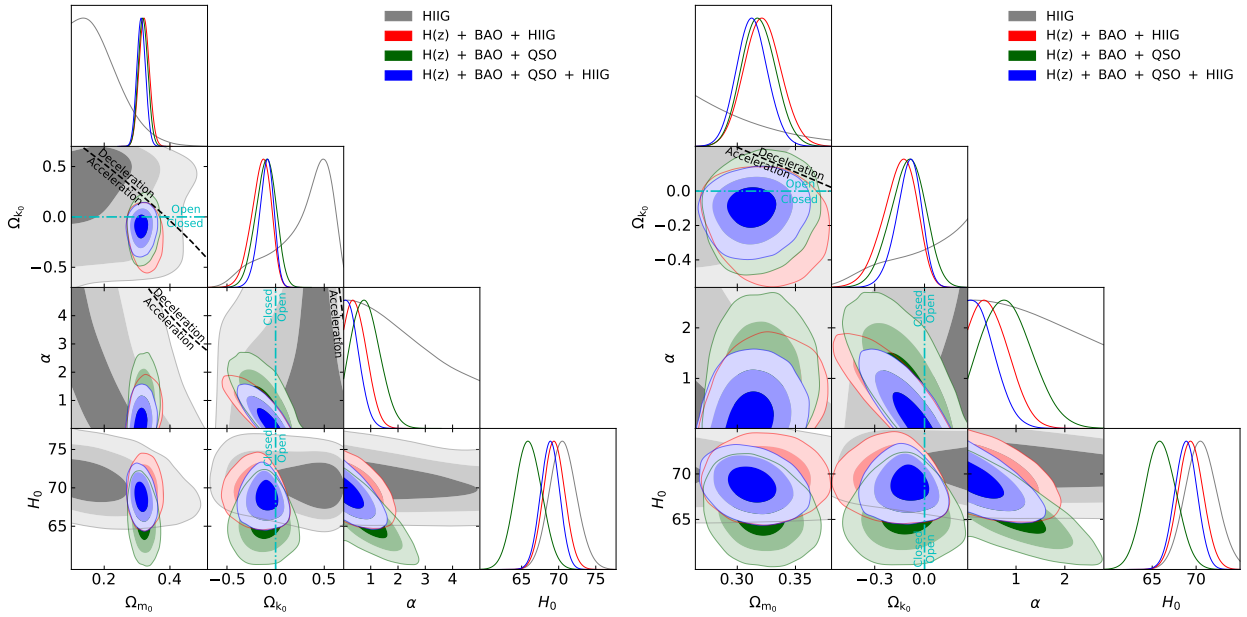

(a) Full parameter range

(b) Zoom in

Figure 3.6: Same as Fig. 3.5 but for non-flat ϕCDM, where the zero-acceleration lines in each of the subpanels are computed for the third cosmological parameter set to the H IIG data only best-fitting values listed in Table 3.2. Currently-accelerating cosmological expansion occurs below these lines. The cyan dash-dot lines represent the flat case, with closed spatial geometry either below or to the left. The $\alpha = 0$ axis is the non-flat ΛCDM model.

estimate of H_0 from Chen & Ratra, 2011 than with the local measurement carried out by Riess et al., 2019; this is because the $H(z)$ and BAO data favor a lower H_0 value) being between $H_0 = 68.36^{+1.05}_{-0.86}$ km s^{-1} Mpc^{-1}(flat ϕCDM) and 70.21 ± 1.33 km s^{-1} Mpc^{-1}(non-flat ΛCDM). We assume that the tension between early- and late-Universe measurements of H_0 is not a major issue here, because the 2D and 1D contours in Fig. 3.1 overlap, and so we compute a combined H_0 value (but if one is concerned about the early- vs late-Universe H_0 tension then one should not compare our combined-data H_0's here, and in Secs. 3.4.3 and 3.4.4, directly to the measurements of Riess et al., 2019 or of Planck Collaboration, 2020).

In contrast to the H II G only cases, when fit to the HzBH data combination the non-flat models mildly favor closed spatial hypersurfaces. This is because the $H(z)$ and BAO data mildly favor closed spatial hypersurfaces; see, e.g. Park & Ratra (2019b) and Ryan et al. (2019). For non-flat ΛCDM, non-flat XCDM, and non-flat ϕCDM, we find $\Omega_{k_0} = -0.029^{+0.049}_{-0.048}$, $\Omega_{k_0} = -0.082^{+0.135}_{-0.119}$, and $\Omega_{k_0} = -0.153^{+0.114}_{-0.079}$, respectively, with the non-flat ϕCDM model favoring closed spatial hypersurfaces at 1.34σ.

The fit to the HzBH data combination produces weaker evidence for dark energy dynamics (in comparison to the H II G only case) with tighter error bars on the measured values of w_X and α. For flat (non-flat) XCDM, $w_X = -1.052^{+0.092}_{-0.082}$ ($w_X = -0.958^{+0.219}_{-0.098}$), with $w_X = -1$ still being within the 1σ range. For flat (non-flat) ϕCDM, $\alpha < 0.411$ ($\alpha = 0.538^{+0.151}_{-0.519}$), where the former is peaked at $\alpha = 0$ but for the latter, $\alpha = 0$ is just out of the 1σ range.

3.4.3 $H(z)$, BAO, and QSO (HzBQ) constraints

The $H(z)$, BAO, and QSO (HzBQ) data combination has previously been studied (Ryan et al., 2019). Relative to that analysis, we use an updated BAO data compilation, a more accurate formula for r_s, and the MCMC formalism (instead of the grid-based χ^2 approach); consequently the parameter constraints derived here slightly differ from those of Ryan et al. (2019).

The 1D probability distributions and 2D confidence regions of the cosmological parameters for all models are presented in Figs. 3.1–3.6, in green. The corresponding best-fitting

results and uncertainties are listed in Tables 3.2 and 3.3.

The measured values of Ω_{m0} here fall within a similar range to the range quoted in the last subsection, being between $0.313^{+0.013}_{-0.015}$ (non-flat ΛCDM) and $0.324^{+0.014}_{-0.015}$ (flat ϕCDM). This range is larger than, but still consistent with, the range of Ω_{m0} reported in Ryan et al. (2019), where the same models are fit to the HzBQ data combination.

The H_0 measurements in this case fall within a broader range than in the HzBH case, being between $65.94^{+1.75}_{-1.73}$ km s^{-1} Mpc^{-1}(non-flat ϕCDM) and 68.60 ± 0.68 km s^{-1} Mpc^{-1}(flat ΛCDM). In addition, they are lower than the corresponding measurements in the HzBH cases, and are in better agreement with the median statistics (Chen & Ratra, 2011) estimate of H_0 than with what is measured from the local expansion rate (Riess et al., 2019). Compared with Ryan et al. (2019), the central values are lower except for the non-flat XCDM model.

For non-flat ΛCDM, non-flat XCDM, and non-flat ϕCDM, we measure $\Omega_{k_0} = 0.029^{+0.056}_{-0.063}$, $\Omega_{k_0} = -0.078^{+0.124}_{-0.112}$, and $\Omega_{k_0} = -0.103^{+0.111}_{-0.091}$, respectively. These results are consistent with their unmarginalized best-fittings (see Table 3.2), where the best-fitting to the non-flat ΛCDM model favors open spatial hypersurfaces, and the best-fittings to the non-flat XCDM parametrization and the non-flat ϕCDM model both favor closed spatial hypersurfaces. Note that the central values are larger than those of Ryan et al. (2019), especially for non-flat ΛCDM (positive instead of negative). In all three models the constraints are consistent with flat spatial hyperfurfaces.

The fit to the HzBQ data combination provides slightly stronger evidence for dark energy dynamics than does the fit to the HzBH data combination. For flat (non-flat) XCDM, $w_{\rm X} = -0.911^{+0.122}_{-0.098}$ ($w_{\rm X} = -0.826^{+0.185}_{-0.088}$), with the former barely within 1σ of $w_{\rm X} = -1$ and the latter almost 2σ away from $w_{\rm X} = -1$. For flat (non-flat) ϕCDM, $\alpha = 0.460^{+0.116}_{-0.440}$ ($\alpha = 0.854^{+0.379}_{-0.594}$), with the former 1.05σ and the latter 1.44σ away from the $\alpha = 0$ cosmological constant. In comparison with Ryan et al. (2019), central values of $w_{\rm X}$ are larger and smaller for flat and non-flat XCDM models, respectively, and that of α are larger for both flat and non-flat ϕCDM models.

3.4.4 $H(z)$, BAO, QSO, and H II G (HzBQH) constraints

Comparing the results of the previous two subsections, we see that when used in conjunction with $H(z)$ and BAO data, the QSO data result in tighter constraints on Ω_{m_0}, Ω_{k_0} (in non-flat XCDM), w_X (in non-flat XCDM), and H_0 (in flat ΛCDM), while the H II G data result in tighter constraints on H_0 (except for flat ΛCDM), Ω_Λ, Ω_{k_0}(in non-flat ΛCDM and ϕCDM), w_X (in flat XCDM), and α. Consequently, it is useful to derive constraints from an analysis of the combined $H(z)$, BAO, QSO, and H II G (HzBQH) data. We present the results of such an analysis in this subsection.

In Figs. 3.1–3.6, we present the 1D probability distributions and 2D confidence constraints for the HzBQH cases in blue. Tables 3.2 and 3.3 list the best-fitting results and uncertainties.

It is interesting that the best-fitting values of Ω_{m_0} in this case are lower compared with both the HzBQ and the HzBH results, being between $0.309^{+0.015}_{-0.014}$ (non-flat XCDM) and 0.319 ± 0.013 (flat ϕCDM). The best-fitting values of H_0 are higher than the HzBQ cases and have central values that are closer to those of the HzBH cases, but are still in better agreement with the lower median statistics estimate of H_0 (Chen & Ratra, 2011) than the higher local expansion rate measurement of H_0 (Riess et al., 2019), being between $68.18^{+0.97}_{-0.75}$ km s^{-1} Mpc^{-1}(flat ϕCDM) and 69.90 ± 1.48 km s^{-1} Mpc^{-1}(flat XCDM).

For non-flat ΛCDM, non-flat XCDM, and non-flat ϕCDM, we measure $\Omega_{k_0} = -0.021^{+0.044}_{-0.048}$, $\Omega_{k_0} = -0.025 \pm 0.092$, and $\Omega_{k_0} = -0.098^{+0.082}_{-0.061}$, respectively. For non-flat ΛCDM and XCDM, the measured values of the curvature energy density parameter are within 0.48σ and 0.27σ of $\Omega_{k_0} = 0$, respectively, while the non-flat ϕCDM model favors a closed geometry with an Ω_{k_0} that is 1.20σ away from zero.

There is not much evidence in support of dark energy dynamics in the HzBQH case, with Λ consistent with this data combination. For flat (non-flat) XCDM, $w_X = -1.053^{+0.091}_{-0.082}$ ($w_X = -1.022^{+0.208}_{-0.104}$). For flat (non-flat) ϕCDM, the 2σ upper limits are $\alpha < 0.411$ ($\alpha < 0.926$), which indicates that $\alpha = 0$ or Λ is consistent with these data.

Table 3.4: $\Delta\chi^2$, ΔAIC, ΔBIC, and $\chi^2_{\rm min}/\nu$ values.

Quantity	Data set	Flat ΛCDM	Non-flat ΛCDM	Flat XCDM	Non-flat XCDM	Flat ϕCDM	Non-flat ϕCDM
$\Delta\chi^2$	H II G	3.06	2.75	3.03	0.00	3.01	2.22
	$H(z)$ + BAO + H II G	1.54	0.63	1.24	0.10	1.61	0.00
	$H(z)$ + BAO + QSO	2.20	2.14	1.27	0.00	1.37	0.15
	$H(z)$ + BAO + QSO + H II G	0.85	0.14	0.54	0.05	0.93	0.00
ΔAIC	H II G	0.00	1.69	1.97	0.94	1.95	3.16
	$H(z)$ + BAO + H II G	0.00	1.09	1.70	2.56	2.07	2.46
	$H(z)$ + BAO + QSO	0.00	1.94	1.07	1.80	1.17	1.95
	$H(z)$ + BAO + QSO + H II G	0.00	1.29	1.69	3.20	2.08	3.15
ΔBIC	H II G	0.00	4.72	5.01	7.00	4.99	9.22
	$H(z)$ + BAO + H II G	0.00	4.35	4.97	9.10	5.34	9.00
	$H(z)$ + BAO + QSO	0.00	5.02	4.15	7.97	4.25	8.12
	$H(z)$ + BAO + QSO + H II G	0.00	5.04	5.44	10.70	5.83	10.65
$\chi^2_{\rm min}/\nu$	H II G	2.72	2.74	2.74	2.74	2.74	2.75
	$H(z)$ + BAO + H II G	2.25	2.26	2.26	2.27	2.26	2.27
	$H(z)$ + BAO + QSO	2.33	2.34	2.34	2.35	2.34	2.35
	$H(z)$ + BAO + QSO + H II G	2.51	2.52	2.52	2.53	2.52	2.53

3.4.5 Model comparison

From Table 3.4, we see that the reduced χ^2 for all models is relatively large (being between 2.25 and 2.75). This could probably be attributed to underestimated systematic uncertainties in the H II G data.[13] This is suggested by González-Morán et al. (2019), who also found relatively large values of χ^2/ν in their cosmological model fits to the H II G data (though not as large as ours, because they compute a different χ^2, as explained in footnote 7 in Section 3.3). They note that an additional systematic uncertainty of ~ 0.22 could bring their χ^2/ν down to ~ 1. As mentioned previously, we do not account for H II G systematic uncertainties in our analysis.

One thing that is clear, regardless of the absolute size of H II G or QSO systematics (and ignoring the large values of χ^2/ν), is that the flat ΛCDM model remains the most favored model among the six models we studied, based on the AIC and BIC criteria (see Table 3.4).[14] In Table 3.4 we define $\Delta\chi^2$, ΔAIC, and ΔBIC, respectively, as the differences between the values of the χ^2, AIC, and BIC associated with a given model and their corresponding

[13] Underestimated systematic uncertainties might also explain the large reduced χ^2 of QSO data (Ryan et al., 2019).

[14] Note that based on the $\Delta\chi^2$ results of Table 3.4 non-flat XCDM has the minimum χ^2 in the H II G and HzBQ cases, whereas non-flat ϕCDM has the minimum χ^2 for the HzBH and HzBQH cases. The $\Delta\chi^2$ values do not, however, penalize a model for having more parameters.

minimum values among all models.

From the H IIG results for ΔAIC and ΔBIC listed in Table 3.4, we see that the evidence against non-flat ΛCDM, flat XCDM, and flat ϕCDM is weak (according to ΔAIC) and positive (according to ΔBIC) where, among these three models, the flat XCDM model is the least favored. The evidence against the non-flat XCDM model is weak regarding ΔAIC but strong based on ΔBIC, while the evidence against non-flat ϕCDM in this case is positive (ΔAIC) and strong (ΔBIC), respectively, with it being the least favored model overall.

Largely similar conclusions result from ΔAIC and ΔBIC values for the H IIG and HzBQ data. The exception is that the HzBQ ΔAIC value gives only weak evidence against non-flat ϕCDM, instead of the positive evidence against it from the H IIG ΔAIC value.

The HzBH and HzBQH values of ΔAIC and ΔBIC result in the following conclusions:

1) the evidence against both non-flat ΛCDM and flat XCDM is weak (HzBH) and positive (HzBQH) for ΔAIC and ΔBIC;

2) the evidence against flat ϕCDM is positive;

3) non-flat XCDM is the least favored model with non-flat ϕCDM doing almost as badly. ΔAIC gives positive evidence against non-flat XCDM and non-flat ϕCDM, while ΔBIC strongly disfavors (HzBH) and very strongly disfavors (HzBQH) both of these non-flat models.

3.5 Conclusions

In this paper, we have constrained cosmological parameters in six flat and non-flat cosmological models by analyzing a total of 315 observations, comprising 31 $H(z)$, 11 BAO, 120 QSO, and 153 H IIG measurements. The QSO angular size and H IIG apparent magnitude measurements are particularly noteworthy, as they reach to $z \sim 2.7$ and $z \sim 2.4$ respectively (somewhat beyond the highest $z \sim 2.3$ reached by BAO data) and into a much less studied area of redshift space. While the current H IIG and QSO data do not provide very restrictive constraints, they do tighten the limits when they are used in conjunction with BAO + $H(z)$ data.

By measuring cosmological parameters in a variety of cosmological models, we are able to draw some relatively model-independent conclusions (i.e. conclusions that do not differ significantly between the different models). Specifically, for the full data set (i.e the HzBQH data), we find quite restrictive constraints on Ω_{m0}, a reasonable summary perhaps being $\Omega_{\mathrm{m_0}} = 0.310 \pm 0.013$, in good agreement with many other recent estimates. H_0 is also fairly tightly constrained, with a reasonable summary perhaps being $H_0 = 69.5 \pm 1.2$ km s^{-1} Mpc^{-1}, which is in better agreement with the results of Chen & Ratra (2011) and Planck Collaboration (2020) than that of Riess et al. (2019). The HzBQH measurements are consistent with the standard spatially-flat ΛCDM model, but do not strongly rule out mild dark energy dynamics or a little spatial curvature energy density. More and better-quality H II G, QSO, and other data at $z \sim 2$–4 will significantly help to test these extensions.

Chapter 4

Cosmological constraints from higher-redshift gamma-ray burst, H II starburst galaxy, and quasar (and other) data

This chapter is based on Cao et al. (2021a). Figures and tables by Shulei Cao, from analyses conducted independently by Shulei Cao, Joseph Ryan, and Narayan Khadka.

4.1 Introduction

There is a large body of evidence indicating that the Universe recently transitioned from a decelerated to an accelerated phase of expansion (at redshift $z \sim 3/4$; see e.g. Farooq et al., 2017) and has been undergoing accelerated expansion ever since (for reviews, see e.g. Coley & Ellis, 2020; Martin, 2012; Ratra & Vogeley, 2008). In the standard model of cosmology, called the ΛCDM model (Peebles, 1984), the accelerated expansion is powered by a constant dark energy density (the cosmological constant, Λ). This model also assumes that spatial hypersurfaces are flat on cosmological scales, and that the majority of non-relativistic matter

in the Universe consists of cold dark matter (CDM).

Out of all the models that have been devised to explain the observed accelerated expansion of the Universe, the ΛCDM model is currently the most highly favored in terms of both observational data and theoretical parsimony (see e.g. eBOSS Collaboration, 2021; Farooq et al., 2017; Planck Collaboration, 2020; Scolnic et al., 2018). In spite of these virtues, however, there are some indications that the ΛCDM model may not tell the whole story. On the observational side, some workers have found evidence of discrepancies between the ΛCDM model and cosmological observations (Martinelli & Tutusaus, 2019; Riess, 2019) and on the theoretical side, the origin of Λ has yet to be explained in fundamental terms (e.g., Martin, 2012). One way to pin down the nature of dark energy is by studying its dynamics phenomenologically. It is possible that the dark energy density may evolve in time (Peebles & Ratra, 1988), and many dark energy models exhibiting this behavior have been proposed.

Cosmological models have largely been tested in the redshift range $0 \lesssim z \lesssim 2.3$, with baryon acoustic oscillation (BAO[1]) measurements probing the upper end of this range, and at $z \sim 1100$, using cosmic microwave background (CMB) anisotropy data. To determine the accuracy of our cosmological models, we also need to test them in the redshift range $2.3 \lesssim z \lesssim 1100$. Quasar angular size (QSO-AS), H II starburst galaxy (H IIG), quasar X-ray and UV flux (QSO-Flux), and gamma-ray burst (GRB) measurements are some of the handful of data available in this range. The main goal of this paper is, therefore, to examine the effect that QSO-AS, H IIG, and GRB data have on cosmological model parameter constraints, in combination with each other, and in combination with more well-known probes.[2]

Gamma-ray bursts are promising cosmological probes for two reasons. First, it is believed that they can be used as standardizable candles (Amati et al., 2002, 2008, 2009; Demianski & Piedipalumbo, 2011; Ghirlanda et al., 2004; Lamb & Reichart, 2000, 2001; Wang et al., 2015). Second, they cover a redshift range that is wider than most other commonly-used cosmological probes, having been observed up to $z \sim 8.2$ (Amati et al., 2008, 2009, 2019;

[1]In our BAO data analyses in this paper the sound horizon computation assumes a value for the current baryonic matter physical density parameter $\Omega_{b_0}h^2$, appropriate for the model under study, computed from Planck CMB anisotropy data.

[2]We relegate the analysis of QSO-Flux data to Appendix A, the reasons for which are discussed there.

Demianski & Piedipalumbo, 2011; Demianski et al., 2017, 2021; Fana Dirirsa et al., 2019; Khadka & Ratra, 2020c; Samushia & Ratra, 2010; Wang et al., 2016). In particular, the $z \sim 2.7$–8.2 part of the Universe is primarily accessed by GRBs,[3] so if GRBs can be standardized, they could provide useful information about a large, mostly unexplored, part of the Universe.

QSO-AS data currently reach to $z \sim 2.7$. These data, consisting of measurements of the angular size of astrophysical radio sources, furnish a standard ruler that is independent of that provided by the BAO sound horizon scale. The intrinsic linear size l_m of intermediate luminosity QSOs has recently been accurately determined by Cao et al. (2017b), opening the way for QSOs to, like GRBs, test cosmological models in a little-explored region of redshift space.[4]

H IIG data reach to $z \sim 2.4$, just beyond the range of current BAO data. Measurements of the luminosities of the Balmer lines in H II galaxies can be correlated with the velocity dispersion of the radiating gas, making H II galaxies a standard candle that can complement both GRBs and lower-redshift standard candles like supernovae (Chávez et al., 2014; González-Morán et al., 2019; Mania & Ratra, 2012; Plionis et al., 2009; Siegel et al., 2005).

Current QSO-Flux measurements reach to $z \sim 5.1$, but they favor a higher value of the current (denoted by the subscript "0") non-relativistic matter density parameter ($\Omega_{\rm m_0}$) than what is currently thought to be reasonable. The $\Omega_{\rm m_0}$ values obtained using QSO-Flux data, in a number of cosmological models, are in nearly 2σ tension with the values obtained by using other well-established cosmological probes like CMB, BAO, and Type Ia supernovae (Khadka & Ratra, 2020b; Risaliti & Lusso, 2019; Wei & Melia, 2020; Yang et al., 2020). Techniques for standardizing QSO-Flux measurements are still under development, so it might be too early to draw strong conclusions about the cosmological constraints obtained from QSO-Flux measurements. Therefore, in this paper, we use QSO-Flux data alone and in combination with other data to constrain cosmological parameters in four different models, and record these results in Appendix A.

[3]Though QSO-Flux measurements can reach up to $z \sim 5.1$.

[4]The use of QSO-AS measurements to constrain cosmological models dates back to near the turn of the century (e.g. Chen & Ratra, 2003; Gurvits et al., 1999; Lima & Alcaniz, 2002; Vishwakarma, 2001; Zhu & Fujimoto, 2002), but, as discussed in Ryan et al. (2019), these earlier results are suspect, because they are based on an inaccurate determination of l_m.

We find that the GRB, H IIG, and QSO-AS constraints are largely mutually consistent, and that their joint constraints are consistent with those from more widely used, and more restrictive, BAO and Hubble parameter ($H(z)$) data. When used jointly with the $H(z)$ + BAO data, these higher-z data tighten the $H(z)$ + BAO constraints.

This paper is organized as follows. In Section 4.2 we introduce the data we use. The models we analyze are described in Chapter 2, with a description of our analysis method in Section 4.3. Our results are in Section 4.4. We provide our conclusions in Section 4.5. Additionally, we discuss our results for QSO-Flux measurements in Appendix A.

4.2 Data

We use QSO-AS, H IIG, QSO-Flux, and GRB data to obtain constraints on the cosmological models we study. The QSO-AS data, comprising 120 measurements compiled by Cao et al. (2017b) (listed in Table 1 of that paper) and spanning the redshift range $0.462 \leq z \leq 2.73$, are also used in Ryan et al. (2019); see these papers for descriptions. The H IIG data, comprising 107 low redshift ($0.0088 \leq z \leq 0.16417$) H IIG measurements, used in Chávez et al. (2014) (recalibrated by González-Morán et al., 2019), and 46 high redshift ($0.636427 \leq z \leq 2.42935$) H IIG measurements, used in González-Morán et al. (2019), are also used in Cao et al. (2020). The GRB data, spanning the redshift range $0.48 \leq z \leq 8.2$, are collected from Fana Dirirsa et al. (2019) (25 from Table 2 of that paper (F10), and the remaining 94 from Table 5 of the same, which are a subset of those compiled by Wang et al., 2016) and also used in Khadka & Ratra (2020c). Note that in our analyses here we did not use the correct value of $E_{\rm p} = 871 \pm 123$ keV for GRB081121, as discussed in Ref. Liu et al. (2022), although the effects on the parameter constraints are small. We also add 1598 QSO-Flux measurements spanning the redshift range $0.036 \leq z \leq 5.1003$, from Risaliti & Lusso (2019). These data are used in Khadka & Ratra (2020b); see that paper for details. Results related to these QSO-Flux data are discussed in Appendix A.

In order to be useful as cosmological probes, GRBs need to be standardized, and many phenomenological relations have been proposed for this purpose (Amati et al., 2002, Ghirlanda

et al., 2004, Liang & Zhang, 2005, Muccino, 2020, and references therein). As in Khadka & Ratra (2020c), we use the Amati relation (Amati et al., 2002), which is an observed correlation between the peak photon energy $E_{\rm p}$ and the isotropic-equivalent radiated energy $E_{\rm iso}$ of long-duration GRBs, to standardize GRB measurements. There have been many attempts to standardize GRBs using the Amati relation. Some analyses assume a fixed value of $\Omega_{\rm m_0}$ to calibrate the Amati relation, so they favor a relatively reasonable value of $\Omega_{\rm m_0}$. Others use supernovae data to calibrate the Amati relation, while some use $H(z)$ data to calibrate it. This means that most previous GRB analyses are affected by some non-GRB external factors. In some cases this leads to a circularity problem, in which the models to be constrained by using the Amati relation are also used to calibrate the Amati relation itself (Demianski et al., 2017, 2021; Fana Dirirsa et al., 2019; Liu & Wei, 2015). In other cases, the data used in the calibration process dominate the analysis results. To overcome these problems, we fit the parameters of the Amati relation simultaneously with the parameters of the cosmological models we study (as done in Khadka & Ratra, 2020c; also see Wang et al., 2016).

The isotropic radiated energy $E_{\rm iso}$ of a source in its rest frame at a luminosity distance D_L is

$$E_{\rm iso} = \frac{4\pi D_L^2}{1+z} S_{\rm bolo}, \tag{4.1}$$

where $S_{\rm bolo}$ is the bolometric fluence, and D_L (defined below) depends on z and on the parameters of our cosmological models. $E_{\rm iso}$ is connected to the source's peak energy output $E_{\rm p}$ via the Amati relation (Amati et al., 2008, 2009)

$$\log E_{\rm iso} = a + b \log E_{\rm p}, \tag{4.2}$$

where a and b are free parameters that we vary in our model fits.[5] Note here that the peak energy $E_{\rm p} = (1+z)E_{\rm p,obs}$ where $E_{\rm p,obs}$ is the observed peak energy.

The correlation between H II G luminosity (L) and velocity dispersion (σ) is shown in

[5] $\log = \log_{10}$ is implied hereinafter.

equation (3.1). One can test a cosmological model with parameters $\mathbf{p}$ by using it to compute a theoretical distance modulus (3.5) and comparing this prediction to the distance modulus computed from observational H II G luminosity and flux (f) data

$$\mu_{\rm obs} = 2.5 \log L - 2.5 \log f - 100.2, \tag{4.3}$$

(González-Morán et al., 2019; Terlevich et al., 2015).

QSO-AS data can be used to test cosmological models by comparing the theoretical angular size of the QSO

$$\theta_{\rm th} = \frac{l_m}{D_A} \tag{4.4}$$

with its observed angular size $\theta_{\rm obs}$. In equation (4.4), l_m is the characteristic linear size of the QSO,[6] and D_A (defined below) is its angular size distance.

Underestimated systematic uncertainties for both H II G and QSO-AS data might be responsible for the large reduced χ^2 (described in Sec. 4.4.4).

The transverse comoving distance $D_M(\mathbf{p}, z)$ is related to the luminosity distance $D_L(\mathbf{p}, z)$ and the angular size distance $D_A(\mathbf{p}, z)$ through equation (1.102), and is a function of z and the parameters $\mathbf{p}$ as shown in equation (1.100).

We also use $H(z)$ and BAO measurements to constrain cosmological parameters. The $H(z)$ data, 31 measurements spanning the redshift range $0.070 \leq z \leq 1.965$, are compiled in Table 2 of Ryan et al. (2018). The BAO data, 11 measurements spanning the redshift range $0.38 \leq z \leq 2.34$, are listed in Table 1 of Cao et al. (2020).

Systematic errors that affect $H(z)$ measurements include assumptions about the stellar metallicity of the galaxies in which cosmic chronometers are found, progenitor bias, the presence of a population of young stars in these galaxies, and assumptions about stellar population synthesis models. These effects were studied in Moresco et al. (2012, 2016, 2018, 2020). Moresco et al. (2020) found that the dominant contribution to the systematic error budget comes from the choice of stellar population synthesis model, which introduces an

[6] For the data sample we use, this quantity is equal to 11.03 ± 0.25 pc; see Cao et al. (2017b).

average systematic error of $\sim$ 8.9% (though the authors say that this can be reduced to $\sim$ 4.5% by removing an outlier model from the analysis). The impacts of a population of young stars and of the progenitor bias were found to be negligible in Moresco et al. (2012, 2018), and Moresco et al. (2020) found that the impact of a $\sim$ 5–10% uncertainty in the metallicity estimates produces a $\sim$ 4–9% systematic error in the $H(z)$ measurements.

The systematic uncertainties of BAO from Alam et al. (2017) (described in Sec. 7) are included in their covariance matrix. The BAO data from Carter et al. (2018) is the combined result of the 6dF Galaxy Survey1 (6dFGS) and the SDSS DR7 MGS, where the systematic effects are described in detail in Jones et al. (2009) and Ross et al. (2015) (negligible), respectively. As described in DES Collaboration (2019b), the BAO systematic uncertainty is 15% of their statistical uncertainty and thus negligible. The same negligible systematic effect applies to the BAO measurement from Ata et al. (2018). de Sainte Agathe et al. (2019) added polynomial terms to the correlation function, so as to test the sensitivity of the slowly-varying part of the correlation function to systematic effects. They found that this shifted the BAO peak position by less than 1σ relative to its position in their fiducial model.

4.3 Data Analysis Methodology

By using the PYTHON module EMCEE (Foreman-Mackey et al., 2013), we perform a Markov chain Monte Carlo (MCMC) analysis to maximize the likelihood function, $\mathscr{L}$, and thereby determine the best-fitting values of the free parameters. The flat cosmological parameter priors are the same as those used in Cao et al. (2020) and the flat priors of the parameters of the Amati relation are non-zero over $0 \leq \sigma_{\rm ext} \leq 10$ (described below), $40 \leq a \leq 60$, and $0 \leq b \leq 5$.

The likelihood functions associated with $H(z)$, BAO, H II G, and QSO-AS data are described in Cao et al. (2020). For GRB data, the natural log of its likelihood function

(D'Agostini, 2005) is

$$\ln \mathscr{L}_{\rm GRB} = -\frac{1}{2}\left[\chi^2_{\rm GRB} + \sum_{i=1}^{119} \ln\left(2\pi(\sigma^2_{\rm ext} + \sigma^2_{y_i} + b^2\sigma^2_{x_i})\right)\right], \tag{4.5}$$

where

$$\chi^2_{\rm GRB} = \sum_{i=1}^{119}\left[\frac{(y_i - bx_i - a)^2}{(\sigma^2_{\rm ext} + \sigma^2_{y_i} + b^2\sigma^2_{x_i})}\right], \tag{4.6}$$

$x = \log\frac{E_{\rm p}}{\rm keV}$, $\sigma_x = \frac{\sigma_{E_{\rm p}}}{E_{\rm p}\ln 10}$, $y = \log\frac{E_{\rm iso}}{\rm erg}$, and $\sigma_{\rm ext}$ is the extrinsic scatter parameter, which contains the unknown systematic uncertainty. For the GRB with σ_z uncertainty in z,

$$\sigma^2_y = \left(\frac{\sigma_{S_{\rm bolo}}}{S_{\rm bolo}\ln 10}\right)^2 + \left(\frac{2(1+z)\frac{\partial D_M}{\partial z} + D_M}{(1+z)D_M\ln 10}\sigma_z\right)^2, \tag{4.7}$$

and for those without z uncertainties $\sigma_z = 0$ (the non-zero σ_z has a negligible effect on our results).

The Akaike Information Criterion (AIC) and the Bayesian Information Criterion (BIC) are used to compare the goodness of fit of models with different numbers of parameters, where

$$AIC = -2\ln\mathscr{L}_{\rm max} + 2n, \tag{4.8}$$

and

$$BIC = -2\ln\mathscr{L}_{\rm max} + n\ln N. \tag{4.9}$$

In these equations, $\mathscr{L}_{\rm max}$ is the maximum value of the relevant likelihood function, n is the number of free parameters of the model under consideration, and N is the number of data points (e.g., for GRB $N = 119$).

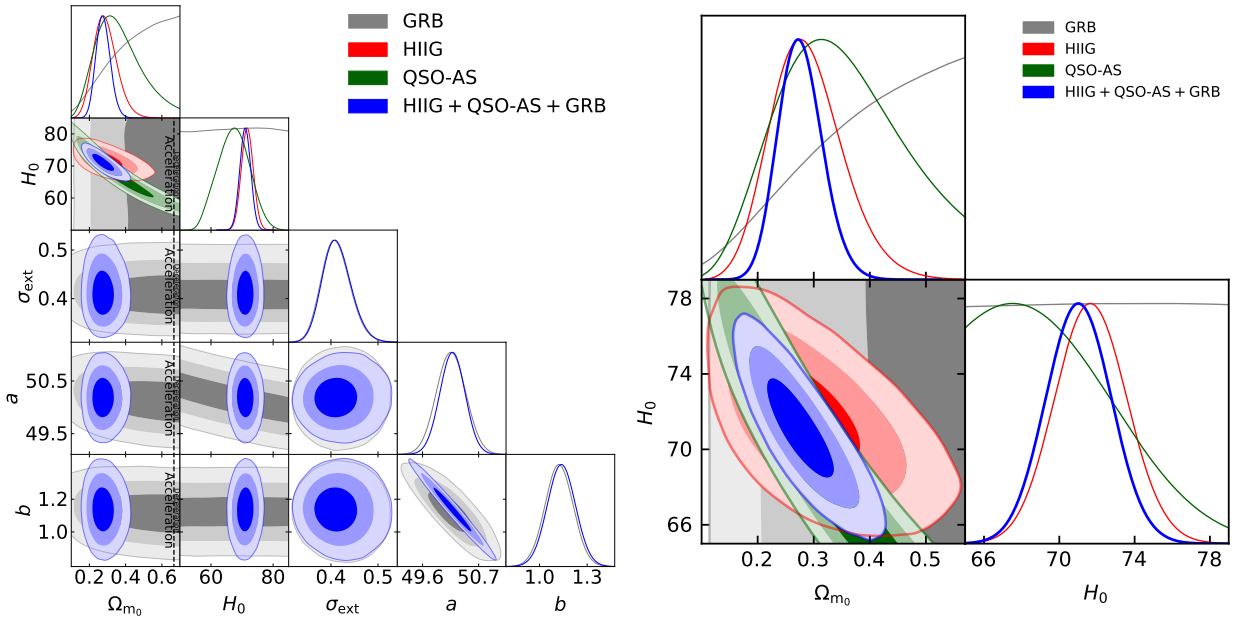

(a) All parameters

(b) Cosmological parameters zoom in

Figure 4.1: 1σ, 2σ, and 3σ confidence contours for flat ΛCDM, where the right panel is the cosmological parameters comparison zoomed in. The black dotted lines in the left sub-panels of the left panel are the zero-acceleration lines, which divide the parameter space into regions associated with currently-accelerating (left) and currently-decelerating (right) cosmological expansion.

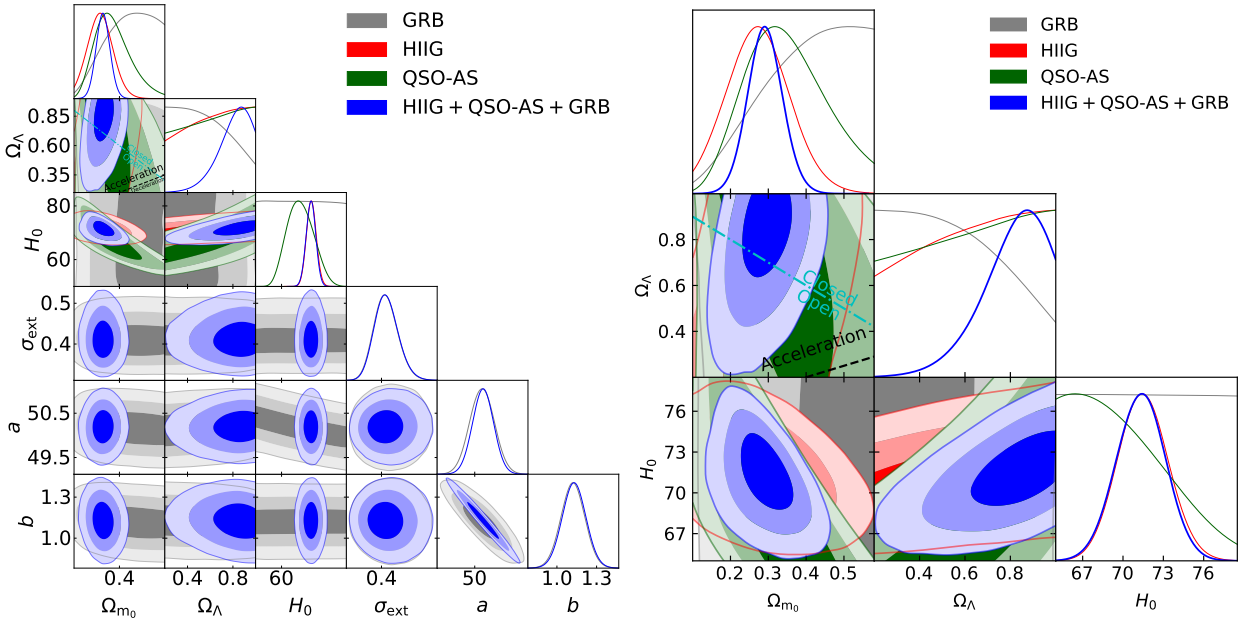

(a) All parameters

(b) Cosmological parameters zoom in

Figure 4.2: Same as Fig. 4.1 but for non-flat ΛCDM. The cyan dash-dot line represents the flat ΛCDM case, with closed spatial hypersurfaces to the upper right. The black dotted line is the zero-acceleration line, which divides the parameter space into regions associated with currently-accelerating (above left) and currently-decelerating (below right) cosmological expansion.

4.4 Results

4.4.1 H II G, QSO-AS, and GRB constraints, individually

We present the posterior one-dimensional (1D) probability distributions and two-dimensional (2D) confidence regions of the cosmological and Amati relation parameters for the six flat and non-flat models in Figs. 4.1–4.6, in gray (GRB), red (H II G), and green (QSO-AS). The unmarginalized best-fitting parameter values are listed in Table 4.1, along with the corresponding χ^2, $-2\ln\mathscr{L}_{\max}$, AIC, BIC, and degrees of freedom ν (where $\nu \equiv N - n$).[7] The values of $\Delta\chi^2$, ΔAIC, and ΔBIC reported in Table 4.1 are discussed in Section 4.4.4, where we define $\Delta\chi^2$, ΔAIC, and ΔBIC, respectively, as the differences between the values of the χ^2, AIC, and BIC associated with a given model and their corresponding minimum values among all models. The marginalized best-fitting parameter values and uncertainties ($\pm1\sigma$ error bars or 2σ limits) are given in Table 4.2.[8] From Table 4.2 we find that the QSO-AS constraints on Ω_{m0} are consistent with other results within a 1σ range but with large error bars, ranging from a low of $0.329^{+0.086}_{-0.171}$ (flat ϕCDM) to a high of $0.364^{+0.083}_{-0.150}$ (flat ΛCDM).

The QSO-AS constraints on H_0 are between $H_0 = 61.91^{+2.83}_{-4.92}$ km s^{-1} Mpc^{-1}(non-flat ϕCDM) and $H_0 = 68.39^{+6.14}_{-8.98}$ km s^{-1} Mpc^{-1}(flat XCDM), with large error bars and relatively low values for non-flat XCDM and the ϕCDM models.

The non-flat models mildly favor open geometry, but are also consistent, given the large error bars, with spatially-flat hypersurfaces (except for non-flat ϕCDM, where the open case is favored at 2.76σ). For non-flat ΛCDM, non-flat XCDM, and non-flat ϕCDM, we find $\Omega_{k_0} = 0.017^{+0.184}_{-0.277}$, $\Omega_{k_0} = 0.115^{+0.466}_{-0.293}$, and $\Omega_{k_0} = 0.254^{+0.304}_{-0.092}$, respectively.[9]

The fits to the QSO-AS data favor dark energy being a cosmological constant but do not strongly disfavor dark energy dynamics. For flat (non-flat) XCDM, $w_X = -1.161^{+0.430}_{-0.679}$

[7] Note that the χ^2 values listed in Tables 4.1 and A.1 are computed from the best-fitting parameter values and are not necessarily the minimum (especially when including GRB and QSO-Flux data).

[8] We use the PYTHON package GETDIST (Lewis, 2019) to plot these figures and compute the central values (posterior means) and uncertainties of the free parameters listed in Table 4.2.

[9] From Table 4.2 we see that GRB data are also consistent with flat spatial geometry in the non-flat ΛCDM and XCDM cases, but also favor, at 2.92σ, open spatial geometry in the case of non-flat ϕCDM.

($w_{\rm X} = -1.030^{+0.593}_{-0.548}$), and for flat (non-flat) ϕCDM, 2σ upper limits of α are $\alpha < 2.841$ ($\alpha < 4.752$). In the former case, both results are within 1σ of $w_{\rm X} = -1$, and in the latter case, both 1D likelihoods peak at $\alpha = 0$.

Constraints on cosmological model parameters derived solely from H II G data are discussed in Sec. 5.1 of Cao et al. (2020), while those derived from GRB data are described in Sec. 5.1 of Khadka & Ratra (2020a) (though there are slight differences coming from the different treatments of H_0 and the different ranges of flat priors used there and here); both are listed in Table 4.2 here. In contrast to the H II G and QSO-AS data sets, the GRB data alone cannot constrain H_0 because there is a degeneracy between the intercept parameter (a) of the Amati relation and H_0; for consistency with the analyses of the H II G and QSO-AS data, we treat H_0 as a free parameter in the GRB data analysis here.

Cosmological constraints obtained using the H II G, QSO-AS, and GRB data sets are mutually consistent, and are also consistent with those obtained from most other cosmological probes. This is partially a consequence of the larger H II G, QSO-AS, and GRB data error bars, which lead to relatively weaker constraints on cosmological parameters when each of these data sets is used alone (see Table 4.2). However, because the H II G, QSO-AS, and GRB constraints are mutually consistent, we may jointly analyze these data. Their combined cosmological constraints will therefore be more restrictive than when they are analyzed individually.

We note, from Figs. 4.1–4.6, that a significant part of the likelihood of each of these three data sets lies in the parameter space part with currently-accelerating cosmological expansion.

4.4.2 H II G, QSO-AS, and GRB (HQASG) joint constraints

Because the H II G, QSO-AS, and GRB contours are mutually consistent for all six of the models we study, we jointly analyze these data to obtain HQASG constraints.

The 1D probability distributions and 2D confidence regions of the cosmological and Amati relation parameters from the HQASG data are in Figs. 4.1–4.6, in blue, Figs. 4.7–4.12, in green, and panels (a) of Figs. A.4–A.4, in red. The best-fitting results and uncertainties are

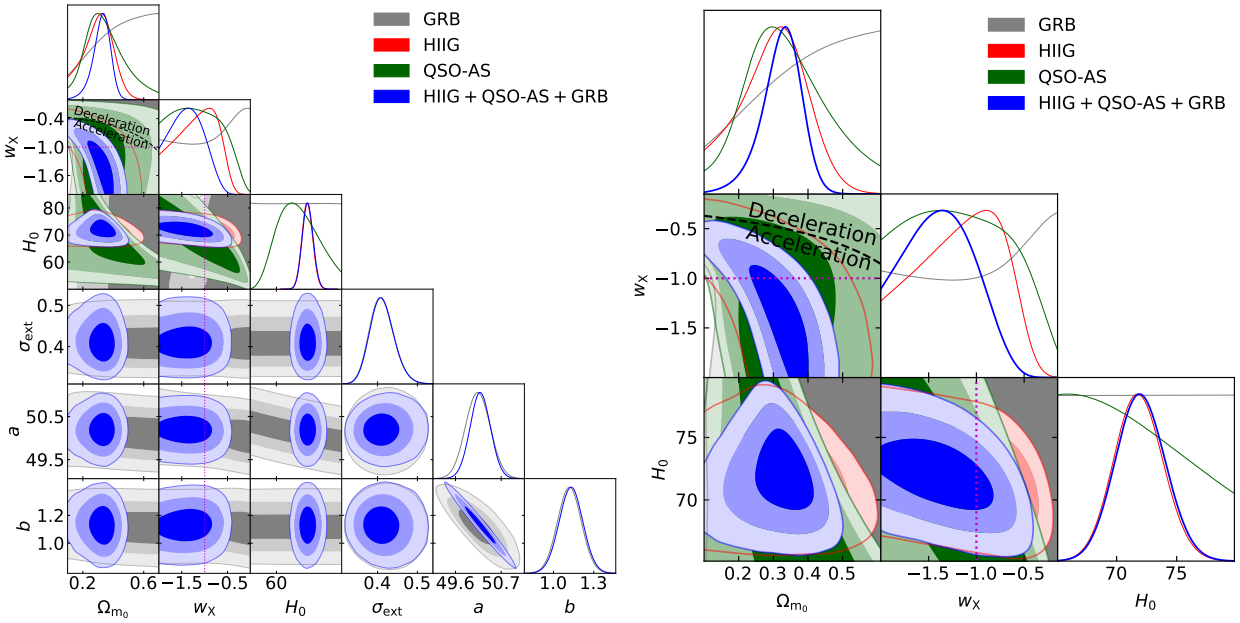

(a) All parameters

(b) Cosmological parameters zoom in

Figure 4.3: 1σ, 2σ, and 3σ confidence contours for flat XCDM. The black dotted line is the zero-acceleration line, which divides the parameter space into regions associated with currently-accelerating (below left) and currently-decelerating (above right) cosmological expansion. The magenta lines denote $w_X = -1$, i.e. the flat ΛCDM model.

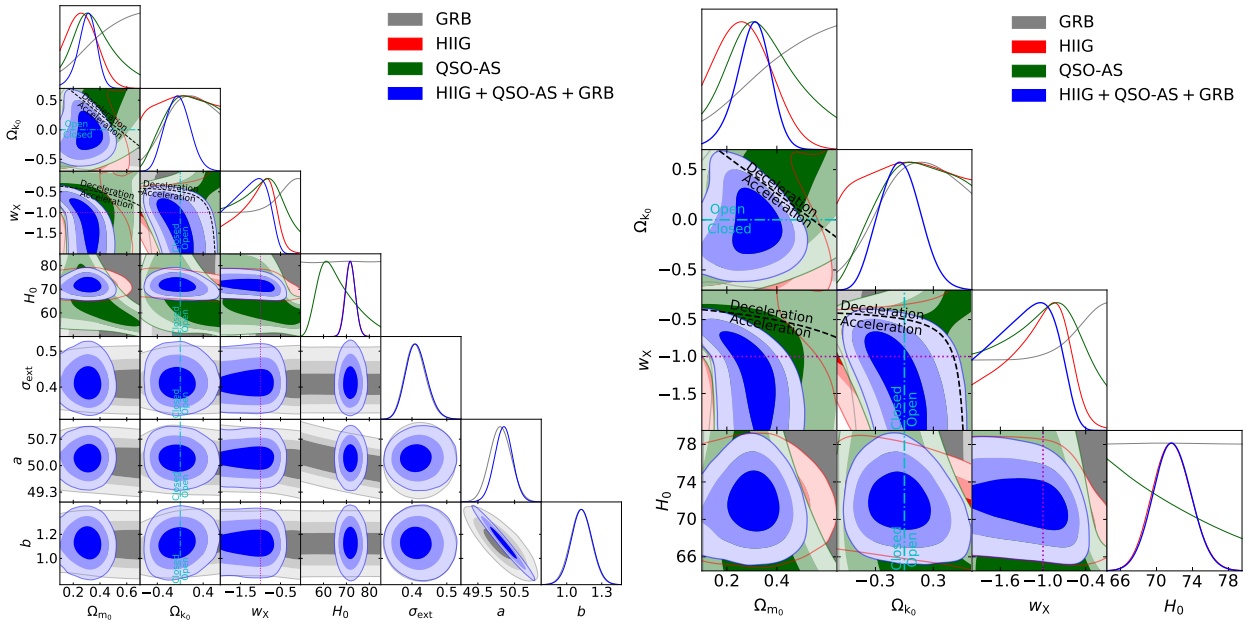

(a) All parameters

(b) Cosmological parameters zoom in

Figure 4.4: Same as Fig. 4.3 but for non-flat XCDM, where the zero acceleration lines in each of the three subpanels are computed for the third cosmological parameter set to the $H(z)$ + BAO data best-fitting values listed in Table 4.1. Currently-accelerating cosmological expansion occurs below these lines. The cyan dash-dot lines represent the flat XCDM case, with closed spatial hypersurfaces either below or to the left. The magenta lines indicate $w_X = -1$, i.e. the non-flat ΛCDM model.

in Tables 4.1 and 4.2.

We find that the HQASG data combination favors currently-accelerating cosmological expansion.

The fit to the HQASG data produces best-fitting values of Ω_{m0} that lie between $0.205^{+0.044}_{-0.094}$ (non-flat ϕCDM) at the low end, and $0.322^{+0.062}_{-0.044}$ (flat XCDM) at the high end. This range is smaller than the ranges within which Ω_{m0} falls when it is determined from the H II G, QSO-AS, and GRB data individually, but the low and high ends of the range are still somewhat mutually inconsistent, being 2.66σ away from each other. This is a consequence of the low Ω_{m0} value for non-flat ϕCDM; the Ω_{m0} values for ΛCDM and XCDM are quite consistent with the recent estimate of Planck Collaboration (2020). In contrast, the best-fitting values of H_0 that we measure from the HQASG data are mutually very consistent (within 0.65σ), with $H_0 = 70.30 \pm 1.68$ km s^{-1} Mpc^{-1}(flat ϕCDM) at the low end of the range and $H_0 = 72.00^{+1.99}_{-1.98}$ km s^{-1} Mpc^{-1}(flat XCDM) at the high end of the range. These measurements are 0.83σ (flat XCDM) and 1.70σ (flat ϕCDM) lower than the local Hubble constant measurement of $H_0 = 74.03 \pm 1.42$ km s^{-1} Mpc^{-1}(Riess et al., 2019), and 0.70σ (flat ϕCDM) and 1.16σ (flat XCDM) higher than the median statistics estimate of $H_0 = 68 \pm 2.8$ km s^{-1} Mpc^{-1}(Chen & Ratra, 2011).[10]

In contrast to the H II G, QSO-AS, and GRB only cases, when fitted to the HQASG data combination the non-flat models mildly favor closed spatial hypersurfaces. For non-flat ΛCDM, non-flat XCDM, and non-flat ϕCDM, we find $\Omega_{k_0} = -0.093^{+0.092}_{-0.190}$, $\Omega_{k_0} = -0.044^{+0.193}_{-0.217}$, and $\Omega_{k_0} = -0.124^{+0.127}_{-0.253}$, respectively, with the non-flat ΛCDM model favoring closed spatial hypersurfaces at 1.01σ.

The fit to the HQASG data combination produces stronger evidence for dark energy dynamics in the flat and non-flat XCDM parametrizations but weaker evidence in the flat

[10]Other local expansion rate determinations have slightly lower central values with slightly larger error bars (Breuval et al., 2020; Dhawan et al., 2018; Efstathiou, 2020; Fernández Arenas et al., 2018; Freedman et al., 2019, 2020; Khetan et al., 2021; Rameez & Sarkar, 2019; Rigault et al., 2015; Zhang et al., 2017). Our H_0 measurements are consistent with earlier median statistics estimates (Chen et al., 2003; Gott et al., 2001) and with other recent H_0 determinations (Birrer et al., 2020; Blum et al., 2020; Chen et al., 2017; Cuceu et al., 2019; DES Collaboration, 2018; Denzel et al., 2021; Domínguez et al., 2019; Gómez-Valent & Amendola, 2018; Lin & Ishak, 2021; Lyu et al., 2020; Martinelli & Tutusaus, 2019; Philcox et al., 2020; Planck Collaboration, 2020; Schöneberg et al., 2019; Zeng & Yan, 2019; Zhang, 2018; Zhang & Huang, 2021).

and non-flat ϕCDM models (in comparison to the H II G and QSO-AS only cases) with tighter error bars on the measured values of $w_{\rm X}$ and α. For flat (non-flat) XCDM, $w_{\rm X} = -1.379^{+0.361}_{-0.375}$ ($w_{\rm X} = -1.273^{+0.501}_{-0.321}$), with $w_{\rm X} = -1$ being within the 1σ range for non-flat XCDM and being 1.05σ larger for flat XCDM. For flat (non-flat) ϕCDM, $\alpha < 2.584$ ($\alpha < 3.414$), where both likelihoods peak at $\alpha = 0$.

The constraints on the Amati relation parameters from the HQASG data are also model-independent, but with slightly larger central values and smaller error bars for the parameter a. A reasonable summary is $\sigma_{\rm ext} = 0.413^{+0.026}_{-0.032}$, $a = 50.19 \pm 0.24$, and $b = 1.133 \pm 0.086$.

The HQASG cosmological constraints are largely consistent with those from other data, like the constraints from the $H(z)$ + BAO data used in Cao et al. (2020) and Khadka & Ratra (2020c), that are shown in red in Figs. 4.7–4.12. We note, however, that there is some mild tension between ϕCDM Ω_{m0} values, and between XCDM and ϕCDM H_0 values determined from $H(z)$ + BAO and HQASG data, with the 2.46σ difference between Ω_{m0} values estimated from the two different data combinations in the non-flat ϕCDM model being the only somewhat troubling difference (see Table 4.2).

4.4.3 $H(z)$, BAO, H II G, QSO-AS, and GRB (HzBHQASG) constraints

Given the good mutual consistency between constraints derived from $H(z)$ + BAO data and those derived from HQASG data, in this subsection we determine more restrictive joint constraints from the combined $H(z)$, BAO, H II G, QSO-AS, and GRB (HzBHQASG) data on the parameters of our six cosmological models.

The 1D probability distributions and 2D confidence regions of the cosmological and Amati relation parameters for all models from the HzBHQASG data are in blue in Figs. 4.7–4.12, and in red in panels (b) of Figs. A.4–A.4. The best-fitting results and uncertainties are in Tables 4.1 and 4.2.

The measured values of Ω_{m0} here are a little larger, and significantly more restrictively constrained, than the ones in the HQASG cases (except for flat XCDM), being between

Table 4.1: Unmarginalized best-fitting parameter values for all models from various combinations of data.

Model	Data set	Ω_{m_0}	Ω_Λ	Ω_{k_0}	w_X	α	H_0[c]	σ_{ext}	a	b	χ^2	ν	$-2\ln\mathscr{L}_{max}$	AIC	BIC	$\Delta\chi^2$	ΔAIC	ΔBIC
Flat ΛCDM	GRB	0.698	0.302	–	–	–	80.36	0.404	49.92	1.113	117.98	114	130.12	140.12	154.01	1.08	0.00	0.00
	H II G	0.276	0.724	–	–	–	71.81	–	–	–	410.75	151	410.75	414.75	420.81	3.15	0.00	0.00
	QSO-AS	0.315	0.685	–	–	–	68.69	–	–	–	352.05	118	352.05	356.05	361.62	1.76	0.00	0.00
	HQASG[d]	0.271	0.729	–	–	–	71.13	0.407	50.18	1.138	879.42	387	895.05	905.05	924.91	0.12	0.00	0.00
	$H(z)$ + BAO	0.314	0.686	–	–	–	68.53	–	–	–	20.82	40	20.82	24.82	28.29	2.39	0.00	0.00
	HzBHQASG[e]	0.317	0.683	–	–	–	69.06	0.404	50.19	1.134	903.61	429	917.79	927.79	948.16	4.05	0.00	0.00
Non-flat ΛCDM	GRB	0.691	0.203	0.106	–	–	77.03	0.402	49.96	1.115	117.37	113	129.96	141.96	158.64	0.47	1.84	4.63
	H II G	0.311	1.000	−0.311	–	–	72.41	–	–	–	410.44	150	410.44	416.44	425.53	2.84	1.69	4.72
	QSO-AS	0.266	1.000	−0.268	–	–	74.73	–	–	–	351.30	117	351.30	357.30	365.66	1.01	1.25	4.04
	HQASG[d]	0.291	0.876	−0.167	–	–	72.00	0.406	50.22	1.120	879.30	386	894.02	906.02	929.85	0.00	0.97	4.94
	$H(z)$ + BAO	0.308	0.643	0.049	–	–	67.52	–	–	–	20.52	39	20.52	26.52	31.73	2.09	1.70	3.44
	HzBHQASG[e]	0.309	0.716	−0.025	–	–	69.77	0.402	50.17	1.141	904.47	428	917.17	929.17	953.61	4.91	1.38	5.45
Flat XCDM	GRB	0.102	–	–	−0.148	–	55.30	0.400	50.22	1.117	118.28	113	129.79	141.79	158.47	1.38	1.67	4.46
	H II G	0.251	–	–	−0.899	–	71.66	–	–	–	410.72	150	410.72	416.72	425.82	3.12	1.97	5.01
	QSO-AS	0.267	–	–	−2.000	–	81.70	–	–	–	351.84	117	351.84	357.84	366.20	1.55	1.79	4.58
	HQASG[d]	0.320	–	–	−1.306	–	72.03	0.404	50.20	1.131	880.47	386	894.27	906.27	930.10	1.17	1.22	5.19
	$H(z)$ + BAO	0.319	–	–	−0.865	–	65.83	–	–	–	19.54	39	19.54	25.54	30.76	1.11	0.72	2.47
	HzBHQASG[e]	0.313	–	–	−1.052	–	69.90	0.407	50.19	1.132	902.09	428	917.55	929.55	953.99	2.53	1.76	5.83
Non-flat XCDM	GRB	0.695	–	0.556	−1.095	–	57.64	0.399	50.13	1.133	118.43	112	129.73	143.73	163.19	1.53	3.61	9.18
	H II G	0.100	–	−0.702	−0.655	–	72.57	–	–	–	407.60	149	407.60	415.60	427.72	0.00	0.85	6.91
	QSO-AS	0.100	–	−0.548	−0.670	–	74.04	–	–	–	350.29	116	350.29	358.29	369.44	0.00	2.24	7.82
	HQASG[d]	0.300	–	−0.161	−1.027	–	80.36	0.405	50.21	1.122	879.48	385	894.01	908.01	935.81	0.18	2.96	10.90
	$H(z)$ + BAO	0.327	–	−0.159	−0.730	–	65.97	–	–	–	18.43	38	18.43	26.43	33.38	0.00	1.61	5.09
	HzBHQASG[e]	0.312	–	−0.045	−0.959	–	69.46	0.402	50.23	1.117	904.17	427	917.07	931.07	959.58	4.61	3.28	11.42
Flat ϕCDM	GRB	0.674	–	–	–	2.535	84.00	0.399	49.88	1.104	119.15	113	130.14	142.14	158.82	2.25	2.02	4.81
	H II G	0.255	–	–	–	0.260	71.70	–	–	–	410.70	150	410.70	416.70	425.80	3.10	1.95	4.99
	QSO-AS	0.319	–	–	–	0.012	68.47	–	–	–	352.05	117	352.05	358.05	366.41	1.76	2.00	4.79
	HQASG[d]	0.282	–	–	–	0.012	70.81	0.402	50.19	1.135	882.56	386	895.28	907.28	931.11	3.26	2.23	6.20
	$H(z)$ + BAO	0.318	–	–	–	0.364	66.04	–	–	–	19.65	39	19.65	25.65	30.86	1.22	0.83	2.57
	HzBHQASG[e]	0.316	–	–	–	0.013	69.15	0.405	50.24	1.114	903.52	428	918.12	930.12	954.56	3.96	2.33	6.40
Non-flat ϕCDM	GRB	0.664	–	0.188	–	4.269	59.65	0.403	50.17	1.111	116.90	112	129.93	143.93	163.39	0.00	3.81	9.38
	H II G	0.114	–	−0.437	–	2.680	72.14	–	–	–	409.91	149	409.91	417.91	430.03	2.31	3.16	9.22
	QSO-AS	0.100	–	−0.433	–	2.948	72.37	–	–	–	350.98	116	350.98	358.98	370.13	0.69	2.93	8.51
	HQASG[d]	0.276	–	−0.185	–	0.145	72.11	0.402	50.16	1.142	881.09	385	894.24	908.24	936.03	1.79	3.19	11.12
	$H(z)$ + BAO	0.321	–	−0.137	–	0.887	66.41	–	–	–	18.61	39	18.61	26.61	33.56	0.18	1.79	5.27
	HzBHQASG[e]	0.310	–	−0.052	–	0.193	69.06	0.411	50.21	1.126	899.56	427	917.26	931.26	959.77	0.00	3.47	11.61

[c] km s^{-1} Mpc^{-1}.

[d] H II G + QSO-AS + GRB.

[e] $H(z)$ + BAO + H II G + QSO-AS + GRB.

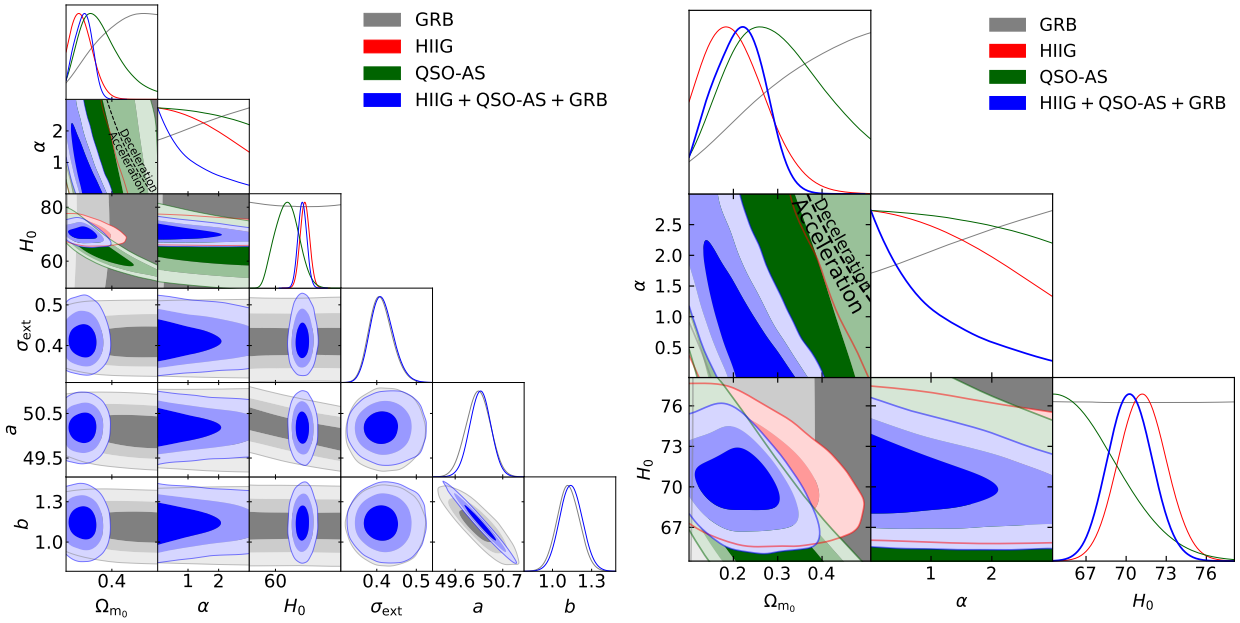

(a) All parameters

(b) Cosmological parameters zoom in

Figure 4.5: 1σ, 2σ, and 3σ confidence contours for flat ϕCDM. The black dotted zero-acceleration line splits the parameter space into regions of currently-accelerating (below left) and currently-decelerating (above right) cosmological expansion. The $\alpha = 0$ axis is the flat ΛCDM model.

0.310 ± 0.014 (non-flat XCDM) and 0.320 ± 0.013 (flat ϕCDM). The H_0 measurements are a little lower, and more tightly constrained, than in the HQASG cases, and are in better agreement with the lower median statistics estimate of H_0 (Chen & Ratra, 2011) than the higher local expansion rate measurement of H_0 (Riess et al., 2019), being between $68.16^{+1.01}_{-0.80}$ km s^{-1} Mpc^{-1}(flat ϕCDM) and $69.85^{+1.42}_{-1.55}$ km s^{-1} Mpc^{-1}(flat XCDM).

For non-flat ΛCDM, non-flat XCDM, and non-flat ϕCDM, we measure $\Omega_{k_0} = -0.019^{+0.043}_{-0.048}$, $\Omega_{k_0} = -0.024^{+0.092}_{-0.093}$, and $\Omega_{k_0} = -0.094^{+0.082}_{-0.064}$, respectively, where the central values are a little higher (closer to 0) than what was measured in the HQASG cases. The joint constraints are more restrictive, with non-flat ΛCDM and XCDM within 0.44σ and 0.26σ of $\Omega_{k_0} = 0$, respectively. The non-flat ϕCDM model, on the other hand, still favors a closed geometry with an Ω_{k_0} that is 1.15σ away from zero.

The HzBHQASG case has slightly larger measured values and tighter error bars for w_X and α than the HQASG case, so there is also not much evidence in support of dark energy dynamics. For flat (non-flat) XCDM, $w_X = -1.050^{+0.090}_{-0.081}$ ($w_X = -1.019^{+0.202}_{-0.099}$). For flat (non-flat) ϕCDM, the 2σ upper limits are $\alpha < 0.418$ ($\alpha < 0.905$).

The cosmological model-independent constraints from the HzBHQASG data combination on the parameters of the Amati relation can be summarized as $\sigma_{ext} = 0.412^{+0.026}_{-0.032}$, $a = 50.19 \pm 0.24$, and $b = 1.132 \pm 0.085$.

4.4.4 Model comparison

From Table 4.1, we see that the reduced χ^2 values determined from GRB data alone are around unity for all models (being between 1.03 and 1.06) while those values determined from the $H(z)$ + BAO data combination range from 0.48 to 0.53, with the lower reduced χ^2 here being due to the $H(z)$ data (that probably have overestimated error bars). As discussed in Ryan et al. (2019) and Cao et al. (2020), the cases that involve H II G and QSO-AS data have a larger reduced χ^2 (between 2.11 and 3.02), which is probably due to underestimated systematic uncertainties in both cases.

Based on the AIC and the BIC (see Table 4.1), the flat ΛCDM model remains the most

favored model, across all data combinations, among the six models we study.[11] From ΔAIC and ΔBIC, we find mostly weak or positive evidence against the models we considered, and only in a few cases do we find strong evidence against them. According to ΔBIC, the evidence against non-flat XCDM is strong for the H II G, QSO-AS, and GRB only cases, and very strong for the HQASG and HzBHQASG cases. Similarly, the evidence against flat ϕCDM is strong for the HQASG and HzBHQASG cases, and the evidence against non-flat ϕCDM is strong for the H II G, QSO-AS, and GRB only cases, and very strong for the HQASG and HzBHQASG cases.

Among these six models, a comparison of the ΔBIC values from Table 4.1 shows that the most disfavored model is non-flat ϕCDM, and that the second most disfavored model is non-flat XCDM. This is especially true when these models are fitted to the HQASG and HzBHQASG data combinations, in which cases non-flat ϕCDM and non-flat XCDM are very strongly disfavored. These models aren't as strongly disfavored by the AIC, however; from a comparison of the ΔAIC values in Table 4.1, we see that the evidence against the most disfavored model (non-flat ϕCDM) is only positive.

4.5 Conclusion

We find that cosmological constraints determined from higher-z GRB, H II G, and QSO-AS data are mutually consistent. It is both reassuring and noteworthy that these higher-z data jointly favor currently-accelerating cosmological expansion, and that their constraints are consistent with the constraints imposed by more widely used and more restrictive $H(z)$ and BAO data. Using a data set consisting of 31 $H(z)$, 11 BAO, 120 QSO-AS, 153 H II G, and 119 GRB measurements, we jointly constrain the parameters of the GRB Amati relation and of six cosmological models.

The GRB measurements are of special interest because they reach to $z \sim 8.2$ (far beyond

[11] Note that based on the $\Delta\chi^2$ results of Table 4.1 non-flat ΛCDM has the minimum χ^2 in the HQASG case and non-flat XCDM has the minimum χ^2 in the H II G, QSO-AS, and $H(z)$ + BAO cases, whereas non-flat ϕCDM has the minimum χ^2 for the GRB and HzBHQASG cases. The $\Delta\chi^2$ values do not, however, penalize a model for having more parameters.

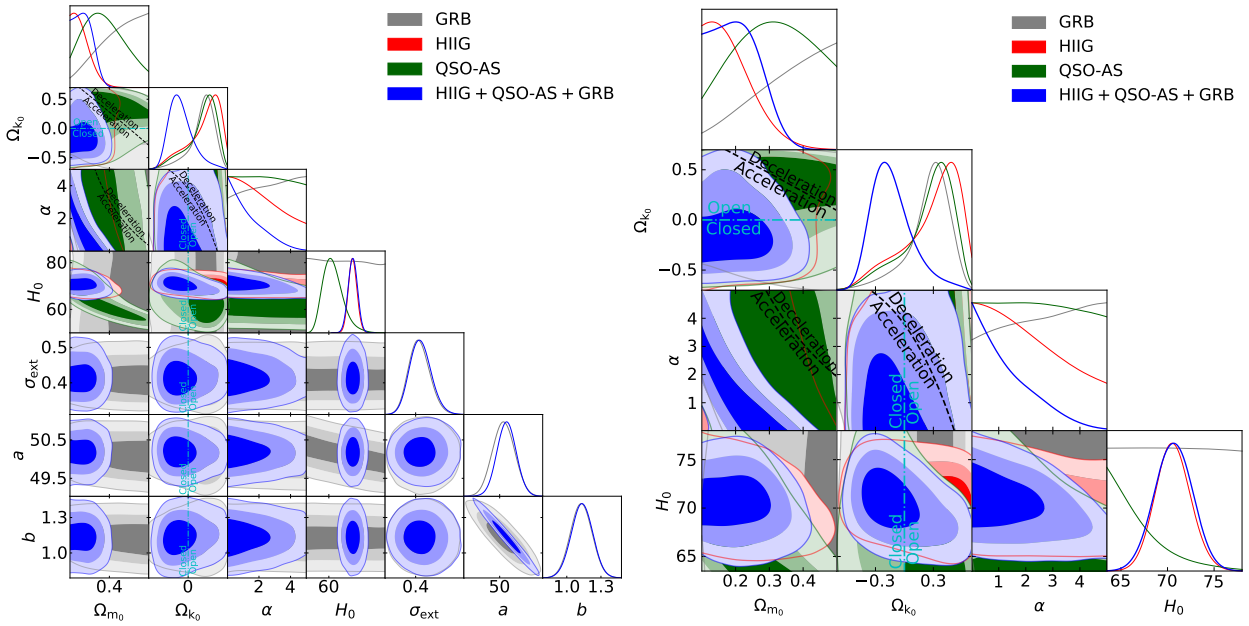

(a) All parameters (b) Cosmological parameters zoom in

Figure 4.6: Same as Fig. 4.5 but for non-flat ϕCDM, where the zero-acceleration lines in each of the sub-panels are computed for the third cosmological parameter set to the $H(z)$ + BAO data best-fitting values listed in Table 4.1. Currently-accelerating cosmological expansion occurs below these lines. The cyan dash-dot lines represent the flat ϕCDM case, with closed spatial geometry either below or to the left. The $\alpha = 0$ axis is the non-flat ΛCDM model.

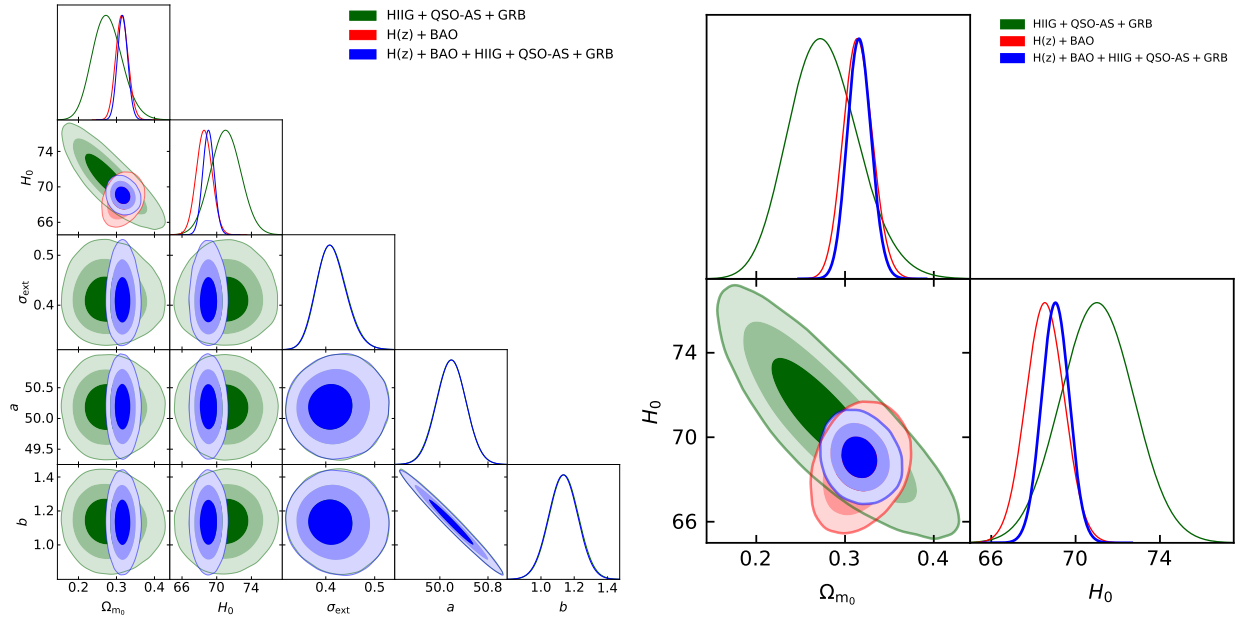

(a) All parameters (b) Cosmological parameters zoom in

Figure 4.7: Same as Fig. 4.1 (flat ΛCDM) but for different combinations of data.

Table 4.2: One-dimensional marginalized best-fitting parameter values and uncertainties ($\pm 1\sigma$ error bars or 2σ limits) for all models from various combinations of data.

Model	Data set	Ω_{m_0}	Ω_Λ	Ω_{k_0}	w_X	α	H_0[c]	σ_{ext}	a	b
Flat ΛCDM	GRB	> 0.208	–	–	–	–	–	$0.411^{+0.026}_{-0.032}$	50.16 ± 0.27	1.123 ± 0.085
	H II G	$0.289^{+0.053}_{-0.071}$	–	–	–	–	71.70 ± 1.83	–	–	–
	QSO-AS	$0.364^{+0.083}_{-0.150}$	–	–	–	–	$67.29^{+4.93}_{-5.07}$	–	–	–
	HQASG[e]	$0.277^{+0.034}_{-0.041}$	–	–	–	–	71.03 ± 1.67	$0.413^{+0.026}_{-0.032}$	50.19 ± 0.24	1.138 ± 0.085
	$H(z)$ + BAO	$0.315^{+0.015}_{-0.017}$	–	–	–	–	68.55 ± 0.87	–	–	–
	HzBHQASG[f]	0.316 ± 0.013	–	–	–	–	$69.05^{+0.62}_{-0.63}$	$0.412^{+0.026}_{-0.032}$	50.19 ± 0.23	1.133 ± 0.085
Non-flat ΛCDM	GRB	$0.463^{+0.226}_{-0.084}$	< 0.658[d]	$-0.007^{+0.251}_{-0.234}$	–	–	–	$0.412^{+0.026}_{-0.032}$	50.17 ± 0.28	1.121 ± 0.086
	H II G	$0.275^{+0.081}_{-0.078}$	> 0.501[d]	$0.094^{+0.237}_{-0.363}$	–	–	$71.50^{+1.80}_{-1.81}$	–	–	–
	QSO-AS	$0.357^{+0.082}_{-0.135}$	–	$0.017^{+0.184}_{-0.277}$	–	–	$67.32^{+4.49}_{-5.44}$	–	–	–
	HQASG[e]	0.292 ± 0.044	$0.801^{+0.191}_{-0.055}$	$-0.093^{+0.092}_{-0.190}$	–	–	$71.33^{+1.75}_{-1.77}$	$0.413^{+0.026}_{-0.032}$	50.19 ± 0.24	1.130 ± 0.086
	$H(z)$ + BAO	0.309 ± 0.016	$0.636^{+0.081}_{-0.072}$	$0.055^{+0.082}_{-0.074}$	–	–	67.44 ± 2.33	–	–	–
	HzBHQASG[f]	$0.311^{+0.012}_{-0.014}$	$0.708^{+0.053}_{-0.046}$	$-0.019^{+0.043}_{-0.048}$	–	–	69.72 ± 1.10	$0.412^{+0.026}_{-0.032}$	50.19 ± 0.23	1.132 ± 0.085
Flat XCDM	GRB	> 0.366[d]	–	–	–	–	–	$0.411^{+0.025}_{-0.032}$	50.14 ± 0.28	1.119 ± 0.085
	H II G	$0.300^{+0.106}_{-0.083}$	–	–	$-1.180^{+0.560}_{-0.330}$	–	71.85 ± 1.96	–	–	–
	QSO-AS	$0.349^{+0.090}_{-0.143}$	–	–	$-1.161^{+0.430}_{-0.679}$	–	$68.39^{+6.14}_{-8.98}$	–	–	–
	HQASG[e]	$0.322^{+0.062}_{-0.044}$	–	–	$-1.379^{+0.361}_{-0.375}$	–	$72.00^{+1.99}_{-1.98}$	$0.412^{+0.026}_{-0.032}$	50.20 ± 0.24	1.130 ± 0.085
	$H(z)$ + BAO	$0.319^{+0.016}_{-0.017}$	–	–	$-0.888^{+0.126}_{-0.098}$	–	$66.26^{+2.32}_{-2.63}$	–	–	–
	HzBHQASG[f]	$0.313^{+0.014}_{-0.015}$	–	–	$-1.050^{+0.090}_{-0.081}$	–	$69.85^{+1.42}_{-1.55}$	$0.412^{+0.026}_{-0.032}$	50.19 ± 0.24	1.134 ± 0.085
Non-flat XCDM	GRB	> 0.386[d]	–	$0.121^{+0.464}_{-0.275}$	> -1.218[d]	–	–	$0.411^{+0.026}_{-0.032}$	50.12 ± 0.28	1.122 ± 0.087
	H II G	$0.275^{+0.084}_{-0.125}$	–	$0.011^{+0.457}_{-0.460}$	$-1.125^{+0.537}_{-0.321}$	–	$71.71^{+2.07}_{-2.08}$	–	–	–
	QSO-AS	$0.359^{+0.111}_{-0.174}$	–	$0.115^{+0.466}_{-0.293}$	$-1.030^{+0.593}_{-0.548}$	–	$65.92^{+4.54}_{-9.54}$	–	–	–
	HQASG[e]	$0.303^{+0.073}_{-0.058}$	–	$-0.044^{+0.193}_{-0.217}$	$-1.273^{+0.501}_{-0.321}$	–	71.77 ± 2.02	$0.413^{+0.026}_{-0.031}$	50.20 ± 0.24	1.129 ± 0.085
	$H(z)$ + BAO	$0.323^{+0.021}_{-0.020}$	–	$-0.105^{+0.187}_{-0.162}$	$-0.818^{+0.212}_{-0.071}$	–	$66.20^{+2.29}_{-2.55}$	–	–	–
	HzBHQASG[f]	0.310 ± 0.014	–	$-0.024^{+0.092}_{-0.093}$	$-1.019^{+0.202}_{-0.099}$	–	$69.63^{+1.45}_{-1.62}$	$0.412^{+0.026}_{-0.031}$	50.19 ± 0.23	1.132 ± 0.085
Flat ϕCDM	GRB	> 0.376[d]	–	–	–	–	–	$0.411^{+0.025}_{-0.032}$	50.13 ± 0.28	1.121 ± 0.087
	H II G	$0.210^{+0.043}_{-0.092}$	–	–	–	< 2.784	$71.23^{+1.79}_{-1.80}$	–	–	–
	QSO-AS	$0.329^{+0.086}_{-0.171}$	–	–	–	< 2.841	$64.42^{+4.47}_{-4.62}$	–	–	–
	HQASG[e]	$0.214^{+0.057}_{-0.061}$	–	–	–	< 2.584	70.30 ± 1.68	$0.413^{+0.026}_{-0.032}$	50.18 ± 0.24	1.142 ± 0.087
	$H(z)$ + BAO	$0.319^{+0.016}_{-0.017}$	–	–	–	$0.550^{+0.169}_{-0.494}$	$65.25^{+2.25}_{-1.82}$	–	–	–
	HzBHQASG[f]	0.320 ± 0.013	–	–	–	< 0.418	$68.16^{+1.01}_{-0.80}$	$0.412^{+0.027}_{-0.033}$	50.20 ± 0.24	1.131 ± 0.088
Non-flat ϕCDM	GRB	> 0.189	–	$0.251^{+0.247}_{-0.086}$	–	–	–	$0.411^{+0.026}_{-0.032}$	50.11 ± 0.28	1.128 ± 0.089
	H II G	< 0.321	–	$0.291^{+0.348}_{-0.113}$	–	< 4.590	$70.60^{+1.68}_{-1.84}$	–	–	–
	QSO-AS	$0.362^{+0.117}_{-0.193}$	–	$0.254^{+0.304}_{-0.092}$	–	< 4.752	$61.91^{+2.83}_{-4.92}$	–	–	–
	HQASG[e]	$0.205^{+0.044}_{-0.094}$	–	$-0.124^{+0.127}_{-0.253}$	–	< 3.414	70.66 ± 1.90	$0.414^{+0.027}_{-0.033}$	50.19 ± 0.24	1.134 ± 0.088
	$H(z)$ + BAO	0.321 ± 0.017	–	$-0.126^{+0.157}_{-0.130}$	–	$0.938^{+0.439}_{-0.644}$	65.93 ± 2.33	–	–	–
	HzBHQASG[f]	0.313 ± 0.013	–	$-0.094^{+0.082}_{-0.064}$	–	< 0.905	68.79 ± 1.22	$0.412^{+0.027}_{-0.033}$	50.20 ± 0.24	1.126 ± 0.087

[c] km s^{-1} Mpc^{-1}.

[d] This is the 1σ limit. The 2σ limit is set by the prior, and is not shown here.

[e] H II G + QSO-AS + GRB.

[f] $H(z)$ + BAO + H II G + QSO-AS + GRB.

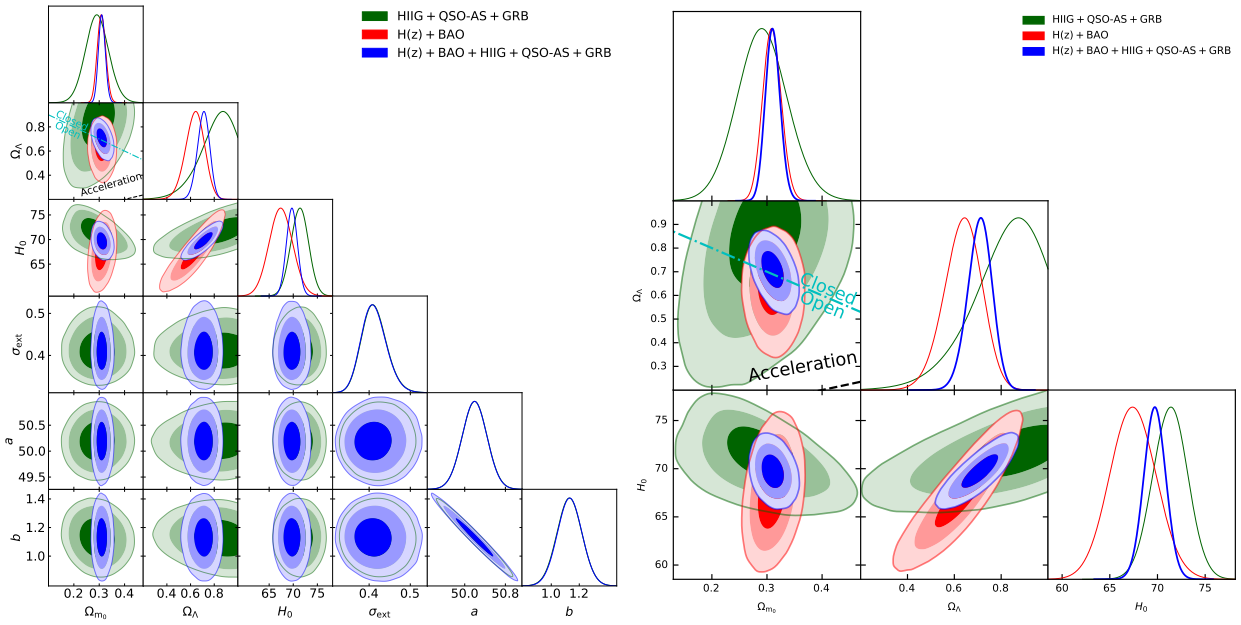

(a) All parameters

(b) Cosmological parameters zoom in

Figure 4.8: Same as Fig. 4.2 (non-flat ΛCDM) but for different combinations of data.

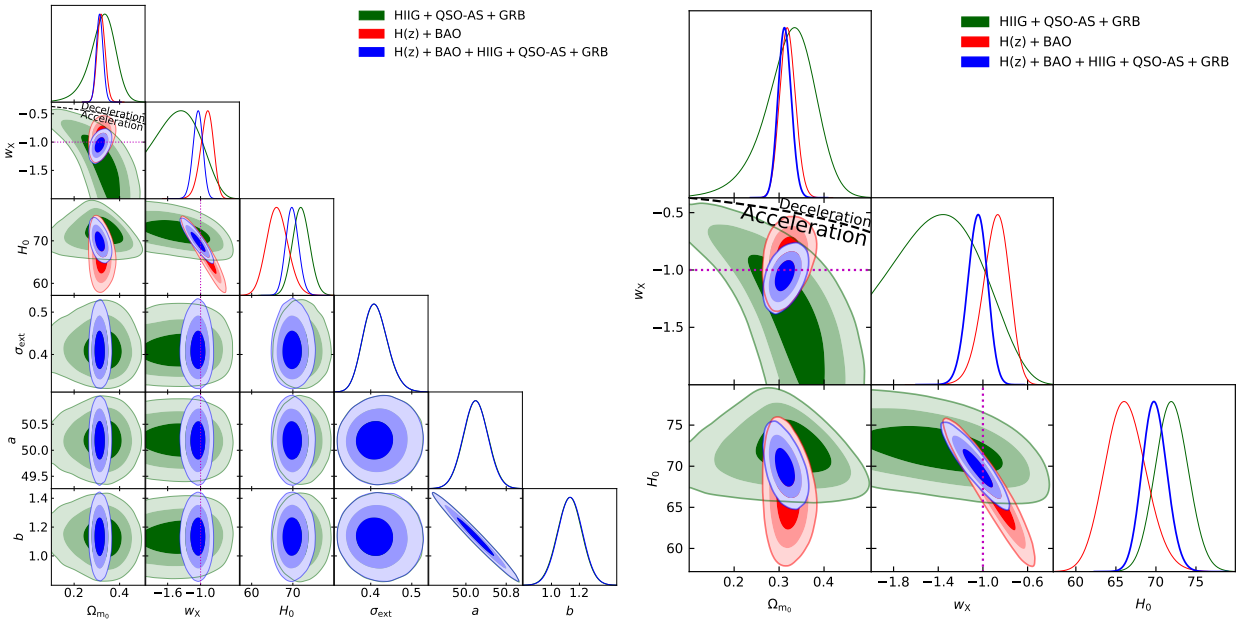

(a) All parameters

(b) Cosmological parameters zoom in

Figure 4.9: Same as Fig. 4.3 (flat XCDM) but for different combinations of data.

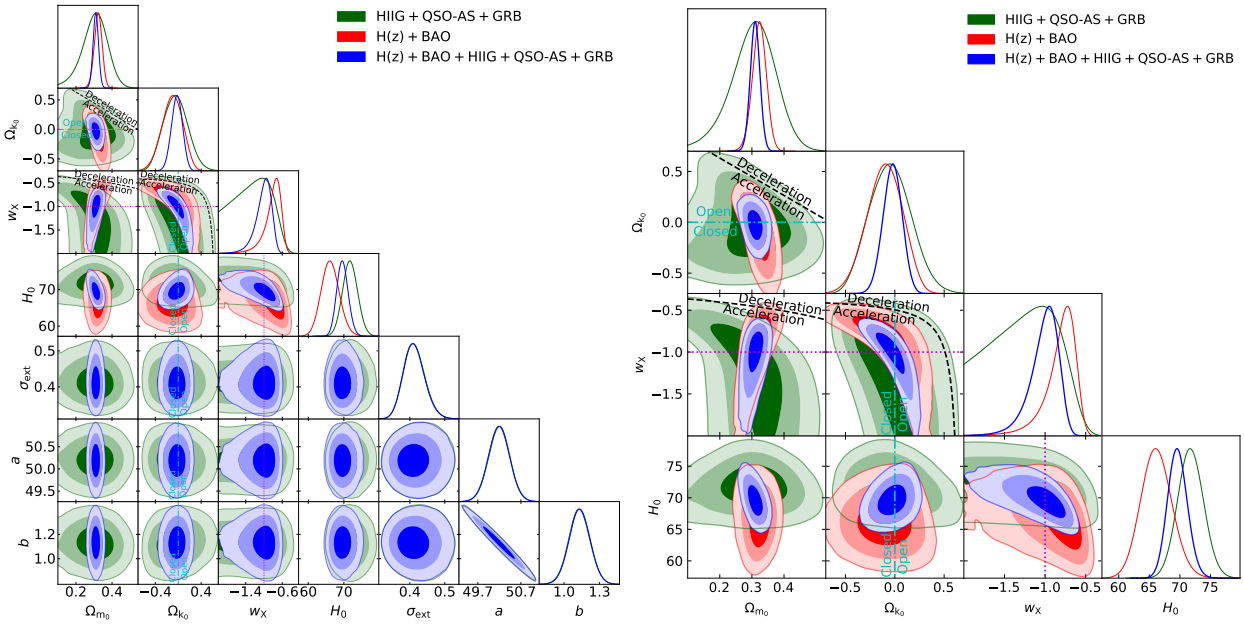

(a) All parameters (b) Cosmological parameters zoom in

Figure 4.10: Same as Fig. 4.4 (non-flat XCDM) but for different combinations of data.

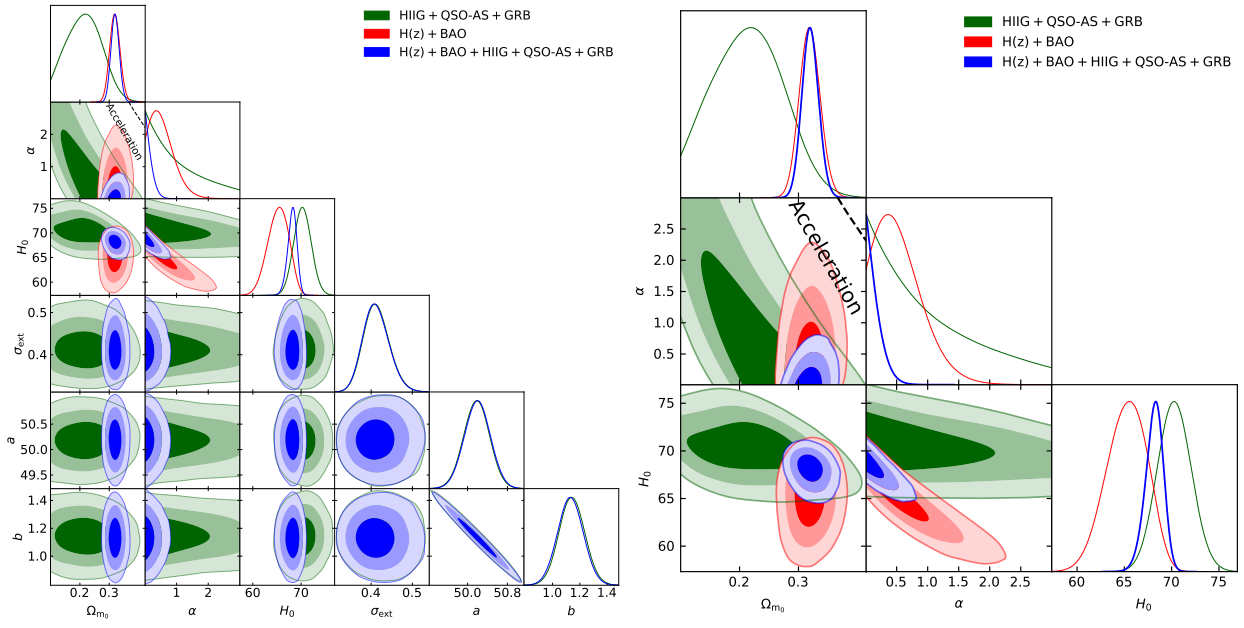

(a) All parameters (b) Cosmological parameters zoom in

Figure 4.11: Same as Fig. 4.5 (flat ϕCDM) but for different combinations of data.

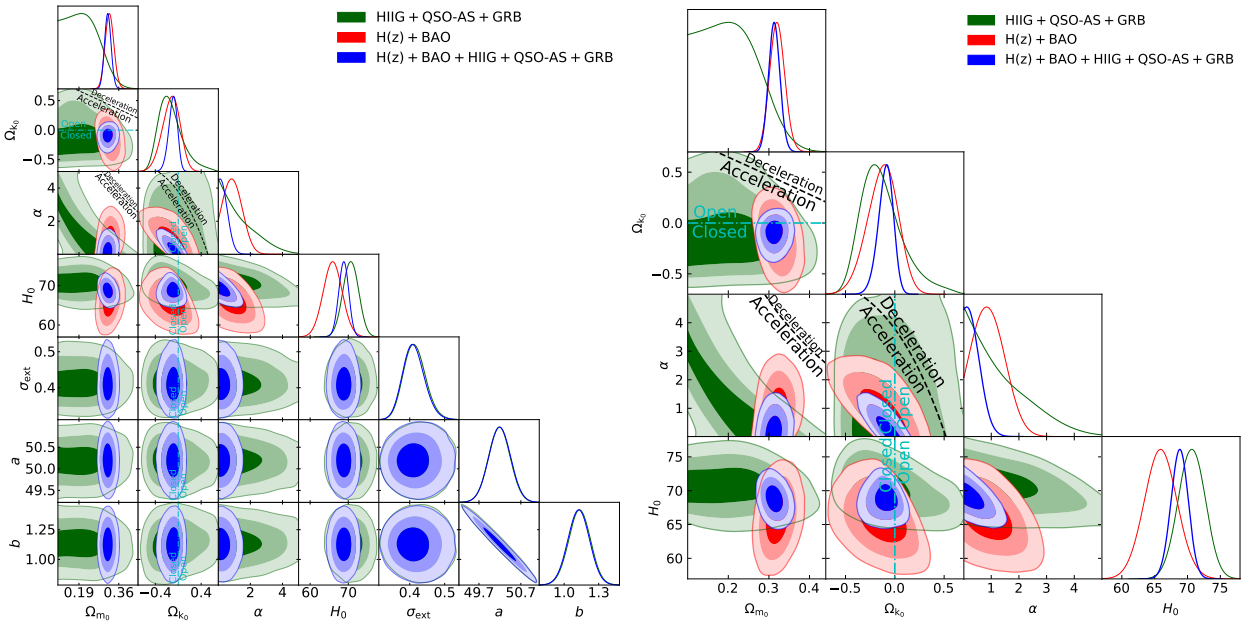

(a) All parameters

(b) Cosmological parameters zoom in

Figure 4.12: Same as Fig. 4.6 (non-flat ϕCDM) but for different combinations of data.

the highest $z \sim 2.3$ reached by BAO data) and into a much less studied area of redshift space. Current GRB data do not provide very restrictive constraints on cosmological model parameters, but in the near future we expect there to be more GRB observations (Shirokov et al., 2020) which should improve the GRB data and provide more restrictive cosmological constraints.

Some of our conclusions do not differ significantly between models and so are model-independent. In particular, for the HzBHQASG data (the full data set excluding QSO-Flux data), we find a fairly restrictive summary value of $\Omega_{m_0} = 0.313 \pm 0.013$ that agrees well with many other recent measurements. From these data we also find a fairly restrictive summary value of $H_0 = 69.3 \pm 1.2$ km s^{-1} Mpc^{-1} that is in better agreement with the results of Chen & Ratra (2011) and Planck Collaboration (2020) than with the result of Riess et al. (2019); note that we do not take the H_0 tension issue into account (for a review, see Riess, 2019). The HzBHQASG measurements are consistent with flat ΛCDM, but do not rule out mild dark energy dynamics or a little spatial curvature energy density. More and better-quality higher-z GRB, H II G, QSO, and other data will significantly help to test these extensions of

flat ΛCDM.

Chapter 5

Using Pantheon and DES supernova, baryon acoustic oscillation, and Hubble parameter data to constrain the Hubble constant, dark energy dynamics, and spatial curvature

This chapter is based on Cao et al. (2021b). Figures and tables by Shulei Cao, from analyses conducted independently by Shulei Cao and Joseph Ryan.

5.1 Introduction

That the Universe is currently in a phase of accelerated expansion is well-supported by observations but not fully explained by fundamental theory (see e.g. Coley & Ellis, 2020; Martin, 2012; Ratra & Vogeley, 2008). The standard spatially flat ΛCDM model (Peebles, 1984) interprets this phenomenon as a consequence of dark energy with negative pressure (a cosmological constant, Λ) and requires the major part of the energy budget of the Universe

to consist of time-independent dark energy and cold dark matter (CDM). Although flat ΛCDM is consistent with many observations (see e.g. eBOSS Collaboration, 2021; Farooq et al., 2017; Planck Collaboration, 2020; Scolnic et al., 2018),[1] there exist some potential observational discrepancies (Martinelli & Tutusaus, 2019; Riess, 2019) and theoretical puzzles (e.g., Martin, 2012), which leaves room for other cosmological models, including non-flat ΛCDM. As the quality and quantity of observational data grow in time, constraining these models is within reach. Many workers have investigated the merits of the flat and non-flat XCDM parametrizations and ϕCDM models, where dark energy dynamics and spatial curvature come into play.[2][3]

Many observational data sets have been used to place constraints on the parameters of cosmological models, such as the equation of state parameter (w) of dark energy. Most recently, in Cao et al. (2020), we used Hubble parameter ($H(z)$), baryon acoustic oscillation (BAO), quasar angular size (QSO), quasar X-ray and UV flux, H II starburst galaxy (H IIG), and gamma-ray burst (GRB) data to constrain this parameter (among others). The tightest constraints on w, we found, come from low-redshift $H(z)$ (cosmic chronometer) and BAO (standard ruler) data, with the standard candle data (H IIG and GRB) giving very broad constraints. In this paper we combine measurements of the distances to 1255 Type Ia supernovae (SNe Ia) with our set of $H(z)$ and BAO data (along with QSO and H IIG observations) to obtain tight cosmological parameter constraints.

The usefulness of SN Ia data to cosmology is well-known. SN Ia measurements revealed the accelerated expansion of the Universe over twenty years ago, and they are employed today to place constraints on cosmological parameters and to break parameter degeneracies. Over

[1] Note that the *Planck* TT,TE,EE+lowE+lensing data favor positive spatial curvature (Planck Collaboration, 2020) but are consistent with a spatially flat model at 1.63σ.

[2] For observational constraints on spatial curvature see Farooq et al. (2015), Chen et al. (2016), Rana et al. (2017), Ooba et al. (2018a,b,c), Yu et al. (2018), Park & Ratra (2018, 2019a,c, 2020), Wei (2018), DES Collaboration (2019a), Handley (2021), Jesus et al. (2021), Li et al. (2020), Geng et al. (2020), Kumar et al. (2021), Efstathiou & Gratton (2020), Di Valentino et al. (2021b), Di Valentino et al. (2021a), Gao et al. (2020), Abbassi & Abbassi (2020), Yang & Gong (2021), Agudelo Ruiz et al. (2020), Velasquez-Toribio & Fabris (2020), Vagnozzi et al. (2021a,b), and references therein.

[3] For observational constraints on the ϕCDM model see Yashar et al. (2009), Samushia et al. (2010), Campanelli et al. (2012), Avsajanishvili et al. (2015), Solà et al. (2017), Solà Peracaula et al. (2018, 2019), Zhai et al. (2017), Ooba et al. (2018b, 2019), Sangwan et al. (2018), Singh et al. (2019), Khadka & Ratra (2020a,b,c, 2021), Ureña-López & Roy (2020), and references therein.

this time period, the sample size of SN Ia distance measurements has grown considerably, and the analysis and mitigation of systematic uncertainties has improved (DES Collaboration, 2019c,d). Supernovae are therefore a reasonably empirically well-understood cosmological probe[4], and so can be used to obtain reliable constraints on cosmological model parameters.

In our earlier studies that made use of BAO data (e.g., Cao et al., 2020; Ryan et al., 2019), we relied on CMB-derived values of the baryon density[5] $\Omega_b h^2$ in order to compute the size of the sound horizon r_s. The size of the sound horizon is needed to calibrate the BAO scale (see Table 5.1), so the constraints we derived from our BAO measurements were indirectly dependent on CMB physics. Park & Ratra (2018, 2019a,c) computed $\Omega_b h^2$ within each of the six models we study (namely flat/non-flat ΛCDM, flat/non-flat XCDM, and flat/non-flat ϕCDM) from CMB data using primordial energy density fluctuation power spectra $P(k)$ appropriate for flat and curved geometries (Lucchin & Matarrese, 1985; Ratra, 1989, 2017; Ratra & Peebles, 1995). Other power spectra have been considered in the non-flat case (Bonga et al., 2016; Handley, 2019; Lesgourgues & Tram, 2014; Thavanesan et al., 2021). Since we do not make use of $P(k)$, the controversy associated with $P(k)$ in non-flat models is avoided in our analyses here.

The constraints from $H(z)$ + BAO data and from SN Ia data are not inconsistent, and so these data can be jointly used to constrain cosmological parameters. Park & Ratra (2019b) used $H(z)$, BAO, and Pantheon SN Ia apparent magnitude (SN-Pantheon) measurements in such a joint analysis. Here we use a more recent BAO data compilation and new DES-3yr binned SN Ia apparent magnitude (SN-DES) data. We find for all combinations of data we study here that all or almost all of the favored parameter space corresponds to currently accelerating cosmological expansion. The most reliable constraints come from the $H(z)$ + BAO + SN-Pantheon + SN-DES (HzBSNPD) data combination, with fairly model-independent determinations of the Hubble constant, $H_0 = 68.8 \pm 1.8$ km s^{-1} Mpc^{-1}, and the non-relativistic matter density parameter, $\Omega_{m_0} = 0.294 \pm 0.020$. The estimate of H_0 is in better agreement with the median statistics $H_0 = 68 \pm 2.8$ km s^{-1} Mpc^{-1} estimate of Chen &

[4]Though the relatively simpler physics underlying cosmic microwave background (CMB) anisotropies and BAO makes those probes better understood than SNe Ia.

[5]Here Ω_{b_0} is the baryon density parameter and $h = H_0/(100$ km s^{-1} Mpc$^{-1})$.

Ratra (2011) and the Planck Collaboration (2020) estimate of $H_0 = 67.4 \pm 0.5$ km s^{-1} Mpc^{-1} than with the local $H_0 = 74.03 \pm 1.42$ km s^{-1} Mpc^{-1} measurement of Riess et al. (2019). The combined measurements are consistent with the spatially flat ΛCDM model, but also favor some dark energy dynamics, as well as a little non-zero spatial curvature energy density. More restrictive constraints are derived when these data are combined with QSO and H II G data.

This paper is organized as follows. We use the cosmological models described in Chapter 2. In Section 5.2 the data used are introduced and our method of analyzing these data is described in Section 5.3. We present our results in Section 5.4, and our conclusions in Section 5.5.

5.2 Data

In this paper, we use a combination of $H(z)$, BAO, SN-Pantheon, SN-DES, QSO, and H II G data to constrain the cosmological models we study.

The $H(z)$ data, compiled in Table 2 of Ryan et al. (2018), consist of 31 measurements spanning the redshift range $0.070 \leq z \leq 1.965$. The BAO data, which have been updated relative to Cao et al. (2020), consist of 11 measurements spanning the redshift range $0.38 \leq z \leq 2.334$, listed in Table 5.1.

The SN-Pantheon data, compiled by Scolnic et al. (2018), consist of 1048 SN Ia measurements spanning the redshift range $0.01 < z < 2.3$. The SN-DES data, compiled by DES Collaboration (2019d), consist of 20 binned measurements of 207 SN Ia measurements spanning the redshift range $0.015 \leq z \leq 0.7026$.

The QSO data, listed in Table 1 of Cao et al. (2017b), consist of 120 measurements of the angular size

$$\theta(z) = \frac{l_{\rm m}}{D_A(z)}, \tag{5.1}$$

spanning the redshift range $0.462 \leq z \leq 2.73$. $l_{\rm m}$ is the characteristic linear size of the quasars in the sample. This quantity is determined by using the Gaussian Process method to

Table 5.1: BAO data.

z	Measurement[a]	Value	Ref.
0.38	$D_M\,(r_{s,\mathrm{fid}}/r_s)$	1512.39	Alam et al. (2017)[b]
0.38	$H(z)\,(r_s/r_{s,\mathrm{fid}})$	81.2087	Alam et al. (2017)[b]
0.51	$D_M\,(r_{s,\mathrm{fid}}/r_s)$	1975.22	Alam et al. (2017)[b]
0.51	$H(z)\,(r_s/r_{s,\mathrm{fid}})$	90.9029	Alam et al. (2017)[b]
0.61	$D_M\,(r_{s,\mathrm{fid}}/r_s)$	2306.68	Alam et al. (2017)[b]
0.61	$H(z)\,(r_s/r_{s,\mathrm{fid}})$	98.9647	Alam et al. (2017)[b]
0.122	$D_V\,(r_{s,\mathrm{fid}}/r_s)$	539 ± 17	Carter et al. (2018)
0.81	D_A/r_s	10.75 ± 0.43	DES Collaboration (2019b)
1.52	$D_V\,(r_{s,\mathrm{fid}}/r_s)$	3843 ± 147	Ata et al. (2018)
2.334	D_M/r_s	37.5	du Mas des Bourboux et al. (2020)[c]
2.334	D_H/r_s	8.99	du Mas des Bourboux et al. (2020)[c]

[a] D_M, D_V, r_s, $r_{s,\mathrm{fid}}$, D_A, and D_H have units of Mpc, while $H(z)$ has units of km s^{-1} Mpc^{-1}.
[b] The six measurements from Alam et al. (2017) are correlated; see equation (20) of Ryan et al. (2019) for their correlation matrix.
[c] The two measurements from du Mas des Bourboux et al. (2020) are correlated; see equation (5.2) below for their correlation matrix.

reconstruct the expansion history of the Universe from 24 cosmic chronometer measurements over $z < 1.2$. This $H(z)$ function is used to reconstruct the angular size distance $D_A(z)$, which can then be used to compute l_m given measurements ($\theta_\mathrm{obs}(z)$) of quasar angular sizes. QSO and $H(z)$ data are therefore somewhat correlated, but the error bars on the constraints derived from QSO data are so large that we do not believe this correlation to be an issue.

The H II G data consist of 107 low redshift ($0.0088 \leq z \leq 0.16417$) measurements, used in Chávez et al. (2014) (recalibrated by González-Morán et al., 2019), and 46 high redshift ($0.636427 \leq z \leq 2.42935$) measurements.

The covariance matrix $\mathbf{C}$ for the BAO data, taken from Alam et al. (2017), is given in equation (20) of Ryan et al. (2019). For the BAO data from du Mas des Bourboux et al. (2020), the covariance matrix is

$$\mathbf{C} = \begin{bmatrix} 1.3225 & -0.1009 \\ -0.1009 & 0.0380 \end{bmatrix}. \tag{5.2}$$

The scale of BAO measurements is set by the sound horizon (r_s) during the epoch of radiation drag. To compute this quantity, we use the approximate formula (1.107) (Aubourg et al., 2015).

In our previous studies we did not vary $\Omega_b h^2$ as a free parameter. Instead we used CMB-derived, model-dependent values of $\Omega_b h^2$ to compute r_s. Because we vary $\Omega_b h^2$ as a free parameter in this paper, our computations of the sound horizon (and therefore our calibration of the scale of our BAO measurements) are fully independent of CMB physics (at the cost of enlarging the parameter space and so somewhat weakening the constraints).

Following Conley et al. (2011) and Deng & Wei (2018), we define the theoretical magnitude of a supernova to be

$$m_{\rm th} = 5 \log \mathscr{D}_L(z) + \mathscr{M}, \tag{5.3}$$

where $\mathscr{M}$ is a nuisance parameter to be marginalized over, and $\mathscr{D}_L(z)$ is

$$\mathscr{D}_L(z) \equiv (1 + z_{\rm hel}) \int_0^{z_{\rm cmb}} \frac{d\tilde{z}}{E\left(\tilde{z}\right)}. \tag{5.4}$$

In this equation, $z_{\rm hel}$ is the heliocentric redshift, and $z_{\rm cmb}$ is the CMB-frame redshift. In Conley et al. (2011), equation (5.4) is called the "Hubble-constant free luminosity distance", because $E(z)$ does not contain H_0. In our case, because we use h, $\Omega_b h^2$, and $\Omega_c h^2$ as free parameters, our expansion rate function (and thus our luminosity distance) depends on the Hubble constant. We therefore obtain weak constraints on H_0 from the supernova data, unlike Conley et al. (2011) and Deng & Wei (2018) (see Section 5.4, below).

5.3 Data Analysis Methodology

We use the PYTHON module EMCEE (Foreman-Mackey et al., 2013) to maximize the likelihood functions, thereby determining the constraints on the free parameters. In our analyses here the priors on the cosmological parameters are different from zero (and flat) over the ranges $0.005 \leq \Omega_{\rm b_0} h^2 \leq 0.1$, $0.001 \leq \Omega_{\rm c_0} h^2 \leq 0.99$, $0.2 \leq h \leq 1.0$, $-3 \leq w_{\rm X} \leq 0.2$,

$-0.7 \leq \Omega_{k_0} \leq 0.7$, and $0 < \alpha \leq 10$. Ω_{m0} is a derived parameter and depends on h. Our approach here differs from that of those earlier papers in that, instead of varying the non-relativistic matter density parameter Ω_{m0} as a free parameter, we vary the baryonic ($\Omega_b h^2$) and cold dark matter ($\Omega_c h^2$) densities as free parameters, treating Ω_{m0} as a derived parameter.[6]

The likelihood functions of $H(z)$, BAO, H II G, and QSO data are described in Cao et al. (2020) and Cao et al. (2021a). For the SN Ia (SN-Pantheon and SN-DES) data, the likelihood function is

$$\mathscr{L}_{\rm SN} = e^{-\chi^2_{\rm SN}/2}, \tag{5.5}$$

where, as in Park & Ratra (2019b), $\chi^2_{\rm SN}$ takes the form of equation (C1) in Appendix C of Conley et al. (2011) with $\mathscr{M}$ being marginalized. The covariance matrices of the SN Ia data, $\mathbf{C}_{\rm SN}$ are the sum of the diagonal statistical uncertainty covariance matrices, $\mathbf{C}_{\rm stat} = {\rm diag}(\sigma^2_{\rm SN})$, and the systematic uncertainty covariance matrices, $\mathbf{C}_{\rm sys}$: $\mathbf{C}_{\rm SN} = \mathbf{C}_{\rm stat} + \mathbf{C}_{\rm sys}$.[7] $\sigma_{\rm SN}$ are the SN Ia statistical uncertainties.

As in Cao et al. (2021a), we use the Akaike Information Criterion (AIC) in equation (4.8) and the Bayesian Information Criterion (BIC) in equation (4.9) to compare the quality of models with different numbers of parameters.

5.4 Results

The posterior one-dimensional (1D) probability distributions and two-dimensional (2D) confidence regions of the cosmological parameters for the six flat and non-flat models are shown in Figs. 5.1–5.6, in gray ($H(z)$+BAO), red ($H(z)$ + BAO + SN-Pantheon, HzBSNP), green ($H(z)$ + BAO + SN-DES, HzBSND), blue ($H(z)$ + BAO + SN-Pantheon + SN-DES, HzBSNPD), and purple ($H(z)$ + BAO + SN-Pantheon + SN-DES + QSO + H II G, HzBSNPDQH). We list the unmarginalized best-fitting parameter values, as well as the cor-

[6] We do this to eliminate the dependence of the BAO data on CMB physics; see Section 5.2 for details.

[7] Note that the covariance matrices for the SN-DES data are the ones described in equation (18) of DES Collaboration (2019d).

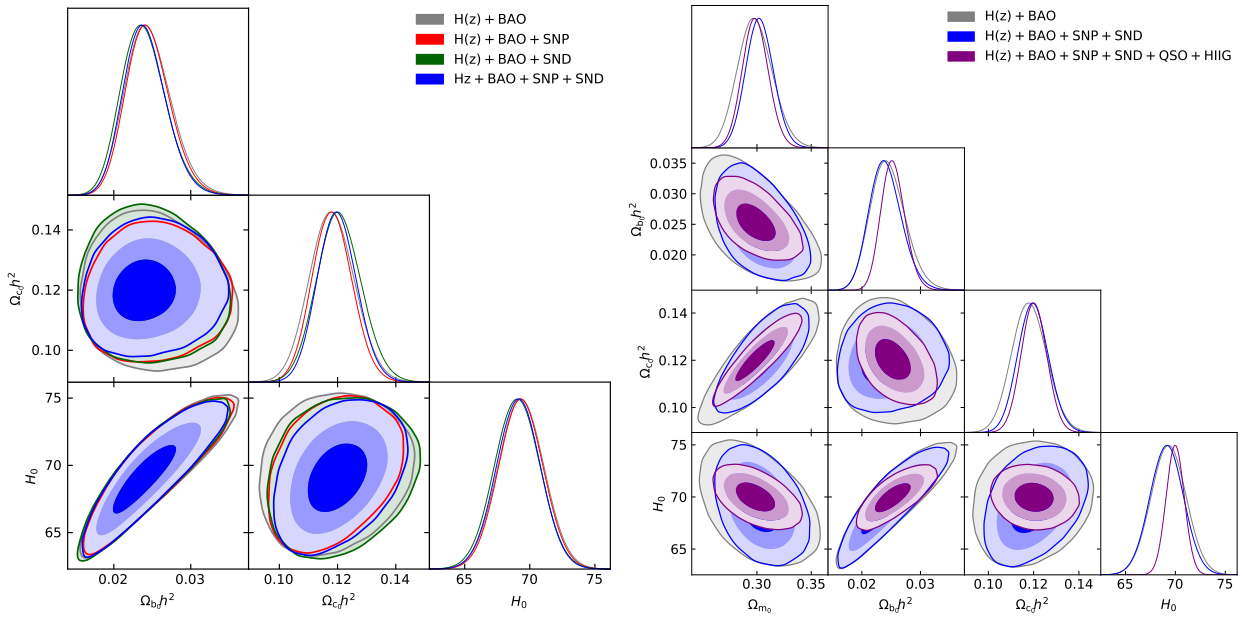

(a) (b)

Figure 5.1: 1σ, 2σ, and 3σ confidence contours for flat ΛCDM, where the right panel is the comparison including derived cosmological matter density parameter Ω_{m0}. In all cases, the favored parameter space is associated with currently-accelerating cosmological expansion.

responding χ^2, AIC, BIC, and degrees of freedom ν ($\nu \equiv N - n$) for all models and data combinations, in Table 5.2. The marginalized best-fitting parameter values and uncertainties ($\pm 1\sigma$ error bars or 2σ limits), for all models and data combinations, are listed in Table 5.3.[8]

5.4.1 $H(z)$ + BAO, HzBSNP, and HzBSND constraints

The 1D marginalized $H(z)$ + BAO constraints on the cosmological parameters are listed in Table 5.3. These are (slightly) different from the ones obtained by Khadka & Ratra (2021), because of the different treatments of both the prior ranges and the coefficient κ in the ϕCDM models.[9]

The $H(z)$, BAO, and SN-Pantheon data combinations have previously been studied (Park & Ratra, 2019b). Relative to that analysis, we use the updated BAO data, shown in Table 5.1, in our analysis here. In the HzBSNP case, we find that the determinations of Ω_{k0} are

[8]The PYTHON package GETDIST (Lewis, 2019) is used to analyze the samples.

[9]We treated κ as a derived constant determined from the parameter α (see e.g. eq. (14) of Cao et al., 2021a), while Khadka & Ratra (2021) treated it as a constant derived from the energy budget equation.

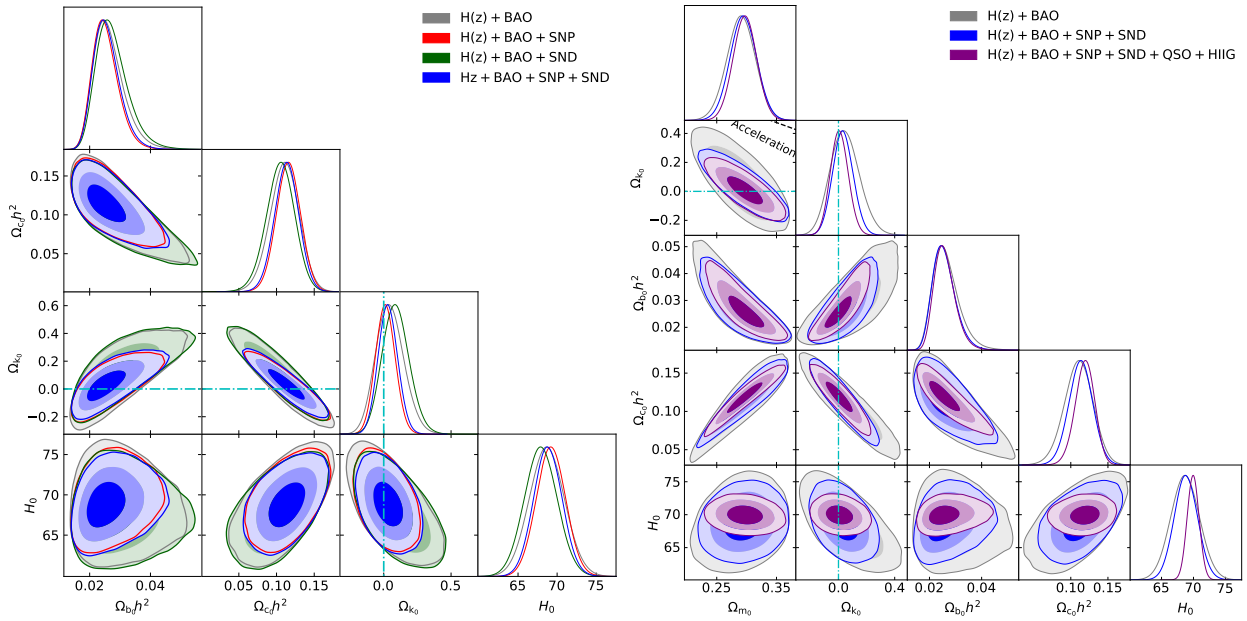

(a) (b)

Figure 5.2: Same as Fig. 5.1 but for non-flat ΛCDM, where the cyan dash-dot lines represent the flat ΛCDM case, with closed spatial hypersurfaces either below or to the left. The black dotted line in the right subpanel is the zero-acceleration line, which divides the parameter space into regions associated with currently-accelerating (below left) and currently-decelerating (above right) cosmological expansion. In all cases, the favored parameter space is associated with currently-accelerating cosmological expansion.

more consistent with flat spatial hypersurfaces than what Park & Ratra (2019b) found and dark energy dynamics favors less deviation from a cosmological constant in the XCDM cases, while favoring a somewhat stronger deviation from $\alpha = 0$ in the non-flat ϕCDM case.

Because the $H(z)$, BAO, and SN-DES constraints are consistent across all six of the models we study, we also perform a joint analysis of these data to determine HzBSND constraints. Relative to the HzBSNP constraints, the measured values of $\Omega_{\mathrm{b}_0}h^2$, $\Omega_{\mathrm{c}_0}h^2$, and Ω_{m0} are a little higher, lower, and lower (except for flat ΛCDM) than those values measured from the HzBSNP case, respectively. Given the error bars, these differences are not statistically significant. The measured values of H_0 are lower than those for the HzBSNP case. The non-flat XCDM and ϕCDM models favor more and less closed geometry than in the HzBSNP case. The non-flat ΛCDM model favors more open geometry than in the HzBSNP case. The constraints for all three non-flat models are consistent with spatially flat hypersurfaces. The fits to the HzBSND data produce stronger evidence for dark energy dynamics than the fits to the HzBSNP data.

5.4.2 HzBSNPD constraints

The results of the previous three subsections show that, when combined with $H(z)$ + BAO data, SN-Pantheon data produce tighter constraints on almost all cosmological parameters, than do SN-DES data (with a few exceptions including $\Omega_{\mathrm{b}_0}h^2$ for non-flat ΛCDM, $\Omega_{\mathrm{c}_0}h^2$ for non-flat ϕCDM, and Ω_{m0} and H_0 for flat and non-flat ϕCDM). Since the $H(z)$ + BAO, SN-Pantheon, and SN-DES data constraints are not inconsistent, it is useful to derive constraints from an analysis of the combined $H(z)$, BAO, SN-Pantheon, and SN-DES (HzBSNPD) data. The results of such an analysis are presented in this subsection. We discuss these results in some detail here because, as discussed in Sec. 5.4.4, we believe that the constraints we obtain from the HzBSNPD data combination are more reliable than the constraints we obtain from the other data combinations we study.

The measured values of $\Omega_{\mathrm{b}_0}h^2$ range from a low of $0.0241^{+0.0024}_{-0.0030}$ (flat ΛCDM) to a high of $0.0279^{+0.0031}_{-0.0048}$ (flat ϕCDM) and those of $\Omega_{\mathrm{c}_0}h^2$ range from a low of $0.1047^{+0.0125}_{-0.0096}$ (flat ϕCDM)

Table 5.2: Unmarginalized best-fitting parameter values for all models from various combinations of data.

Model	Data set	$\Omega_{b_0}h^2$	$\Omega_{c_0}h^2$	Ω_{m_0}	Ω_{k_0}	w_X	α	H_0[a]	χ^2	ν	AIC	BIC
Flat ΛCDM	$H(z)$ + BAO	0.0240	0.1179	0.299	–	–	–	69.11	23.64	39	29.64	34.86
	HzBSNP[b]	0.0240	0.1180	0.299	–	–	–	69.10	1053.22	1087	1059.22	1074.21
	HzBSND[c]	0.0234	0.1203	0.305	–	–	–	68.82	50.83	59	56.83	63.21
	HzBSNPD[d]	0.0236	0.1196	0.303	–	–	–	68.91	1080.46	1107	1086.46	1101.50
	HzBSNPDQH[e]	0.0251	0.1203	0.299	–	–	–	69.92	1844.99	1380	1850.99	1866.69
Non-flat ΛCDM	$H(z)$ + BAO	0.0248	0.1136	0.294	0.026	–	–	68.75	23.58	38	31.58	38.53
	HzBSNP[b]	0.0241	0.1172	0.298	0.004	–	–	69.06	1053.22	1086	1061.22	1081.20
	HzBSND[c]	0.0258	0.1081	0.292	0.071	–	–	67.92	50.28	58	58.28	66.79
	HzBSNPD[d]	0.0245	0.1150	0.297	0.023	–	–	68.68	1080.35	1106	1088.35	1108.40
	HzBSNPDQH[e]	0.0249	0.1209	0.300	−0.004	–	–	69.93	1844.99	1379	1852.99	1873.92
Flat XCDM	$H(z)$ + BAO	0.0323	0.0860	0.280	–	−0.696	–	65.12	19.65	38	27.65	34.60
	HzBSNP[b]	0.0254	0.1120	0.292	–	−0.951	–	68.72	1052.63	1086	1060.63	1080.61
	HzBSND[c]	0.0300	0.0934	0.286	–	−0.752	–	65.90	45.46	58	53.46	61.97
	HzBSNPD[d]	0.0256	0.1107	0.293	–	−0.932	–	68.43	1079.23	1106	1087.23	1107.28
	HzBSNPDQH[e]	0.0268	0.1136	0.291	–	−0.949	–	69.63	1844.27	1379	1852.27	1873.20
Non-flat XCDM	$H(z)$ + BAO	0.0302	0.0956	0.294	−0.155	−0.650	–	65.55	18.31	37	28.31	37.00
	HzBSNP[b]	0.0234	0.1231	0.307	−0.103	−0.895	–	69.25	1051.82	1085	1061.82	1086.79
	HzBSND[c]	0.0277	0.1046	0.301	−0.136	−0.711	–	66.45	44.34	57	54.34	64.98
	HzBSNPD[d]	0.0236	0.1220	0.307	−0.107	−0.877	–	68.98	1078.36	1105	1088.36	1113.42
	HzBSNPDQH[e]	0.0242	0.1217	0.303	−0.092	−0.900	–	69.54	1843.25	1378	1853.25	1879.41
Flat ϕCDM	$H(z)$ + BAO	0.0361	0.0758	0.264	–	–	1.484	65.30	19.48	38	27.48	34.43
	HzBSNP[b]	0.0260	0.1145	0.292	–	–	0.101	69.51	1051.46	1086	1059.46	1079.44
	HzBSND[c]	0.0328	0.0860	0.273	–	–	1.061	66.16	45.17	58	53.17	61.68
	HzBSNPD[d]	0.0254	0.1102	0.292	–	–	0.168	68.35	1078.18	1106	1086.18	1106.22
	HzBSNPDQH[e]	0.0264	0.1135	0.290	–	–	0.132	69.57	1842.95	1379	1850.95	1871.88
Non-flat ϕCDM	$H(z)$ + BAO	0.0354	0.0811	0.269	−0.148	–	1.819	66.06	18.16	37	28.16	36.85
	HzBSNP[b]	0.0234	0.1225	0.305	−0.133	–	0.393	69.32	1050.31	1085	1060.31	1085.28
	HzBSND[c]	0.0319	0.0933	0.282	−0.140	–	1.411	66.84	44.09	57	54.09	64.72
	HzBSNPD[d]	0.0256	0.1159	0.298	−0.080	–	0.377	69.09	1077.13	1105	1087.13	1112.19
	HzBSNPDQH[e]	0.0258	0.1155	0.293	−0.078	–	0.354	69.55	1842.00	1378	1852.00	1878.16

[a] km s^{-1} Mpc^{-1}.
[b] $H(z)$ + BAO + SN-Pantheon.
[c] $H(z)$ + BAO + SN-DES.
[d] $H(z)$ + BAO + SN-Pantheon + SN-DES.
[e] $H(z)$ + BAO + SN-Pantheon + SN-DES + QSO + H II G.

to a high of 0.1199 ± 0.0067 (flat ΛCDM). The derived constraints on Ω_{m0} range from a low of $0.284^{+0.017}_{-0.016}$ (flat ϕCDM) to a high of 0.303 ± 0.013 (flat ΛCDM). These measurements are consistent with what is measured by Planck Collaboration (2020). In particular, for flat ΛCDM, comparing to the TT,TE,EE+lowE+lensing results in Table 2 of Planck Collaboration (2020) the error bars we find here for $\Omega_b h^2$, $\Omega_c h^2$, and Ω_{m0} are a factor of 18, 5.6, and 1.8, respectively, larger than the *Planck* error bars, and our estimates here for the quantities differ from the *Planck* estimates by 0.58σ, 0.015σ, and 0.82σ, respectively.

The constraints on H_0 are between $H_0 = 68.48^{+1.71}_{-1.70}$ km s^{-1} Mpc^{-1} (flat ϕCDM) and $H_0 = 69.14 \pm 1.68$ km s^{-1} Mpc^{-1} (flat ΛCDM), which are 0.35σ (flat ΛCDM) and 0.15σ (flat ϕCDM) higher than the median statistics estimate of $H_0 = 68 \pm 2.8$ km s^{-1} Mpc^{-1} (Chen & Ratra, 2011), and 2.22σ (flat ΛCDM) and 2.50σ (flat ϕCDM) lower than the local Hubble constant measurement of $H_0 = 74.03 \pm 1.42$ km s^{-1} Mpc^{-1} (Riess et al., 2019).[10] For flat ΛCDM our H_0 error bar is a factor of 3.1 larger than that from the *Planck* data and our H_0 estimate is 1.01σ higher than that of *Planck*.

For non-flat ΛCDM, non-flat XCDM, and non-flat ϕCDM, we find $\Omega_{k_0} = 0.032 \pm 0.072$, $\Omega_{k_0} = -0.071^{+0.110}_{-0.123}$, and $\Omega_{k_0} = -0.105 \pm 0.104$, respectively, with non-flat ϕCDM favoring closed geometry at 1.01σ. The non-flat XCDM and ϕCDM models favor closed geometry, while the non-flat ΛCDM model favors open geometry. The constraints for non-flat ΛCDM and XCDM models are consistent with spatially flat hypersurfaces.

The fits to the HzBSNPD data favor dark energy dynamics, where for flat (non-flat) XCDM, $w_X = -0.932 \pm 0.061$ ($w_X = -0.904^{+0.098}_{-0.058}$), with best-fitting value being 1.11σ (1.66σ) away from $w_X = -1$; and for flat (non-flat) ϕCDM, $\alpha = 0.320^{+0.108}_{-0.277}$ ($\alpha = 0.509^{+0.212}_{-0.370}$), with best-fitting value being 1.16σ (1.38σ) away from $\alpha = 0$.

[10] Other local expansion rate H_0 measurements result in slightly lower central values with slightly larger error bars (Breuval et al., 2020; Dhawan et al., 2018; Efstathiou, 2020; Fernández Arenas et al., 2018; Freedman et al., 2020; Khetan et al., 2021; Rameez & Sarkar, 2019; Rigault et al., 2015; Zhang et al., 2017). Our H_0 determinations are consistent with earlier median statistics determinations (Chen et al., 2003; Gott et al., 2001) as well as with other recent H_0 measurements (Birrer et al., 2020; Blum et al., 2020; Boruah et al., 2021; Chen et al., 2017; Cuceu et al., 2019; DES Collaboration, 2018; Denzel et al., 2021; Domínguez et al., 2019; Gómez-Valent & Amendola, 2018; Harvey, 2020; Kim et al., 2020; Lin & Ishak, 2021; Lyu et al., 2020; Philcox et al., 2020; Planck Collaboration, 2020; Pogosian et al., 2020; Schöneberg et al., 2019; Zeng & Yan, 2019; Zhang & Huang, 2021).

Table 5.3: One-dimensional marginalized best-fitting parameter values and uncertainties ($\pm1\sigma$ error bars or 2σ limits) for all models from various combinations of data.

Model	Data set	$\Omega_{b_0}h^2$	$\Omega_{c_0}h^2$	Ω_{m_0}	Ω_{k_0}	w_X	α	H_0[a]
Flat ΛCDM	$H(z)$ + BAO	$0.0245^{+0.0026}_{-0.0032}$	0.1182 ± 0.0077	$0.298^{+0.015}_{-0.017}$	–	–	–	69.33 ± 1.75
	HzBSNP[b]	$0.0245^{+0.0025}_{-0.0031}$	0.1182 ± 0.0068	0.298 ± 0.013	–	–	–	69.32 ± 1.70
	HzBSND[c]	$0.0239^{+0.0025}_{-0.0032}$	0.1206 ± 0.0076	$0.305^{+0.015}_{-0.017}$	–	–	–	69.04 ± 1.74
	HzBSNPD[d]	$0.0241^{+0.0024}_{-0.0030}$	0.1199 ± 0.0067	0.303 ± 0.013	–	–	–	69.14 ± 1.68
	HzBSNPDQH[e]	$0.0253^{+0.0019}_{-0.0022}$	0.1202 ± 0.0057	0.299 ± 0.012	–	–	–	69.98 ± 0.91
Non-flat ΛCDM	$H(z)$ + BAO	$0.0265^{+0.0035}_{-0.0059}$	0.1104 ± 0.0192	0.291 ± 0.024	$0.047^{+0.095}_{-0.112}$	–	–	68.71 ± 2.24
	HzBSNP[b]	$0.0253^{+0.0033}_{-0.0049}$	$0.1158^{+0.0161}_{-0.0160}$	0.296 ± 0.022	0.013 ± 0.073	–	–	69.22 ± 1.86
	HzBSND[c]	$0.0276^{+0.0038}_{-0.0062}$	$0.1049^{+0.0188}_{-0.0187}$	0.288 ± 0.024	$0.090^{+0.093}_{-0.106}$	–	–	67.92 ± 2.10
	HzBSNPD[d]	$0.0257^{+0.0033}_{-0.0050}$	0.1133 ± 0.0160	0.295 ± 0.022	0.032 ± 0.072	–	–	68.83 ± 1.82
	HzBSNPDQH[e]	$0.0260^{+0.0031}_{-0.0046}$	$0.1188^{+0.0138}_{-0.0123}$	0.297 ± 0.020	0.007 ± 0.063	–	–	69.95 ± 0.93
Flat XCDM	$H(z)$ + BAO	$0.0372^{+0.0045}_{-0.0138}$	$0.0777^{+0.0351}_{-0.0182}$	$0.270^{+0.036}_{-0.022}$	–	$-0.688^{+0.174}_{-0.109}$	–	$65.22^{+2.21}_{-2.64}$
	HzBSNP[b]	$0.0261^{+0.0030}_{-0.0041}$	0.1118 ± 0.0105	0.292 ± 0.016	–	-0.951 ± 0.063	–	68.91 ± 1.76
	HzBSND[c]	$0.0331^{+0.0038}_{-0.0091}$	$0.0881^{+0.0235}_{-0.0137}$	$0.279^{+0.027}_{-0.019}$	–	$-0.739^{+0.110}_{-0.108}$	–	65.95 ± 2.08
	HzBSNPD[d]	$0.0264^{+0.0031}_{-0.0042}$	0.1105 ± 0.0107	0.292 ± 0.016	–	-0.932 ± 0.061	–	68.62 ± 1.73
	HzBSNPDQH[e]	$0.0273^{+0.0026}_{-0.0035}$	$0.1131^{+0.0104}_{-0.0095}$	0.291 ± 0.015	–	-0.949 ± 0.059	–	$69.67^{+0.97}_{-0.96}$
Non-flat XCDM	$H(z)$ + BAO	$0.0367^{+0.0049}_{-0.0145}$	$0.0822^{+0.0376}_{-0.0233}$	$0.278^{+0.041}_{-0.030}$	$-0.122^{+0.137}_{-0.136}$	$-0.647^{+0.159}_{-0.084}$	–	$65.39^{+2.18}_{-2.59}$
	HzBSNP[b]	$0.0251^{+0.0031}_{-0.0049}$	0.1186 ± 0.0167	0.301 ± 0.023	$-0.066^{+0.111}_{-0.124}$	$-0.923^{+0.104}_{-0.060}$	–	69.24 ± 1.87
	HzBSND[c]	$0.0315^{+0.0039}_{-0.0091}$	$0.0956^{+0.0260}_{-0.0190}$	$0.290^{+0.031}_{-0.026}$	-0.099 ± 0.133	$-0.714^{+0.116}_{-0.089}$	–	66.30 ± 2.14
	HzBSNPD[d]	$0.0253^{+0.0032}_{-0.0048}$	$0.1178^{+0.0166}_{-0.0165}$	0.301 ± 0.023	$-0.071^{+0.110}_{-0.123}$	$-0.904^{+0.098}_{-0.058}$	–	69.00 ± 1.85
	HzBSNPDQH[e]	$0.0256^{+0.0030}_{-0.0046}$	$0.1182^{+0.0136}_{-0.0121}$	0.299 ± 0.020	$-0.063^{+0.087}_{-0.097}$	$-0.919^{+0.085}_{-0.056}$	–	69.59 ± 0.97
Flat ϕCDM	$H(z)$ + BAO	$0.0480^{+0.0113}_{-0.0195}$	$0.0524^{+0.0246}_{-0.0427}$	$0.240^{+0.024}_{-0.044}$	–	–	$2.418^{+1.197}_{-1.331}$	$64.67^{+1.86}_{-2.22}$
	HzBSNP[b]	$0.0278^{+0.0030}_{-0.0046}$	$0.1055^{+0.0119}_{-0.0091}$	0.284 ± 0.016	–	–	< 0.666	$68.71^{+1.73}_{-1.74}$
	HzBSND[c]	$0.0429^{+0.0071}_{-0.0170}$	$0.0641^{+0.0371}_{-0.0235}$	$0.251^{+0.038}_{-0.031}$	–	–	$1.863^{+0.674}_{-1.316}$	$65.41^{+1.91}_{-2.08}$
	HzBSNPD[d]	$0.0279^{+0.0031}_{-0.0048}$	$0.1047^{+0.0125}_{-0.0096}$	$0.284^{+0.017}_{-0.016}$	–	–	$0.320^{+0.108}_{-0.277}$	$68.48^{+1.71}_{-1.70}$
	HzBSNPDQH[e]	$0.0289^{+0.0025}_{-0.0040}$	$0.1073^{+0.0116}_{-0.0081}$	$0.283^{+0.016}_{-0.014}$	–	–	$0.261^{+0.067}_{-0.254}$	69.57 ± 0.94
Non-flat ϕCDM	$H(z)$ + BAO	$0.0482^{+0.0126}_{-0.0190}$	$0.0544^{+0.0194}_{-0.0497}$	$0.242^{+0.024}_{-0.046}$	-0.103 ± 0.132	–	$2.618^{+1.213}_{-1.226}$	$65.14^{+2.02}_{-2.29}$
	HzBSNP[b]	$0.0260^{+0.0033}_{-0.0051}$	$0.1159^{+0.0163}_{-0.0161}$	0.296 ± 0.022	-0.106 ± 0.102	–	$0.454^{+0.174}_{-0.372}$	69.33 ± 1.86
	HzBSND[c]	$0.0427^{+0.0076}_{-0.0177}$	$0.0670^{+0.0379}_{-0.0282}$	$0.253^{+0.037}_{-0.039}$	-0.097 ± 0.130	–	$2.058^{+0.779}_{-1.269}$	65.86 ± 2.09
	HzBSNPD[d]	$0.0264^{+0.0034}_{-0.0052}$	0.1139 ± 0.0161	0.295 ± 0.022	-0.105 ± 0.104	–	$0.509^{+0.212}_{-0.370}$	$69.06^{+1.84}_{-1.83}$
	HzBSNPDQH[e]	$0.0265^{+0.0031}_{-0.0048}$	$0.1142^{+0.0141}_{-0.0123}$	0.293 ± 0.020	-0.085 ± 0.081	–	$0.399^{+0.159}_{-0.313}$	69.53 ± 0.95

[a] km s^{-1} Mpc^{-1}.
[b] $H(z)$ + BAO + SN-Pantheon.
[c] $H(z)$ + BAO + SN-DES.
[d] $H(z)$ + BAO + SN-Pantheon + SN-DES.
[e] $H(z)$ + BAO + SN-Pantheon + SN-DES + QSO + H II G.

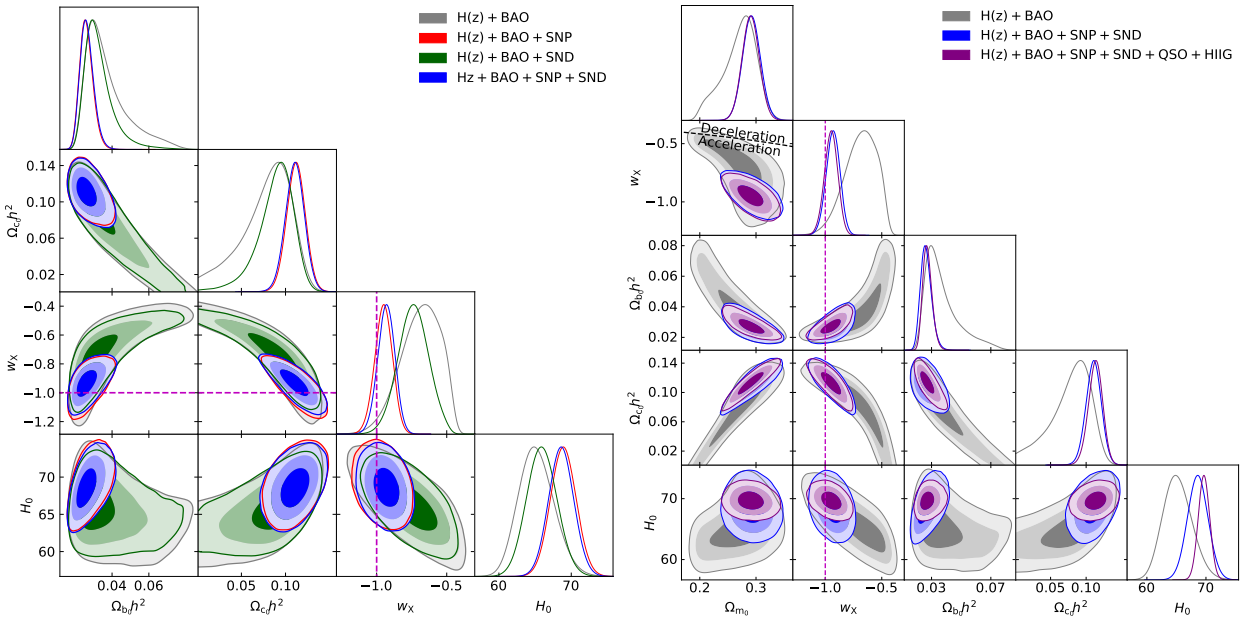

(a) (b)

Figure 5.3: 1σ, 2σ, and 3σ confidence contours for flat XCDM. The black dotted line in the right panel is the zero-acceleration line, which divides the parameter space into regions associated with currently-accelerating (below) and currently-decelerating (above) cosmological expansion. In all cases, almost all of the favored parameter space is associated with currently-accelerating cosmological expansion. The magenta lines denote $w_X = -1$, i.e. the flat ΛCDM model.

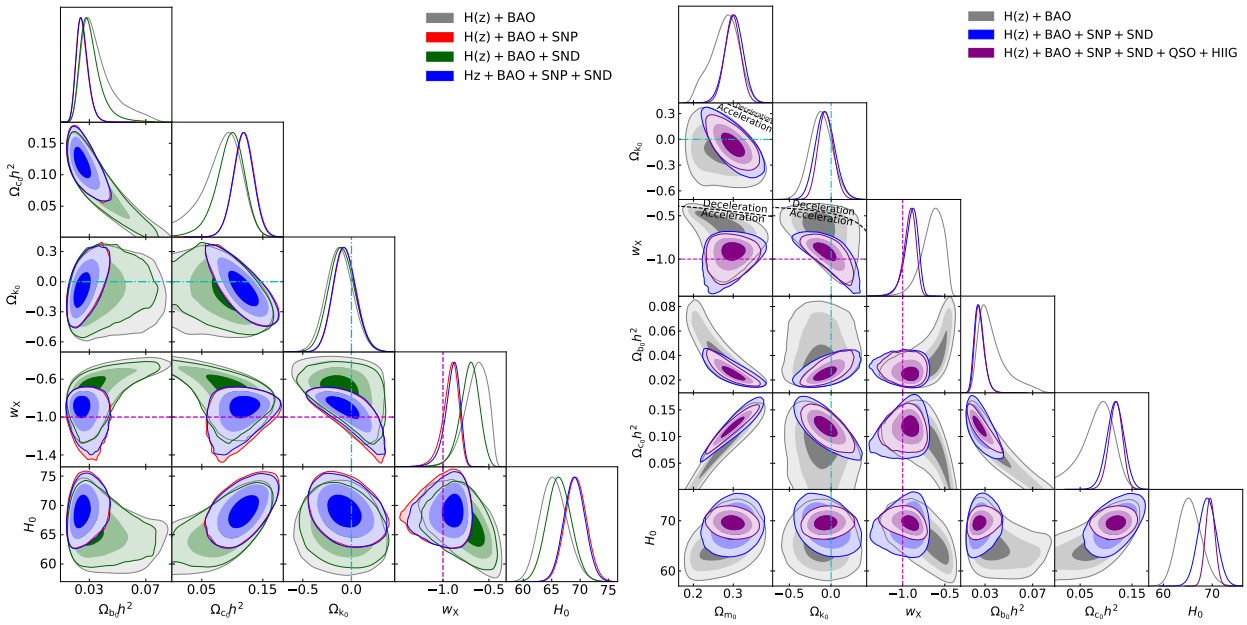

Figure 5.4: Same as Fig. 5.3 but for non-flat XCDM, where the zero acceleration lines in each of the three subpanels of the right panel are computed for the third cosmological parameter set to the $H(z)$ + BAO data best-fitting values listed in Table 5.2. Currently-accelerating cosmological expansion occurs below these lines. The cyan dash-dot lines represent the flat XCDM case, with closed spatial hypersurfaces either below or to the left. In all cases, almost all of the favored parameter space is associated with currently-accelerating cosmological expansion. The magenta lines indicate $w_{\rm X} = -1$, i.e. the non-flat ΛCDM model.

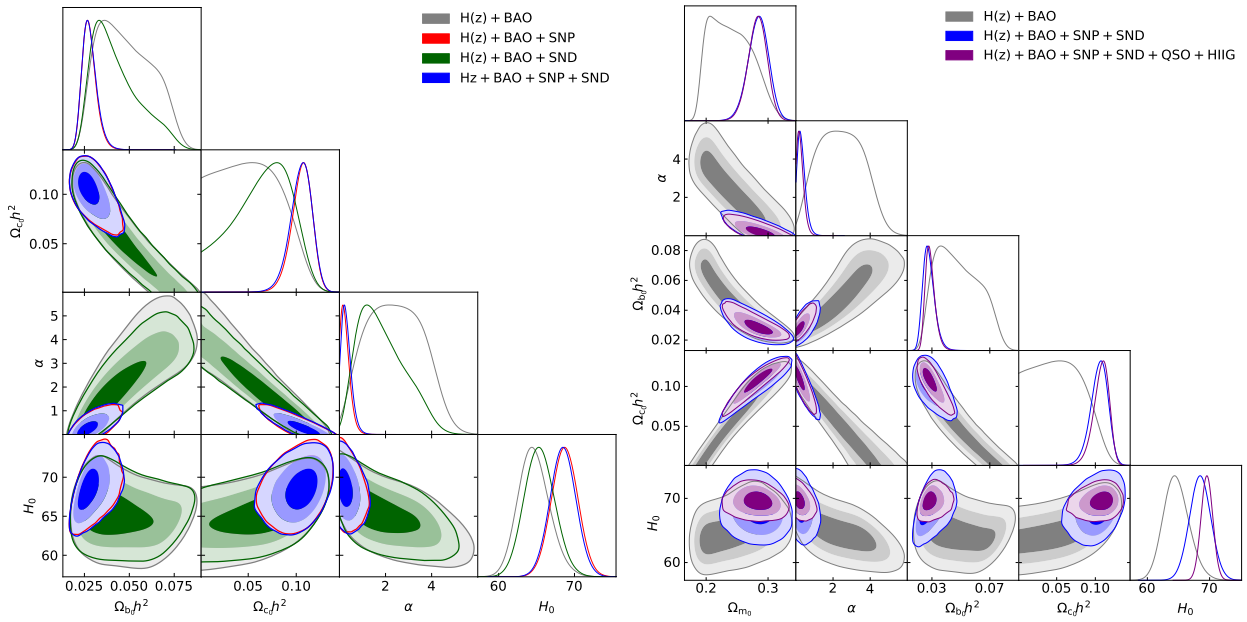

(a) (b)

Figure 5.5: 1σ, 2σ, and 3σ confidence contours for flat ϕCDM. In all cases, the favored parameter space is associated with currently-accelerating cosmological expansion. The $\alpha = 0$ axis is the flat ΛCDM model.

5.4.3 HzBSNPDQH constraints

Since the constraints derived from $H(z)$, BAO, SN-Pantheon, SN-DES, QSO, and H II G data are not inconsistent, in this subsection we jointly analyze HzBSNPDQH data to determine more restrictive constraints on the cosmological parameters (though as discussed in Sec. 5.4.4, we believe these constraints to be less reliable than those that stem from the HzSNPD combination, so we only describe the broad outlines here).

For flat ΛCDM, the error bars we derive for $\Omega_b h^2$, $\Omega_c h^2$, and Ω_{m0} are larger than the *Planck* error bars, though our central estimates of these quantities are broadly consistent with those derived from *Planck*. In a similar fashion, we find larger error bars on H_0 in flat ΛCDM than does *Planck*, though our central estimate is higher than theirs. Generally, the constraints we derive on H_0 are more consistent with the median statistics estimate of $H_0 = 68 \pm 2.8$ km s^{-1} Mpc^{-1} (Chen & Ratra, 2011), than with the local Hubble constant measurement of $H_0 = 74.03 \pm 1.42$ km s^{-1} Mpc^{-1} (Riess et al., 2019).

We find mild evidence for spatial curvature, with non-flat XCDM and ϕCDM favoring

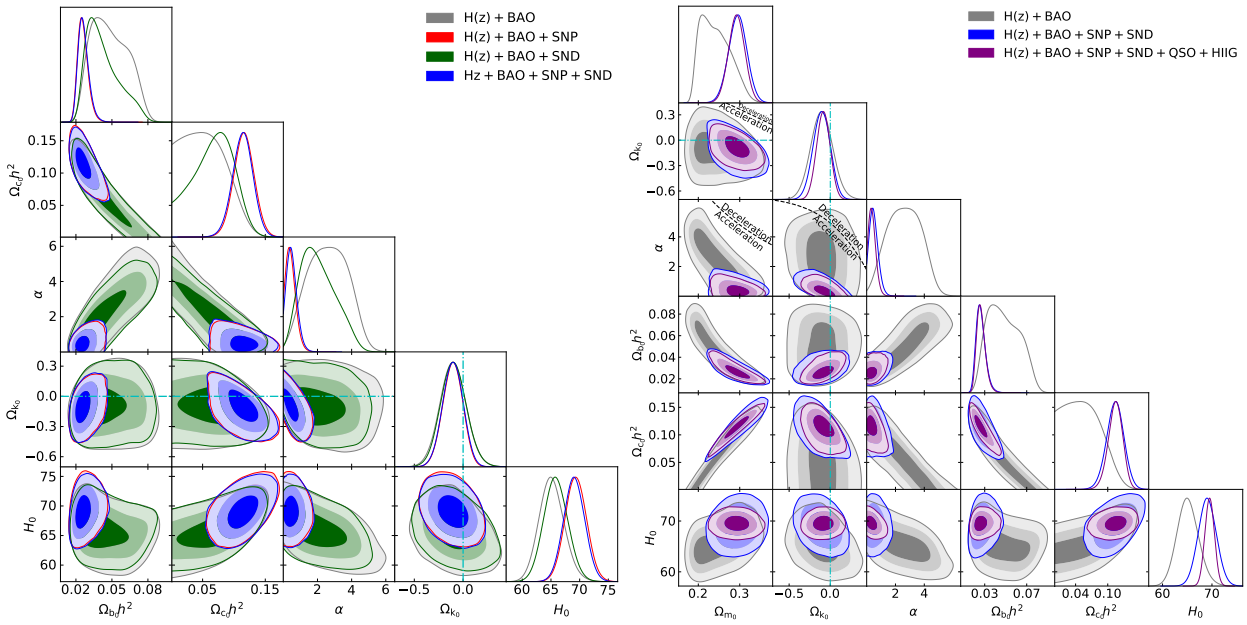

(a) (b)

Figure 5.6: Same as Fig. 5.5 but for non-flat ϕCDM, where the zero-acceleration lines in each of the sub-panels of the right panel are computed for the third cosmological parameter set to the $H(z)$ + BAO data best-fitting values listed in Table 5.2. Currently-accelerating cosmological expansion occurs below these lines. In all cases, almost all of the favored parameter space is associated with currently-accelerating cosmological expansion. The cyan dash-dot lines represent the flat ϕCDM case, with closed spatial geometry either below or to the left. The $\alpha = 0$ axis is the non-flat ΛCDM model.

closed geometry, and non-flat ΛCDM mildly favoring open geometry. The constraints from non-flat ΛCDM and XCDM are consistent with spatially flat hypersurfaces to within less than 1σ. Additionally, we find mild evidence for dark energy dynamics, with the best-fitting value of $w_{\rm X}$ being 0.86σ (1.45σ) away from $w_{\rm X} = -1$ in flat (non-flat) XCDM, and the best-fitting value of α being 1.03σ (1.27σ) away from $\alpha = 0$ in flat (non-flat) ϕCDM.

5.4.4 Model comparison

The values of $\Delta\chi^2$, ΔAIC, ΔBIC, and the reduced χ^2 (χ^2/ν) are reported in Table 5.4, where $\Delta\chi^2$, ΔAIC, and ΔBIC, respectively, are defined as the differences between the values of the χ^2, AIC, and BIC for a given model and their corresponding minimum values among all models. From Table 5.4, we see that the reduced χ^2 values determined from the $H(z)$ + BAO data combination range from 0.49 to 0.62, which is probably due to the $H(z)$ data having overestimated error bars (see Cao et al., 2021a for discussions of the systematic errors of these data). As discussed in Ryan et al. (2019) and Cao et al. (2020), the underestimated systematic uncertainties in QSO and H II G data[11] result in larger reduced χ^2 (~ 1.34) for the models in the HzBSNPDQH case. The reduced χ^2 values for the HzBSNP and HzBSNPD cases are around unity for all models and for the HzBSND case range from 0.77 to 0.87. Of the combinations we study here, on the basis of these reduced χ^2 values, the HzBSNPD constraints should be viewed as the most reliable ones.

We find that based on the AIC and BIC, flat ΛCDM and flat ϕCDM are the most favored models in different data combination cases. The ΔAIC results show that the most favored model is flat ΛCDM in the HzBSNP case, while the most favored model is flat ϕCDM in the rest of the data combinations. The ΔBIC results show that the most favored model is flat ϕCDM in the $H(z)$ + BAO and HzBSND cases, and is flat ΛCDM in the remaining cases. For both ΔAIC and ΔBIC results, the most disfavored model is non-flat ΛCDM in the $H(z)$ + BAO and HzBSND cases, and is non-flat XCDM in all other cases, with positive

[11] Roberto Terlevich and his colleagues are currently investigating the systematic uncertainties of the H II G data, the results of which they plan to publish in a future paper (Roberto Terlevich, private communication, 2021).

Table 5.4: $\Delta\chi^2$, ΔAIC, ΔBIC, and $\chi^2_{\rm min}/\nu$ values.

Quantity	Data set	Flat ΛCDM	Non-flat ΛCDM	Flat XCDM	Non-flat XCDM	Flat ϕCDM	Non-flat ϕCDM
	$H(z)$ + BAO	5.48	5.42	1.49	0.15	1.32	0.00
	HzBSNP[a]	2.91	2.91	2.32	1.51	1.15	0.00
$\Delta\chi^2$	HzBSND[b]	6.74	6.19	1.37	0.25	1.08	0.00
	HzBSNPD[c]	3.33	3.22	2.10	1.23	1.05	0.00
	HzBSNPDQH[d]	2.99	2.99	2.27	1.25	0.95	0.00
	$H(z)$ + BAO	2.16	4.10	0.17	0.83	0.00	0.68
	HzBSNP[a]	0.00	2.00	1.41	2.60	0.24	1.09
ΔAIC	HzBSND[b]	3.66	5.11	0.29	1.17	0.00	0.92
	HzBSNPD[c]	0.28	2.17	1.05	2.18	0.00	0.95
	HzBSNPDQH[d]	0.04	2.04	1.32	2.30	0.00	1.05
	$H(z)$ + BAO	0.43	4.10	0.17	2.57	0.00	2.42
	HzBSNP[a]	0.00	6.99	6.40	12.58	5.23	11.07
ΔBIC	HzBSND[b]	1.53	5.11	0.29	3.30	0.00	3.04
	HzBSNPD[c]	0.00	6.90	5.78	11.92	4.72	10.69
	HzBSNPDQH[d]	0.00	7.23	6.51	12.72	5.19	11.47
	$H(z)$ + BAO	0.61	0.62	0.52	0.49	0.51	0.49
	HzBSNP[a]	0.97	0.97	0.97	0.97	0.97	0.97
$\chi^2_{\rm min}/\nu$	HzBSND[b]	0.86	0.87	0.78	0.78	0.78	0.77
	HzBSNPD[c]	0.98	0.98	0.98	0.98	0.97	0.97
	HzBSNPDQH[d]	1.34	1.34	1.34	1.34	1.34	1.34

[a] $H(z)$ + BAO + SN-Pantheon.
[b] $H(z)$ + BAO + SN-DES.
[c] $H(z)$ + BAO + SN-Pantheon + SN-DES.
[d] $H(z)$ + BAO + SN-Pantheon + SN-DES + QSO + H II G.

evidence against non-flat ΛCDM and either positive or very strong evidence (depending on the data combination) against non-flat XCDM.

Overall, the ΔAIC results show no strong evidence against any model, and neither do the ΔBIC results for the $H(z)$ + BAO and HzBSND cases. However, in the HzBSNP and HzBSNPDQH cases, the ΔBIC results show strong evidence against the non-flat ΛCDM and flat XCDM models, and very strong evidence against the non-flat ϕCDM and XCDM models. In the HzBSNPD case, the evidence against flat XCDM and flat ϕCDM is positive, the evidence against non-flat ΛCDM is strong, and the evidence against non-flat ϕCDM and non-flat XCDM is very strong. Based on the $\Delta\chi^2$ results, non-flat ϕCDM has the minimum χ^2 in all cases.

In summary, the HzBSNPD data favor flat ϕCDM (AIC) or flat ΛCDM (BIC) among the six models we study here.

5.5 Conclusion

By analyzing a total of 1383 measurements, consisting of 31 $H(z)$, 11 BAO, 1048 SN-Pantheon, 20 SN-DES, 120 QSO, and 153 H II G data points, we jointly constrain cosmological parameters in six flat and non-flat cosmological models.

From the constraints derived using the cosmological models, we can identify some relatively model-independent features. As discussed in Sec. 5.4.4, the $H(z)$ + BAO + SN-Pantheon + SN-DES (HzBSNPD) data combination produces the most reliable constraints. In particular, for the HzBSNPD data combination, we find a reasonable and fairly restrictive summary value of $\Omega_{m_0} = 0.294 \pm 0.020$,[12] which is in good agreement with many other recent measurements (e.g. 0.315 ± 0.007 from Planck Collaboration, 2020). A fairly restrictive summary value of $H_0 = 68.8 \pm 1.8$ km s^{-1} Mpc^{-1} is found to be in better agreement with the estimates of Chen & Ratra (2011) and Planck Collaboration (2020) than with the measurement of Riess et al. (2019); note that the constraints from BAO data do not depend on physics of the early Universe (with $\Omega_{b_0}h^2$ being a free parameter that is fitted to the data used here). There is some room for dark energy dynamics or a little spatial curvature energy density in the HzBSNPD constraints, but based on AIC and BIC criteria, flat ϕCDM or flat ΛCDM are the best candidate models.

[12]Here we take the summary central value to be the mean of the two of six central-most values. As for the uncertainty, we call the difference between the two central-most values twice the systematic uncertainty and the average of the two central-most error bars the statistical uncertainty, and compute the summary error bar as the quadrature sum of the two uncertainties.

Chapter 6

Cosmological constraints from H II starburst galaxy, quasar angular size, and other measurements

This chapter is based on Cao et al. (2022a).

6.1 Introduction

Many observations indicate that the Universe is currently in a phase of accelerated expansion, however, the theory behind this is not yet well-established. Although the spatially flat ΛCDM model[1] (Peebles, 1984) is consistent with most observations (see e.g. eBOSS Collaboration, 2021; Farooq et al., 2017; Planck Collaboration, 2020; Scolnic et al., 2018), some potential observational discrepancies and theoretical puzzles (see e.g. Di Valentino et al., 2021a; Perivolaropoulos & Skara, 2022) suggest that there still is room for other cosmological models, including, for example, non-flat ΛCDM (the Planck Collaboration, 2020 cosmic microwave background (CMB) anisotropy TT,TE,EE+lowE+lensing data favor positive spa-

[1]The flat ΛCDM model has flat spatial hypersurfaces and a time-independent dark energy, a cosmological constant Λ, that provides approximately 70% of the current cosmological energy budget. Non-relativistic cold dark matter (CDM) accounts for approximately 25% and non-relativistic baryonic matter accounts for almost all of the remaining $\sim 5\%$ of the energy budget.

tial curvature) as well as dynamical dark energy. These discrepancies and puzzles motivate us to also study dynamical dark energy models and spatially non-flat models in this paper.

In this paper we use the new González-Morán et al. (2021) H II starburst galaxy (H IIG) measured fluxes and inferred absolute luminosities (from their correlation with their measured ionized gas velocity dispersions) as standard candles to constrain cosmological models.[2] These new H IIG data reach to a slightly higher redshift $z \sim 2.5$, somewhat higher than the baryon acoustic oscillation (BAO) standard ruler data that reach to $z \sim 2.3$, that we also use in this paper. In order to determine the expansion rate and geometry of the Universe, it is vital to measure distances using either standard candles or standard rules. More data sets probing wider redshift regions would provide more information and make more contributions to a better understanding of our Universe, so it is worthwhile to seek additional standard rulers. The angular sizes of quasars (QSOs) provide one such additional probe, reaching to $z \sim 2.7$, which we have explored in previous work (Cao et al., 2020, 2021a,b; Ryan et al., 2019). As described in those papers and in Sec. 6.2 below, intermediate luminosity QSOs have, over a fairly wide range of redshifts ($0.46 \lesssim z \lesssim 2.7$), very similar intrinsic lengths $l_{\rm m} = 11.03 \pm 0.25$ pc (Cao et al., 2017b). A knowledge of this intrinsic length scale, combined with measurements of the angular sizes of these QSOs allows one to determine the angular diameter distance out to the redshifts of the QSOs.

The QSO data that we have used in the past (from Cao et al., 2017b) have the following drawback, however: $l_{\rm m}$ was determined with a Gaussian process interpolation (Seikel et al., 2012) of the Hubble parameter from Hubble parameter ($H(z)$) data (as described in Cao et al., 2017b), many of which we have used in our previous analyses and also use in this paper. We have discussed this correlation between our QSO data and our $H(z)$ data in the past (Cao et al., 2021b; Ryan, 2021b), although we made the assumption in our earlier analyses that the correlation is not significant enough to have a strong effect on our results (owing to the weakness of the constraints from QSO data). Here we sidestep this problem

[2]Our analyses of the earlier González-Morán et al. (2019) data are described in Cao et al. (2020) (also see Cao et al., 2021a,b; Johnson et al., 2022). For analyses of earlier H IIG data, see Chávez et al. (2014, 2016); Mania & Ratra (2012); Melnick et al. (2000); Plionis et al. (2011); Siegel et al. (2005); Terlevich et al. (2015), and references therein. For recent analyses of the González-Morán et al. (2021) H IIG measurements, see Martínez-Aldama et al. (2019); Tsiapi et al. (2021).

by treating $l_{\rm m}$ as a free (nuisance) parameter, thereby constraining its value directly from our analysis. As discussed in Sec. 6.4, we find that the value of $l_{\rm m}$ is almost independent of cosmological model, and is consistent with the value $l_{\rm m} = 11.03 \pm 0.25$ pc from Cao et al. (2017b) that we used in our earlier work. This finding suggests that these QSOs are close to being standard rulers, and it validates the result of Cao et al. (2017b), independently of their method.

Significant constraints on cosmology now largely come from only a few data sets, at low $z \lesssim 2.3$, including BAO, Type Ia supernova (SN Ia), and $H(z)$ measurements, and at $z \sim 1100$ from CMB anisotropy observations. As mentioned above, it is useful and important to develop new probes, especially in the intermediate $2.3 \lesssim z \lesssim 1100$ redshift range. H II G is an example, as are QSO angular sizes that have been under discussion for a longer time (see e.g. Chen & Ratra, 2003; Gurvits et al., 1999; Lima & Alcaniz, 2002; Vishwakarma, 2001; Zhu & Fujimoto, 2002) with the compilation of Cao et al. (2017b) being a significant step forward. Other probes under development now include reverberation-measured Mg II time-lag radius-luminosity relation QSOs that reach to $z \sim 1.9$ (Czerny et al., 2021; Khadka et al., 2021a; Martínez-Aldama et al., 2019; Yu et al., 2021; Zajaček et al., 2021). High redshift options include QSO X-ray and UV flux measurements which extend to $z \sim 7.5$ (Khadka & Ratra, 2020a,b, 2021, 2022; Li et al., 2021; Lian et al., 2021; Lusso et al., 2020; Risaliti & Lusso, 2015, 2019; Yang et al., 2020),[3] and gamma-ray burst (GRB) data that extend to $z \sim 8.2$ (Amati et al., 2008, 2019; Demianski et al., 2021; Fana Dirirsa et al., 2019; Hu et al., 2021; Khadka & Ratra, 2020c; Khadka et al., 2021b; Samushia & Ratra, 2010; Wang et al., 2016, 2022).[4] As of now, all five of these probes provide mostly only weak cosmological constraints, but new data should yield tighter constraints that have the potential to soon usefully probe the largely unexplored $2 \lesssim z \lesssim 8$ part of cosmological redshift space.

Our comparisons here between the constraints from the new González-Morán et al. (2021) data and the old González-Morán et al. (2019) data show that the new data provide more

[3]However the current QSO compilation is standardizable up to only $z \sim 1.5$–1.7 (Khadka & Ratra, 2021, 2022).

[4]Only a smaller sample of 118 GRBs is reliable enough to be used for cosmological purposes, but include GRBs that probe to $z \sim 8.2$ (Khadka & Ratra, 2020c; Khadka et al., 2021b).

restrictive constraints on most cosmological parameters. As noted above, QSO angular size data provide relatively cosmological model-independent estimates of $l_{\rm m}$. We find that the cosmological constraints from $H(z)$, BAO, SN Ia, QSO, and the new H II G measurements are not mutually inconsistent, thus we combine them to provide more restrictive constraints on the cosmological and nuisance parameters. The almost model-independent summary constraints from this data combination are measurements of the Hubble constant, $H_0 = 69.7 \pm 1.2$ km s^{-1} Mpc^{-1}, the non-relativistic matter density parameter, $\Omega_{\rm m_0} = 0.293 \pm 0.021$, and the QSO characteristic linear size, $l_{\rm m} = 10.93 \pm 0.25$ pc. The estimate of H_0 is in better agreement with the median statistics estimate of Chen & Ratra (2011) ($H_0 = 68 \pm 2.8$ km s^{-1} Mpc^{-1}) than with the measurements of Planck Collaboration (2020) ($H_0 = 67.4 \pm 0.5$ km s^{-1} Mpc^{-1}) and Riess et al. (2021) ($H_0 = 73.2 \pm 1.3$ km s^{-1} Mpc^{-1}). Although the most-favored model is the spatially-flat ΛCDM model, there is room for some mild dark energy dynamics and a little non-zero spatial curvature energy density. We also find that currently accelerating cosmological expansion is favored by most of the data combinations we study (except for QSO data alone).

This paper is organized as follows. The models we study are described in Chapter 2. The data we used are introduced in Section 6.2 with the data analysis method presented in Section 6.3. We summarize our results and conclusions in Sections 6.4 and 6.5.

6.2 Data

In this paper our main focus is on a new set of H II G data (González-Morán et al., 2021, which we dub "H II G-2021"). We compare cosmological constraints from these H II G-2021 data to those from earlier H II G data. We also use these H II G-2021 data and BAO, $H(z)$, SN Ia, and QSO angular size measurements to constrain cosmological parameters in the models we study.

The 31 $H(z)$ measurements we use, that span the redshift range $0.070 \leq z \leq 1.965$, are given in Table 2 of Ryan et al. (2018).[5] The 11 BAO measurements we use, that span the

[5]These measurements were taken from Simon et al. (2005), Stern et al. (2010), Moresco et al. (2012),

redshift range $0.38 \leq z \leq 2.334$, are listed in Table 1 of Cao et al. (2021b).[6] Information on systematic errors of these data can be found in Cao et al. (2021a).

The SN-Pantheon data we use consist of 1048 SN Ia measurements, spanning the redshift range $0.01 < z < 2.3$, compiled in Scolnic et al. (2018). The SN-DES data we use consist of 20 binned measurements (of 207 SN Ia measurements), spanning the redshift range $0.015 \leq z \leq 0.7026$, compiled in DES Collaboration (2019d). See Cao et al. (2021b) for a description of how we use these SN Ia data.

The QSO data we use, that span the redshift range $0.462 \leq z \leq 2.73$, are listed in Table 1 of Cao et al. (2017b). These consist of 120 measurements of the angular size

$$\theta(z) = \frac{l_{\rm m}}{D_A(z)}. \tag{6.1}$$

Here $l_{\rm m}$ is the characteristic linear size of QSOs in the sample and D_A (defined below) is the angular size distance. Here we improve on the approach of Cao et al. (2017b), Ryan et al. (2019), and Cao et al. (2020, 2021a,b), by treating $l_{\rm m}$ as a nuisance parameter to be determined from these measurements so that these QSO data are independent of $H(z)$ data.

The old H II G data (which we dub "H II G-2019") consist of 107 low redshift measurements that span $0.0088 \leq z \leq 0.16417$, used in Chávez et al. (2014) (recalibrated by González-Morán et al., 2019), and 46 high redshift measurements that span $0.636427 \leq z \leq 2.42935$. The new H II G-2021 data, comprising the original 107 low redshift measurements and 74 updated high redshift measurements (that now span $0.636427 \leq z \leq 2.545$), are listed in Table A3 of González-Morán et al. (2021).

The correlation between H II G luminosity (L) and velocity dispersion (σ) is in equation (3.1). Note that the systematic uncertainties of both H II G and QSO data are not considered so that the reduced χ^2's are relatively large.

The transverse comoving distance $D_M(z)$ in equation (1.100), the luminosity distance $D_L(z)$, and the angular size distance $D_A(z)$ are related through equation (1.102).

Zhang et al. (2014), Moresco (2015), Moresco et al. (2016), and Ratsimbazafy et al. (2017).

[6] These measurements were taken from Alam et al. (2017), Ata et al. (2018), Carter et al. (2018), DES Collaboration (2019b), and du Mas des Bourboux et al. (2020).

6.3 Data Analysis Methodology

In this paper we use the CLASS code to compute cosmological model predictions as a function of the cosmological model and other parameters. These predictions are compared to observational data using the Markov chain Monte Carlo (MCMC) code MONTEPYTHON (Audren et al., 2013) to maximize the likelihood function, $\mathscr{L}$, and thereby determine the best-fitting values of the free parameters. The priors on the cosmological parameters are flat and nonzero over the same ranges as used in Cao et al. (2021b), except that now $\Omega_b h^2 \in [0.00499, 0.03993]$.[7] The prior range of the QSO nuisance parameter $l_{\rm m}$ is not bounded. We assume a minimal neutrino sector, with three massless neutrino species, with the effective number of relativistic neutrino species $N_{\rm eff} = 3.046$. We neglect the late-time contribution of non-relativistic neutrinos and treat the baryonic ($\Omega_b h^2$) and cold dark matter ($\Omega_c h^2$) energy density parameters as free cosmological parameters to be determined from the data. The non-relativistic matter density parameter $\Omega_{m0} = (\Omega_b h^2 + \Omega_c h^2)/h^2$ is a derived parameter.

The computation of the likelihood functions of $H(z)$, BAO, H II G, and QSO data are described in Cao et al. (2020) and Cao et al. (2021a), whereas that of the likelihood functions of SN Ia measurements can be found in Cao et al. (2021b). One can also find the definitions of the Akaike Information Criterion (AIC) and the Bayesian Information Criterion (BIC) in those papers.

6.4 Results

The posterior one-dimensional (1D) probability distributions and two-dimensional (2D) confidence regions of the cosmological and nuisance parameters for the six flat and non-flat models are shown in Figs. 6.1–6.6, in gray (QSO), pink (H II G-2019), green (H II G-2021), blue ($H(z)$ + BAO), red ($H(z)$ + BAO + SN-Pantheon + SN-DES, HzBSNPD), and purple

[7] The value of primordial Helium abundance $Y_{\rm p}$ is set using a standard big-bang nucleosynthesis prediction by interpolation on a grid of values computed using version 1.2 of the PArthENoPE BBN code for a neutron lifetime of 880.2 s. Since we choose the effective number of relativistic neutrino species $N_{\rm eff} = 3.046$, $\Omega_b h^2$ is therefore limited to the range of [0.00499, 0.03993] by the correlated predictions of $Y_{\rm p}$.

($H(z)$ + BAO + SN-Pantheon + SN-DES + QSO + H IIG-2021, HzBSNPDQH). We list the unmarginalized best-fitting parameter values, as well as the corresponding χ^2, AIC, BIC, degrees of freedom ν ($\nu \equiv N - n$), reduced χ^2 (χ^2/ν), $\Delta\chi^2$, ΔAIC, and ΔBIC for all models and data combinations, in Table 6.1. The marginalized posterior mean parameter values and uncertainties ($\pm 1\sigma$ error bars or 2σ limits), for all models and data combinations, are listed in Table 6.2.[8]

6.4.1 Constraints from H IIG-2021 versus H IIG-2019

Here we compare constraints from the current compilation of H IIG data (H IIG-2021) with the constraints from the older compilation (H IIG-2019).

For both data sets, from the figures, most of the probability lies in the part of parameter space that corresponds to currently accelerating cosmological expansion.

For both the flat and non-flat ΛCDM models, H IIG-2021 data favor lower values of $\Omega_c h^2$ and Ω_{m0}. For the non-flat case, the H IIG-2021 data prefer a lower (more negative) value of Ω_{k0} than the H IIG-2019 data. It is worth noting that H_0 is not particularly sensitive to the change in the H IIG data. It is also worth noting that the H IIG-2021 compilation provides constraints on $\Omega_b h^2$ in the flat case, in contrast to H IIG-2019, although these constraints are not as tight as those obtained from the other data combinations. H IIG-2021 data also more tightly constrain Ω_{k0} compared to the H IIG-2019 data. In comparison with the flat ΛCDM H IIG-2021 constraints given in González-Morán et al. (2021), $h = 0.717 \pm 0.018$ and $\Omega_{m0} = 0.243^{+0.039}_{-0.050}$, our constraints, $h = 0.7191 \pm 0.0192$ and $\Omega_{m0} = 0.243^{+0.039}_{-0.051}$, are a bit less restrictive (due to our models having more free parameters) but are consistent with theirs.

In the flat and non-flat XCDM parametrizations, the H IIG-2021 data favor lower values of $\Omega_c h^2$, Ω_{m0}, $w_{\rm X}$, and Ω_{k0} than those favored by the H IIG-2019 data, while the constraints on $\Omega_b h^2$ and H_0 are consistent with each other. The flat XCDM H IIG-2021 constraints are $\{h, \Omega_{m0}, w_{\rm X}\} = \{0.719 \pm 0.020, 0.250^{+0.10}_{-0.061}, -1.19^{+0.46}_{-0.38}\}$ in González-Morán et al. (2021), whereas our results are $\{h, \Omega_{m0}, w_{\rm X}\} = \{0.7266 \pm 0.0219, 0.288^{+0.087}_{-0.058}, -1.527^{+0.786}_{-0.391}\}$ and con-

[8] We use the PYTHON package GETDIST (Lewis, 2019) to determine the posterior means and uncertainties and to generate the marginalized likelihood contours.

Table 6.1: Unmarginalized best-fitting parameter values for all models from various combinations of data.

Model	Data set	$\Omega_{b_0}h^2$	$\Omega_{c_0}h^2$	Ω_{m_0}	Ω_{k_0}	w_X	α	H_0[a]	l_m[b]	χ^2	ν	AIC	BIC	χ^2/ν	$\Delta\chi^2$	ΔAIC	ΔBIC
Flat ΛCDM	$H(z)$ + BAO	0.0239	0.1187	0.298	–	–	–	69.13	–	23.66	39	29.66	34.87	0.61	0.00	0.00	0.00
	H II G-2019	0.0200	0.1215	0.274	–	–	–	71.86	–	410.75	150	416.75	425.84	2.74	0.00	0.00	0.00
	H II G-2021	0.0156	0.1058	0.235	–	–	–	71.89	–	433.86	178	439.86	449.45	2.44	0.00	0.00	0.00
	QSO	0.0095	0.0172	0.315	–	–	–	29.14	25.99	352.04	116	360.04	371.19	3.03	0.00	0.00	0.00
	HzBSNPD[c]	0.0235	0.1200	0.302	–	–	–	68.90	–	1080.48	1107	1086.48	1101.52	0.98	0.00	0.00	0.00
	HzBSNPDQH[d]	0.0248	0.1205	0.298	–	–	–	69.83	10.98	1868.64	1407	1876.64	1897.64	1.33	0.00	0.00	0.00
Non-flat ΛCDM	$H(z)$ + BAO	0.0247	0.1140	0.294	0.029	–	–	68.68	–	23.60	38	31.60	38.55	0.62	−0.06	1.94	3.68
	H II G-2019	0.0075	0.1585	0.314	−0.424	–	–	72.70	–	410.40	149	418.40	430.52	2.75	−0.35	1.65	4.68
	H II G-2021	0.0114	0.1282	0.260	−0.490	–	–	73.20	–	432.79	177	440.79	453.58	2.45	−1.07	0.93	4.13
	QSO	0.0320	0.1277	0.236	−0.363	–	–	82.31	10.52	351.12	115	361.12	375.06	3.05	−0.92	1.08	3.87
	HzBSNPD[c]	0.0243	0.1153	0.296	0.025	–	–	68.61	–	1080.38	1106	1088.38	1108.42	0.98	−0.10	1.90	6.90
	HzBSNPDQH[d]	0.0249	0.1192	0.296	0.005	–	–	69.76	10.99	1868.63	1406	1878.63	1904.89	1.33	−0.01	1.99	7.25
Flat XCDM	$H(z)$ + BAO	0.0304	0.0891	0.281	–	−0.701	–	65.18	–	19.65	38	27.65	34.60	0.52	−4.01	−2.01	−0.27
	H II G-2019	0.0107	0.1180	0.251	–	−0.896	–	71.62	–	410.72	149	418.72	430.85	2.76	−0.03	1.97	5.01
	H II G-2021	0.0291	0.0942	0.239	–	−1.013	–	71.88	–	433.86	177	441.86	454.65	2.45	0.00	2.00	5.20
	QSO	0.0173	0.0050	0.253	–	−2.137	–	29.68	31.24	351.83	115	361.83	375.77	3.06	−0.21	1.79	4.58
	HzBSNPD[c]	0.0254	0.1119	0.293	–	−0.934	–	68.51	–	1079.24	1106	1087.24	1107.29	0.98	−1.24	0.76	5.77
	HzBSNPDQH[d]	0.0266	0.1135	0.289	–	−0.948	–	69.63	10.95	1867.85	1406	1877.85	1904.11	1.33	−0.79	1.21	6.47
Non-flat XCDM	$H(z)$ + BAO	0.0290	0.0980	0.295	−0.152	−0.655	–	65.59	–	18.31	37	28.31	37.00	0.49	−5.35	−1.35	2.13
	H II G-2019	0.0128	0.0011	0.027	−0.625	−0.630	–	72.24	–	405.56	148	415.56	430.72	2.74	−5.19	−1.19	4.88
	H II G-2021	0.0260	0.0066	0.062	−0.573	−0.680	–	72.43	–	430.07	176	440.07	456.06	2.44	−3.79	0.21	6.61
	QSO	0.0153	0.0122	0.060	−0.570	−0.617	–	67.92	11.82	350.22	114	362.22	378.95	3.07	−1.82	2.18	7.76
	HzBSNPD[c]	0.0234	0.1232	0.309	−0.111	−0.876	–	68.94	–	1078.38	1105	1088.38	1113.44	0.98	−2.10	1.90	11.92
	HzBSNPDQH[d]	0.0246	0.1208	0.299	−0.083	−0.900	–	69.72	10.89	1867.11	1405	1879.11	1910.63	1.33	−1.53	2.47	12.99
Flat ϕCDM	$H(z)$ + BAO	0.0333	0.0788	0.264	–	–	1.504	65.20	–	19.49	38	27.49	34.44	0.51	−4.17	−2.17	−0.43
	H II G-2019	0.0304	0.1038	0.261	–	–	0.174	71.75	–	410.74	149	418.74	430.86	2.76	−0.01	1.99	5.02
	H II G-2021	0.0334	0.0876	0.234	–	–	0.001	71.94	–	433.86	177	441.86	454.65	2.45	0.00	2.00	5.20
	QSO	0.0370	0.0960	0.316	–	–	0.001	64.91	11.66	352.05	115	362.05	375.98	3.06	0.01	2.01	4.79
	HzBSNPD[c]	0.0257	0.1097	0.290	–	–	0.226	68.38	–	1079.09	1106	1087.09	1107.14	0.98	−1.39	0.61	5.62
	HzBSNPDQH[d]	0.0270	0.1125	0.288	–	–	0.174	69.63	10.94	1867.75	1406	1877.75	1904.01	1.33	−0.89	1.11	6.37
Non-flat ϕCDM	$H(z)$ + BAO	0.0334	0.0816	0.266	−0.147	–	1.915	65.70	–	18.15	37	28.15	36.84	0.49	−5.51	−1.51	1.97
	H II G-2019	0.0251	0.1126	0.265	−0.265	–	0.433	72.04	–	410.37	148	420.37	435.52	2.77	−0.38	3.62	9.68
	H II G-2021	0.0146	0.1014	0.249	−0.246	–	0.101	72.48	–	433.19	176	443.19	459.19	2.46	−0.67	3.33	9.74
	QSO	0.0282	0.0469	0.261	−0.261	–	0.008	53.61	15.39	351.32	114	363.32	380.04	3.08	−0.72	3.28	8.85
	HzBSNPD[c]	0.0243	0.1197	0.302	−0.110	–	0.442	69.05	–	1078.07	1105	1088.07	1113.13	0.98	−2.41	1.59	11.61
	HzBSNPDQH[d]	0.0250	0.1192	0.297	−0.092	–	0.348	69.69	10.87	1866.93	1405	1878.93	1910.45	1.33	−1.71	2.29	12.81

[a] km s^{-1} Mpc^{-1}.

[b] pc.

[c] $H(z)$ + BAO + SN-Pantheon + SN-DES.

[d] $H(z)$ + BAO + SN-Pantheon + SN-DES + QSO + H II G-2021.

sistent with theirs within 1σ, although due to different prior ranges the posterior means deviate more than those for the flat ΛCDM model.

In the flat ϕCDM model, the H II G-2021 data prefer lower values of $\Omega_c h^2$, Ω_{m0}, and α, with consistent constraints on $\Omega_b h^2$ and H_0. The H II G-2021 data constrain α more tightly than the H II G-2019 data, leading to α being consistent with zero to within a little more than 1σ. In the non-flat case, the H II G-2021 data prefer lower values for all parameters. It is worth noting that both H II G-2021 and H II G-2019 data in the flat and non-flat ϕCDM models determine lower values of Ω_{m0}, and H II G-2021 data prefer the lowest Ω_{m0} value in the non-flat ϕCDM model among all models.

H II G-2021 and H II G-2019 data result in higher values of H_0 than the other probes we study in this paper. The highest H_0 values are in the flat XCDM parametrization and are 72.66 ± 2.19 km s^{-1} Mpc^{-1}and $72.37^{+2.18}_{-2.20}$ km s^{-1} Mpc^{-1}, respectively, which are 1.31σ and 1.23σ higher than the median statistics estimate of $H_0 = 68 \pm 2.8$ km s^{-1} Mpc^{-1} (Chen & Ratra, 2011), and 0.21σ and 0.33σ lower than the local Hubble constant measurement of $H_0 = 73.2 \pm 1.3$ km s^{-1} Mpc^{-1} (Riess et al., 2021). The lowest H_0 estimates are in the non-flat ϕCDM model and are 70.49 ± 1.81 km s^{-1} Mpc^{-1}and 70.53 ± 1.79 km s^{-1} Mpc^{-1}, which are 0.75σ and 0.76σ higher than the median statistics estimate of $H_0 = 68 \pm 2.8$ km s^{-1} Mpc^{-1}, and 1.22σ and 1.21σ lower than the local Hubble constant measurement of $H_0 = 73.2 \pm 1.3$ km s^{-1} Mpc^{-1}.

In the non-flat ΛCDM model, H II G-2021 and H II G-2019 data favor closed spatial hypersurfaces, while in the non-flat XCDM parametrization and the non-flat ϕCDM model, they favor open spatial hypersurfaces. Only in the non-flat ϕCDM model, however, is Ω_{k0} more than 1σ away from spatial flatness. Dark energy dynamics is favored by both data sets, but dark energy being a cosmological constant is not disfavored (it is within 1σ or just a little bit more away).

6.4.2 QSO constraints alone and in comparison to those from other probes

In this subsection we discuss the constraints we obtain solely from the QSO data. As mentioned in Sec. 6.2, in this paper we improve on earlier analyses of the QSO angular size data by now treating $l_{\rm m}$, the characteristic linear size of QSOs, as a nuisance parameter to be determined from the observational data. From QSO data alone, in Table 6.2, $l_{\rm m}$ ranges from a low of $10.26^{+1.24}_{-3.42}$ pc for the non-flat ϕCDM model to a high of $11.90^{+1.52}_{-4.17}$ pc for the flat XCDM parametrization, differing by just 0.38σ. These values are consistent from model to model, largely justifying the use of QSOs as standard rulers, with $l_{\rm m} = 11.03$ pc, the value we used in our previous studies (taken from Cao et al., 2017b). However, ignoring the dependence on cosmological model and the $l_{\rm m}$ errors, as we and others have previously done, results in mildly biased and somewhat more restrictive QSO angular size constraints than is warranted by data. These deficiencies are corrected in our improved analyses here.[9] Additionally, we note that in Table 6.1, the best-fitting values of H_0 in flat ΛCDM and flat XCDM appear to be unreasonably low. This strange behavior is caused by the large values of $l_{\rm m}$, which push the H_0 values lower to obtain locally minimized χ^2 values. Specifically, from the form of the model-predicted angular size of a quasar,

$$\theta\left(z\right) \propto \frac{l_{\rm m} H_0}{d_{\rm M}(z)} \tag{6.2}$$

(where $d_{\rm M}(z) := \frac{H_0}{c} D_{\rm M}(z)$ and suppressing irrelevant parameters), we can see that a large value of $l_{\rm m}$ requires a small value of H_0 in order to keep $\theta\left(z\right)$ constant. Since $l_{\rm m}$ has an unbounded prior range, it can roam over a larger region of parameter space than H_0. It therefore has the freedom to move into regions of parameter space where its value is unusually large; if this happens, then H_0 must be made small to compensate. This is only a partial answer, since it does not account for the variation of Ω_{k0} (the effect of which is more complex,

[9] When QSO data are combined with other probes, as in the HzBSNPDQH combination, the model-independence of $l_{\rm m}$ is evident and the determination here is consistent with $l_{\rm m} = 11.03 \pm 0.25$ pc found by Cao et al. (2017b).

as Ω_{k0} is coupled to the redshift z through the function $d_{\rm M}(z)$), and so does not fully capture the behavior of $\theta(z)$ across all models, but it does give some insight into the apparently anomalously low values of H_0 that appear in some cases.[10]

From the results listed in Table 6.2, we can draw the following conclusions. First, QSO data alone can only constrain the values of $\Omega_b h^2$ in the flat and non-flat ϕCDM models. Second, QSO data alone prefer higher values of Ω_{m0}, which are consistent with almost all other probes except for the non-flat ϕCDM H II G-2021 case (the posterior mean values being 1.1σ away from each other in this case). Furthermore, QSO data alone do not give tight constraints on H_0 or Ω_{k0}. Although in each non-flat model open geometry is favored, given the large error bars, flat geometry is within 1σ.

QSO data favor higher central values of $\Omega_c h^2$ and Ω_{m0}, in both flat and non-flat ΛCDM, compared to the central values favored by the other probes (although QSO constraints have wider error bars than the other constraints). QSO data only very weakly constrain the value of H_0 in the flat ΛCDM model, while the fit of QSO data to the non-flat ΛCDM model produces a tighter constraint whose central value is closer to that of the H II G data and the local value favored by Riess et al. (2021) (with wide error bars, however). In both the flat and non-flat cases, the marginalized values of $l_{\rm m}$ are close to the value obtained by Cao et al. (2017b), with the central value in the flat ΛCDM model here being only 0.02 pc away from that of Cao et al. (2017b) (with wider error bars than what they found). QSO data do not provide strong evidence for non-zero spatial curvature in the non-flat ΛCDM model, as the marginalized posterior mean value of Ω_{k0} is consistent with $\Omega_{k0}= 0$ to within 1σ.

When we look at the flat and non-flat XCDM parametrizations, we find that QSO data again favor somewhat large values of $\Omega_c h^2$ and Ω_{m0} (but, as with flat and non-flat ΛCDM, these have wide error bars) and weak constraints on H_0. The central value of H_0 in the

[10]The relatively higher values of H_0 seen in the ϕCDM models pose an apparent challenge to this explanation, but here the best-fitting values of $\Omega_b h^2$ and $\Omega_c h^2$ need to be taken into account. In comparing, for example, the flat ΛCDM model to the flat ϕCDM model (both of which have nearly identical best-fitting values of Ω_{m0}), we can see that the flat ϕCDM model has larger best-fitting values of both $\Omega_b h^2$ and $\Omega_c h^2$. From the defining relationship $\Omega_{m0} = (\Omega_b h^2 + \Omega_c h^2)/h^2$, keeping Ω_{m0} constant requires $\Omega_b h^2 + \Omega_c h^2$ and H_0 to vary in tandem. If $\Omega_b h^2$ and $\Omega_c h^2$ both increase, as they do in going from flat ΛCDM to flat ϕCDM, then H_0 must also increase. This then has the effect of lowering $l_{\rm m}$ (all other parameters being held fixed).

non-flat case is more consistent with Riess et al. (2021) and with the values derived from the H IIG data. In both cases we find that the marginalized values of $l_{\rm m}$ are consistent with that of Cao et al. (2017b). We also find that QSO data favor values of $w_{\rm X}$ that are in the phantom regime (consistent with the findings from the H IIG data). In the non-flat case, QSO data favor a relatively large and positive central value (0.170) for Ω_{k0}, corresponding to a spatially open universe, but the error bars are wide enough that this result is still consistent with spatial flatness.

Both the flat and non-flat ϕCDM models have central values of $\Omega_b h^2$ from QSO data that are similar to earlier findings (specifically, they are close to the values of $\Omega_b h^2$ obtained for the flat ΛCDM and ϕCDM models by Park & Ratra, 2018, 2019c). Both flat and non-flat ϕCDM have relatively high central values of $\Omega_c h^2$ and Ω_{m0} (compared to the other probes), both favor similar large values of α (consistent with $\alpha = 0$, however, to within 1.15σ and 1.29σ in the flat and non-flat cases, respectively), and both show weak constraints on H_0. Both flat and non-flat ϕCDM favor posterior mean values of $l_{\rm m}$ that are consistent to within 1σ with the central value obtained by Cao et al. (2017b). Like non-flat XCDM, non-flat ϕCDM favors a relatively large and positive value of Ω_{k0}, that is nevertheless consistent with spatial flatness to within 1σ.

6.4.3 Joint analyses results

Since the constraints derived from $H(z)$, BAO, SN-Pantheon, SN-DES, QSO, H IIG-2019, and H IIG-2021 data are not mutually inconsistent, we jointly analyze combinations of these data and summarize these results in this subsection.

The $H(z)$ + BAO and HzBSNPD results are different from, but consistent with, what we obtained in Cao et al. (2021b). The differences arise from the different codes that we used to analyze the data; in Cao et al. (2021b) we used EMCEE, whereas here we used CLASS and MONTEPYTHON. It is worth recalling here that, as mentioned above, CLASS constrains $\Omega_b h^2$ in the range $0.00499 \leq \Omega_b h^2 \leq 0.03993$. Therefore the parameter constraints differ more when the model and data prefer higher values of $\Omega_b h^2$; this is especially true of the ϕCDM

Table 6.2: One-dimensional posterior mean parameter values and uncertainties ($\pm1\sigma$ error bars or 2σ limits) for all models from various combinations of data.

Model	Data set	$\Omega_{b_0}h^2$	$\Omega_{c_0}h^2$	Ω_{m_0}	Ω_{k_0}	w_X	α	H_0 [a]	l_m [b]
Flat ΛCDM	$H(z)$ + BAO	0.0241 ± 0.0029	$0.1193^{+0.0082}_{-0.0090}$	$0.299^{+0.017}_{-0.019}$	–	–	–	$69.29^{+1.84}_{-1.85}$	–
	H II G-2019	–	$0.1258^{+0.0278}_{-0.0335}$	$0.289^{+0.054}_{-0.074}$	–	–	–	71.80 ± 1.94	–
	H II G-2021	0.0225 ± 0.0108	$0.1023^{+0.0197}_{-0.0229}$	$0.243^{+0.039}_{-0.051}$	–	–	–	71.91 ± 1.92	–
	QSO	–	$0.1874^{+0.0592}_{-0.1595}$	$0.387^{+0.078}_{-0.177}$	–	–	–	> 38.09	$11.05^{+1.10}_{-3.85}$
	HzBSNPD[c]	0.0237 ± 0.0028	0.1208 ± 0.0074	$0.303^{+0.013}_{-0.014}$	–	–	–	69.10 ± 1.80	–
	HzBSNPDQH[d]	0.0250 ± 0.0021	0.1208 ± 0.0064	0.298 ± 0.013	–	–	–	69.95 ± 1.18	10.96 ± 0.26
Non-flat ΛCDM	$H(z)$ + BAO	$0.0253^{+0.0040}_{-0.0049}$	$0.1134^{+0.0196}_{-0.0197}$	0.293 ± 0.025	$0.040^{+0.102}_{-0.115}$	–	–	68.75 ± 2.45	–
	H II G-2019	0.0224 ± 0.0108	$0.1245^{+0.0413}_{-0.0380}$	0.285 ± 0.077	$-0.052^{+0.289}_{-0.530}$	–	–	71.95 ± 2.04	–
	H II G-2021	0.0225 ± 0.0108	$0.1035^{+0.0328}_{-0.0268}$	$0.243^{+0.060}_{-0.055}$	$-0.100^{+0.216}_{-0.484}$	–	–	$72.15^{+2.05}_{-2.04}$	–
	QSO	–	$0.1797^{+0.0610}_{-0.1489}$	$0.385^{+0.074}_{-0.191}$	$0.043^{+0.265}_{-0.464}$	–	–	$71.33^{+26.04}_{-9.82}$	$11.27^{+0.91}_{-3.92}$
	HzBSNPD[c]	$0.0248^{+0.0036}_{-0.0043}$	0.1157 ± 0.0164	0.296 ± 0.023	0.027 ± 0.074	–	–	68.82 ± 2.02	–
	HzBSNPDQH[d]	$0.0256^{+0.0035}_{-0.0042}$	0.1188 ± 0.0138	0.295 ± 0.021	0.011 ± 0.067	–	–	69.90 ± 1.18	10.96 ± 0.25
Flat XCDM	$H(z)$ + BAO	$0.0297^{+0.0046}_{-0.0053}$	$0.0934^{+0.0195}_{-0.0169}$	$0.283^{+0.023}_{-0.021}$	–	$-0.751^{+0.152}_{-0.106}$	–	$65.85^{+2.38}_{-2.65}$	–
	H II G-2019	0.0224 ± 0.0109	$0.1491^{+0.0596}_{-0.0390}$	$0.327^{+0.108}_{-0.077}$	–	$-1.494^{+0.858}_{-0.411}$	–	$72.37^{+2.18}_{-2.20}$	–
	H II G-2021	0.0223 ± 0.0108	$0.1297^{+0.0493}_{-0.0308}$	$0.288^{+0.087}_{-0.058}$	–	$-1.527^{+0.786}_{-0.391}$	–	72.66 ± 2.19	–
	QSO	–	$0.1785^{+0.0536}_{-0.1603}$	$0.373^{+0.072}_{-0.187}$	–	$-1.709^{+0.696}_{-0.882}$	–	> 39.72	$11.90^{+1.52}_{-4.17}$
	HzBSNPD[c]	$0.0256^{+0.0031}_{-0.0035}$	$0.1121^{+0.0107}_{-0.0108}$	0.293 ± 0.016	–	-0.935 ± 0.063	–	68.57 ± 1.74	–
	HzBSNPDQH[d]	$0.0267^{+0.0029}_{-0.0033}$	0.1142 ± 0.0103	0.290 ± 0.016	–	-0.950 ± 0.062	–	69.69 ± 1.20	10.94 ± 0.25
Non-flat XCDM	$H(z)$ + BAO	$0.0288^{+0.0049}_{-0.0054}$	$0.0997^{+0.0210}_{-0.0211}$	0.294 ± 0.027	$-0.112^{+0.136}_{-0.137}$	$-0.706^{+0.135}_{-0.084}$	–	66.01 ± 2.43	–
	H II G-2019	0.0223 ± 0.0107	$0.1288^{+0.0548}_{-0.0620}$	$0.291^{+0.109}_{-0.110}$	$0.089^{+0.484}_{-0.283}$	$-1.409^{+0.810}_{-0.402}$	–	$71.96^{+2.06}_{-2.29}$	–
	H II G-2021	0.0224 ± 0.0107	$0.1109^{+0.0472}_{-0.0514}$	0.255 ± 0.090	$0.078^{+0.417}_{-0.322}$	$-1.461^{+0.777}_{-0.361}$	–	$72.23^{+2.08}_{-2.28}$	–
	QSO	–	$0.1905^{+0.0461}_{-0.1731}$	$0.403^{+0.093}_{-0.225}$	$0.170^{+0.403}_{-0.256}$	$-1.455^{+1.014}_{-0.776}$	–	> 38.43	$11.08^{+1.19}_{-4.05}$
	HzBSNPD[c]	$0.0245^{+0.0036}_{-0.0043}$	0.1193 ± 0.0170	0.302 ± 0.024	-0.069 ± 0.119	$-0.907^{+0.099}_{-0.062}$	–	68.95 ± 1.96	–
	HzBSNPDQH[d]	$0.0255^{+0.0035}_{-0.0041}$	$0.1189^{+0.0136}_{-0.0135}$	0.297 ± 0.020	-0.054 ± 0.096	$-0.926^{+0.091}_{-0.062}$	–	$69.73^{+1.19}_{-1.20}$	10.89 ± 0.26
Flat ϕCDM	$H(z)$ + BAO	$0.0323^{+0.0060}_{-0.0034}$	$0.0810^{+0.0188}_{-0.0185}$	0.267 ± 0.025	–	–	$1.530^{+0.644}_{-0.904}$	$65.09^{+2.23}_{-2.24}$	–
	H II G-2019	$0.0214^{+0.0084}_{-0.0128}$	$0.0561^{+0.0157}_{-0.0541}$	$0.155^{+0.047}_{-0.097}$	–	–	< 7.803	$70.97^{+1.91}_{-1.89}$	–
	H II G-2021	$0.0213^{+0.0080}_{-0.0130}$	$0.0468^{+0.0152}_{-0.0431}$	$0.135^{+0.043}_{-0.077}$	–	–	$2.454^{+0.587}_{-2.434}$	$71.15^{+1.90}_{-1.89}$	–
	QSO	$0.0221^{+0.0179}_{-0.0171}$	< 0.3644	$0.305^{+0.081}_{-0.212}$	–	–	$4.526^{+1.546}_{-4.464}$	$70.79^{+24.27}_{-12.67}$	$10.32^{+1.08}_{-3.54}$
	HzBSNPD[c]	$0.0273^{+0.0032}_{-0.0039}$	$0.1051^{+0.0122}_{-0.0103}$	0.284 ± 0.017	–	–	$0.351^{+0.132}_{-0.284}$	68.33 ± 1.81	–
	HzBSNPDQH[d]	$0.0284^{+0.0027}_{-0.0035}$	$0.1078^{+0.0112}_{-0.0090}$	0.282 ± 0.016	–	–	$0.288^{+0.098}_{-0.252}$	69.54 ± 1.17	10.92 ± 0.25
Non-flat ϕCDM	$H(z)$ + BAO	$0.0319^{+0.0061}_{-0.0037}$	$0.0849^{+0.0178}_{-0.0217}$	$0.271^{+0.025}_{-0.028}$	$-0.074^{+0.104}_{-0.111}$	–	$1.646^{+0.680}_{-0.840}$	65.48 ± 2.26	–
	H II G-2019	$0.0216^{+0.0089}_{-0.0121}$	$0.0560^{+0.0198}_{-0.0476}$	$0.157^{+0.047}_{-0.091}$	$0.314^{+0.310}_{-0.182}$	–	$3.983^{+1.228}_{-3.932}$	70.53 ± 1.79	–
	H II G-2021	$0.0210^{+0.0076}_{-0.0129}$	$0.0407^{+0.0116}_{-0.0381}$	$0.125^{+0.037}_{-0.069}$	$0.302^{+0.278}_{-0.221}$	–	< 8.046	70.49 ± 1.81	–
	QSO	0.0222 ± 0.0109	$0.1444^{+0.0391}_{-0.1352}$	$0.330^{+0.108}_{-0.183}$	$0.207^{+0.244}_{-0.241}$	–	$4.773^{+2.487}_{-3.699}$	$70.15^{+20.58}_{-15.20}$	$10.26^{+1.24}_{-3.42}$
	HzBSNPD[c]	$0.0259^{+0.0037}_{-0.0043}$	0.1136 ± 0.0156	0.294 ± 0.022	$-0.088^{+0.105}_{-0.075}$	–	$0.495^{+0.208}_{-0.344}$	68.84 ± 1.88	–
	HzBSNPDQH[d]	$0.0267^{+0.0035}_{-0.0041}$	0.1141 ± 0.0133	0.290 ± 0.020	$-0.072^{+0.074}_{-0.073}$	–	$0.405^{+0.165}_{-0.304}$	69.62 ± 1.17	10.87 ± 0.26

[a] km s^{-1} Mpc^{-1}.

[b] pc.

[c] $H(z)$ + BAO + SN-Pantheon + SN-DES.

[d] $H(z)$ + BAO + SN-Pantheon + SN-DES + QSO + H II G-2021.

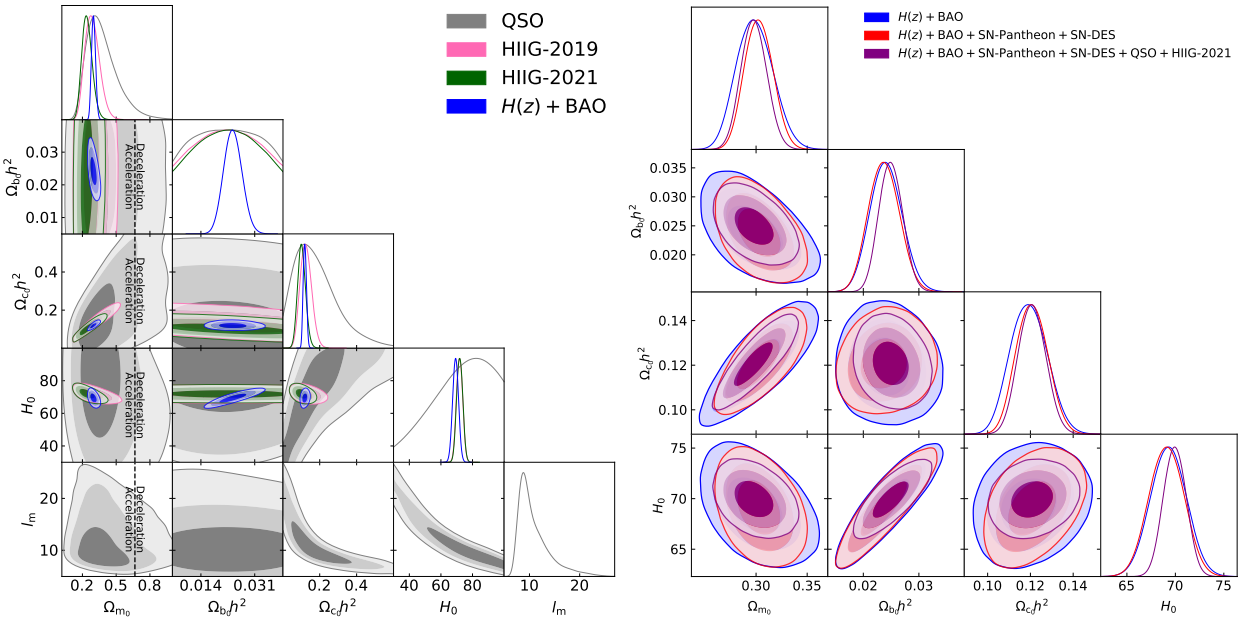

(a) (b)

Figure 6.1: One-dimensional likelihoods and 1σ, 2σ, and 3σ two-dimensional likelihood confidence contours for flat ΛCDM. Left panel shows individual data set and $H(z)$ + BAO results and the right panel shows joint data sets constraints. The zero-acceleration lines are shown as black dashed lines in the left panel, which divide the parameter space into regions associated with currently-accelerating (left) and currently-decelerating (right) cosmological expansion, while in the right panel the joint analyses favor currently-accelerating expansion.

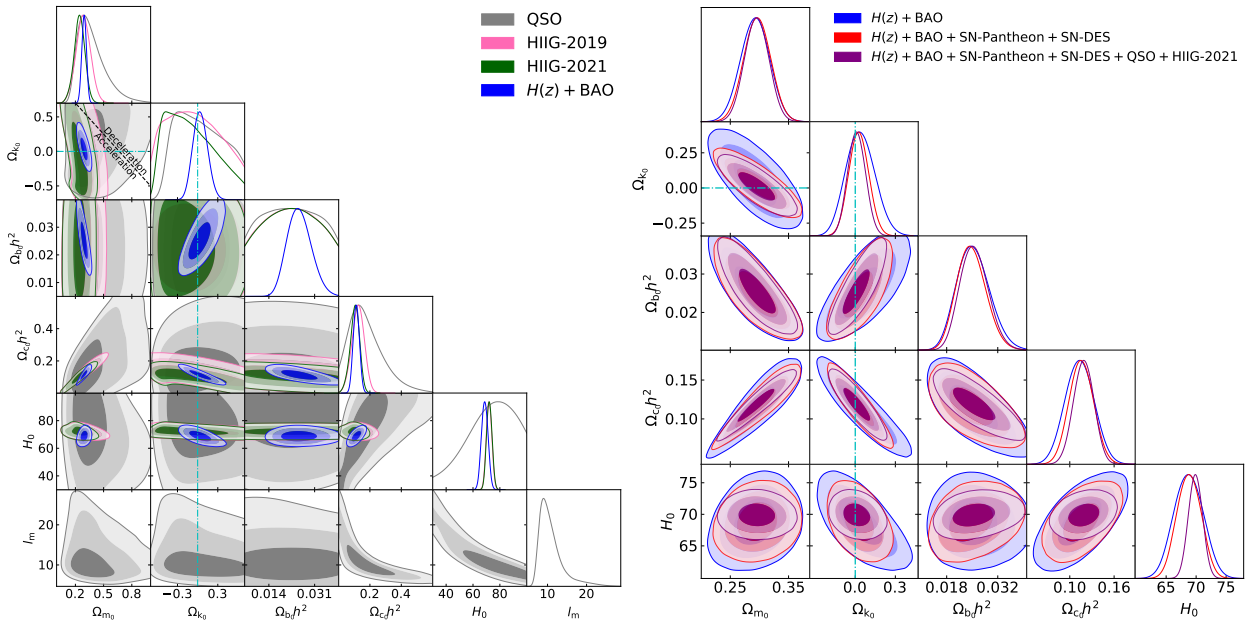

(a) (b)

Figure 6.2: Same as Fig. 6.1 but for non-flat ΛCDM. The flat ΛCDM case is shown as the cyan dash-dot lines, with closed spatial hypersurfaces either below or to the left. The black dashed line in the left panel is the zero-acceleration line, which divides the parameter space into regions associated with currently-accelerating (below left) and currently-decelerating (above right) cosmological expansion. In the right panel, the joint analyses favor currently-accelerating expansion.

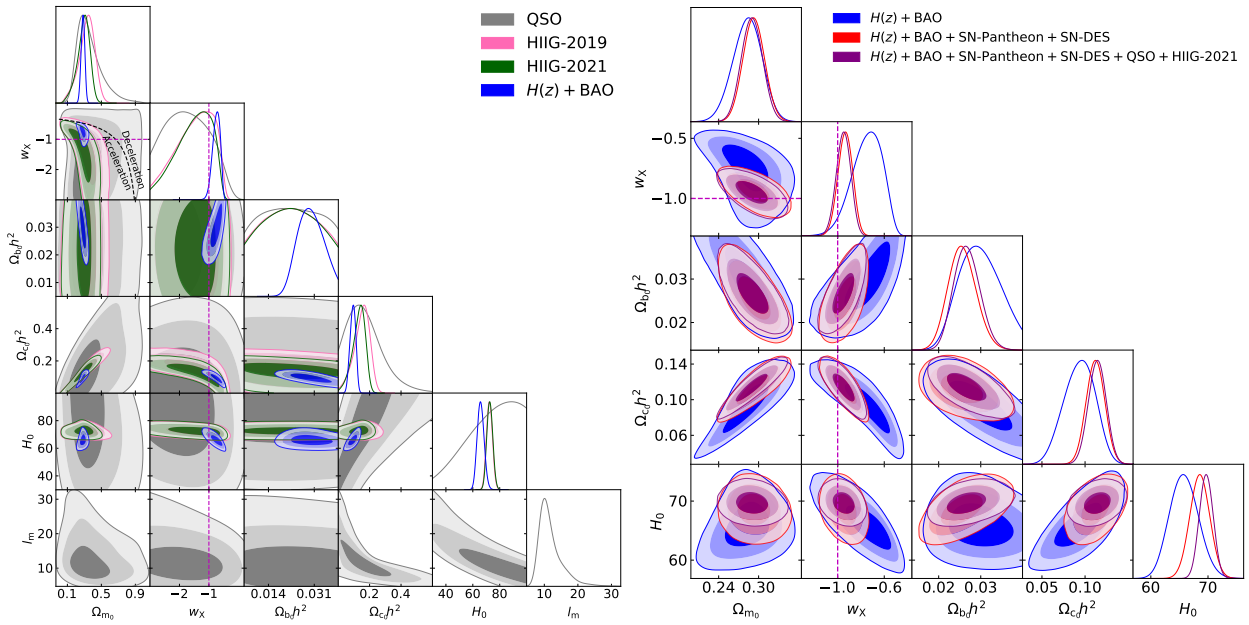

(a) (b)

Figure 6.3: One-dimensional likelihoods and 1σ, 2σ, and 3σ two-dimensional likelihood confidence contours for flat XCDM. The black dashed line in the left panel is the zero-acceleration line, which divides the parameter space into regions associated with currently-accelerating (below left) and currently-decelerating (above right) cosmological expansion. In the right panel, the joint analyses favor currently-accelerating expansion. The magenta lines represent $w_{\rm X} = -1$, i.e. the flat ΛCDM model.

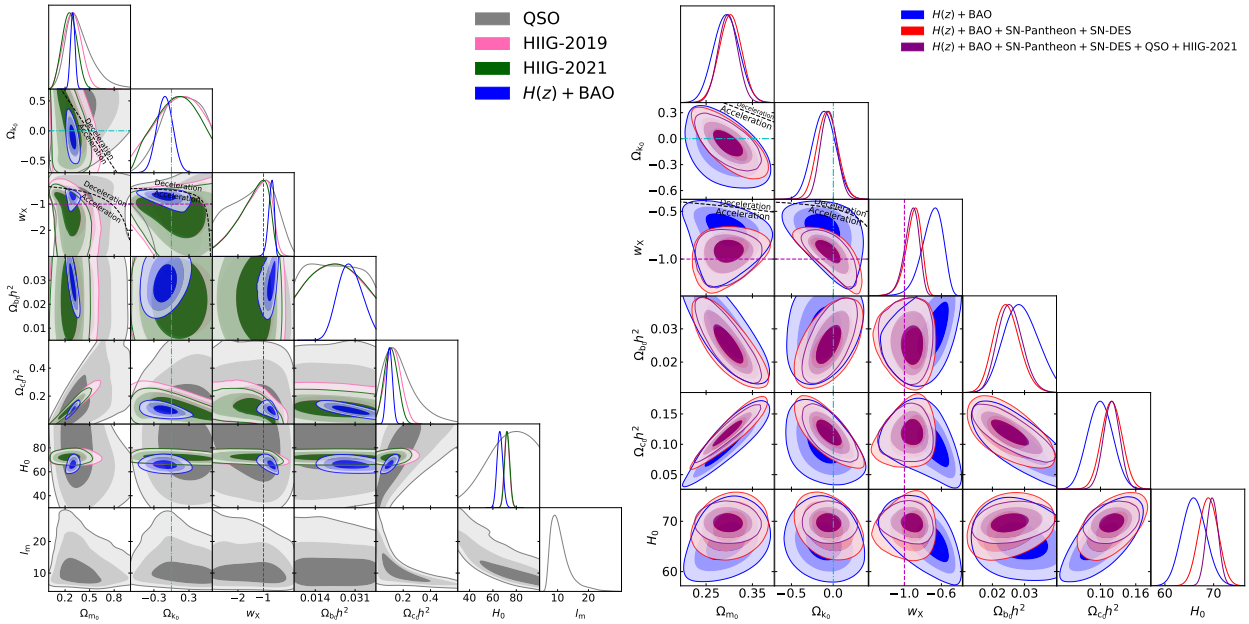

(a) (b)

Figure 6.4: Same as Fig. 6.3 but for non-flat XCDM, where the black dashed zero-acceleration lines are computed for the third cosmological parameter set to the $H(z)$ + BAO data best-fitting values listed in Table 6.1, with currently-accelerating cosmological expansion residing below left. The flat XCDM case is denoted as the cyan dash-dot lines, with closed spatial hypersurfaces either below or to the left. The magenta lines represent $w_{\rm X} = -1$, i.e. the non-flat ΛCDM model. In all cases except for the QSO only case, almost all of the favored parameter space is associated with currently-accelerating cosmological expansion.

model when it is fitted to the $H(z)$ + BAO data combination. As a result, the present constraints on Ω_{m0} and α in ϕCDM with $H(z)$ + BAO data are higher and lower than the ones given in Cao et al. (2021b). The HzBSNPD results are, however, consistent.

The fit to the HzBSNPDQH data combination produces, for all models, the most interesting results. By adding QSO and H II G-2021 data to HzBSNPD combination, the constraints are slightly tightened. Although the posterior means of $\Omega_b h^2$ and $\Omega_c h^2$ are relatively higher, those of Ω_{m0} are lower than the constraints from HzBSNPD. The Ω_{m0} constraints range from a low of 0.282 ± 0.016 (flat ϕCDM) to a high of 0.298 ± 0.013 (flat ΛCDM), a difference of only 0.78σ.

The constraints on H_0 are between $H_0 = 69.54 \pm 1.17$ km s^{-1} Mpc^{-1} (flat ϕCDM) and $H_0 = 69.95 \pm 1.18$ km s^{-1} Mpc^{-1} (flat ΛCDM) — a difference of only 0.25σ — which are 0.64σ (flat ΛCDM) and 0.51σ (flat ϕCDM) higher than the median statistics estimate of $H_0 = 68 \pm 2.8$ km s^{-1} Mpc^{-1} (Chen & Ratra, 2011), and 1.85σ (flat ΛCDM) and 2.09σ (flat ϕCDM) lower than the local Hubble constant measurement of $H_0 = 73.2 \pm 1.3$ km s^{-1} Mpc^{-1} (Riess et al., 2021).[11]

For non-flat ΛCDM, non-flat XCDM, and non-flat ϕCDM, we find $\Omega_{k_0} = 0.011 \pm 0.067$, $\Omega_{k_0} = -0.054 \pm 0.096$, and $\Omega_{k_0} = -0.072^{+0.074}_{-0.073}$, respectively. The non-flat XCDM and ϕCDM models favor closed geometry, while the non-flat ΛCDM model favors open geometry. Note, however, that these results are all consistent with spatially flat hypersurfaces to within 1σ.

Our results show a slight preference for dark energy dynamics. For flat (non-flat) XCDM, $w_X = -0.950 \pm 0.062$ ($w_X = -0.926^{+0.091}_{-0.062}$), with central values being 0.81σ (1.19σ) away from $w_X = -1$; and for flat (non-flat) ϕCDM, $\alpha = 0.288^{+0.098}_{-0.252}$ ($\alpha = 0.405^{+0.165}_{-0.304}$), with central values being 1.14σ (1.33σ) away from $\alpha = 0$.

[11] Other local expansion rate H_0 measurements result in slightly lower central values with slightly larger error bars (Breuval et al., 2020; Dhawan et al., 2018; Efstathiou, 2020; Fernández Arenas et al., 2018; Freedman, 2021; Khetan et al., 2021; Rameez & Sarkar, 2021; Rigault et al., 2015; Zhang et al., 2017). Our H_0 estimates are consistent with earlier median statistics determinations (Calabrese et al., 2012; Gott et al., 2001) as well as with other recent H_0 measurements (Birrer et al., 2020; Blum et al., 2020; Boruah et al., 2021; Chen et al., 2017; Cuceu et al., 2019; DES Collaboration, 2018; Denzel et al., 2021; Domínguez et al., 2019; Gómez-Valent & Amendola, 2018; Harvey, 2020; Kim et al., 2020; Lin & Ishak, 2021; Lyu et al., 2020; Philcox et al., 2020; Planck Collaboration, 2020; Pogosian et al., 2020; Schöneberg et al., 2019; Zeng & Yan, 2019; Zhang & Huang, 2021).

The constraints on the nuisance parameter $l_{\rm m}$ are between $l_{\rm m} = 10.87 \pm 0.26$ pc (non-flat ϕCDM) and $l_{\rm m} = 10.96 \pm 0.26$ pc (flat ΛCDM), which differ by 0.24σ and so are effectively model-independent, and consistent with $l_{\rm m} = 11.03 \pm 0.25$ pc (Cao et al., 2017b).

6.4.4 Model comparison

The values of the reduced χ^2 (χ^2/ν), $\Delta\chi^2$, ΔAIC, and ΔBIC are reported in Table 6.1, where $\Delta\chi^2$, ΔAIC, and ΔBIC, are the differences between the values of the χ^2, AIC, and BIC for a given model and the ones for flat ΛCDM. Here a negative (positive) value of $\Delta\chi^2$, ΔAIC, or ΔBIC means that the given statistic favors (disfavors) the model under consideration relative to flat ΛCDM. We find that, except for a few of the $H(z)$ + BAO and H II G-2019 cases, the flat ΛCDM model is the most favored model among all six models we study. The AIC does not show strong evidence against any of the models.[12] However, we find that some data combinations show strong evidence against the models we study, when these models are analyzed using the BIC, as follows. First, the HzBSNPD combination strongly disfavors non-flat ΛCDM and very strongly disfavors non-flat XCDM and non-flat ϕCDM. Second, the HzBSNPDQH combination strongly disfavors non-flat ΛCDM, flat XCDM, and flat ϕCDM, and very strongly disfavors non-flat XCDM and non-flat ϕCDM. Furthermore, strong evidence against non-flat XCDM as well as non-flat ϕCDM are provided by the H II G-2021 and QSO data.

6.5 Conclusion

We find that the new H II G-2021 data provide more restrictive cosmological parameter constraints and also prefer lower values of Ω_{m0}, $w_{\rm X}$, and Ω_{k0} than those favored by the H II G-2019 data.

We find that the QSO characteristic linear size $l_{\rm m}$ is relatively model-independent, so

[12] There is weak evidence for the reference model when $\Delta AIC(BIC) \in [0, 2]$, positive evidence when $\Delta AIC(BIC) \in (2, 6]$, strong evidence when $\Delta AIC(BIC) \in (6, 10]$, and very strong evidence when $\Delta AIC(BIC) > 10$ (Kass & Raftery, 1995).

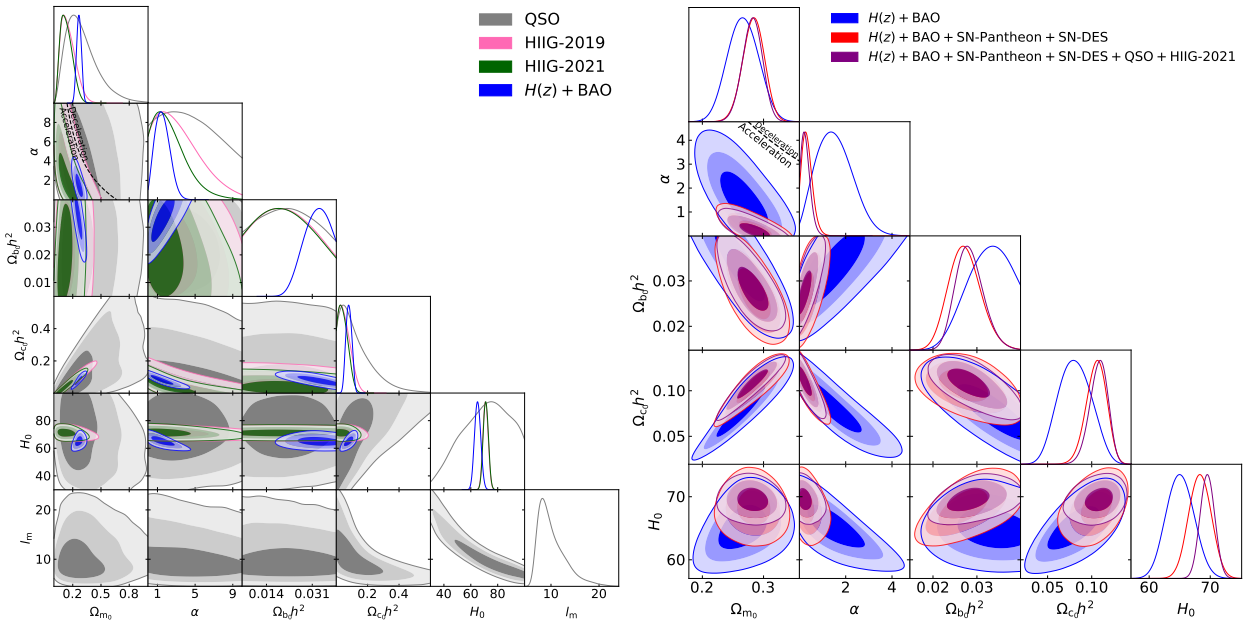

(a) (b)

Figure 6.5: One-dimensional likelihoods and 1σ, 2σ, and 3σ two-dimensional likelihood confidence contours for flat ϕCDM. The black dashed lines are the zero-acceleration lines, which divides the parameter space into regions associated with currently-accelerating (below left) and currently-decelerating (above right) cosmological expansion. The $\alpha = 0$ axis is the flat ΛCDM model. In all cases except for the QSO only case, almost all of the favored parameter space is associated with currently-accelerating cosmological expansion.

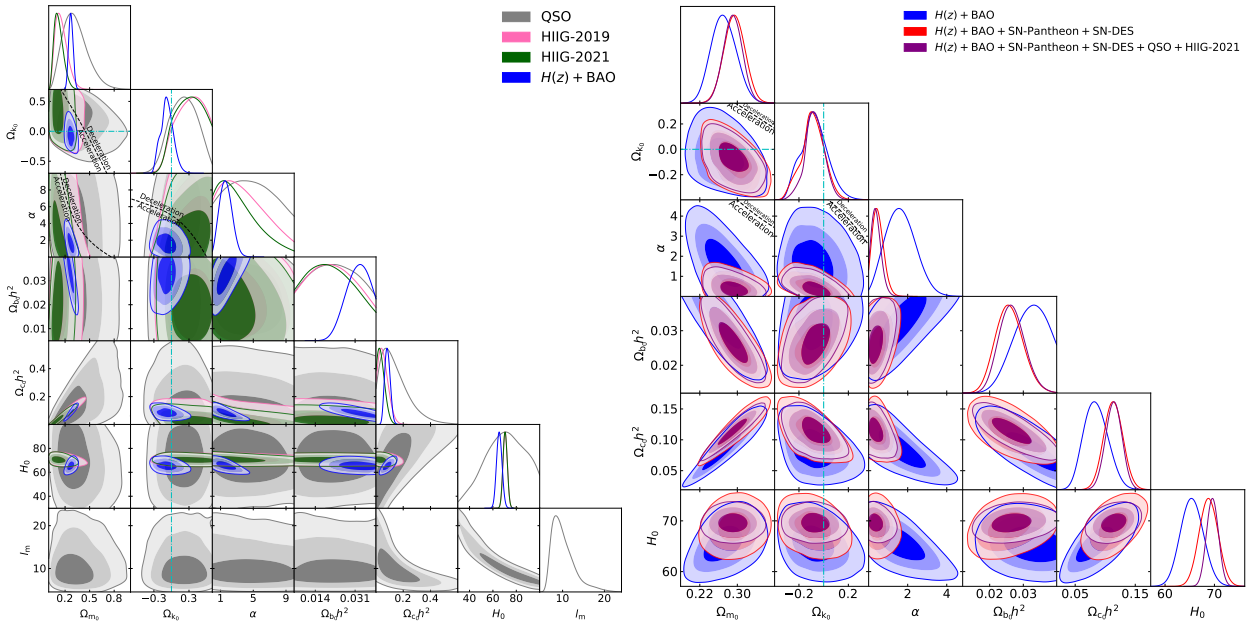

(a) (b)

Figure 6.6: Same as Fig. 6.5 but for non-flat ϕCDM, where the black dashed zero-acceleration lines are computed for the third cosmological parameter set to the $H(z)$ + BAO data best-fitting values listed in Table 6.1. Currently-accelerating cosmological expansion occurs below left of these lines. The cyan dash-dot lines represent the flat ϕCDM case, with closed spatial geometry either below or to the left. The $\alpha = 0$ axis is the non-flat ΛCDM model. In the right panel, the joint analyses favor currently-accelerating expansion.

QSOs can be treated as approximate standard rulers but the uncertainty in $l_{\rm m}$ must be accounted for in the analysis.

We also jointly analyzed a total of 1411 measurements, consisting of 31 $H(z)$, 11 BAO, 1048 SN-Pantheon, 20 SN-DES, 120 QSO, and 181 H II G-2021 data points to constrain cosmological and nuisance parameters in six flat and non-flat cosmological models. We can describe the relatively model-independent summary features of the constraints obtained from this $H(z)$ + BAO + SN-Pantheon + SN-DES + QSO + H II G-2021 (HzBSNPDQH) data combination as follows.[13] First, the constraint on $l_{\rm m}$ is $l_{\rm m} = 10.93 \pm 0.25$ pc, which is consistent with the $l_{\rm m} = 11.03 \pm 0.25$ pc of Cao et al. (2017b). Second, the constraint on Ω_{m0} is $\Omega_{\rm m_0} = 0.293 \pm 0.021$, which is in good agreement with many other recent measurements (e.g. 0.315 ± 0.007 from TT,TE,EE+lowE+lensing CMB anisotropy data in the flat ΛCDM model of Planck Collaboration, 2020). Third, the determination of H_0 is $H_0 = 69.7 \pm 1.2$ km s^{-1} Mpc^{-1}, which is in better agreement with the estimate of Chen & Ratra (2011) than with the measurements of Planck Collaboration (2020) and Riess et al. (2021). There is some room for dark energy dynamics or a little spatial curvature energy density, but overall the flat ΛCDM model is the best candidate model.

[13]The following summary values are obtained with the same method used in Cao et al. (2021b), where we take the summary central value to be the mean of the two of six central-most values. As for the uncertainty, we call the difference between the two central-most values twice the systematic uncertainty and the average of the two central-most error bars the statistical uncertainty, and compute the summary error bar as the quadrature sum of the two uncertainties.

Chapter 7

Standardizing Dainotti-correlated gamma-ray bursts, and using them with standardized Amati-correlated gamma-ray bursts to constrain cosmological model parameters

This chapter is based on Cao et al. (2022b), from analyses conducted independently by Shulei Cao and Narayan Khadka.

7.1 Introduction

The observed currently accelerated cosmological expansion indicates that — if general relativity provides an accurate description of gravitation on cosmological scales — dark energy must contribute significantly to the current cosmological energy budget. The simpler spatially-flat ΛCDM model (Peebles, 1984) is consistent with this and other observations. Fits of this model to most better-established cosmological data suggest that a

time-independent cosmological constant (Λ) provides $\sim 70\%$ of the current cosmological energy budget, non-relativistic cold dark matter (CDM) provides $\sim 25\%$, and non-relativistic baryonic matter provides most of the remaining $\sim 5\%$ (see, e.g. eBOSS Collaboration, 2021; Farooq et al., 2017; Planck Collaboration, 2020; Scolnic et al., 2018). While the spatially-flat ΛCDM model is consistent with most observations (see, e.g. Di Valentino et al., 2021b; Perivolaropoulos & Skara, 2022), observational data do not strongly rule out a little spatial curvature or dynamical dark energy. In this paper, in addition to the spatially-flat ΛCDM model, we also study spatially non-flat and dynamical dark energy models.

Observational astronomy now provides many measurements that can be used to test cosmological models. Largely, these data are either at low or at high redshift. So cosmological models are mostly tested at low and high redshifts, remaining poorly tested in the intermediate redshift regime. The highest redshift of the better-established low-redshift data, ~ 2.3, is reached through baryon acoustic oscillation (BAO) observations; the high redshift region, $z \sim 1100$, is probed by better-established cosmic microwave background anisotropy data. Fits of these better-established data to cosmological models provide mostly mutually consistent results. However, for a better understanding of our Universe, it is necessary to also test cosmological models in the intermediate redshift range of $2.3 \lesssim z \lesssim 1100$. Some progress has been achieved: methods that test cosmological models in the intermediate redshift region include the use of H II starburst galaxy measurements which reach to $z \sim 2.4$ (Cao et al., 2020, 2021a,b; Chávez et al., 2014; González-Morán et al., 2019, 2021; Johnson et al., 2022; Mania & Ratra, 2012), quasar angular size measurements which reach to ~ 2.7 (Cao et al., 2017a, 2020, 2021a; Lian et al., 2021; Ryan et al., 2019; Zheng et al., 2021), and quasar flux measurements which reach to ~ 7.5 (Khadka & Ratra, 2020a,b, 2021, 2022; Li et al., 2021; Lian et al., 2021; Luongo et al., 2022; Lusso et al., 2020; Rezaei et al., 2022; Risaliti & Lusso, 2015, 2019; Yang et al., 2020; Zhao & Xia, 2021).[1]

Gamma-ray burst (GRB) measurements are another high redshift probe and reach to $z \sim 8.2$ (Amati et al., 2008, 2019; Cardone et al., 2010; Dainotti & Del Vecchio, 2017;

[1]Note that in the latest Lusso et al. (2020) quasar flux compilation, their assumed UV–X-ray correlation is valid only to a much lower redshift, $z \sim 1.5 - 1.7$, and so these quasars can be used to derive only lower-z cosmological constraints (Khadka & Ratra, 2021, 2022).

Dainotti et al., 2013a; Demianski et al., 2021; Fana Dirirsa et al., 2019; Khadka & Ratra, 2020c; Khadka et al., 2021b; Luongo & Muccino, 2021; Luongo et al., 2022; Salvaterra et al., 2009; Samushia & Ratra, 2010; Tanvir et al., 2009; Wang et al., 2015, 2016). While there are quite a few Amati correlation long GRBs that have been used to constrain cosmological parameters, currently only a smaller fraction of 118 such GRBs (hereafter A118) that cover the redshift range $0.3399 \leq z \leq 8.2$ (Khadka & Ratra, 2020c; Khadka et al., 2021a) are reliable enough to be used to constrain cosmological parameters. To date, this is the lower-z data set used to constrain cosmological parameters that spans the widest range of redshifts. These A118 data provide cosmological constraints which are consistent with those obtained from the better-established cosmological probes but the GRB constraints are significantly less restrictive. To obtain tighter cosmological constraints using GRB data, we need to make use of more GRBs.

Recently Wang et al. (2022) and Hu et al. (2021) have compiled smaller GRB data sets that together probe the redshift range $0.35 \leq z \leq 5.91$. These are GRBs whose plateau phase luminosity L_0 and spin-down characteristic time t_b are correlated through the Dainotti ($L_0 - t_b$) correlation (Dainotti et al., 2013b, 2017). This correlation between L_0 and t_b allows one to use these GRBs for cosmological purposes. These GRBs can be classified in two categories depending on whether the plateau phase is dominated by magnetic dipole (MD) radiation or gravitational wave (GW) emission (Hu et al., 2021; Wang et al., 2022). In this paper we use long and short GRBs whose plateau phase is dominated by MD radiation (hereafter MD-LGRBs and MD-SGRBs) and long GRBs whose plateau phase is dominated by GW emission (hereafter GW-LGRBs). All three sets of GRBs obey the Dainotti correlation but each set can have different correlation parameters. We use the three individual GRB data sets, as well as some combinations of them, to constrain cosmological model parameters and Dainotti correlation parameters simultaneously.[2] We find that these GRBs are standardizable, as was assumed in Wang et al. (2022) and Hu et al. (2021). However, cosmological constraints

[2]The advantage of fitting cosmological and GRB correlation parameters simultaneously is that the fitting process is free from the circularity problem. More specifically, this procedure allows us to determine whether the GRB correlation parameters depend on the assumed cosmological model and so determine whether the GRBs are standardizable.

obtained from these Dainotti correlation GRB data sets are very weak.

When we combine the MD-LGRB or GW-LGRB data sets with the 115 non-overlapping Amati correlation GRBs from the A118 data set, they slightly tighten the constraints from the 115 Amati correlation GRBs, but not significantly so. Each of the individual Amati or Dainotti correlation GRB data sets, as well as combinations of these GRB data sets, mostly provide only lower limits on the current value of the non-relativistic matter energy density parameter $\Omega_{\rm m0}$ and the resulting cosmological parameter constraints are mostly consistent with those obtained from better-established cosmological data.

In this paper, we use a combination of Hubble parameter ($H(z)$) and BAO data, $H(z)$ + BAO, results as a proxy for better-established data results, to compare with our GRB data results. Qualitatively, results from the individual GRB data sets, as well as those from combinations of GRB data sets, are consistent with those from the $H(z)$ + BAO data which favor $\Omega_{\rm m0} \sim 0.3$, but there are a few combinations of GRB data sets with constraints on Ω_{m0} being more than 2σ away from 0.3 in the ΛCDM models.

This paper is structured as follows. We use the cosmological models described in Chapter 2. In Sec. 7.2 we describe the data sets we analyze. In Sec. 7.3 we summarize our analyses techniques. In Sec. 7.4 we present our results. We conclude in Sec. 7.5.

7.2 Data

In this paper, we analyze four different GRB data sets as well as some combinations of these data sets. We also use a joint $H(z)$ + BAO data set. These data sets are summarized in Table 7.1 and described in what follows.[3]

MD-LGRB sample. This includes 31 long GRBs, with burst duration longer than 2 seconds, listed in Table 1 of Wang et al. (2022). For this data set, measured quantities for a GRB are redshift z, X-ray flux F_0, characteristic time scale t_b, and spectral index

[3]In this table and elsewhere, for compactness, we sometimes use ML, MS, and GL as abbreviations for the MD-LGRB, MD-SGRB, and GW-LGRB data sets compiled by Wang et al. (2022) and Hu et al. (2021).

during the plateau phase β'.[4] This sample probes the redshift range $1.45 \leq z \leq 5.91$.

MD-SGRB sample. This includes 5 short GRBs, with burst duration shorter than 2 seconds, listed in Table 1 of Hu et al. (2021). For this data set, measured quantities for a GRB are the same as those for the MD-LGRB sample. This data set probes the redshift range $0.35 \leq z \leq 2.6$.

GW-LGRB sample. This includes 24 long GRBs listed in Table 1 of Hu et al. (2021). For this data set, measured quantities for a GRB are the same as those for the MD-LGRB sample. This sample probes the redshift range $0.55 \leq z \leq 4.81$.

A118 sample. This sample include 118 long GRBs listed in Table 7 of Khadka et al. (2021a). For this data set, measured quantities for a GRB are z, rest-frame spectral peak energy $E_{\rm p}$, and measured bolometric fluence $S_{\rm bolo}$, computed in the standard rest-frame energy band $1-10^4$ keV. This sample probes the redshift range $0.3399 \leq z \leq 8.2$. Note that in our analyses here we did not use the correct value of $E_{\rm p} = 871 \pm 123$ keV for GRB081121, as discussed in Ref. Liu et al. (2022), although the effects on the parameter constraints are small.

The A118 data and the MD-LGRB data sets have 3 common GRBs, GRB060526, GRB081008, and GRB090516. We exclude these common GRBs from the A118 data set to form the A115 data set for joint analyses with the MD-LGRB data set. There are also 3 common GRBs between the A118 data set and the GW-LGRB data set, GRB060206, GRB091029, and GRB131105A. We exclude these common GRBs from the A118 data set to form the A115$'$ data set for joint analyses with the GW-LGRB data set.

***H(z)* and BAO data**. In addition to the GRB data, we also use 31 $H(z)$ and 11 BAO measurements. These $H(z)$ and BAO measurements probe the redshift range $0.07 \leq z \leq 1.965$ and $0.0106 \leq z \leq 2.33$, respectively. The $H(z)$ data are in Table 2 of

[4]ML, MS, and GL data error bars on F_0 and t_b are mostly asymmetric. We symmetrize these error bars using the method applied in Wang et al. (2022) and Hu et al. (2021), with the symmetrized error bar $\sigma = \sqrt{(\sigma_u^2 + \sigma_d^2)/2}$, where σ_u and σ_d are the asymmetric upper and lower error bars.

Table 7.1: Summary of data sets used.

Data set	N (Number of points)	Redshift range
ML	31	$1.45 \leq z \leq 5.91$
MS	5	$0.35 \leq z \leq 2.6$
GL	24	$0.55 \leq z \leq 4.81$
MS + GL	29	$0.35 \leq z \leq 4.81$
A118	118	$0.3399 \leq z \leq 8.2$
A115[a]	115	$0.3399 \leq z \leq 8.2$
A115′[b]	115	$0.3399 \leq z \leq 8.2$
$H(z)$	31	$0.070 \leq z \leq 1.965$
BAO	11	$0.38 \leq z \leq 2.334$

[a] Excluding from A118 those GRBs in common with MD-LGRB (GRB060526, GRB081008, and GRB090516).
[b] Excluding from A118 those GRBs in common with GW-LGRB (GRB060206, GRB091029, and GRB131105A).

Ryan et al. (2018) and the BAO data are in Table 1 of Khadka & Ratra (2020c). We use cosmological constraints from the better-established $H(z)$ + BAO data to compare with those obtained from the GRB data sets.

7.3 Data Analysis Methodology

For GRBs which obey the Dainotti correlation the luminosity of the plateau phase is (Dainotti et al., 2008, 2010, 2011b)

$$L_0 = \frac{4\pi D_L^2 F_0}{(1+z)^{1-\beta'}}, \tag{7.1}$$

where F_0 is the GRB X-ray flux, β' is the spectral index in the plateau phase, and D_L is the luminosity distance.

Table 7.2: Flat priors of the constrained parameters.

Parameter	Prior
Cosmological Parameters	
H_0 [a]	[None, None]
$\Omega_b h^2$ [b]	[0, 1]
$\Omega_c h^2$ [c]	[0, 1]
Ω_{k0}	[-2, 2]
α	[0, 10]
$w_{\rm X}$	[-5, 0.33]
GRB Nuisance Parameters[d]	
k	[-10, 10]
b [e]	[0, 10]
$\sigma_{\rm int}$	[0, 5]
β	[0, 5]
γ	[0, 300]

[a] km s^{-1} Mpc^{-1}. In the GRB alone cases, H_0 is set to be 70 km s^{-1} Mpc^{-1}, while in the $H(z)$ + BAO case, the prior range is irrelevant (unbounded).
[b] In the GRB alone cases, $\Omega_b h^2$ is set to be 0.0245, i.e. $\Omega_b = 0.05$.
[c] In the GRB alone cases, $\Omega_c \in [-0.05, 0.95]$ to ensure $\Omega_{m0} \in [0, 1]$.
[d] Note that k, b, and $\sigma_{\rm int}$ of MD-LGRBs are different from those of MD-SGRBs/GW-LGRBs, but with the same prior ranges.
[e] $b < 0$ values are possible for MD-SGRBs (due to fewer data points) but, as discussed below, requiring $b \geq 0$ does not have significant consequences.

D_L, as a function of redshift z and cosmological parameters $\boldsymbol{p}$, is given by

$$\frac{H_0\sqrt{|\Omega_{\rm k0}|}D_L(z,\boldsymbol{p})}{c(1+z)} = \begin{cases} \sinh\left[g(z,\boldsymbol{p})\right] & \text{if } \Omega_{\rm k0} > 0, \\ g(z,\boldsymbol{p}) & \text{if } \Omega_{\rm k0} = 0, \\ \sin\left[g(z,\boldsymbol{p})\right] & \text{if } \Omega_{\rm k0} < 0, \end{cases} \tag{7.2}$$

where

$$g(z,\boldsymbol{p}) = H_0\sqrt{|\Omega_{\rm k0}|}\int_0^z \frac{dz'}{H(z',\boldsymbol{p})}, \tag{7.3}$$

c is the speed of light, and $H(z,\boldsymbol{p})$ is the Hubble parameter that is described in Chapter 2 for each cosmological model.

For these GRBs the luminosity of the plateau phase L_0 and the characteristic time scale t_b are correlated through the Dainotti or luminosity-time relation

$$y \equiv \log\left(\frac{L_0}{10^{47}\ \mathrm{erg/s}}\right) = k\log\frac{t_b}{10^3(1+z)\ \mathrm{s}} + b \equiv kx + b, \tag{7.4}$$

where $\log = \log_{10}$ and the slope k and the intercept b are free parameters to be determined from the data.

We predict L_0 as a function of cosmological parameters $\boldsymbol{p}$ at the redshift of each GRB by using eqs. (7.1), (7.2), and (7.4). We then compare predicted and measured values of L_0 by using the natural log of the likelihood function (D'Agostini, 2005)

$$\ln\mathscr{L}_{\rm GRB} = -\frac{1}{2}\left[\chi^2_{\rm GRB} + \sum_{i=1}^{N}\ln\left(2\pi(\sigma^2_{\rm int} + \sigma^2_{y_i} + k^2\sigma^2_{x_i})\right)\right], \tag{7.5}$$

where

$$\chi^2_{\rm GRB} = \sum_{i=1}^{N}\left[\frac{(y_i - kx_i - b)^2}{(\sigma^2_{\rm int} + \sigma^2_{y_i} + k^2\sigma^2_{x_i})}\right]. \tag{7.6}$$

Here N is the number of data points (e.g., for MD-LGRB $N = 31$), and $\sigma_{\rm int}$ is the intrinsic scatter parameter (which also contains the unknown systematic uncertainty).

For GRBs which obey the Amati correlation the rest frame isotropic radiated energy $E_{\rm iso}$ is

$$E_{\rm iso} = \frac{4\pi D_L^2}{1+z} S_{\rm bolo}, \tag{7.7}$$

where $S_{\rm bolo}$ is the bolometric fluence.

For these GRBs the rest frame peak photon energy $E_{\rm p}$ and $E_{\rm iso}$ are correlated through the Amati (or $E_{\rm p} - E_{\rm iso}$) relation (4.2) (Amati et al., 2008, 2009).

We predict $E_{\rm iso}$ as a function of cosmological parameters $\boldsymbol{p}$ at the redshift of each GRB by using eqs. (7.2), (7.7), and (4.2). We then compare predicted and measured values of $E_{\rm iso}$ by using the natural log of the likelihood function (D'Agostini, 2005)

$$\ln \mathscr{L}_{\rm A118} = -\frac{1}{2}\left[\chi^2_{\rm A118} + \sum_{i=1}^{N} \ln\left(2\pi(\sigma^2_{\rm int} + \sigma^2_{y'_i} + \beta^2\sigma^2_{x'_i})\right)\right], \tag{7.8}$$

where

$$\chi^2_{\rm A118} = \sum_{i=1}^{N}\left[\frac{(y'_i - \beta x'_i - \gamma)^2}{(\sigma^2_{\rm int} + \sigma^2_{y'_i} + \beta^2\sigma^2_{x'_i})}\right]. \tag{7.9}$$

Here $x' = \log(E_{\rm p}/{\rm keV})$, $\sigma_{x'} = \sigma_{E_{\rm p}}/(E_{\rm p}\ln 10)$, $y' = \log(E_{\rm iso}/{\rm erg})$, and $\sigma_{\rm int}$ is the intrinsic scatter parameter, which also contains the unknown systematic uncertainty.

The $H(z)$ + BAO data analyses follow the method described in Sec. 4 of Khadka & Ratra (2022).

We maximize the likelihood function using the Markov chain Monte Carlo (MCMC) method as implemented in the MontePython code (Brinckmann & Lesgourgues, 2019) and determine the best-fitting and posterior mean values and the corresponding uncertainties for all free parameters. We assure convergence of the MCMC chains for each free parameter from the Gelman-Rubin criterion ($R - 1 < 0.05$). Flat priors used for the free parameters are given in Table 7.2.

The Akaike Information Criterion (AIC) in equation (4.8) and the Bayesian Information Criterion (BIC) in equation (4.9) are used to compare the goodness of fit of models with different numbers of parameters.

Table 7.3: One-dimensional marginalized posterior means and 68.27% limits of the Dainotti correlation parameters for the ML, GL, and MS data sets using the flat ΛCDM model with $\Omega_{m0} = 0.3$ and $H_0 = 70$ km s^{-1} Mpc^{-1}, and comparison with the results given in Wang et al. (2022) and Hu et al. (2021).

Data set	Source	k	b	σ_{int}
ML	[a]	$-1.02^{+0.09}_{-0.08}$	$1.72^{+0.07}_{-0.07}$	–
	[b]	-1.026 ± 0.085	1.726 ± 0.074	$0.303^{+0.032}_{-0.050}$
	[c]	-1.026 ± 0.086	1.726 ± 0.074	$0.303^{+0.032}_{-0.050}$
GL	[d]	$-1.77^{+0.20}_{-0.20}$	$0.66^{+0.01}_{-0.01}$	$0.42^{+0.08}_{-0.06}$
	[b]	$-1.753^{+0.187}_{-0.208}$	$0.642^{+0.100}_{-0.071}$	$0.428^{+0.053}_{-0.086}$
	[c]	-1.769 ± 0.205	0.656 ± 0.094	$0.431^{+0.054}_{-0.088}$
MS	[d]	$-1.38^{+0.17}_{-0.19}$	$0.33^{+0.17}_{-0.16}$	$0.35^{+0.20}_{-0.12}$
	[b]	$-1.381^{+0.209}_{-0.213}$	$0.327^{+0.195}_{-0.189}$	$0.420^{+0.086}_{-0.242}$
	[c]	$-1.397^{+0.247}_{-0.241}$	$0.354^{+0.195}_{-0.242}$	$0.525^{+0.044}_{-0.358}$

[a] Results from Wang et al. (2022) with the prior ranges of the parameters being $k \in (-1.3, -0.75)$, $b \in (1.4, 2.0)$, and $\sigma_{int} \in (0.1, 0.6)$ for ML.
[b] Our results with the same prior ranges of the parameters as Wang et al. (2022) or Hu et al. (2021).
[c] Our results with wider prior ranges of the parameters $k \in [-10, 10]$, $b \in [0, 10]$ ($b \in [-0.5, 10]$), and $\sigma_{int} \in [0, 3]$ for ML and GL (MS).
[d] Results from Hu et al. (2021) with the prior ranges of the parameters being $k \in (-2.2, -1)$, $b \in (0.1, 0.8)$, and $\sigma_{int} \in (0.01, 0.8)$ for GL and being $k \in (-2.1, -0.55)$, $b \in (-0.5, 1.0)$, and $\sigma_{int} \in (0.01, 1)$ for MS.

7.4 Results

7.4.1 Constraints from ML, MS, and GL data

In Table 7.3 we list Dainotti correlation parameters computed using the ML, GL, and MS data sets. These are computed in the flat ΛCDM model with $\Omega_{m0} = 0.3$ and $H_0 = 70$ km s^{-1} Mpc^{-1}, the same model and parameter values used in Wang et al. (2022) and Hu et al. (2021). The first line of parameter values in each of the three subpanels of Table 7.3 are taken from these papers.[5] To compare to these results, we used EMCEE (Foreman-Mackey

[5] Wang et al. (2022) do not list a value for σ_{int} in the ML case.

et al., 2013) to compute the values listed in the second and third lines of each subpanel. Comparing the first and second lines in each subpanel, we find that they are consistent, except: i) for the GL case our b uncertainties are larger than those of Hu et al. (2021); and, ii) for the MS case we have larger b and k error bars and a larger central value of $\sigma_{\rm int}$ than those of Hu et al. (2021), but they agree within 1σ. In the third line of each subpanel we list results obtained assuming wider prior ranges of the parameters. We find that the ML results do not change, the GL results are shifted closer to those of Hu et al. (2021), except for the values of $\sigma_{\rm int}$, and the MS results are shifted away from those of Hu et al. (2021) with larger error bars, especially for $\sigma_{\rm int}$.

We now record and discuss results when these data sets are used to jointly constrain the Dainotti parameters and the cosmological parameters of the six spatially-flat and non-flat dark energy cosmological models. Figure 7.1 shows the flat ΛCDM Dainotti correlations for the ML, MS, GL, and MS + GL data sets. The unmarginalized best-fitting results and the one-dimensional (1D) posterior mean values and uncertainties are reported in Tables 7.4 and 7.5, respectively. The corresponding posterior 1D probability distributions and two-dimensional (2D) confidence regions of these parameters are shown in Figs. 7.2–7.4, in blue (ML), gray (MS), green (GL), pink (ML + MS), violet (ML + GL), orange (MS + GL), and red ($H(z)$ + BAO, as a baseline). Note that $H_0 = 70$ km s^{-1} Mpc^{-1} and $\Omega_b = 0.05$ are applied in the GRB cases.

ML, MS, and GL GRB data have almost cosmological-model independent Dainotti parameters. This means that it is not unreasonable to treat the ML, MS, and GL GRBs as standardizable candles, as was assumed in Wang et al. (2022) and Hu et al. (2021).

In the ML case (with subscript "ML" in the first line of Tables 7.4, 7.5, 7.7, and 7.8), the slope k ranges from a high of -0.996 ± 0.097 (non-flat XCDM) to a low of -1.017 ± 0.090 (flat ΛCDM), the intercept b ranges from a high of $1.611^{+0.113}_{-0.277}$ (flat XCDM) to a low of $1.448^{+0.120}_{-0.165}$ (non-flat ϕCDM), and the intrinsic scatter $\sigma_{\rm int}$ ranges from a high of $0.306^{+0.036}_{-0.054}$ (flat XCDM) to a low of $0.303^{+0.035}_{-0.053}$ (non-flat ϕCDM), with central values of each pair being 0.16σ, 0.54σ, and 0.05σ away from each other, respectively.

In the MS case (with subscript "MS" in the first line of Tables 7.4 and 7.5) with prior

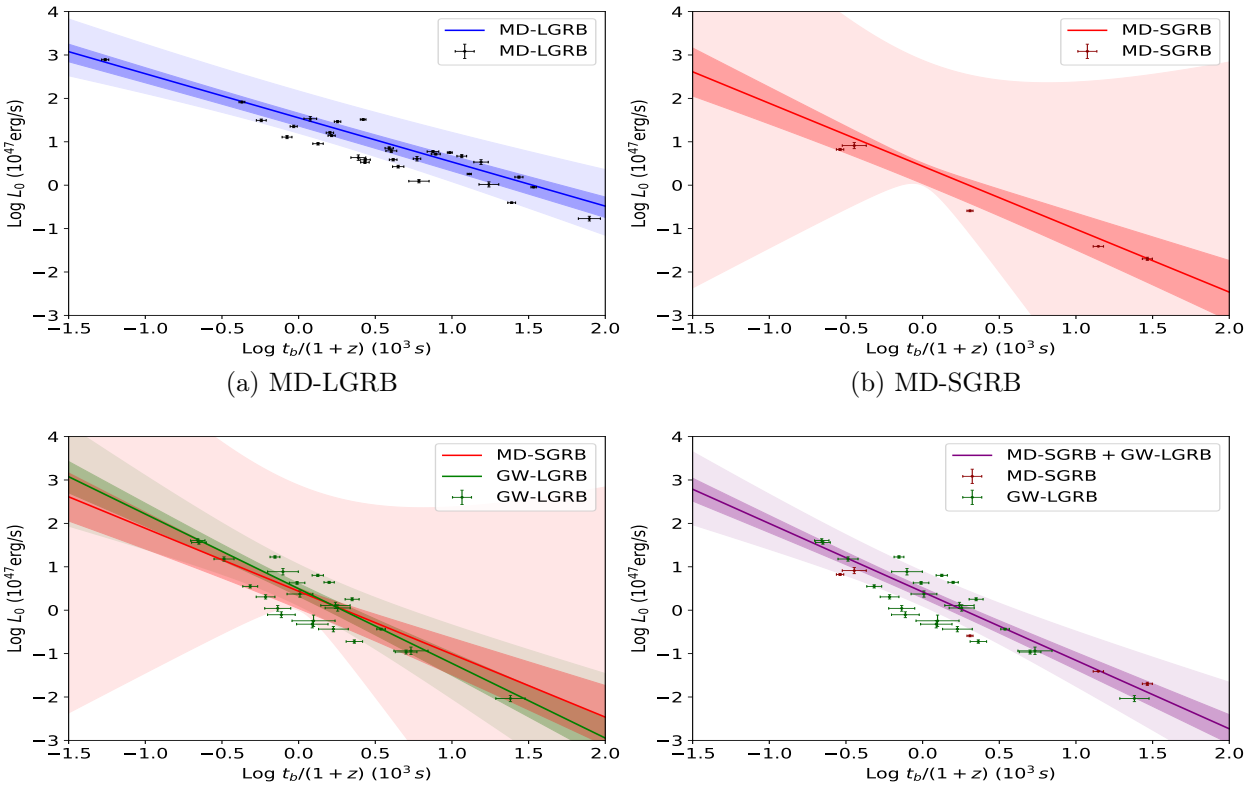

(a) MD-LGRB

(b) MD-SGRB

(c) GW-LGRB and MD-SGRB

(d) MD-SGRB + GW-LGRB

Figure 7.1: $L_0 - t_b$ correlations for MD-LGRB, MD-SGRB, GW-LGRB, and MD-SGRB + GW-LGRB data using the flat ΛCDM model. The MD-LGRB, MD-SGRB, and GW-LGRB data with error bars are shown in black, dark red, and dark green, respectively. The solid lines are the $L_0 - t_b$ correlations with posterior mean values for the slopes and intercepts listed in Table 7.5, for MD-LGRB (blue), MD-SGRB (red), GW-LGRB (green), and MD-SGRB + GW-LGRB (purple) data. The 1σ and 3σ confidence regions are the dark and light colored shaded regions with the uncertainties propagated from those of k and b (without considering $\sigma_{\rm int}$).

Table 7.4: Unmarginalized best-fitting parameter values for all models from various combinations of data.

Model	Data set	$\Omega_b h^2$	$\Omega_c h^2$	Ω_{m0}	Ω_{k0}	w_X	α	H_0[a]	$\sigma_{int,ML}$	b_{ML}	k_{ML}	$\sigma_{int,MS}$	b_{MS}	k_{MS}	$\sigma_{int,GL}$	b_{GL}	k_{GL}	$\sigma_{int,MS+GL}$	b_{MS+GL}	k_{MS+GL}	$-2\ln\mathscr{L}_{max}$	AIC	BIC	ΔAIC	ΔBIC
	$H(z)$ + BAO	0.0239	0.1187	0.298	–	–	–	69.13	–	–	–	–	–	–	–	–	–	–	–	–	23.66	29.66	34.87	0.00	0.00
	ML	0.0245	0.4645	0.998	–	–	–	70	0.275	1.383	−1.010	–	–	–	–	–	–	–	–	–	8.68	16.68	22.41	0.00	0.00
	MS	0.0245	0.4651	0.999	–	–	–	70	–	–	–	0.159	0.105	−1.310	–	–	–	–	–	–	−3.49	4.51	2.95	0.00	0.00
Flat ΛCDM	GL	0.0245	0.4641	0.997	–	–	–	70	–	–	–	–	–	–	0.370	0.359	−1.675	–	–	–	22.94	30.94	35.65	0.00	0.00
	MS + GL	0.0245	0.4652	0.999	–	–	–	70	–	–	–	–	–	–	–	–	–	0.361	0.313	−1.545	25.59	33.59	38.30	0.00	0.00
	ML + GL	0.0245	0.4642	0.997	–	–	–	70	0.274	1.378	−1.008	–	–	–	0.362	0.358	−1.708	–	–	–	31.66	45.66	59.71	0.00	0.00
	ML + MS	0.0245	0.463	0.995	–	–	–	70	0.274	1.388	−1.013	0.148	0.080	−1.322	–	–	–	–	–	–	5.34	19.34	30.42	0.00	0.00
	$H(z)$ + BAO	0.0247	0.1140	0.294	0.029	–	–	68.68	–	–	–	–	–	–	–	–	–	–	–	–	23.60	31.60	38.55	1.94	3.68
	ML	0.0245	0.4410	0.950	−0.973	–	–	70	0.268	1.316	−0.967	–	–	–	–	–	–	–	–	–	7.48	17.48	24.65	0.80	2.24
	MS	0.0245	0.2727	0.607	−1.730	–	–	70	–	–	–	0.007	0.023	−0.919	–	–	–	–	–	–	−15.81	−5.81	−7.76	−10.32	−10.71
Non-flat ΛCDM	GL	0.0245	0.4640	0.997	−1.703	–	–	70	–	–	–	–	–	–	0.329	0.238	−1.377	–	–	–	17.00	27.00	32.89	−3.94	−2.76
	MS + GL	0.0245	0.4649	0.999	−1.738	–	–	70	–	–	–	–	–	–	–	–	–	0.304	0.220	−1.303	16.02	26.02	31.91	−7.57	−6.39
	ML + GL	0.0245	0.4330	0.934	−1.288	–	–	70	0.269	1.248	−0.953	–	–	–	0.336	0.330	−1.529	–	–	–	26.79	42.79	58.84	−2.87	−0.87
	ML + MS	0.0245	0.4625	0.994	−1.130	–	–	70	0.259	1.278	−0.966	0.136	0.159	−1.249	–	–	–	–	–	–	2.91	18.91	31.58	−0.43	1.14
	$H(z)$ + BAO	0.0304	0.0891	0.281	–	−0.701	–	65.18	–	–	–	–	–	–	–	–	–	–	–	–	19.65	27.65	34.60	−2.01	−0.27
	ML	0.0245	0.0327	0.117	–	0.133	–	70	0.275	1.288	−0.997	–	–	–	–	–	–	–	–	–	8.14	18.14	25.31	1.46	2.90
	MS	0.0245	0.0939	0.242	–	0.141	–	70	–	–	–	0.160	0.054	−1.285	–	–	–	–	–	–	−4.23	5.77	3.81	1.26	0.86
Flat XCDM	GL	0.0245	0.0035	0.057	–	0.139	–	70	–	–	–	–	–	–	0.364	0.259	−1.651	–	–	–	21.97	31.97	37.86	1.03	2.21
	MS + GL	0.0245	0.0058	0.062	–	0.141	–	70	–	–	–	–	–	–	–	–	–	0.346	0.248	−1.518	23.92	33.92	39.81	0.33	1.51
	ML + GL	0.0245	0.0735	0.200	–	0.143	–	70	0.273	1.300	−1.015	–	–	–	0.359	0.273	−1.636	–	–	–	30.20	46.20	62.26	0.54	6.55
	ML + MS	0.0245	−0.0207	0.008	–	0.137	–	70	0.278	1.269	−0.984	0.175	0.031	−1.282	–	–	–	–	–	–	3.99	19.99	32.65	0.65	2.23
	$H(z)$ + BAO	0.0290	0.0980	0.295	−0.152	−0.655	–	65.59	–	–	–	–	–	–	–	–	–	–	–	–	18.31	28.31	37.00	−1.35	2.13
	ML	0.0245	0.1525	0.361	−1.893	0.036	–	70	0.269	0.949	−0.976	–	–	–	–	–	–	–	–	–	7.39	19.39	27.99	2.71	5.58
	MS	0.0245	0.3596	0.784	−1.915	−1.108	–	70	–	–	–	0.057	0.098	−0.995	–	–	–	–	–	–	−13.61	−1.61	−3.95	−6.12	−6.90
Non-flat XCDM	GL	0.0245	0.0378	0.127	−0.174	−4.518	–	70	–	–	–	–	–	–	0.327	1.237	−1.299	–	–	–	16.61	28.61	35.68	−2.33	0.03
	MS + GL	0.0245	0.4212	0.910	−1.218	−2.308	–	70	–	–	–	–	–	–	–	–	–	0.298	0.403	−1.248	15.65	27.65	34.72	−5.94	−3.58
	ML + GL	0.0245	0.3594	0.783	−0.789	−4.432	–	70	0.269	1.449	−0.927	–	–	–	0.338	0.576	−1.429	–	–	–	26.04	44.04	62.11	−1.62	2.40
	ML + MS	0.0245	0.1499	0.306	−1.993	0.130	–	70	0.281	0.881	−0.978	0.095	−0.164	−1.206	–	–	–	–	–	–	−0.04	17.96	32.21	−1.38	1.79
	$H(z)$ + BAO	0.0333	0.0788	0.264	–	–	1.504	65.20	–	–	–	–	–	–	–	–	–	–	–	–	19.49	27.49	34.44	−2.17	−0.43
	ML	0.0245	0.4651	0.999	–	–	5.225	70	0.275	1.383	−1.011	–	–	–	–	–	–	–	–	–	8.68	18.68	25.85	2.00	3.44
	MS	0.0245	0.4649	0.999	–	–	8.046	70	–	–	–	0.160	0.099	−1.306	–	–	–	–	–	–	−3.49	6.51	4.56	2.00	1.61
Flat ϕCDM	GL	0.0245	0.4641	0.997	–	–	4.299	70	–	–	–	–	–	–	0.372	0.360	−1.674	–	–	–	22.94	32.94	38.83	2.00	3.18
	MS + GL	0.0245	0.4653	1.000	–	–	6.323	70	–	–	–	–	–	–	–	–	–	0.359	0.314	−1.545	25.59	35.59	41.48	2.00	3.18
	ML + GL	0.0245	0.4648	0.999	–	–	7.886	70	0.274	1.375	−1.013	–	–	–	0.371	0.333	−1.647	–	–	–	31.72	47.72	63.78	2.06	4.07
	ML + MS	0.0245	0.4611	0.991	–	–	6.029	70	0.268	1.371	−0.997	0.148	0.113	−1.317	–	–	–	–	–	–	5.32	21.32	33.99	1.98	3.57
	$H(z)$ + BAO	0.0334	0.0816	0.266	−0.147	–	1.915	65.70	–	–	–	–	–	–	–	–	–	–	–	–	18.15	28.15	36.84	−1.51	1.97
	ML	0.0245	0.4558	0.980	−0.980	–	0.423	70	0.266	1.296	−0.973	–	–	–	–	–	–	–	–	–	7.48	19.48	28.09	2.80	5.68
	MS	0.0245	0.4482	0.965	−0.964	–	8.262	70	–	–	–	0.132	0.003	−1.261	–	–	–	–	–	–	−5.25	6.75	4.40	2.24	1.45
Non-flat ϕCDM	GL	0.0245	0.4644	0.998	−0.993	–	0.173	70	–	–	–	–	–	–	0.340	0.337	−1.547	–	–	–	20.15	32.15	39.22	1.21	3.57
	MS + GL	0.0245	0.4601	0.989	−0.982	–	0.011	70	–	–	–	–	–	–	–	–	–	0.315	0.310	−1.484	21.46	33.46	40.53	−0.13	2.23
	ML + GL	0.0245	0.4465	0.961	−0.950	–	0.232	70	0.255	1.290	−0.969	–	–	–	0.348	0.356	−1.600	–	–	–	28.04	46.04	64.11	0.38	4.40
	ML + MS	0.0245	0.4628	0.995	−0.936	–	8.517	70	0.281	1.202	−0.994	0.152	0.027	−1.291	–	–	–	–	–	–	2.71	20.71	34.96	1.36	4.53

[a] km s^{-1} Mpc^{-1}. In the GRB only cases, H_0 is set to be 70 km s^{-1} Mpc^{-1}.

Table 7.5: One-dimensional marginalized posterior mean values and uncertainties ($\pm1\sigma$ error bars or 2σ limits) of the parameters for all models from various combinations of data.

Model	Data set	$\Omega_b h^2$	$\Omega_c h^2$	Ω_{m0}	Ω_{k0}	w_X	α	H_0[a]	$\sigma_{int,ML}$	b_{ML}	k_{ML}	$\sigma_{int,MS}$	b_{MS}	k_{MS}	$\sigma_{int,GL}$	b_{GL}	k_{GL}	$\sigma_{int,MS+GL}$	b_{MS+GL}	k_{MS+GL}
	$H(z)$ + BAO	0.0241 ± 0.0029	$0.1193^{+0.0082}_{-0.0090}$	$0.299^{+0.017}_{-0.019}$	–	–	–	69.30 ± 1.84	–	–	–	–	–	–	–	–	–	–	–	–
	ML	–	–	> 0.188	–	–	–	–	$0.305^{+0.035}_{-0.053}$	$1.552^{+0.108}_{-0.189}$	-1.017 ± 0.090	–	–	–	–	–	–	–	–	–
	MS	–	–	$0.520^{+0.379}_{-0.253}$	–	–	–	–	–	–	–	$0.695^{+0.044}_{-0.550}$	$0.437^{+0.073}_{-0.400}$	$-1.450^{+0.362}_{-0.258}$	–	–	–	–	–	–
Flat ΛCDM	GL	–	–	> 0.202	–	–	–	–	–	–	–	–	–	–	$0.429^{+0.059}_{-0.094}$	$0.495^{+0.120}_{-0.173}$	-1.720 ± 0.219	–	–	–
	MS + GL	–	–	> 0.293	–	–	–	–	–	–	–	–	–	–	–	–	–	$0.412^{+0.052}_{-0.079}$	$0.421^{+0.101}_{-0.141}$	-1.577 ± 0.155
	ML + GL	–	–	> 0.294	–	–	–	–	$0.301^{+0.033}_{-0.051}$	$1.507^{+0.095}_{-0.151}$	-1.015 ± 0.089	–	–	–	$0.424^{+0.056}_{-0.090}$	$0.465^{+0.113}_{-0.149}$	-1.708 ± 0.210	–	–	–
	ML + MS	–	–	> 0.206	–	–	–	–	$0.302^{+0.034}_{-0.052}$	$1.542^{+0.104}_{-0.184}$	-1.016 ± 0.091	$0.613^{+0.010}_{-0.479}$	$0.379^{+0.049}_{-0.350}$	$-1.426^{+0.312}_{-0.210}$	–	–	–	–	–	–
	$H(z)$ + BAO	$0.0253^{+0.0041}_{-0.0050}$	$0.1135^{+0.0196}_{-0.0197}$	0.293 ± 0.025	$0.039^{+0.102}_{-0.115}$	–	–	$68.75^{+2.37}_{-2.36}$	–	–	–	–	–	–	–	–	–	–	–	–
	ML	–	–	> 0.241	$-0.131^{+0.450}_{-0.919}$	–	–	–	$0.304^{+0.035}_{-0.053}$	$1.478^{+0.123}_{-0.166}$	-1.000 ± 0.096	–	–	–	–	–	–	–	–	–
	MS	–	–	$0.564^{+0.426}_{-0.149}$	$0.066^{+1.002}_{-1.199}$	–	–	–	–	–	–	$0.670^{+0.024}_{-0.533}$	$0.413^{+0.047}_{-0.393}$	$-1.430^{+0.360}_{-0.239}$	–	–	–	–	–	–
Non-flat ΛCDM	GL	–	–	> 0.290	$-0.762^{+0.271}_{-0.888}$	–	–	–	–	–	–	–	–	–	$0.402^{+0.057}_{-0.090}$	$0.407^{+0.136}_{-0.160}$	-1.536 ± 0.252	–	–	–
	MS + GL	–	–	> 0.391	$-1.165^{+0.225}_{-0.519}$	–	–	–	–	–	–	–	–	–	–	–	–	$0.357^{+0.046}_{-0.070}$	$0.337^{+0.110}_{-0.127}$	$-1.382^{+0.164}_{-0.163}$
	ML + GL	–	–	> 0.338	$-0.737^{+0.299}_{-0.547}$	–	–	–	$0.300^{+0.033}_{-0.051}$	$1.386^{+0.138}_{-0.154}$	-0.966 ± 0.093	–	–	–	$0.397^{+0.053}_{-0.086}$	$0.437^{+0.110}_{-0.142}$	$-1.588^{+0.215}_{-0.214}$	–	–	–
	ML + MS	–	–	> 0.270	$-0.300^{+0.380}_{-0.836}$	–	–	–	$0.302^{+0.034}_{-0.052}$	$1.457^{+0.128}_{-0.163}$	-0.993 ± 0.095	$0.518^{+0.009}_{-0.393}$	$0.339^{+0.056}_{-0.301}$	$-1.385^{+0.271}_{-0.186}$	–	–	–	–	–	–
	$H(z)$ + BAO	$0.0296^{+0.0046}_{-0.0052}$	$0.0939^{+0.0194}_{-0.0171}$	$0.284^{+0.023}_{-0.021}$	–	$-0.754^{+0.155}_{-0.107}$	–	$65.89^{+2.41}_{-2.71}$	–	–	–	–	–	–	–	–	–	–	–	–
	ML	–	–	> 0.123	–	$-2.456^{+2.567}_{-2.180}$	–	–	$0.306^{+0.036}_{-0.054}$	$1.611^{+0.113}_{-0.277}$	-1.014 ± 0.092	–	–	–	–	–	–	–	–	–
	MS	–	–	$0.520^{+0.340}_{-0.276}$	–	$-2.494^{+1.264}_{-2.050}$	–	–	–	–	–	$0.704^{+0.035}_{-0.564}$	$0.497^{+0.086}_{-0.458}$	$-1.441^{+0.366}_{-0.259}$	–	–	–	–	–	–
Flat XCDM	GL	–	–	> 0.141	–	< -0.046	–	–	–	–	–	–	–	–	$0.428^{+0.058}_{-0.092}$	$0.556^{+0.127}_{-0.256}$	-1.706 ± 0.215	–	–	–
	MS + GL	–	–	> 0.192	–	< 0.028	–	–	–	–	–	–	–	–	–	–	–	$0.409^{+0.052}_{-0.078}$	$0.470^{+0.108}_{-0.206}$	-1.570 ± 0.155
	ML + GL	–	–	> 0.164	–	< 0.022	–	–	$0.300^{+0.033}_{-0.051}$	$1.566^{+0.099}_{-0.239}$	-1.012 ± 0.087	–	–	–	$0.424^{+0.057}_{-0.092}$	$0.531^{+0.116}_{-0.240}$	-1.700 ± 0.213	–	–	–
	ML + MS	–	–	> 0.142	–	< -0.072	–	–	$0.303^{+0.034}_{-0.052}$	$1.597^{+0.108}_{-0.255}$	-1.013 ± 0.089	$0.562^{+0.010}_{-0.431}$	$0.409^{+0.066}_{-0.377}$	$-1.408^{+0.288}_{-0.196}$	–	–	–	–	–	–
	$H(z)$ + BAO	$0.0290^{+0.0052}_{-0.0055}$	$0.0990^{+0.0214}_{-0.0215}$	0.293 ± 0.028	-0.116 ± 0.134	$-0.700^{+0.138}_{-0.083}$	–	$65.96^{+2.32}_{-2.55}$	–	–	–	–	–	–	–	–	–	–	–	–
	ML	–	–	> 0.174	$-0.262^{+0.580}_{-0.724}$	$-2.000^{+2.117}_{-1.264}$	–	–	$0.305^{+0.036}_{-0.054}$	$1.462^{+0.194}_{-0.196}$	-0.996 ± 0.097	–	–	–	–	–	–	–	–	–
	MS	–	–	$0.552^{+0.442}_{-0.152}$	$0.134^{+0.793}_{-0.987}$	$-2.234^{+2.159}_{-0.969}$	–	–	–	–	–	$0.733^{+0.031}_{-0.596}$	$0.464^{+0.052}_{-0.444}$	$-1.433^{+0.394}_{-0.270}$	–	–	–	–	–	–
Non-flat XCDM	GL	–	–	> 0.194	$-0.615^{+0.470}_{-0.685}$	$-2.212^{+2.186}_{-0.962}$	–	–	–	–	–	–	–	–	$0.403^{+0.058}_{-0.092}$	$0.480^{+0.177}_{-0.223}$	$-1.532^{+0.259}_{-0.260}$	–	–	–
	MS + GL	–	–	> 0.268	$-0.920^{+0.460}_{-0.386}$	$-2.323^{+2.085}_{-1.095}$	–	–	–	–	–	–	–	–	–	–	–	$0.358^{+0.047}_{-0.072}$	$0.452^{+0.185}_{-0.203}$	-1.363 ± 0.175
	ML + GL	–	–	> 0.196	$-0.696^{+0.484}_{-0.408}$	$-2.158^{+2.254}_{-1.424}$	–	–	$0.298^{+0.033}_{-0.051}$	$1.422^{+0.201}_{-0.221}$	-0.968 ± 0.092	–	–	–	$0.397^{+0.054}_{-0.087}$	$0.480^{+0.205}_{-0.224}$	$-1.561^{+0.220}_{-0.219}$	–	–	–
	ML + MS	–	–	> 0.198	$-0.375^{+0.458}_{-0.611}$	$-2.235^{+2.289}_{-2.007}$	–	–	$0.301^{+0.034}_{-0.052}$	$1.470^{+0.184}_{-0.183}$	$-0.988^{+0.095}_{-0.094}$	$0.525^{+0.007}_{-0.409}$	$0.397^{+0.079}_{-0.364}$	$-1.367^{+0.275}_{-0.193}$	–	–	–	–	–	–
	$H(z)$ + BAO	$0.0321^{+0.0056}_{-0.0039}$	$0.0823^{+0.0186}_{-0.0183}$	0.268 ± 0.024	–	–	$1.467^{+0.637}_{-0.866}$	$65.24^{+2.15}_{-2.35}$	–	–	–	–	–	–	–	–	–	–	–	–
	ML	–	–	> 0.148	–	–	–	–	$0.304^{+0.035}_{-0.053}$	$1.493^{+0.093}_{-0.143}$	-1.017 ± 0.089	–	–	–	–	–	–	–	–	–
	MS	–	–	$0.514^{+0.365}_{-0.275}$	–	–	–	–	–	–	–	$0.597^{+0.029}_{-0.457}$	$0.355^{+0.052}_{-0.331}$	$-1.425^{+0.311}_{-0.221}$	–	–	–	–	–	–
Flat ϕCDM	GL	–	–	> 0.148	–	–	–	–	–	–	–	–	–	–	$0.428^{+0.059}_{-0.094}$	$0.444^{+0.112}_{-0.141}$	-1.710 ± 0.218	–	–	–
	MS + GL	–	–	> 0.222	–	–	–	–	–	–	–	–	–	–	–	–	–	$0.408^{+0.050}_{-0.076}$	$0.384^{+0.092}_{-0.111}$	-1.573 ± 0.151
	ML + GL	–	–	> 0.235	–	–	–	–	$0.301^{+0.033}_{-0.051}$	$1.463^{+0.086}_{-0.119}$	-1.015 ± 0.088	–	–	–	$0.423^{+0.056}_{-0.091}$	$0.423^{+0.104}_{-0.121}$	-1.701 ± 0.209	–	–	–
	ML + MS	–	–	> 0.166	–	–	–	–	$0.303^{+0.034}_{-0.053}$	$1.485^{+0.092}_{-0.137}$	-1.017 ± 0.090	$0.517^{+0.001}_{-0.385}$	$0.304^{+0.033}_{-0.283}$	$-1.410^{+0.268}_{-0.173}$	–	–	–	–	–	–
	$H(z)$ + BAO	$0.0319^{+0.0062}_{-0.0037}$	$0.0848^{+0.0181}_{-0.0220}$	$0.271^{+0.025}_{-0.028}$	$-0.074^{+0.104}_{-0.110}$	–	$1.653^{+0.685}_{-0.856}$	$65.46^{+2.31}_{-2.29}$	–	–	–	–	–	–	–	–	–	–	–	–
	ML	–	–	> 0.207	$-0.163^{+0.355}_{-0.317}$	–	–	–	$0.303^{+0.035}_{-0.053}$	$1.448^{+0.120}_{-0.165}$	-1.011 ± 0.091	–	–	–	–	–	–	–	–	–
	MS	–	–	$0.505^{+0.310}_{-0.313}$	$0.017^{+0.387}_{-0.375}$	–	–	–	–	–	–	$0.589^{+0.023}_{-0.455}$	$0.352^{+0.048}_{-0.331}$	$-1.432^{+0.314}_{-0.207}$	–	–	–	–	–	–
Non-flat ϕCDM	GL	–	–	> 0.207	$-0.193^{+0.364}_{-0.347}$	–	–	–	–	–	–	–	–	–	$0.422^{+0.057}_{-0.092}$	$0.408^{+0.121}_{-0.149}$	$-1.693^{+0.215}_{-0.214}$	–	–	–
	MS + GL	–	–	> 0.313	$-0.293^{+0.330}_{-0.359}$	–	–	–	–	–	–	–	–	–	–	–	–	$0.397^{+0.050}_{-0.076}$	$0.343^{+0.101}_{-0.120}$	-1.546 ± 0.150
	ML + GL	–	–	> 0.340	$-0.327^{+0.321}_{-0.345}$	–	–	–	$0.299^{+0.033}_{-0.051}$	$1.391^{+0.107}_{-0.136}$	-1.004 ± 0.088	–	–	–	$0.414^{+0.055}_{-0.088}$	$0.374^{+0.113}_{-0.128}$	$-1.668^{+0.207}_{-0.208}$	–	–	–
	ML + MS	–	–	> 0.238	$-0.198^{+0.351}_{-0.321}$	–	–	–	$0.301^{+0.034}_{-0.052}$	$1.435^{+0.114}_{-0.156}$	-1.010 ± 0.089	$0.507^{+0.003}_{-0.379}$	$0.292^{+0.025}_{-0.281}$	$-1.393^{+0.258}_{-0.173}$	–	–	–	–	–	–

[a] km s^{-1} Mpc^{-1}. In the GRB only cases, H_0 is set to be 70 km s^{-1} Mpc^{-1}.

range of $b \in [0, 10]$, the slope k ranges from a high of $-1.425^{+0.311}_{-0.221}$ (flat ϕCDM) to a low of $-1.450^{+0.362}_{-0.258}$ (flat ΛCDM), the intercept b ranges from a high of $0.497^{+0.086}_{-0.458}$ (flat XCDM) to a low of $0.352^{+0.048}_{-0.331}$ (non-flat ϕCDM), and the intrinsic scatter $\sigma_{\rm int}$ ranges from a high of $0.733^{+0.031}_{-0.596}$ (non-flat XCDM) to a low of $0.589^{+0.023}_{-0.455}$ (non-flat ϕCDM), with central values of each pair being 0.06σ, 0.54σ, and 0.05σ away from each other, respectively.[6]

In the GL case (with subscript "GL" in the first line of Tables 7.4, 7.5, 7.7, and 7.8), the slope k ranges from a high of $-1.532^{+0.259}_{-0.260}$ (non-flat XCDM) to a low of -1.720 ± 0.219 (flat ΛCDM), the intercept b ranges from a high of $0.556^{+0.127}_{-0.256}$ (flat XCDM) to a low of $0.407^{+0.136}_{-0.160}$ (non-flat ΛCDM), and the intrinsic scatter $\sigma_{\rm int}$ ranges from a high of $0.429^{+0.059}_{-0.094}$ (flat ΛCDM) to a low of $0.402^{+0.057}_{-0.090}$ (non-flat ϕCDM), with central values of each pair being 0.55σ, 0.51σ, and 0.25σ away from each other, respectively.

Figure 7.1, panel (c), shows that the GL and MS GRBs obey the same Dainotti correlation in the flat ΛCDM model, within the uncertainties.[7] Table 7.6 shows that the differences between the GL and MS Dainotti parameters in all six cosmological models are within 1σ. GL and MS GRBs however follow a different Dainotti correlation than the ML GRBs. Given the similarity of the GL and MS Dainotti correlation parameters, it is not unreasonable to use just three (not six) correlation parameters in joint analyses of MS and GL data (with subscript "MS+GL" in the first line of Tables 7.4 and 7.5). In this case, the slope k ranges from a high of -1.363 ± 0.175 (non-flat XCDM) to a low of -1.577 ± 0.155 (flat ΛCDM), the intercept b ranges from a high of $0.470^{+0.108}_{-0.206}$ (flat XCDM) to a low of $0.337^{+0.110}_{-0.127}$ (non-flat ΛCDM), and the intrinsic scatter $\sigma_{\rm int}$ ranges from a high of $0.412^{+0.052}_{-0.079}$ (flat ΛCDM) to a low of $0.357^{+0.046}_{-0.070}$ (non-flat ΛCDM), with central values of each pair being 0.92σ, 0.57σ, and 0.60σ away from each other, respectively. In contrast to the GL case, the MS + GL case tightens the constraints a little bit, with smaller error bars, and prefers lower values of b

[6] Note, however, that the lower error bars of b and $\sigma_{\rm int}$ are considerably larger than the upper ones due to cut-off prior ranges of the former and skewed distributions of the latter. Therefore here we also consider the MS case with wider prior range of $b \in [-10, 10]$, which are not listed in the tables due to their insignificant differences. Because the lowest and highest values of k, b, and $\sigma_{\rm int}$ from these two MS cases differ from each other at only 0.22σ, 0.56σ, and 0.37σ, respectively, and the constraints of the cosmological parameters are also within 1σ range, the prior range of $b \in [0, 10]$ is an acceptable choice.

[7] It is unclear if this is more than just a coincidence, as the plateau phases in the two cases are dominated by GW emission (GL) and MD radiation (MS), respectively.

and $\sigma_{\rm int}$, and higher values of k. When we jointly analyze ML + GL and ML + MS, the constraints on the Dainotti parameters follow the same pattern as that of MS + GL against GL.

The constraints on the cosmological parameters are very loose for all of these cases. In the flat ΛCDM model, the highest 2σ lower limit of Ω_{m0} among these cases is $\Omega_{m0} > 0.294$ of the ML + GL data. In the non-flat ΛCDM model, the highest 2σ lower limit of Ω_{m0} is $\Omega_{m0} > 0.391$ of the MS + GL case, which is inconsistent with that of the $H(z)$ + BAO case. The MS data favor open hypersufaces while all other cases favor closed hypersufaces, with the favored spatial geometries for GL, ML + GL, and MS + GL data being more than 1σ (or even 2σ) away from flat geometry. In the flat XCDM parametrization, the highest 2σ lower limit of Ω_{m0} is $\Omega_{m0} > 0.192$ for the MS + GL data, and the constraints on the X-fluid equation of state parameter $w_{\rm X}$ are very loose, with the highest 1σ upper limit being 0.111 for the ML case. In the non-flat XCDM parametrization, the highest 2σ lower limit of Ω_{m0} is $\Omega_{m0} > 0.268$ for the MS + GL data, and the constraints on $w_{\rm X}$ are very loose, with the highest 1σ upper limit being 0.238 for the MS + GL data. The favored spatial geometries for these cases follow the same pattern as that for non-flat ΛCDM, but with larger upper limits of Ω_{k0} except for the MS data. In the flat ϕCDM model, the highest 2σ lower limit of Ω_{m0} is $\Omega_{m0} > 0.235$ for the ML + GL data. In the non-flat ϕCDM model, the highest 2σ lower limit of Ω_{m0} is $\Omega_{m0} > 0.340$ for the ML + GL case, which is inconsistent with that of the $H(z)$ + BAO data. Except for the MS case, closed spatial hypersurfaces are favored, but only in the ML + GL case is flat geometry slightly more than 1σ away. There are no constraints on α from these GRB data.

In the ΛCDM and XCDM cases, all GRB data combinations more favor currently accelerating cosmological expansion. They however more favor currently decelerating cosmological expansion in the ϕCDM models, in the $\Omega_{m0} - \alpha$ and $\Omega_{m0} - \Omega_{k0}$ parameter subspaces.

From the AIC and BIC values we compute ΔAIC and ΔBIC values with respect to the flat ΛCDM model. These are listed in the last two columns of Table 7.4. In the ML case, flat ΛCDM is the most favored model but there is only weak or positive evidence against any other model. In the MS case non-flat ΛCDM model is the most favored model and,

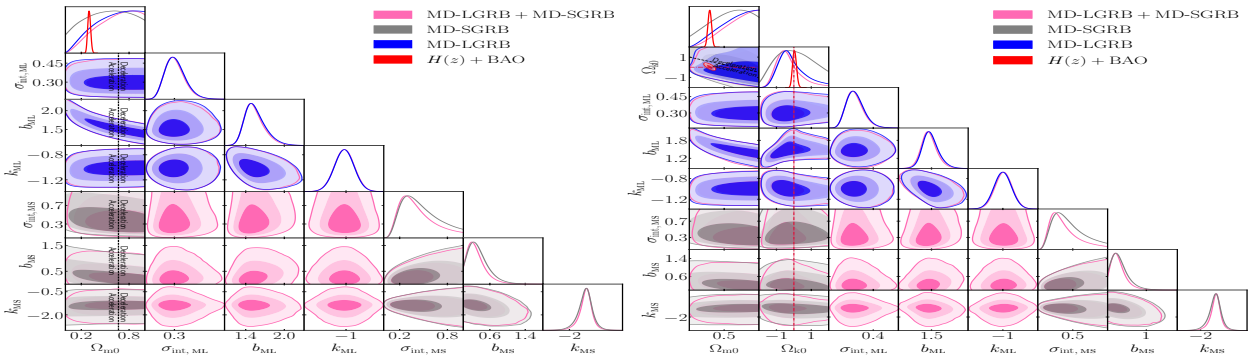

(a) Flat ΛCDM

(b) Non-flat ΛCDM

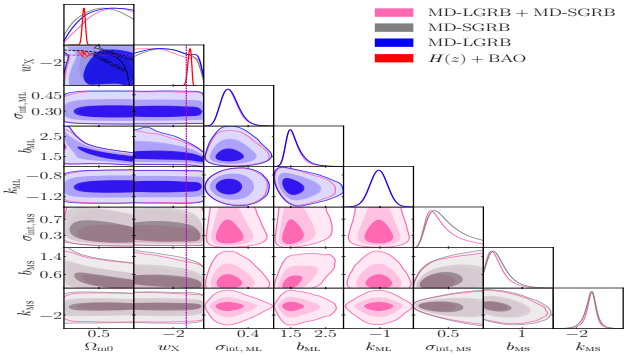

(c) Flat XCDM

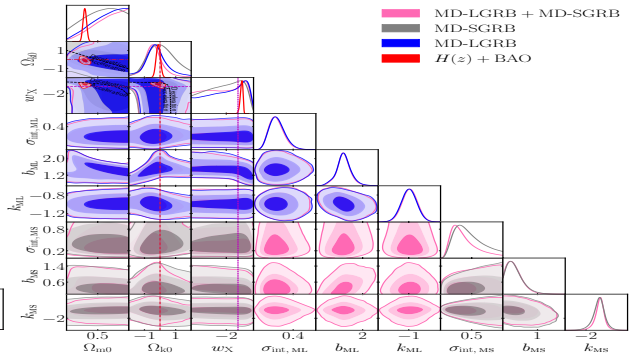

(d) Non-flat XCDM

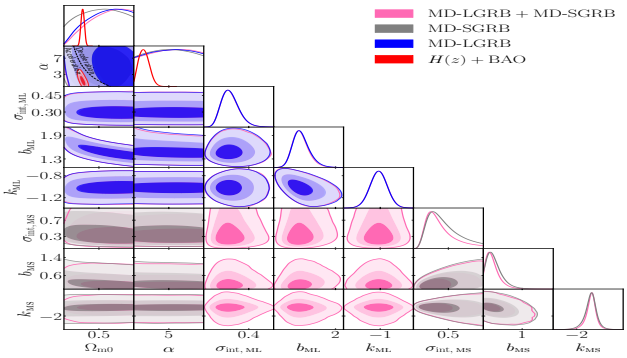

(e) Flat ϕCDM

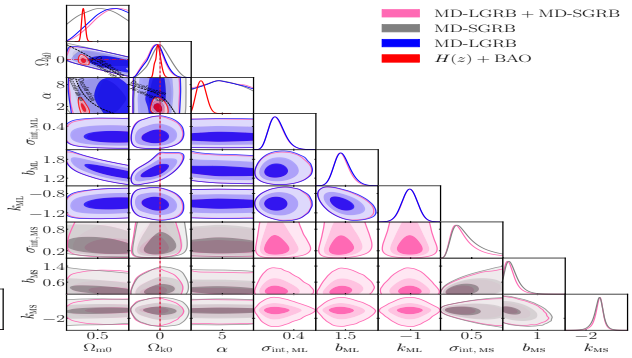

(f) Non-flat ϕCDM

Figure 7.2: One-dimensional likelihoods and 1σ, 2σ, and 3σ two-dimensional likelihood confidence contours from MD-LGRB (blue), MD-SGRB (gray), MD-LGRB + MD-SGRB (pink), and $H(z)$ + BAO (red) data for all six models. The zero-acceleration lines are shown as black dashed lines, which divide the parameter space into regions associated with currently-accelerating and currently-decelerating cosmological expansion. In the non-flat XCDM and non-flat ϕCDM cases, the zero-acceleration lines are computed for the third cosmological parameter set to the $H(z)$ + BAO data best-fitting values listed in Table 7.4. The crimson dash-dot lines represent flat hypersurfaces, with closed spatial hypersurfaces either below or to the left. The magenta lines represent $w_{\rm X} = -1$, i.e. flat or non-flat ΛCDM models. The $\alpha = 0$ axes correspond to flat and non-flat ΛCDM models in panels (e) and (f), respectively.

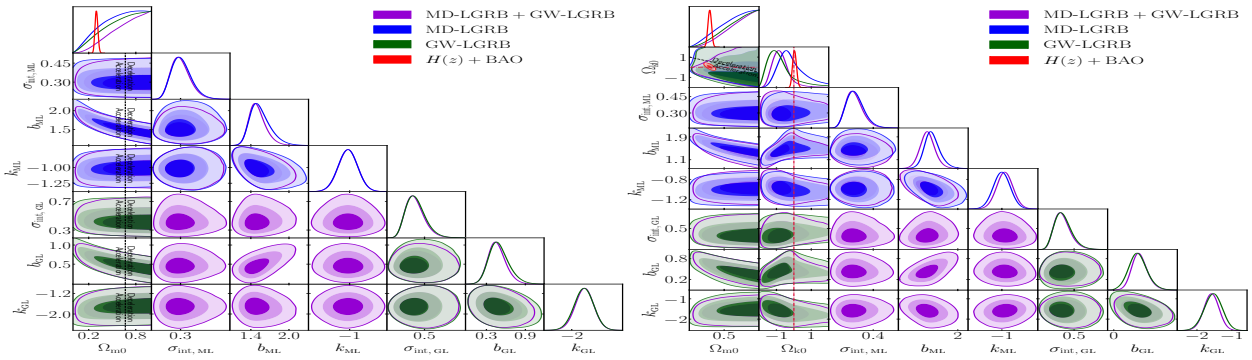

(a) Flat ΛCDM

(b) Non-flat ΛCDM

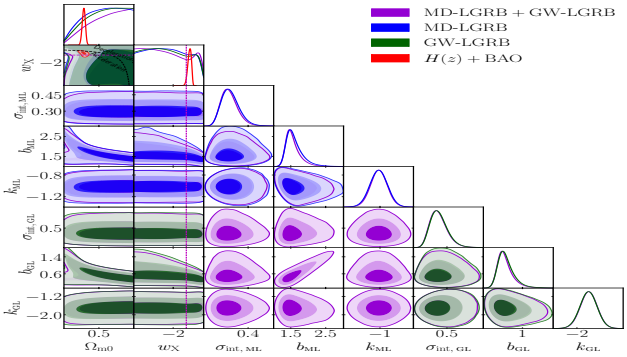

(c) Flat XCDM

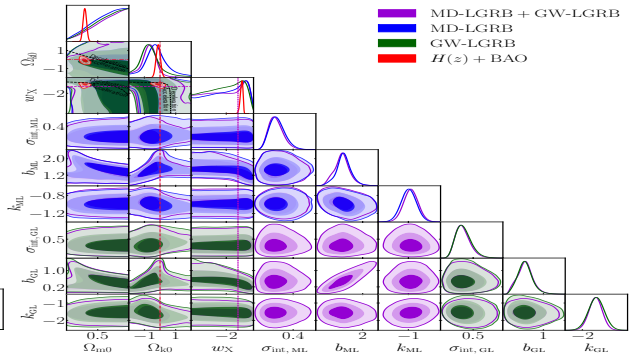

(d) Non-flat XCDM

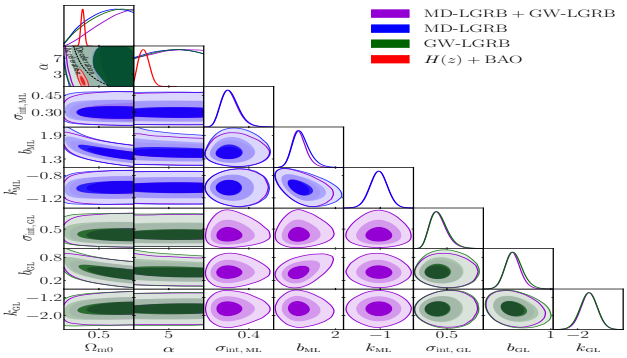

(e) Flat ϕCDM

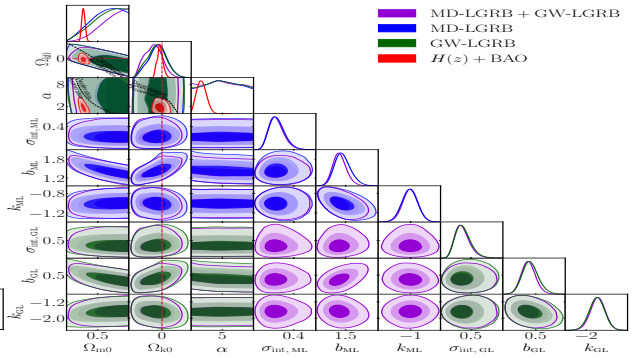

(f) Non-flat ϕCDM

Figure 7.3: One-dimensional likelihoods and 1σ, 2σ, and 3σ two-dimensional likelihood confidence contours from MD-LGRB (blue), GW-LGRB (green), MD-LGRB + GW-LGRB (violet), and $H(z)$ + BAO (red) data for all six models. The zero-acceleration lines are shown as black dashed lines, which divide the parameter space into regions associated with currently-accelerating and currently-decelerating cosmological expansion. In the non-flat XCDM and non-flat ϕCDM cases, the zero-acceleration lines are computed for the third cosmological parameter set to the $H(z)$ + BAO data best-fitting values listed in Table 7.4. The crimson dash-dot lines represent flat hypersurfaces, with closed spatial hypersurfaces either below or to the left. The magenta lines represent $w_{\rm X} = -1$, i.e. flat or non-flat ΛCDM models. The $\alpha = 0$ axes correspond to flat and non-flat ΛCDM models in panels (e) and (f), respectively.

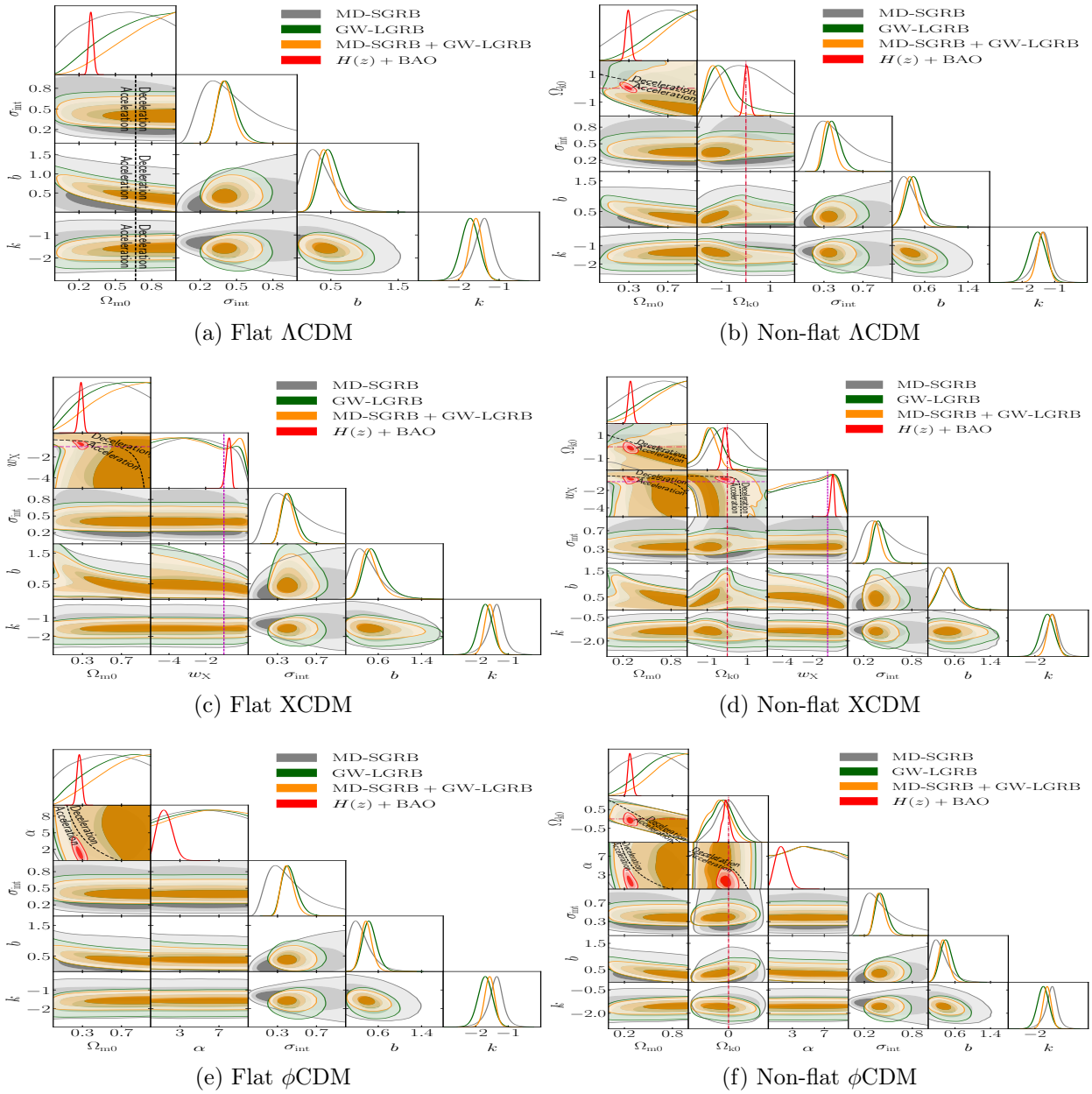

(a) Flat ΛCDM (b) Non-flat ΛCDM

(c) Flat XCDM (d) Non-flat XCDM

(e) Flat ϕCDM (f) Non-flat ϕCDM

Figure 7.4: One-dimensional likelihoods and 1σ, 2σ, and 3σ two-dimensional likelihood confidence contours from MD-SGRB (gray), GW-LGRB (green), MD-SGRB + GW-LGRB (orange), and $H(z)$ + BAO (red) data for all six models, without subscripts on $\sigma_{\rm int}$, k, and b. The zero-acceleration lines are shown as black dashed lines, which divide the parameter space into regions associated with currently-accelerating and currently-decelerating cosmological expansion. In the non-flat XCDM and non-flat ϕCDM cases, the zero-acceleration lines are computed for the third cosmological parameter set to the $H(z)$ + BAO data best-fitting values listed in Table 7.4. The crimson dash-dot lines represent flat hypersurfaces, with closed spatial hypersurfaces either below or to the left. The magenta lines represent $w_{\rm X} = -1$, i.e. flat or non-flat ΛCDM models. The $\alpha = 0$ axes correspond to flat and non-flat ΛCDM models in panels (e) and (f), respectively.

Table 7.6: MD-SGRB and GW-LGRB data $L_0 - t_b$ correlation parameters (and $\sigma_{\rm int}$) differences.

Model	$\Delta\sigma_{\rm int}$	Δk	Δb
Flat ΛCDM	0.48σ	0.31σ	0.80σ
Non-flat ΛCDM	0.50σ	0.31σ	0.01σ
Flat XCDM	0.49σ	0.79σ	0.22σ
Non-flat XCDM	0.55σ	0.26σ	0.07σ
Flat ϕCDM	0.37σ	0.92σ	0.59σ
Non-flat ϕCDM	0.36σ	0.87σ	0.36σ

except for non-flat XCDM (with positive evidence against it), the other models are very strongly disfavored. In the GL case, non-flat ΛCDM is again the most favored model, while the evidence against the others are mostly positive, except for non-flat ϕCDM (with strong BIC evidence against it). In the MS + GL case, similar to the MS case, non-flat ΛCDM is the most favored model and, except for non-flat XCDM (with weak AIC and positive BIC evidence against it), the others are strongly disfavored. In the ML + GL case, non-flat ΛCDM is the most favored model but, except for flat XCDM (with strong BIC evidence against it), the evidence against the other models is either weak or positive. In the ML + MS case, the best candidates are non-flat XCDM based on AIC and flat ΛCDM based on BIC, while the evidence against the other models is either weak or positive.

7.4.2 Constraints from A118, A115 (and jointly with ML), and A115′ (and jointly with GL) data

The A118 data set was previously studied by Khadka et al. (2021b). Here we analyze it along with the truncated A115 and A115′ data sets, which are also used in joint analyses with the ML and GL data sets. The constraints from these data sets on the GRB correlation parameters and on the cosmological model parameters are presented in Tables 7.7 and 7.8. The corresponding posterior 1D probability distributions and 2D confidence regions of these parameters are shown in Figs. 7.5 and 7.6, in gray (A118), red (A115 and A115′), green (ML and GL), and purple (ML + A115 and GL + A115′). Note that these analyses assume

Table 7.7: Unmarginalized best-fitting parameter values for all models from various combinations of data.[a]

Model	Data set	$\Omega_c h^2$	$\Omega_{\rm m0}$	$\Omega_{\rm k0}$	$w_{\rm X}$	α	$\sigma_{\rm int,\,ML}$	$b_{\rm ML}$	$k_{\rm ML}$	$\sigma_{\rm int}$	γ	β	$\sigma_{\rm int,\,GL}$	$b_{\rm GL}$	$k_{\rm GL}$	$-2\ln\mathscr{L}_{\rm max}$	AIC	BIC	ΔAIC	ΔBIC
	A118	0.4089	0.884	–	–	–	–	–	–	0.401	50.02	1.099	–	–	–	128.72	136.72	147.81	0.00	0.00
	ML	0.4645	0.998	–	–	–	0.275	1.383	−1.010	–	–	–	–	–	–	8.68	16.68	22.41	0.00	0.00
	A115	0.4172	0.901	–	–	–	–	–	–	0.405	50.01	1.099	–	–	–	127.97	135.97	146.95	0.00	0.00
Flat ΛCDM	ML + A115	0.4540	0.977	–	–	–	0.274	1.400	−1.019	0.407	50.00	1.097	–	–	–	136.70	150.70	171.59	0.00	0.00
	GL	0.4641	0.997	–	–	–	–	–	–	–	–	–	0.370	0.359	−1.675	22.94	30.94	35.65	0.00	0.00
	A115′	0.4629	0.995	–	–	–	–	–	–	0.403	50.01	1.091	–	–	–	126.34	134.34	145.32	0.00	0.00
	GL + A115′	0.4652	0.999	–	–	–	–	–	–	0.402	49.96	1.110	0.370	0.363	−1.666	149.34	163.34	183.88	0.00	0.00
	A118	0.4622	0.993	0.907	–	–	–	–	–	0.400	49.92	1.115	–	–	–	127.96	137.96	151.82	1.24	4.01
	ML	0.4410	0.950	−0.973	–	–	0.268	1.316	−0.967	–	–	–	–	–	–	7.48	17.48	24.65	0.80	2.24
	A115	0.4631	0.995	1.014	–	–	–	–	–	0.403	49.90	1.118	–	–	–	127.18	137.18	150.90	1.21	3.95
Non-flat ΛCDM	ML + A115	0.4637	0.996	0.062	–	–	0.283	1.383	−1.006	0.410	50.01	1.088	–	–	–	136.74	152.74	176.61	2.04	5.02
	GL	0.4640	0.997	−1.703	–	–	–	–	–	–	–	–	0.329	0.238	−1.377	17.00	27.00	32.89	−3.94	−2.76
	A115′	0.4647	0.998	0.729	–	–	–	–	–	0.404	49.94	1.110	–	–	–	125.93	135.93	149.65	1.59	4.33
	GL + A115′	0.4544	0.977	−0.244	–	–	–	–	–	0.402	50.00	1.100	0.362	0.364	−1.674	149.29	165.29	188.77	1.95	4.89
	A118	−0.0115	0.027	–	−0.098	–	–	–	–	0.399	50.04	1.102	–	–	–	128.43	138.43	152.29	1.71	4.48
	ML	0.0327	0.117	–	0.133	–	0.275	1.288	−0.997	–	–	–	–	–	–	8.14	18.14	25.31	1.46	2.90
	A115	−0.0197	0.010	–	−0.102	–	–	–	–	0.407	50.01	1.115	–	–	–	127.66	137.66	151.38	1.69	4.43
Flat XCDM	ML + A115	0.4065	0.880	–	−4.386	–	0.273	1.431	−1.008	0.403	50.05	1.093	–	–	–	136.70	152.70	176.57	2.00	4.98
	GL	0.0035	0.057	–	0.139	–	–	–	–	–	–	–	0.364	0.259	−1.651	21.97	31.97	37.86	1.03	2.21
	A115′	0.0119	0.074	–	−0.082	–	–	–	–	0.402	50.03	1.100	–	–	–	126.22	136.22	149.94	1.88	4.62
	GL + A115′	0.2817	0.625	–	0.122	–	–	–	–	0.401	49.98	1.084	0.376	0.330	−1.672	149.21	165.21	188.69	1.87	4.81
	A118	0.4603	0.989	0.841	−1.048	–	–	–	–	0.399	49.93	1.112	–	–	–	127.99	139.99	156.61	3.27	8.80
	ML	0.1525	0.361	−1.893	0.036	–	0.269	0.949	−0.976	–	–	–	–	–	–	7.39	19.39	27.99	2.71	5.58
	A115	0.4602	0.989	0.955	−1.097	–	–	–	–	0.404	49.91	1.115	–	–	–	127.18	139.18	155.65	3.21	8.70
Non-flat XCDM	ML + A115	0.3647	0.794	0.002	−4.000	–	0.269	1.478	−1.015	0.404	50.05	1.107	–	–	–	136.75	154.75	181.60	4.05	10.01
	GL	0.0378	0.127	−0.174	−4.518	–	–	–	–	–	–	–	0.327	1.237	−1.299	16.61	28.61	35.68	−2.33	0.03
	A115′	0.4643	0.997	0.783	−0.956	–	–	–	–	0.403	49.94	1.112	–	–	–	125.92	137.92	154.39	3.58	9.07
	GL + A115′	0.4349	0.938	−0.255	−0.043	–	–	–	–	0.410	50.03	1.063	0.358	0.296	−1.616	149.16	167.16	193.57	3.82	9.69
	A118	0.2301	0.520	–	–	9.936	–	–	–	0.402	50.02	1.109	–	–	–	128.56	138.56	152.41	1.84	4.60
	ML	0.4651	0.999	–	–	5.225	0.275	1.383	−1.011	–	–	–	–	–	–	8.68	18.68	25.85	2.00	3.44
	A115	0.2065	0.471	–	–	9.932	–	–	–	0.405	50.04	1.106	–	–	–	127.79	137.79	151.52	1.82	4.57
Flat ϕCDM	ML + A115	0.4563	0.981	–	–	2.762	0.273	1.391	−1.021	0.405	49.99	1.099	–	–	–	136.70	152.70	176.57	2.00	4.98
	GL	0.4641	0.997	–	–	4.299	–	–	–	–	–	–	0.372	0.360	−1.674	22.94	32.94	38.83	2.00	3.18
	A115′	0.3334	0.730	–	–	9.652	–	–	–	0.402	50.02	1.096	–	–	–	126.29	136.29	150.01	1.95	4.69
	GL + A115′	0.4484	0.965	–	–	8.745	–	–	–	0.403	50.05	1.077	0.372	0.348	−1.663	149.36	165.36	188.83	2.02	4.95
	A118	0.3245	0.712	0.245	–	8.862	–	–	–	0.400	50.01	1.116	–	–	–	128.42	140.42	157.04	3.70	9.23
	ML	0.4558	0.980	−0.980	–	0.423	0.266	1.296	−0.973	–	–	–	–	–	–	7.48	19.48	28.09	2.80	5.68
	A115	0.3217	0.706	0.290	–	3.150	–	–	–	0.406	50.05	1.108	–	–	–	127.64	139.64	156.11	3.67	9.16
Non-flat ϕCDM	ML + A115	0.3044	0.671	−0.076	–	8.893	0.274	1.406	−1.001	0.404	50.03	1.095	–	–	–	136.77	154.77	181.62	4.07	10.03
	GL	0.4644	0.998	−0.993	–	0.173	–	–	–	–	–	–	0.340	0.337	−1.547	20.15	32.15	39.22	1.21	3.57
	A115′	0.3787	0.823	0.161	–	7.940	–	–	–	0.404	50.02	1.105	–	–	–	126.21	138.21	154.68	3.87	9.36
	GL + A115′	0.4420	0.952	−0.266	–	8.343	–	–	–	0.400	50.00	1.077	0.372	0.310	−1.622	149.18	167.18	193.59	3.84	9.71

[a] In these GRB cases, Ω_b and H_0 are set to be 0.05 and 70 km s^{-1} Mpc^{-1}, respectively.

Table 7.8: One-dimensional marginalized posterior mean values and uncertainties ($\pm1\sigma$ error bars or 2σ limits) of the parameters for all models from various combinations of data.[a]

Model	Data set	$\Omega_{\rm m0}$	$\Omega_{\rm k0}$	$w_{\rm X}$	α	$\sigma_{\rm int,\,ML}$	$b_{\rm ML}$	$k_{\rm ML}$	$\sigma_{\rm int}$	γ	β	$\sigma_{\rm int,\,GL}$	$b_{\rm GL}$	$k_{\rm GL}$
	A118	> 0.247	–	–	–	–	–	–	$0.412^{+0.027}_{-0.033}$	50.09 ± 0.26	1.110 ± 0.090	–	–	–
	ML	> 0.188	–	–	–	$0.305^{+0.035}_{-0.053}$	$1.552^{+0.108}_{-0.189}$	-1.017 ± 0.090	–	–	–	–	–	–
	A115	$0.630^{+0.352}_{-0.135}$	–	–	–	–	–	–	$0.417^{+0.028}_{-0.035}$	50.09 ± 0.26	1.112 ± 0.093	–	–	–
Flat ΛCDM	ML + A115	> 0.298	–	–	–	$0.301^{+0.033}_{-0.051}$	$1.515^{+0.101}_{-0.151}$	-1.015 ± 0.088	$0.416^{+0.027}_{-0.034}$	50.07 ± 0.25	1.111 ± 0.089	–	–	–
	GL	> 0.202	–	–	–	–	–	–	–	–	–	$0.429^{+0.059}_{-0.094}$	$0.495^{+0.120}_{-0.173}$	-1.720 ± 0.219
	A115′	> 0.264	–	–	–	–	–	–	$0.414^{+0.028}_{-0.034}$	50.10 ± 0.26	1.107 ± 0.090	–	–	–
	GL + A115′	> 0.339	–	–	–	–	–	–	$0.413^{+0.027}_{-0.034}$	50.08 ± 0.25	1.104 ± 0.089	$0.423^{+0.056}_{-0.090}$	$0.458^{+0.112}_{-0.139}$	-1.705 ± 0.210
	A118	> 0.287	$0.694^{+0.626}_{-0.848}$	–	–	–	–	–	$0.412^{+0.027}_{-0.034}$	50.01 ± 0.26	1.121 ± 0.090	–	–	–
	ML	> 0.241	$-0.131^{+0.450}_{-0.919}$	–	–	$0.304^{+0.035}_{-0.053}$	$1.478^{+0.123}_{-0.166}$	-1.000 ± 0.096	–	–	–	–	–	–
	A115	> 0.275	$0.698^{+0.639}_{-0.857}$	–	–	–	–	–	$0.417^{+0.028}_{-0.034}$	50.00 ± 0.27	1.124 ± 0.092	–	–	–
Non-flat ΛCDM	ML + A115	> 0.346	$0.352^{+0.427}_{-0.830}$	–	–	$0.304^{+0.034}_{-0.052}$	$1.486^{+0.096}_{-0.136}$	-1.019 ± 0.091	$0.416^{+0.028}_{-0.034}$	50.03 ± 0.26	1.113 ± 0.091	–	–	–
	GL	> 0.290	$-0.762^{+0.271}_{-0.888}$	–	–	–	–	–	–	–	–	$0.402^{+0.057}_{-0.090}$	$0.407^{+0.136}_{-0.160}$	-1.536 ± 0.252
	A115′	> 0.299	$0.599^{+0.582}_{-0.887}$	–	–	–	–	–	$0.414^{+0.028}_{-0.034}$	50.02 ± 0.26	1.117 ± 0.090	–	–	–
	GL + A115′	> 0.381	$0.214^{+0.428}_{-0.855}$	–	–	–	–	–	$0.414^{+0.027}_{-0.034}$	50.05 ± 0.26	1.103 ± 0.090	$0.423^{+0.056}_{-0.090}$	$0.432^{+0.111}_{-0.132}$	-1.701 ± 0.212
	A118	$0.599^{+0.350}_{-0.175}$	–	$-2.440^{+1.779}_{-1.715}$	–	–	–	–	$0.412^{+0.028}_{-0.034}$	$50.15^{+0.26}_{-0.30}$	1.106 ± 0.089	–	–	–
	ML	> 0.123	–	$-2.456^{+2.567}_{-2.180}$	–	$0.306^{+0.036}_{-0.054}$	$1.611^{+0.113}_{-0.277}$	-1.014 ± 0.092	–	–	–	–	–	–
	A115	$0.589^{+0.357}_{-0.184}$	–	$-2.411^{+1.797}_{-1.729}$	–	–	–	–	$0.417^{+0.028}_{-0.035}$	$50.14^{+0.27}_{-0.31}$	1.109 ± 0.092	–	–	–
Flat XCDM	ML + A115	> 0.191	–	< -0.041	–	$0.300^{+0.033}_{-0.051}$	$1.562^{+0.103}_{-0.220}$	-1.012 ± 0.088	$0.417^{+0.028}_{-0.034}$	$50.13^{+0.27}_{-0.30}$	1.108 ± 0.090	–	–	–
	GL	> 0.141	–	< -0.046	–	–	–	–	–	–	–	$0.428^{+0.058}_{-0.092}$	$0.556^{+0.127}_{-0.256}$	-1.706 ± 0.215
	A115′	$0.605^{+0.394}_{-0.126}$	–	$-2.391^{+1.826}_{-1.758}$	–	–	–	–	$0.414^{+0.028}_{-0.034}$	$50.15^{+0.27}_{-0.30}$	1.103 ± 0.092	–	–	–
	GL + A115′	> 0.205	–	< -0.017	–	–	–	–	$0.413^{+0.027}_{-0.034}$	$50.14^{+0.26}_{-0.30}$	1.101 ± 0.088	$0.421^{+0.055}_{-0.090}$	$0.512^{+0.113}_{-0.210}$	-1.698 ± 0.208
	A118	> 0.246	$0.590^{+0.476}_{-0.796}$	$-2.358^{+2.032}_{-1.154}$	–	–	–	–	$0.412^{+0.027}_{-0.033}$	50.01 ± 0.28	1.121 ± 0.091	–	–	–
	ML	> 0.174	$-0.262^{+0.580}_{-0.724}$	$-2.000^{+2.117}_{-1.264}$	–	$0.305^{+0.036}_{-0.054}$	$1.462^{+0.194}_{-0.196}$	-0.996 ± 0.097	–	–	–	–	–	–
	A115	> 0.240	$0.563^{+0.498}_{-0.796}$	$-2.290^{+2.146}_{-1.032}$	–	–	–	–	$0.418^{+0.028}_{-0.034}$	50.01 ± 0.28	1.122 ± 0.093	–	–	–
Non-flat XCDM	ML + A115	> 0.231	$0.202^{+0.376}_{-0.635}$	$-2.155^{+2.224}_{-1.156}$	–	$0.302^{+0.033}_{-0.051}$	$1.489^{+0.122}_{-0.167}$	-1.016 ± 0.089	$0.417^{+0.027}_{-0.034}$	50.05 ± 0.28	1.109 ± 0.090	–	–	–
	GL	> 0.194	$-0.615^{+0.470}_{-0.685}$	$-2.212^{+2.186}_{-0.962}$	–	–	–	–	–	–	–	$0.403^{+0.058}_{-0.092}$	$0.480^{+0.177}_{-0.223}$	$-1.532^{+0.259}_{-0.260}$
	A115′	> 0.236	$0.451^{+0.469}_{-0.789}$	$-2.210^{+2.208}_{-0.946}$	–	–	–	–	$0.415^{+0.028}_{-0.034}$	50.03 ± 0.28	1.114 ± 0.091	–	–	–
	GL + A115′	> 0.226	$0.014^{+0.408}_{-0.604}$	$-2.080^{+2.201}_{-1.138}$	–	–	–	–	$0.415^{+0.027}_{-0.033}$	$50.09^{+0.27}_{-0.30}$	1.096 ± 0.090	$0.416^{+0.055}_{-0.088}$	$0.446^{+0.142}_{-0.183}$	-1.682 ± 0.208
	A118	$0.568^{+0.332}_{-0.230}$	–	–	–	–	–	–	$0.411^{+0.027}_{-0.033}$	50.05 ± 0.25	1.110 ± 0.089	–	–	–
	ML	> 0.148	–	–	–	$0.304^{+0.035}_{-0.053}$	$1.493^{+0.093}_{-0.143}$	-1.017 ± 0.089	–	–	–	–	–	–
	A115	$0.565^{+0.339}_{-0.228}$	–	–	–	–	–	–	$0.416^{+0.028}_{-0.034}$	50.04 ± 0.25	1.113 ± 0.091	–	–	–
Flat ϕCDM	ML + A115	> 0.198	–	–	–	$0.302^{+0.033}_{-0.051}$	$1.477^{+0.091}_{-0.126}$	-1.016 ± 0.088	$0.416^{+0.027}_{-0.034}$	50.03 ± 0.25	1.110 ± 0.089	–	–	–
	GL	> 0.148	–	–	–	–	–	–	–	–	–	$0.428^{+0.059}_{-0.094}$	$0.444^{+0.112}_{-0.141}$	-1.710 ± 0.218
	A115′	$0.586^{+0.391}_{-0.156}$	–	–	–	–	–	–	$0.414^{+0.028}_{-0.034}$	50.06 ± 0.25	1.106 ± 0.089	–	–	–
	GL + A115′	> 0.231	–	–	–	–	–	–	$0.413^{+0.027}_{-0.033}$	50.05 ± 0.24	1.102 ± 0.088	$0.423^{+0.055}_{-0.090}$	$0.426^{+0.105}_{-0.119}$	-1.703 ± 0.210
	A118	$0.560^{+0.256}_{-0.247}$	$-0.002^{+0.294}_{-0.286}$	–	$5.203^{+3.808}_{-2.497}$	–	–	–	$0.412^{+0.027}_{-0.033}$	50.05 ± 0.25	$1.111^{+0.089}_{-0.090}$	–	–	–
	ML	> 0.207	$-0.163^{+0.355}_{-0.317}$	–	–	$0.303^{+0.035}_{-0.053}$	$1.448^{+0.120}_{-0.165}$	-1.011 ± 0.091	–	–	–	–	–	–
	A115	$0.546^{+0.260}_{-0.253}$	$0.011^{+0.299}_{-0.291}$	–	–	–	–	–	$0.417^{+0.028}_{-0.034}$	50.04 ± 0.26	1.115 ± 0.092	–	–	–
Non-flat ϕCDM	ML + A115	$0.630^{+0.286}_{-0.181}$	$-0.108^{+0.296}_{-0.263}$	–	–	$0.301^{+0.033}_{-0.051}$	$1.453^{+0.115}_{-0.139}$	-1.013 ± 0.089	$0.416^{+0.027}_{-0.034}$	50.03 ± 0.25	1.106 ± 0.090	–	–	–
	GL	> 0.207	$-0.193^{+0.364}_{-0.347}$	–	–	–	–	–	–	–	–	$0.422^{+0.057}_{-0.092}$	$0.408^{+0.121}_{-0.149}$	$-1.693^{+0.215}_{-0.214}$
	A115′	$0.581^{+0.254}_{-0.247}$	$-0.033^{+0.296}_{-0.290}$	–	$5.215^{+3.853}_{-2.429}$	–	–	–	$0.414^{+0.028}_{-0.034}$	50.05 ± 0.25	1.106 ± 0.091	–	–	–
	GL + A115′	$0.666^{+0.327}_{-0.106}$	$-0.169^{+0.317}_{-0.270}$	–	–	–	–	–	$0.413^{+0.027}_{-0.034}$	50.04 ± 0.25	1.096 ± 0.089	$0.419^{+0.055}_{-0.089}$	$0.401^{+0.115}_{-0.128}$	-1.686 ± 0.209

[a] In these GRB cases, Ω_b and H_0 are set to be 0.05 and 70 km s^{-1} Mpc^{-1}, respectively.

$H_0 = 70$ km s^{-1} Mpc^{-1} and $\Omega_b = 0.05$.

The constraints from A115 data and from ML data, and from A115′ data and from GL data, are not mutually inconsistent, so it is not unreasonable to examine joint ML + A115 and GL + A115′ constraints. The ML data have the smallest intrinsic dispersion, $\sim 0.30 - 0.31$, with A115, A115′, and GL having larger intrinsic dispersion, $\sim 0.40 - 0.43$

The constraints on the Amati parameters are quite cosmological-model-independent for these GRB data sets. In the A118 case, the slope β ranges from a high of 1.121 ± 0.091 (non-flat XCDM) to a low of 1.106 ± 0.089 (flat XCDM), the intercept γ ranges from a high of $50.15^{+0.26}_{-0.30}$ (flat XCDM) to a low of 50.01 ± 0.26 (non-flat ΛCDM), and the intrinsic scatter $\sigma_{\rm int}$ ranges from a high of $0.412^{+0.028}_{-0.034}$ (flat XCDM) to a low of $0.411^{+0.027}_{-0.033}$ (flat ϕCDM), with central values of each pair being 0.12σ, 0.35σ, and 0.02σ away from each other, respectively.

In the A115 case, the slope β ranges from a high of 1.124 ± 0.092 (non-flat ΛCDM) to a low of 1.109 ± 0.092 (flat XCDM), the intercept γ ranges from a high of $50.14^{+0.27}_{-0.31}$ (flat XCDM) to a low of 50.00 ± 0.27 (non-flat ΛCDM), and the intrinsic scatter $\sigma_{\rm int}$ ranges from a high of $0.418^{+0.028}_{-0.034}$ (non-flat XCDM) to a low of $0.416^{+0.028}_{-0.034}$ (flat ϕCDM), with central values of each pair being 0.12σ, 0.34σ, and 0.05σ away from each other, respectively.

In the A115′ case, the slope β ranges from a high of 1.117 ± 0.090 (non-flat ΛCDM) to a low of 1.103 ± 0.092 (flat XCDM), the intercept γ ranges from a high of $50.15^{+0.27}_{-0.30}$ (flat XCDM) to a low of 50.02 ± 0.26 (non-flat ΛCDM), and the intrinsic scatter $\sigma_{\rm int}$ ranges from a high of $0.415^{+0.028}_{-0.034}$ (non-flat XCDM) to a low of $0.414^{+0.028}_{-0.034}$ (the others), with central values of each pair being 0.11σ, 0.33σ, and 0.02σ away from each other, respectively.

The lowest and highest values of β, γ, and $\sigma_{\rm int}$ from the A118, A115, and A115′ cases differ from each other at 0.16σ, 0.37σ, and 0.16σ, respectively. This implies that excluding three GRBs from A118 does not significantly affect the constraints on the Amati parameters.

In the joint analysis of ML and A115 (ML + A115) data, β ranges from a high of 1.113 ± 0.091 (non-flat ΛCDM) to a low of 1.106 ± 0.090 (non-flat ϕCDM), γ ranges from a high of $50.13^{+0.27}_{-0.30}$ (flat XCDM) to a low of 50.03 ± 0.25 (flat and non-flat ϕCDM), and $\sigma_{\rm int}$ ranges from a high of $0.417^{+0.028}_{-0.034}$ (flat XCDM) to a low of $0.416^{+0.027}_{-0.034}$ (flat ΛCDM, and flat and non-flat ϕCDM), with central values of each pair being 0.05σ, 0.26σ, and 0.02σ away

from each other, respectively; also k ranges from a high of -1.012 ± 0.088 (flat XCDM) to a low of -1.019 ± 0.091 (non-flat ΛCDM), b ranges from a high of $1.562^{+0.103}_{-0.220}$ (flat XCDM) to a low of $1.453^{+0.115}_{-0.139}$ (non-flat ϕCDM), and $\sigma_{\mathrm{int,\,ML}}$ ranges from a high of $0.304^{+0.034}_{-0.052}$ (non-flat ΛCDM) to a low of $0.300^{+0.033}_{-0.051}$ (flat XCDM), with central values of each pair being 0.06σ, 0.44σ, and 0.06σ away from each other, respectively. The lowest and highest values of β, γ, and σ_{int} from the A115 and ML + A115 cases differ from each other at 0.14σ, 0.32σ, and 0.05σ, respectively; also those of k, b, and $\sigma_{\mathrm{int,\,ML}}$ differ from each other at 0.17σ, 0.53σ, and 0.09σ, respectively.

In the joint analysis of GL and A115′ (GL + A115′) data, β ranges from a high of 1.104 ± 0.089 (flat ΛCDM) to a low of 1.096 ± 0.089 (non-flat ϕCDM), γ ranges from a high of $50.14^{+0.26}_{-0.30}$ (flat XCDM) to a low of 50.04 ± 0.25 (non-flat ϕCDM), and σ_{int} ranges from a high of $0.415^{+0.027}_{-0.033}$ (non-flat XCDM) to a low of $0.413^{+0.027}_{-0.034}$ (flat ΛCDM, flat XCDM, and non-flat ϕCDM), with central values of each pair being 0.06σ, 0.26σ, and 0.05σ away from each other, respectively; also k ranges from a high of -1.682 ± 0.208 (non-flat XCDM) to a low of -1.705 ± 0.210 (flat ΛCDM), b ranges from a high of $0.512^{+0.113}_{-0.210}$ (flat XCDM) to a low of $0.401^{+0.115}_{-0.128}$ (non-flat ϕCDM), and $\sigma_{\mathrm{int,\,GL}}$ ranges from a high of $0.423^{+0.056}_{-0.090}$ (flat and non-flat ΛCDM) to a low of $0.416^{+0.055}_{-0.088}$ (non-flat XCDM), with central values of each pair being 0.08σ, 0.46σ, and 0.07σ away from each other, respectively. The lowest and highest values of β, γ, and σ_{int} from the A115′ and GL + A115′ cases differ from each other at 0.17σ, 0.30σ, and 0.05σ, respectively; also those of k, b, and $\sigma_{\mathrm{int,\,GL}}$ differ from each other at 0.52σ, 0.47σ, and 0.20σ, respectively.

Judging from the constraints on the parameters of the Amati and Dainotti correlations, those from the joint analyses do not deviate much from the individual cases. We next focus on constraints on cosmological model parameters.

Similar to GRB data from Sec. 7.4.1, these data more favor currently accelerating cosmological expansion in the ΛCDM and XCDM cases, but also more favor currently decelerating cosmological expansion in the ϕCDM models, in the $\Omega_{m0} - \alpha$ and $\Omega_{m0} - \Omega_{k0}$ parameter subspaces.

In the flat ΛCDM model, the A118, A115, and A115′ 2σ constraints on Ω_{m0} are mutually

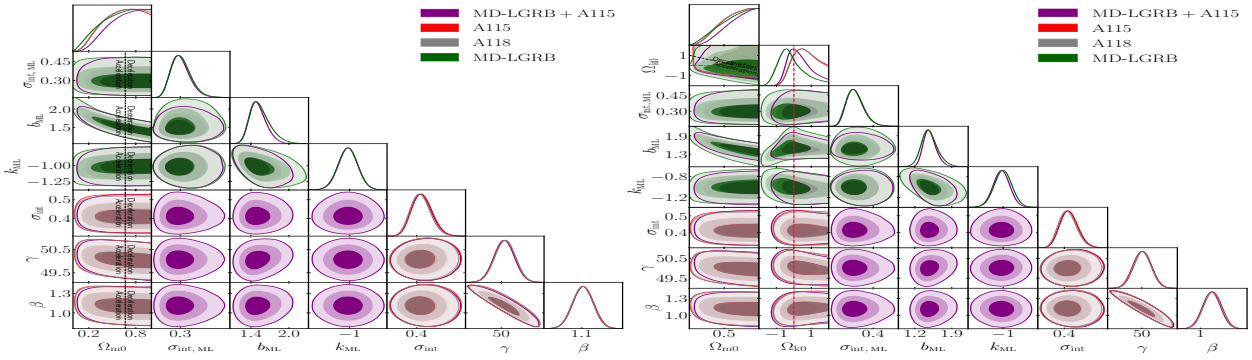

(a) Flat ΛCDM

(b) Non-flat ΛCDM

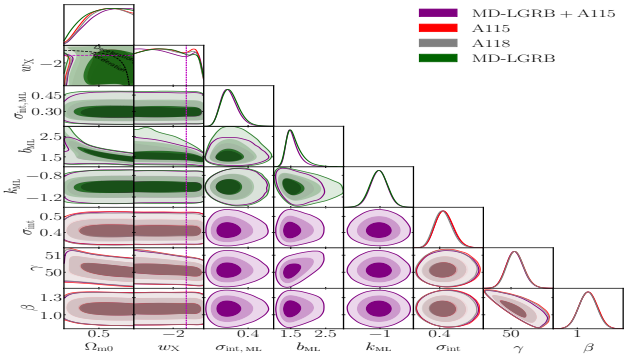

(c) Flat XCDM

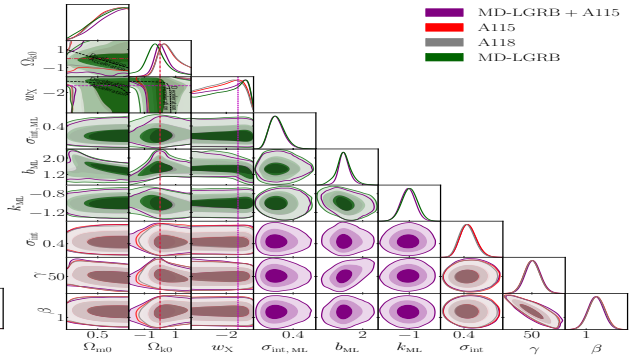

(d) Non-flat XCDM

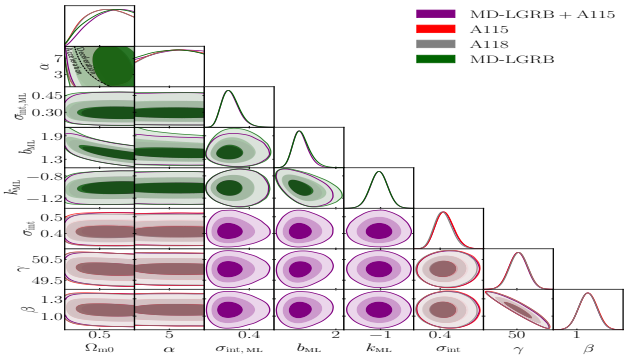

(e) Flat ϕCDM

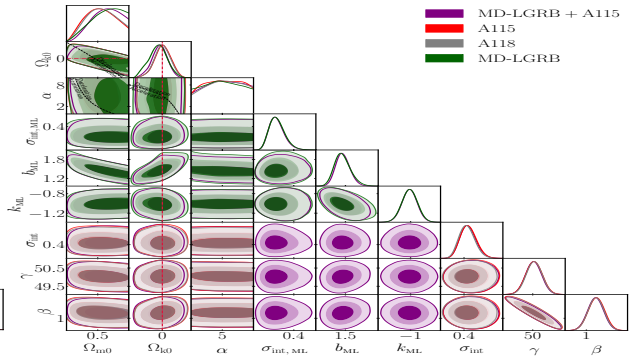

(f) Non-flat ϕCDM

Figure 7.5: One-dimensional likelihoods and 1σ, 2σ, and 3σ two-dimensional likelihood confidence contours from MD-LGRB (green), A118 (gray), A115 (red), and MD-LGRB + A115 (purple) data for all six models. The zero-acceleration lines are shown as black dashed lines, which divide the parameter space into regions associated with currently-accelerating and currently-decelerating cosmological expansion. In the non-flat XCDM and non-flat ϕCDM cases, the zero-acceleration lines are computed for the third cosmological parameter set to the $H(z)$ + BAO data best-fitting values listed in Table 7.7. The crimson dash-dot lines represent flat hypersurfaces, with closed spatial hypersurfaces either below or to the left. The magenta lines represent $w_{\rm X} = -1$, i.e. flat or non-flat ΛCDM models. The $\alpha = 0$ axes correspond to flat and non-flat ΛCDM models in panels (e) and (f), respectively.

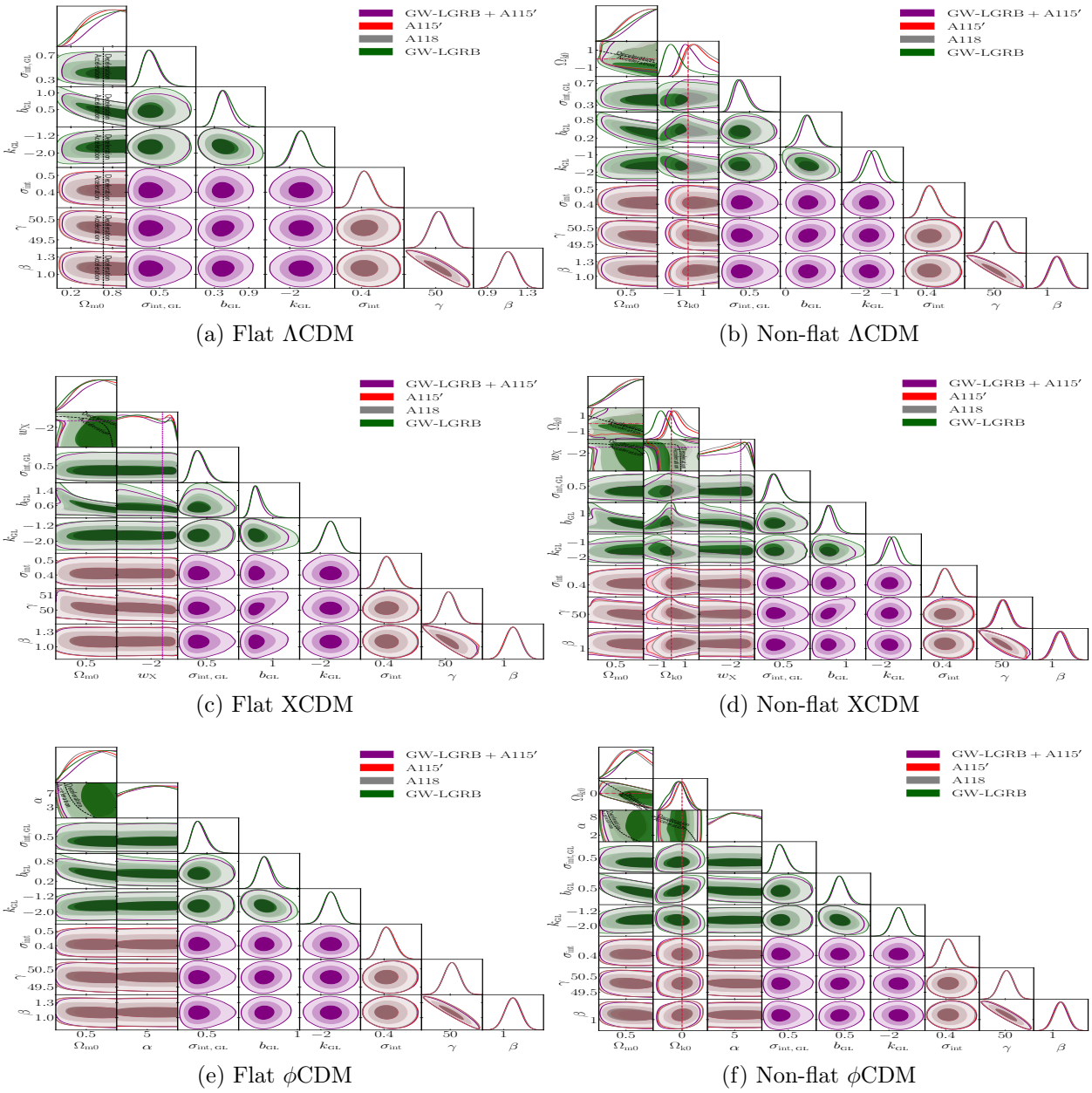

(a) Flat ΛCDM

(b) Non-flat ΛCDM

(c) Flat XCDM

(d) Non-flat XCDM

(e) Flat ϕCDM

(f) Non-flat ϕCDM

Figure 7.6: One-dimensional likelihoods and 1σ, 2σ, and 3σ two-dimensional likelihood confidence contours from GW-LGRB (green), A118 (gray), A115′ (red), and GW-LGRB + A115′ (purple) data for all six models. The zero-acceleration lines are shown as black dashed lines, which divide the parameter space into regions associated with currently-accelerating and currently-decelerating cosmological expansion. In the non-flat XCDM and non-flat ϕCDM cases, the zero-acceleration lines are computed for the third cosmological parameter set to the $H(z)$ + BAO data best-fitting values listed in Table 7.7. The crimson dash-dot lines represent flat hypersurfaces, with closed spatial hypersurfaces either below or to the left. The magenta lines represent $w_{\rm X} = -1$, i.e. flat or non-flat ΛCDM models. The $\alpha = 0$ axes correspond to flat and non-flat ΛCDM models in panels (e) and (f), respectively.

consistent (A115 with $\Omega_{m0} > 0.241$), but they favor higher values of Ω_{m0} than do ML and GL while the joint ML + A115 and GL + A115′ cases favor even higher values of > 0.298 and > 0.339, respectively. In fact, this is also true for the ML + GL case ($\Omega_{m0} > 0.294$).

In the non-flat ΛCDM model, the A118, A115, and A115′ 2σ constraints on Ω_{m0} are also mutually consistent, but they favor slightly higher values of Ω_{m0} than in the flat ΛCDM case, with $\Omega_{m0} > 0.299$ in the A115′ non-flat ΛCDM case. The joint ML + A115, GL + A115′, and ML + GL cases favor higher Ω_{m0} 2σ limits of > 0.346, > 0.381, and > 0.338, respectively. The A118, A115, ML + A115, A115′, and GL + A115′ data mildly favor open hypersurfaces in the non-flat ΛCDM model, being less than 1σ away from flatness.

In the flat and non-flat XCDM parametrizations, the 2σ constraints on Ω_{m0} are mutually consistent in all cases, where in the flat XCDM parametrization, the 2σ limits are $\Omega_{m0} > 0.181$ (A118), > 0.170 (A115), and > 0.185 (A115′). The constraints on $w_{\rm X}$ are very loose, and thus affected by the $w_{\rm X}$ prior, and consistent with each other in all cases, and mildly favor phantom dark energy (but Λ is less than 1σ away). In the non-flat XCDM parametrization, the A118, A115, ML + A115, A115′, and GL + A115′ data also mildly favor open hypersurfaces, with flatness being less than 1σ away.

In the flat ϕCDM model, the A118, A115, and A115′ constraints on Ω_{m0} are mutually consistent, with 2σ limits of $\Omega_{m0} > 0.149$ (A118), > 0.145 (A115), and > 0.159 (A115′), which are consistent with the other cases. These GRB data do not provide constraints on α in the flat ϕCDM model, while in the non-flat ϕCDM model, A118 and A115′ provide constraints of $\alpha = 5.203^{+3.808}_{-2.497}$ and $\alpha = 5.215^{+3.853}_{-2.429}$, respectively. Note that $\alpha = 0$ is still within 2σ for both cases. Similar trends hold for non-flat ϕCDM Ω_{m0} constraints, but ML + A115 and GL + A115′ data constraints posterior mean values are larger than for the individual data sets. The 2σ limits are $\Omega_{m0} > 0.183$ (A118), $\Omega_{m0} = 0.546^{+0.449}_{-0.384}$ (A115), $\Omega_{m0} > 0.198$ (A115′), > 0.251 (ML + A115), and > 0.286 (GL + A115′). Except for the A115 data, non-flat ϕCDM constraints favor closed hypersurfaces (unlike non-flat ΛCDM and non-flat XCDM), but with flatness well within 1σ for all cases.

The ΔAIC and ΔBIC values with respect to the flat ΛCDM model are listed in the last two columns of Table 7.7. In all cases (except for the GL case, which is discussed in Sec.

7.4.1 above), the flat ΛCDM model is the most favored model but the evidence against the other models are either weak or positive, except that, based on BIC, the evidence against non-flat XCDM and non-flat ϕCDM are strong. For ML + A115 data the non-flat ϕCDM model is very strongly disfavored with $\Delta BIC = 10.03$.

In summary, while the joint analyses do slightly tighten the constraints, the improvements relative to those from A118 data alone are not significant.

7.5 Conclusion

We have used six different cosmological models in analyses of the three (ML, MS, and GL) Dainotti ($L_0 - t_b$) correlation GRB data sets compiled by Wang et al. (2022) and Hu et al. (2021). We find for each data sets, as well as the MS + GL, ML + GL, and ML + MS combinations, that the GRB correlation parameters are independent of cosmological model. Our results thus indicate that these GRBs are standardizable through the Dainotti correlation and so can be used to constrain cosmological parameters, justifying the assumption made by Wang et al. (2022) and Hu et al. (2021). These results also mean that the circularity problem does not affect cosmological parameter constraints derived from these GRB data.

In contrast to Wang et al. (2022) and Hu et al. (2021) we do not use $H(z)$ data to calibrate these GRB data, instead we use these data to derive GRB only cosmological constraints. We find that ML, MS, GL, MS + GL, ML + GL, and ML + MS GRBs provide only weak restrictions on cosmological parameters.

We have also used the more-restrictive ML and GL Dainotti data sets in joint analyses with the largest available reliable compilation of Amati ($E_{\rm p} - E_{\rm iso}$) correlation A118 GRB data (Khadka et al., 2021b), but excluding three overlapping GRBs from the A118 data in the joint analyses. While the joint analyses do result in slightly tighter constraints, typically with larger lower limits on Ω_{m0} than those from the ML, GL, or A118 data alone, the improvements relative to the A118 data constraints are not significant.

Current GRB data provide quite weak constraints on cosmological parameters but do favor currently accelerated cosmological expansion in the ΛCDM models and the XCDM

parametrizations. We hope that in the near future there will be more and better-quality GRB measurements that will result in more restrictive GRB cosmological constraints. GRBs probe a very wide range of cosmological redshift space, a significant part of which is as yet unprobed, so it is worth putting effort into further developing GRB cosmological constraints.

Chapter 8

Standardizing Platinum Dainotti-correlated gamma-ray bursts, and using them with standardized Amati-correlated gamma-ray bursts to constrain cosmological model parameters

This chapter is based on Cao et al. (2022c).

8.1 Introduction

Currently accelerated cosmological expansion and other cosmological observations are reasonably well accommodated in the spatially-flat ΛCDM model (Peebles, 1984) with $\sim 70\%$ of the current cosmological energy budget being a time-independent cosmological constant (Λ), $\sim 25\%$ being non-relativistic cold dark matter (CDM), and most of the remaining $\sim 5\%$ being non-relativistic baryonic matter (see, e.g. eBOSS Collaboration, 2021; Farooq et al., 2017; Planck Collaboration, 2020; Scolnic et al., 2018). In this paper we also study cosmolog-

ical models with a little spatial curvature or dynamical dark energy, since the observations do not rule out such models, and since some sets of measurements seem mutually incompatible when analyzed in the spatially-flat ΛCDM model (see, e.g. Di Valentino et al., 2021b; Perivolaropoulos & Skara, 2022).

It is still unclear whether this incompatibility is evidence against the spatially-flat ΛCDM model or is caused by unidentified systematic errors in one of the established cosmological probes or by evolution of the parameters themselves with the redshift (Dainotti et al., 2021c, 2022a). Newer, alternate cosmological probes could help alleviate this issue. Recent examples of such probes include reverberation-mapped quasar (QSO) measurements that reach to redshift $z \sim 1.9$ (Czerny et al., 2021; Khadka et al., 2021a, 2022a; Yu et al., 2021; Zajaček et al., 2021), H II starburst galaxy measurements that reach to $z \sim 2.4$ (Cao et al., 2020, 2021a, 2022a; Chávez et al., 2014; González-Morán et al., 2019, 2021; Johnson et al., 2022; Mania & Ratra, 2012; Mehrabi et al., 2022), QSO angular size measurements that reach to $z \sim 2.7$ (Cao et al., 2017a, 2020, 2021a; Lian et al., 2021; Ryan et al., 2019; Zheng et al., 2021), QSO flux measurements that reach to $z \sim 7.5$ (Khadka & Ratra, 2020a,b, 2021, 2022; Li et al., 2021; Lian et al., 2021; Luongo et al., 2022; Lusso et al., 2020; Rezaei et al., 2022; Risaliti & Lusso, 2015, 2019; Yang et al., 2020; Zhao & Xia, 2021),[1] and the main subject of this paper, gamma-ray burst (GRB) measurements that reach to $z \sim 8.2$ (Amati et al., 2008, 2019; Cao et al., 2021a; Cardone et al., 2009, 2010; Dai et al., 2021; Dainotti et al., 2013a,b; Demianski et al., 2021; Fana Dirirsa et al., 2019; Hu et al., 2021; Khadka & Ratra, 2020c; Khadka et al., 2021b; Luongo & Muccino, 2021; Luongo et al., 2022; Postnikov et al., 2014; Samushia & Ratra, 2010; Wang et al., 2015, 2016, 2022). Some of these probes might eventually allow for a reliable extension of the Hubble diagram to $z \sim 3-4$, well beyond the reach of Type Ia supernovae. GRBs have been detected to $z \sim 9.4$ (Cucchiara et al., 2011), and might be detectable to $z = 20$ (Lamb & Reichart, 2000), so in principle GRBs could act as a cosmological probe to higher redshifts than 8.2.

Cao et al. (2022b) recently used the A118 two-parameter Amati-correlated GRB data set

[1]The most recent Lusso et al. (2020) QSO flux compilation assumes a UV–X-ray correlation model that is invalid above a significantly lower redshift, $z \sim 1.5-1.7$, so these QSOs can only be used to derive lower-z cosmological constraints (Khadka & Ratra, 2021, 2022).

(Khadka et al., 2021b) and the long GRB whose plateau phase is dominated by magnetic dipole radiation (MD-LGRB) and gravational wave emission (GW-LGRB), and short GRB whose plateau phase is dominated by magnetic dipole radiation (MD-SGRB) two-parameter Dainotti-correlated GRB data sets (Hu et al., 2021; Wang et al., 2022) to constrain cosmological parameters.[2] The circularity problem was circumvented by simultaneously constraining cosmological model parameters and GRB correlation parameters (see Dainotti et al., 2013b for a more extended discussion) and the cosmological-model-independence of the GRB correlation parameters shows that these GRBs are standardizable (Cao et al., 2022b; Khadka & Ratra, 2020c). Not only does the simultaneous fitting method circumvent the circularity problem, it also allows for the derivation of unbiased GRB-only constraints (unlike the constraints derived from GRBs that have been calibrated by using other data, that are correlated with the calibrating data), that can be straightforwardly used to compare with other constraints derived from other data, such as $H(z)$ + BAO data as we have done here. The A118, MD-LGRB, GW-LGRB, and MD-SGRB GRBs provide cosmological constraints that are mostly compatible with those determined using better-established cosmological probes (Cao et al., 2022b).

Here, we use the new Platinum compilation of 50 long GRBs, spanning $0.553 \leq z \leq 5.0$, that obey the three-parameter fundamental plane (Dainotti) correlation between the peak prompt luminosity, the luminosity at the end of the plateau emission and its rest frame duration (Dainotti et al., 2016, 2017, 2020) to constrain cosmological model parameters and GRB correlation parameters. The platinum sample is listed in Table 8.2. Note, however, that this table is incorrect. The correct table should be Table B.1 in Appendix B, where we reanalyzed the Platinum constraints in Cao et al. (2022d) and found that the differences are not significant. For this data set, measured quantities for a GRB are redshift z, characteristic time scale T_X^*, which marks the end of the plateau emission, the measured γ-ray energy flux F_X at T_X^* and the prompt peak flux $F_{\rm peak}$ over a 1 s interval, and X-ray spectral index

[2]The Amati correlation relates the rest-frame peak photon energy and the rest-frame isotropic radiated energy (Amati et al., 2008) and the two-dimensional Dainotti correlation relates the luminosity at the end of the plateau phase and the rest-frame end-time of plateau emission (Dainotti et al., 2008, 2010, 2011b, 2013a, 2015a, 2017). As discussed below, in this paper we use three-dimensional Dainotti and two-dimensional Amati correlation GRBs.

of the plateau phase β'. This sample spans the redshift range $0.553 \leq z \leq 5.0$. We find that the Platinum GRBs are standardizable through the Dainotti correlation and they also provides cosmological parameter constraints compatible with those from better-established cosmological probes, as well as with those derived from A118 GRB data. We also combine the Platinum data set with the 101 non-overlapping Amati-correlated GRBs (A101) from the A118 data set to perform a joint (Platinum + A101) analysis. We find that this joint GRB data set provides slightly more restrictive cosmological constraints (in which the twice-as-large A101 data set dominates the statistics and so plays a more dominant role) that are consistent with those from a combined analysis of baryon acoustic oscillation (BAO) and Hubble parameter $[H(z)]$ data. However, the cosmological constraints from Platinum, A118, A101, and Platinum + A101 data are less restrictive (precise) than those from $H(z)$ + BAO data because there are more parameters to be constrained in the GRB cases but not yet enough precise-enough data points to determine more precise GRB constraints. A joint analysis of the $H(z)$ + BAO + Platinum + A101 data results in slightly more restrictive cosmological constraints relative to those from just $H(z)$ + BAO data.

Our paper is organized as follows. We use the cosmological models described in Chapter 2 and outline the data sets adopted in Sec. 8.2. We then describe our analyses methods in Sec. 8.3 and discuss results in Sec. 8.4. We summarize our conclusions in Sec. 8.5.

8.2 Data

In this paper we analyze two different GRB data sets as well as combinations of them and the joint $H(z)$ + BAO data set. These data sets are summarized in Table 8.1 and described below.[3]

Platinum sample. This includes 50 long GRBs which exhibit a plateau phase with an angle $< 41°$, that do not have a flare during the plateau, and have a plateau with duration longer than 500 s. The first criterion is based on evidence that the plateau

[3]In this table and elsewhere, for compactness, we sometimes use Plat. as an abbreviation for the Platinum data set.

angles are Gaussianly distributed and those with angle $> 41^\circ$ are outliers; the second criterion allows one to eliminate cases contaminated by the presence of flaring activity; and, the third criterion allows one to eliminate cases where prompt emission may mask the plateau to the point that the definition of the plateau is uncertain (Willingale et al., 2007, 2010). As discussed below, the Platinum GRBs obey the three-dimensional Dainotti relation. The correct platinum sample is listed in Table B.1. For this data set, measured quantities for a GRB are redshift z, characteristic time scale T_X^*, which marks the end of the plateau emission, the measured γ-ray energy flux F_X at T_X^* and the prompt peak flux $F_{\rm peak}$ over a 1 s interval, and X-ray spectral index of the plateau phase β'. This sample spans the redshift range $0.553 \leq z \leq 5.0$.

A118 sample. This sample include 118 long GRBs, listed in Table 7 of Khadka et al. (2021b), that obey the two-dimensional Amati relation. For this data set, measured quantities for a GRB are z, rest-frame spectral peak energy $E_{\rm p}$, and measured bolometric fluence $S_{\rm bolo}$, computed in the standard rest-frame energy band $1 - 10^4$ keV. This sample spans the redshift range $0.3399 \leq z \leq 8.2$. Note that in our analyses here we did not use the correct value of $E_{\rm p} = 871 \pm 123$ keV for GRB081121, as discussed in Ref. Liu et al. (2022), although the effects on the parameter constraints are small.

A101 sample. The A118 data and the Platinum data have 17 common GRBs that are listed in the footnote of Table 8.1. We exclude these common GRBs from the A118 data set to form the A101 data set for joint analyses with the Platinum data set. This sample spans the redshift range $0.3399 \leq z \leq 8.2$.

Platinum + A101 sample. This combination GRB sample includes 151 GRBs. This sample spans the redshift range $0.3399 \leq z \leq 8.2$.

***H(z)* and BAO data**. There are 31 $H(z)$ and 11 BAO measurements that have a redshift range $0.07 \leq z \leq 1.965$ and $0.0106 \leq z \leq 2.33$, respectively. The $H(z)$ data are in Table 2 of Ryan et al. (2018) and the BAO data are in Table 1 of Cao et al. (2021b). We compare cosmological constraints from $H(z)$ + BAO data with those

Table 8.1: Summary of data sets used.

Data set	N (Number of points)	Redshift range
Platinum	50	$0.553 \leq z \leq 5.0$
A118	118	$0.3399 \leq z \leq 8.2$
A101[a]	101	$0.3399 \leq z \leq 8.2$
Plat. + A101	151	$0.3399 \leq z \leq 8.2$
$H(z)$	31	$0.070 \leq z \leq 1.965$
BAO	11	$0.38 \leq z \leq 2.334$

[a] Excluding from A118 those GRBs in common with Platinum [060418, 080721, 081008, 090418(A), 091020, 091029, 110213(A), 110818(A), 111008(A), 120811C, 120922(A), 121128(A), 131030A, 131105A, 140206A, 150314A, and 150403A].

obtained from the GRB data sets, and also jointly analyze GRB and $H(z)$ + BAO data.

8.3 Data Analysis Methodology

Luminosity distance, D_L, as a function of z and cosmological parameters $\boldsymbol{p}$, is given by

$$D_L(z,\boldsymbol{p}) = \begin{cases} \frac{c(1+z)}{H_0\sqrt{\Omega_{\rm k0}}} \sinh\left[\frac{\sqrt{\Omega_{\rm k0}}H_0}{c} D_C(z,\boldsymbol{p})\right] & \text{if } \Omega_{\rm k0} > 0, \\ (1+z) D_C(z,\boldsymbol{p}) & \text{if } \Omega_{\rm k0} = 0, \\ \frac{c(1+z)}{H_0\sqrt{|\Omega_{\rm k0}|}} \sin\left[\frac{H_0\sqrt{|\Omega_{\rm k0}|}}{c} D_C(z,\boldsymbol{p})\right] & \text{if } \Omega_{\rm k0} < 0, \end{cases} \tag{8.1}$$

where the comoving distance is in equation (1.101), and $H(z,\boldsymbol{p})$ is the Hubble parameter that is described in Chapter 2 for each cosmological model.

For Platinum GRBs the X-ray source rest-frame luminosity L_X, time T_X^* at the end of the plateau emission, and the peak prompt luminosity $L_{\rm peak}$ are correlated through the three-parameter fundamental plane relation (Dainotti et al., 2016, 2017, 2020, 2021a)

$$\log L_X = C_o + a \log T_X^* + b \log L_{\rm peak}, \tag{8.2}$$

Table 8.2: 50 Platinum GRB samples, which are incorrect. The correct ones are listed in Table B.1 of Appendix B.

GRB	z	$\log T_X^*$ (s)	$\log F_X$ (erg cm^{-2} s^{-1})	β'	$F_{\rm peak}$ (10^{-8} erg cm^{-2} s^{-1})
060418	1.49	$3.11887^{+0.05725}_{-0.05724}$	-9.79296 ± 0.04904	1.98	49.9 ± 1.63
060605	3.8	$4.04162^{+0.03738}_{-0.03737}$	$-11.2609^{+0.0531}_{-0.0532}$	1.835	4.73 ± 0.693
060708	1.92	$3.50569^{+0.06273}_{-0.06272}$	$-10.8688^{+0.0611}_{-0.0612}$	2.485	6.89 ± 0.796
060714	2.71	$3.73449^{+0.04676}_{-0.04677}$	-10.8586 ± 0.0352	1.87	9.13 ± 0.549
060814	0.84	$4.22387^{+0.03485}_{-0.03486}$	-10.9108 ± 0.0353	1.97	60.6 ± 1.48
060906	3.685	$4.33479^{+0.07214}_{-0.07215}$	$-11.8833^{+0.0885}_{-0.0884}$	2.06	12.2 ± 1.18
061121	1.314	3.78753 ± 0.01703	$-10.0299^{+0.0126}_{-0.0127}$	1.9485	196 ± 2.43
061222A	2.088	$3.92091^{+0.02444}_{-0.02443}$	-9.95369 ± 0.02311	1.86	73.3 ± 1.51
070110	2.352	$4.26825^{+0.05399}_{-0.05400}$	$-11.0488^{+0.0547}_{-0.0548}$	2.186	4.73 ± 0.648
070306	1.4959	4.86926 ± 0.02824	-11.2737 ± 0.0335	1.831	20.1 ± 0.899
070508	0.82	3.02525 ± 0.01189	$-9.16118^{+0.01080}_{-0.01079}$	1.764	224 ± 3.07
070521	0.553	3.55243 ± 0.04844	$-10.01250^{+0.04902}_{-0.04900}$	1.98	8.71 ± 1.2
070529	2.4996	$3.09323^{+0.06805}_{-0.06804}$	-10.2468 ± 0.0552	1.76	11.1 ± 1.84
080310	2.4266	$4.326080559^{+0.037986760}_{-0.037986759}$	$-11.39909559 \pm 0.04247343$	1.878	7.52 ± 0.893
080430	0.767	$4.217629106^{+0.038388523}_{-0.038388522}$	$-11.17223461^{+0.02818096}_{-0.02818097}$	4.18	18.2 ± 0.808
080721	2.6	$2.878762860^{+0.007554815}_{-0.007554816}$	$-8.713485538^{+0.007019298}_{-0.007019299}$	1.735	193 ± 10.3
081008	1.967	$3.855508334 \pm 0.056285684$	$-10.79325557 \pm 0.06052989$	1.84	10.5 ± 0.813
081221	2.26	$2.931957486 \pm 0.031176651$	$-9.354590372 \pm 0.024985500$	1.991	147 ± 2.46
090418A	1.608	$3.528136567^{+0.030759021}_{-0.030759020}$	$-10.04734554^{+0.02865941}_{-0.02865940}$	1.98	15.8 ± 1.66
091018	0.971	$2.896555345^{+0.034497877}_{-0.034497878}$	$-9.626765539^{+0.024288604}_{-0.024288603}$	1.91	59.1 ± 1.22
091020	1.71	$2.952650108 \pm 0.045271255$	$-9.712875280 \pm 0.034480687$	1.895	36.4 ± 1.71
091029	2.752	$4.303689975^{+0.034224003}_{-0.034224002}$	$-11.34682089 \pm 0.02563352$	2.064	10.9 ± 0.786
100219A	4.7	$4.721899099 \pm 0.103773463$	$-12.13530676^{+0.32639562}_{-0.32639563}$	1.46	3.15 ± 0.721
110213A	1.46	$3.84089^{+0.02576}_{-0.02127}$	$-9.89698^{+0.03865}_{-0.03311}$	2.1905	7.15 ± 1.88
110818A	3.36	$3.846274153 \pm 0.059648416$	$-11.28292779 \pm 0.05514905$	1.83	14.1 ± 1.5
111008A	5	$3.989933926 \pm 0.035676696$	$-10.66765993^{+0.02851108}_{-0.02851109}$	1.829	54.1 ± 3.91
120118B	2.943	$3.68307^{+0.15437}_{-0.10916}$	$-10.9560^{+0.1224}_{-0.1120}$	2.01	13.8 ± 1.32
120404A	2.88	$3.79948^{+0.09188}_{-0.04469}$	$-11.0269^{+0.0927}_{-0.1414}$	1.69	7.62 ± 0.109
120811C	2.67	$3.159095907^{+0.084200302}_{-0.084200301}$	$-10.14322956 \pm 0.05294686$	1.65	26 ± 1.1
120922A	3.1	$3.59799^{+0.21328}_{-0.05347}$	$-10.5957^{+0.1158}_{-0.2115}$	2.17	10.6 ± 0.757
121128A	2.2	$3.233929220^{+0.029795567}_{-0.029795568}$	$-9.618411717^{+0.028690024}_{-0.028690023}$	1.9455	104 ± 2.1
131030A	1.29	$2.84594^{+0.02758}_{-0.02757}$	$-9.29414^{+0.02517}_{-0.02518}$	1.693	265 ± 4.61
131105A	1.686	$3.94880^{+0.04788}_{-0.04789}$	$-10.9111^{+0.0333}_{-0.0334}$	1.94	26.8 ± 0.204
140206A	2.7	$3.59073^{+0.02132}_{-0.02133}$	$-9.72980^{+0.01300}_{-0.01299}$	1.672	169 ± 2.62
140419A	3.956	3.68383 ± 0.02442	$-10.00560^{+0.02397}_{-0.02400}$	1.678	41.8 ± 1.28
140506A	0.889	3.30686 ± 0.06882	-9.90438 ± 0.05516	1.9	86.7 ± 4.56
140509A	2.4	$3.58709^{+0.11327}_{-0.06416}$	$-11.0977^{+0.0897}_{-0.0782}$	1.86	11.8 ± 1.77
140629A	2.3	2.85608 ± 0.06161	$-9.84891^{+0.04278}_{-0.04279}$	1.815	35 ± 1.87
150314A	1.758	$2.49217^{+0.01586}_{-0.01585}$	$-8.60990^{+0.01503}_{-0.01502}$	1.73	381 ± 6.06
150403A	2.06	$3.19694^{+0.00698}_{-0.00697}$	$-8.82118^{+0.00510}_{-0.00511}$	1.679	171 ± 3.81
150910A	1.36	3.85419 ± 0.02868	$-9.97065^{+1.37578}_{-0.03215}$	1.6645	8.28 ± 2.18
151027A	0.81	3.99907 ± 0.01731	-9.93519 ± 0.02221	1.9235	58.2 ± 2.88
160121A	1.96	$3.82440^{+0.12038}_{-0.12039}$	-11.1726 ± 0.0694	2.02	7.79 ± 0.823
160227A	2.38	4.47751 ± 0.03885	$-10.9957^{+0.0305}_{-0.0306}$	1.679	4.88 ± 0.688
160327A	4.99	3.76407 ± 0.06033	-11.2238 ± 0.0673	1.78	12.5 ± 0.877
170202A	3.645	$3.77629^{+0.06866}_{-0.06865}$	$-10.6535^{+0.0449}_{-0.0448}$	2.04	39.2 ± 1.79
170705A	2.01	3.63746 ± 0.06603	$-10.1867^{+0.0406}_{-0.0405}$	1.66	113 ± 2.41
180329B	1.998	4.02296 ± 0.04314	$-11.1493^{+0.0483}_{-0.0482}$	1.77	9.09 ± 2.02
190106A	1.86	$4.19124^{+0.03109}_{-0.03110}$	$-10.4325^{+0.0285}_{-0.0286}$	2.9365	33.6 ± 1.3
190114A	3.37	$3.74534^{+0.04221}_{-0.04222}$	$-10.7527^{+0.0336}_{-0.0337}$	1.86	4.12 ± 0.953

Table 8.3: Flat priors of the constrained parameters.

Parameter	Prior
Cosmological Parameters	
H_0 [a]	[None, None]
$\Omega_b h^2$ [b]	[0, 1]
$\Omega_c h^2$ [c]	[0, 1]
Ω_{k0}	[-2, 2]
α	[0, 10]
$w_{\rm X}$	[-5, 0.33]
GRB Correlation Parameters	
a	[-5, 5]
b	[-5, 5]
C_o	[-50, 50]
$\sigma_{\rm int}$	[0, 5]
β	[0, 5]
γ	[0, 300]

[a] km s^{-1} Mpc^{-1}. In all four GRB-only analyses, H_0 is set to be 70 km s^{-1} Mpc^{-1}, while in other cases the prior range is irrelevant (unbounded).
[b] In all four GRB-only analyses, $\Omega_b h^2$ is set to be 0.0245, i.e. $\Omega_b = 0.05$.
[c] In all four GRB-only analyses, the Ω_c range is adjusted to ensure $\Omega_{m0} \in [0, 1]$.

where

$$L_X = \frac{4\pi D_L^2}{(1+z)^{1-\beta'}} F_X, \tag{8.3}$$

$$L_{\rm peak} = \frac{4\pi D_L^2}{(1+z)^{1-\beta'}} F_{\rm peak}, \tag{8.4}$$

C_o is the intercept parameter, and a and b are the slope parameters, with all three to be determined from data. F_X and $F_{\rm peak}$ are the measured γ-ray energy flux (erg cm^{-2} s^{-1}) at T_X^* and in the peak of the prompt emission over a 1 s interval, respectively, and β' is the X-ray spectral index of the plateau phase. Note, however, that these expressions are incorrect, where the corrected expressions are described in Chapter 9 from Cao et al. (2022d).

We compute L_X and $L_{\rm peak}$ as functions of cosmological parameters $\boldsymbol{p}$ at the redshift of each GRB by using eqs. (7.2), (8.3), and (8.4). We then compute the natural log of the likelihood function (D'Agostini, 2005)

$$\ln \mathscr{L}_{\rm GRB} = -\frac{1}{2}\left[\chi^2_{\rm GRB} + \sum_{i=1}^{N} \ln\left(2\pi\sigma^2_{{\rm tot},i}\right)\right], \tag{8.5}$$

where

$$\chi^2_{\rm GRB} = \sum_{i=1}^{N}\left[\frac{(\log L_{X,i} - C_o - a\log T^*_{X,i} - b\log L_{{\rm peak},i})^2}{\sigma^2_{{\rm tot},i}}\right], \tag{8.6}$$

with

$$\sigma^2_{{\rm tot},i} = \sigma^2_{{\rm int,\,P}} + \sigma^2_{\log L_{X,i}} + a^2\sigma^2_{\log T^*_{X,i}} + b^2\sigma^2_{\log L_{{\rm peak},i}}. \tag{8.7}$$

where $\sigma_{\rm int,\,P}$ is the Platinum GRB data intrinsic scatter parameter, that also contains the unknown systematic uncertainty, and N is the number of data points.

For GRBs which obey the Amati correlation, a detailed description of the procedure can be found in Sec. 4 of Cao et al. (2022b). Here we denote its intrinsic scatter parameter as $\sigma_{\rm int,\,A}$ as opposed to the Platinum one, $\sigma_{\rm int,\,P}$.

Detailed descriptions of the $H(z)$ + BAO data analysis procedure can be found in Sec. 4 of Cao et al. (2020) and Cao et al. (2021b).

The flat priors of the free parameters are listed in Table 8.3. The best-fitting values and

posterior distributions of all free parameters are obtained through maximizing the likelihood functions using the Markov chain Monte Carlo (MCMC) code MontePython (Brinckmann & Lesgourgues, 2019), with the physics coded in class. The convergence of the MCMC chains for each free parameter is guaranteed by the Gelman-Rubin criterion ($R-1<0.05$). The python package getdist (Lewis, 2019) is used to compute the posterior means and uncertainties and plot the marginalized likelihood distributions and contours.

We use the Akaike Information Criterion (AIC) and the Bayesian Information Criterion (BIC) to compare the goodness of fit of models with different numbers of parameters. Their definitions can be found in Cao et al. (2022b). We also compare the goodness of fit using the deviance information criterion (DIC) (Amati et al., 2019; Kunz et al., 2006) defined as

$$DIC = -2\ln\mathscr{L}_{\rm max} + 2n_{\rm eff}, \tag{8.8}$$

where $n_{\rm eff} = \langle -2\ln\mathscr{L}\rangle + 2\ln\mathscr{L}_{\rm max}$ is the number of effectively constrained parameters with brackets representing the average over the posterior distribution. We compute ΔAIC, ΔBIC, and ΔDIC differences of the other five cosmological models with respect to the flat ΛCDM reference model. Positive (negative) values of ΔAIC, ΔBIC, or ΔDIC indicate that the model under study fits the data worse (better) than does the reference model. Relative to the model with minimum $AIC(BIC/DIC)$, $\Delta AIC(BIC/DIC) \in (0,2]$ is said to be weak evidence against the candidate model, $\Delta AIC(BIC/DIC) \in (2,6]$ is positive evidence against the candidate model, while $\Delta AIC(BIC/DIC) \in (6,10]$ is strong evidence against the candidate model, with $\Delta AIC(BIC/DIC) > 10$ being very strong evidence against the candidate model.

Here we consider one massive and two massless neutrino species, with the effective number of relativistic neutrino species $N_{\rm eff} = 3.046$ and the total neutrino mass $\sum m_\nu = 0.06$ eV. The non-relativistic neutrino physical energy density parameter is $\Omega_\nu h^2 = \sum m_\nu/(93.14\ {\rm eV})$, where h is the reduced Hubble constant in units of 100 km s^{-1} Mpc^{-1}. With the baryonic ($\Omega_b h^2$) and cold dark matter ($\Omega_c h^2$) physical energy density parameters as free cosmological parameters to be constrained, the derived non-relativistic matter density parameter is

therefore $\Omega_{m0} = (\Omega_\nu h^2 + \Omega_b h^2 + \Omega_c h^2)/h^2$.

8.4 Results

We show the posterior one-dimensional (1D) probability distributions and two-dimensional (2D) confidence regions of cosmological-model and GRB-correlation parameters for the six cosmological models in Figs. 8.1–8.7, in gray (Platinum), green (A118 and A101), orange (Platinum + A101), red [$H(z)$ + BAO], and blue [$H(z)$ + BAO + Platinum, in short HzBP, and $H(z)$ + BAO + Platinum + A101, in short HzBPA101]. The unmarginalized best-fitting parameter values, as well as the values of maximum likelihood $\mathscr{L}_{\rm max}$, AIC, BIC, DIC, ΔAIC, ΔBIC, and ΔDIC, for all models and data combinations, are listed in Table 8.4. We list the marginalized posterior mean parameter values and uncertainties ($\pm 1\sigma$ error bars and 1 or 2σ limits), for all models and data combinations, in Table 8.5.

8.4.1 Constraints from Platinum, A118, A101, and Platinum + A101 data

As in Khadka et al. (2021b) and Cao et al. (2022b), in the four GRB-only cases here we set $H_0 = 70$ km s^{-1} Mpc^{-1} and $\Omega_b = 0.05$.

The constraints on the Platinum GRB correlation parameters in the six different cosmological models are mutually consistent, so the three-dimensional Dainotti correlation Platinum data set is standardizable. The constraints on the intrinsic scatter parameter $\sigma_{\rm int,\,P}$ are almost identical, ranging from $0.346^{+0.032}_{-0.044}$ (flat ϕCDM) to $0.347^{+0.034}_{-0.046}$ (non-flat ΛCDM). The constraints on the slope a range from a low of -0.727 ± 0.109 (non-flat ΛCDM and non-flat XCDM) to a high of -0.714 ± 0.104 (flat ΛCDM), the constraints on the slope b range from a low of $0.736^{+0.102}_{-0.087}$ (non-flat XCDM) to a high of 0.756 ± 0.083 (flat ΛCDM), and the constraints on the intercept C_o range from a low of 11.52 ± 4.45 (flat ΛCDM) to a high of $12.62^{+4.65}_{-5.51}$ (non-flat XCDM), with central values of each pair being 0.09σ, 0.15σ, and 0.16σ away from each other, respectively. We note that a compilation of (the two-parameter)

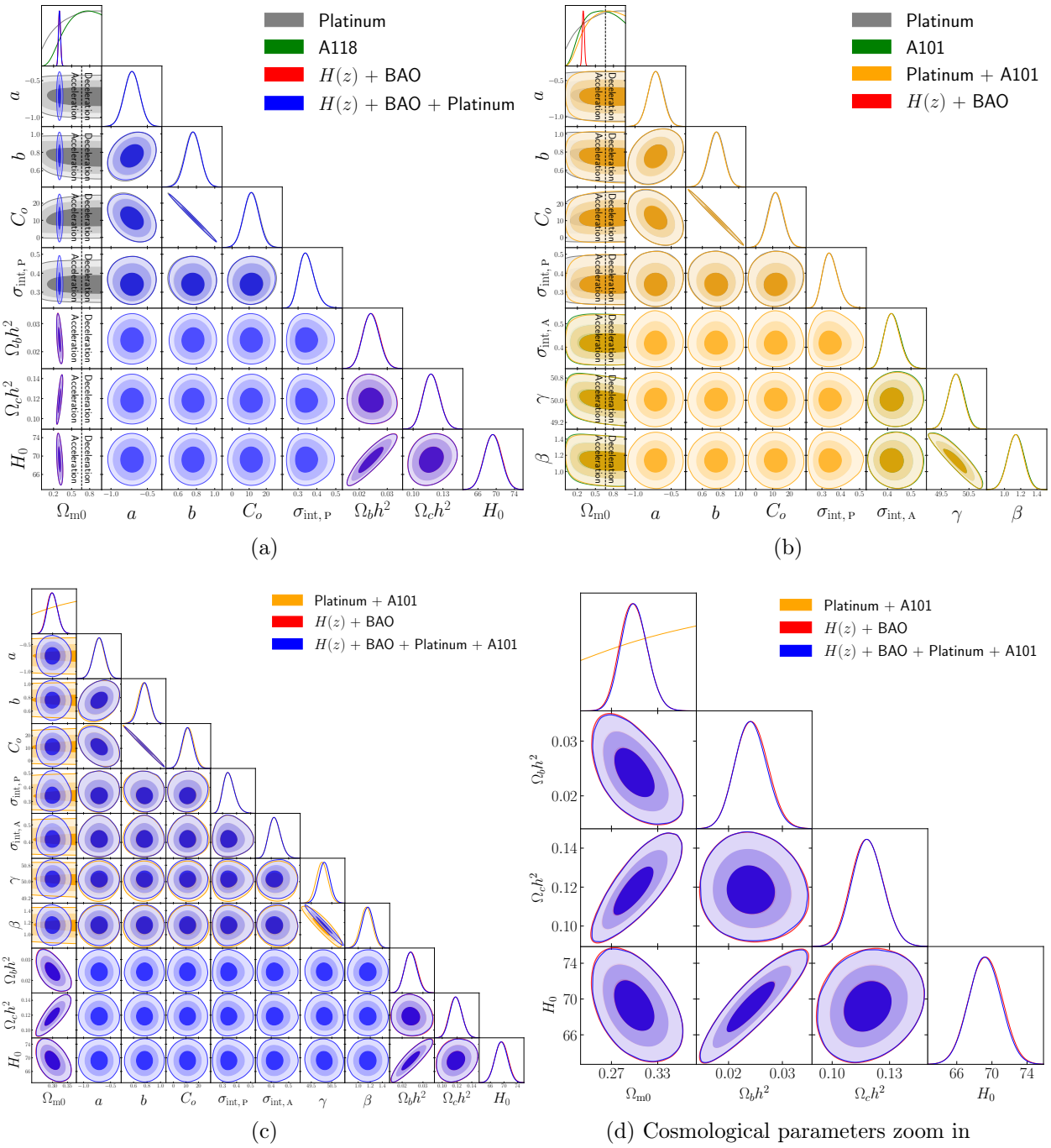

(a) (b) (c) (d) Cosmological parameters zoom in

Figure 8.1: One-dimensional likelihood distributions and 1σ, 2σ, and 3σ two-dimensional likelihood confidence contours for flat ΛCDM from various combinations of data. The zero-acceleration black dashed lines in panels (a) and (b) divide the parameter space into regions associated with currently-accelerating (left) and currently-decelerating (right) cosmological expansion.

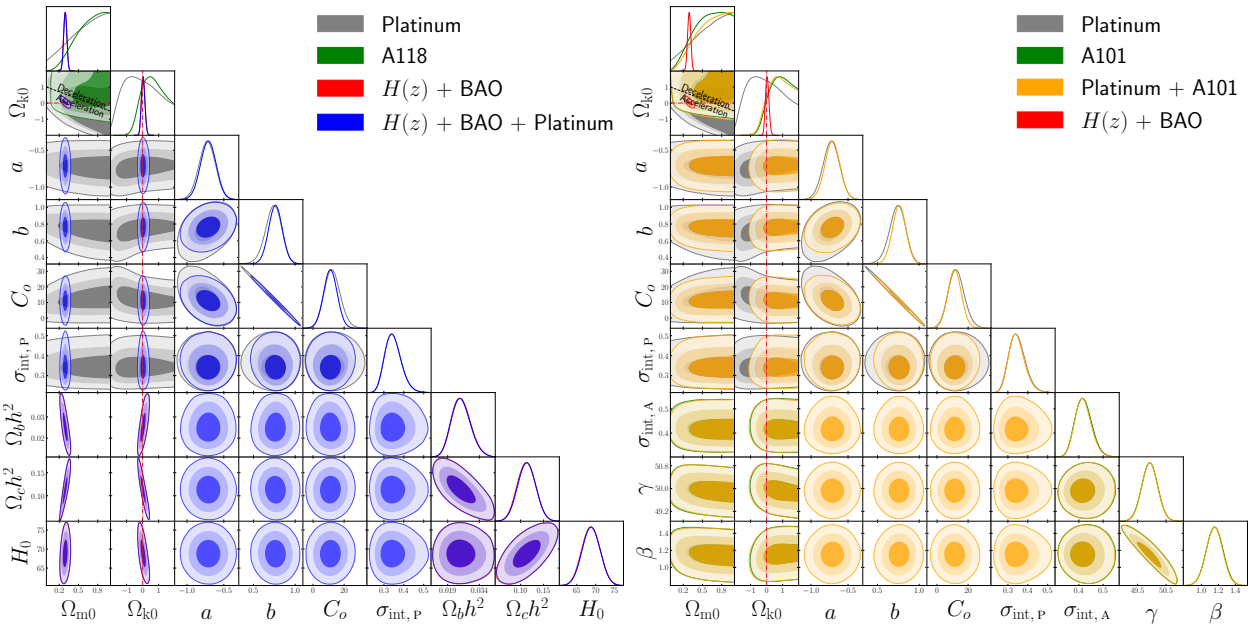

(a)

(b)

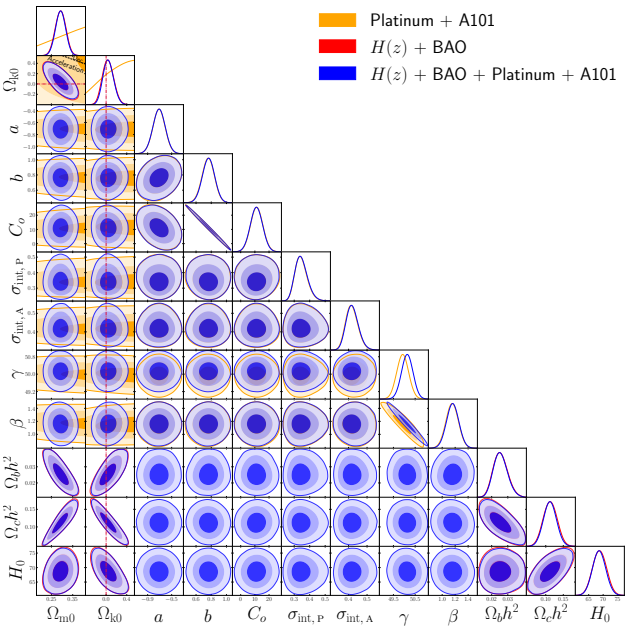

(c)

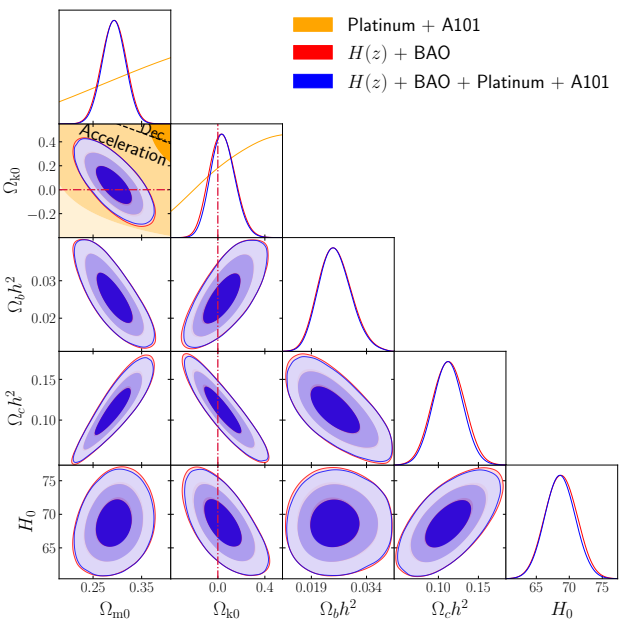

(d) Cosmological parameters zoom in

Figure 8.2: Same as Fig. 8.1 but for non-flat ΛCDM. The zero-acceleration black dashed lines divide the parameter space into regions associated with currently-accelerating (below left) and currently-decelerating (above right) cosmological expansion.

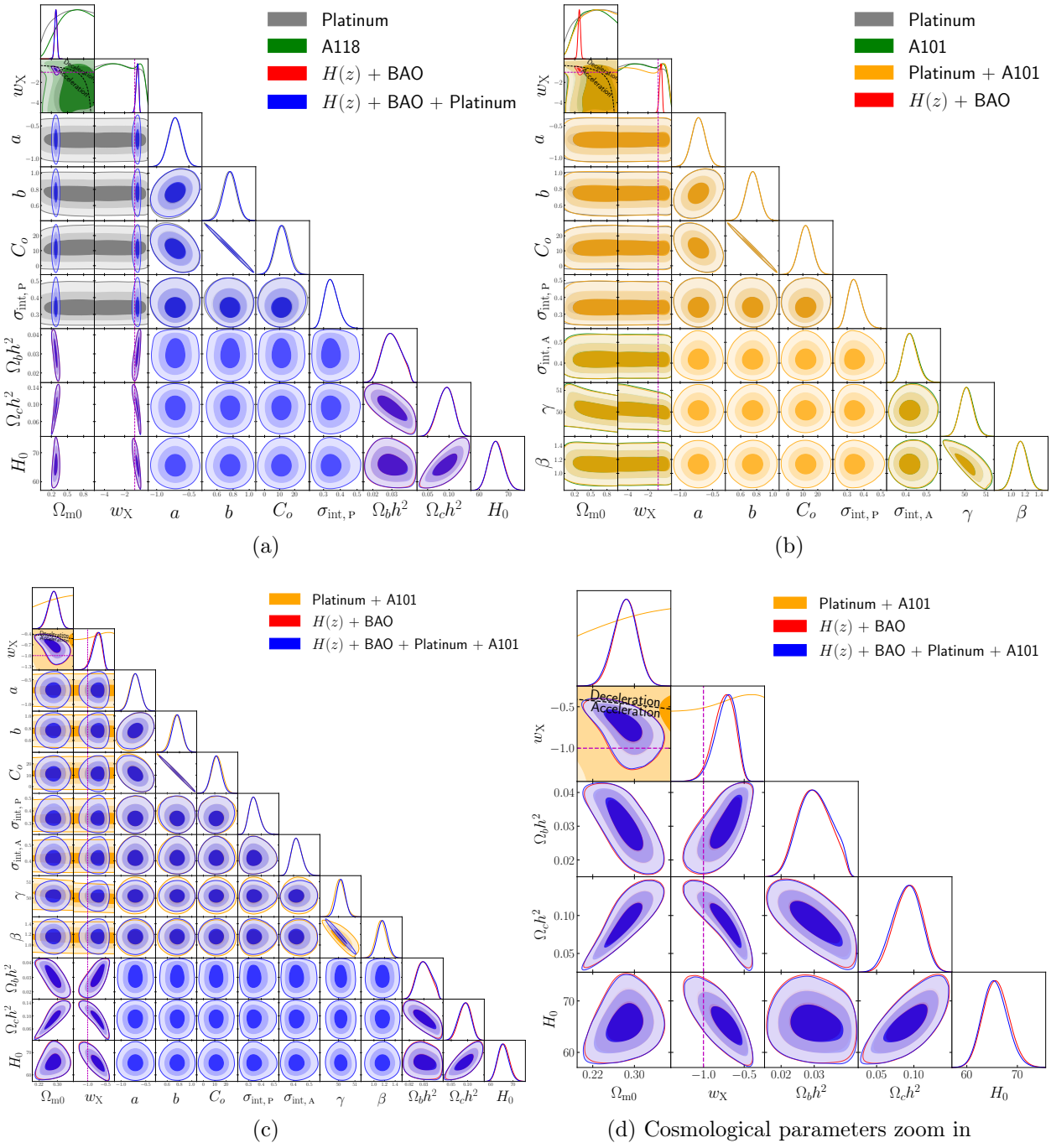

Figure 8.3: One-dimensional likelihood distributions and 1σ, 2σ, and 3σ two-dimensional likelihood confidence contours for flat XCDM from various combinations of data. The zero-acceleration black dashed lines divide the parameter space into regions associated with currently-accelerating (either below left or below) and currently-decelerating (either above right or above) cosmological expansion. The magenta dashed lines represent $w_{\rm X} = -1$, i.e. flat ΛCDM.

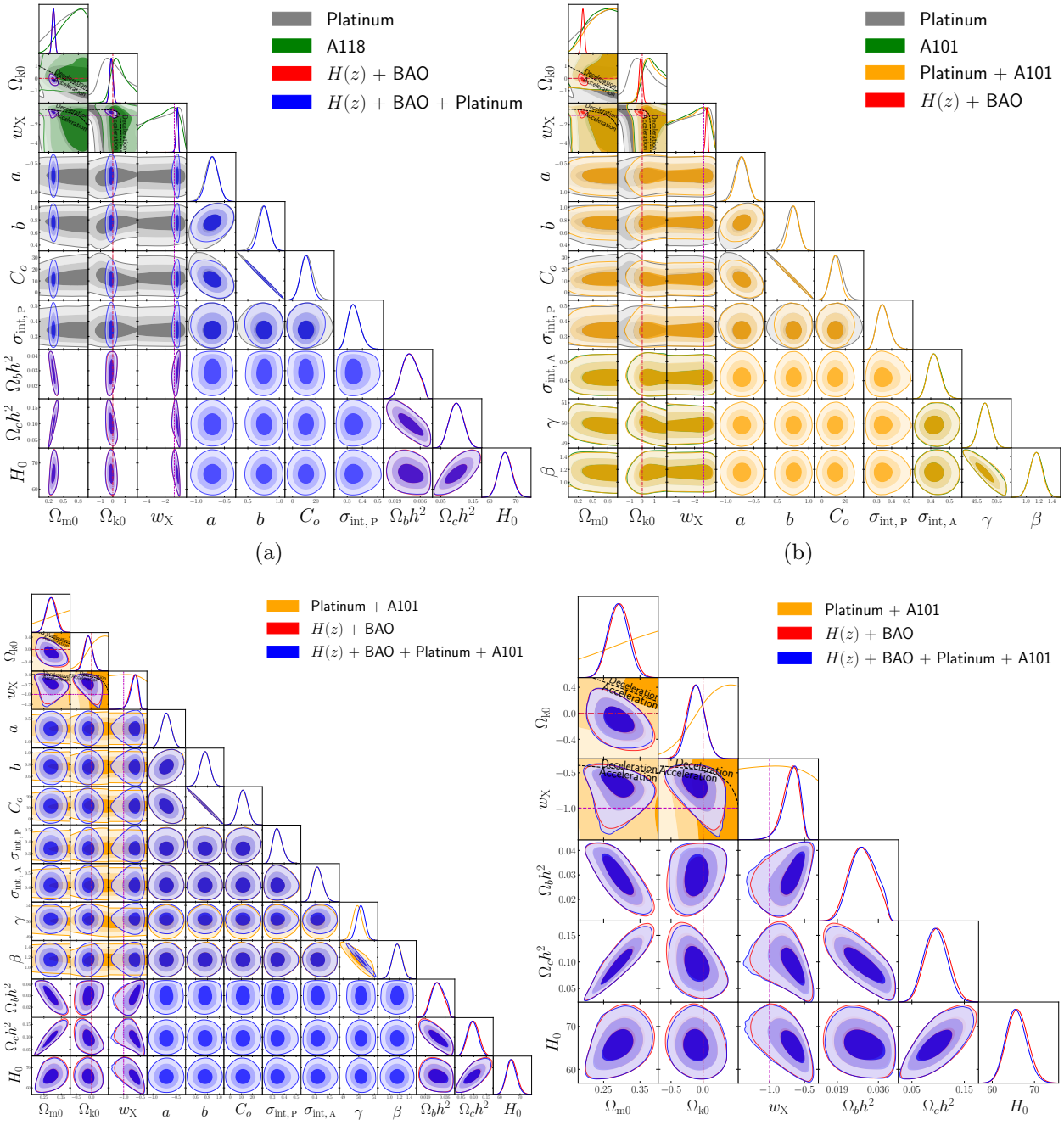

(a)

(b)

(c)

(d) Cosmological parameters zoom in

Figure 8.4: Same as Fig. 8.3 but for non-flat XCDM. The zero-acceleration black dashed lines are computed for the third cosmological parameter set to the $H(z)$ + BAO data best-fitting values listed in Table 8.4, and divide the parameter space into regions associated with currently-accelerating (either below left or below) and currently-decelerating (either above right or above) cosmological expansion. The crimson dash-dot lines represent flat hypersurfaces, with closed spatial hypersurfaces either below or to the left. The magenta dashed lines represent $w_X = -1$, i.e. non-flat ΛCDM.

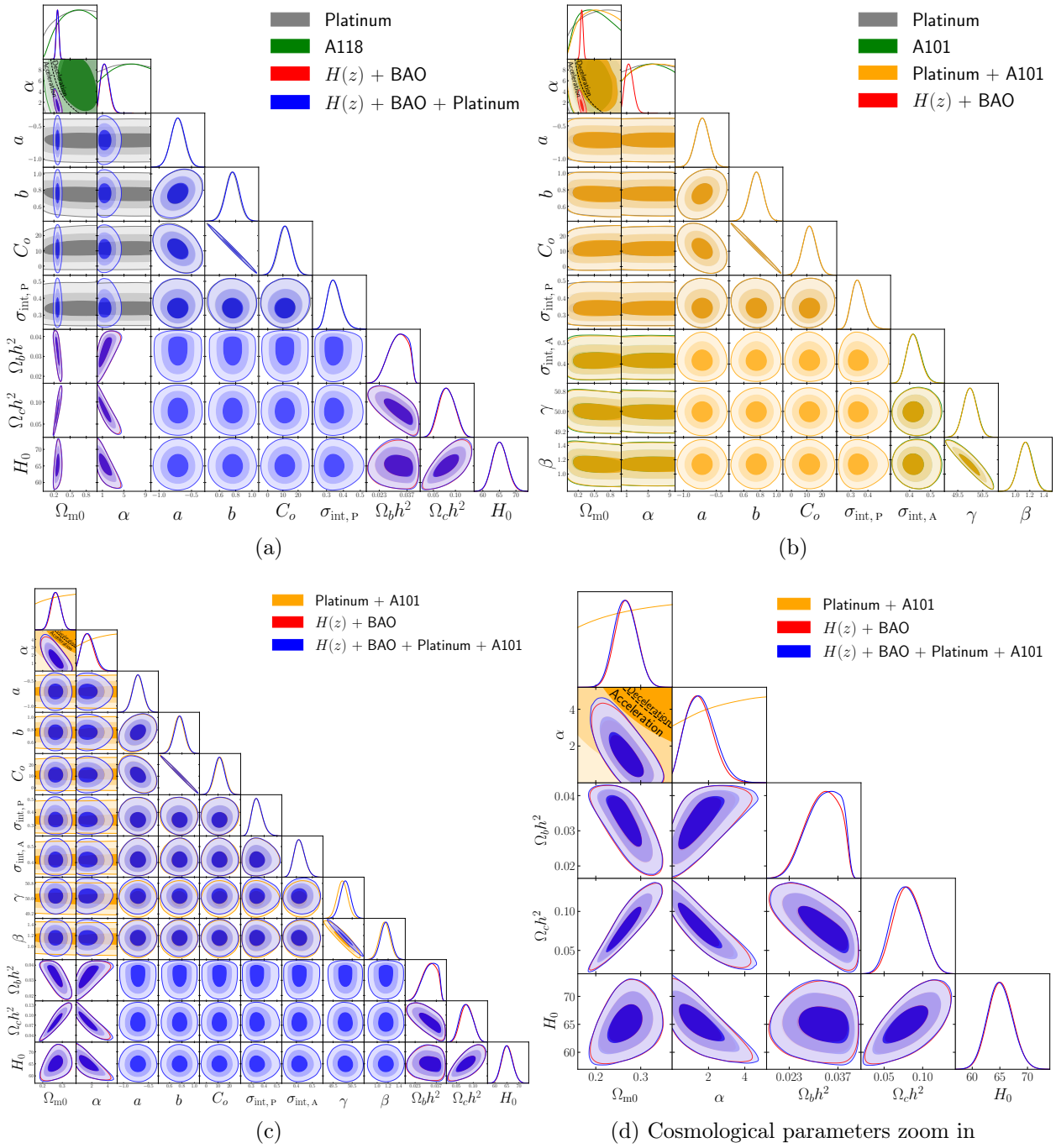

(a) (b) (c) (d) Cosmological parameters zoom in

Figure 8.5: One-dimensional likelihood distributions and 1σ, 2σ, and 3σ two-dimensional likelihood confidence contours for flat ϕCDM from various combinations of data. The zero-acceleration black dashed lines divide the parameter space into regions associated with currently-accelerating (below left) and currently-decelerating (above right) cosmological expansion. The $\alpha = 0$ axes correspond to flat ΛCDM.

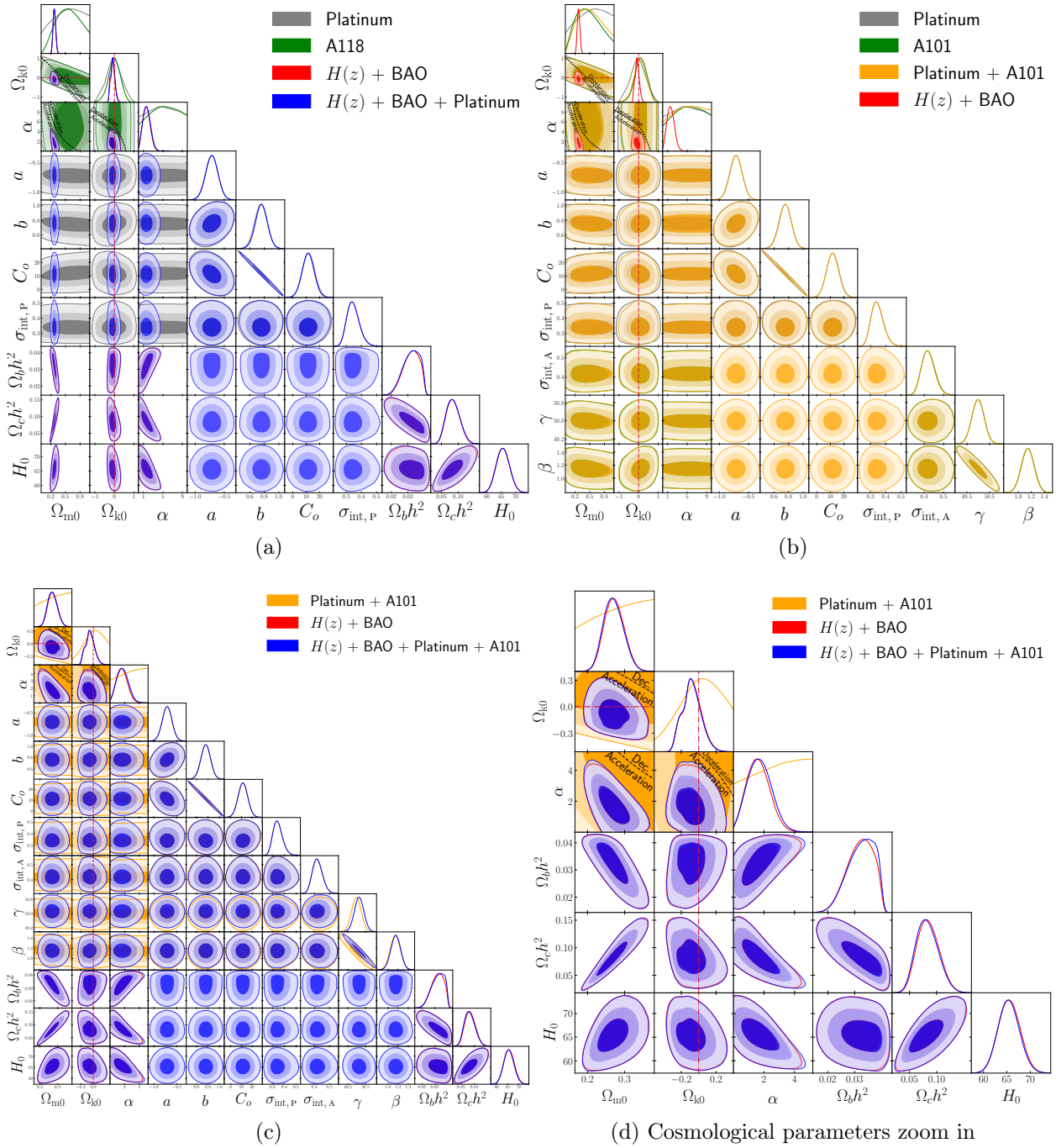

(a) (b) (c) (d) Cosmological parameters zoom in

Figure 8.6: Same as Fig. 8.5 but for non-flat ϕCDM. The zero-acceleration black dashed lines are computed for the third cosmological parameter set to the $H(z)$ + BAO data best-fitting values listed in Table 8.4, and divide the parameter space into regions associated with currently-accelerating (below left) and currently-decelerating (above right) cosmological expansion. The crimson dash-dot lines represent flat hypersurfaces, with closed spatial hypersurfaces either below or to the left. The $\alpha = 0$ axes correspond to non-flat ΛCDM.

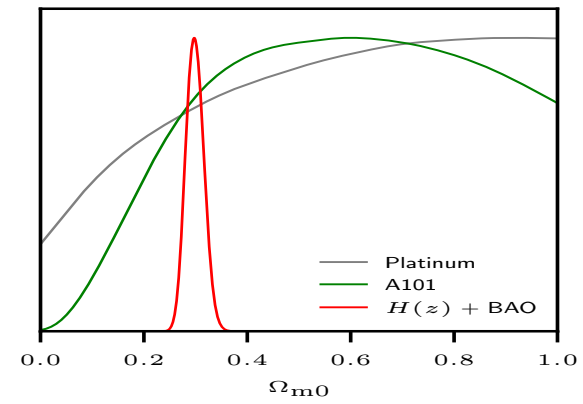

(a) Flat ΛCDM

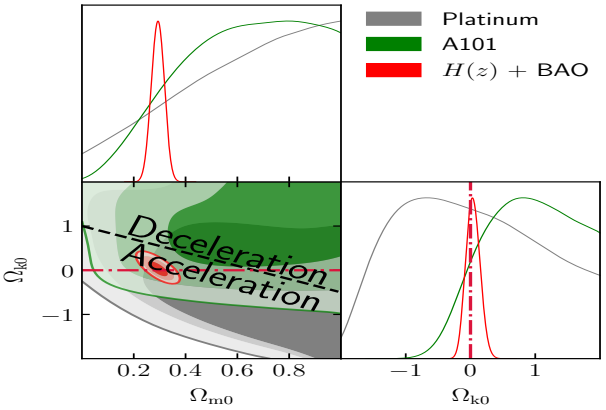

(b) Non-flat ΛCDM

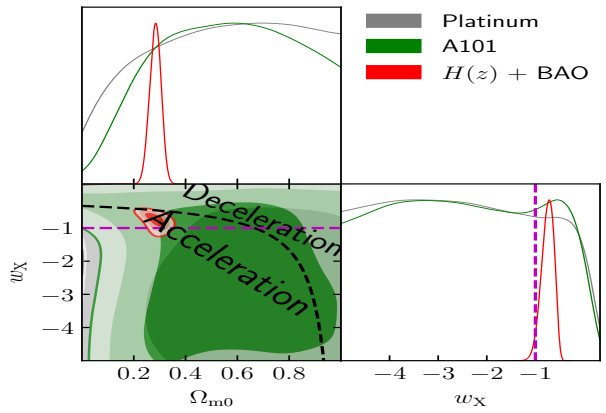

(c) Flat XCDM

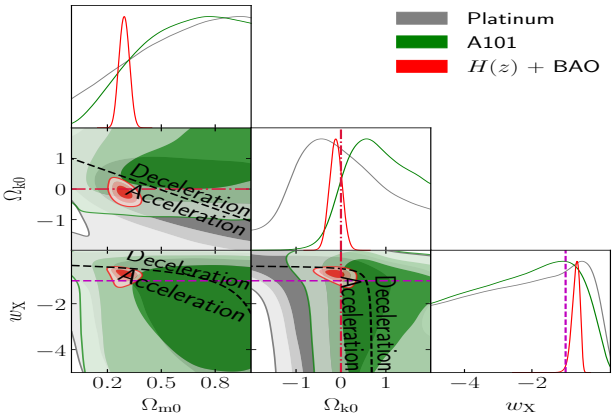

(d) Non-flat XCDM

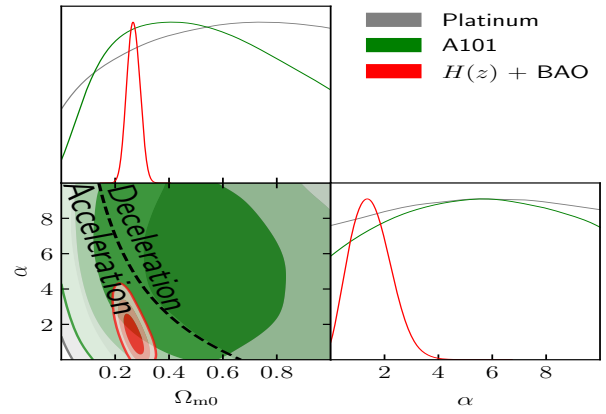

(e) Flat ϕCDM

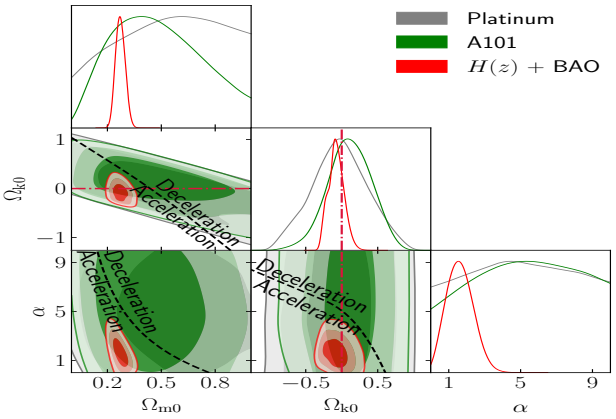

(f) Non-flat ϕCDM

Figure 8.7: One-dimensional likelihood distributions and 1σ, 2σ, and 3σ two-dimensional likelihood confidence contours for some cosmological parameters of the six cosmological models from Platinum data (gray), A101 data (green), and $H(z)$ + BAO data (red), which more clearly show the cosmological parameter overlaps between Platinum/A101 data and $H(z)$ + BAO data.

Table 8.4: Unmarginalized best-fitting parameter values for all models from various combinations of data.

Model	Data set	$\Omega_b h^2$ [a]	$\Omega_c h^2$	$\Omega_{\rm m0}$	$\Omega_{\rm k0}$	$w_{\rm X}/\alpha$ [b]	H_0 [c]	$\sigma_{\rm int,\,P}$	a	b	C_o	$\sigma_{\rm int,\,A}$	γ	β	$-2\ln\mathscr{L}_{\rm max}$	AIC	BIC	DIC	ΔAIC	ΔBIC	ΔDIC
	Platinum	–	0.4560	0.982	–	–	–	0.322	−0.716	0.743	12.19	–	–	–	32.99	42.99	52.55	42.80	0.00	0.00	0.00
	A118	–	0.4088	0.886	–	–	–	–	–	–	–	0.402	50.02	1.099	128.72	136.72	147.81	136.05	0.00	0.00	0.00
	A101	–	0.2547	0.571	–	–	–	–	–	–	–	0.409	50.04	1.135	112.81	120.81	131.27	120.16	0.00	0.00	0.00
Flat	Plat. + A101	–	0.3505	0.767	–	–	–	0.324	−0.694	0.753	11.60	0.413	49.98	1.125	146.08	162.08	186.22	162.07	0.00	0.00	0.00
ΛCDM	$H(z)$ + BAO	0.0240	0.1177	0.298	–	–	69.11	–	–	–	–	–	–	–	23.66	29.66	34.87	30.23	0.00	0.00	0.00
	HzBP[d]	0.0243	0.1169	0.298	–	–	69.04	0.325	−0.715	0.757	11.53	–	–	–	57.33	73.33	88.99	72.58	0.00	0.00	0.00
	HzBPA101[e]	0.0236	0.1155	0.296	–	–	68.71	0.324	−0.707	0.760	11.35	0.412	50.16	1.153	170.63	190.63	223.26	191.94	0.00	0.00	0.00
	Platinum	–	0.1178	0.292	−0.992	–	–	0.292	−0.700	0.829	7.59	–	–	–	24.51	36.51	47.98	51.00	−6.48	−4.57	8.20
	A118	–	0.4625	0.995	1.094	–	–	–	–	–	–	0.401	49.90	1.117	127.96	137.96	151.82	136.72	1.24	4.01	0.67
	A101	–	0.4606	0.991	1.993	–	–	–	–	–	–	0.405	49.78	1.151	111.08	121.08	134.16	120.04	0.27	2.89	−0.12
Non-flat	Plat. + A101	–	0.4300	0.929	1.857	–	–	0.326	−0.712	0.746	11.99	0.400	49.75	1.167	144.65	162.65	189.80	161.75	0.57	3.58	−0.32
ΛCDM	$H(z)$ + BAO	0.0247	0.1141	0.295	0.023	–	68.78	–	–	–	–	–	–	–	23.59	31.59	38.54	32.21	1.93	3.67	1.99
	HzBP[d]	0.0245	0.1149	0.294	0.010	–	68.99	0.328	−0.719	0.752	11.81	–	–	–	57.31	73.31	93.48	74.65	−0.02	4.49	2.07
	HzBPA101[e]	0.0237	0.1115	0.295	0.032	–	67.91	0.328	−0.726	0.750	11.91	0.410	50.13	1.164	170.70	192.70	228.59	193.50	2.07	5.33	1.56
	Platinum	–	0.0809	0.216	–	0.137	–	0.323	−0.724	0.735	12.59	–	–	–	32.81	44.81	56.28	42.83	1.82	3.73	0.04
	A118	–	−0.0198	0.011	–	−0.139	–	–	–	–	–	0.402	50.04	1.112	128.42	138.42	152.28	136.65	1.70	4.47	0.61
	A101	–	−0.0221	0.006	–	−0.251	–	–	–	–	–	0.406	50.01	1.148	111.99	121.99	135.06	121.23	1.18	3.79	1.08
Flat	Plat. + A101	–	0.1570	0.372	–	−0.193	–	0.317	−0.712	0.753	11.65	0.405	50.02	1.115	145.74	163.74	190.90	162.40	1.66	4.68	0.33
XCDM	$H(z)$ + BAO	0.0309	0.0870	0.280	–	−0.694	65.11	–	–	–	–	–	–	–	19.65	27.65	34.60	28.11	−2.01	−0.27	−2.11
	HzBP[d]	0.0302	0.0899	0.284	–	−0.711	65.22	0.320	−0.709	0.758	11.46	–	–	–	53.26	69.26	89.44	70.25	−4.07	0.45	−2.33
	HzBPA101[e]	0.0301	0.0891	0.282	–	−0.709	69.13	0.325	−0.724	0.756	11.63	0.408	50.17	1.150	166.30	188.30	224.19	188.98	−2.33	0.93	−2.96
	Platinum	–	0.0918	0.239	−0.760	−1.123	–	0.286	−0.761	0.788	10.04	–	–	–	24.58	38.58	51.97	51.01	−4.41	−0.58	8.21
	A118	–	0.4644	0.999	0.998	−1.137	–	–	–	–	–	0.398	49.91	1.113	127.97	139.97	156.60	137.16	3.25	8.79	1.11
	A101	–	0.4444	0.958	1.849	−1.222	–	–	–	–	–	0.410	49.73	1.164	111.14	123.14	138.83	120.59	2.33	7.56	0.44
Non-flat	Plat. + A101	–	0.4120	0.892	1.526	−1.208	–	0.335	−0.707	0.758	11.34	0.405	49.77	1.163	144.69	164.69	194.86	162.75	2.61	8.64	0.67
XCDM	$H(z)$ + BAO	0.0295	0.0962	0.294	−0.159	−0.648	65.62	–	–	–	–	–	–	–	18.31	28.31	37.00	28.96	−1.35	2.13	−1.26
	HzBP[d]	0.0301	0.0933	0.290	−0.164	−0.640	65.39	0.324	−0.709	0.746	12.04	–	–	–	51.90	69.90	92.60	70.74	−3.43	3.61	−1.85
	HzBPA101[e]	0.0299	0.0883	0.284	−0.112	−0.640	64.65	0.319	−0.714	0.767	11.01	0.414	50.19	1.137	165.30	189.30	228.45	189.85	−1.33	5.19	−2.09
	Platinum	–	0.4615	0.993	–	4.896	–	0.322	−0.723	0.744	12.14	–	–	–	32.99	44.99	56.46	42.37	2.00	3.91	−0.43
	A118	–	0.2119	0.484	–	9.617	–	–	–	–	–	0.400	50.04	1.105	128.56	138.56	152.41	135.74	1.84	4.60	−0.31
	A101	–	0.0764	0.207	–	9.922	–	–	–	–	–	0.409	49.99	1.152	112.26	122.26	135.33	119.96	1.45	4.06	−0.20
Flat	Plat. + A101	–	0.0936	0.242	–	7.330	–	0.326	−0.723	0.755	11.62	0.410	50.04	1.135	145.75	163.75	190.90	161.62	1.67	4.68	−0.46
ϕCDM	$H(z)$ + BAO	0.0332	0.0789	0.265	–	1.455	65.24	–	–	–	–	–	–	–	19.49	27.49	34.44	26.96	−2.17	−0.43	−3.27
	HzBP[d]	0.0343	0.0746	0.259	–	1.633	64.98	0.331	−0.714	0.765	11.10	–	–	–	53.12	69.12	89.29	69.20	−4.21	0.30	−3.39
	HzBPA101[e]	0.0374	0.0663	0.246	–	1.968	65.20	0.327	−0.703	0.759	11.38	0.412	50.10	1.172	166.28	188.28	224.17	187.99	−2.35	0.91	−3.95
	Platinum	–	0.4366	0.942	−0.905	0.061	–	0.325	−0.735	0.725	13.16	–	–	–	32.53	46.53	59.92	43.06	3.54	7.37	0.26
	A118	–	0.3331	0.731	0.234	5.269	–	–	–	–	–	0.402	50.02	1.111	128.42	140.42	157.04	136.67	3.70	9.23	0.63
	A101	–	0.2367	0.534	0.460	8.680	–	–	–	–	–	0.406	49.99	1.151	111.89	123.89	139.58	120.48	3.08	8.31	0.33
Non-flat	Plat. + A101	–	0.3063	0.677	0.317	9.746	–	0.319	−0.728	0.742	12.27	0.412	49.96	1.140	145.40	165.40	195.57	162.44	3.32	9.35	0.36
ϕCDM	$H(z)$ + BAO	0.0344	0.0786	0.263	−0.149	2.014	65.71	–	–	–	–	–	–	–	18.15	28.15	36.84	27.39	−1.51	1.97	−2.84
	HzBP[d]	0.0326	0.0851	0.271	−0.176	1.826	66.10	0.322	−0.727	0.752	11.78	–	–	–	51.79	69.79	92.49	69.44	−3.54	3.50	−3.14
	HzBPA101[e]	0.0353	0.0730	0.257	−0.135	2.199	65.09	0.321	−0.729	0.758	11.52	0.403	50.16	1.144	165.08	189.08	228.23	188.65	−1.55	4.97	−3.29

[a] In the four GRB-only cases $\Omega_b h^2$ is set to 0.0245.
[b] $w_{\rm X}$ corresponds to flat/non-flat XCDM and α corresponds to flat/non-flat ϕCDM.
[c] km s^{-1} Mpc^{-1}. In the four GRB-only cases H_0 is set to 70 km s^{-1} Mpc^{-1}.
[d] $H(z)$ + BAO + Platinum.
[e] $H(z)$ + BAO + Platinum + A101.

Table 8.5: One-dimensional marginalized posterior mean values and uncertainties ($\pm1\sigma$ error bars or 2σ limits) of the parameters for all models from various combinations of data.

Model	Data set	$\Omega_b h^2$ [a]	$\Omega_c h^2$	$\Omega_{\rm m0}$	$\Omega_{\rm k0}$	$w_{\rm X}/\alpha$ [b]	H_0 [c]	$\sigma_{\rm int,\,P}$	a	b	C_o	$\sigma_{\rm int,\,A}$	γ	β
	Platinum	–	–	> 0.411 [d]	–	–	–	$0.347^{+0.033}_{-0.046}$	-0.714 ± 0.104	0.756 ± 0.083	11.52 ± 4.45	–	–	–
	A118	–	–	> 0.256	–	–	–	–	–	–	–	$0.412^{+0.027}_{-0.033}$	50.09 ± 0.25	1.109 ± 0.089
	A101	–	–	$0.584^{+0.298}_{-0.240}$	–	–	–	–	–	–	–	$0.422^{+0.030}_{-0.037}$	50.03 ± 0.28	1.140 ± 0.098
Flat	Plat. + A101	–	–	$0.614^{+0.380}_{-0.130}$	–	–	–	$0.347^{+0.033}_{-0.046}$	-0.717 ± 0.102	0.751 ± 0.083	11.80 ± 4.45	$0.421^{+0.029}_{-0.036}$	50.03 ± 0.27	1.138 ± 0.095
ΛCDM	$H(z)$ + BAO	0.0243 ± 0.0029	$0.1184^{+0.0077}_{-0.0084}$	$0.299^{+0.016}_{-0.018}$	–	–	69.27 ± 1.85	–	–	–	–	–	–	–
	HzBP [e]	0.0242 ± 0.0029	$0.1184^{+0.0076}_{-0.0084}$	$0.299^{+0.016}_{-0.018}$	–	–	69.24 ± 1.81	$0.347^{+0.033}_{-0.045}$	-0.711 ± 0.104	0.762 ± 0.081	11.23 ± 4.35	–	–	–
	HzBPA101 [f]	$0.0242^{+0.0027}_{-0.0030}$	$0.1187^{+0.0075}_{-0.0083}$	$0.300^{+0.016}_{-0.018}$	–	–	69.20 ± 1.79	$0.347^{+0.032}_{-0.045}$	-0.711 ± 0.104	0.762 ± 0.080	11.23 ± 4.32	$0.421^{+0.029}_{-0.036}$	50.13 ± 0.26	1.159 ± 0.094
	Platinum	–	–	> 0.491 [d]	$-0.023^{+0.869}_{-1.401}$	–	–	$0.347^{+0.034}_{-0.046}$	-0.727 ± 0.109	$0.738^{+0.102}_{-0.088}$	$12.49^{+4.71}_{-5.46}$	–	–	–
	A118	–	–	> 0.295	$0.701^{+0.636}_{-0.844}$	–	–	–	–	–	–	$0.411^{+0.027}_{-0.033}$	50.00 ± 0.26	1.123 ± 0.088
	A101	–	–	> 0.212	$0.886^{+0.819}_{-0.614}$	–	–	–	–	–	–	$0.419^{+0.030}_{-0.037}$	49.93 ± 0.27	1.156 ± 0.096
Non-flat	Plat. + A101	–	–	> 0.235	$0.840^{+0.758}_{-0.720}$	–	–	$0.346^{+0.031}_{-0.044}$	-0.711 ± 0.100	0.759 ± 0.080	$11.33^{+4.28}_{-4.27}$	$0.418^{+0.029}_{-0.036}$	49.93 ± 0.27	1.154 ± 0.095
ΛCDM	$H(z)$ + BAO	$0.0255^{+0.0040}_{-0.0048}$	0.1127 ± 0.0195	0.293 ± 0.025	$0.039^{+0.100}_{-0.114}$	–	68.76 ± 2.36	–	–	–	–	–	–	–
	HzBP [e]	$0.0253^{+0.0039}_{-0.0048}$	$0.1135^{+0.0192}_{-0.0193}$	0.294 ± 0.024	$0.034^{+0.098}_{-0.113}$	–	68.80 ± 2.32	$0.347^{+0.033}_{-0.046}$	-0.710 ± 0.104	0.763 ± 0.080	11.18 ± 4.30	–	–	–
	HzBPA101 [f]	$0.0255^{+0.0038}_{-0.0047}$	$0.1121^{+0.0181}_{-0.0182}$	0.293 ± 0.023	$0.043^{+0.094}_{-0.107}$	–	68.62 ± 2.24	$0.347^{+0.033}_{-0.045}$	-0.710 ± 0.102	0.764 ± 0.079	11.15 ± 4.27	$0.421^{+0.029}_{-0.036}$	50.13 ± 0.26	1.161 ± 0.093
	Platinum	–	–	> 0.386 [d]	–	< -0.078	–	$0.347^{+0.033}_{-0.046}$	-0.717 ± 0.103	0.749 ± 0.083	11.90 ± 4.45	–	–	–
	A118	–	–	$0.599^{+0.360}_{-0.166}$	–	$-2.412^{+1.790}_{-1.730}$	–	–	–	–	–	$0.412^{+0.028}_{-0.034}$	$50.15^{+0.27}_{-0.30}$	1.106 ± 0.090
	A101	–	–	$0.558^{+0.285}_{-0.280}$	–	$-2.423^{+1.765}_{-1.716}$	–	–	–	–	–	$0.422^{+0.030}_{-0.037}$	$50.10^{+0.29}_{-0.33}$	1.134 ± 0.097
Flat	Plat. + A101	–	–	$0.576^{+0.382}_{-0.182}$	–	< -0.089	–	$0.346^{+0.033}_{-0.046}$	-0.718 ± 0.105	0.749 ± 0.084	11.94 ± 4.54	$0.421^{+0.029}_{-0.036}$	$50.08^{+0.28}_{-0.32}$	1.133 ± 0.094
XCDM	$H(z)$ + BAO	$0.0299^{+0.0046}_{-0.0052}$	$0.0926^{+0.0192}_{-0.0170}$	$0.283^{+0.023}_{-0.021}$	–	$-0.750^{+0.149}_{-0.104}$	$65.83^{+2.34}_{-2.63}$	–	–	–	–	–	–	–
	HzBP [e]	$0.0301^{+0.0046}_{-0.0053}$	$0.0917^{+0.0196}_{-0.0171}$	$0.283^{+0.023}_{-0.021}$	–	$-0.743^{+0.153}_{-0.101}$	$65.73^{+2.31}_{-2.63}$	$0.347^{+0.033}_{-0.046}$	-0.711 ± 0.104	0.763 ± 0.081	11.24 ± 4.32	–	–	–
	HzBPA101 [f]	$0.0303^{+0.0047}_{-0.0053}$	$0.0904^{+0.0196}_{-0.0173}$	$0.282^{+0.023}_{-0.021}$	–	$-0.731^{+0.150}_{-0.096}$	$65.54^{+2.26}_{-2.58}$	$0.347^{+0.032}_{-0.046}$	-0.711 ± 0.102	0.762 ± 0.080	11.21 ± 4.38	$0.420^{+0.029}_{-0.036}$	50.14 ± 0.26	1.159 ± 0.093
	Platinum	–	–	> 0.457 [d]	$0.011^{+0.821}_{-1.158}$	$-2.212^{+2.279}_{-1.046}$	–	$0.346^{+0.034}_{-0.046}$	-0.727 ± 0.109	$0.736^{+0.102}_{-0.087}$	$12.62^{+4.65}_{-5.51}$	–	–	–
	A118	–	–	> 0.257	$0.569^{+0.474}_{-0.790}$	$-2.289^{+1.998}_{-1.087}$	–	–	–	–	–	$0.412^{+0.027}_{-0.033}$	50.01 ± 0.27	1.120 ± 0.088
	A101	–	–	> 0.193	$0.824^{+0.644}_{-0.749}$	$-2.338^{+2.038}_{-1.083}$	–	–	–	–	–	$0.421^{+0.030}_{-0.037}$	49.91 ± 0.30	1.157 ± 0.098
Non-flat	Plat. + A101	–	–	> 0.207	$0.743^{+0.618}_{-0.800}$	$-2.305^{+2.139}_{-1.049}$	–	$0.346^{+0.033}_{-0.046}$	-0.711 ± 0.103	0.759 ± 0.081	$11.33^{+4.38}_{-4.34}$	$0.420^{+0.029}_{-0.036}$	49.91 ± 0.29	1.154 ± 0.096
XCDM	$H(z)$ + BAO	$0.0291^{+0.0055}_{-0.0053}$	$0.0986^{+0.0218}_{-0.0220}$	0.294 ± 0.028	$-0.116^{+0.135}_{-0.136}$	$-0.702^{+0.139}_{-0.083}$	$65.98^{+2.36}_{-2.58}$	–	–	–	–	–	–	–
	HzBP [e]	$0.0292^{+0.0051}_{-0.0057}$	$0.0983^{+0.0215}_{-0.0218}$	0.294 ± 0.028	$-0.128^{+0.135}_{-0.134}$	$-0.695^{+0.141}_{-0.080}$	$65.93^{+2.27}_{-2.53}$	$0.347^{+0.033}_{-0.046}$	-0.713 ± 0.103	0.758 ± 0.082	11.46 ± 4.44	–	–	–
	HzBPA101 [f]	$0.0298^{+0.0053}_{-0.0055}$	$0.0948^{+0.0212}_{-0.0214}$	0.290 ± 0.027	-0.106 ± 0.128	$-0.690^{+0.144}_{-0.076}$	$65.65^{+2.24}_{-2.53}$	$0.346^{+0.033}_{-0.045}$	-0.713 ± 0.103	0.758 ± 0.081	11.44 ± 4.38	$0.421^{+0.029}_{-0.036}$	50.14 ± 0.26	1.151 ± 0.094
	Platinum	–	–	> 0.379 [d]	–	–	–	$0.346^{+0.032}_{-0.044}$	-0.715 ± 0.102	0.753 ± 0.081	11.68 ± 4.33	–	–	–
	A118	–	–	$0.576^{+0.355}_{-0.202}$	–	–	–	–	–	–	–	$0.411^{+0.027}_{-0.033}$	50.05 ± 0.25	1.110 ± 0.089
	A101	–	–	$0.506^{+0.239}_{-0.348}$	–	–	–	–	–	–	–	$0.421^{+0.030}_{-0.037}$	49.99 ± 0.27	1.140 ± 0.097
Flat	Plat. + A101	–	–	$0.541^{+0.301}_{-0.297}$	–	–	–	$0.346^{+0.033}_{-0.045}$	-0.716 ± 0.103	0.751 ± 0.082	11.77 ± 4.39	$0.420^{+0.029}_{-0.036}$	49.99 ± 0.26	1.137 ± 0.095
ϕCDM	$H(z)$ + BAO	$0.0324^{+0.0060}_{-0.0034}$	$0.0809^{+0.0180}_{-0.0178}$	0.268 ± 0.024	–	$1.492^{+0.623}_{-0.854}$	65.12 ± 2.18	–	–	–	–	–	–	–
	HzBP [e]	$0.0325^{+0.0071}_{-0.0030}$	$0.0805^{+0.0177}_{-0.0195}$	0.267 ± 0.024	–	$1.509^{+0.639}_{-0.904}$	$65.15^{+2.13}_{-2.34}$	$0.347^{+0.033}_{-0.045}$	-0.711 ± 0.104	0.762 ± 0.081	11.24 ± 4.37	–	–	–
	HzBPA101 [f]	$0.0328^{+0.0069}_{-0.0023}$	$0.0794^{+0.0174}_{-0.0198}$	$0.266^{+0.024}_{-0.025}$	–	$1.568^{+0.652}_{-0.911}$	$65.03^{+2.10}_{-2.30}$	$0.347^{+0.033}_{-0.046}$	-0.711 ± 0.103	0.762 ± 0.082	$11.23^{+4.39}_{-4.38}$	$0.420^{+0.029}_{-0.036}$	50.14 ± 0.26	1.158 ± 0.093
	Platinum	–	–	$0.537^{+0.427}_{-0.187}$	$-0.026^{+0.391}_{-0.384}$	–	–	$0.346^{+0.033}_{-0.046}$	-0.717 ± 0.105	0.751 ± 0.084	$11.78^{+4.51}_{-4.52}$	–	–	–
	A118	–	–	$0.559^{+0.258}_{-0.249}$	$-0.002^{+0.300}_{-0.292}$	$5.185^{+3.757}_{-2.564}$	–	–	–	–	–	$0.412^{+0.027}_{-0.033}$	50.05 ± 0.25	1.110 ± 0.090
	A101	–	–	$0.477^{+0.199}_{-0.310}$	$0.107^{+0.306}_{-0.294}$	$5.205^{+3.974}_{-2.507}$	–	–	–	–	–	$0.421^{+0.030}_{-0.037}$	49.99 ± 0.27	1.146 ± 0.098
Non-flat	Plat. + A101	–	–	$0.514^{+0.225}_{-0.300}$	$0.061^{+0.308}_{-0.297}$	–	–	$0.346^{+0.033}_{-0.045}$	-0.715 ± 0.103	0.754 ± 0.083	11.64 ± 4.42	$0.420^{+0.030}_{-0.036}$	49.98 ± 0.26	1.142 ± 0.097
ϕCDM	$H(z)$ + BAO	$0.0320^{+0.0060}_{-0.0037}$	$0.0847^{+0.0179}_{-0.0218}$	$0.272^{+0.025}_{-0.028}$	$-0.076^{+0.106}_{-0.114}$	$1.623^{+0.670}_{-0.821}$	$65.53^{+2.30}_{-2.29}$	–	–	–	–	–	–	–
	HzBP [e]	$0.0321^{+0.0069}_{-0.0031}$	$0.0847^{+0.0179}_{-0.0226}$	$0.272^{+0.024}_{-0.029}$	$-0.090^{+0.092}_{-0.130}$	$1.674^{+0.697}_{-0.850}$	65.57 ± 2.27	$0.347^{+0.033}_{-0.046}$	-0.713 ± 0.104	0.760 ± 0.081	11.37 ± 4.35	–	–	–
	HzBPA101 [f]	$0.0324^{+0.0073}_{-0.0024}$	$0.0829^{+0.0175}_{-0.0223}$	$0.270^{+0.024}_{-0.029}$	$-0.079^{+0.104}_{-0.112}$	$1.714^{+0.713}_{-0.856}$	65.39 ± 2.24	$0.346^{+0.032}_{-0.045}$	-0.712 ± 0.103	0.760 ± 0.082	11.36 ± 4.40	$0.420^{+0.029}_{-0.036}$	50.14 ± 0.26	1.153 ± 0.094

[a] In the four GRB-only cases $\Omega_b h^2$ is set to 0.0245.

[b] $w_{\rm X}$ corresponds to flat/non-flat XCDM and α corresponds to flat/non-flat ϕCDM.

[c] km s^{-1} Mpc^{-1}. In the four GRB-only cases H_0 is set to 70 km s^{-1} Mpc^{-1}.

[d] This is the 1σ limit. The 2σ limit is set by the prior and not shown here.

[e] $H(z)$ + BAO + Platinum.

[f] $H(z)$ + BAO + Platinum + A101.

Dainotti-correlation GRBs, the 31 MD-LGRBs of Wang et al. (2022), have a somewhat smaller intrinsic dispersion, $\sigma_{\rm int} \sim 0.303 - 0.306$, Table 5 of Cao et al. (2022b), than the $\sigma_{\rm int,\,P} \sim 0.346 - 0.347$ of the 50 Platinum GRBs.[4] A possible reason for the smaller scatter of the 2-parameter MD-LGRB sample is due to how the sample was chosen. In principle one can retain fewer GRBs that lie exactly on the plane, or are much closer to the plane, thus reducing the scatter. However, further investigation is needed in order to draw a definite conclusion. Probably as a consequence of the smaller $\sigma_{\rm int}$, the MD-LGRB constraints on Ω_{m0} and Ω_{k0} are more restrictive than the constraints from Platinum data.

Compared with the analyses in Cao et al. (2022b) where we neglect massive neutrinos (setting $\Omega_\nu h^2 = 0$), here we include a non-zero $\Omega_\nu h^2$. The constraints on the A118 GRB correlation parameters here are almost identical to those listed in Table 8 of Cao et al. (2022b) and are cosmological-model-independent implying that the A118 GRBs are standardizable. For the 118 GRBs A118 data $\sigma_{\rm int,\,A} \sim 0.411 - 0.412$, larger than the $\sigma_{\rm int,\,P} \sim 0.346 - 0.347$ of the 50 Platinum GRBs. The constraints on the A101 GRB correlation parameters are also cosmological-model-independent, so A101 GRBs are also standardizable. The constraints on the A101 intrinsic scatter parameter $\sigma_{\rm int,\,A}$ range from a low of $0.419^{+0.030}_{-0.037}$ (non-flat ΛCDM) to a high of $0.422^{+0.030}_{-0.037}$ (flat ΛCDM and flat XCDM), which are slightly (0.2σ at most) higher than those from A118 data; the constraints on the slope β range from a low of 1.140 ± 0.098 (flat ΛCDM) to a high of 1.157 ± 0.098 (non-flat XCDM), which are slightly (0.28σ at most) higher than those from A118 data; and the constraints on the intercept γ range from a low of 49.91 ± 0.30 (non-flat XCDM) to a high of $50.10^{+0.29}_{-0.33}$ (flat XCDM), which are slightly (0.25σ at most) lower than those from A118 data; with central values of each pair being 0.06σ, 0.12σ, and 0.43σ away from each other, respectively.

Below we discuss cosmological parameter constraints in more detail. From Fig. 8.7 we see

[4]There are 12 common GRBs between the Platinum and MD-LGRB data sets (060605, 060906, 061222A, 070306, 080310, 081008, 120404A, 160121A, 160227A, 180329B, 190106A, and 190114A). There are also common GRBs between the Platinum and the (two-parameter) Dainotti-correlated GW-LGRB compilation of Hu et al. (2021) [091029, 120118B, 131105A, 170202A, 170705A, and 151027A (same name but different redshifts)]. Because of the significant number of overlapping GRBs in these cases, we believe it would not be that useful to perform joint analyses of the Platinum and truncated (to remove the overlapping GRBs) MD-LGRB or GW-LGRB data sets.

that the overlap of the constraints on the cosmological parameters indicate that Platinum data and A101 data cosmological constraints are mutually consistent and so these two data sets can be jointly analyzed. The Platinum + A101 data combination is also standardizable with cosmological-model-independent constraints on GRB correlation parameters that are consistent (well within 1σ) with those from both Platinum data and A101 data individually.

We find that in the flat ΛCDM model and the flat XCDM parametrization all GRB data more favor currently accelerating cosmological expansion. In the non-flat ΛCDM model, all but the Platinum GRBs more favor currently decelerating cosmological expansion. In the non-flat XCDM parametrization, in the $\Omega_{k0} - \Omega_{m0}$ parameter subspace, all but the Platinum GRBs more favor currently decelerating cosmological expansion, while in the $w_{\rm X} - \Omega_{m0}$ ($w_{\rm X} - \Omega_{k0}$) parameter subspace, all (all but the A101) GRBs more favor currently accelerating cosmological expansion. In the flat and non-flat ϕCDM models, currently decelerating cosmological expansion is slightly more favored.

Cosmological constraints from Platinum data are less restrictive than those from A118 and A101 data, which contain a little more than twice as many GRBs than the Platinum compilation. Comparing the Platinum + A101 constraints with the Platinum constraints and with the A101 constraints, we see that A101 data, with double the number of GRBs compared to Platinum, play a more dominant role in the combination.

In the flat and non-flat ΛCDM models, the Platinum, A118, A101, and Platinum + A101 2σ constraints on Ω_{m0} are mutually consistent and also consistent with those of $H(z)$ + BAO, with the 2σ lower limits in the flat (non-flat) ΛCDM model being None (None), > 0.256 (> 0.295), > 0.191 (> 0.212), and > 0.216 (> 0.235), respectively. In the flat ΛCDM model, the A101 constraint on Ω_{m0} is more consistent (than the Platinum and Platinum + A101 constraints) with that from $H(z)$ + BAO data, differing by only 1.18σ. In both models Platinum + A101 data favor a higher 1σ lower limit of Ω_{m0} than do Platinum data or A101 data. In the non-flat ΛCDM model, the constraints on Ω_{k0} from the four GRB data sets are mutually consistent within 1σ, with all but Platinum data slightly favoring open spatial hypersurfaces. Platinum and A118 data are consistent with flat hypersurfaces within 1σ, while A101 and Platinum + A101 data are 1.44σ and 1.17σ, respectively, away from flat.

The posterior mean value of Ω_{k0} from A101 data is 1.36σ away from that from $H(z)$ + BAO data, while those from the other three GRB data sets are consistent with that from $H(z)$ + BAO data within 1σ.

In the flat and non-flat XCDM parametrizations, the Platinum, A118, A101, and Platinum + A101 2σ constraints on Ω_{m0} are mutually consistent and also consistent with those of $H(z)$ + BAO, with the 2σ lower limits in the flat (non-flat) XCDM parametrization being None (None), > 0.181 (> 0.257), > 0.148 (> 0.193), and > 0.151 (> 0.207), respectively. In flat XCDM, the A101 constraint on Ω_{m0} is consistent with that from $H(z)$ + BAO within 1σ. Platinum + A101 data also favor a higher 1σ lower limit of Ω_{m0} than do Platinum or A101 data in both XCDM parametrizations. The constraints on $w_{\rm X}$ are weak, thus affected by the $w_{\rm X}$ prior, and consistent with each other. They mildly favor phantom dark energy, but Λ is less than 1σ away, except for the flat XCDM Platinum and Platinum + A101 cases (where Λ is still within 2σ), as is the case for the $w_{\rm X}$ constraints from $H(z)$ + BAO data.[5] In non-flat XCDM, the constraints on Ω_{k0} from the four GRB data sets are mutually consistent within 1σ, and they slightly favor open hypersurfaces. Platinum, A118, and Platinum + A101 data are consistent with flat hypersurfaces within 1σ, while A101 data are 1.10σ away from flat. The posterior mean value of Ω_{k0} from A101 data is 1.24σ away from that from $H(z)$ + BAO data, while those from the other three GRB data sets are consistent with that from $H(z)$ + BAO data within 1σ.

In the flat and non-flat ϕCDM models, the Platinum, A118, A101, and Platinum + A101 constraints on Ω_{m0} are mutually consistent within 1σ and the A101 and Platinum + A101 (Platinum and A118) constraints are within 1σ (2σ) of those from $H(z)$ + BAO data. Only A118 and A101 data provide (very weak) constraints on α with Λ being more than 1σ away but within 2σ. In non-flat ϕCDM, the constraints on Ω_{k0} from the four GRB data sets are mutually consistent and consistent with that from $H(z)$ + BAO data and flat hypersurfaces are within 1σ.

From the ΔAIC and ΔBIC values listed in Table 8.4, in the Platinum case, non-flat ΛCDM is the most favored model, while the evidence against other models are positive,

[5] These are computed 2σ constraints, not necessarily twice the 1σ ones, and are not shown in the table.

strong, and very strong (non-flat ϕCDM). In the A118, A101, and Platinum + A101 cases, the flat ΛCDM model is the most favored model and, except for non-flat XCDM and non-flat ϕCDM (with strong BIC evidence against them), the evidence against other models are either weak or positive. However, based on ΔDIC, in theses cases, flat ϕCDM is the most favored model; in the A118, A101, and Platinum + A101 cases, the evidence against other models are weak; whereas in the Platinum case, the evidence against other models are either weak or strong (non-flat ΛCDM and non-flat XCDM).

8.4.2 Constraints from $H(z)$ + BAO data in combination with Platinum (HzBP) and Platinum + A101 (HzBPA101) data

Since the $H(z)$ + BAO, Platinum, and Platinum + A101 cosmological constraints are mutually consistent, we jointly analyze combinations of these data to determine more restrictive constraints on cosmological and GRB correlation parameters. We find that the new constraints on GRB correlation parameters are more restrictive but change less than 1σ compared to those from the GRB-only analyses. The correlation parameter constraints remain cosmological-model-independent, indicating again that these GRBs are standardizable. In what follows we discuss how the $H(z)$ + BAO data cosmological parameter constraints are altered when these GRB data are jointly analyzed with $H(z)$ + BAO data.

Compared to the $H(z)$ + BAO constraints, the HzBP constraints on Ω_{m0} are almost unchanged in all models, but there are small changes in other cosmological parameter constraints. The constraints on H_0 are slightly tightened, with posterior means being $0.01-0.03\sigma$ smaller or larger from model to model; the constraints on $w_{\rm X}$ are slightly shifted away from Λ, with posterior means being $\sim 0.04\sigma$ larger; the constraints on α are slightly shifted away from Λ, with posterior means being 0.02σ (0.05σ) larger in flat (non-flat) ϕCDM; and the constraints on Ω_{k0} are slightly shifted away from flat, with posterior means being 0.06σ (0.10σ) smaller in non-flat XCDM (ϕCDM).

Compared to $H(z)$ + BAO, the HzBPA101 data provide mildly different constraints on Ω_{m0} in all models, but the effects on other cosmological parameter constraints are more

noticeable. The constraints on H_0 are slightly tightened, with posterior means being $0.03-0.10\sigma$ smaller from model to model; the constraints on $w_{\rm X}$ are slightly shifted away from Λ, with posterior means being 0.11σ (0.08σ) larger in flat (non-flat) XCDM; the constraints on α are slightly shifted away from Λ, with posterior means being 0.07σ (0.08σ) larger in flat (non-flat) ϕCDM; and the constraints on Ω_{k0} are slightly shifted towards (away) from flat, with posterior means being 0.05σ (0.02σ) larger (smaller) in non-flat XCDM (ϕCDM), respectively.

From the ΔAIC, ΔBIC, and ΔDIC values listed in Table 8.4, in both the HzBP and the HzBPA101 cases, following the patterns of the $H(z)$ + BAO case, flat ϕCDM is the most favored model but the evidence against other models are only either weak or positive. As expected, the better-established $H(z)$ + BAO data play the dominant role in these combined analyses and therefore currently accelerating cosmological expansion is favored.

8.5 Conclusion

We have analyzed the 50 Platinum GRBs, that obey the three-parameter fundamental plane (or Dainotti) relation, using six different cosmological models. By simultaneously constraining cosmological model and GRB correlation parameters our approach circumvents the circularity problem. We find that the Platinum GRB correlation parameters are cosmological-model-independent so the Platinum sample is standardizable through the three-parameter Dainotti correlation and can be used to constrain cosmological parameters. Since the cosmological constraints from Platinum data are consistent with those from $H(z)$ + BAO data, we have combined Platinum and $H(z)$ + BAO data to perform a joint (HzBP) analysis and find mild changes of the cosmological parameter constraints relative to those from $H(z)$ + BAO data, with the central values in the two cases agreeing to two significant figures.

We have also reanalyzed the A118 GRBs that obey the Amati ($E_{\rm p}-E_{\rm iso}$) correlation (Cao et al., 2022b; Khadka et al., 2021b), because of different, improved modeling of neutrino physics here, and, by excluding the 17 overlapping (with Platinum) GRBs from the larger A118 data set to form the truncated A101 data set, we have also performed a joint analysis

of Platinum and A101 data. The twice as large A101 data set plays a dominant role in the joint Platinum + A101 analysis, and the cosmological constraints from Platinum + A101 data are closer to those from A101 data. The results show that the Platinum + A101 GRBs are also standardizable and their cosmological constraints are also more consistent (than the A118 ones) with those from $H(z)$ + BAO data. The joint analyses of $H(z)$ + BAO and Platinum + A101 (HzBPA101) data show that Platinum + A101 data do have more impact on the joint constraints than do Platinum data, however, $H(z)$ + BAO data still play the dominant role.

Current compilations of GRBs provide some improvements on the cosmological constraints determined using $H(z)$ + BAO data. Importantly, GRBs are the only currently reliable probes of the $z \sim 3 - 8$ part of cosmological redshift space and so are well worth improving upon. With the upcoming SVOM mission (Cordier, 2019) in 2023, and possibly Theseus (Amati et al., 2021) in 2037 if approved in the new ESA call, there soon will be larger GRB data sets over a wider range of redshifts that will allow for improved GRB cosmological constraints.

Chapter 9

Using lower-redshift, non-CMB, data to constrain the Hubble constant and other cosmological parameters

This chapter is based on Cao & Ratra (2022).

9.1 Introduction

The expansion of the Universe is currently accelerating. This is well-supported by many observations but the underlying theory remains obscure. If general relativity is valid on cosmological scales, a dark energy that has negative pressure is thought to be responsible for the accelerated cosmological expansion. In the well-known spatially-flat ΛCDM model (Peebles, 1984), dark energy is a cosmological constant Λ and contributes $\sim 70\%$ of the current cosmological energy budget (see, e.g. eBOSS Collaboration, 2021; Farooq et al., 2017; Planck Collaboration, 2020; Scolnic et al., 2018). However, potential observational discrepancies (see, e.g. Abdalla et al., 2022; Di Valentino et al., 2021b; Perivolaropoulos & Skara, 2022) motivate consideration of other cosmological models besides flat ΛCDM. In our

analyses here we also allow for non-zero spatial curvature[1] as well as dark energy dynamics.

Many observations have been used to compare the goodness of fit of cosmological models and determine cosmological parameter constraints. These include CMB anisotropy data (see, e.g. Planck Collaboration, 2020) that largely probe the high-redshift, $z \sim 1100$, Universe, as well as lower-z cosmological measurements that we make use of here, such as reverberation-measured Hβ quasar (QSO) and Mg II QSO observations that reach to $z \sim 1.9$ (see, e.g. Czerny et al., 2021; Khadka et al., 2021a, 2022a; Yu et al., 2021; Zajaček et al., 2021)[2], Hubble parameter $[H(z)]$ data that reach to $z \sim 2$ (see, e.g. Cao et al., 2022a; Farooq et al., 2017; Moresco et al., 2016; Ryan et al., 2019), type Ia supernova (SN Ia) observations that reach to $z \sim 2.3$ (see, e.g. DES Collaboration, 2019d; Scolnic et al., 2018), baryon acoustic oscillation (BAO) measurements that reach to $z \sim 2.3$ (see, e.g. Cao et al., 2022a; eBOSS Collaboration, 2021), H II starburst galaxy apparent magnitude data that reach to $z \sim 2.4$ (see, e.g. Cao et al., 2022a; Chávez et al., 2014; González-Morán et al., 2021; Johnson et al., 2022; Mania & Ratra, 2012; Mehrabi et al., 2022), QSO angular size (QSO-AS) measurements that reach to $z \sim 2.7$ (see, e.g. Cao et al., 2017b, 2020, 2022a; Lian et al., 2021; Ryan et al., 2019; Zheng et al., 2021), QSO flux observations that reach to $z \sim 7.5$ (Dainotti et al., 2022d; Khadka & Ratra, 2020a,b, 2021, 2022; Li et al., 2021; Lian et al., 2021; Luongo et al., 2022; Lusso et al., 2020; Rezaei et al., 2022; Risaliti & Lusso, 2015, 2019; Yang et al., 2020; Zhao & Xia, 2021)[3], and gamma-ray burst (GRB) data that reach to $z \sim 8.2$ (see, e.g. Amati et al., 2019; Cao et al., 2022b,c,d; Dai et al., 2021; Dainotti et al., 2016, 2017, 2020, 2022c; Demianski et al., 2021; Fana Dirirsa et al., 2019; Hu et al., 2021; Khadka & Ratra, 2020c; Khadka et al., 2021b; Liu et al., 2022; Luongo & Muccino, 2021; Wang et al., 2016, 2022)[4].

In this paper, we use most of the aforementioned non-CMB data sets to jointly constrain

[1]The *Planck* TT,TE,EE+lowE+lensing cosmic microwave background (CMB) anisotropy data favor positive spatial curvature over flatness (Planck Collaboration, 2020).

[2]Current Hβ QSO data probe to $z \sim 0.9$ and the resulting cosmological parameter constraints from these data are in $\sim 2\sigma$ tension with those from better-established cosmological probes (Khadka et al., 2022a) so we do not use these data in our analyses here.

[3]We do not use these data in this paper since the latest Lusso et al. (2020) QSO flux compilation assumes a UV–X-ray correlation model that is invalid above $z \sim 1.5 - 1.7$ (Khadka & Ratra, 2021, 2022).

[4]Only a subset containing 118 Amati-correlated GRBs are suitable for cosmological purposes (Cao et al., 2021a; Khadka & Ratra, 2020c; Khadka et al., 2021b), and these are the Amati-correlated GRBs we use in our analyses here.

cosmological parameters. In Cao et al. (2021b), by using $H(z)$ + BAO + SN data (SN refers to Pantheon and DES-3yr SN Ia data, discussed in Sec. 9.2 below), we estimated summary values of the current non-relativistic matter density parameter $\Omega_{m0} = 0.294 \pm 0.020$ and the Hubble constant $H_0 = 68.8 \pm 1.8$ km s^{-1} Mpc^{-1}. In Cao et al. (2022a), by using $H(z)$ + BAO + SN + QSO-AS + H IIG data, summary values of $\Omega_{m0} = 0.293 \pm 0.021$ and $H_0 = 69.7 \pm 1.2$ km s^{-1} Mpc^{-1} were obtained. Compared to our earlier analysis, the addition of QSO-AS and H IIG data results in similar constraints on Ω_{m0} with a slightly larger 1σ uncertainty and more restrictive (1σ uncertainty reduced by 50%) H_0 constraints, with a higher central value of H_0 (0.42σ higher).

In our analysis here we improve on our earlier work by more correctly accounting for the neutrinos. We also use updated BAO and $H(z)$ data and now also include Mg II QSO and A118 GRB data.[5] Here the joint analyses of $H(z)$ + BAO + SN + QSO-AS + H IIG + Mg II QSO + A118 data provide model-independent values of $\Omega_{m0} = 0.295 \pm 0.017$ and $H_0 = 69.7 \pm 1.2$ km s^{-1} Mpc^{-1}. Our H_0 measurement is in better agreement with the median statistics H_0 estimate of Chen & Ratra (2011) than with the local expansion rate H_0 estimate of Riess et al. (2021). Flat ΛCDM is favored the most, but mild dark energy dynamics or a little spatial curvature energy density is not ruled out. Although here we use updated $H(z)$ and BAO data, and add Mg II QSO and A118 data, the constraint on H_0 is identical to that of Cao et al. (2022a)[6], whereas the new constraint on Ω_{m0} is more restrictive (1σ uncertainty reduced by $\sim 24\%$) and $\sim 0.15\sigma$ higher.

This paper is organized as follows. In Chapter 2 we described the cosmological models/parametrizations used in our analyses. In Sec. 9.2 we describe the data sets used in our analyses, with the methods we use summarized in Sec. 9.3. We discuss our cosmological parameter constraints results in Sec. 9.4 and summarize our conclusions in Sec. 9.5.

[5] We also examined constraints from mutually consistent Platinum + A101 GRB data used in Cao et al. (2022c) and jointly analyzed them with QSO-AS, H IIG, and Mg II QSO data. Cosmological constraints from the joint QSO-AS + H IIG + Mg II QSO + Platinum + A101 data are similar to those from the QSO-AS + H IIG + Mg II QSO + A118 data, so we decided to perform further analyses with the latter that constrain fewer non-cosmological parameters.

[6] Mg II QSO and A118 data do not have the power to constrain H_0 and updated $H(z)$ and BAO data we use here provide similar constraints to those from older BAO and $H(z)$ data.

9.2 Data

In this paper we use updated $H(z)$ and BAO data, as well as other data sets, to constrain cosmological parameters. These are summarized next.

***H(z)* data**. There are 32 $H(z)$ measurements listed in Table 9.1, spanning the redshift range $0.07 \leq z \leq 1.965$. Compared with what is given in table 1 of Ryan et al. (2018), the updated $H(z)$ data here have one additional data point from Borghi et al. (2022).

BAO data. There are 12 BAO measurements listed in Table 9.2, spanning the redshift range $0.122 \leq z \leq 2.334$. The covariance matrices for given BAO data are summarized below.

The covariance matrix $\mathbf{C}$ for BAO data from du Mas des Bourboux et al. (2020) is

$$\begin{bmatrix} 1.3225 & -0.1009 \\ -0.1009 & 0.0380 \end{bmatrix}, \tag{9.1}$$

for BAO data from Gil-Marín et al. (2020) $\mathbf{C}$ is

$$\begin{bmatrix} 0.02860520 & -0.04939281 & 0.01489688 & -0.01387079 \\ -0.04939281 & 0.5307187 & -0.02423513 & 0.1767087 \\ 0.01489688 & -0.02423513 & 0.04147534 & -0.04873962 \\ -0.01387079 & 0.1767087 & -0.04873962 & 0.3268589 \end{bmatrix}, \tag{9.2}$$

for BAO data from Gil-Marín et al. (2020) and Bautista et al. (2021) $\mathbf{C}$ is

$$\begin{bmatrix} 0.1076634008565565 & -0.05831820341302727 \\ -0.05831820341302727 & 0.2838176386340292 \end{bmatrix}, \tag{9.3}$$

Table 9.1: Updated $H(z)$ data.

z	$H(z)$[a]	Reference
0.07	69.0 ± 19.6	Zhang et al. (2014)
0.09	69.0 ± 12.0	Simon et al. (2005)
0.12	68.6 ± 26.2	Zhang et al. (2014)
0.17	83.0 ± 8.0	Simon et al. (2005)
0.179	75.0 ± 4.0	Moresco et al. (2012)
0.199	75.0 ± 5.0	Moresco et al. (2012)
0.2	72.9 ± 29.6	Zhang et al. (2014)
0.27	77.0 ± 14.0	Simon et al. (2005)
0.28	88.8 ± 36.6	Zhang et al. (2014)
0.352	83.0 ± 14.0	Moresco et al. (2012)
0.3802	83.0 ± 13.5	Moresco et al. (2016)
0.4	95.0 ± 17.0	Simon et al. (2005)
0.4004	77.0 ± 10.2	Moresco et al. (2016)
0.4247	87.1 ± 11.2	Moresco et al. (2016)
0.4497	92.8 ± 12.9	Moresco et al. (2016)
0.47	89.0 ± 50.0	Ratsimbazafy et al. (2017)
0.4783	80.9 ± 9.0	Moresco et al. (2016)
0.48	97.0 ± 62.0	Stern et al. (2010)
0.593	104.0 ± 13.0	Moresco et al. (2012)
0.68	92.0 ± 8.0	Moresco et al. (2012)
0.75	98.8 ± 33.6	Borghi et al. (2022)
0.781	105.0 ± 12.0	Moresco et al. (2012)
0.875	125.0 ± 17.0	Moresco et al. (2012)
0.88	90.0 ± 40.0	Stern et al. (2010)
0.9	117.0 ± 23.0	Simon et al. (2005)
1.037	154.0 ± 20.0	Moresco et al. (2012)
1.3	168.0 ± 17.0	Simon et al. (2005)
1.363	160.0 ± 33.6	Moresco (2015)
1.43	177.0 ± 18.0	Simon et al. (2005)
1.53	140.0 ± 14.0	Simon et al. (2005)
1.75	202.0 ± 40.0	Simon et al. (2005)
1.965	186.5 ± 50.4	Moresco (2015)

[a] km s^{-1} Mpc^{-1}.

Table 9.2: Updated BAO data.

z	Measurement[a]	Value	Reference
0.122	$D_V\,(r_{s,\mathrm{fid}}/r_s)$	539 ± 17	Carter et al. (2018)
0.38	D_M/r_s	10.23406	Gil-Marín et al. (2020)[b]
0.38	D_H/r_s	24.98058	Gil-Marín et al. (2020)[b]
0.51	D_M/r_s	13.36595	Gil-Marín et al. (2020)[b]
0.51	D_H/r_s	22.31656	Gil-Marín et al. (2020)[b]
0.698	D_M/r_s	17.85823691865007	[c]
0.698	D_H/r_s	19.32575373059217	[c]
0.81	D_A/r_s	10.75 ± 0.43	DES Collaboration (2019b)
1.48	D_M/r_s	30.6876	[d]
1.48	D_H/r_s	13.2609	[d]
2.334	D_M/r_s	37.5	[e]
2.334	D_H/r_s	8.99	[e]

[a] D_V, r_s, $r_{s,\mathrm{fid}}$, D_M, D_H, and D_A have units of Mpc.
[b] The four measurements from Gil-Marín et al. (2020) are correlated; see equation (9.2) for their correlation matrix.
[c] The two measurements from Gil-Marín et al. (2020) and Bautista et al. (2021) are correlated; see equation (9.3) for their correlation matrix.
[d] The two measurements from Neveux et al. (2020) and Hou et al. (2021) are correlated; see equation (9.4) for their correlation matrix.
[e] The two measurements from du Mas des Bourboux et al. (2020) are correlated; see equation (9.1) for their correlation matrix.

and for BAO data from Neveux et al. (2020) and Hou et al. (2021) $\mathbf{C}$ is

$$\begin{bmatrix} 0.63731604 & 0.1706891 \\ 0.1706891 & 0.30468415 \end{bmatrix}. \tag{9.4}$$

SN Ia data. As in Cao et al. (2022a), we use SN Ia data that consist of 1048 Pantheon (Scolnic et al., 2018) and 20 binned DES 3yr (DES Collaboration, 2019d) SNe Ia, spanning the redshift ranges $0.01 < z < 2.3$ and $0.015 \leq z \leq 0.7026$, respectively.

QSO angular size (QSO-AS) data. There are 120 QSO-AS measurements listed in table 1 of Cao et al. (2017b), spanning the redshift range $0.462 \leq z \leq 2.73$. The measured quantities are z and the angular size $\theta(z)$ with the characteristic linear size of QSOs in the sample, $l_{\rm m}$, as a free parameter to be constrained. The angular size $\theta(z) = l_{\rm m}/D_A(z)$, where $D_A(z)$ is the angular diameter distance. A detailed description of the use of these data can be found in Cao et al. (2022a).

H II G data. There are 181 H II G measurements listed in table A3 of González-Morán et al. (2021), with 107 low-z data from Chávez et al. (2014) recalibrated by González-Morán et al. (2019), spanning the redshift range $0.0088 \leq z \leq 0.16417$, and 74 high-$z$ data spanning the redshift range $0.63427 \leq z \leq 2.545$. The measured quantities are z, H II G flux $F(\mathrm{H}\beta)$, and velocity dispersion σ.

Mg II QSO sample. The Mg II QSO sample consists of 78 QSOs listed in table A1 of Khadka et al. (2021a), spanning the redshift range $0.0033 \leq z \leq 1.89$. Mg II QSO data obey the radius-luminosity $(R-L)$ relation and the measured quantities are the time delay τ and QSO flux F_{3000} measured at 3000 Å.

A118 sample. The A118 sample includes 118 long GRBs listed in table 7 of Khadka et al. (2021b), spanning the redshift range $0.3399 \leq z \leq 8.2$. A118 data obey the Amati (or $E_{\rm p} - E_{\rm iso}$) correlation and the measured quantities are z, rest-frame spectral peak energy $E_{\rm p}$, and measured bolometric fluence $S_{\rm bolo}$, computed in the standard

rest-frame energy band $1 - 10^4$ keV.[7]

Platinum + A101 sample. The Platinum sample includes 50 long GRBs listed in table A1 of Cao et al. (2022c), spanning the redshift range $0.553 \leq z \leq 5.0$. The A101 sample includes 101 long GRBs with common GRBs between the Platinum and the A118 samples excluded, spanning the redshift range $0.3399 \leq z \leq 8.2$. The Platinum GRBs obey the three-dimensional Dainotti correlation and the measured quantities are z, characteristic time scale T_X^*, the measured γ-ray energy flux F_X at T_X^*, the prompt peak flux $F_{\rm peak}$ over a 1 s interval, and the X-ray spectral index of the plateau phase β'.

9.3 Data Analysis Methodology

In this paper we determine constraints on the cosmological model parameters, and non-cosmological parameters related to different data sets, by maximizing the likelihood function, $\mathscr{L}$. These analyses are performed by using the Markov chain Monte Carlo (MCMC) code MontePython (Audren et al., 2013), with the physics coded in the class code. In Table 9.3, we list the flat prior ranges of the constrained free parameters.

The detailed descriptions for the likelihood functions of $H(z)$, BAO, H II G, QSO-AS, and SN Ia data can be found in Cao et al. (2020, 2021a,b), whereas those of Platinum, A118/A101, and Mg II QSO data can be found in Cao et al. (2022c) and Khadka et al. (2021a). One can also find the definitions of the Akaike Information Criterion (AIC) and the Bayesian Information Criterion (BIC) as well as the deviance information criterion (DIC) in Cao et al. (2022c).[8] We compute ΔAIC, ΔBIC, and ΔDIC differences for the other five cosmological models relative to the flat ΛCDM reference model values. Negative (positive)

[7] As noted in Liu et al. (2022), the $E_{\rm p}$ value for GRB081121 reported in table 5 of Fana Dirirsa et al. (2019), and used in our analysis here, is incorrect. One should instead use the correct value provided in table 4 of Wang et al. (2016), $E_{\rm p} = 871 \pm 123$ keV. However, since this data point has negligible effect on the cosmological-model and GRB-correlation parameter constraints and the conclusions remain unchanged after correcting it, we do not revise our Amati-correlated GRB results here and in Cao et al. (2021a, 2022b,c). In future analyses we will use the correct Wang et al. (2016) value.

[8] Unlike AIC and BIC, DIC estimates the effective number of free parameters.

values of ΔAIC, ΔBIC, or ΔDIC indicate that the model under investigation fits the data compilation better (worse) than does the reference model. Relative to the model with minimum AIC(BIC/DIC), ΔAIC(BIC/DIC) $\in (0, 2]$ is defined to be weak evidence against the model under investigation, ΔAIC(BIC/DIC) $\in (2, 6]$ is positive evidence against the model under investigation, ΔAIC(BIC/DIC) $\in (6, 10]$ is strong evidence against the model under investigation, and ΔAIC(BIC/DIC) > 10 is very strong evidence against the model under investigation.

As in Cao et al. (2022c), we assume one massive and two massless neutrino species, with the effective number of relativistic neutrino species $N_{\rm eff} = 3.046$ and the total neutrino mass $\sum m_\nu = 0.06$ eV. Therefore, here the current value of the non-relativistic neutrino physical energy density parameter, $\Omega_\nu h^2 = \sum m_\nu/(93.14\ {\rm eV})$, is not a free parameter, and along with the current values of the observationally-constrained baryonic ($\Omega_b h^2$) and cold dark matter ($\Omega_c h^2$) physical energy density parameters, Ω_{m0} is derived as $\Omega_{m0} = (\Omega_\nu h^2 + \Omega_b h^2 + \Omega_c h^2)/h^2$, where h is the Hubble constant in units of 100 km s^{-1} Mpc^{-1}.

9.4 Results

The posterior one-dimensional probability distributions and two-dimensional confidence regions of the cosmological and non-cosmological parameters are shown in Figs. 9.1–9.6, in red (QSO-AS + H II G and $H(z)$ + BAO + SN), green (QSO-AS + H II G + Mg II QSO + A118), orange (Mg II QSO + A118 and QSO-AS + H II G + Mg II QSO + Platinum + A101, QHMPA101), and blue ($H(z)$ + BAO + SN + QSO-AS + H II G + Mg II QSO + A118, HzBSNQHMA). The unmarginalized best-fitting parameter values, as well as the corresponding $-2\ln\mathscr{L}_{\rm max}$, AIC, BIC, DIC, ΔAIC, ΔBIC, and ΔDIC values, for all models and data combinations, are listed in Table 9.4, whereas the marginalized posterior mean parameter values and uncertainties ($\pm1\sigma$ error bars or 2σ limits), for all models and data combinations, are listed in Table 9.5.[9]

In the non-flat ΛCDM and flat and non-flat ϕCDM models, Mg II QSO + A118 data

[9]We use PYTHON package GETDIST (Lewis, 2019) to analyze the samples and generate the plots.

Table 9.3: Flat priors of the constrained parameters.

Parameter	Prior
Cosmological Parameters	
H_0 [a]	[None, None]
$\Omega_b h^2$ [b]	[0, 1]
$\Omega_c h^2$ [c]	[0, 1]
Ω_{k0}	[-2, 2]
α	[0, 10]
$w_{\rm X}$	[-5, 0.33]
Non-Cosmological Parameters	
k	[0, 5]
$b_{\rm M}$	[0, 10]
$\sigma_{\rm int}$	[0, 5]
a	[-5, 5]
$b_{\rm P}$	[-5, 5]
C_o	[-50, 50]
β	[0, 5]
γ	[0, 300]
$l_{\rm m}$	[None, None]

[a] km s^{-1} Mpc^{-1}. In the Mg II QSO + A118 case, H_0 is set to be 70 km s^{-1} Mpc^{-1}, while in other cases, the prior range is irrelevant (unbounded).
[b] In the Mg II QSO + A118 case, $\Omega_b h^2$ is set to be 0.0245, i.e. $\Omega_b = 0.05$.
[c] In the Mg II QSO + A118 case, $\Omega_{m0} \in [0, 1]$ is ensured.

mildly favor currently decelerating cosmological expansion, which is most likely caused by the choice of fixed Ω_b and H_0 values. All other data combinations more favor currently accelerating cosmological expansion.

9.4.1 Constraints from $H(z)$, BAO, and SN Ia data

The updated $H(z)$ + BAO results derived here are quite similar to the $H(z)$ + BAO results given in Cao et al. (2022c), so we do not discuss them in detail. $H(z)$ + BAO + SN is a more important data combination, so here we discuss these constraints in more detail. While the computation of the $H(z)$ + BAO + SN results reported in Cao et al. (2022a) neglected the late-time contribution of non-relativistic neutrinos, in this paper, where we account for the contributions of one massive and two massless neutrino species, we find very similar constraints.

The constraints from $H(z)$ + BAO + SN data on Ω_{m0} range from a low of 0.287 ± 0.017 (flat ϕCDM) to a high of $0.304^{+0.014}_{-0.015}$ (flat ΛCDM), with a difference of 0.75σ.

The H_0 constraints range from a low of 68.29 ± 1.78 km s^{-1} Mpc^{-1} (flat ϕCDM) to a high of 69.04 ± 1.77 km s^{-1} Mpc^{-1} (flat ΛCDM), with a difference of 0.30σ, which are 0.09σ (flat ϕCDM) and 0.31σ (flat ΛCDM) higher than the median statistics estimate of $H_0 = 68 \pm 2.8$ km s^{-1} Mpc^{-1} (Chen & Ratra, 2011), and 2.23σ (flat ϕCDM) and 1.89σ (flat ΛCDM) lower than the local Hubble constant measurement of $H_0 = 73.2 \pm 1.3$ km s^{-1} Mpc^{-1} (Riess et al., 2021).

The constraints on Ω_{k0} are 0.040 ± 0.070, -0.001 ± 0.098, and $-0.038^{+0.071}_{-0.085}$ for non-flat ΛCDM, XCDM, and ϕCDM, respectively. Although non-flat hypersurfaces are mildly favored, flat hypersurfaces are well within 1σ.

There is a slight preference for dark energy dynamics. For flat (non-flat) XCDM, $w_{\rm X} = -0.941 \pm 0.064$ ($w_{\rm X} = -0.948^{+0.098}_{-0.068}$), with central values being 0.92σ (0.76σ) higher than $w_{\rm X} = -1$; and for flat (non-flat) ϕCDM, $\alpha = 0.324^{+0.122}_{-0.264}$ ($\alpha = 0.382^{+0.151}_{-0.299}$), with central values being 1.23σ (1.28σ) away from $\alpha = 0$.

9.4.2 Constraints from QSO-AS, H II G, Mg II QSO, A118, and Platinum + A101 data

Given our improved treatment of neutrinos in this paper, compared to our earlier analyses, we have reanalyzed data we had previously studied.

As shown in Cao et al. (2022a), QSO-AS data alone do not deal well with H_0, so an unbounded prior range for H_0 makes it hard for the computation to converge and results in an unreasonably high H_0 value and so an unreasonably low $l_{\rm m}$ value. However, we expect constraints on the other cosmological parameters consistent with those given in Cao et al. (2022a). Constraints from H II G data are consistent with what are given in Cao et al. (2022a). Constraints from Mg II QSO data are consistent with those described in Khadka et al. (2021a) while those from A118 and Platinum + A101 data are consistent with those in Cao et al. (2022c). We find that cosmological parameter constraints from those four data sets are mutually consistent so they can be used to do joint analyses. As expected, cosmological parameter constraints from the joint QSO-AS + H II G data and Mg II QSO + A118 data are indeed mutually consistent, as seen in Tables 9.4 and 9.5. We do not discuss these results in detail since there are no significant changes compared to those derived in our earlier analyses. We consider the joint analyses results of QSO-AS + H II G + Mg II QSO + A118 data to be more useful and discuss these in more detail next.[10]

The constraints from QSO-AS + H II G + Mg II QSO + A118 data on Ω_{m0} range from a low of $0.175^{+0.075}_{-0.081}$ (flat ϕCDM) to a high of $0.314^{+0.051}_{-0.044}$ (flat XCDM), with a difference of 1.60σ. Following the pattern of H II G data, the Ω_{m0} difference is relatively large.

The H_0 constraints range from a low of 70.38 ± 1.84 km s^{-1} Mpc^{-1} (non-flat ϕCDM) to a high of $73.14^{+2.14}_{-2.48}$ km s^{-1} Mpc^{-1} (flat XCDM), with a difference of 0.89σ, which are 0.71σ (non-flat ϕCDM) and 1.37σ (flat XCDM) higher than the median statistics estimate of $H_0 = 68 \pm 2.8$ km s^{-1} Mpc^{-1} (Chen & Ratra, 2011), and 1.25σ (non-flat ϕCDM) and

[10]We note that cosmological parameter constraints from Platinum, A101, and Platinum + A101 data are also consistent with those from QSO-AS, H II G, and Mg II QSO data, so we also investigate the joint QSO-AS + H II G + Mg II QSO + Platinum + A101 (QHPMAP101) data combination. As seen in Tables 9.4 and 9.5, we find no significant differences between the QHPMAP101 cosmological constraints and those from the QSO-AS + H II G + Mg II QSO + A118 data combination that contains fewer non-cosmological parameters.

0.02σ (flat XCDM) lower than the local Hubble constant measurement of $H_0 = 73.2 \pm 1.3$ km s^{-1} Mpc^{-1} (Riess et al., 2021).

The constraints on Ω_{k0} are $-0.139^{+0.116}_{-0.228}$, $0.054^{+0.227}_{-0.238}$, and $0.044^{+0.104}_{-0.256}$ for non-flat ΛCDM, XCDM, and ϕCDM, respectively. As opposed to $H(z)$ + BAO + SN results, non-flat ΛCDM mildly favors closed hypersurfaces, whereas non-flat XCDM and non-flat ϕCDM mildly favor open hypersurfaces. However, flat hypersurfaces are well within 1σ.

There are mild preferences for dark energy dynamics. For flat (non-flat) XCDM, $w_{\rm X} = -1.836^{+0.804}_{-0.419}$ ($w_{\rm X} = -2.042^{+1.295}_{-0.451}$), with central values being 1.04σ (0.80σ) lower than $w_{\rm X} = -1$; and for flat (non-flat) ϕCDM, $\alpha < 6.756$ ($\alpha < 7.239$), with $\alpha = 0$ being within 1σ.

9.4.3 Constraints from $H(z)$ + BAO + SN + QSO-AS + H II G + Mg II QSO + A118 (HzBSNQHMA) data

Cosmological parameter constraints from $H(z)$ + BAO + SN data are consistent with those from QSO-AS + H II G + Mg II QSO + A118 data. From model to model, there are differences, ranging from -0.41σ (flat XCDM) to 1.45σ (flat ϕCDM), between Ω_{m0} constraints from $H(z)$ + BAO + SN data and those from QSO-AS + H II G + Mg II QSO + A118 data; and there are differences, ranging from 0.73σ (non-flat ϕCDM) to 1.48σ (flat XCDM), between H_0 constraints from QSO-AS + H II G + Mg II QSO + A118 data and those from $H(z)$ + BAO + SN data. For the XCDM parametrizations, $H(z)$ + BAO + SN data slightly prefer non-phantom dark energy dynamics, whereas QSO-AS + H II G + Mg II QSO + A118 data prefer phantom dark energy dynamics, however, their differences are within 1σ. As can be seen in the (d) panels of Figs. 9.1–9.6, the two-dimensional posterior cosmological constraints from $H(z)$ + BAO + SN data and QSO-AS + H II G + Mg II QSO + A118 data are significantly more mutually consistent than the less than 1.5σ differences between the maximum and minimum one-dimensional posterior mean values discussed above. Consequently we can combine these data in a joint HzBSNQHMA data analysis; we discuss the results from this analysis next.

The constraints from HzBSNQHMA data on Ω_{m0} range from a low of 0.286 ± 0.015 (flat

ϕCDM) to a high of 0.300 ± 0.012 (flat ΛCDM), with a difference of 0.73σ.

The H_0 constraints range from a low of 69.50 ± 1.14 km s^{-1} Mpc^{-1} (flat ϕCDM) to a high of 69.87 ± 1.13 km s^{-1} Mpc^{-1} (flat ΛCDM), with a difference of 0.23σ, which are 0.50σ (flat ϕCDM) and 0.62σ (flat ΛCDM) higher than the median statistics estimate of $H_0 = 68 \pm 2.8$ km s^{-1} Mpc^{-1} (Chen & Ratra, 2011), and 2.14σ (flat ϕCDM) and 1.93σ (flat ΛCDM) lower than the local Hubble constant measurement of $H_0 = 73.2 \pm 1.3$ km s^{-1} Mpc^{-1} (Riess et al., 2021).[11]

The constraints on Ω_{k0} are 0.018 ± 0.059, $-0.009^{+0.077}_{-0.083}$, and $-0.040^{+0.064}_{-0.072}$ for non-flat ΛCDM, XCDM, and ϕCDM, respectively. Following the same pattern as $H(z)$ + BAO + SN data results, flat hypersurfaces are also well within 1σ.

There is a slight preference for dark energy dynamics. For flat (non-flat) XCDM, $w_{\rm X} = -0.959 \pm 0.059$ ($w_{\rm X} = -0.959^{+0.090}_{-0.063}$), with central values being 0.69σ (0.65σ) higher than $w_{\rm X} = -1$; and for flat (non-flat) ϕCDM, $\alpha = 0.249^{+0.069}_{-0.239}$ ($\alpha = 0.316^{+0.101}_{-0.292}$), with central values being 1.04σ (1.08σ) away from $\alpha = 0$.

9.4.4 Model Comparison

From the AIC, BIC, and DIC values listed in Table 9.4, we find the following results:

1) **AIC** $H(z)$ + BAO data favor flat ϕCDM the most, Mg II QSO + A118 data favor flat XCDM the most, QSO-AS + H IIG data favor non-flat XCDM the most, and the other data combinations favor flat ΛCDM the most. However the evidence against the rest of the models/parametrizations is either only weak or positive.

2) **BIC** All data combinations favor flat ΛCDM the most. $H(z)$ + BAO data only provide weak or positive evidence against other models/parametrizations.

[11] Other local determinations of H_0 result in somewhat lower central values with somewhat larger error bars (Breuval et al., 2020; Dhawan et al., 2018; Efstathiou, 2020; Fernández Arenas et al., 2018; Freedman, 2021; Khetan et al., 2021; Rameez & Sarkar, 2021; Rigault et al., 2015; Zhang et al., 2017). Our H_0 determinations here are consistent with earlier median statistics estimates (Calabrese et al., 2012; Gott et al., 2001) and with other recent H_0 determinations (Birrer et al., 2020; Blum et al., 2020; Boruah et al., 2021; Chen et al., 2017; Cuceu et al., 2019; DES Collaboration, 2018; Denzel et al., 2021; Domínguez et al., 2019; Gómez-Valent & Amendola, 2018; Harvey, 2020; Kim et al., 2020; Lin & Ishak, 2021; Lyu et al., 2020; Philcox et al., 2020; Planck Collaboration, 2020; Pogosian et al., 2020; Schöneberg et al., 2019; Wu et al., 2022; Zeng & Yan, 2019; Zhang & Huang, 2021).

Both Mg II QSO + A118 and QSO-AS + H IIG data provide strong (very strong) evidence against non-flat XCDM (non-flat ϕCDM) and positive evidence against the others.

QSO-AS + H IIG + Mg II QSO + A118 data provide strong (very strong) evidence against flat ϕCDM (non-flat XCDM and non-flat ϕCDM) and positive evidence against non-flat ΛCDM and flat XCDM.

$H(z)$ + BAO + SN data provide strong (very strong) evidence against non-flat ΛCDM (non-flat XCDM and non-flat ϕCDM) and positive evidence against flat XCDM and flat ϕCDM.

$H(z)$ + BAO + SN + QSO-AS + H IIG + Mg II QSO + A118 data provide very strong evidence against non-flat XCDM and non-flat ϕCDM, and strong evidence against the others.

QSO-AS + H IIG + Mg II QSO + Platinum + A101 data provide strong (very strong) evidence against flat ϕCDM (non-flat XCDM and non-flat ϕCDM) and positive evidence against non-flat ΛCDM and flat XCDM.

3) **DIC** $H(z)$ + BAO, Mg II QSO + A118, and $H(z)$ + BAO + SN data favor flat ϕCDM the most, and the other data combinations favor flat ΛCDM the most. There is strong evidence against non-flat XCDM from QSO-AS + H IIG data, strong evidence against non-flat ϕCDM from QSO-AS + H IIG, QSO-AS + H IIG + Mg II QSO + A118, and QSO-AS + H IIG + Mg II QSO + Platinum + A101 data, and weak or positive evidence against the others from the remaining data sets.

Perhaps the most reliable summary conclusion is that, based on DIC, the $H(z)$ + BAO + SN + QSO-AS + H IIG + Mg II QSO + A118 data combination does not provide strong evidence against any of the cosmological models/parametrizations.

9.5 Conclusion

In this paper we use many of the most up-to-date available non-CMB data sets to determine cosmological constraints. We analyze 32 $H(z)$, 12 BAO, 1048 Pantheon SN Ia, 20 binned DES-3yr SN Ia, 120 QSO-AS, 181 H II G, 78 Mg II QSO, 118 (101) A118 (A101) GRB, and 50 Platinum GRB measurements and find that the cosmological constraints from each data set are mutually consistent. We find very small differences between cosmological constraints determined from QSO-AS + H II G + Mg II QSO + A118 data and those from QSO-AS + H II G + Mg II QSO + Platinum + A101 data, so report only the cosmological constraints from joint $H(z)$ + BAO + SN + QSO-AS + H II G + Mg II QSO + A118 (HzBSNQHMA) data.

The HzBSNQHMA data provide a fairly restrictive summary value[12] of $\Omega_{m0} = 0.295 \pm 0.017$ that agrees well with many other recent measurements and a fairly restrictive summary value of $H_0 = 69.7 \pm 1.2$ km s^{-1} Mpc^{-1} that is in better agreement with the result of Chen & Ratra (2011) than with the result of Riess et al. (2021).[13] Our H_0 measurement here lies in the middle of the flat ΛCDM model result of Planck Collaboration (2020) and the local expansion rate result of Riess et al. (2021), slightly closer to the former. Based on DIC, the HzBSNQHMA data compilation prefers flat ΛCDM the most, but does not rule out mild dark energy dynamics or a little spatial curvature energy density (evidence against them is either weak or positive).

We hope that in the near future the quality and amount of the types of lower-redshift, non-CMB, data we have used here will improve enough to result in cosmological parameter error bars comparable to those from *Planck* CMB anisotropy data.

[12] As in Cao et al. (2021b, 2022a), the summary central value is computed from the mean of the two central-most of the six mean values and the summary uncertainty is computed from the quadrature sum of the systematic uncertainty, defined to be half of the difference between the two central-most mean values, and the statistical uncertainty, defined to be the average of the error bars of the two central-most results.

[13] Our model-independent H_0 error bar is slightly smaller than that of Riess et al. (2021) and is a factor of 2.2 larger than that of the flat ΛCDM model (Planck Collaboration, 2020) TT,TE,EE+lowE+lensing CMB anisotropy H_0 error bar while our Ω_{m0} error bar is a factor of 2.3 larger than the corresponding *Planck* flat ΛCDM one.

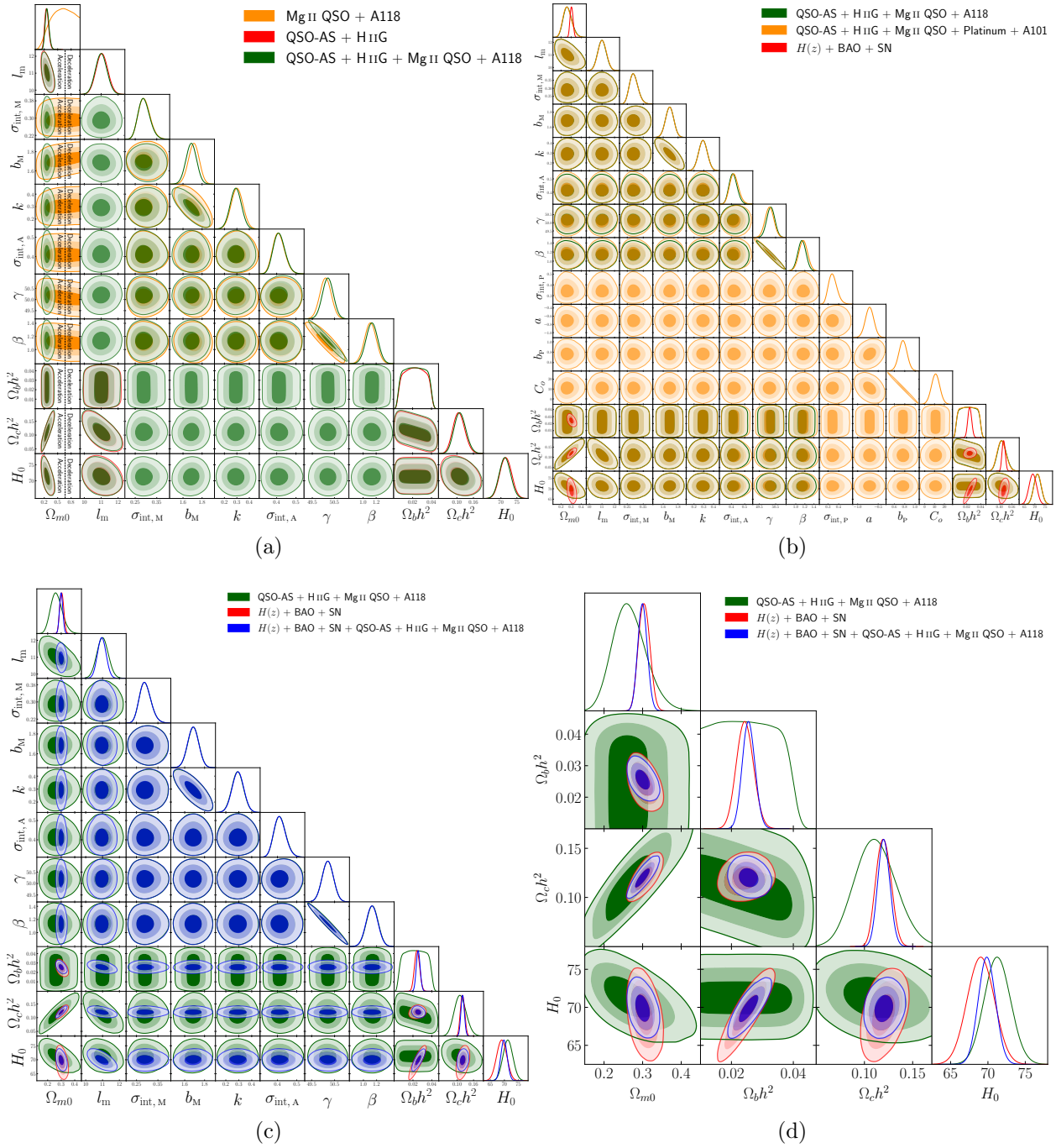

Figure 9.1: One-dimensional likelihood distributions and 1σ, 2σ, and 3σ two-dimensional likelihood confidence contours for flat ΛCDM from various combinations of data. The zero-acceleration black dashed lines in some (a) panels divide the parameter space into regions associated with currently-accelerating (left) and currently-decelerating (right) cosmological expansion.

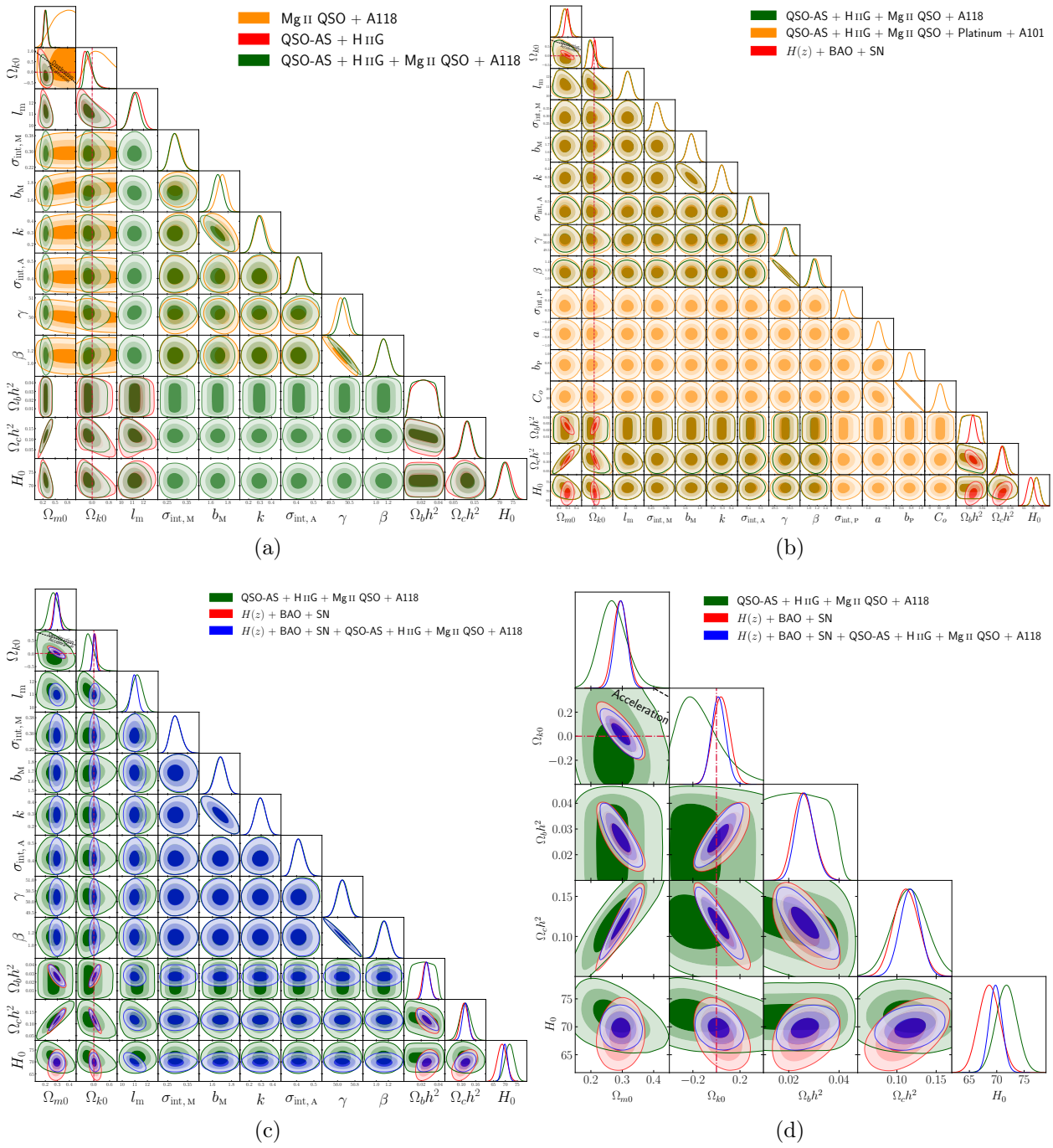

Figure 9.2: Same as Fig. 9.1 but for non-flat ΛCDM. The zero-acceleration black dashed lines divide the parameter space into regions associated with currently-accelerating (below left) and currently-decelerating (above right) cosmological expansion.

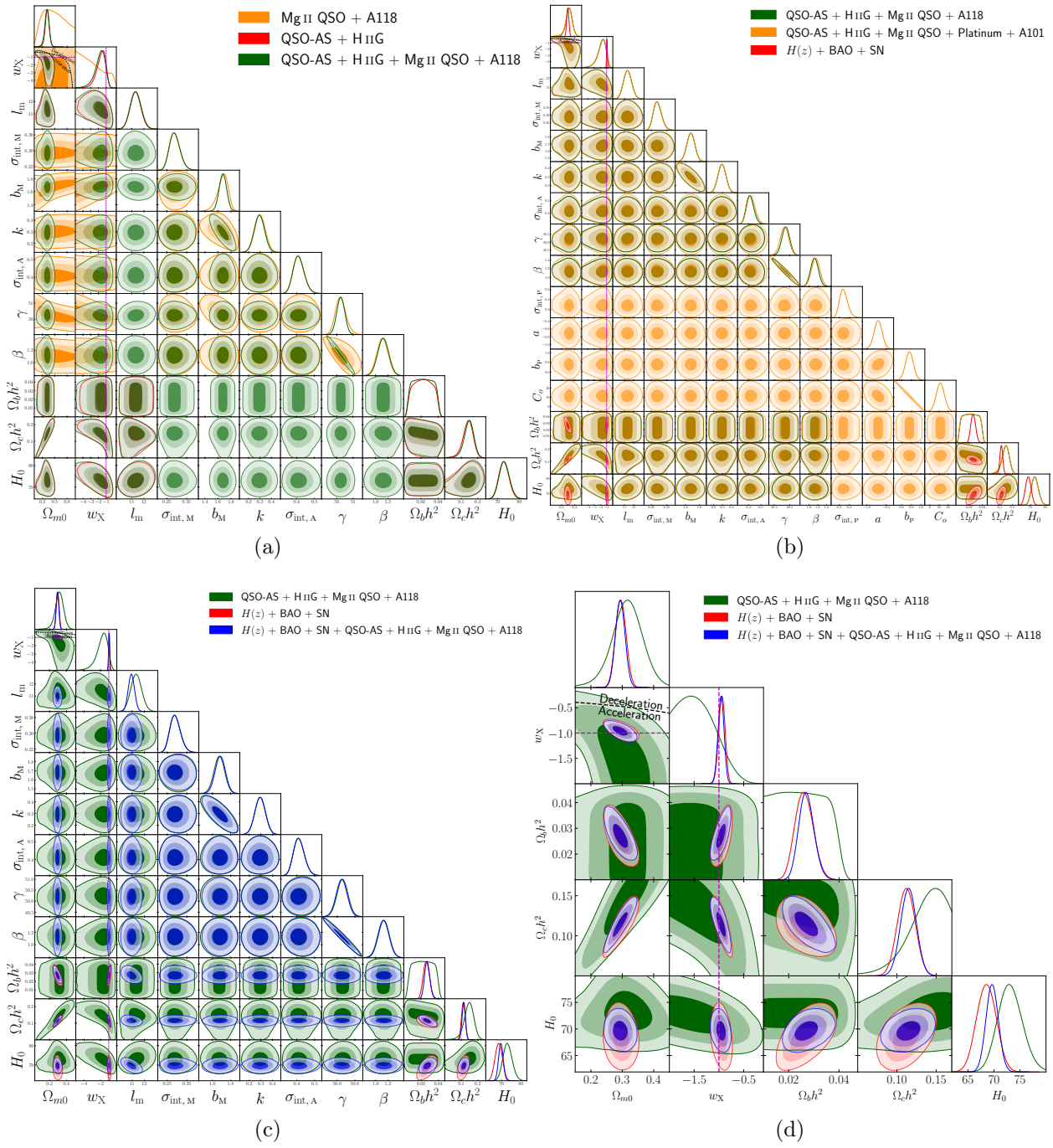

Figure 9.3: One-dimensional likelihood distributions and 1σ, 2σ, and 3σ two-dimensional likelihood confidence contours for flat XCDM from various combinations of data. The zero-acceleration black dashed lines divide the parameter space into regions associated with currently-accelerating (either below left or below) and currently-decelerating (either above right or above) cosmological expansion. The magenta dashed lines represent $w_{\rm X} = -1$, i.e. flat ΛCDM.

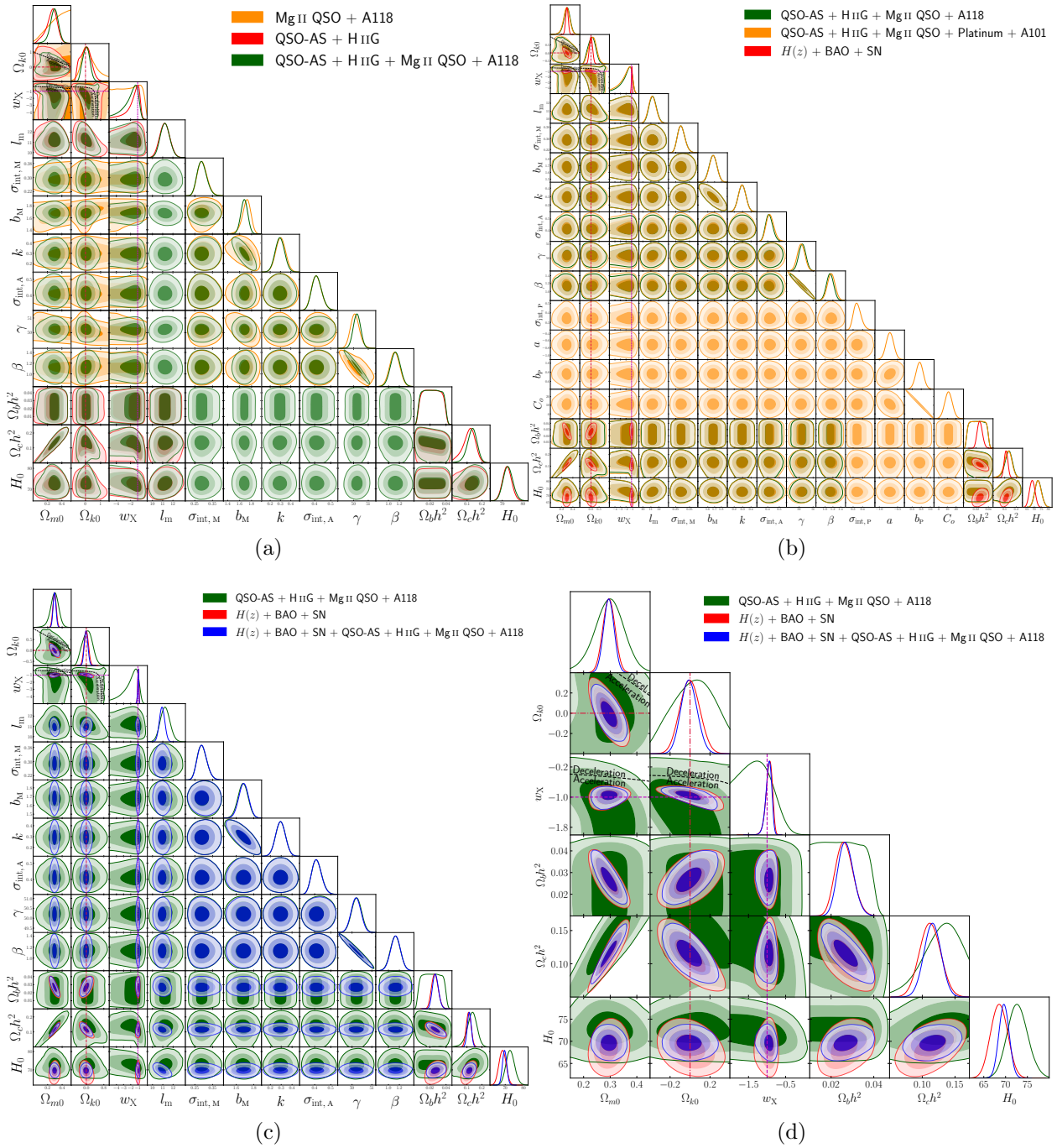

Figure 9.4: Same as Fig. 9.3 but for non-flat XCDM. The zero-acceleration black dashed lines are computed for the third cosmological parameter set to the $H(z)$ + BAO data best-fitting values listed in Table 9.4, and divide the parameter space into regions associated with currently-accelerating (either below left or below) and currently-decelerating (either above right or above) cosmological expansion. The crimson dash-dot lines represent flat hypersurfaces, with closed spatial hypersurfaces either below or to the left. The magenta dashed lines represent $w_{\rm X} = -1$, i.e. non-flat ΛCDM.

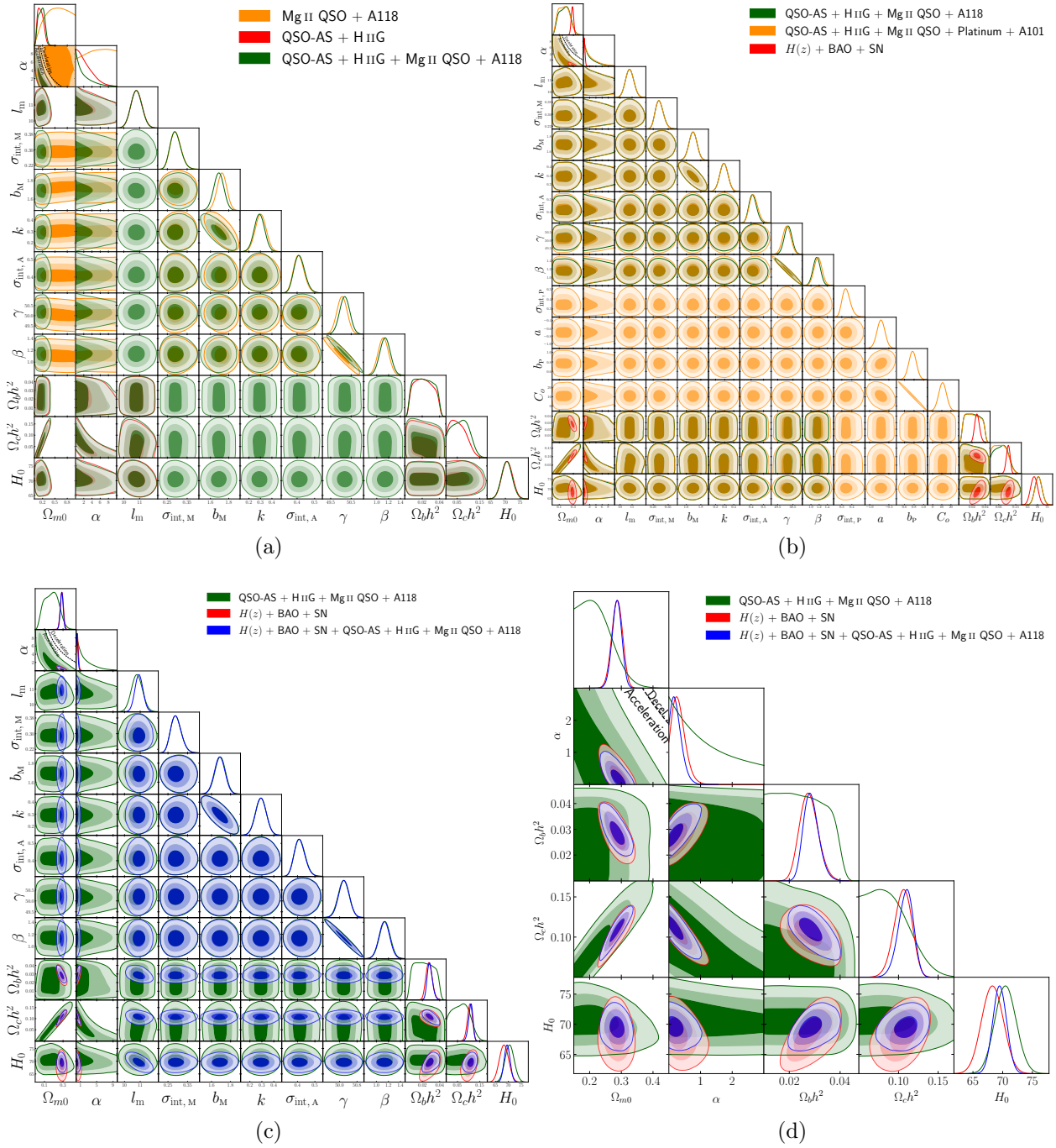

Figure 9.5: One-dimensional likelihood distributions and 1σ, 2σ, and 3σ two-dimensional likelihood confidence contours for flat ϕCDM from various combinations of data. The zero-acceleration black dashed lines divide the parameter space into regions associated with currently-accelerating (below left) and currently-decelerating (above right) cosmological expansion. The $\alpha = 0$ axes correspond to flat ΛCDM.

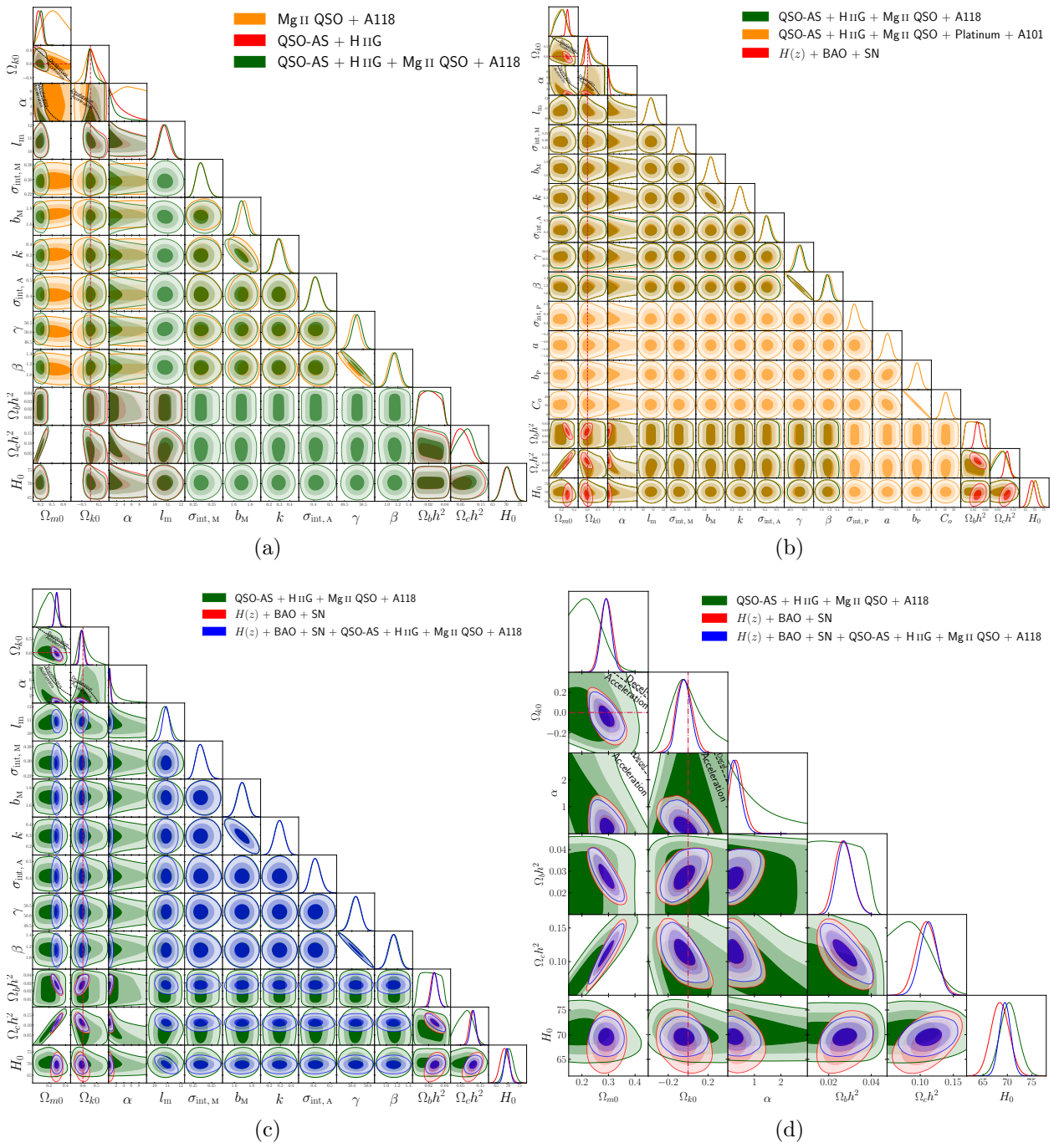

Figure 9.6: Same as Fig. 9.5 but for non-flat ϕCDM. The zero-acceleration black dashed lines are computed for the third cosmological parameter set to the $H(z)$ + BAO data best-fitting values listed in Table 9.4, and divide the parameter space into regions associated with currently-accelerating (below left) and currently-decelerating (above right) cosmological expansion. The crimson dash-dot lines represent flat hypersurfaces, with closed spatial hypersurfaces either below or to the left. The $\alpha = 0$ axes correspond to non-flat ΛCDM.

Table 9.4: Unmarginalized best-fitting parameter values for all models from various combinations of data.

Model	Data set	$\Omega_b h^2$	$\Omega_c h^2$	Ω_{m0}	Ω_{k0}	$w_{\rm X}/\alpha$[a]	H_0[b]	$l_{\rm m}$[c]	$\sigma_{\rm int,M}$	$b_{\rm M}$	k	$\sigma_{\rm int,A}$	γ	β	$\sigma_{\rm int,P}$	a	$b_{\rm P}$	C_o	$-2\ln\mathscr{L}_{\rm max}$	AIC	BIC	DIC	ΔAIC	ΔBIC	ΔDIC
	$H(z)$ + BAO	0.0244	0.1181	0.301	–	–	68.98	–	–	–	–	–	–	–	–	–	–	–	25.64	31.64	36.99	32.32	0.00	0.00	0.00
	Mg II QSO + A118	–	0.2526	0.567	–	–	–	–	0.286	1.711	0.300	0.398	50.12	1.105	–	–	–	–	159.64	173.64	196.59	173.37	0.00	0.00	0.00
Flat	QSO-AS + H II G	0.0332	0.0947	0.251	–	–	71.53	11.06	–	–	–	–	–	–	–	–	–	–	786.45	794.45	809.28	792.69	0.00	0.00	0.00
ΛCDM	QSO-AS + H II G + Mg II QSO + A118	0.0183	0.1127	0.258	–	–	71.50	11.04	0.282	1.682	0.294	0.404	50.23	1.124	–	–	–	–	947.34	967.34	1009.43	966.23	0.00	0.00	0.00
	$H(z)$ + BAO + SN	0.0242	0.1191	0.304	–	–	68.86	–	–	–	–	–	–	–	–	–	–	–	1082.39	1088.39	1103.44	1089.92	0.00	0.00	0.00
	HzNBSNQHMA[e]	0.0258	0.1207	0.300	–	–	70.06	10.93	0.286	1.671	0.296	0.406	50.26	1.110	–	–	–	–	2031.30	2051.30	2105.13	2051.86	0.00	0.00	0.00
	QHMPA101[e]	0.0197	0.1144	0.264	–	–	71.41	11.02	0.283	1.673	0.315	0.410	50.11	1.169	0.321	−0.746	0.773	10.81	964.62	992.62	1052.44	990.65	0.00	0.00	0.00
	$H(z)$ + BAO	0.0260	0.1098	0.292	0.048	–	68.35	–	–	–	–	–	–	–	–	–	–	–	25.30	33.30	40.43	33.87	1.66	3.44	1.54
	Mg II QSO + A118	–	0.2692	0.601	0.252	–	–	–	0.281	1.713	0.308	0.401	50.07	1.117	–	–	–	–	159.65	175.65	201.87	174.46	2.01	5.28	1.09
Non-flat	QSO-AS + H II G	0.0228	0.1145	0.260	−0.360	–	72.91	11.60	–	–	–	–	–	–	–	–	–	–	784.18	794.18	812.71	793.24	−0.27	3.43	0.55
ΛCDM	QSO-AS + H II G + Mg II QSO + A118	0.0261	0.1186	0.278	−0.254	–	72.25	11.29	0.282	1.678	0.299	0.410	50.27	1.106	–	–	–	–	945.97	967.97	1014.27	966.91	0.63	4.84	0.69
	$H(z)$ + BAO + SN	0.0255	0.1121	0.295	0.035	–	68.53	–	–	–	–	–	–	–	–	–	–	–	1082.11	1090.11	1110.16	1091.17	1.72	6.72	1.24
	HzBSNQHMA[d]	0.0261	0.1182	0.297	0.008	–	69.90	10.94	0.281	1.674	0.301	0.400	50.20	1.126	–	–	–	–	2031.26	2053.26	2112.48	2053.69	1.96	7.35	1.84
	QHMPA101[e]	0.0246	0.1161	0.276	−0.221	–	71.56	11.37	0.287	1.682	0.304	0.411	50.20	1.132	0.329	−0.674	0.790	9.64	963.83	993.83	1057.92	992.04	1.21	5.48	1.39
	$H(z)$ + BAO	0.0296	0.0951	0.290	–	−0.754	65.79	–	–	–	–	–	–	–	–	–	–	–	22.39	30.39	37.52	30.63	−1.25	0.53	−1.69
	Mg II QSO + A118	–	0.0448	0.143	–	−4.972	–	–	0.279	1.554	0.292	0.407	50.65	1.126	–	–	–	–	156.84	172.84	199.07	174.36	−0.80	2.48	0.99
Flat	QSO-AS + H II G	0.0174	0.1308	0.285	–	−1.280	72.32	11.23	–	–	–	–	–	–	–	–	–	–	786.05	796.05	814.58	795.03	1.60	5.30	2.34
XCDM	QSO-AS + H II G + Mg II QSO + A118	0.0069	0.1558	0.307	–	−1.505	72.94	11.32	0.282	1.679	0.290	0.401	50.24	1.122	–	–	–	–	946.23	968.23	1014.52	967.53	0.89	5.09	1.31
	$H(z)$ + BAO + SN	0.0258	0.1115	0.295	–	−0.940	68.37	–	–	–	–	–	–	–	–	–	–	–	1081.34	1089.34	1109.40	1090.43	0.95	5.96	0.50
	HzBSNQHMA[d]	0.0266	0.1162	0.296	–	−0.975	69.62	10.94	0.280	1.696	0.278	0.406	50.24	1.118	–	–	–	–	2030.88	2052.88	2112.10	2053.30	1.58	6.97	1.44
	QHMPA101[e]	0.0176	0.1450	0.311	–	−1.573	72.46	11.41	0.276	1.686	0.294	0.417	50.12	1.168	0.326	−0.682	0.756	11.45	963.77	993.77	1057.86	992.26	1.15	5.42	1.61
	$H(z)$ + BAO	0.0289	0.0985	0.296	−0.053	−0.730	65.76	–	–	–	–	–	–	–	–	–	–	–	22.13	32.13	41.05	32.51	0.49	4.06	0.19
	Mg II QSO + A118	–	0.0169	0.086	−0.027	−5.000	–	–	0.279	1.473	0.298	0.396	50.91	1.118	–	–	–	–	156.52	174.52	204.03	177.50	0.88	7.44	4.13
Non-flat	QSO-AS + H II G	0.0300	0.0031	0.065	−0.560	−0.651	71.87	11.45	–	–	–	–	–	–	–	–	–	–	781.18	793.18	815.43	799.59	−1.27	6.15	6.90
XCDM	QSO-AS + H II G + Mg II QSO + A118	0.0365	0.1224	0.307	−0.087	−1.278	72.14	11.33	0.292	1.677	0.287	0.398	50.23	1.123	–	–	–	–	946.08	970.08	1020.59	969.33	2.74	11.16	3.11
	$H(z)$ + BAO + SN	0.0255	0.1155	0.300	−0.030	−0.922	68.68	–	–	–	–	–	–	–	–	–	–	–	1081.28	1091.28	1116.35	1092.47	2.89	12.91	2.55
	HzBSNQHMA[d]	0.0260	0.1158	0.295	−0.016	−0.947	69.53	10.94	0.288	1.697	0.277	0.409	50.15	1.151	–	–	–	–	2030.78	2054.78	2119.38	2055.42	3.48	14.25	3.56
	QHMPA101[e]	0.0354	0.1154	0.292	−0.048	−1.221	72.03	11.31	0.272	1.680	0.294	0.313	50.06	1.178	0.313	−0.736	0.769	10.98	963.91	995.91	1064.28	993.76	3.29	11.84	3.11
	$H(z)$ + BAO	0.0310	0.0900	0.280	–	1.010	65.89	–	–	–	–	–	–	–	–	–	–	–	22.31	30.31	37.45	29.90	−1.33	0.46	−2.42
	Mg II QSO + A118	–	0.2760	0.615	–	0.353	–	–	0.279	1.714	0.308	0.403	50.09	1.105	–	–	–	–	159.69	175.69	201.91	172.93	2.05	5.32	−0.44
Flat	QSO-AS + H II G	0.0198	0.1066	0.249	–	0.000	71.42	11.10	–	–	–	–	–	–	–	–	–	–	786.46	796.46	815.00	796.31	2.01	5.72	3.62
ϕCDM	QSO-AS + H II G + Mg II QSO + A118	0.0098	0.1196	0.253	–	0.020	71.63	10.98	0.283	1.683	0.289	0.416	50.18	1.145	–	–	–	–	947.60	969.60	1015.89	970.30	2.26	6.46	4.07
	$H(z)$ + BAO + SN	0.0263	0.1097	0.292	–	0.203	68.39	–	–	–	–	–	–	–	–	–	–	–	1081.22	1089.22	1109.28	1089.91	0.83	5.84	−0.01
	HzBSNQHMA[d]	0.0274	0.1116	0.289	–	0.150	69.51	10.97	0.280	1.685	0.292	0.409	50.23	1.121	–	–	–	–	2030.52	2052.52	2111.74	2053.18	1.22	6.61	1.33
	QHMPA101[e]	0.0388	0.0884	0.251	–	0.105	71.31	11.13	0.287	1.679	0.293	0.402	50.11	1.168	0.317	−0.664	0.775	10.43	964.97	994.97	1059.07	994.25	2.35	6.63	3.60
	$H(z)$ + BAO	0.0306	0.0920	0.284	−0.058	1.200	65.91	–	–	–	–	–	–	–	–	–	–	–	22.05	32.05	40.97	31.30	0.41	3.98	−1.02
	Mg II QSO + A118	–	0.2233	0.507	0.101	6.181	–	–	0.280	1.723	0.303	0.401	50.04	1.115	–	–	–	–	159.63	177.63	207.13	173.84	3.99	10.54	0.47
Non-flat	QSO-AS + H II G	0.0338	0.0979	0.251	−0.250	0.000	72.53	11.47	–	–	–	–	–	–	–	–	–	–	784.61	796.61	818.85	801.32	2.16	9.57	8.63
ϕCDM	QSO-AS + H II G + Mg II QSO + A118	0.0073	0.1290	0.265	−0.228	0.115	71.91	11.29	0.288	1.673	0.300	0.412	50.23	1.120	–	–	–	–	946.09	970.09	1020.59	972.93	2.75	11.16	6.70
	$H(z)$ + BAO + SN	0.0261	0.1119	0.295	−0.023	0.253	68.56	–	–	–	–	–	–	–	–	–	–	–	1081.12	1091.12	1116.19	1091.27	2.73	12.75	1.35
	HzBSNQHMA[d]	0.0251	0.1207	0.300	−0.056	0.195	69.84	10.91	0.284	1.699	0.279	0.411	50.19	1.132	–	–	–	–	2030.76	2054.76	2119.36	2055.13	3.46	14.23	3.28
	QHMPA101[e]	0.0370	0.0977	0.260	−0.217	0.066	72.15	11.23	0.274	1.689	0.277	0.408	50.08	1.180	0.335	−0.703	0.777	10.42	963.77	995.77	1064.14	997.14	3.15	11.70	6.49

[a] $w_{\rm X}$ corresponds to flat/non-flat XCDM and α corresponds to flat/non-flat ϕCDM.
[b] km s^{-1} Mpc^{-1}. In these GRB cases, Ω_b and H_0 are set to be 0.05 and 70 km s^{-1} Mpc^{-1}, respectively.
[c] pc.
[d] $H(z)$ + BAO + SN + QSO-AS + H II G + Mg II QSO + A118.
[e] QSO-AS + H II G + Mg II QSO + Platinum + A101.

Table 9.5: One-dimensional marginalized posterior mean values and uncertainties ($\pm1\sigma$ error bars or 2σ limits) of the parameters for all models from various combinations of data.

Model	Data set	$\Omega_b h^2$	$\Omega_c h^2$	Ω_{m0}	Ω_{k0}	w_X/α[a]	H_0[b]	l_m[c]	$\sigma_{int,M}$	b_M	k	$\sigma_{int,A}$	γ	β	$\sigma_{int,P}$	a	b_P	C_o
	$H(z)$ + BAO	0.0247 ± 0.0030	$0.1186^{+0.0076}_{-0.0083}$	$0.301^{+0.016}_{-0.018}$	–	–	69.14 ± 1.85	–	–	–	–	–	–	–	–	–	–	–
	Mg II QSO + A118	–	–	$0.609^{+0.294}_{-0.210}$	–	–	–	–	$0.293^{+0.023}_{-0.030}$	1.712 ± 0.056	0.301 ± 0.047	$0.411^{+0.027}_{-0.033}$	50.10 ± 0.25	1.112 ± 0.088	–	–	–	–
Flat	QSO-AS + H II G	0.0225 ± 0.0113	$0.1076^{+0.0197}_{-0.0224}$	$0.257^{+0.037}_{-0.047}$	–	–	71.52 ± 1.79	11.04 ± 0.34	–	–	–	–	–	–	–	–	–	–
ΛCDM	QSO-AS + H II G + Mg II QSO + A118	0.0224 ± 0.0116	$0.1118^{+0.0197}_{-0.0223}$	$0.266^{+0.037}_{-0.047}$	–	–	71.28 ± 1.73	11.00 ± 0.33	$0.292^{+0.023}_{-0.029}$	1.686 ± 0.055	0.291 ± 0.044	$0.414^{+0.027}_{-0.033}$	50.20 ± 0.24	1.135 ± 0.087	–	–	–	–
	$H(z)$ + BAO + SN	0.0244 ± 0.0027	0.1199 ± 0.0076	$0.304^{+0.014}_{-0.015}$	–	–	69.04 ± 1.77	–	–	–	–	–	–	–	–	–	–	–
	HzBSNQHMA[d]	0.0256 ± 0.0020	0.1201 ± 0.0061	0.300 ± 0.012	–	–	69.87 ± 1.13	10.96 ± 0.25	$0.292^{+0.023}_{-0.029}$	1.684 ± 0.055	0.293 ± 0.044	$0.413^{+0.026}_{-0.033}$	50.20 ± 0.24	1.131 ± 0.087	–	–	–	–
	QHMPA101[e]	$0.0225^{+0.0117}_{-0.0118}$	$0.1105^{+0.0197}_{-0.0223}$	$0.264^{+0.036}_{-0.047}$	–	–	$71.34^{+1.73}_{-1.74}$	11.02 ± 0.34	$0.291^{+0.023}_{-0.029}$	1.686 ± 0.055	0.291 ± 0.044	$0.421^{+0.029}_{-0.036}$	50.12 ± 0.26	1.164 ± 0.094	$0.346^{+0.032}_{-0.045}$	-0.710 ± 0.101	0.765 ± 0.078	11.06 ± 4.19
	$H(z)$ + BAO	$0.0266^{+0.0039}_{-0.0045}$	0.1088 ± 0.0166	0.291 ± 0.023	$0.059^{+0.081}_{-0.091}$	–	68.37 ± 2.10	–	–	–	–	–	–	–	–	–	–	–
	Mg II QSO + A118	–	–	> 0.274	$0.521^{+0.512}_{-0.872}$	–	–	–	$0.294^{+0.023}_{-0.030}$	$1.730^{+0.058}_{-0.053}$	0.302 ± 0.047	$0.411^{+0.027}_{-0.033}$	50.03 ± 0.26	1.118 ± 0.089	–	–	–	–
Non-flat	QSO-AS + H II G	0.0224 ± 0.0111	$0.1122^{+0.0223}_{-0.0218}$	$0.260^{+0.039}_{-0.045}$	$-0.196^{+0.112}_{-0.295}$	–	72.25 ± 1.99	11.35 ± 0.49	–	–	–	–	–	–	–	–	–	–
ΛCDM	QSO-AS + H II G + Mg II QSO + A118	0.0225 ± 0.0116	0.1162 ± 0.0218	$0.271^{+0.038}_{-0.045}$	$-0.139^{+0.116}_{-0.228}$	–	71.77 ± 1.87	11.19 ± 0.42	$0.291^{+0.022}_{-0.029}$	1.680 ± 0.055	0.292 ± 0.044	$0.415^{+0.027}_{-0.033}$	50.23 ± 0.24	1.122 ± 0.088	–	–	–	–
	$H(z)$ + BAO + SN	$0.0260^{+0.0037}_{-0.0043}$	0.1119 ± 0.0157	0.294 ± 0.022	0.040 ± 0.070	–	68.62 ± 1.90	–	–	–	–	–	–	–	–	–	–	–
	HzBSNQHMA[d]	$0.0265^{+0.0032}_{-0.0038}$	0.1168 ± 0.0127	0.295 ± 0.019	0.018 ± 0.059	–	69.79 ± 1.14	10.96 ± 0.25	$0.292^{+0.023}_{-0.029}$	1.685 ± 0.055	0.293 ± 0.044	$0.413^{+0.027}_{-0.033}$	50.20 ± 0.24	1.131 ± 0.086	–	–	–	–
	QHMPA101[e]	0.0224 ± 0.0117	$0.1138^{+0.0226}_{-0.0224}$	$0.267^{+0.039}_{-0.046}$	$-0.096^{+0.127}_{-0.251}$	–	$71.65^{+1.86}_{-1.85}$	11.15 ± 0.42	$0.291^{+0.023}_{-0.029}$	1.682 ± 0.055	0.292 ± 0.044	$0.424^{+0.029}_{-0.036}$	50.14 ± 0.26	1.154 ± 0.095	$0.346^{+0.032}_{-0.045}$	-0.712 ± 0.102	0.760 ± 0.080	11.37 ± 4.34
	$H(z)$ + BAO	$0.0295^{+0.0042}_{-0.0050}$	$0.0969^{+0.0178}_{-0.0152}$	0.289 ± 0.020	–	$-0.784^{+0.140}_{-0.107}$	$66.22^{+2.31}_{-2.54}$	–	–	–	–	–	–	–	–	–	–	–
	Mg II QSO + A118	–	–	$0.493^{+0.209}_{-0.353}$	–	< -0.218	–	–	$0.291^{+0.023}_{-0.030}$	$1.670^{+0.095}_{-0.062}$	0.301 ± 0.046	$0.412^{+0.027}_{-0.033}$	$50.25^{+0.28}_{-0.36}$	1.110 ± 0.088				
Flat	QSO-AS + H II G	0.0224 ± 0.0112	$0.1391^{+0.0333}_{-0.0256}$	$0.305^{+0.056}_{-0.047}$	–	$-1.683^{+0.712}_{-0.387}$	$72.92^{+2.15}_{-2.40}$	11.31 ± 0.43	–	–	–	–	–	–	–	–	–	–
XCDM	QSO-AS + H II G + Mg II QSO + A118	0.0224 ± 0.0117	$0.1449^{+0.0314}_{-0.0246}$	$0.314^{+0.051}_{-0.044}$	–	$-1.836^{+0.804}_{-0.419}$	$73.14^{+2.14}_{-2.48}$	11.34 ± 0.43	$0.291^{+0.023}_{-0.029}$	1.675 ± 0.056	0.294 ± 0.044	$0.413^{+0.027}_{-0.033}$	50.24 ± 0.24	1.124 ± 0.087	–	–	–	–
	$H(z)$ + BAO + SN	$0.0262^{+0.0033}_{-0.0037}$	0.1120 ± 0.0110	0.295 ± 0.016	–	-0.941 ± 0.064	68.55 ± 1.85	–	–	–	–	–	–	–	–	–	–	–
	HzBSNQHMA[d]	$0.0271^{+0.0027}_{-0.0031}$	$0.1147^{+0.0098}_{-0.0097}$	0.294 ± 0.015	–	-0.959 ± 0.059	69.66 ± 1.16	10.94 ± 0.25	$0.292^{+0.023}_{-0.029}$	1.685 ± 0.055	0.293 ± 0.044	$0.413^{+0.027}_{-0.033}$	50.20 ± 0.24	1.131 ± 0.087	–	–	–	–
	QHMPA101[e]	0.0224 ± 0.0118	$0.1429^{+0.0333}_{-0.0248}$	$0.310^{+0.054}_{-0.044}$	–	$-1.801^{+0.814}_{-0.421}$	$73.09^{+2.13}_{-2.48}$	11.33 ± 0.43	$0.290^{+0.022}_{-0.029}$	1.675 ± 0.056	0.294 ± 0.044	$0.421^{+0.029}_{-0.036}$	50.16 ± 0.26	1.152 ± 0.094	$0.346^{+0.032}_{-0.045}$	-0.713 ± 0.102	0.758 ± 0.081	11.45 ± 4.35
	$H(z)$ + BAO	$0.0294^{+0.0047}_{-0.0050}$	$0.0980^{+0.0186}_{-0.0187}$	0.292 ± 0.025	-0.027 ± 0.109	$-0.770^{+0.149}_{-0.098}$	$66.13^{+2.35}_{-2.36}$	–	–	–	–	–	–	–	–	–	–	–
	Mg II QSO + A118	–	–	> 0.170	$0.309^{+0.347}_{-0.650}$	< -0.132	–	–	$0.293^{+0.023}_{-0.030}$	$1.711^{+0.081}_{-0.058}$	0.302 ± 0.047	$0.413^{+0.027}_{-0.033}$	$50.10^{+0.28}_{-0.32}$	1.114 ± 0.091	–	–	–	–
Non-flat	QSO-AS + H II G	0.0224 ± 0.0114	$0.1122^{+0.0473}_{-0.0326}$	$0.258^{+0.086}_{-0.057}$	$0.018^{+0.345}_{-0.383}$	$-1.670^{+1.063}_{-0.245}$	72.34 ± 2.16	11.20 ± 0.49	–	–	–	–	–	–	–	–	–	–
XCDM	QSO-AS + H II G + Mg II QSO + A118	0.0225 ± 0.0118	$0.1327^{+0.0348}_{-0.0286}$	$0.294^{+0.059}_{-0.051}$	$0.054^{+0.227}_{-0.238}$	$-2.042^{+1.205}_{-0.451}$	$72.79^{+2.18}_{-2.42}$	$11.23^{+0.44}_{-0.49}$	$0.291^{+0.023}_{-0.030}$	1.678 ± 0.057	0.294 ± 0.045	$0.414^{+0.027}_{-0.033}$	50.23 ± 0.25	1.127 ± 0.089	–	–	–	–
	$H(z)$ + BAO + SN	$0.0262^{+0.0037}_{-0.0043}$	0.1119 ± 0.0157	0.295 ± 0.022	-0.001 ± 0.098	$-0.948^{+0.098}_{-0.068}$	68.53 ± 1.90	–	–	–	–	–	–	–	–	–	–	–
	HzBSNQHMA[d]	$0.0269^{+0.0033}_{-0.0039}$	$0.1155^{+0.0128}_{-0.0127}$	0.295 ± 0.019	$-0.009^{+0.077}_{-0.083}$	$-0.959^{+0.090}_{-0.063}$	69.65 ± 1.16	10.93 ± 0.26	$0.292^{+0.023}_{-0.029}$	1.685 ± 0.055	0.293 ± 0.044	$0.413^{+0.027}_{-0.033}$	50.20 ± 0.24	1.130 ± 0.087	–	–	–	–
	QHMPA101[e]	0.0225 ± 0.0118	$0.1283^{+0.0354}_{-0.0290}$	$0.286^{+0.060}_{-0.052}$	$0.104^{+0.232}_{-0.244}$	$-2.131^{+1.385}_{-0.524}$	$72.70^{+2.19}_{-2.43}$	11.19 ± 0.46	$0.291^{+0.023}_{-0.029}$	1.679 ± 0.056	0.293 ± 0.044	$0.421^{+0.029}_{-0.036}$	50.14 ± 0.26	1.159 ± 0.095	$0.346^{+0.032}_{-0.045}$	-0.711 ± 0.102	0.761 ± 0.080	11.28 ± 4.32
	$H(z)$ + BAO	$0.0320^{+0.0054}_{-0.0041}$	$0.0855^{+0.0175}_{-0.0174}$	0.275 ± 0.023	–	$1.267^{+0.536}_{-0.807}$	$65.47^{+2.22}_{-2.21}$	–	–	–	–	–	–	–	–	–	–	–
	Mg II QSO + A118	–	–	$0.561^{+0.332}_{-0.241}$	–	–	–	–	$0.293^{+0.023}_{-0.030}$	1.725 ± 0.052	0.303 ± 0.046	$0.411^{+0.026}_{-0.032}$	50.05 ± 0.25	1.110 ± 0.087	–	–	–	–
Flat	QSO-AS + H II G	$0.0217^{+0.0081}_{-0.0138}$	$0.0543^{+0.0225}_{-0.0471}$	$0.154^{+0.053}_{-0.086}$	–	< 6.506	70.64 ± 1.80	10.81 ± 0.34	–	–	–	–	–	–	–	–	–	–
ϕCDM	QSO-AS + H II G + Mg II QSO + A118	$0.0219^{+0.0076}_{-0.0165}$	$0.0644^{+0.0384}_{-0.0410}$	$0.175^{+0.075}_{-0.081}$	–	< 6.756	70.50 ± 1.76	10.80 ± 0.34	$0.292^{+0.023}_{-0.029}$	1.691 ± 0.055	0.291 ± 0.044	$0.414^{+0.027}_{-0.033}$	50.18 ± 0.24	1.140 ± 0.088	–	–	–	–
	$H(z)$ + BAO + SN	$0.0278^{+0.0032}_{-0.0039}$	$0.1054^{+0.0117}_{-0.0100}$	0.287 ± 0.017	–	$0.324^{+0.122}_{-0.264}$	68.29 ± 1.78	–	–	–	–	–	–	–	–	–	–	–
	HzBSNQHMA[d]	$0.0286^{+0.0025}_{-0.0033}$	$0.1089^{+0.0103}_{-0.0083}$	0.286 ± 0.015	–	$0.249^{+0.069}_{-0.239}$	69.50 ± 1.14	10.92 ± 0.25	$0.292^{+0.023}_{-0.029}$	1.686 ± 0.054	0.293 ± 0.044	$0.413^{+0.027}_{-0.033}$	50.20 ± 0.24	1.132 ± 0.086	–	–	–	–
	QHMPA101[e]	$0.0217^{+0.0088}_{-0.0164}$	$0.0607^{+0.0296}_{-0.0493}$	$0.167^{+0.067}_{-0.088}$	–	< 7.149	70.53 ± 1.76	10.80 ± 0.34	$0.292^{+0.023}_{-0.029}$	1.691 ± 0.054	0.291 ± 0.044	$0.421^{+0.029}_{-0.036}$	50.10 ± 0.26	1.172 ± 0.093	$0.347^{+0.032}_{-0.045}$	-0.707 ± 0.102	0.768 ± 0.078	10.89 ± 4.21
	$H(z)$ + BAO	$0.0320^{+0.0057}_{-0.0038}$	$0.0865^{+0.0172}_{-0.0198}$	$0.277^{+0.023}_{-0.026}$	$-0.034^{+0.087}_{-0.098}$	$1.360^{+0.584}_{-0.819}$	65.53 ± 2.19	–	–	–	–	–	–	–	–	–	–	–
	Mg II QSO + A118	–	–	$0.549^{+0.241}_{-0.268}$	$-0.001^{+0.296}_{-0.286}$	–	–	–	$0.293^{+0.023}_{-0.030}$	1.725 ± 0.052	0.303 ± 0.047	$0.412^{+0.027}_{-0.033}$	50.05 ± 0.25	1.111 ± 0.089	–	–	–	–
Non-flat	QSO-AS + H II G	$0.0219^{+0.0093}_{-0.0130}$	$0.0576^{+0.0268}_{-0.0424}$	$0.163^{+0.058}_{-0.081}$	$0.181^{+0.180}_{-0.339}$	< 7.875	70.21 ± 1.83	$10.70^{+0.36}_{-0.41}$	–	–	–	–	–	–	–	–	–	–
ϕCDM	QSO-AS + H II G + Mg II QSO + A118	$0.0222^{+0.0098}_{-0.0135}$	$0.0725^{+0.0398}_{-0.0368}$	$0.193^{+0.077}_{-0.071}$	$0.044^{+0.104}_{-0.256}$	< 7.239	70.38 ± 1.84	$10.79^{+0.38}_{-0.41}$	$0.292^{+0.024}_{-0.030}$	1.691 ± 0.055	0.292 ± 0.045	$0.415^{+0.028}_{-0.033}$	50.18 ± 0.25	1.140 ± 0.089	–	–	–	–
	$H(z)$ + BAO + SN	$0.0271^{+0.0038}_{-0.0043}$	0.1095 ± 0.0152	0.292 ± 0.022	$-0.038^{+0.071}_{-0.085}$	$0.382^{+0.151}_{-0.299}$	68.48 ± 1.85	–	–	–	–	–	–	–	–	–	–	–
	HzBSNQHMA[d]	$0.0277^{+0.0034}_{-0.0040}$	0.1126 ± 0.0128	0.291 ± 0.019	$-0.040^{+0.064}_{-0.072}$	$0.316^{+0.101}_{-0.292}$	69.52 ± 1.15	10.89 ± 0.25	$0.292^{+0.023}_{-0.030}$	1.685 ± 0.055	0.294 ± 0.044	$0.413^{+0.027}_{-0.033}$	50.20 ± 0.24	1.128 ± 0.087	–	–	–	–
	QHMPA101[e]	$0.0221^{+0.0094}_{-0.0138}$	$0.0677^{+0.0368}_{-0.0389}$	$0.183^{+0.072}_{-0.076}$	$0.084^{+0.119}_{-0.275}$	< 7.625	70.33 ± 1.83	$10.76^{+0.37}_{-0.41}$	$0.292^{+0.023}_{-0.030}$	1.692 ± 0.054	0.291 ± 0.044	$0.421^{+0.029}_{-0.036}$	50.09 ± 0.26	1.172 ± 0.094	$0.347^{+0.033}_{-0.046}$	-0.707 ± 0.102	0.769 ± 0.078	10.87 ± 4.22

[a] w_X corresponds to flat/non-flat XCDM and α corresponds to flat/non-flat ϕCDM.

[b] km s^{-1} Mpc^{-1}. In Mg II QSO, A118, and Mg II QSO + A118 cases, Ω_b and H_0 are set to be 0.05 and 70 km s^{-1} Mpc^{-1}, respectively.

[c] pc.

[d] $H(z)$ + BAO + SN + QSO-AS + H II G + Mg II QSO + A118.

[e] QSO-AS + H II G + Mg II QSO + Platinum + A101.

Chapter 10

Gamma-ray burst data strongly favour the three-parameter fundamental plane (Dainotti) correlation over the two-parameter one

This chapter is based on Cao et al. (2022d).

10.1 Introduction

In the standard general-relativistic spatially-flat ΛCDM model (Peebles, 1984), dark energy is a time-independent cosmological constant Λ that sources $\sim 70\%$ of the current cosmological energy budget and the observed currently accelerating cosmological expansion. The predictions of this model are consistent with most current cosmological observations, such as Hubble parameter $[H(z)]$, type Ia supernova (SNIa) apparent magnitude, cosmic microwave background (CMB) anisotropy, and baryon acoustic oscillation (BAO) measurements (see, e.g. eBOSS Collaboration, 2021; Farooq et al., 2017; Planck Collaboration, 2020; Scolnic et al., 2018). The measurements, however, are not yet decisive enough (see, e.g. Abdalla

et al., 2022; Dainotti et al., 2021c, 2022a; Di Valentino et al., 2021b; Perivolaropoulos & Skara, 2022) to disallow other cosmological models. Here we also consider dynamical dark energy models as well as models with non-zero spatial curvature.

In addition to the better-established cosmological probes mentioned above, developing cosmological probes can play a significant role in paring down the theoretical options. Developing cosmological probes that are under active debate now include H II starburst galaxy measurements that reach to $z \sim 2.4$ (Cao et al., 2020, 2021b; Chávez et al., 2014; González-Morán et al., 2021; Johnson et al., 2022; Mania & Ratra, 2012; Mehrabi et al., 2022), quasar (QSO) angular size observations that reach to $z \sim 2.7$ (Cao et al., 2017a, 2022a; Lian et al., 2021; Ryan et al., 2019; Zheng et al., 2021), reverberation-mapped QSO observations that reach to redshift $z \sim 3.4$ (Cao et al., 2022e; Czerny et al., 2021; Khadka et al., 2021a, 2022a,b; Yu et al., 2021; Zajaček et al., 2021), QSO flux measurements that reach to $z \sim 7.5$ (Colgáin et al., 2022; Dainotti et al., 2022d; Khadka & Ratra, 2020a,b, 2021, 2022; Leizerovich et al., 2022; Luongo et al., 2022; Lusso et al., 2020; Rezaei et al., 2022; Risaliti & Lusso, 2015, 2019; Zhao & Xia, 2021),[1] and — the main subject of our paper — gamma-ray burst (GRB) observations that reach to $z \sim 8.2$ (Amati et al., 2019; Cao et al., 2021a; Cardone et al., 2009, 2010; Dainotti & Amati, 2018; Dainotti & Del Vecchio, 2017; Dainotti et al., 2013a; Dainotti et al., 2018; Dainotti et al., 2022b,c; Demianski et al., 2021; Fana Dirirsa et al., 2019; Hu et al., 2021; Khadka & Ratra, 2020c; Khadka et al., 2021b; Liu et al., 2022; Luongo & Muccino, 2021; Luongo et al., 2022; Postnikov et al., 2014; Samushia & Ratra, 2010; Wang et al., 2015, 2016, 2022). In this paper the highest redshift GRB we use is at $z = 9.4$ (Cucchiara et al., 2011), but GRBs might be detectable to $z = 20$ (Lamb & Reichart, 2000), because they are in principle free from dust extinction. The highest low-z better-established BAO and SNIa observations reach to $z \sim 2.3$, while the high-z better-established CMB anisotropy measurements largely probe $z \sim 1100$, mostly leaving the exploration of the intermediate part of redshift space to the developing probes.

[1]The latest Lusso et al. (2020) QSO flux compilation assumes a model for the QSO UV–X-ray correlation that is not valid above a much lower redshift, $z \sim 1.5 - 1.7$ (i.e., above these redshifts the assumed QSO UV–X-ray luminosities correlation relation is different in different cosmological models), meaning that these QSOs can be used to determine only much lower-z cosmological constraints (Khadka & Ratra, 2021, 2022).

In this paper we study long GRBs, those GRBs with burst duration longer than 2 s. The measured quantities for the GRBs are the redshift z, the characteristic time scale T_X^* which marks the end of the plateau emission, the measured X-ray energy flux F_X at T_X^*, the measured γ-ray energy flux $F_{\rm peak}$ in the peak of the prompt emission over a 1 s interval, and the X-ray photon indices of the plateau phase $\alpha_{\rm plateau}$ and of the prompt emission $\alpha_{\rm prompt}$. We make use of the 50 Platinum GRBs, spanning the redshift range $0.553 \leq z \leq 5.0$, introduced in Dainotti et al. (2020), that we previously studied (Cao et al., 2022c), and a new LGRB95 sample consisting of 95 long GRBs, spanning $0.297 \leq z \leq 9.4$ and also taken from Dainotti et al. (2020), as well as the combined LGRB145 data set of 145 GRBs, to test whether they are better described by the three-dimensional (3D) fundamental plane (Dainotti) correlation between the peak prompt luminosity, the luminosity at the end of the plateau emission, and its rest frame duration (Dainotti et al., 2016, 2017, 2020, 2021a,b; Srinivasaragavan et al., 2020) or by the two-dimensional (2D) Dainotti correlation between the luminosity at the end of the plateau emission and its rest frame duration (Dainotti et al., 2008, 2010, 2011b, 2013a, 2015b, 2017),[2] and to constrain cosmological-model and GRB-correlation parameters. The Platinum sample is a compilation of the higher-quality (lower intrinsic dispersion) GRBs considered in Dainotti et al. (2020), and are tabulated in Table B.1.[3] The remaining 95 long GRBs considered in Dainotti et al. (2020) constitute the LGRB95 sample listed in Table B.2. LGRB95 data have a $\sim 50\%$ larger intrinsic scatter parameter, which contains the unknown systematic errors, than the Platinum data.

Based on information criteria, we discover that Platinum, LGRB95, and LGRB145 data strongly prefer the 3D Dainotti correlation over the 2D one. Although LGRB95 data have $\sim 50\%$ larger intrinsic scatter parameter values than Platinum data, they provide consistent but slightly tighter cosmological-model and GRB-correlation parameter constraints than do Platinum data, perhaps solely due to the larger number of data points, 95 versus 50. LGRB145 data provide tighter constraints on GRB-correlation parameters than those from

[2]The 2D and 3D Dainotti correlation relations are discussed in Sec. 10.3

[3]This is a correction of table A1 of Cao et al. (2022c) that incorrectly accounted for the GRB K-corrections. In Sec. 10.3 we discuss our improved method of accounting for the spectral evolution of GRBs and both the prompt and afterglow photon indices. These corrections are not appreciable and do not affect any of the qualitative conclusions of Cao et al. (2022c).

the individual GRB data sets.

Our paper is organized as follows. We use the cosmological models described in Chapter 2 and describe the data sets we use in Sec. 10.2. We outline our analyses methods in Sec. 10.3 and present results in Sec. 10.4. Our summary and conclusions are in Sec. 10.5.

10.2 Data

In this paper we analyze three different GRB data sets to study two-parameter or two-dimensional (2D) Dainotti correlation and the three-parameter or 3D fundamental-plane (Dainotti) correlation. These contain only long GRBs, with burst duration longer than 2 s, and are taken from the compilation of Dainotti et al. (2020). For these data sets, the measured quantities for a GRB are the redshift z, the characteristic time scale T_X^* which marks the end of the plateau emission, the measured X-ray energy flux F_X at T_X^*, the prompt peak γ-ray energy flux $F_{\rm peak}$ over a 1 s interval, and the X-ray photon indices of the plateau phase $\alpha_{\rm plateau}$ and of the prompt emission $\alpha_{\rm prompt}$. The data sets we use here are summarized next.

Platinum sample. This includes 50 long GRBs that have a plateau phase with angle $< 41^\circ$, that do not flare during the plateau phase, and that have a plateau phase that lasts longer than 500 s. The first criterion follows from the evidence that those with angle $> 41^\circ$ are outliers of the Gaussian distribution; the second criterion eliminates flaring-contaminated cases; and, the third criterion eliminates cases where prompt emission might mask the plateau (Willingale et al., 2007, 2010). The Platinum GRBs are listed in Table B.1 of Appendix B, which is a correction of table A1 of Cao et al. (2022c). This sample spans the redshift range $0.553 \leq z \leq 5.0$.

LGRB95 sample. This sample includes the remaining 95 long GRBs from the compilation of Dainotti et al. (2020). As discussed below, this GRB data set has a larger intrinsic scatter parameter $\sigma_{\rm int}$ than the Platinum GRBs. These GRBs are listed in Table B.2 of Appendix B. This sample spans the redshift range $0.297 \leq z \leq 9.4$.

LGRB145 sample. This sample is a combination of the Platinum sample and the LGRB95 sample and spans the redshift range $0.297 \leq z \leq 9.4$.

10.3 Data Analysis Methodology

The 3D fundamental plane (or 3D Dainotti) correlation (Dainotti et al., 2016, 2017, 2020, 2021a) is

$$\log L_X = C_o + a \log T_X^* + b \log L_{\rm peak}, \tag{10.1}$$

where the X-ray source rest-frame luminosity

$$L_X = 4\pi D_L^2 F_X K_{\rm plateau}, \tag{10.2}$$

with the power-law (PL) plateau K-correction

$$K_{\rm plateau} = (1+z)^{\alpha_{\rm plateau}-2}, \tag{10.3}$$

the peak prompt luminosity

$$L_{\rm peak} = 4\pi D_L^2 F_{\rm peak} K_{\rm prompt}, \tag{10.4}$$

with the prompt K-correction

$$K_{\rm prompt} = \frac{\int_{15/(1+z)}^{150/(1+z)} E f(E) dE}{\int_{15}^{150} E f(E) dE}, \tag{10.5}$$

where E is the photon energy and the differential photon spectrum (Sakamoto et al., 2011)

$$f(E) = \begin{cases} K_{50}^{\rm PL} \left(\frac{E}{50\ \rm keV}\right)^{\alpha^{\rm PL}} & \text{if PL,} \\ K_{50}^{\rm CPL} \left(\frac{E}{50\ \rm keV}\right)^{\alpha^{\rm CPL}} \exp\left[\frac{-E\left(2+\alpha^{\rm CPL}\right)}{E_{\rm peak}}\right] & \text{if CPL.} \end{cases} \tag{10.6}$$

Here $K_{50}^{\rm PL}$ and $K_{50}^{\rm CPL}$ are the normalization at 50 keV in units of photons cm^{-2} s^{-1} keV^{-1} in the PL and cutoff power-law (CPL) models, respectively, $\alpha^{\rm PL}$ and $\alpha^{\rm CPL}$ are the PL and CPL photon indices, respectively, and $E_{\rm peak}$ is the peak energy in the νF_ν spectrum in units of keV, where ν is the photon frequency proportional to E and F_ν is the photon energy flux per unit frequency. When $\Delta\chi^2 \equiv \chi^2_{\rm PL} - \chi^2_{\rm CPL} > 6$, the CPL model is used to compute the prompt K-correction, otherwise the PL model is used. In the preceding equations, $\{C_o, a, b\}$ are the GRB correlation parameters to be constrained, T_X^* (s) is the time at the end of the plateau emission, F_X and $F_{\rm peak}$ are the measured X-ray and γ-ray energy flux (erg cm^{-2} s^{-1}) at T_X^* and in the peak of the prompt emission over a 1 s interval, respectively. The luminosity distance is defined in equation (8.1).

Here we have improved upon the analysis of Cao et al. (2022c), that assumed the GRB K-corrections are the same throughout the burst duration, by also considering the prompt emission photon index. We consider the sliced photon index in the spectrum starting from the time of the beginning of plateau emission to the time of the end of plateau emission. We use the photon counting (PC) mode for the majority of cases and the window timing (WT) mode for only a few cases where we do not have the PC mode. This procedure differs from previous analyses in which photon indices were computed using an average of both WT and PC modes.

The 3D fundamental plane (or 3D Dainotti) correlation reduces to the 2D Dainotti correlation when $b = 0$. Note that the 3D fundamental plane Dainotti relation is a combination of this 2D Dainotti $L_X - T_X^*$ correlation and another 2D Dainotti correlation between the peak prompt luminosity and the luminosity at the end of the plateau emission (Dainotti et al., 2011a, 2015a).

The natural log of the likelihood function (D'Agostini, 2005) is

$$\ln \mathscr{L}_{\rm GRB} = -\frac{1}{2}\left[\chi^2_{\rm GRB} + \sum_{i=1}^{N} \ln\left(2\pi\sigma^2_{{\rm tot},i}\right)\right], \tag{10.7}$$

Table 10.1: Flat priors of the constrained parameters.

Parameter	Prior
Cosmological Parameters	
Ω_c	[-0.051315, 0.948685]
Ω_{k0}	[-2, 2]
α	[0, 10]
$w_{\rm X}$	[-5, 0.33]
GRB Correlation Parameters	
a	[-2, -0.001]
b[a]	[0, 2]
C_o	[-10, 60]
$\sigma_{\rm int}$	[0, 5]

[a] In two-dimensional GRB analyses, $b = 0$.

where, in the 3D fundamental plane relation case,

$$\chi^2_{\rm GRB} = \sum_{i=1}^{N} \left[\frac{(\log L_{X,i} - C_o - a \log T^*_{X,i} - b \log L_{{\rm peak},i})^2}{\sigma^2_{{\rm tot},i}} \right], \tag{10.8}$$

with

$$\sigma^2_{{\rm tot},i} = \sigma^2_{\rm int} + \sigma^2_{\log L_{X,i}} + a^2 \sigma^2_{\log T^*_{X,i}} + b^2 \sigma^2_{\log L_{{\rm peak},i}}. \tag{10.9}$$

N is the number of data points and $\sigma_{\rm int}$ is the intrinsic scatter parameter that contains the unknown systematic uncertainty. Note that $\sigma_{\log L_X} = \sigma_{\log {\rm FK}_{\rm plateau}}$ and $\sigma_{\log L_{\rm peak}} = \sigma_{\log {\rm FK}_{\rm prompt}}$, where $\log {\rm FK}_{\rm plateau} \equiv \log F_X + \log K_{\rm plateau}$ and $\log {\rm FK}_{\rm prompt} \equiv \log F_{\rm peak} + \log K_{\rm prompt}$. In the 2D Dainotti correlation case we fix $b = 0$ in equations (10.8) and (10.9).

We avoid the circularity problem by simultaneously constraining cosmological-model and GRB-correlation parameters, and if the GRB correlation parameters are independent of the cosmological models used in the analysis then the GRBs are standardizable (Khadka & Ratra, 2020c). The simultaneous fitting technique also allows for the determination of GRB-only cosmological constraints, unlike the cosmological constraints determined from GRBs that have been calibrated using other data (which are then correlated with data used in the calibration process), that can be directly compared to (or combined with) constraints

determined from other data.

We list the flat priors of the free cosmological and GRB correlation parameters in Table 10.1. Since these GRB data sets cannot constrain Ω_b and H_0, we set $\Omega_b = 0.05$ and $H_0 = 70$ km s^{-1} Mpc^{-1} in our analyses. By maximizing the likelihood functions, we obtain the unmarginalized best-fitting values and posterior distributions of all free cosmological-model and GRB-correlation parameters. We use the Markov chain Monte Carlo (MCMC) code MontePython (Audren et al., 2013; Brinckmann & Lesgourgues, 2019) that interacts with the class code cosmological model physics. We use the python package getdist (Lewis, 2019) to perform our analyses.

The definitions of the Akaike Information Criterion (AIC), the Bayesian Information Criterion (BIC), and the deviance information criterion (DIC) can be found in our previous papers (see, e.g. Cao et al., 2022b,c). ΔAIC, ΔBIC, and ΔDIC are the differences between the AIC, BIC, and DIC values of the other five cosmological models and those of the flat ΛCDM reference model, while ΔAIC$'$, ΔBIC$'$, and ΔDIC$'$ are the differences between values of 2D and 3D Dainotti correlations in the same cosmological model. Negative (positive) values of these ΔICs indicate that the model under investigation fits the data better (worse) than does the reference model. Relative to the model with the minimum IC, $\Delta\text{IC} \in (0, 2]$ is defined to be weak evidence against the model under investigation, $\Delta\text{IC} \in (2, 6]$ is positive evidence against the model under investigation, $\Delta\text{IC} \in (6, 10]$ is strong evidence against the model under investigation, and $\Delta\text{IC} > 10$ is very strong evidence against the model under investigation.

As in Cao & Ratra (2022), we assume one massive and two massless neutrino species, with the non-relativistic neutrino physical energy density parameter $\Omega_\nu h^2 = \sum m_\nu/(93.14 \text{ eV}) = 0.06 \text{ eV}/(93.14 \text{ eV})$, where h is the Hubble constant in units of 100 km s^{-1} Mpc^{-1}. The non-relativistic matter density parameter $\Omega_{m0} = (\Omega_\nu h^2 + \Omega_b h^2 + \Omega_c h^2)/h^2$, where the current value of the baryonic matter energy density parameter is set to $\Omega_b = 0.05$[4] and the current value of the cold dark matter energy density parameter (Ω_c) is constrained as a free cosmological parameter.

[4]Since GRB data are unable to constrain Ω_b.

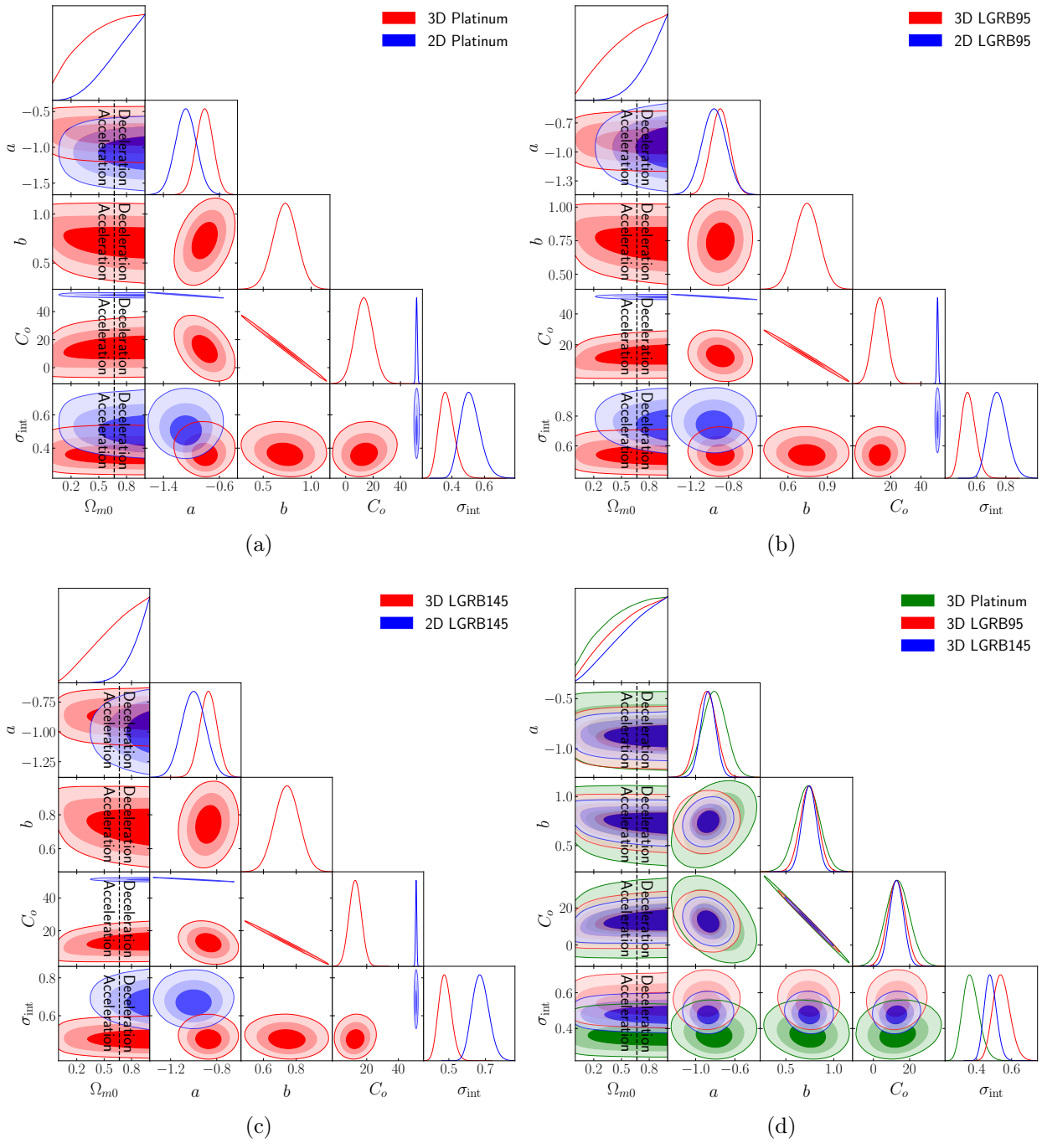

Figure 10.1: One-dimensional likelihood distributions and 1σ, 2σ, and 3σ two-dimensional likelihood confidence contours for flat ΛCDM from various combinations of data. The zero-acceleration black dashed lines in panels (a) and (b) divide the parameter space into regions associated with currently-accelerating (left) and currently-decelerating (right) cosmological expansion.

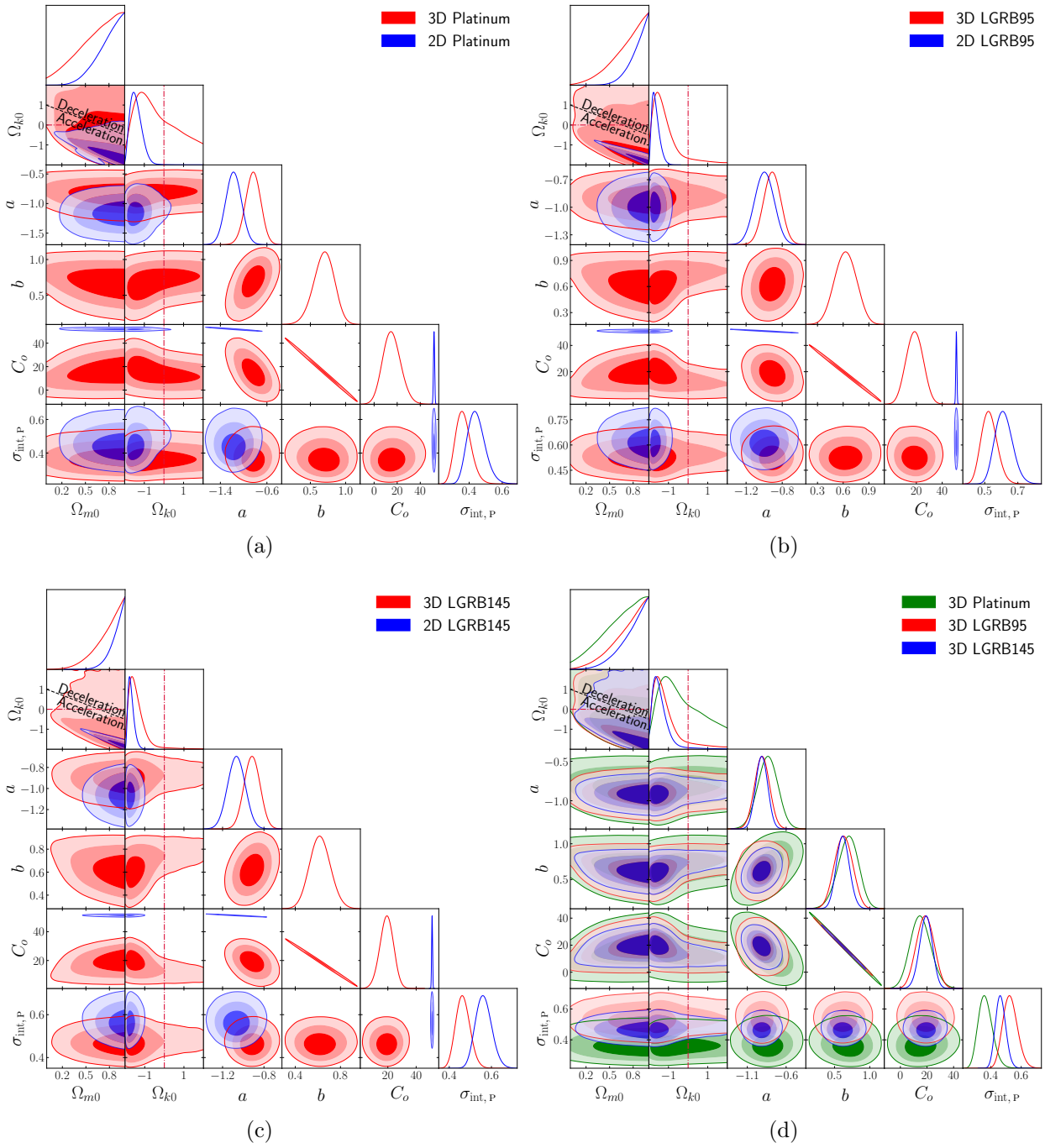

Figure 10.2: Same as Fig. 10.1 but for non-flat ΛCDM. The zero-acceleration black dashed lines divide the parameter space into regions associated with currently-accelerating (below left) and currently-decelerating (above right) cosmological expansion.

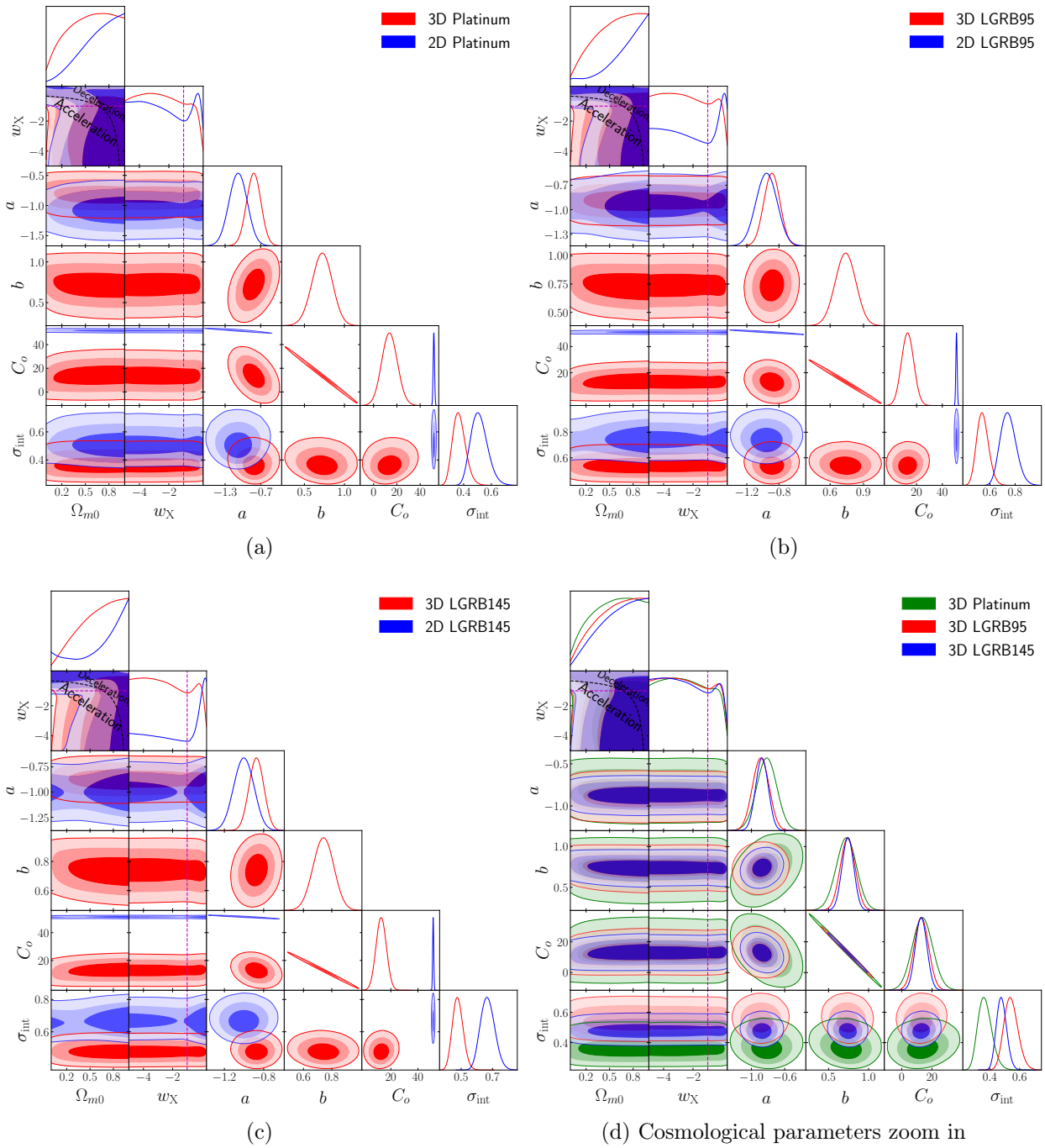

Figure 10.3: One-dimensional likelihood distributions and 1σ, 2σ, and 3σ two-dimensional likelihood confidence contours for flat XCDM from various combinations of data. The zero-acceleration black dashed lines divide the parameter space into regions associated with currently-accelerating (either below left or below) and currently-decelerating (either above right or above) cosmological expansion. The magenta dashed lines represent $w_{\rm X} = -1$, i.e. flat ΛCDM.

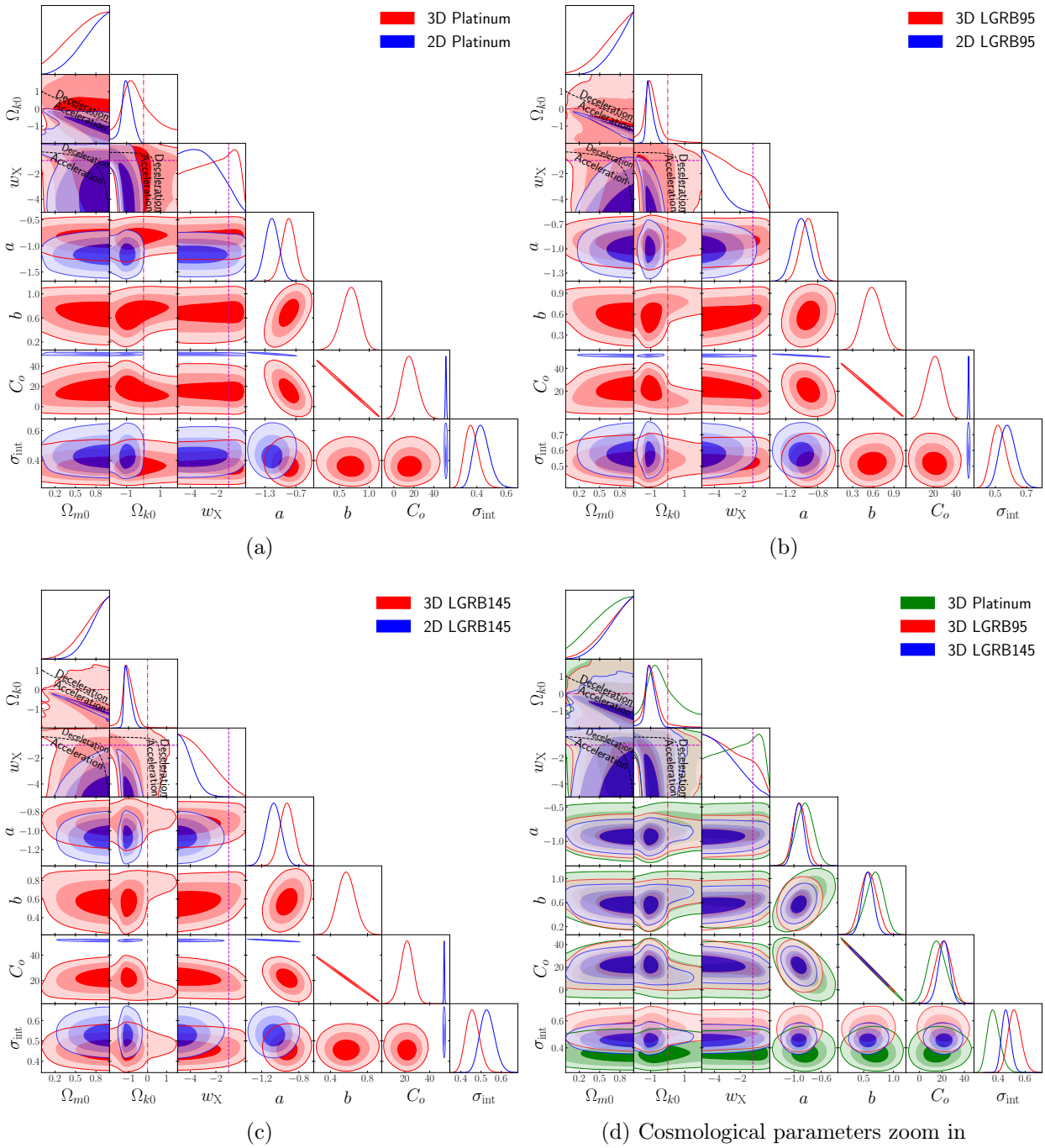

Figure 10.4: Same as Fig. 10.3 but for non-flat XCDM. The zero-acceleration black dashed lines are computed for the third cosmological parameter set to the $H(z)$ + BAO data best-fitting values listed in table 4 of Cao & Ratra (2022), and divide the parameter space into regions associated with currently-accelerating (either below left or below) and currently-decelerating (either above right or above) cosmological expansion. The crimson dash-dot lines represent flat hypersurfaces, with closed spatial hypersurfaces either below or to the left. The magenta dashed lines represent $w_X = -1$, i.e. non-flat ΛCDM.

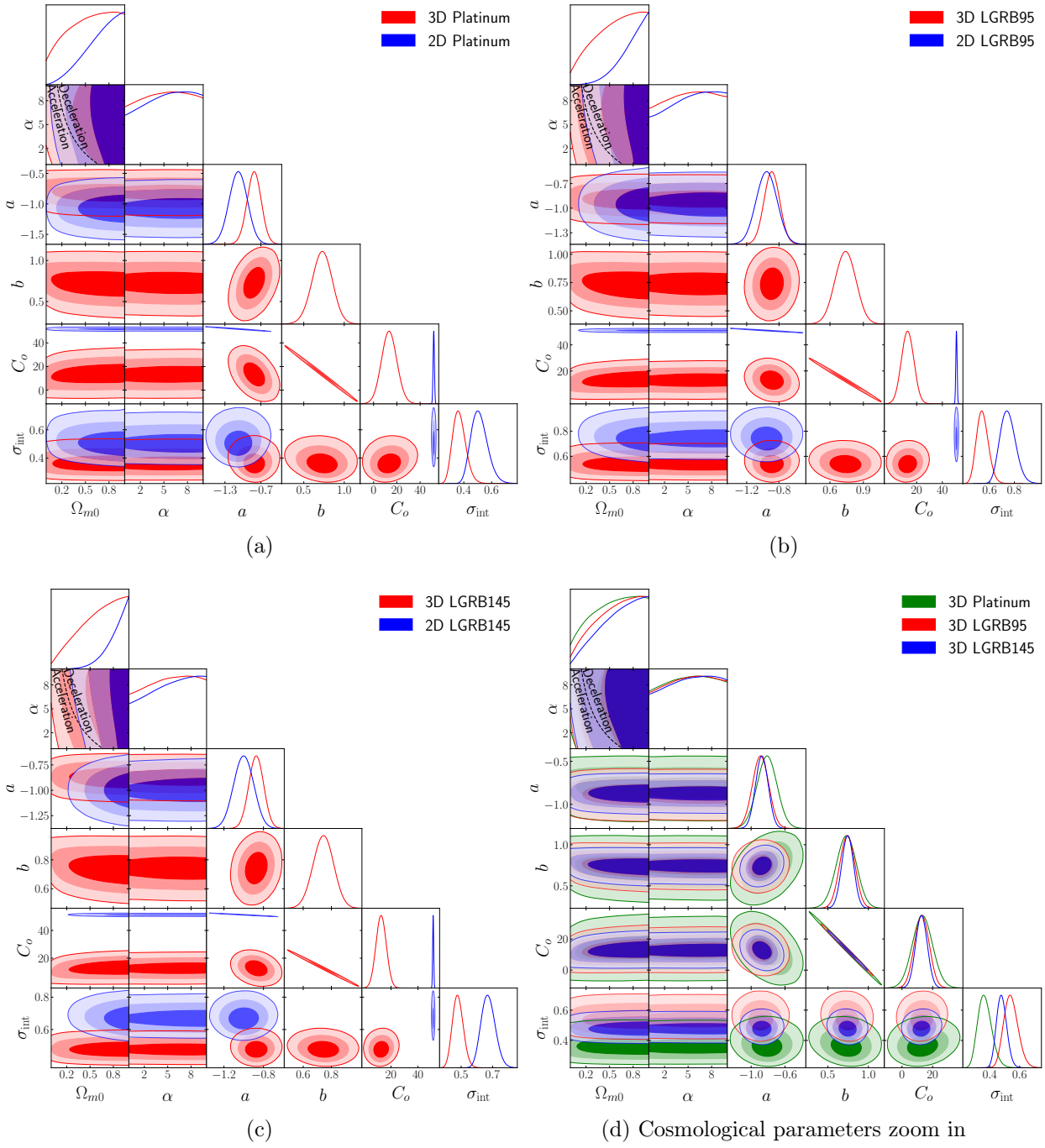

(a) (b)

(c) (d) Cosmological parameters zoom in

Figure 10.5: One-dimensional likelihood distributions and 1σ, 2σ, and 3σ two-dimensional likelihood confidence contours for flat ϕCDM from various combinations of data. The zero-acceleration black dashed lines divide the parameter space into regions associated with currently-accelerating (below left) and currently-decelerating (above right) cosmological expansion. The $\alpha = 0$ axes correspond to flat ΛCDM.

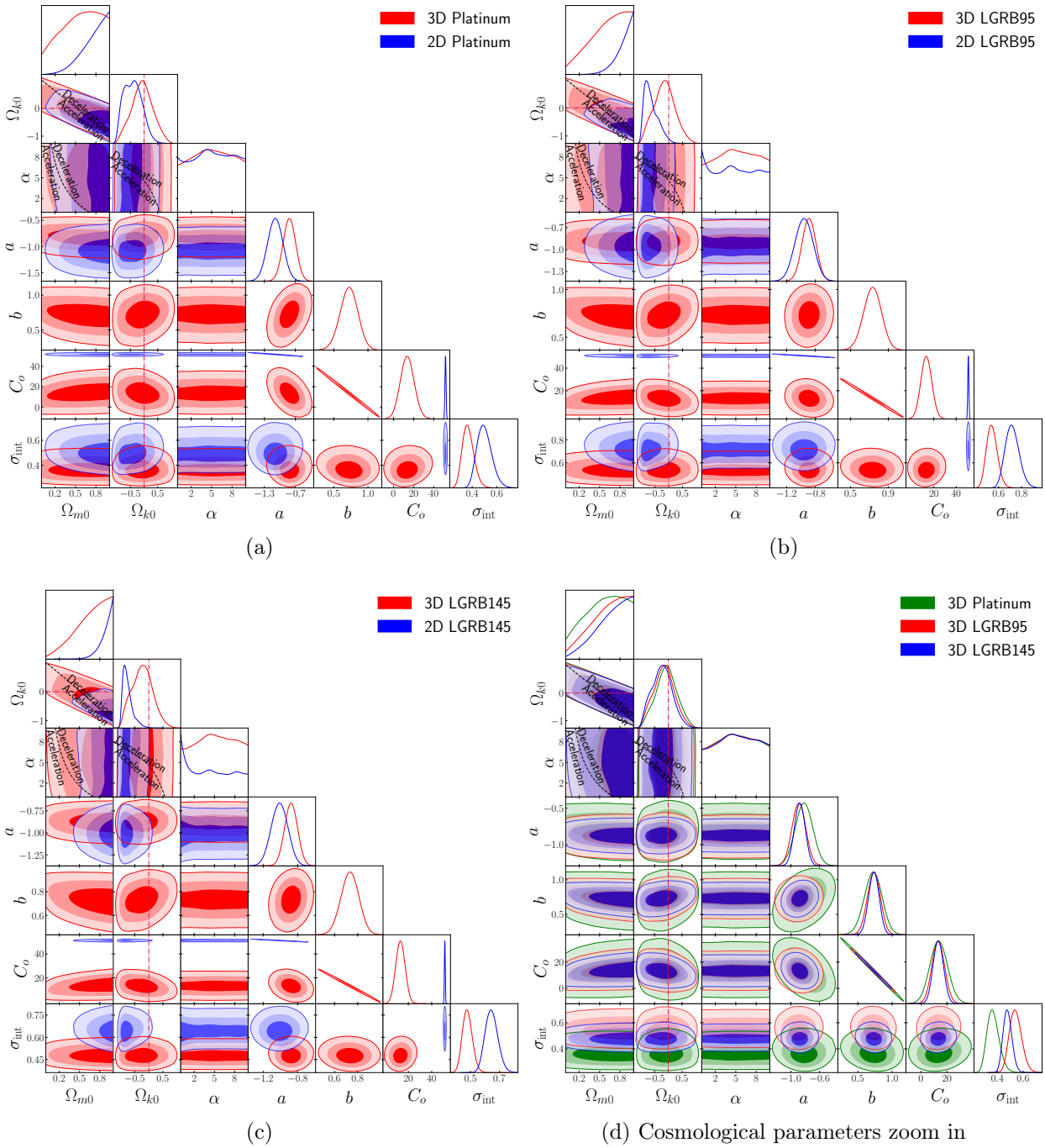

(a) (b)

(c) (d) Cosmological parameters zoom in

Figure 10.6: Same as Fig. 10.5 but for non-flat ϕCDM. The zero-acceleration black dashed lines are computed for the third cosmological parameter set to the $H(z)$ + BAO data best-fitting values listed in table 4 of Cao & Ratra (2022), and divide the parameter space into regions associated with currently-accelerating (below left) and currently-decelerating (above right) cosmological expansion. The crimson dash-dot lines represent flat hypersurfaces, with closed spatial hypersurfaces either below or to the left. The $\alpha = 0$ axes correspond to non-flat ΛCDM.

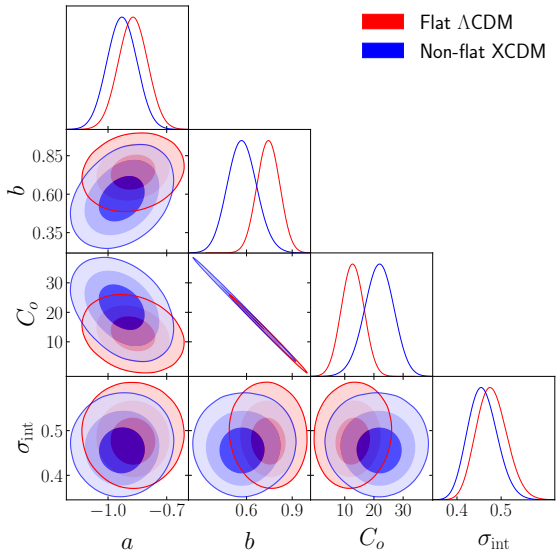

Figure 10.7: Comparisons between 3D Dainotti correlation parameters of flat ΛCDM and those of non-flat XCDM from LGRB145 data, where their two-dimensional likelihood confidence contours are mutually consistent within 1σ.

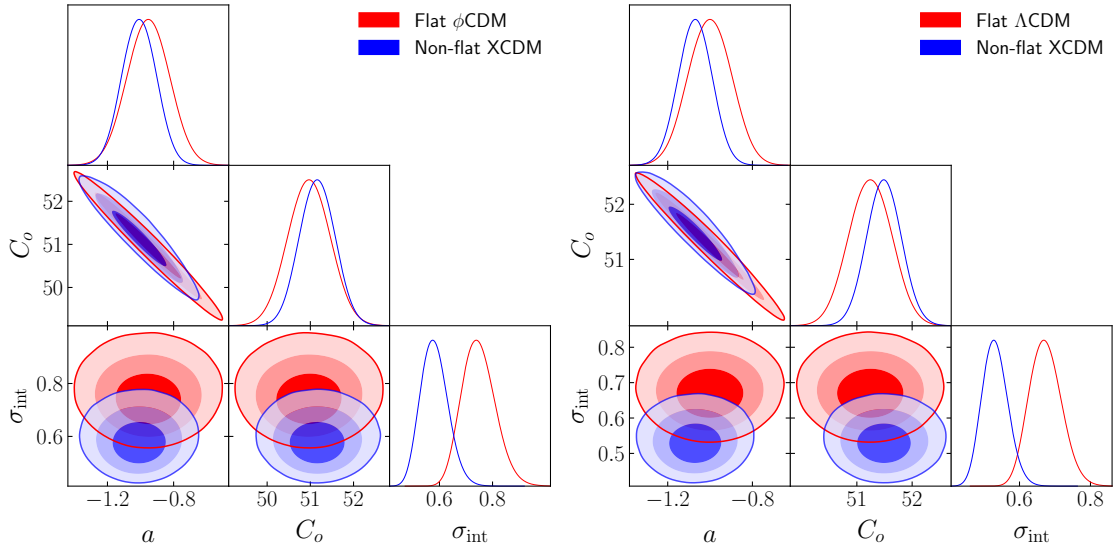

(a) 2D LGRB95 (b) 2D LGRB145

Figure 10.8: Comparisons between 2D Dainotti correlation parameters of different cosmological models.

10.4 Results

The posterior one-dimensional probability distributions and two-dimensional confidence regions of cosmological-model and GRB-correlation parameters for the six cosmological models are shown in Figs. 10.1–10.6, where in panels (a)–(c) of each figure results of the 3D and 2D Dainotti correlation analyses are shown in red and blue, respectively; while in panel (d) of each figure 3D Dainotti correlation results are shown in green (Platinum), red (LGRB95), and blue (LGRB145). The unmarginalized best-fitting parameter values, as well as the values of maximum likelihood $\mathscr{L}_{\rm max}$, AIC, BIC, DIC, ΔAIC$'$, ΔBIC$'$, ΔDIC$'$, ΔAIC, ΔBIC, and ΔDIC, for all models and data sets, are listed in Table 10.2. We list the marginalized posterior mean parameter values and uncertainties ($\pm1\sigma$ error bars and 1 or 2σ limits), for all models and data sets, in Table 10.3.

In Cao et al. (2022c) we showed that the 3D Dainotti correlation parameters in all six cosmological models, determined from the Platinum data set, were mutually consistent, confirming that the 3D Dainotti correlation Platinum GRBs are standardizable.[5] When we compare the 3D Dainotti correlation parameters results in Table 10.3 for the six different cosmological models, we see that the 3D Dainotti correlation LGRB95 GRBs are standardizable.[6] Similarly, the determined 2D Dainotti correlation parameters, a and C_o, are independent (within the errors) of the cosmological model used in the analysis, for the Platinum, LGRB95, and LGRB145 GRBs. However, unlike the 3D Dainotti correlation cases and the 2D Dainotti Platinum case, from the cosmological models which result in the largest and smallest $\sigma_{\rm int}$ values, in the 2D Dainotti correlation LGRB95 and LGRB145 cases, although 1D marginalized $\sigma_{\rm int}$ constraints are in $> 2\sigma$ tension, as shown in panels (a) and (b) of Fig. 10.8, their 2D marginalized contours are within 2σ. These results indicate that the 2D Dainotti correlation LGRB95 and LGRB145 data need more careful study.

For the 3D Platinum data set, the constraints on the intrinsic scatter parameter $\sigma_{\rm int}$

[5]The corrected results in Tables 10.2 and 10.3 show that the conclusions of Cao et al. (2022c) do not change.

[6]Note that although the highest (non-flat XCDM) and lowest (flat ΛCDM) values of 1D marginalized b and C_o constraints from LGRB145 data differ by 1.44σ and 1.45σ, respectively, as shown in Fig. 10.7 their 1σ 2D marginalized contours overlap so the 3D Dainotti correlation LGRB145 GRBs are also standardizable.

range from a low of $0.365^{+0.038}_{-0.052}$ (non-flat XCDM) to a high of $0.369^{+0.038}_{-0.052}$ (flat ΛCDM), with a difference of 0.06σ. The constraints on the slope a range from a low of -0.842 ± 0.127 (non-flat XCDM) to a high of -0.812 ± 0.119 (flat ΛCDM), with a difference of 0.17σ. The constraints on the slope b range from a low of $0.680^{+0.160}_{-0.136}$ (non-flat XCDM) to a high of 0.728 ± 0.122 (flat ΛCDM), with a difference of 0.24σ. The constraints on the intercept C_o range from a low of 13.38 ± 6.45 (flat ΛCDM) to a high of $15.93^{+7.22}_{-8.52}$ (non-flat XCDM), with a difference of 0.24σ.

For the 3D LGRB95 data set, the constraints on the intrinsic scatter parameter $\sigma_{\rm int}$ range from a low of $0.524^{+0.042}_{-0.051}$ (non-flat XCDM) to a high of $0.543^{+0.042}_{-0.052}$ (flat ΛCDM), with a difference of 0.28σ, which are larger ($> 2\sigma$) than those from Platinum data. The constraints on the slope a range from a low of -0.918 ± 0.095 (non-flat XCDM) to a high of -0.887 ± 0.097 (flat ΛCDM), with a difference of 0.23σ, which are lower ($\sim 0.5\sigma$) than those from Platinum data. The constraints on the slope b range from a low of $0.588^{+0.140}_{-0.138}$ (non-flat XCDM) to a high of 0.743 ± 0.091 (flat ΛCDM), with a difference of 0.93σ, which are either lower ($\sim -0.3/0.5\sigma$) or higher ($\sim 0.1\sigma$) than those from Platinum data. The constraints on the intercept C_o range from a low of 12.73 ± 4.69 (flat ΛCDM) to a high of $20.75^{+7.14}_{-7.22}$ (non-flat XCDM), with a difference of 0.93σ, which are either higher ($\sim 0.3/0.8\sigma$) or lower ($\sim -0.1\sigma$) than those from Platinum data. Although the constraints of $\sigma_{\rm int}$ from LGRB95 data are $> 2\sigma$ larger than those from Platinum data, which means that LGRB95 data do not fit the 3D Dainotti correlation as well as Platinum data do, the LGRB95 and Platinum 3D Dainotti correlation parameters (a, b, and C_o) are mutually consistent within 1σ, so they both obey same 3D Dainotti correlation and so can be jointly analyzed.

For the joint 3D LGRB145 data set, the constraints on the intrinsic scatter parameter $\sigma_{\rm int}$ range from a low of $0.458^{+0.030}_{-0.035}$ (non-flat XCDM) to a high of $0.480^{+0.030}_{-0.036}$ (flat ϕCDM), with a difference of 0.47σ. The constraints on the slope a range from a low of -0.929 ± 0.074 (non-flat XCDM) to a high of -0.872 ± 0.073 (flat ΛCDM), with a difference of 0.55σ. The constraints on the slope b range from a low of 0.572 ± 0.094 (non-flat XCDM) to a high of 0.743 ± 0.073 (flat ΛCDM), with a difference of 1.44σ. The constraints on the intercept C_o range from a low of 12.71 ± 3.78 (flat ΛCDM) to a high of $21.68^{+4.93}_{-4.91}$ (non-flat XCDM), with

a difference of 1.45σ. Although the constraints of b and C_o from LGRB145 data are $\sim 1.4\sigma$ away, their 2D contours overlap within 1σ.

These results show that for both GRB samples the correlation slope a remains consistent within 1σ with the value of the correlation slope corrected for selection biases, $a' = (-0.75 \pm 0.11,\ -0.69 \pm 0.07)$ for the Gold and Long GRBs, respectively (Dainotti et al., 2017), highlighting that the physics of the correlation, i.e. that the energy reservoir remains constant, is consistently maintained, independent of the sample and cosmology used (here we do account for the selection biases correction as in Dainotti et al., 2022c). Also, the positive correlation between $L_{\rm peak}$ and L_X is maintained at the 1σ level when compared with the intrinsic correlation corrected for selection biases which yield $b = (0.7 \pm 0.07,\ 0.64 \pm 0.11)$ for the Long and Gold GRBs, respectively (Dainotti et al., 2017). Again, regardless of the sample and cosmological model used, the underlying physics of the correlation is preserved confirming the reliability of our results.

In comparison with the cosmological parameter constraints from Platinum data, LGRB95 data provide slightly tighter constraints. For Ω_{m0} constraints, LGRB95 data provide higher 1 or 2σ lower limits than most of those from Platinum data with only 1σ lower limits. For Ω_{k0} constraints, LGRB95 data provide more restrictive and lower posterior mean values than those from Platinum data. Closed hypersurfaces are favoured but except for non-flat ϕCDM, flatness is more than 1σ away. LGRB95 data provide lower 2σ upper limits of $w_{\rm X}$ than those provided by Platinum data, while they do not constrain α. It is worth noting that LGRB95 data provide slightly more restrictive constraints on both the cosmological-model and the 3D Dainotti correlation parameters, than do Platinum data, likely a consequence of the larger number of data points, 95 versus 50, more than compensating for the larger $\sigma_{\rm int}$ value, $\sim 0.52 - 0.54$ versus ~ 0.37.

Although the cosmological parameter constraints from joint LGRB145 data are more restrictive than those from individual data sets, due to it containing more data points, the resulting constraints are not yet comparable with those from SNIa data. However, LGRB145 data favour higher values of Ω_{m0} and lower values of Ω_{k0} (closed geometry) than do Platinum data and LGRB95 data. LGRB145 data provide 2σ lower limits of Ω_{m0}, ranging from > 0.157

(flat ϕCDM) to > 0.444 (non-flat ΛCDM). In the non-flat ΛCDM model, LGRB145 data provide tighter and lower Ω_{k0} values of $-1.396^{+0.125}_{-0.487}$ (1σ) and < -0.520 (2σ), away from flatness to $> 2\sigma$. In the non-flat XCDM parametrization, LGRB145 data provide tighter and lower Ω_{k0} values of $-0.991^{+0.240}_{-0.307}$ (1σ) and $-0.991^{+0.682}_{-0.673}$ (2σ), away from flatness to $> 2\sigma$. In the non-flat ϕCDM model, LGRB145 data provide tighter and lower Ω_{k0} value of $-0.226^{+0.357}_{-0.388}$ (1σ), with flatness within 1σ (0.63σ).

Based on AIC and BIC, non-flat XCDM is favoured the most by both LGRB95 and LGRB145 data, with the evidence against non-flat XCDM and non-flat ΛCDM being either weak or positive, and with the evidence against the remaining models being either strong or very strong. However, based on DIC, non-flat ΛCDM and non-flat XCDM are the most favoured model by LGRB95 and LGRB145 data, with positive evidence against the remaining models, and with positive evidence against non-flat ΛCDM and either strong or very strong evidence against the remaining models, respectively.

From the AIC, BIC, and DIC results we find that the 3D Dainotti correlation is very strongly favoured over the 2D Dainotti correlation by all three of the GRB data sets. Therefore, although some of the cosmological parameter constraints are more restrictive in the 2D Dainotti correlation cases, possibly because there is one less free parameter to constrain in the 2D correlation cases, we do not discuss them in detail. Leaving aside the 2D Dainotti correlation LGRB145 data set, we briefly discuss the results from the 2D correlation Platinum and LGRB95 data. Overall, these GRB data used with the 2D Dainotti correlation prefer higher values of Ω_{m0} and lower values of Ω_{k0} and $w_{\rm X}$ (non-flat XCDM), whereas they do not provide restrictive constraints on $w_{\rm X}$ in flat XCDM (except for Platinum data) and α in ϕCDM models. However, the constraints on the Platinum and LGRB95 2D Dainotti correlation parameters a and C_o are cosmological model-independent, with the 2D a values being more negative and less restrictive and the 2D C_o values being larger and more restrictive than those from the corresponding 3D Dainotti correlation data sets.

10.5 Summary and Conclusion

In addition to 50 Platinum GRBs, we use LGRB95 data that contains 95 long GRBs, as well as the joint 145 GRB data compilation, to study whether the 2D or 3D Dainotti correlation is more favoured by data, as well as to constrain cosmological-model and GRB-correlation parameters, in six flat and non-flat dark energy cosmological models. Based on AIC, BIC, and DIC results, we find that the 3D Dainotti correlation is much more strongly favoured than the 2D one by the GRB data sets we study.

We also find that LGRB95 data obey the 3D Dainotti correlation and are standardizable. Platinum and LGRB95 data provide mutually consistent constraints on both cosmological-model and GRB-correlation parameters, and also provide cosmological-model independent 3D Dainotti correlation parameter constraints. Therefore, we can combine Platinum with LGRB95 data to form the LGRB145 data set and use it for similar analyses. We find that while LGRB95 data have $\sim 42-49\%$ larger values of intrinsic scatter parameter $\sigma_{\rm int} \sim 0.524-0.543$ than $\sigma_{\rm int} \sim 0.365-0.369$ of Platinum data, they provide somewhat tighter constraints on cosmological-model and GRB-correlation parameters, perhaps mostly due to the larger number of data points, 95 versus 50. We recommend that when compiling GRB data for the purpose of constraining cosmological parameters, given the quality of current GRB data, attention be placed on also expanding the sample size, in addition to attempting to reduce the value of $\sigma_{\rm int}$ of the compilation.[7]

LGRB95 data favour higher values of Ω_{m0} and lower values of Ω_{k0} than do Platinum data, whereas the joint LGRB145 data favour even higher and lower values of Ω_{m0} and Ω_{k0} than both Platinum and LGRB95 data, respectively. All these GRB data do not provide restrictive constraints on $w_{\rm X}$ and α. LGRB145 data also provide tighter constraints on GRB-correlation parameters and the intrinsic scatter parameter.

Given the current paucity of GRB data it is therefore necessary to increase the sample size to allow the 3D correlation to have cosmological constraints comparable to those from SNIa data. A detailed study on simulating GRB constraints based on the Platinum sample

[7]This recommendation also holds for QSO and related data.

to determine the number of Platinum-quality GRBs needed to reach constraints similar to those from a number of recent SNIa data sets is presented in Dainotti et al. (2022c). To achieve similar GRB constraints one needs to wait for more GRB data from future missions, and one can use machine learning techniques and lightcurves reconstruction on these larger data sets that can enable smaller scatter (47.5%) on the 2D and 3D correlation parameters.

We note that a major restriction on the use of more current GRBs as cosmological tools is the lack of redshift for many GRBs. Only 26% of the total number of GRBs observed by Swift have reliable redshifts. Work on the inference of redshifts is underway (Dainotti et al., 2019) and does not require waiting for a new mission. Once reliable redshifts are determined for the GRBs with X-ray plateaus, we anticipate having a Platinum-quality sample twice as large as the current one as well as also anticipate doubling the size of the LGRB95-quality sample.

Current GRB data alone cannot provide very restrictive cosmological constraints comparable to those from better-established probes such as CMB, BAO, $H(z)$, or SNIa measurements, but one can do joint analyses of GRB data with these data to get more restrictive cosmological parameter constraints (Cao & Ratra, 2022; Cao et al., 2022b,c; Xu et al., 2021).

We also look forward to a larger, better-quality, compilation of GRB data from the *SVOM* mission scheduled to be launched in 2023 (Atteia et al., 2022), and possibly the *THESEUS* mission (Amati et al., 2021) in 2037. In conjunction with machine learning techniques, these new data should provide significantly more restrictive GRB cosmological parameter constraints that could be comparable with those from SNIa data.

Table 10.2: Unmarginalized best-fitting parameter values for all models from different data sets.[a]

Model	Data set	$\Omega_c h^2$	$\Omega_{\rm m0}$	$\Omega_{\rm k0}$	$w_{\rm X}/\alpha$[b]	$\sigma_{\rm int}$	a	b	C_o	$-2\ln\mathscr{L}_{\rm max}$	AIC	BIC	DIC	ΔAIC$'$	ΔBIC$'$	ΔDIC$'$	ΔAIC	ΔBIC	ΔDIC
	3D Platinum	0.4555	0.981	–	–	0.341	−0.817	0.711	14.23	41.72	51.72	61.28	51.88	–	–	–	–	–	–
	3D LGRB95	0.4644	0.999	–	–	0.522	−0.891	0.729	13.44	156.64	166.64	179.41	167.20	–	–	–	–	–	–
Flat	3D LGRB145	0.4635	0.997	–	–	0.468	−0.882	0.733	13.27	209.18	219.18	234.06	219.88	–	–	–	–	–	–
ΛCDM	2D Platinum	0.4648	1.000	–	–	0.478	−1.079	–	51.66	69.58	77.58	85.23	79.28	25.86	23.95	27.40	–	–	–
	2D LGRB95	0.4642	0.999	–	–	0.720	−0.957	–	50.94	210.61	218.61	228.83	220.95	51.97	49.42	53.75	–	–	–
	2D LGRB145	0.4647	1.000	–	–	0.658	−1.000	–	51.20	294.75	302.75	314.66	305.16	83.58	80.60	85.28	–	–	–
	3D Platinum	0.0307	0.114	−0.495	–	0.307	−0.858	0.667	16.65	33.89	45.89	57.36	57.84	–	–	–	−5.83	−3.92	5.96
	3D LGRB95	0.4641	0.999	−1.915	–	0.491	−0.923	0.541	23.03	147.73	157.73	175.06	164.80	–	–	–	−6.90	−4.35	−2.39
Non-flat	3D LGRB145	0.4606	0.991	−1.889	–	0.447	−0.940	0.578	21.28	197.47	209.47	227.34	213.18	–	–	–	−9.70	−6.72	−6.70
ΛCDM	2D Platinum	0.4644	0.999	−1.819	–	0.408	−1.189	–	51.88	54.84	64.84	74.40	67.11	18.95	17.04	9.27	−12.75	−10.83	−12.17
	2D LGRB95	0.4648	1.000	−1.898	–	0.590	−1.000	–	50.85	174.93	184.93	197.70	187.31	25.20	22.65	22.51	−33.68	−31.12	−33.64
	2D LGRB145	0.4639	0.998	−1.880	–	0.547	−1.070	–	51.22	246.10	256.10	270.98	258.28	45.62	43.65	45.09	−46.66	−43.68	−46.89
	3D Platinum	0.0041	0.060	–	0.131	0.348	−0.826	0.701	14.72	41.37	53.37	64.84	51.95	–	–	–	1.65	3.56	0.07
	3D LGRB95	−0.0188	0.013	–	0.121	0.523	−0.884	0.697	15.02	155.96	167.96	183.28	167.34	–	–	–	1.32	3.88	0.14
Flat	3D LGRB145	−0.0246	0.001	–	0.135	0.459	−0.864	0.718	13.94	208.12	220.12	237.98	220.31	–	–	–	0.95	3.92	0.43
XCDM	2D Platinum	−0.0242	0.002	–	0.140	0.468	−1.086	–	51.59	67.15	77.15	86.71	81.30	23.78	21.87	29.35	−0.43	1.48	2.02
	2D LGRB95	−0.0132	0.024	–	0.141	0.699	−0.974	–	50.92	205.84	215.84	228.61	224.19	47.89	45.33	56.85	−2.77	−0.21	3.24
	2D LGRB145	−0.0149	0.021	–	0.141	0.636	−1.017	–	51.17	287.71	297.71	312.59	308.85	77.59	74.61	88.54	−5.04	−2.07	3.69
	3D Platinum	0.1032	0.262	−1.446	−0.696	0.310	−0.803	0.706	14.34	35.58	49.58	62.96	57.71	–	–	–	−2.14	−1.68	3.83
	3D LGRB95	0.0721	0.199	−1.518	−0.605	0.471	−0.943	0.616	19.24	140.12	154.12	171.99	168.13	–	–	–	−12.52	−7.41	0.93
Non-flat	3D LGRB145	0.4611	0.992	−1.228	−4.971	0.441	−0.941	0.517	24.48	192.09	206.09	226.93	210.37	–	–	–	−13.09	−7.13	−9.51
XCDM	2D Platinum	0.4568	0.983	−1.182	−4.983	0.389	−1.182	–	52.04	51.73	63.73	75.20	65.25	14.16	12.24	9.53	−13.85	−10.02	−14.03
	2D LGRB95	0.4609	0.992	−1.232	−4.912	0.553	−1.009	–	51.05	163.56	175.56	190.88	178.23	21.44	18.89	10.10	−43.05	−37.94	−42.71
	2D LGRB145	0.4633	0.997	−1.232	−4.998	0.511	−1.078	–	51.41	229.92	241.92	259.78	243.77	35.83	32.85	33.40	−60.83	−54.88	−61.40
	3D Platinum	0.4564	0.983	–	8.469	0.342	−0.828	0.698	14.90	41.72	53.72	65.19	51.56	–	–	–	2.00	3.91	−0.32
	3D LGRB95	0.4614	0.993	–	4.276	0.524	−0.894	0.724	13.70	156.64	168.64	183.97	166.90	–	–	–	2.01	4.56	−0.30
Flat	3D LGRB145	0.4598	0.990	–	8.582	0.466	−0.871	0.732	13.28	209.19	221.19	239.05	219.62	–	–	–	2.01	4.99	−0.26
ϕCDM	2D Platinum	0.4647	1.000	–	6.040	0.477	−1.079	–	51.65	69.58	79.58	89.14	79.15	25.86	23.95	27.59	2.00	3.91	−0.13
	2D LGRB95	0.4648	1.000	–	4.187	0.723	−0.949	–	50.91	210.61	220.61	233.38	220.64	51.96	49.41	53.74	2.00	4.55	−0.31
	2D LGRB145	0.4647	1.000	–	9.417	0.654	−1.010	–	51.23	294.76	304.76	319.65	304.90	83.58	80.60	85.28	2.01	4.98	−0.26
	3D Platinum	0.4359	0.941	−0.939	0.024	0.333	−0.818	0.670	16.30	40.75	54.75	68.13	52.57	–	–	–	3.03	6.85	0.69
	3D LGRB95	0.4566	0.983	−0.969	0.381	0.515	−0.896	0.670	16.47	154.66	168.66	186.54	168.06	–	–	–	2.03	7.14	0.86
Non-flat	3D LGRB145	0.4634	0.997	−0.970	0.352	0.461	−0.877	0.694	15.20	206.38	220.38	241.22	221.01	–	–	–	1.20	7.16	1.13
ϕCDM	2D Platinum	0.4634	0.997	−0.985	0.000	0.449	−1.093	–	51.67	63.73	75.73	87.21	80.15	20.98	19.07	27.58	−1.85	1.98	0.87
	2D LGRB95	0.4647	1.000	−0.991	0.003	0.679	−0.981	–	51.04	198.63	210.63	225.96	218.39	41.97	39.42	50.33	−7.98	−2.87	−2.56
	2D LGRB145	0.4628	0.996	−0.994	0.000	0.611	−1.004	–	51.20	277.29	289.29	307.15	299.79	68.91	65.93	78.78	−13.47	−7.51	−5.37

[a] Ω_b is set to 0.05 and H_0 is set to 70 km s^{-1} Mpc^{-1}.

[b] $w_{\rm X}$ corresponds to flat/non-flat XCDM and α corresponds to flat/non-flat ϕCDM.

Table 10.3: One-dimensional marginalized posterior mean values and uncertainties ($\pm 1\sigma$ error bars or 2σ limits) of the parameters for all models from different data sets.[a]

Model	Data set	$\Omega_{\rm m0}$	$\Omega_{\rm k0}$	$w_{\rm X}/\alpha$[b]	$\sigma_{\rm int}$	a	b	C_o
	3D Platinum	> 0.441[c]	–	–	$0.369^{+0.038}_{-0.052}$	-0.812 ± 0.119	0.728 ± 0.122	13.38 ± 6.45
	3D LGRB95	> 0.155	–	–	$0.543^{+0.042}_{-0.052}$	-0.887 ± 0.097	0.743 ± 0.091	12.73 ± 4.69
Flat	3D LGRB145	> 0.213	–	–	$0.479^{+0.031}_{-0.036}$	-0.872 ± 0.073	0.743 ± 0.073	12.71 ± 3.78
ΛCDM	2D Platinum	> 0.372	–	–	$0.515^{+0.049}_{-0.066}$	-1.080 ± 0.146	–	51.75 ± 0.55
	2D LGRB95	> 0.526	–	–	$0.747^{+0.055}_{-0.069}$	-0.953 ± 0.125	–	50.98 ± 0.48
	2D LGRB145	> 0.628	–	–	$0.673^{+0.040}_{-0.048}$	-1.001 ± 0.100	–	51.24 ± 0.38
	3D Platinum	> 0.170	$-0.304^{+0.630}_{-1.452}$	–	$0.366^{+0.038}_{-0.052}$	-0.839 ± 0.128	$0.690^{+0.153}_{-0.133}$	$15.36^{+7.02}_{-8.12}$
	3D LGRB95	> 0.321	$-1.111^{+0.112}_{-0.790}$	–	$0.528^{+0.042}_{-0.051}$	-0.911 ± 0.095	0.628 ± 0.125	$18.63^{+6.42}_{-6.45}$
Non-flat	3D LGRB145	> 0.444	$-1.396^{+0.125}_{-0.487}$	–	$0.465^{+0.030}_{-0.035}$	-0.915 ± 0.075	$0.620^{+0.087}_{-0.094}$	19.12 ± 4.69
ΛCDM	2D Platinum	> 0.475	$-1.415^{+0.196}_{-0.367}$	–	$0.445^{+0.043}_{-0.059}$	-1.173 ± 0.132	–	51.93 ± 0.49
	2D LGRB95	> 0.622	$-1.648^{+0.104}_{-0.240}$	–	$0.616^{+0.046}_{-0.057}$	-0.997 ± 0.106	–	50.91 ± 0.41
	2D LGRB145	> 0.700	$-1.693^{+0.084}_{-0.186}$	–	$0.563^{+0.034}_{-0.041}$	-1.066 ± 0.083	–	51.26 ± 0.31
	3D Platinum	> 0.407[c]	–	$-2.470^{+2.578}_{-2.342}$	$0.368^{+0.038}_{-0.052}$	-0.816 ± 0.119	0.720 ± 0.124	13.78 ± 6.58
	3D LGRB95	> 0.128	–	< -0.023	$0.543^{+0.041}_{-0.051}$	-0.888 ± 0.097	0.738 ± 0.091	13.01 ± 4.69
Flat	3D LGRB145	> 0.159	–	< -0.002	$0.479^{+0.030}_{-0.036}$	-0.874 ± 0.074	0.741 ± 0.071	$12.87^{+3.72}_{-3.71}$
XCDM	2D Platinum	> 0.208	–	< 0.065	$0.514^{+0.049}_{-0.067}$	-1.081 ± 0.150	–	51.79 ± 0.57
	2D LGRB95	> 0.172	–	–	$0.746^{+0.054}_{-0.067}$	-0.955 ± 0.127	–	51.02 ± 0.50
	2D LGRB145	> 0.587[c]	–	–	$0.669^{+0.041}_{-0.048}$	-1.002 ± 0.100	–	51.25 ± 0.39
	3D Platinum	> 0.499[c]	$-0.251^{+0.697}_{-1.117}$	$-2.210^{+2.295}_{-0.985}$	$0.365^{+0.038}_{-0.052}$	-0.842 ± 0.127	$0.680^{+0.160}_{-0.136}$	$15.93^{+7.22}_{-8.52}$
	3D LGRB95	> 0.267	$-0.861^{+0.310}_{-0.511}$	< -0.327	$0.524^{+0.042}_{-0.051}$	-0.918 ± 0.095	$0.588^{+0.140}_{-0.138}$	$20.75^{+7.14}_{-7.22}$
Non-flat	3D LGRB145	> 0.363	$-0.991^{+0.240}_{-0.307}$	< -0.964	$0.458^{+0.030}_{-0.035}$	-0.929 ± 0.074	0.572 ± 0.094	$21.68^{+4.93}_{-4.91}$
XCDM	2D Platinum	> 0.327	$-0.987^{+0.322}_{-0.282}$	< -0.746	$0.434^{+0.043}_{-0.059}$	-1.166 ± 0.130	–	52.08 ± 0.50
	2D LGRB95	> 0.477	$-1.035^{+0.135}_{-0.239}$	< -2.386	$0.581^{+0.045}_{-0.055}$	-1.008 ± 0.102	–	51.16 ± 0.40
	2D LGRB145	> 0.513	$-1.029^{+0.105}_{-0.226}$	< -2.960	$0.531^{+0.032}_{-0.039}$	-1.070 ± 0.078	–	51.49 ± 0.31
	3D Platinum	> 0.406[c]	–	–	$0.368^{+0.038}_{-0.052}$	-0.813 ± 0.116	0.726 ± 0.123	13.45 ± 6.48
	3D LGRB95	> 0.453[c]	–	–	$0.543^{+0.041}_{-0.051}$	-0.888 ± 0.094	0.739 ± 0.091	12.95 ± 4.72
Flat	3D LGRB145	> 0.157	–	–	$0.480^{+0.030}_{-0.036}$	-0.873 ± 0.073	0.743 ± 0.071	12.73 ± 3.71
ϕCDM	2D Platinum	> 0.287	–	–	$0.513^{+0.048}_{-0.066}$	-1.077 ± 0.149	–	51.71 ± 0.55
	2D LGRB95	> 0.390	–	–	$0.748^{+0.054}_{-0.068}$	-0.953 ± 0.126	–	50.97 ± 0.48
	2D LGRB145	> 0.548	–	–	$0.672^{+0.040}_{-0.047}$	-1.000 ± 0.099	–	51.23 ± 0.37
	3D Platinum	> 0.425[c]	$-0.065^{+0.384}_{-0.382}$	–	$0.368^{+0.038}_{-0.052}$	-0.817 ± 0.120	0.721 ± 0.127	13.71 ± 6.72
	3D LGRB95	> 0.150	$-0.153^{+0.371}_{-0.392}$	–	$0.541^{+0.041}_{-0.051}$	-0.889 ± 0.094	0.732 ± 0.093	$13.29^{+4.79}_{-4.78}$
Non-flat	3D LGRB145	> 0.215	$-0.226^{+0.357}_{-0.388}$	–	$0.479^{+0.030}_{-0.036}$	-0.876 ± 0.074	0.732 ± 0.075	13.28 ± 3.91
ϕCDM	2D Platinum	> 0.405	$-0.402^{+0.256}_{-0.404}$	–	$0.501^{+0.049}_{-0.067}$	-1.089 ± 0.146	–	51.69 ± 0.55
	2D LGRB95	> 0.594	$-0.628^{+0.104}_{-0.324}$	–	$0.719^{+0.053}_{-0.065}$	-0.958 ± 0.123	–	50.90 ± 0.47
	2D LGRB145	> 0.688	$-0.749^{+0.062}_{-0.210}$	–	$0.645^{+0.039}_{-0.046}$	-1.010 ± 0.095	–	51.17 ± 0.36

[a] Ω_b is set to 0.05 and H_0 is set to 70 km s^{-1} Mpc^{-1}.
[b] $w_{\rm X}$ corresponds to flat/non-flat XCDM and α corresponds to flat/non-flat ϕCDM.
[c] This is the 1σ limit. The 2σ limit is set by the prior and not shown here.

Chapter 11

Standardizing reverberation-measured C IV time-lag quasars, and using them with standardized Mg II quasars to constrain cosmological parameters

This chapter is based on Cao et al. (2022e).

11.1 Introduction

The well-established observed currently accelerated expansion of the Universe has motivated many theoretical cosmological models. In the standard general-relativistic spatially-flat ΛCDM cosmological model (Peebles, 1984) dark energy in the form of a time-independent cosmological constant Λ powers the currently accelerated cosmological expansion and contributes $\sim 70\%$ of the current cosmological energy budget, with non-relativistic cold dark matter (CDM) and baryonic matter contributing $\sim 25\%$ and $\sim 5\%$, respectively. Although the flat ΛCDM model makes predictions consistent with most observations (see, e.g. eBOSS Collaboration, 2021; Planck Collaboration, 2020; Scolnic et al., 2018; Yu et al., 2018), it has

some potential observational discrepancies (Abdalla et al., 2022; Di Valentino et al., 2021b; Perivolaropoulos & Skara, 2022) that motivate us to also study dynamical dark energy models as well as models with non-zero spatial curvature.

There are better-established cosmological probes, such as baryon acoustic oscillation (BAO), type Ia supernova apparent magnitude, and Hubble parameter $[H(z)]$ measurements that, when jointly analyzed, provide fairly restrictive cosmological parameter constraints (see, e.g. Cao & Ratra, 2022). Cosmological probes that are now under active development can tighten these constraints. Amongst these developing probes are H II starburst galaxy apparent magnitude data that reach to redshift $z \sim 2.4$ (Cao et al., 2020, 2021b; Chávez et al., 2014; González-Morán et al., 2021; Johnson et al., 2022; Mania & Ratra, 2012; Mehrabi et al., 2022), quasar (QSO) angular size measurements that reach to $z \sim 2.7$ (Cao et al., 2017a, 2022a; Lian et al., 2021; Ryan et al., 2019; Zheng et al., 2021), QSO flux observations that reach to $z \sim 7.5$ (Colgáin et al., 2022; Dainotti et al., 2022d; Khadka & Ratra, 2020a,b, 2021, 2022; Leizerovich et al., 2022; Luongo et al., 2022; Lusso et al., 2020; Rezaei et al., 2022; Risaliti & Lusso, 2015, 2019; Zhao & Xia, 2021),[1] gamma-ray burst data that reach to $z \sim 8.2$ (Cao et al., 2021a, 2022b,c,d; Dainotti et al., 2022c; Demianski et al., 2021; Fana Dirirsa et al., 2019; Hu et al., 2021; Khadka & Ratra, 2020c; Khadka et al., 2021b; Liu et al., 2022; Luongo & Muccino, 2021; Wang et al., 2016, 2022), and — the main subject of our paper — reverberation-mapped (RM) QSO data that reach to $z \sim 3.4$ (Czerny et al., 2021; Khadka et al., 2021a, 2022a,a; Zajaček et al., 2021, and this paper).

Khadka et al. (2021a, 2022a,a) derived cosmological constraints from RM Hβ and Mg II QSO data. In this paper, we show that RM C IV QSO data, that extend to higher z, are standardizable and derive the first cosmological constraints from C IV data.

With its ionization potential energy of $\sim$ 64.5 eV, C IV (λ1549) belongs to the high-ionization line (HIL) component of the QSO broad-line region (BLR; Baskin & Laor, 2005; Collin-Souffrin et al., 1988; Karas et al., 2021), which can partially form an outflow that is manifested by the blueshifted centroid of the line (see e.g. Britzen et al., 2021) as well as by

[1]Note however that the Lusso et al. (2020) QSO flux compilation assumes a model for the QSO UV–X-ray correlation that is invalid above redshifts $z \sim 1.5 - 1.7$ so this is the limit to which the Lusso et al. (2020) QSOs can be used to determine cosmological constraints (Khadka & Ratra, 2021, 2022).

the frequent blueward line-emission asymmetry (Baskin & Laor, 2005). It is therefore not yet established whether all of the C IV material is virialized and if the standard reverberation mapping (hereafter RM[2]) of HILs can lead to the reliable measurements of the SMBH masses, as was previously done using the low-ionization lines (LILs) for several hundreds of objects (mainly using the Balmer line Hβ and the resonance Mg II line).

However, the BLR radius-luminosity ($R-L$) relationship for the C IV line, in the flat ΛCDM model, appears to now be well established with a significant positive correlation and a relatively small dispersion (Grier et al., 2019; Kaspi et al., 2007, 2021; Lira et al., 2018), which allows for the possibility of using this relation for constraining cosmological parameters as we previously did for Hβ and Mg II lines (Czerny et al., 2021; Khadka et al., 2021a, 2022a,a; Martínez-Aldama et al., 2019; Panda et al., 2019a; Zajaček et al., 2021).

In this paper, we use 38 high-quality C IV QSO measurements, which span eight orders of magnitude in luminosity $\sim 10^{40-48}$ erg s^{-1} and the redshift range $0.001064 \leq z \leq 3.368$, to constrain, for the first time, cosmological-model and $R-L$ relation parameters, in six general relativistic dark energy cosmological models, using a more correct technique to account for the asymmetric errors of the time-lag measurements. We find that the C IV $R-L$ relation parameters are independent of cosmological model, so C IV QSO data are standardizable through the C IV $R-L$ relation. Mg II QSO data were also found to be standardizable through the Mg II $R-L$ relation (Khadka et al., 2021a, 2022a). We find that cosmological constraints from C IV and Mg II QSO data are mutually consistent and are also consistent with those from $H(z)$ + BAO data. Although the cosmological constraints from the joint analysis of C IV + Mg II QSO data are weak, jointly analyzing C IV + Mg II data with $H(z)$ + BAO data results in a mild ($< 0.1\sigma$) tightening of the $H(z)$ + BAO cosmological constraints.

This paper is organized as follows. We describe the cosmological models/parametrizations we study in Chapter 2. In Sections 11.2 and 11.3, we outline the data sets and the analysis methods we use, respectively. Our constrained cosmological parameter and $R-L$ relation parameter results are presented and discussed in Sections 11.4 and 11.5. We summarize our

[2]Depending on the context, we use the abbreviation RM for both reverberation mapping as a method and for reverberation-mapped quasars interchangeably.

conclusions in Section 11.6.

11.2 Data

In this work, we use C IV QSO, Mg II QSO, and $H(z)$ + BAO data, as well as combinations of these data sets, to constrain cosmological-model and QSO $R - L$ relation parameters. These data sets are summarized next, with the emphasis on the C IV QSO sample.

C IV QSO data. Here we describe the sample of high-quality 38 C IV RM QSOs. The first time-lag measurements of the broad C IV line were inferred by Peterson et al. (2005, 2006) for 4 sources. The source NGC4151 was monitored by Metzroth et al. (2006). The C IV time-lag for the intensively monitored NGC5548 was determined by De Rosa et al. (2015). Lira et al. (2018) performed RM for 17 high-luminosity QSOs for over 10 years, out of which 8 QSOs were reported to have statistically significant ($> 1\sigma$) C IV time-lag measurements. Hoormann et al. (2019) report 2 C IV detections for quasars at $z = 1.905$ and $z = 2.593$ from the photometric Dark Energy Survey Supernova Program (DES-SN) and the spectroscopic Australian Dark Energy Survey (Oz-DES). Within the Sloan Digital Sky Survey Reverberation Mapping project (SDSS-RM), Grier et al. (2019) determined C IV time-lag measurements for 48 QSOs with an average false-positive rate of 10%. Of these, 16 QSOs pass the highest-quality criteria, in the redshift range of $1.4 < z < 2.8$ and the monochromatic luminosity range $44.5 < \log\left[L_{1350}\,(\mathrm{erg\,s^{-1}})\right] < 45.6$. Shen et al. (2019) showed that adding more photometric data points and spectroscopic data ($9 + 5$ years of photometric and spectroscopic measurements, respectively, in comparison to $4 + 4$ years of spectroscopic and photometric monitoring performed by Grier et al., 2019) results in the significant detection of 3 more C IV time-lag measurements. Using 20 years of photometric and spectrophotometric data, Kaspi et al. (2021) report significant C IV time-delays for 3 QSOs at redshifts $z = 2.172$, 2.646, and 3.192.

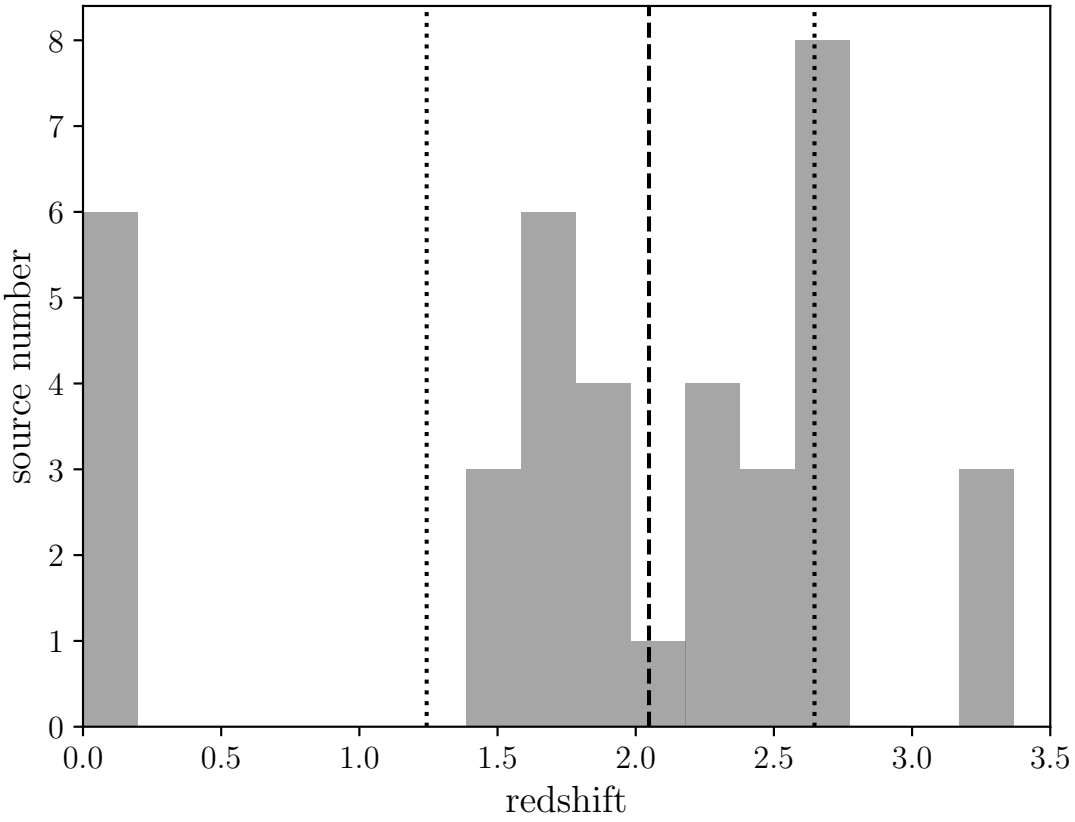

Figure 11.1: The redshift distribution for the "golden" sample of 38 C IV QSOs from Kaspi et al. (2021). The dashed line stands for the redshift median at 2.048, while the dotted lines represent 16% and 84% percentiles at 1.244 and 2.647, respectively. The histogram bin size is $\Delta z \simeq 0.2$.

Kaspi et al. (2021) compiled (with a few corrections) available C IV RM sources, finding 38 QSOs with significantly measured C IV time-delays, including their 3 QSOs. The time-delays were determined by using either the interpolated cross-correlation function (ICCF) or the z-transformed dicrete correlation function (zDCF) or a combination of both, which ensures a relative homogeneity of the sample in terms of the time-delay methodology in comparison with, e.g., the Hβ sample where several different methods are applied and combined, see e.g. Zajaček et al. (2019) or Rakshit (2020) for overviews. We refer to this sample of 38 C IV QSOs as "golden" and it covers the redshift range $0.001064 \leq z \leq 3.368$, with the median redshift of 2.048 and 16-% and 84-% percentile redshifts of 1.244 and 2.647, respectively. The redshift distribution is shown in Fig. 11.1. The sources belonging to the golden sample are listed in Table C.1, including their redshift, flux density at 1350 Å, monochromatic luminosity at 1350 Å (computed assuming a flat ΛCDM model with $H_0 = 70\,\mathrm{km\,s^{-1}\,Mpc^{-1}}$, $\Omega_{m0} = 0.3$, and $\Omega_\Lambda = 0.7$), and the rest-frame C IV time-lag τ (typically with asymmetrical error bars).

The correlation between the rest-frame C IV time-delay and the UV monochromatic luminosity at 1350 Å is significant, with the Pearson correlation coefficient $r = 0.898$ ($p = 2.082 \times 10^{-14}$) and the Spearman rank-order correlation coefficient $s = 0.799$ ($p = 1.751 \times 10^{-9}$). Given the large correlation coefficient, we fit the golden dataset with the power-law relation $\log \tau = \beta_\mathrm{C} + \gamma_\mathrm{C} \log\left(L_{1350}/10^{44}\,\mathrm{erg\,s^{-1}}\right)$, where $\log \equiv \log_{10}$, and find the best-fit intercept $\beta_\mathrm{C} = 1.04 \pm 0.07$ and the best-fit slope $\gamma_\mathrm{C} = 0.42 \pm 0.03$, for which the individual time-delay errors were neglected in the Levenberg-Marquardt algorithm. This results in an intrinsic scatter of $\sigma = 0.32$ dex and $\chi^2 = 31.8$ (36 degrees of freedom). When we consider individual symmetrized time-delay errors (see the discussion in the paragraph below eq. (11.10)), we obtain $\gamma_\mathrm{C} = 0.56 \pm 0.04$ and $\beta_\mathrm{C} = 0.98 \pm 0.07$ with $\sigma = 0.41$ dex and $\chi^2 = 16.6$. See Fig. 11.2 for the best-fitting relations, which were inferred using the `curve_fit` function from the `scipy` library. To add information about the accretion state of each QSO from our sample in the $R - L$ relation, we estimate the Eddington ratio $\lambda_\mathrm{Edd} = L_\mathrm{bol}/L_\mathrm{Edd}$, where $L_\mathrm{bol} = \kappa_\mathrm{bol} L_{1350}$ is

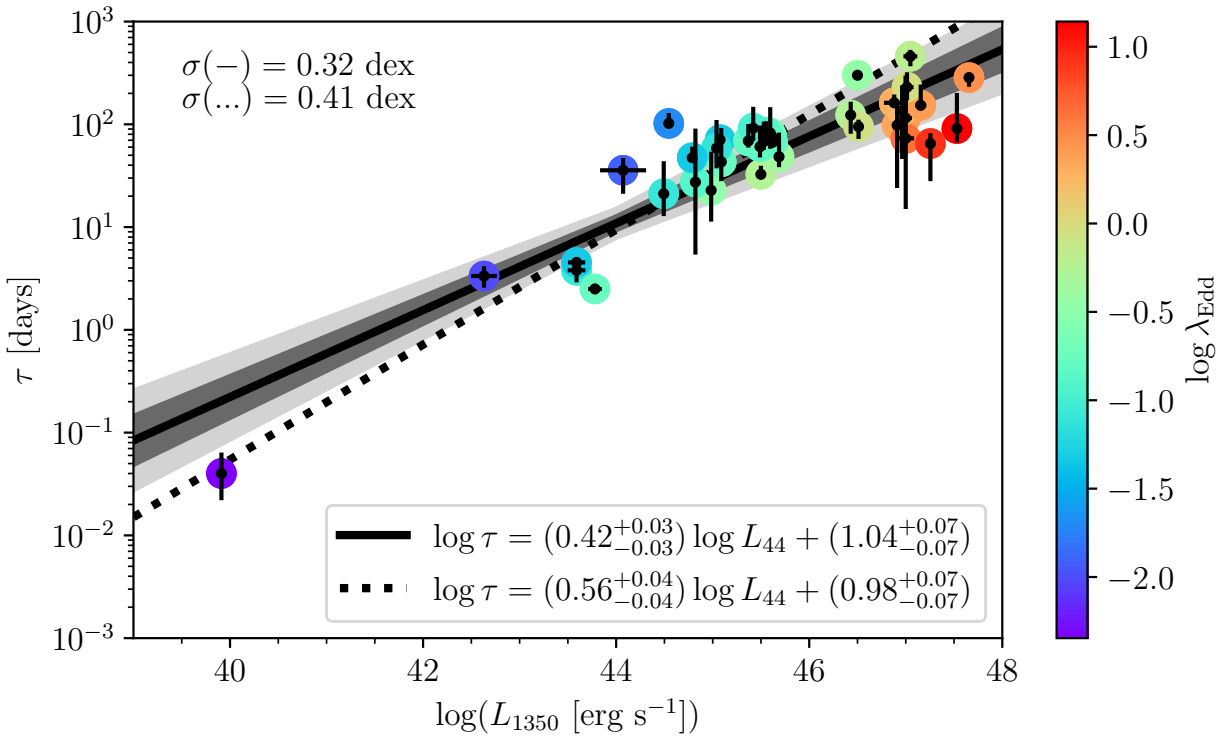

Figure 11.2: Radius-luminosity relationship for the "golden" sample of 38 C IV QSOs (see also Kaspi et al., 2021). The luminosity at 1350 Å is based on the flat ΛCDM model (with $H_0 = 70\,\mathrm{km\,s^{-1}\,Mpc^{-1}}$, $\Omega_{m0} = 0.3$, and $\Omega_\Lambda = 0.7$). The points are colour-coded with respect to the calculated Eddington ratio $\lambda_{\rm Edd} = L_{\rm bol}/L_{\rm Edd}$ of the source. When we neglect individual time-delay errors, the best-fit relation (black solid line) determined by the Levenberg-Marquardt algorithm has a slope of $\gamma_{\rm C} = 0.42 \pm 0.03$ and a scatter of $\sigma = 0.32$ dex. The dark and light gray areas around the best-fit solid line are one and two sigma confidence regions. Considering individual time-delay errors yields the best-fit relation (dotted line) with a larger slope of $\gamma_{\rm C} = 0.56 \pm 0.04$ and the scatter of data around this relation is $\sigma = 0.41$ dex.

the bolometric luminosity calculated using the luminosity-dependent bolometric factor $\kappa_{\rm bol}$ according to Netzer (2019), and $L_{\rm Edd}$ is the Eddington luminosity (Eckart et al., 2017; Zajaček et al., 2014, 2020b). To obtain $L_{\rm Edd}$, the supermassive black hole (SMBH) mass was calculated using the virial relation $M_\bullet = f_{\rm vir} c\tau \mathrm{FWHM}^2/G$, where the virial factor $f_{\rm vir}$ was estimated using the fitted formula that inversely scales with the full width at half maximum, FWHM, see Mejía-Restrepo et al. (2018). The FWHM and τ values were adopted from the compilation of Kaspi et al. (2021). In Fig. 11.2 each source is coloured by the corresponding value of $\log \lambda_{\rm Edd}$.

Apart from the "golden" C IV AGN sample reported by Kaspi et al. (2021), there are

additional lower-quality C IV time-lag detections reported in literature. Grier et al. (2019) report additional 32 C IV detections with a lower quality rating of 1, 2, and 3.[3] As a follow-up of the Oz-DES RM project, Penton et al. (2022) designed a quality-cut methodology and out of 6 test sources, 2 at redshifts 1.93 and 2.74 pass all the quality criteria. These additional 34 sources will be considered in a future study.

Mg II QSO data. As listed in table A1 of Khadka et al. (2021a), the Mg II QSO sample consists of 78 QSOs and spans the redshift range $0.0033 \leq z \leq 1.89$. Detailed descriptions of Mg II QSO data can be found in Khadka et al. (2021a) and Martínez-Aldama et al. (2020b), where it was shown that they obey the $R - L$ relation, with measured quantities being time-delay τ' and QSO flux F_{3000} measured at 3000 Å; see also Prince et al. (2022) for an updated Mg II QSO $R - L$ relation in the fixed flat ΛCDM cosmology. We note that the Mg II QSO sample is relatively homogeneous since 57 significant time-delay detections (hence 73% of Mg II QSO sources) were determined by Homayouni et al. (2020), who applied a consistent time-delay method to all the sources based on JAVELIN (Zu et al., 2011), which was compared with the CREAM results that were generally consistent (Starkey et al., 2016). However, the time-delay uncertainties for this sample are not completely homogeneous and a consistent treatment of the continuum and the line-emission light-curve correlation and the time-delay inference is needed to homogenize the sample of the best Mg II QSO time delays and their uncertainties.

$H(z)$ + BAO data. There are 32 $H(z)$ and 12 BAO measurements listed in Tables 1 and 2 of Cao & Ratra (2022), spanning the redshift ranges $0.07 \leq z \leq 1.965$ and $0.122 \leq z \leq 2.334$, respectively.

[3] Grier et al. (2019) assign the quality flag of 1 to the lowest-quality time-lag detections, while 5 is the highest quality rating. There are different factors considered in the rating scheme, such as the clear correlation between the continuum and C IV emission-line light curves, overall consistency between JAVELIN, CREAM, and ICCF time-lag detections, and the presence of multiple significant time-lag peaks.

11.3 Data Analysis Methodology

We utilize the $R-L$ relation parametrization according to Bentz et al. (2013), where we replace the monochromatic luminosity and rest-frame time-delay taking into account the C IV-region emission properties

$$\log \frac{\tau}{\text{days}} = \beta_{\text{C}} + \gamma_{\text{C}} \log \frac{L_{1350}}{10^{44}\,\text{erg s}^{-1}}, \tag{11.1}$$

where τ, β_{C}, and γ_{C} are the C IV time-lag, the intercept parameter, and the slope parameter, respectively, and the monochromatic luminosity at 1350 Å

$$L_{1350} = 4\pi D_L^2 F_{1350}, \tag{11.2}$$

with measured quasar flux F_{1350} at 1350 Å in units of erg s^{-1} cm^{-2}. The luminosity distance in equation (8.1) is a function of redshift z and the cosmological parameters.

The Mg II QSO $R-L$ relation is

$$\log \frac{\tau'}{\text{days}} = \beta_{\text{M}} + \gamma_{\text{M}} \log \frac{L_{3000}}{10^{44}\,\text{erg s}^{-1}}, \tag{11.3}$$

where τ', β_{M}, and γ_{M} are the Mg II time-lag, the intercept parameter, and the slope parameter, respectively, and the monochromatic luminosity at 3000 Å

$$L_{3000} = 4\pi D_L^2 F_{3000}, \tag{11.4}$$

with measured quasar flux F_{3000} at 3000 Å in units of erg s^{-1} cm^{-2}.

The natural log of the C IV likelihood function (D'Agostini, 2005) is

$$\ln \mathscr{L}_{\text{C IV}} = -\frac{1}{2}\left[\chi^2_{\text{C IV}} + \sum_{i=1}^{N} \ln\left(2\pi\sigma^2_{\text{tot,C},i}\right)\right], \tag{11.5}$$

where

$$\chi^2_{\rm C\,IV} = \sum_{i=1}^{N} \left[\frac{(\log \tau_{{\rm obs},i} - \beta_{\rm C} - \gamma_{\rm C} \log L_{1350,i})^2}{\sigma^2_{{\rm tot,C},i}} \right] \tag{11.6}$$

with total uncertainty

$$\sigma^2_{{\rm tot,C},i} = \sigma^2_{{\rm int,\,C}} + \sigma^2_{\log \tau_{{\rm obs},i}} + \gamma^2_{\rm C} \sigma^2_{\log F_{1350,i}}, \tag{11.7}$$

where $\sigma_{\rm int,\,C}$ is the C IV QSO intrinsic scatter parameter which also contains the unknown systematic uncertainty, and N is the number of data points.

The natural log of the Mg II likelihood function is

$$\ln \mathscr{L}_{\rm Mg\,II} = -\frac{1}{2} \left[\chi^2_{\rm Mg\,II} + \sum_{i=1}^{N} \ln \left(2\pi \sigma^2_{{\rm tot,M},i} \right) \right], \tag{11.8}$$

where

$$\chi^2_{\rm Mg\,II} = \sum_{i=1}^{N} \left[\frac{(\log \tau'_{{\rm obs},i} - \beta_{\rm M} - \gamma_{\rm M} \log L_{3000,i})^2}{\sigma^2_{{\rm tot,M},i}} \right] \tag{11.9}$$

with total uncertainty

$$\sigma^2_{{\rm tot,M},i} = \sigma^2_{{\rm int,\,M}} + \sigma^2_{\log \tau'_{{\rm obs},i}} + \gamma^2_{\rm M} \sigma^2_{\log F_{3000,i}}, \tag{11.10}$$

where $\sigma_{\rm int,\,M}$ is the Mg II QSO intrinsic scatter parameter which also contains the unknown systematic uncertainty.

The τ error bars are typically asymmetric. As used for Mg II QSOs in Khadka et al. (2021a) and Cao & Ratra (2022), in what follows, τ symmetrized errors mean that we are using symmetrized σ_τ's defined as $\sigma_\tau = [2\sigma_{\tau,+}\sigma_{\tau,-}/(\sigma_{\tau,+} + \sigma_{\tau,-}) + \sqrt{\sigma_{\tau,+}\sigma_{\tau,-}}]/2$, where $\sigma_{\tau,+}$ and $\sigma_{\tau,-}$ are the upper and lower errors of τ, respectively. On the other hand, τ asymmetric errors mean that we directly use asymmetric $\sigma_{\tau,+}$ and $\sigma_{\tau,-}$ as follows: when the theoretical prediction for $\log \tau$ is larger (smaller) than the observed value, $\sigma_\tau = \sigma_{\tau,+}$ ($\sigma_\tau = \sigma_{\tau,-}$).

The detailed descriptions for the likelihood functions of $H(z)$ and BAO data can be found in Cao et al. (2020).

Table 11.1: Flat priors of the constrained parameters.

Parameter	Prior
Cosmological-Model Parameters	
H_0 [a]	[None, None]
$\Omega_b h^2$ [b]	[0, 1]
$\Omega_c h^2$ [c]	[0, 1]
Ω_{k0}	[-2, 2]
α	[0, 10]
$w_{\rm X}$	[-5, 0.33]
$R-L$ Relation Parameters	
γ	[0, 5]
β	[0, 10]
$\sigma_{\rm int}$	[0, 5]

[a] km s^{-1} Mpc^{-1}. In the C IV QSO and Mg II QSO alone cases, H_0 is set to be 70 km s^{-1} Mpc^{-1}, while in other cases, the prior range is irrelevant (unbounded).
[b] In the C IV QSO and Mg II QSO alone cases, $\Omega_b h^2$ is set to be 0.0245, i.e. $\Omega_b = 0.05$.
[c] In the C IV QSO and Mg II QSO alone cases, $\Omega_{m0} \in [0, 1]$ is ensured.

We list the flat priors of the free cosmological-model and $R-L$ relation parameters in Table 11.1. By maximizing the likelihood functions, we obtain the unmarginalized best-fitting values and posterior distributions of all free cosmological-model and $R-L$ relation parameters. The Markov chain Monte Carlo (MCMC) code MontePython (Audren et al., 2013; Brinckmann & Lesgourgues, 2019), the class code, and the python package getdist (Lewis, 2019) are used to perform our analyses.

One can find the definitions of the Akaike Information Criterion (AIC), the Bayesian Information Criterion (BIC), and the Deviance Information Criterion (DIC) in our previous paper (see, e.g. Cao et al., 2022c). ΔAIC, ΔBIC, and ΔDIC are computed as the differences between the AIC, BIC, and DIC values of the other five cosmological dark energy models and those of the flat ΛCDM reference model. Positive (negative) values of these ΔICs show that the model under investigation fits the data worse (better) than does the flat ΛCDM reference model. In comparison with the model with the minimum IC, $\Delta\mathrm{IC} \in (0, 2]$ indicates weak evidence against the model under investigation, $\Delta\mathrm{IC} \in (2, 6]$ indicates positive evidence against the model under investigation, $\Delta\mathrm{IC} \in (6, 10]$ indicates strong evidence against the model under investigation, and $\Delta\mathrm{IC} > 10$ indicates very strong evidence against the model under investigation.

We assume one massive and two massless neutrino species with the non-relativistic neutrino physical energy density parameter $\Omega_\nu h^2 = \sum m_\nu/(93.14\ \mathrm{eV}) = 0.06\ \mathrm{eV}/(93.14\ \mathrm{eV})$, where h is the Hubble constant H_0 in units of 100 km s^{-1} Mpc^{-1}. The non-relativistic matter density parameter $\Omega_{m0} = (\Omega_\nu h^2 + \Omega_b h^2 + \Omega_c h^2)/h^2$, where $\Omega_b h^2$ and $\Omega_c h^2$ are the current values of the observationally-constrained baryonic and cold dark matter physical energy density parameters, respectively.[4] Including neutrino species is more accurate even though it only has a mild effect on the constraints from Mg II and C IV data.

[4]In the C IV QSO and Mg II QSO alone cases, the current value of the baryonic matter energy density parameter and the Hubble constant are set to $\Omega_b = 0.05$ and $H_0 = 70$ km s^{-1} Mpc^{-1}, respectively, because these data alone are unable to constrain Ω_b and H_0.

11.4 Results

The posterior one-dimensional probability distributions and two-dimensional confidence regions of cosmological-model and $R - L$ relation parameters for the six cosmological models are shown in Figs. 11.3–11.8, where in panel (a) of each figure results of the C IV data analyses with symmetrized errors and asymmetric errors are shown in green and red, respectively; in panel (b) of each figure results of the Mg II data analyses with symmetrized errors and asymmetric errors are shown in green and red, respectively; in panel (c) of each figure the results of the C IV, Mg II, and joint C IV + Mg II data analyses with asymmetric errors, and the $H(z)$ + BAO data analysis are shown in red, green, blue, and black, respectively; and in panels (d) and (e) of each figure the results of the joint (asymmetric errors) C IV + Mg II, $H(z)$ + BAO, and $H(z)$ + BAO + C IV + Mg II data analyses are shown in grey, blue, and red, respectively. The unmarginalized best-fitting parameter values, as well as the values of maximum likelihood $\mathscr{L}_{\max}$, AIC, BIC, DIC, ΔAIC, ΔBIC, and ΔDIC, for all models and data sets, are listed in Table 11.2. The marginalized posterior mean parameter values and uncertainties ($\pm 1\sigma$ error bars and 1 or 2σ limits), for all models and data sets, are listed in Table 11.3.

In all six cosmological models, all data combinations more favour currently accelerating cosmological expansion. This is also the case with Mg II QSO data (Khadka et al., 2021a, 2022a), but differs from what happens with Hβ QSO data, which more favour currently decelerated cosmological expansion (Khadka et al., 2022a).

11.4.1 Constraints from C IV, Mg II, and C IV + Mg II QSO data

As shown in panels (a) and (b) of Figs. 11.3–11.8 and Table 11.3, we find that results from C IV QSO and Mg II QSO symmetrized errors data analyses are only mildly different (less than 1σ) from those of C IV QSO and Mg II QSO asymmetric errors data analyses. Since the analyses with asymmetric errors are the more correct ones, we summarize the asymmetric errors C IV results in what follows. The symmetric errors Mg II results are discussed in Khadka et al. (2021a).

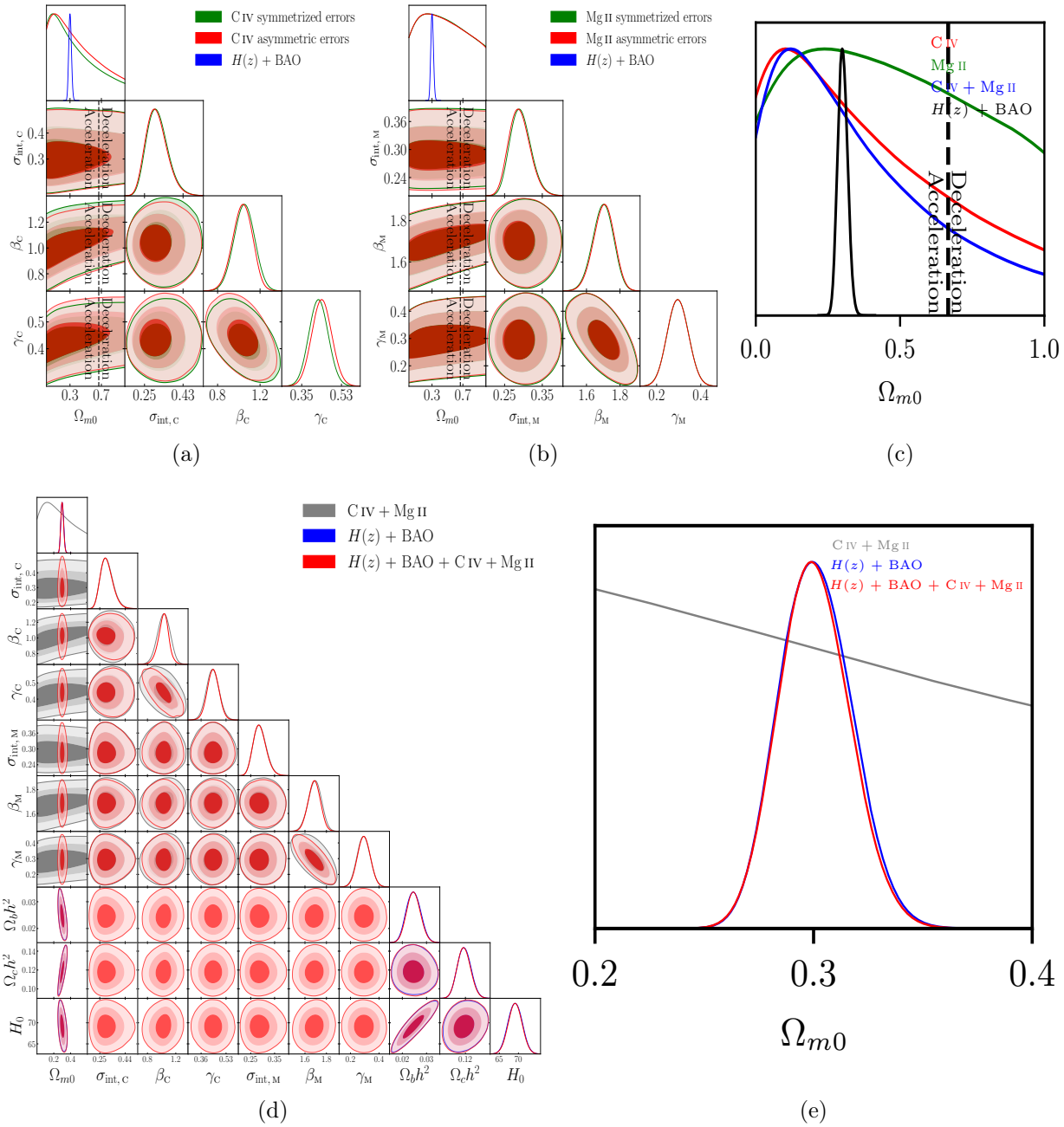

Figure 11.3: One-dimensional likelihood distributions and 1σ, 2σ, and 3σ two-dimensional likelihood confidence contours for flat ΛCDM from various combinations of data. The zero-acceleration black dashed lines in panels (a) and (b) divide the parameter space into regions associated with currently-accelerating (left) and currently-decelerating (right) cosmological expansion.

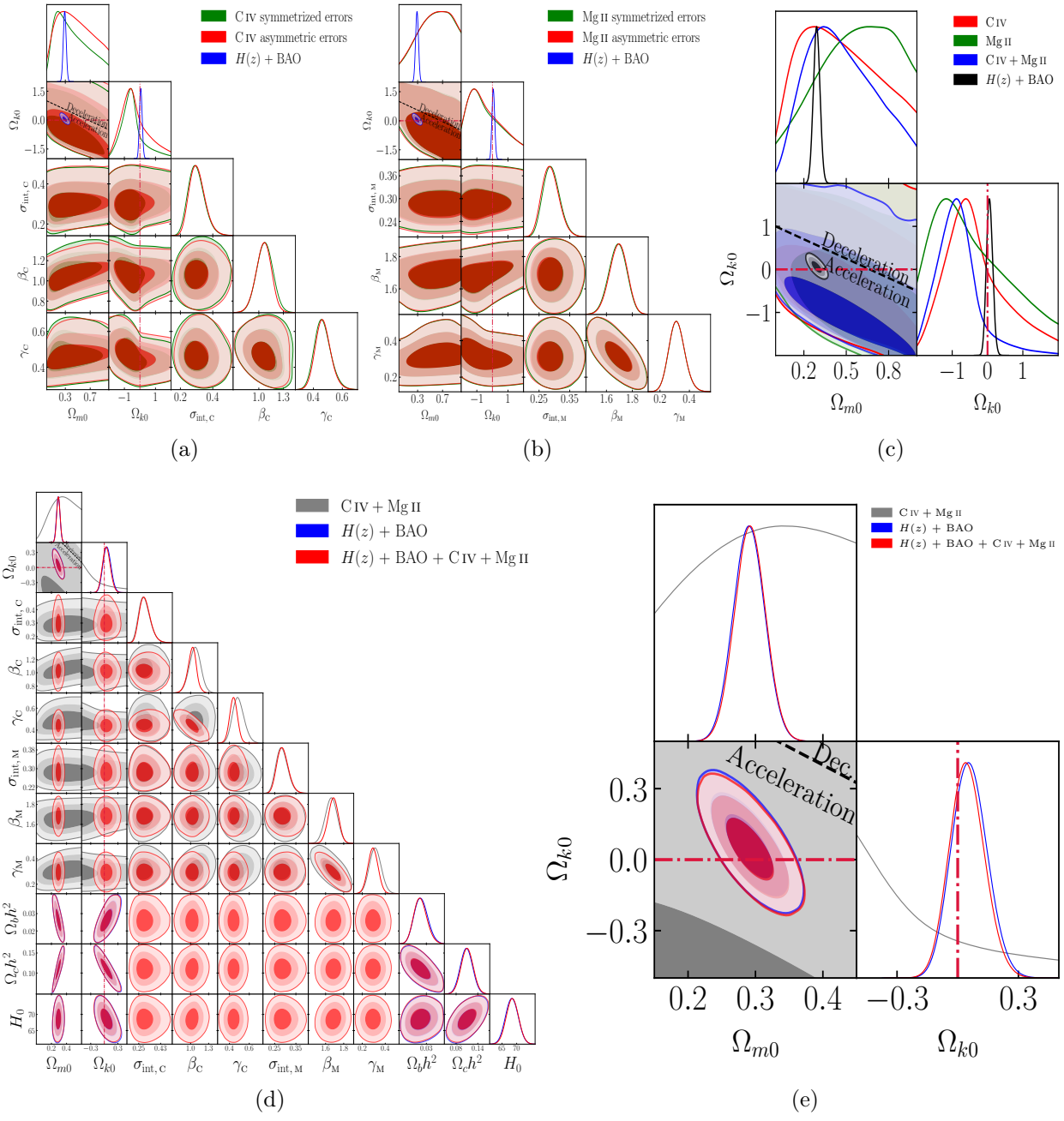

Figure 11.4: Same as Fig. 11.3 but for non-flat ΛCDM. The zero-acceleration black dashed lines divide the parameter space into regions associated with currently-accelerating (below left) and currently-decelerating (above right) cosmological expansion.

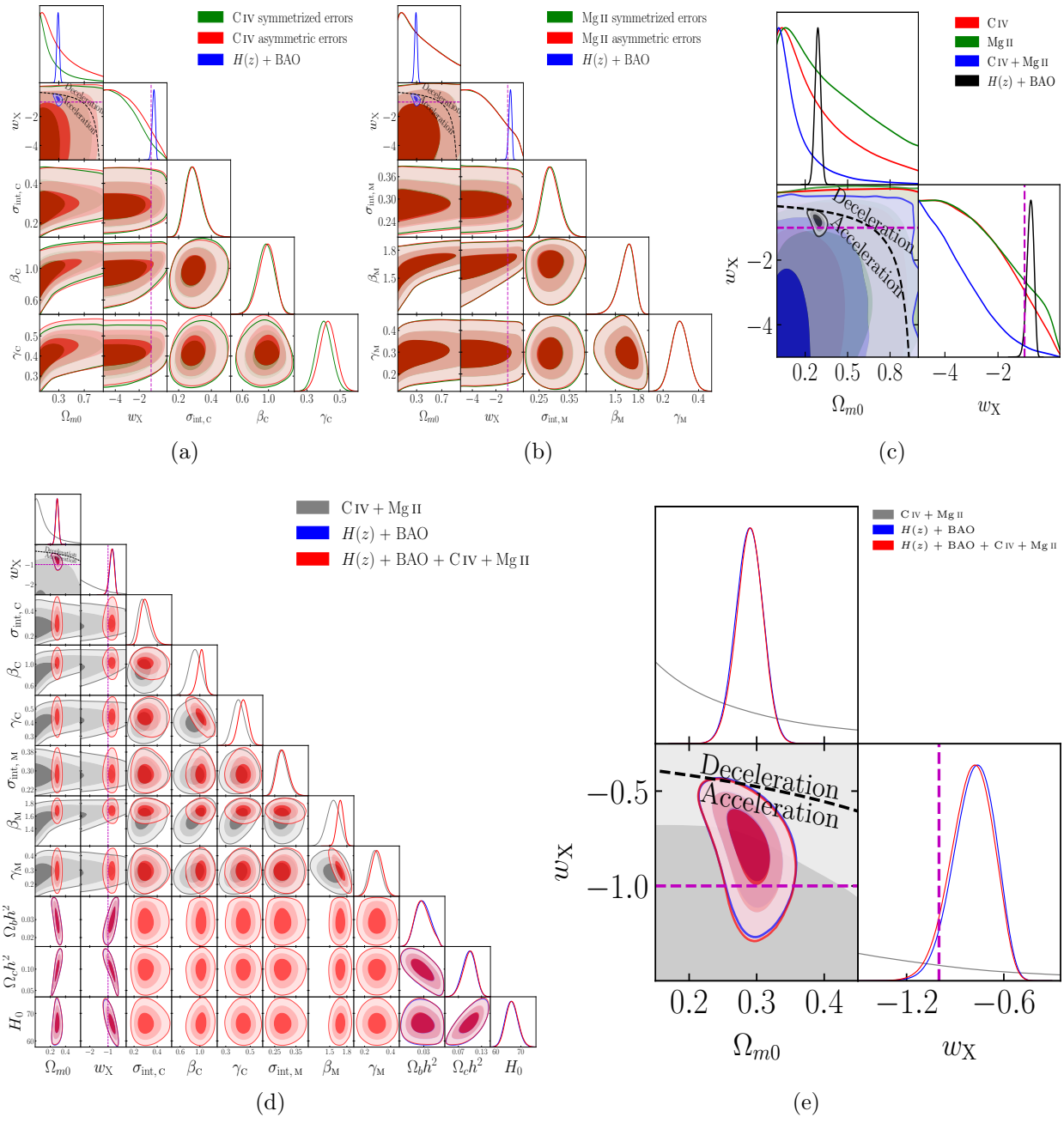

Figure 11.5: One-dimensional likelihood distributions and 1σ, 2σ, and 3σ two-dimensional likelihood confidence contours for flat XCDM from various combinations of data. The zero-acceleration black dashed lines divide the parameter space into regions associated with currently-accelerating (either below left or below) and currently-decelerating (either above right or above) cosmological expansion. The magenta dashed lines represent $w_{\rm X} = -1$, i.e. flat ΛCDM.

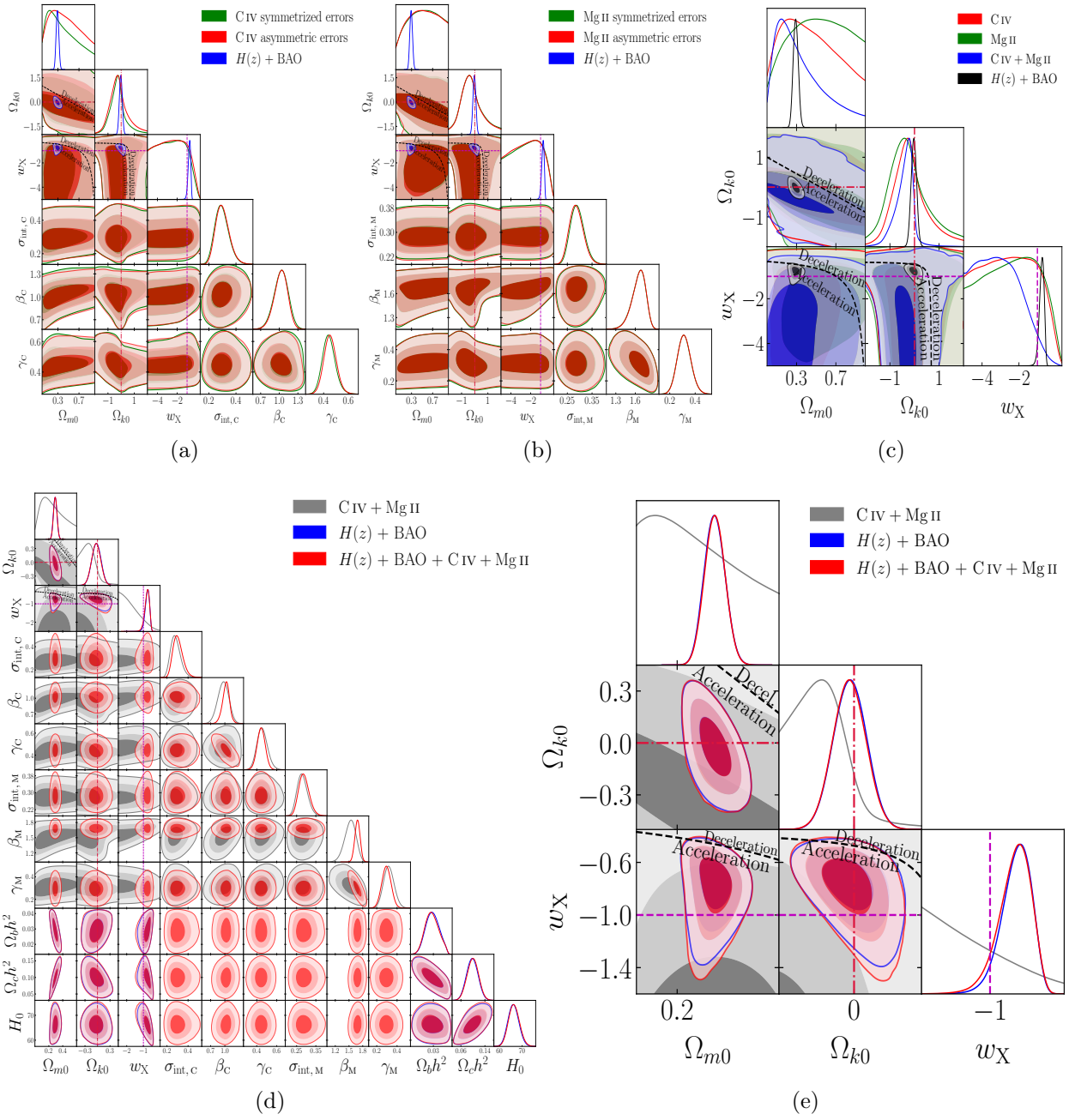

Figure 11.6: Same as Fig. 11.5 but for non-flat XCDM. The zero-acceleration black dashed lines are computed for the third cosmological parameter set to the $H(z)$ + BAO data best-fitting values listed in Table 11.2, and divide the parameter space into regions associated with currently-accelerating (either below left or below) and currently-decelerating (either above right or above) cosmological expansion. The crimson dash-dot lines represent flat hypersurfaces, with closed spatial hypersurfaces either below or to the left. The magenta dashed lines represent $w_{\rm X} = -1$, i.e. non-flat ΛCDM.

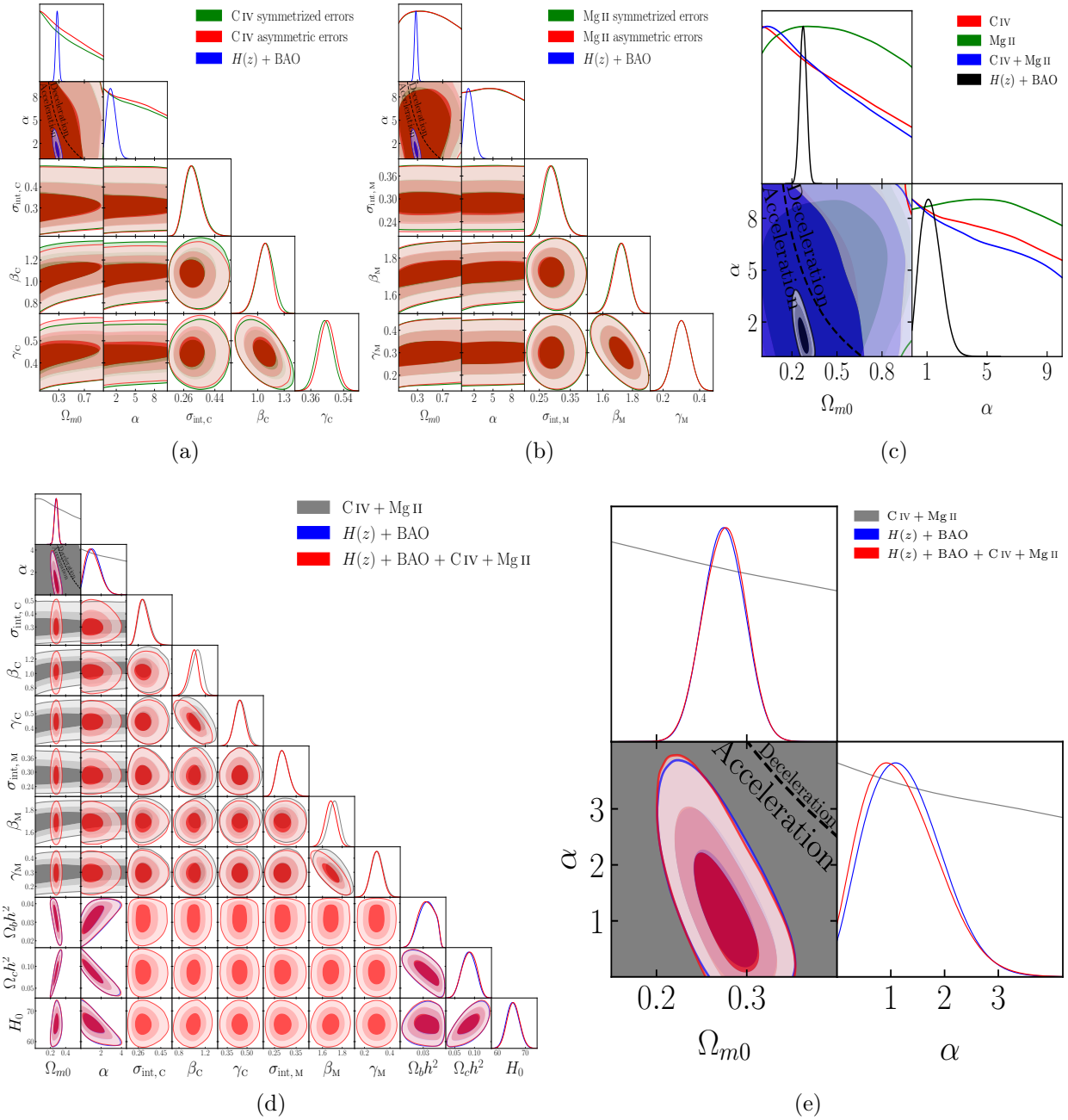

Figure 11.7: One-dimensional likelihood distributions and 1σ, 2σ, and 3σ two-dimensional likelihood confidence contours for flat ϕCDM from various combinations of data. The zero-acceleration black dashed lines divide the parameter space into regions associated with currently-accelerating (below left) and currently-decelerating (above right) cosmological expansion. The $\alpha = 0$ axes correspond to flat ΛCDM.

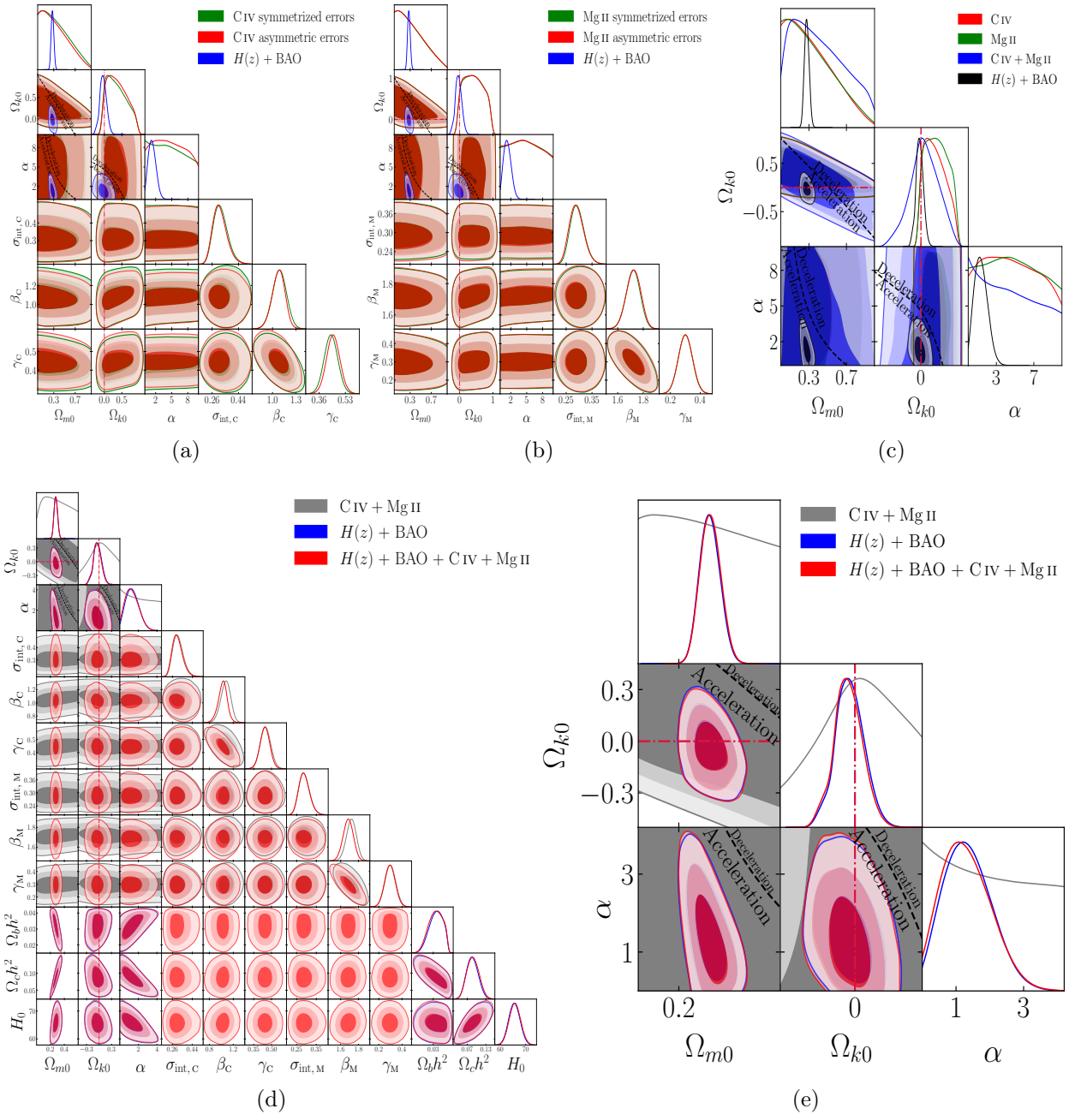

Figure 11.8: Same as Fig. 11.7 but for non-flat ϕCDM. The zero-acceleration black dashed lines are computed for the third cosmological parameter set to the $H(z)$ + BAO data best-fitting values listed in Table 11.2, and divide the parameter space into regions associated with currently-accelerating (below left) and currently-decelerating (above right) cosmological expansion. The crimson dash-dot lines represent flat hypersurfaces, with closed spatial hypersurfaces either below or to the left. The $\alpha = 0$ axes correspond to non-flat ΛCDM.

The Ω_{m0} constraints from C IV data range from a low of < 0.840 (2σ, flat XCDM) to a high of $0.467^{+0.199}_{-0.378}$ (1σ, non-flat ΛCDM).

The Ω_{k0} constraints from C IV data are $-0.330^{+0.534}_{-1.060}$, $-0.168^{+0.451}_{-0.789}$, and $0.096^{+0.359}_{-0.337}$ for non-flat ΛCDM, XCDM, and ϕCDM, respectively. Although C IV data favour closed hypersurfaces in non-flat ΛCDM and non-flat XCDM, and favour open hypersurfaces in non-flat ϕCDM, flat hypersurfaces are well within 1σ. C IV data only provide very weak constraints of $w_{\rm X}$ and α.

From panels (c) of Figs. 11.3–11.8, we see that the cosmological-model parameter constraints from C IV QSO data and from Mg II QSO data are mutually consistent, as are the cosmological constraints from C IV QSO and $H(z)$ + BAO data and from Mg II QSO and $H(z)$ + BAO data.[5] It is therefore reasonable to perform joint analyses of C IV QSO and Mg II QSO data. As shown in panels (d) and (e) of Figs. 11.3–11.8, the cosmological-model parameter constraints from C IV + Mg II QSO data and from $H(z)$ + BAO data are mutually consistent at $\lesssim 1.5\sigma$,[6] so these data sets can be jointly analyzed.

The constraints on the C IV $R-L$ relation parameters in the six different cosmological models are mutually consistent, so the $R-L$ relation C IV data set is standardizable. The constraints on the intrinsic scatter parameter of the C IV $R-L$ relation, $\sigma_{\rm int,\,C}$, range from a low of $0.296^{+0.041}_{-0.056}$ (flat XCDM) to a high of $0.314^{+0.038}_{-0.055}$ (flat ϕCDM), with a difference of 0.26σ, which are $\sim 0.1-0.4\sigma$ larger than those of Mg II ($\sigma_{\rm int,\,M}$). The constraints on the slope parameter of the C IV $R-L$ relation, $\gamma_{\rm C}$, range from a low of 0.426 ± 0.049 (flat XCDM) to a high of $0.468^{+0.046}_{-0.056}$ (non-flat ΛCDM), with a difference of 0.56σ. The constraints on the intercept parameter of the C IV $R-L$ relation, $\beta_{\rm C}$, range from a low of $0.970^{+0.136}_{-0.108}$ (flat XCDM) to a high of $1.076^{+0.087}_{-0.074}$ (non-flat ϕCDM), with a difference of 0.68σ.

A summary value of the measured C IV $R-L$ relation slope, $\gamma_{\rm C} \simeq 0.45 \pm 0.04$, indicates that it is about 1σ lower than and consistent with the prediction of simple photoionization theory ($\gamma = 0.5$, Karas et al., 2021; Panda, 2022), on the other hand a summary value of the

[5] Khadka et al. (2021a, 2022a) had earlier shown that the symmetric errors Mg II cosmological constraints are mutually consistent with those from $H(z)$ + BAO data. This differs from the Hβ QSOs cosmological constraints, which are $\sim 2\sigma$ inconsistent with those from $H(z)$ + BAO data (Khadka et al., 2022a).

[6] I.e., in the two-dimensional contour plots all or most of the 1σ $H(z)$ + BAO data contour always lie inside the 2σ C IV + Mg II QSO data contour.

measured Mg II $R-L$ relation slope, $\gamma_{\rm M} \simeq 0.3 \pm 0.05$ (also see Khadka et al., 2021a, 2022a), indicates that it is about 4σ lower than $\gamma = 0.5$.

The Ω_{m0} constraints from (asymmetric errors) C IV + Mg II data range from a low of < 0.563 (2σ, flat XCDM) to a high of < 0.537 (1σ, flat ϕCDM).

The Ω_{k0} constraints from C IV + Mg II data are $-0.818^{+0.391}_{-0.637}$ (< 0.474, 2σ), $-0.410^{+0.368}_{-0.222}$ ($-0.410^{+0.698}_{-0.846}$, 2σ), and $0.088^{+0.384}_{-0.364}$ ($0.088^{+0.732}_{-0.722}$, 2σ) for non-flat ΛCDM, XCDM, and ϕCDM, respectively. C IV + Mg II data favour closed hypersurfaces in non-flat ΛCDM and non-flat XCDM, being $> 1\sigma$ (but $< 2\sigma$) and $\sim 1.1\sigma$ away from flat hypersurfaces, respectively, and favour open hypersurfaces in non-flat ϕCDM, with flat hypersurfaces being within 1σ. C IV + Mg II data still provide weak constraints on $w_{\rm X}$ and α, but $w_{\rm X}$ constraints are more than 2σ away from $w_{\rm X} = -1$ (ΛCDM).

C IV + Mg II data provide consistent (within 1σ) constraints on the intrinsic scatter, slope, and intercept parameters of both C IV and Mg II $R-L$ relations, which confirms that C IV and Mg II QSOs are standardizable through different $R-L$ relations.

11.4.2 Constraints from $H(z)$ + BAO + C IV + Mg II data

The mutually consistent cosmological-model parameter constraints allow us to jointly analyze $H(z)$ + BAO and C IV + Mg II data. In what follows we summarize the cosmological-model parameter constraints from $H(z)$ + BAO + C IV + Mg II data and contrast them with those from $H(z)$ + BAO data.

The $H(z)$ + BAO + C IV + Mg II data provide Ω_{m0} constraints ranging from a low of 0.275 ± 0.023 (flat ϕCDM) to a high of $0.301^{+0.015}_{-0.017}$ (flat ΛCDM), with a difference of 0.91σ, which only slightly differ from those determined using only $H(z)$ + BAO data.

The H_0 constraints from $H(z)$ + BAO + C IV + Mg II data range from a low of $65.68^{+2.20}_{-2.19}$ km s^{-1} Mpc^{-1} (flat ϕCDM) to a high of 69.15 ± 1.77 km s^{-1} Mpc^{-1} (flat ΛCDM), with a difference of 1.23σ, which are 0.65σ (flat ϕCDM) lower than and 0.35σ (flat ΛCDM) higher than the median statistics estimate of $H_0 = 68 \pm 2.8$ km s^{-1} Mpc^{-1} (Chen & Ratra, 2011), and 2.94σ (flat ϕCDM) and 1.84σ (flat ΛCDM) lower than the local Hubble constant

measurement of $H_0 = 73.2 \pm 1.3$ km s^{-1} Mpc^{-1} (Riess et al., 2021). The $H(z)$ + BAO + C IV + Mg II data provide H_0 constraints that are slightly higher ($\sim 0.1\sigma$ at most) and mostly more restrictive ($\sim 4\%$ at most) than those from $H(z)$ + BAO data.

The Ω_{k0} constraints from $H(z)$ + BAO + C IV + Mg II data are $0.047^{+0.079}_{-0.089}$, -0.031 ± 0.108, and $-0.044^{+0.090}_{-0.094}$ for non-flat ΛCDM, XCDM, and ϕCDM, respectively, which are slightly lower ($\sim 0.1\sigma$ at most) than those from $H(z)$ + BAO data. Similar to the $H(z)$ + BAO data results, non-flat ΛCDM mildly favours open hypersurfaces, whereas non-flat XCDM and non-flat ϕCDM mildly favour closed hypersurfaces. However, flat hypersurfaces are well within 1σ.

Dark energy dynamics is favoured. For flat (non-flat) XCDM, $w_{\rm X} = -0.799^{+0.143}_{-0.111}$ ($w_{\rm X} = -0.787^{+0.165}_{-0.102}$), with central values being 1.81σ ($< 2\sigma$) higher than $w_{\rm X} = -1$; and for flat (non-flat) ϕCDM, $\alpha = 1.202^{+0.490}_{-0.862}$ ($\alpha = 1.320^{+0.572}_{-0.869}$), with central values being 1.39σ (1.52σ) away from $\alpha = 0$. The addition of C IV + Mg II data to $H(z)$ + BAO data bring $w_{\rm X}$ and α values lower, and closer to ΛCDM model values.

As expected, the constraints on the C IV and Mg II $R - L$ relation parameters are consistent with those from the individual data sets and the C IV + Mg II data.

11.4.3 Model Comparison

From the AIC, BIC, and DIC values listed in Table 11.2, we find the following results (from the more correct C IV and Mg II asymmetric errors analyses):

1) **AIC.** $H(z)$ + BAO and $H(z)$ + BAO + C IV + Mg II data favour flat ϕCDM the most, and the evidence against the rest of the models/parametrizations is either only weak or positive.

   C IV, Mg II, and C IV + Mg II data favour non-flat XCDM the most, however, in the C IV case, the evidence against non-flat ΛCDM and flat XCDM is only weak, the evidence against flat ΛCDM is positive, and the evidence against flat and non-flat ϕCDM is strong; in the Mg II case, the evidence against non-flat ΛCDM and flat XCDM is positive, the evidence against flat ΛCDM and flat ϕCDM is strong, and the evidence

against non-flat ϕCDM is very strong; and in the C IV + Mg II case, the evidence against flat XCDM is positive, the evidence against non-flat ΛCDM is strong, and other models are very strongly disfavoured.

2) **BIC.** $H(z)$ + BAO and $H(z)$ + BAO + C IV + Mg II data favour flat ΛCDM the most, and in the former case, the evidence against the rest of the models/parametrizations is either only weak or positive, while in the latter case, the evidence against the rest of the models/parametrizations is either positive or strong (non-flat XCDM and non-flat ϕCDM).

   C IV data favour non-flat ΛCDM the most, and the evidence against flat and non-flat XCDM is only weak, the evidence against flat ΛCDM is positive, and the evidence against flat and non-flat ϕCDM is strong.

   Mg II and C IV + Mg II data favour non-flat XCDM the most, however, in the Mg II case, the evidence against non-flat ΛCDM, flat XCDM, and non-flat XCDM is only weak, the evidence against flat ϕCDM is strong, and the evidence against non-flat ϕCDM is very strong; and in the C IV + Mg II case, the evidence against non-flat ΛCDM and flat XCDM is positive, the evidence against flat ΛCDM is strong, and non-flat XCDM and non-flat ϕCDM are very strongly disfavoured.

3) **DIC.** $H(z)$ + BAO and $H(z)$ + BAO + C IV + Mg II data favour flat ϕCDM the most, and the evidence against the rest of the models/parametrizations is either only weak or positive.

   C IV and Mg II data favour flat ΛCDM the most, however, in the former case, the evidence against the rest of the models/parametrizations is either only weak or positive, whereas in the latter case, the evidence against flat and non-flat ϕCDM is only weak, the evidence against non-flat ΛCDM and flat XCDM is positive, and the evidence against non-flat XCDM is strong.

   C IV + Mg II data favour non-flat XCDM the most, and the evidence against the rest of the models/parametrizations is either only weak or positive.

Based on the more reliable DIC (Liddle, 2007; Spiegelhalter et al., 2002), except for the Mg II data set, these data sets do not provide strong evidence against any of the cosmological models/parametrizations.

11.5 Discussion

We have shown that QSOs with measured C IV time-delays can be standardized and so can be used as cosmological probes. Mg II QSOs are also standardizable and so can be jointly analyzed with C IV QSOs to constrain cosmological model parameters. This is not true for current Hβ QSOs (Khadka et al., 2022a) and more work is needed to clarify the Hβ QSO situation.

However, we find a 2.3σ difference in the measured slopes of the C IV and Mg II $R-L$ relations, in the flat ΛCDM model asymmetric error bars results of Table 11.3, or from the summary values of the measured C IV and Mg II $R-L$ relation slopes, $\gamma_{\rm C} \simeq 0.45 \pm 0.04$ and $\gamma_{\rm M} \simeq 0.3 \pm 0.05$. And while the C IV slope is only about 1σ lower than the $\gamma = 0.5$ slope predicted by simple photoionization theory (Bentz et al., 2013; Karas et al., 2021; Panda, 2022) or a dust-based model of the BLR (Czerny & Hryniewicz, 2011; Müller et al., 2022; Naddaf & Czerny, 2022; Naddaf et al., 2021), the Mg II slope is about 4σ lower than $\gamma = 0.5$, which is more statistically significant.

In this section we examine potential (selection effect produced) differences between the C IV and Mg II compilations and conclude that the ones we study here are not very significant. We begin by computing the Eddington ratio $\lambda_{\rm Edd}$ for the 78 Mg II sources and the 38 C IV sources. We use the definition $\lambda_{\rm Edd} = L_{\rm bol}/L_{\rm Edd}$ where the bolometric luminosity is estimated as a multiple of the corresponding monochromatic luminosity (L_{1350} for the C IV sample and L_{3000} for the Mg II sample; for the calculations in this section we adopt the fixed flat ΛCDM model with $\Omega_{m0} = 0.3$, $\Omega_\Lambda = 0.7$, and $H_0 = 70\,{\rm km\,s^{-1}\,Mpc^{-1}}$), taking into account the monochromatic luminosity-dependent bolometric correction factors according to Netzer (2019). Subsequently, we evaluate the correlations between $\lambda_{\rm Edd}$ and the monochromatic luminosity and the redshift.

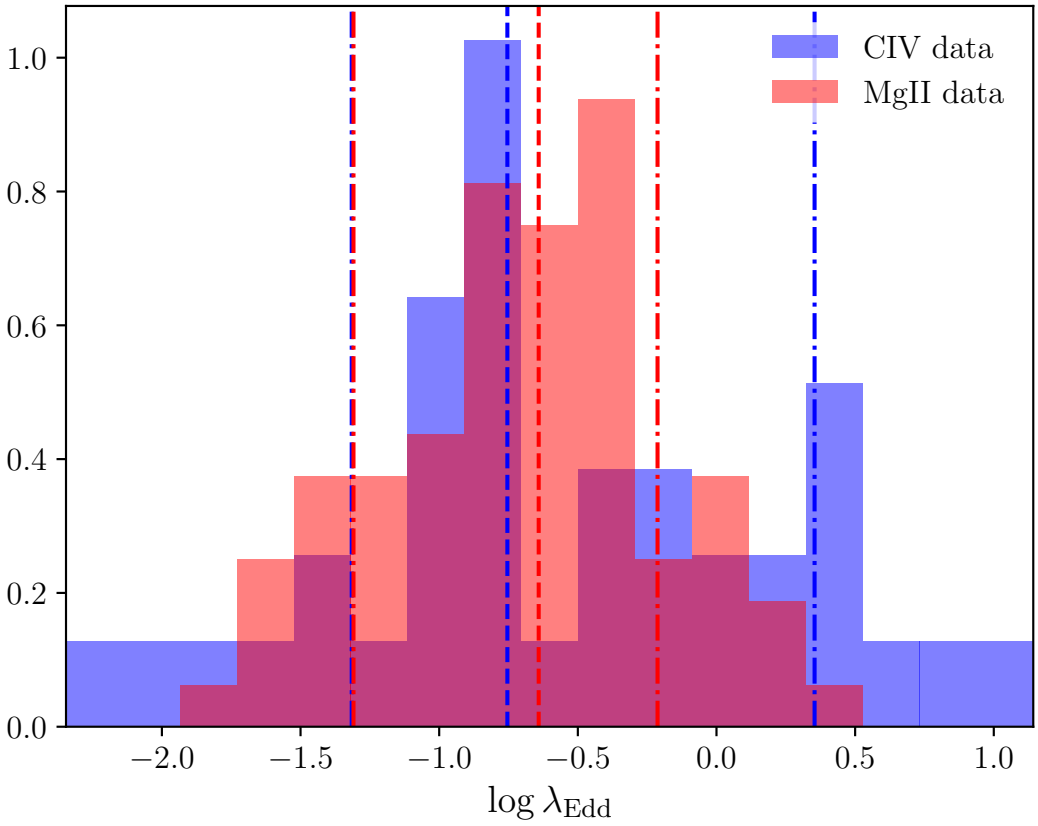

Figure 11.9: Normalized distributions of the Eddington ratio ($\log \lambda_{\rm Edd}$) for the C IV sample (blue histogram) and for the Mg II sample (pink histogram). Vertical dashed lines stand for median values, while the dot-dashed lines represent 16- and 84-% percentiles. The bin size is $\Delta(\log \lambda_{\rm Edd}) \sim 0.205$.

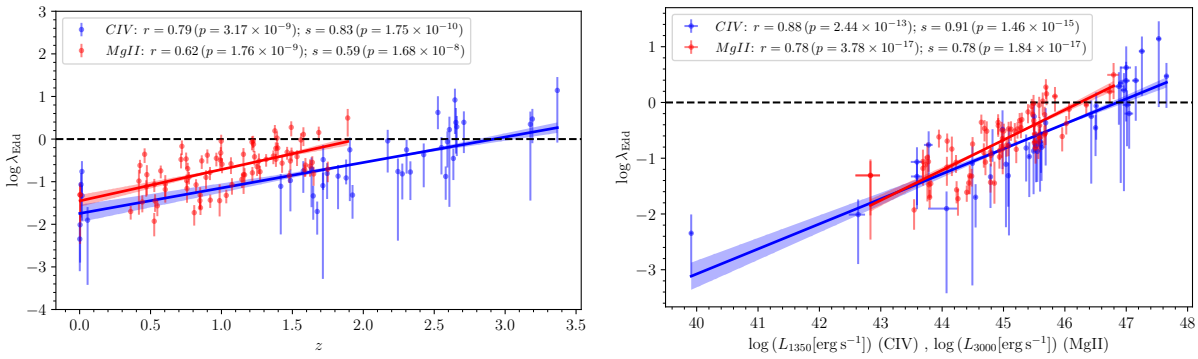

Figure 11.10: The Eddington ration $\lambda_{\rm Edd} = L_{\rm bol}/L_{\rm Edd}$ as a function of the source redshift (left panel) and as a function of the monochromatic luminosities L_{1350} or L_{3000} (right panel) for C IV (blue points) and Mg II (red points) sources. In both panels, we include the Pearson (r) and the Spearman rank-order correlation coefficients (s), which indicate significant positive correlations between $\lambda_{\rm Edd}$ and z as well as $\lambda_{\rm Edd}$ and L_{1350} (or L_{3000}). The horizontal dashed line stands for the Eddington limit ($\log \lambda_{\rm Edd} = 0$). The solid blue and red lines stand for the best-fitting linear relations for the C IV and Mg II datasets, respectively, see Eqs. (11.11) and Eqs. (11.12) for the best-fitting slopes and intercepts including 1σ uncertainties.

The Eddington-ratio normalized distributions for the C IV and Mg II samples are shown in Fig. 11.9, represented by blue and pink histograms, respectively. The vertical dashed lines stand for the distribution medians, while vertical dot-dashed lines mark 16- and 84-% percentiles. For the Mg II sample, the $\lambda_{\rm Edd}$ distribution median is -0.64, while 16- and 84-% percentiles are -1.31 and -0.21, respectively. For the C IV sample, the median of the $\lambda_{\rm Edd}$ distribution is -0.75, while 16- and 84-% percentiles are -1.32 and 0.35, respectively. The median $\lambda_{\rm Edd}$ of the Mg II sources is larger than the median $\lambda_{\rm Edd}$ of the C IV sources. However, the C IV distribution is skewed significantly towards higher $\lambda_{\rm Edd}$ values, with a total range of $(-2.35, 1.14)$, in comparison with the range of $(-1.93, 0.50)$ for the Mg II sample. Also note that the Eddington ratios of the super-Eddington sources generally have large error bars, being consistent with the Eddington limit as well.

The $\lambda_{\rm Edd}$-z and $\lambda_{\rm Edd}$-L_{1350} or $\lambda_{\rm Edd}$-L_{3000} correlations are positive, see Fig. 11.10, left and right panels, respectively. The correlation significance is evaluated using Pearson and Spearman rank-order correlation coefficients, see the legend in Fig. 11.10. For both C IV and Mg II samples, the $\lambda_{\rm Edd}$-z correlation is positive and significant, being slightly stronger and more significant for C IV sources. The correlation between $\lambda_{\rm Edd}$ and the corresponding

monochromatic luminosity is also positive and significant for both samples. Here we stress that the correlation between the Eddington ratio $\lambda_{\rm Edd}$ and the corresponding monochromatic luminosities is enhanced intrinsically due to the definition of $\lambda_{\rm Edd} = L_{\rm bol}/L_{\rm Edd}$, where the bolometric luminosity is proportional to the monochromatic luminosity. However, the relative comparison of the correlation slopes provides hints about the similarities/differences of the two samples.

The slopes and the intercepts of the best-fitting linear relations between $\lambda_{\rm Edd}$ and z are

$$\begin{aligned} \log \lambda_{\rm Edd}({\rm C\,IV}) &= (0.60 \pm 0.10)z - (1.75 \pm 0.20)\,, \\ \log \lambda_{\rm Edd}({\rm Mg\,II}) &= (0.74 \pm 0.12)z - (1.45 \pm 0.14)\,, \end{aligned} \tag{11.11}$$

while for the best-fitting linear relations between $\lambda_{\rm Edd}$ and the monochromatic luminosity we obtain

$$\begin{aligned} \log \lambda_{\rm Edd}({\rm C\,IV}) &= (0.45 \pm 0.04) \log L_{1350} - (21.03 \pm 1.97)\,, \\ \log \lambda_{\rm Edd}({\rm Mg\,II}) &= (0.54 \pm 0.05) \log L_{3000} - (25.01 \pm 2.25)\,. \end{aligned} \tag{11.12}$$

The best-fitting relations are depicted in Fig. 11.10 including 1σ uncertainties of the best-fitting parameters. Compared to the C IV case, the Mg II Eddington ratios for the sample of 78 sources appear to increase more steeply with both redshift and monochromatic luminosity, though the Mg II and C IV slopes are consistent within 1.0σ (for the $\lambda_{\rm Edd}$ vs. z correlations) and 1.4σ (for the $\lambda_{\rm Edd}$ vs. monochromatic luminosity correlations), respectively. The differences in slopes may merely be due to the limited number of sources in each sample, and hence a selection effect.

However, when we study how the time-delay difference between the measured value and the value predicted from the best-fit $R - L$ relation (in the fixed flat ΛCDM model) — $\Delta\tau \equiv \log(\tau/\tau_{\rm RL})$ (Martínez-Aldama et al., 2019; Zajaček et al., 2020a) — correlates with the Eddington ratio, the (anti)correlation is more significant and steeper for Mg II sources. This is shown in Fig. 11.11 for both C IV (blue points) and Mg II sources (red points). As

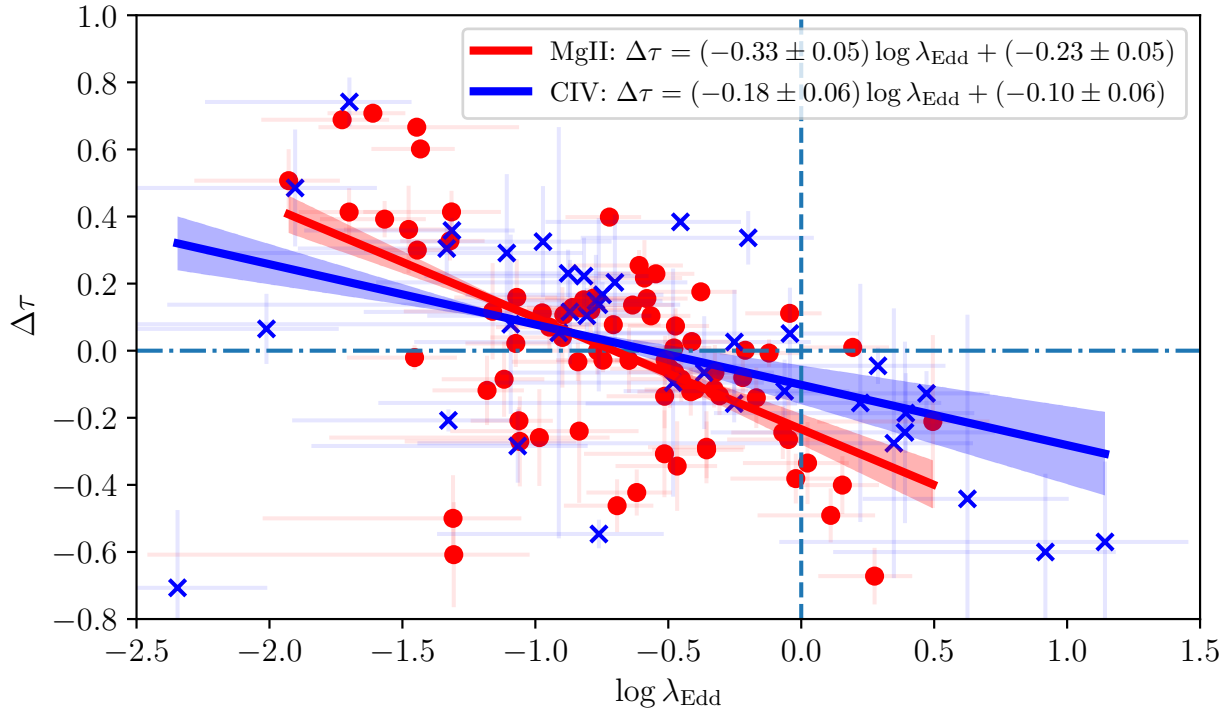

Figure 11.11: (Anti)correlation between $\Delta\tau \equiv \log(\tau/\tau_{\rm RL})$ and the Eddington ratio $\lambda_{\rm Edd}$ for both C IV sources (blue points) and Mg II sources (red points). The correlation is more signifcant for the Mg II sample with a Spearman rank-order correlation coefficient of -0.53 ($p = 4.76 \times 10^{-7}$) in comparison with -0.50 ($p = 0.0015$) for the C IV sample. The slope of the anticorrelation is steeper for Mg II sources, see Eq. (11.13) for the comparison.

a caveat, we note that unless the SMBH mass is inferred independently of the RM, $\Delta\tau$ and $\log\lambda_{\rm Edd}$ are intrinsically correlated as $\Delta\tau \propto -\log\tau$, which implies anticorrelation.[7] Therefore, we can only assess the different behaviour between $\Delta\tau$ and $\lambda_{\rm Edd}$ based on the relative comparison of the correlation coefficients and the correlation slopes for the two samples. The anticorrelation between $\Delta\tau$ and $\log\lambda_{\rm Edd}$ is more significant for the Mg II sample with a Spearman rank-order correlation coefficient of $s = -0.53$ ($p = 4.76 \times 10^{-7}$), while for the C IV sample we obtain $s = -0.50$ ($p = 0.0015$). When we fit a linear function to the anticorrelations we get

$$\Delta\tau({\rm C\,IV}) = (-0.18 \pm 0.06)\log\lambda_{\rm Edd} + (-0.10 \pm 0.06)\,,$$
$$\Delta\tau({\rm Mg\,II}) = (-0.33 \pm 0.05)\log\lambda_{\rm Edd} + (-0.23 \pm 0.05)\,. \qquad (11.13)$$

Hence, the anticorrelation is significantly steeper for the Mg II sample (by nearly a factor of two) in comparison with the current C IV sample. A combination of steeper $\Delta\tau$ – $\log\lambda_{\rm Edd}$ anticorrelation with a slightly steeper correlation between $\log\lambda_{\rm Edd}$ and the monochromatic luminosity for the Mg II sources can qualitatively account for the flatter Mg II $R-L$ relation with respect to the C IV one. However, with a future increase in the number of Mg II and C IV RM sources, both towards lower and higher redshifts, the difference in the correlation slopes is expected to become progressively weaker, since the general trends appear to be consistent between the Mg II and the C IV samples and the differences can be traced to a few outlying sources.

There may also be a potential problem in the way $\lambda_{\rm Edd}$ was measured in the C IV QSOs. Such measurements are uncertain, particularly for C IV. The C IV-emitting material is likely not completely virialized as revealed by its blueshift and blueward asymmetry with respect to low-ionization lines, which hints at an outflow approaching the observer. Therefore,

[7] It is generally thought advisable to use independent accretion-rate proxies, such as the relative Fe II strength $\mathscr{R}_{\rm Fe\,II}$ the variability factor $F_{\rm var}$ (Martínez-Aldama et al., 2020b), or the shape of the ionizing continuum (Ferland et al., 2020; Fonseca Alvarez et al., 2020; Panda et al., 2019b), rather than the Eddington ratio, due to the interdependency on the rest-frame time delay and the monochromatic luminosity that appear in the $R-L$ correlation. However, here we focus on a relative comparison between the Mg II and C IV samples instead of the absolute values of the correlation slopes and normalizations.

the SMBH mass determination may be biased (Baskin & Laor, 2005). The anticorrelation between the virial factor and the C IV FWHM is also the most uncertain among broad lines due to the smallest correlation coefficient as investigated by Mejía-Restrepo et al. (2018), which results in larger errorbars of C IV Eddington ratios in comparison with Mg II ones in Fig. 11.10. Looking at how the C IV sample was selected might suggest that the histogram in Fig. 11.9 may not well represent the true C IV $\lambda_{\rm Edd}$ values. One of the criteria used when selecting the final C IV QSOs from the SDSS-RM sample is the variability of the light curve. Sources with no significant variability were excluded from the final sample to ensure a reliable time-lag estimate (Grier et al., 2019). Several papers claim that there is a negative correlation between the variability and the Eddington ratio (e.g. De Cicco et al., 2022, and references therein). This suggests that the criterion of the variability applied to the SDSS-RM sample excludes highly-radiating QSOs. Such QSOs flatten the $R-L$ relation and increase the scatter in the case of the Hβ $R-L$ relation, which is not observed in the C IV $R-L$ relation. In addition, Kaspi et al. (2021) claim that their three sources do not show strong outflows, which are usually found in QSOs with high Eddington ratios (Coatman et al., 2017; Martínez-Aldama et al., 2018). We performed a visual inspection of the rest of the sources and most of them show spectral features associated with low Eddington ratios (symmetric profiles in C IV λ1549, moderate He II λ1640 contribution, strong contribution of C III] λ1909, and low contributions of Fe II and Fe III). All these facts, in contradiction to Fig. 11.9, suggest that the C IV sample mainly includes low Eddington sources. However, a detailed analysis of variability and spectral properties is needed to confirm the accretion state of sources in the C IV sample.

The C IV sample spans eight orders of luminosity ($L_{1350} \sim 10^{40-48}$ erg s^{-1}) and covers a large redshift range ($0.001 < z < 3.37$), and is standardizable and suitable for constraining cosmological models. The Mg II sample has smaller luminosity and redshift ranges ($L_{3000} \sim 10^{43-47}$ erg s^{-1}, $0 < z < 1.8$), but is standardizable and also suitable for constraining cosmological parameters (Khadka et al., 2021a, 2022a), and can be jointly analyzed with the C IV sample. The same is not true for the Hβ sample. Although the Hβ sample spans almost five orders of luminosity ($L_{5100} = 10^{41.5-46}$ erg s^{-1}), the redshift range is narrow ($0.002 <$

$z < 0.9$), but most importantly the current Hβ sample appears to be not standardizable (Khadka et al., 2022a). Therefore, we cannot jointly use the Mg II, C IV and Hβ samples, which is unfortunate since they together contain more sources over large luminosity and redshift ranges, all of which are beneficial if such QSOs are to be useful for cosmological purposes.

With future missions and surveys, such as the Black Hole Mapper by the SDSS-V (Kollmeier et al., 2017), long-term spectroscopic and photometric measurements of reverberation lags for the continuum and the "major" emission lines (C IV, Mg II, and Hβ/Hα) will be obtained for a large sample of quasars, adding wide-area, multi-epoch optical spectroscopy to the era of time-domain imaging. With the photometric Legacy Survey of Space and Time performed by the Vera C. Rubin observatory (Ivezić et al., 2019), many more RM objects will be obtained, e.g. the Rubin Deep Drilling Field should result in a few thousand measurements at redshifts $\sim 1-2$ (Brandt et al., 2018; Kovačević et al., 2022). This will lead to the decrease in the statistical error. The source monitoring will be performed photometrically in six broad optical bands, which will be used to probe the continuum accretion-disc response as well as the BLR response using the photometric RM (see e.g., Martinez Aldama et al., 2020a; Panda et al., 2019a, for the assessment of the photometric RM for BLR RM and the future application in cosmology). Currently, we obtain a difference with respect to BAO+$H(z)$ data constraints by at most 0.1σ when 116 C IV + Mg II sources are included, hence a QSO dataset larger by an order of magnitude can naturally influence the overall cosmological constraints more. It is more challenging to lower the dispersion in the individual time-delay measurements. Using a consistent methodology for all the RM QSOs to infer time-delays will be necessary to avoid systematic errors introduced by combining different subsets of RM sources into one large dataset. Specifically, surveys and RM projects typically select sources in a narrow luminosity range, which can result in a problem. For instance, if the time-delay method used for higher-luminosity sources is systematically susceptible to yield smaller lags in comparison with the method used for lower-luminosity sources, it can lead to a systematically smaller slope of the R-L relation compared to the case when the same method is applied to all the sources across several orders of magnitude in luminosity.

11.6 Conclusions

In this paper, for the first time, we use 38 highest-quality C IV QSO data to simultaneously constrain cosmological model parameters, in six cosmological models, and C IV $R-L$ relation parameters. We use a new technique we have developed to more correctly take into account the asymmetric time-lag τ error bars and applied it to both C IV and Mg II QSO data (Khadka et al., 2021a) for the first time. We find that similar to Mg II QSO data, C IV QSO data are also standardizable through the $R-L$ relation since the C IV $R-L$ relation parameters are cosmological model-independent. Unlike the Hβ QSOs cosmological constraints (Khadka et al., 2022a), those from C IV and Mg II QSO data are consistent with cosmological constraints from better established $H(z)$ + BAO data.

The mutually consistent cosmological parameter constraints from C IV, Mg II, and $H(z)$ + BAO data allow us to perform joint analyses on C IV + Mg II data as well as on $H(z)$ + BAO + C IV + Mg II data. Although the joint C IV + Mg II cosmological constraints are still weak, they do slightly ($\sim 0.1\sigma$ at most) alter the $H(z)$ + BAO constraints when jointly analyzed.

The Rubin Observatory Legacy Survey of Space and Time (Ivezić et al., 2019), as well as the SDSS-V Black Hole Mapper (Kollmeier et al., 2017), will find many more C IV and Mg II QSOs. These new QSOs will result in significantly more restrictive C IV (and Mg II) cosmological constraints than the first ones we have derived here.

Table 11.2: Unmarginalized best-fitting parameter values for all models from various combinations of data.

Model	Data set	$\Omega_b h^2$	$\Omega_c h^2$	Ω_{m0}	Ω_{k0}	$w_{\rm X}/\alpha$[a]	H_0[b]	$\sigma_{\rm int,\,C}$	$\gamma_{\rm C}$	$\beta_{\rm C}$	$\sigma_{\rm int,\,M}$	$\gamma_{\rm M}$	$\beta_{\rm M}$	$-2\ln\mathscr{L}_{\rm max}$	AIC	BIC	DIC	ΔAIC	ΔBIC	ΔDIC
	$H(z)$ + BAO	0.0244	0.1181	0.301	–	–	68.98	–	–	–	–	–	–	25.64	31.64	36.99	32.32	0.00	0.00	0.00
	Mg II QSO symm	–	0.0518	0.157	–	–	–	–	–	–	0.282	0.285	1.670	30.16	38.16	47.59	37.68	0.00	0.00	0.00
Flat	Mg II QSO asymm	–	0.0472	0.148	–	–	–	–	–	–	0.278	0.282	1.676	30.18	38.18	47.61	37.86	0.00	0.00	0.00
ΛCDM	C IV QSO symm	–	−0.0007	0.050	–	–	–	0.275	0.403	0.989	–	–	–	20.61	28.61	35.16	31.10	0.00	0.00	0.00
	C IV QSO asymm	–	−0.0026	0.046	–	–	–	0.265	0.411	0.980	–	–	–	20.51	28.51	35.06	32.74	0.00	0.00	0.00
	C IV QSO asymm + Mg II QSO asymm	–	0.0082	0.068	–	–	–	0.274	0.412	0.995	0.280	0.286	1.647	50.94	64.94	84.21	69.10	0.00	0.00	0.00
	$H(z)$ + BAO + C IV QSO asymm + Mg II QSO asymm	0.0245	0.1148	0.295	–	–	68.86	0.284	0.421	1.079	0.279	0.288	1.688	78.31	96.31	123.98	98.13	0.00	0.00	0.00
	$H(z)$ + BAO	0.0260	0.1098	0.292	0.048	–	68.35	–	–	–	–	–	–	25.30	33.30	40.43	33.87	1.66	3.44	1.54
	Mg II QSO symm	–	0.1703	0.399	−1.135	–	–	–	–	–	0.275	0.352	1.625	25.39	35.39	47.17	40.12	−2.77	−0.42	2.44
Non-flat	Mg II QSO asymm	–	0.1708	0.400	−1.134	–	–	–	–	–	0.270	0.349	1.635	25.62	35.62	47.40	40.25	−2.56	−0.20	2.38
ΛCDM	C IV QSO symm	–	0.0147	0.081	−0.358	–	–	0.237	0.486	0.968	–	–	–	9.38	19.38	27.57	36.94	−9.23	−7.59	5.84
	C IV QSO asymm	–	0.0378	0.128	−0.471	–	–	0.242	0.498	0.939	–	–	–	14.44	24.44	32.63	36.77	−4.07	−2.43	4.03
	C IV QSO asymm + Mg II QSO asymm	–	0.0791	0.213	−0.678	–	–	0.269	0.512	1.018	0.279	0.293	1.642	42.92	58.92	80.95	68.83	−6.01	−3.26	−0.27
	$H(z)$ + BAO + C IV QSO asymm + Mg II QSO asymm	0.0260	0.1112	0.293	0.036	–	68.64	0.278	0.430	1.045	0.278	0.293	1.684	78.09	98.09	128.84	99.73	1.79	4.86	1.60
	$H(z)$ + BAO	0.0296	0.0951	0.290	–	−0.754	65.79	–	–	–	–	–	–	22.39	30.39	37.52	30.63	−1.25	0.53	−1.69
	Mg II QSO symm	–	−0.0234	0.003	–	−4.949	–	–	–	–	0.270	0.241	1.354	24.39	34.39	46.18	41.19	−3.77	−1.41	3.51
Flat	Mg II QSO asymm	–	−0.0226	0.005	–	−4.983	–	–	–	–	0.267	0.249	1.361	24.35	34.35	46.13	41.14	−3.83	−1.48	3.28
XCDM	C IV QSO symm	–	−0.0237	0.003	–	−4.990	–	0.234	0.321	0.727	–	–	–	12.69	22.69	30.88	31.64	−5.92	−4.29	0.53
	C IV QSO asymm	–	−0.0203	0.010	–	−4.988	–	0.232	0.355	0.736	–	–	–	15.58	25.58	33.77	33.67	−2.93	−1.29	0.93
	C IV QSO asymm + Mg II QSO asymm	–	−0.0212	0.008	–	−4.875	–	0.225	0.337	0.757	0.262	0.248	1.399	40.24	56.24	78.27	66.94	−8.70	−5.95	−2.16
	$H(z)$ + BAO + C IV QSO asymm + Mg II QSO asymm	0.0283	0.1007	0.297	–	−0.792	66.05	0.283	0.425	1.074	0.279	0.286	1.691	75.85	95.85	126.60	97.19	−0.46	2.62	−0.94
	$H(z)$ + BAO	0.0289	0.0985	0.296	−0.053	−0.730	65.76	–	–	–	–	–	–	22.13	32.13	41.05	32.51	0.49	4.06	0.19
	Mg II QSO symm	–	−0.0103	0.030	−0.060	−3.207	–	–	–	–	0.257	0.284	1.382	18.29	30.29	44.43	46.23	−7.87	−3.16	8.54
Non-flat	Mg II QSO asymm	–	−0.0016	0.048	−0.095	−2.947	–	–	–	–	0.260	0.303	1.395	19.66	31.66	45.80	45.06	−6.52	−1.81	7.19
XCDM	C IV QSO symm	–	−0.0161	0.019	−0.035	−3.815	–	0.220	0.428	0.827	–	–	–	6.26	18.26	28.09	38.74	−10.35	−7.08	7.64
	C IV QSO asymm	–	−0.0130	0.025	−0.042	−4.329	–	0.228	0.386	0.828	–	–	–	12.08	24.08	33.90	37.86	−4.43	−1.16	5.12
	C IV QSO asymm + Mg II QSO asymm	–	−0.0149	0.021	−0.034	−5.000	–	0.226	0.374	0.808	0.270	0.285	1.262	32.43	50.43	75.21	68.46	−14.51	−9.00	−0.71
	$H(z)$ + BAO + C IV QSO asymm + Mg II QSO asymm	0.0281	0.1046	0.296	−0.065	−0.779	67.10	0.276	0.434	1.064	0.274	0.298	1.676	75.81	97.81	131.64	98.92	1.51	7.66	0.79
	$H(z)$ + BAO	0.0310	0.0900	0.280	–	1.010	65.89	–	–	–	–	–	–	22.31	30.31	37.45	29.90	−1.33	0.46	−2.42
	Mg II QSO symm	–	0.0414	0.136	–	0.018	–	–	–	–	0.282	0.282	1.668	30.17	40.17	51.96	38.18	2.01	4.37	0.50
Flat	Mg II QSO asymm	–	0.0532	0.160	–	0.047	–	–	–	–	0.279	0.284	1.679	30.20	40.20	51.99	38.40	2.02	4.38	0.52
ϕCDM	C IV QSO symm	–	0.0003	0.052	–	0.030	–	0.274	0.399	0.996	–	–	–	20.67	30.67	38.85	33.47	2.05	3.69	2.37
	C IV QSO asymm	–	−0.0059	0.039	–	0.061	–	0.270	0.410	0.977	–	–	–	20.59	30.59	38.78	34.56	2.08	3.72	1.82
	C IV QSO asymm + Mg II QSO asymm	–	−0.0078	0.035	–	0.014	–	0.263	0.399	0.984	0.283	0.265	1.662	51.19	67.19	89.21	72.04	2.25	5.00	2.94
	$H(z)$ + BAO + C IV QSO asymm + Mg II QSO asymm	0.0289	0.0985	0.288	–	0.663	66.68	0.275	0.430	1.050	0.278	0.304	1.668	75.78	95.78	126.54	96.48	−0.52	2.55	−1.65
	$H(z)$ + BAO	0.0306	0.0920	0.284	−0.058	1.200	65.91	–	–	–	–	–	–	22.05	32.05	40.97	31.30	0.41	3.98	−1.02
	Mg II QSO symm	–	0.1167	0.290	−0.277	0.000	–	–	–	–	0.283	0.290	1.678	29.81	41.81	55.95	38.70	3.65	8.36	1.02
Non-flat	Mg II QSO asymm	–	0.1354	0.328	−0.310	0.042	–	–	–	–	0.275	0.292	1.675	29.91	41.91	56.05	38.65	3.73	8.45	0.78
ϕCDM	C IV QSO symm	–	0.0489	0.151	−0.146	0.065	–	0.272	0.417	1.010	–	–	–	20.42	32.42	42.24	34.07	3.80	7.08	2.96
	C IV QSO asymm	–	0.0367	0.126	−0.125	0.121	–	0.268	0.423	1.006	–	–	–	20.41	32.41	42.24	34.92	3.91	7.18	2.18
	C IV QSO asymm + Mg II QSO asymm	–	0.0611	0.176	−0.173	0.115	–	0.264	0.421	1.034	0.271	0.289	1.659	50.74	68.74	93.52	72.86	3.80	9.31	3.76
	$H(z)$ + BAO + C IV QSO asymm + Mg II QSO asymm	0.0313	0.0882	0.278	−0.044	1.256	65.76	0.281	0.455	1.035	0.276	0.292	1.687	75.73	97.73	131.55	97.61	1.42	7.57	−0.52

[a] $w_{\rm X}$ corresponds to flat/non-flat XCDM and α corresponds to flat/non-flat ϕCDM.
[b] km s^{-1} Mpc^{-1}. Ω_b and H_0 are set to be 0.05 and 70 km s^{-1} Mpc^{-1}, respectively.

Table 11.3: One-dimensional marginalized posterior mean values and uncertainties ($\pm 1\sigma$ error bars or 2σ limits) of the parameters for all models from various combinations of data.

Model	Data set	$\Omega_b h^2$	$\Omega_c h^2$	Ω_{m0}	Ω_{k0}	$w_{\rm X}/\alpha$[a]	H_0[b]	$\sigma_{\rm int,\,C}$	$\gamma_{\rm C}$	$\beta_{\rm C}$	$\sigma_{\rm int,\,M}$	$\gamma_{\rm M}$	$\beta_{\rm M}$
	$H(z)$ + BAO	0.0247 ± 0.0030	$0.1186^{+0.0076}_{-0.0083}$	$0.301^{+0.016}_{-0.018}$	–	–	69.14 ± 1.85	–	–	–	–	–	–
	Mg II QSO symm	–	–	$0.470^{+0.199}_{-0.426}$	–	–	–	–	–	–	$0.293^{+0.023}_{-0.030}$	0.297 ± 0.047	$1.698^{+0.063}_{-0.058}$
Flat	Mg II QSO asymm	–	–	$0.470^{+0.196}_{-0.430}$	–	–	–	–	–	–	$0.290^{+0.024}_{-0.030}$	0.296 ± 0.047	$1.703^{+0.064}_{-0.057}$
ΛCDM	C IV QSO symm	–	–	< 0.471[c]	–	–	–	$0.311^{+0.039}_{-0.056}$	0.427 ± 0.043	1.051 ± 0.096	–	–	–
	C IV QSO asymm	–	–	< 0.503[c]	–	–	–	$0.307^{+0.039}_{-0.056}$	0.441 ± 0.044	$1.034^{+0.097}_{-0.087}$	–	–	–
	C IV QSO asymm + Mg II QSO asymm	–	–	< 0.444[c]	–	–	–	$0.305^{+0.037}_{-0.054}$	0.440 ± 0.042	1.030 ± 0.089	$0.289^{+0.023}_{-0.030}$	0.292 ± 0.045	1.691 ± 0.061
	$H(z)$ + BAO + C IV QSO asymm + Mg II QSO asymm	0.0247 ± 0.0028	$0.1183^{+0.0073}_{-0.0080}$	$0.301^{+0.015}_{-0.017}$	–	–	69.15 ± 1.77	$0.303^{+0.036}_{-0.053}$	0.442 ± 0.039	$1.026^{+0.075}_{-0.065}$	$0.288^{+0.023}_{-0.029}$	0.294 ± 0.044	1.686 ± 0.056
	$H(z)$ + BAO	$0.0266^{+0.0039}_{-0.0045}$	0.1088 ± 0.0166	0.291 ± 0.023	$0.059^{+0.081}_{-0.091}$	–	68.37 ± 2.10	–	–	–	–	–	–
	Mg II QSO symm	–	–	$0.568^{+0.359}_{-0.196}$	$-0.427^{+0.546}_{-1.453}$	–	–	–	–	–	$0.291^{+0.024}_{-0.030}$	$0.315^{+0.049}_{-0.056}$	1.687 ± 0.067
Non-flat	Mg II QSO asymm	–	–	$0.567^{+0.365}_{-0.192}$	$-0.419^{+0.560}_{-1.449}$	–	–	–	–	–	$0.288^{+0.024}_{-0.031}$	$0.316^{+0.048}_{-0.057}$	$1.692^{+0.070}_{-0.064}$
ΛCDM	C IV QSO symm	–	–	$0.417^{+0.153}_{-0.353}$	$-0.478^{+0.346}_{-0.851}$	–	–	$0.300^{+0.041}_{-0.055}$	$0.465^{+0.047}_{-0.062}$	1.072 ± 0.098	–	–	–
	C IV QSO asymm	–	–	$0.467^{+0.199}_{-0.378}$	$-0.330^{+0.534}_{-1.060}$	–	–	$0.305^{+0.039}_{-0.055}$	$0.468^{+0.046}_{-0.056}$	$1.059^{+0.097}_{-0.086}$	–	–	–
	C IV QSO asymm + Mg II QSO asymm	–	–	$0.473^{+0.187}_{-0.311}$	$-0.818^{+0.391}_{-0.637}$	–	–	$0.299^{+0.036}_{-0.053}$	$0.491^{+0.050}_{-0.064}$	$1.073^{+0.093}_{-0.094}$	$0.285^{+0.023}_{-0.030}$	$0.314^{+0.048}_{-0.052}$	1.662 ± 0.065
	$H(z)$ + BAO + C IV QSO asymm + Mg II QSO asymm	$0.0262^{+0.0037}_{-0.0044}$	0.1105 ± 0.0165	0.292 ± 0.022	$0.047^{+0.079}_{-0.089}$	–	68.55 ± 2.05	$0.303^{+0.035}_{-0.052}$	0.441 ± 0.039	$1.023^{+0.075}_{-0.064}$	$0.288^{+0.023}_{-0.030}$	0.294 ± 0.043	1.685 ± 0.055
	$H(z)$ + BAO	$0.0295^{+0.0042}_{-0.0050}$	$0.0969^{+0.0178}_{-0.0152}$	0.289 ± 0.020	–	$-0.784^{+0.140}_{-0.107}$	$66.22^{+2.31}_{-2.54}$	–	–	–	–	–	–
	Mg II QSO symm	–	–	< 0.515[c]	–	< -0.371	–	–	–	–	$0.291^{+0.024}_{-0.030}$	0.294 ± 0.048	$1.640^{+0.118}_{-0.073}$
Flat	Mg II QSO asymm	–	–	< 0.512[c]	–	< -0.370	–	–	–	–	$0.288^{+0.024}_{-0.030}$	0.295 ± 0.047	$1.644^{+0.118}_{-0.072}$
XCDM	C IV QSO symm	–	–	< 0.737	–	< -0.926	–	$0.292^{+0.041}_{-0.056}$	0.403 ± 0.047	0.957 ± 0.128	–	–	–
	C IV QSO asymm	–	–	< 0.840	–	< -0.636	–	$0.296^{+0.041}_{-0.056}$	0.426 ± 0.049	$0.970^{+0.136}_{-0.108}$	–	–	–
	C IV QSO asymm + Mg II QSO asymm	–	–	< 0.563	–	< -1.509	–	$0.282^{+0.038}_{-0.054}$	0.405 ± 0.047	$0.900^{+0.122}_{-0.121}$	$0.283^{+0.023}_{-0.029}$	$0.282^{+0.042}_{-0.046}$	$1.557^{+0.117}_{-0.101}$
	$H(z)$ + BAO + C IV QSO asymm + Mg II QSO asymm	$0.0292^{+0.0040}_{-0.0050}$	$0.0983^{+0.0181}_{-0.0144}$	$0.290^{+0.020}_{-0.018}$	–	$-0.799^{+0.143}_{-0.111}$	$66.45^{+2.28}_{-2.53}$	$0.305^{+0.036}_{-0.053}$	0.443 ± 0.039	$1.021^{+0.077}_{-0.065}$	$0.289^{+0.023}_{-0.030}$	0.295 ± 0.044	1.684 ± 0.056
	$H(z)$ + BAO	$0.0294^{+0.0047}_{-0.0050}$	$0.0980^{+0.0186}_{-0.0187}$	0.292 ± 0.025	-0.027 ± 0.109	$-0.770^{+0.149}_{-0.098}$	$66.13^{+2.35}_{-2.36}$	–	–	–	–	–	–
	Mg II QSO symm	–	–	$0.526^{+0.351}_{-0.268}$	$-0.235^{+0.555}_{-0.936}$	$-2.416^{+1.894}_{-1.260}$	–	–	–	–	$0.291^{+0.024}_{-0.031}$	$0.313^{+0.049}_{-0.055}$	$1.649^{+0.124}_{-0.079}$
	Mg II QSO asymm	–	–	$0.523^{+0.341}_{-0.280}$	$-0.245^{+0.544}_{-0.917}$	$-2.448^{+1.834}_{-1.321}$	–	–	–	–	$0.287^{+0.024}_{-0.030}$	$0.314^{+0.049}_{-0.055}$	$1.651^{+0.122}_{-0.079}$
Non-flat	C IV QSO symm	–	–	$0.399^{+0.140}_{-0.375}$	$-0.247^{+0.360}_{-0.645}$	$-2.636^{+1.523}_{-1.570}$	–	$0.297^{+0.042}_{-0.057}$	$0.443^{+0.045}_{-0.055}$	$1.028^{+0.121}_{-0.106}$	–	–	–
XCDM	C IV QSO asymm	–	–	$0.452^{+0.186}_{-0.394}$	$-0.168^{+0.451}_{-0.789}$	$-2.573^{+1.568}_{-1.605}$	–	$0.302^{+0.040}_{-0.056}$	$0.453^{+0.046}_{-0.051}$	$1.025^{+0.115}_{-0.096}$	–	–	–
	C IV QSO asymm + Mg II QSO asymm	–	–	$0.338^{+0.101}_{-0.299}$	$-0.410^{+0.368}_{-0.222}$	< -1.124	–	$0.282^{+0.037}_{-0.053}$	$0.456^{+0.047}_{-0.056}$	$0.966^{+0.119}_{-0.110}$	$0.280^{+0.023}_{-0.030}$	$0.319^{+0.048}_{-0.054}$	$1.526^{+0.132}_{-0.108}$
	$H(z)$ + BAO + C IV QSO asymm + Mg II QSO asymm	$0.0290^{+0.0044}_{-0.0053}$	$0.0997^{+0.0186}_{-0.0188}$	0.293 ± 0.025	-0.031 ± 0.108	$-0.787^{+0.165}_{-0.102}$	$66.41^{+2.26}_{-2.49}$	$0.305^{+0.036}_{-0.053}$	0.444 ± 0.040	$1.023^{+0.077}_{-0.065}$	$0.289^{+0.023}_{-0.030}$	0.295 ± 0.045	1.685 ± 0.056
	$H(z)$ + BAO	$0.0320^{+0.0054}_{-0.0041}$	$0.0855^{+0.0175}_{-0.0174}$	0.275 ± 0.023	–	$1.267^{+0.536}_{-0.807}$	$65.47^{+2.22}_{-2.21}$	–	–	–	–	–	–
	Mg II QSO symm	–	–	–	–	–	–	–	–	–	$0.294^{+0.023}_{-0.029}$	0.301 ± 0.046	1.719 ± 0.054
Flat	Mg II QSO asymm	–	–	–	–	–	–	–	–	–	$0.290^{+0.024}_{-0.030}$	0.301 ± 0.046	$1.724^{+0.055}_{-0.051}$
ϕCDM	C IV QSO symm	–	–	< 0.553[c]	–	< 6.291[c]	–	$0.318^{+0.039}_{-0.055}$	0.436 ± 0.043	1.086 ± 0.090	–	–	–
	C IV QSO asymm	–	–	< 0.565[c]	–	–	–	$0.314^{+0.038}_{-0.055}$	0.450 ± 0.044	$1.070^{+0.092}_{-0.075}$	–	–	–
	C IV QSO asymm + Mg II QSO asymm	–	–	< 0.537[c]	–	< 6.202[c]	–	$0.312^{+0.037}_{-0.054}$	0.449 ± 0.043	$1.069^{+0.091}_{-0.074}$	$0.289^{+0.023}_{-0.030}$	0.299 ± 0.046	$1.717^{+0.059}_{-0.053}$
	$H(z)$ + BAO + C IV QSO asymm + Mg II QSO asymm	$0.0318^{+0.0053}_{-0.0045}$	$0.0866^{+0.0190}_{-0.0171}$	0.275 ± 0.023	–	$1.202^{+0.490}_{-0.862}$	$65.68^{+2.20}_{-2.19}$	$0.306^{+0.036}_{-0.053}$	0.444 ± 0.040	$1.019^{+0.078}_{-0.066}$	$0.289^{+0.023}_{-0.030}$	0.295 ± 0.044	1.683 ± 0.056
	$H(z)$ + BAO	$0.0320^{+0.0057}_{-0.0038}$	$0.0865^{+0.0172}_{-0.0198}$	$0.277^{+0.023}_{-0.026}$	$-0.034^{+0.087}_{-0.098}$	$1.360^{+0.584}_{-0.819}$	65.53 ± 2.19	–	–	–	–	–	–
	Mg II QSO symm	–	–	$0.476^{+0.230}_{-0.396}$	$0.042^{+0.390}_{-0.378}$	–	–	–	–	–	$0.294^{+0.023}_{-0.029}$	0.300 ± 0.046	1.721 ± 0.054
Non-flat	Mg II QSO asymm	–	–	$0.473^{+0.216}_{-0.409}$	$0.040^{+0.395}_{-0.383}$	–	–	–	–	–	$0.291^{+0.024}_{-0.030}$	0.301 ± 0.047	1.724 ± 0.056
ϕCDM	C IV QSO symm	–	–	< 0.542[c]	$0.104^{+0.381}_{-0.362}$	–	–	$0.319^{+0.039}_{-0.055}$	0.437 ± 0.043	1.089 ± 0.089	–	–	–
	C IV QSO asymm	–	–	$0.427^{+0.153}_{-0.408}$	$0.096^{+0.359}_{-0.337}$	$4.747^{+2.065}_{-4.304}$	–	$0.313^{+0.037}_{-0.055}$	0.451 ± 0.043	$1.076^{+0.087}_{-0.074}$	–	–	–
	C IV QSO asymm + Mg II QSO asymm	–	–	< 0.536[c]	$0.088^{+0.384}_{-0.364}$	< 6.162[c]	–	$0.312^{+0.037}_{-0.054}$	0.450 ± 0.043	$1.072^{+0.088}_{-0.076}$	$0.290^{+0.023}_{-0.030}$	0.299 ± 0.046	1.719 ± 0.055
	$H(z)$ + BAO + C IV QSO asymm + Mg II QSO asymm	$0.0317^{+0.0058}_{-0.0043}$	$0.0884^{+0.0183}_{-0.0203}$	$0.278^{+0.024}_{-0.026}$	$-0.044^{+0.090}_{-0.094}$	$1.320^{+0.572}_{-0.869}$	65.77 ± 2.21	$0.306^{+0.036}_{-0.053}$	0.445 ± 0.040	$1.021^{+0.079}_{-0.066}$	$0.289^{+0.023}_{-0.030}$	0.296 ± 0.045	1.684 ± 0.056

[a] $w_{\rm X}$ corresponds to flat/non-flat XCDM and α corresponds to flat/non-flat ϕCDM.
[b] km s^{-1} Mpc^{-1}. Ω_b and H_0 are set to be 0.05 and 70 km s^{-1} Mpc^{-1}, respectively.
[c] This is the 1σ limit. The 2σ limit is set by the prior and not shown here.

Chapter 12

Conclusion

In this study we have utilized various non-CMB data sets to constrain cosmological parameters in six different general relativistic dark energy models. By simultaneously constraining both the cosmological and correlation parameters, we discovered that certain correlations can standardize some GRBs and reverberation-measured QSOs, as their constraints are relatively model-independent.

More specifically, we found that the 118 long GRBs (A118) can be standardized through the Amati correlation; the 31 long and 5 short GRBs with the plateau phase dominated by magnetic dipole (MD) radiation, and 24 long GRBs with the plateau phase dominated by gravitational wave (GW) emission can be standardized through the two-parameter Dainotti correlation; the 50 Platinum and 95 long GRBs can be standardized through the three-parameter Dainotti correlation; the 78 reverberation-measured Mg II QSOs can be standardized through the radius-luminosity ($R - L$) correlation; and the 38 reverberation-measured C IV QSOs can be standardized through another $R - L$ correlation.

Although the cosmological constraints obtained from these standardized probes are relatively weaker than those obtained from well-established $H(z)$ + BAO data, their constraints are still mutually consistent and, therefore, can be jointly analyzed. Among the GRB data sets, A118 provides slightly tighter constraints than the others, making it the preferred choice for joint analyses. However, we are still investigating other GRB data sets, and we expect

that more and better quality GRBs will provide fresh insights on cosmological parameter values.

QSO angular size, H II G, and SN Ia data are complementary to the well-established $H(z)$ + BAO data. Although they provide weaker cosmological constraints than $H(z)$ + BAO data, they provide tighter constraints than the standardized GRBs and reverberation-measured QSOs. All these lower-redshift non-CMB data provide mutually consistent cosmological constraints and can be jointly analyzed.

Using advanced data analysis methods and more up-to-date measurements, we have obtained somewhat model-independent constraints on the Hubble constant ($H_0 = 69.7 \pm 1.2$ km s^{-1} Mpc^{-1}) and the non-relativistic matter density parameter ($\Omega_{m0} = 0.3 \pm 0.02$). Nonetheless, the current cosmological parameter constraints from lower-redshift standardized non-CMB measurements are not comparable to those from *Planck* CMB anisotropy data. We hope that in the future, the quality and quantity of non-CMB data will be significantly better, allowing us to measure cosmological parameter error bars comparable to those obtained from *Planck* CMB anisotropy data.

Bibliography

Abbassi M. H., Abbassi A. H., 2020, J. Cosmol. Astropart. Phys., 2020, 042

Abdalla E., et al., 2022, Journal of High Energy Astrophysics, 34, 49

Adil A., Albrecht A., Knox L., 2022, preprint (arXiv:2207.10235)

Agudelo Ruiz J. A., Fabris J. C., Velasquez-Toribio A. M., Shapiro I. L., 2020, Gravitation and Cosmology, 26, 316

Alam S., et al., 2017, Mon. Not. R. Astron. Soc., 470, 2617

Amati L., et al., 2002, Astron. Astrophys., 390, 81

Amati L., Guidorzi C., Frontera F., Della Valle M., Finelli F., Landi R., Montanari E., 2008, Mon. Not. R. Astron. Soc., 391, 577

Amati L., Frontera F., Guidorzi C., 2009, Astron. Astrophys., 508, 173

Amati L., D'Agostino R., Luongo O., Muccino M., Tantalo M., 2019, Mon. Not. R. Astron. Soc., 486, L46

Amati L., et al., 2021, Experimental Astronomy, 52, 183

Ata M., et al., 2018, Mon. Not. R. Astron. Soc., 473, 4773

Atteia J.-L., Cordier B., Wei J., 2022, International Journal of Modern Physics D, 31, 2230008

Aubourg É., et al., 2015, Phys. Rev. D., 92, 123516

Audren B., Lesgourgues J., Benabed K., Prunet S., 2013, J. Cosmol. Astropart. Phys., 2013, 001

Avsajanishvili O., Samushia L., Arkhipova N. A., Kahniashvili T., 2015, preprint, (arXiv:1511.09317)

Baskin A., Laor A., 2005, Mon. Not. R. Astron. Soc., 356, 1029

Bautista J. E., et al., 2021, Mon. Not. R. Astron. Soc., 500, 736

Bentz M. C., et al., 2013, Astrophys. J., 767, 149

Birrer S., et al., 2020, Astron. Astrophys., 643, A165

Blas D., Lesgourgues J., Tram T., 2011, J. Cosmol. Astropart. Phys., 2011, 034

Blum K., Castorina E., Simonović M., 2020, Astrophys. J. Lett., 892, L27

Bonga B., Gupt B., Yokomizo N., 2016, J. Cosmol. Astropart. Phys., 2016, 031

Borghi N., Moresco M., Cimatti A., 2022, Astrophys. J. Lett., 928, L4

Boruah S. S., Hudson M. J., Lavaux G., 2021, Mon. Not. R. Astron. Soc., 507, 2697

Brandt W. N., et al., 2018, preprint, (arXiv:1811.06542)

Breuval L., et al., 2020, Astron. Astrophys., 643, A115

Brinckmann T., Lesgourgues J., 2019, Physics of the Dark Universe, 24, 100260

Britzen S., et al., 2021, Mon. Not. R. Astron. Soc., 503, 3145

Calabrese E., Archidiacono M., Melchiorri A., Ratra B., 2012, Phys. Rev. D., 86, 043520

Campanelli L., Fogli G. L., Kahniashvili T., Marrone A., Ratra B., 2012, European Physical Journal C, 72, 2218

Cao S., Ratra B., 2022, Mon. Not. Roy. Astron. Soc., 513, 5686

Cao S., Biesiada M., Jackson J., Zheng X., Zhao Y., Zhu Z.-H., 2017a, J. Cosmol. Astropart. Phys., 2, 012

Cao S., Zheng X., Biesiada M., Qi J., Chen Y., Zhu Z.-H., 2017b, Astron. Astrophys., 606, A15

Cao S., Ryan J., Ratra B., 2020, Mon. Not. R. Astron. Soc., 497, 3191

Cao S., Ryan J., Khadka N., Ratra B., 2021a, Mon. Not. R. Astron. Soc., 501, 1520

Cao S., Ryan J., Ratra B., 2021b, Mon. Not. R. Astron. Soc., 504, 300

Cao S., Ryan J., Ratra B., 2022a, Mon. Not. R. Astron. Soc., 509, 4745

Cao S., Khadka N., Ratra B., 2022b, Mon. Not. R. Astron. Soc., 510, 2928

Cao S., Dainotti M., Ratra B., 2022c, Mon. Not. R. Astron. Soc., 512, 439

Cao S., Dainotti M., Ratra B., 2022d, Mon. Not. R. Astron. Soc., 516, 1386

Cao S., Zajaček M., Panda S., Martínez-Aldama M. L., Czerny B., Ratra B., 2022e, Mon. Not. Roy. Astron. Soc., 516, 1721

Cardone V. F., Capozziello S., Dainotti M. G., 2009, Mon. Not. R. Astron. Soc., 400, 775

Cardone V. F., Dainotti M. G., Capozziello S., Willingale R., 2010, Mon. Not. R. Astron. Soc., 408, 1181

Carter P., Beutler F., Percival W. J., Blake C., Koda J., Ross A. J., 2018, Mon. Not. R. Astron. Soc., 481, 2371

Chávez R., Terlevich E., Terlevich R., Plionis M., Bresolin F., Basilakos S., Melnick J., 2012, Mon. Not. R. Astron. Soc., 425, L56

Chávez R., Terlevich R., Terlevich E., Bresolin F., Melnick J., Plionis M., Basilakos S., 2014, Mon. Not. R. Astron. Soc., 442, 3565

Chávez R., Plionis M., Basilakos S., Terlevich R., Terlevich E., Melnick J., Bresolin F., González-Morán A. L., 2016, Mon. Not. R. Astron. Soc., 462, 2431

Chen G., Ratra B., 2003, Astrophys. J., 582, 586

Chen G., Ratra B., 2011, PASP, 123, 1127

Chen G., Gott III J. R., Ratra B., 2003, PASP, 115, 1269

Chen Y., Ratra B., Biesiada M., Li S., Zhu Z.-H., 2016, Astrophys. J., 829, 61

Chen Y., Kumar S., Ratra B., 2017, Astrophys. J., 835, 86

Coatman L., Hewett P. C., Banerji M., Richards G. T., Hennawi J. F., Prochaska J. X., 2017, Mon. Not. R. Astron. Soc., 465, 2120

Coley A. A., Ellis G. F. R., 2020, Classical and Quantum Gravity, 37, 013001

Colgáin E. O., Sheikh-Jabbari M. M., Solomon R., Bargiacchi G., Capozziello S., Dainotti M. G., Stojkovic D., 2022, Phys. Rev. D, 106, L041301

Collin-Souffrin S., Dyson J. E., McDowell J. C., Perry J. J., 1988, Mon. Not. R. Astron. Soc., 232, 539

Conley A., et al., 2011, Astrophys. J. Suppl., 192, 1

Cordier B., 2019, Mem. Soc. Ast. It., 90, 242

Cucchiara A., et al., 2011, Astrophys. J., 736, 7

Cuceu A., Farr J., Lemos P., Font-Ribera A., 2019, J. Cosmol. Astropart. Phys., 2019, 044

Czerny B., Hryniewicz K., 2011, Astron. Astrophys., 525, L8

Czerny B., et al., 2021, Acta Physica Polonica A, 139, 389

D'Agostini G., 2005, preprint, (arXiv:physics/0511182)

DES Collaboration 2018, Mon. Not. R. Astron. Soc., 480, 3879

DES Collaboration 2019a, Phys. Rev. D., 99, 123505

DES Collaboration 2019b, Mon. Not. R. Astron. Soc., 483, 4866

DES Collaboration 2019c, Astrophys. J. Lett., 872, L30

DES Collaboration 2019d, Astrophys. J., 874, 150

Dai Y., Zheng X.-G., Li Z.-X., Gao H., Zhu Z.-H., 2021, Astron. Astrophys., 651, L8

Dainotti M. G., Amati L., 2018, PASP, 130, 051001

Dainotti M. G., Del Vecchio R., 2017, New Astronomy Reviews, 77, 23

Dainotti M. G., Cardone V. F., Capozziello S., 2008, Mon. Not. R. Astron. Soc., 391, L79

Dainotti M. G., Willingale R., Capozziello S., Fabrizio Cardone V., Ostrowski M., 2010, Astrophys. J. Lett., 722, L215

Dainotti M. G., Ostrowski M., Willingale R., 2011a, Mon. Not. R. Astron. Soc., 418, 2202

Dainotti M. G., Fabrizio Cardone V., Capozziello S., Ostrowski M., Willingale R., 2011b, Astrophys. J., 730, 135

Dainotti M. G., Cardone V. F., Piedipalumbo E., Capozziello S., 2013a, Mon. Not. R. Astron. Soc., 436, 82

Dainotti M. G., Petrosian V., Singal J., Ostrowski M., 2013b, Astrophys. J., 774, 157

Dainotti M., Petrosian V., Willingale R., O'Brien P., Ostrowski M., Nagataki S., 2015a, Mon. Not. R. Astron. Soc., 451, 3898

Dainotti M. G., Del Vecchio R., Nagataki S., Capozziello S., 2015b, Astrophys. J., 800, 31

Dainotti M. G., Postnikov S., Hernandez X., Ostrowski M., 2016, Astrophys. J. Lett., 825, L20

Dainotti M. G., Nagataki S., Maeda K., Postnikov S., Pian E., 2017, Astron. Astrophys., 600, A98

Dainotti M. G., Del Vecchio R., Tarnopolski M., 2018, Advances in Astronomy, 2018, 4969503

Dainotti M., et al., 2019, preprint, (arXiv:1907.05074)

Dainotti M. G., Lenart A. Ł., Sarracino G., Nagataki S., Capozziello S., Fraija N., 2020, Astrophys. J., 904, 97

Dainotti M. G., Lenart A. Ł., Fraija N., Nagataki S., Warren D. C., De Simone B., Srinivasaragavan G., Mata A., 2021a, PASJ, 73, 970

Dainotti M. G., et al., 2021b, Astrophys. J. Suppl., 255, 13

Dainotti M. G., De Simone B., Schiavone T., Montani G., Rinaldi E., Lambiase G., 2021c, Astrophys. J., 912, 150

Dainotti M. G., De Simone B. D., Schiavone T., Montani G., Rinaldi E., Lambiase G., Bogdan M., Ugale S., 2022a, Galaxies, 10, 24

Dainotti M. G., Sarracino G., Capozziello S., 2022b, PASJ, 74, 1095

Dainotti M. G., Nielson V., Sarracino G., Rinaldi E., Nagataki S., Capozziello S., Gnedin O. Y., Bargiacchi G., 2022c, Mon. Not. R. Astron. Soc., 514, 1828

Dainotti M. G., Bargiacchi G., Lenart A. Ł., Capozziello S., Ó Colgáin E., Solomon R., Stojkovic D., Sheikh-Jabbari M. M., 2022d, Astrophys. J., 931, 106

De Cicco D., et al., 2022, Astron. Astrophys., 664, A117

De Rosa G., et al., 2015, Astrophys. J., 806, 128

de Cruz Perez J., Sola Peracaula J., Gomez-Valent A., Moreno-Pulido C., 2021, preprint, (arXiv:2110.07569)

de Sainte Agathe V., et al., 2019, Astron. Astrophys., 629, A85

Demianski M., Piedipalumbo E., 2011, Mon. Not. R. Astron. Soc., 415, 3580

Demianski M., Piedipalumbo E., Sawant D., Amati L., 2017, Astron. Astrophys., 598, A112

Demianski M., Piedipalumbo E., Sawant D., Amati L., 2021, Mon. Not. R. Astron. Soc., 506, 903

Deng H.-K., Wei H., 2018, European Physical Journal C, 78, 755

Denzel P., Coles J. P., Saha P., Williams L. L. R., 2021, Mon. Not. R. Astron. Soc., 501, 784

Dhawan S., Jha S. W., Leibundgut B., 2018, Astron. Astrophys., 609, A72

Di Valentino E., et al., 2021a, Classical and Quantum Gravity, 38, 153001

Di Valentino E., Melchiorri A., Silk J., 2021b, Astrophys. J. Lett., 908, L9

Domínguez A., et al., 2019, Astrophys. J., 885, 137

du Mas des Bourboux H., et al., 2020, Astrophys. J., 901, 153

eBOSS Collaboration 2021, Phys. Rev. D., 103, 083533

Eckart A., et al., 2017, Foundations of Physics, 47, 553

Efstathiou G., 2020, preprint, (arXiv:2007.10716)

Efstathiou G., Gratton S., 2020, Mon. Not. R. Astron. Soc., 496, L91

Erb D. K., Steidel C. C., Shapley A. E., Pettini M., Reddy N. A., Adelberger K. L., 2006, Astrophys. J., 646, 107

Evans P. A., et al., 2010, Astron. Astrophys., 519, A102

Fana Dirirsa F., et al., 2019, Astrophys. J., 887, 13

Farooq O., 2013, PhD thesis, Kansas State U. (arXiv:1309.3710)

Farooq O., Mania D., Ratra B., 2015, Astrophys. Space Sci., 357, 11

Farooq O., Ranjeet Madiyar F., Crandall S., Ratra B., 2017, Astrophys. J., 835, 26

Ferland G. J., Done C., Jin C., Landt H., Ward M. J., 2020, Mon. Not. R. Astron. Soc., 494, 5917

Fernández Arenas D., et al., 2018, Mon. Not. R. Astron. Soc., 474, 1250

Fonseca Alvarez G., et al., 2020, Astrophys. J., 899, 73

Foreman-Mackey D., Hogg D. W., Lang D., Goodman J., 2013, PASP, 125, 306

Freedman W. L., 2021, Astrophys. J., 919, 16

Freedman W. L., et al., 2019, Astrophys. J., 882, 34

Freedman W. L., et al., 2020, Astrophys. J., 891, 57

Gao C., Chen Y., Zheng J., 2020, Research in Astronomy and Astrophysics, 20, 151

Geng C.-Q., Hsu Y.-T., Yin L., Zhang K., 2020, Chinese Physics C, 44, 105104

Ghirlanda G., Ghisellini G., Lazzati D., 2004, Astrophys. J., 616, 331

Gil-Marín H., et al., 2020, Mon. Not. R. Astron. Soc., 498, 2492

Gómez-Valent A., Amendola L., 2018, J. Cosmol. Astropart. Phys., 4, 051

González-Morán A. L., et al., 2019, Mon. Not. R. Astron. Soc., 487, 4669

González-Morán A. L., et al., 2021, Mon. Not. R. Astron. Soc., 505, 1441

Gordon K. D., Clayton G. C., Misselt K. A., Landolt A. U., Wolff M. J., 2003, Astrophys. J., 594, 279

Gott III J. R., Vogeley M. S., Podariu S., Ratra B., 2001, Astrophys. J., 549, 1

Grier C. J., et al., 2019, Astrophys. J., 887, 38

Gurvits L. I., Kellermann K. I., Frey S., 1999, Astron. Astrophys., 342, 378

Handley W., 2019, Phys. Rev. D., 100, 123517

Handley W., 2021, Phys. Rev. D., 103, L041301

Haridasu B. S., Lukovi ć V. V., Moresco M., Vittorio N., 2018, J. Cosmol. Astropart. Phys., 2018, 015

Harvey D., 2020, Mon. Not. R. Astron. Soc., 498, 2871

Homayouni Y., et al., 2020, Astrophys. J., 901, 55

Hoormann J. K., et al., 2019, Mon. Not. R. Astron. Soc., 487, 3650

Hou J., et al., 2021, Mon. Not. R. Astron. Soc., 500, 1201

Hu J.-P., Wang F.-Y., 2023, Universe, 9, 94

Hu J. P., Wang F. Y., Dai Z. G., 2021, Mon. Not. R. Astron. Soc., 507, 730

Ivezić Ž., et al., 2019, Astrophys. J., 873, 111

Jesus J. F., Valentim R., Moraes P. H. R. S., Malheiro M., 2021, Mon. Not. R. Astron. Soc., 500, 2227

Jesus J. F., Valentim R., Escobal A. A., Pereira S. H., Benndorf D., 2022, J. Cosmol. Astropart. Phys., 2022, 037

Johnson J. P., Sangwan A., Shankaranarayanan S., 2022, J. Cosmol. Astropart. Phys., 2022, 024

Jones D. H., et al., 2009, Mon. Not. R. Astron. Soc., 399, 683

Karas V., Svoboda J., Zajaček M., 2021, in RAGtime: Workshops on black holes and netron stars. p. E1 (arXiv:1901.06507)

Kaspi S., Brandt W. N., Maoz D., Netzer H., Schneider D. P., Shemmer O., 2007, Astrophys. J., 659, 997

Kaspi S., Brandt W. N., Maoz D., Netzer H., Schneider D. P., Shemmer O., Grier C. J., 2021, Astrophys. J., 915, 129

Kass R. E., Raftery A. E., 1995, J. Am. Stat. Assoc., 90, 773

Khadka N., Ratra B., 2020a, Mon. Not. R. Astron. Soc., 492, 4456

Khadka N., Ratra B., 2020b, Mon. Not. R. Astron. Soc., 497, 263

Khadka N., Ratra B., 2020c, Mon. Not. R. Astron. Soc., 499, 391

Khadka N., Ratra B., 2021, Mon. Not. R. Astron. Soc., 502, 6140

Khadka N., Ratra B., 2022, Mon. Not. R. Astron. Soc., 510, 2753

Khadka N., Yu Z., Zajaček M., Martinez-Aldama M. L., Czerny B., Ratra B., 2021a, Mon. Not. R. Astron. Soc., 508, 4722

Khadka N., Luongo O., Muccino M., Ratra B., 2021b, J. Cosmol. Astropart. Phys., 2021, 042

Khadka N., Martínez-Aldama M. L., Zajaček M., Czerny B., Ratra B., 2022a, Mon. Not. R. Astron. Soc., 513, 1985

Khadka N., Zajaček M., Panda S., Martínez-Aldama M. L., Ratra B., 2022b, Mon. Not. R. Astron. Soc., 515, 3729

Khetan N., et al., 2021, Astron. Astrophys., 647, A72

Kim Y. J., Kang J., Lee M. G., Jang I. S., 2020, Astrophys. J., 905, 104

Kollmeier J. A., et al., 2017, preprint, (arXiv:1711.03234)

Kovačević A. B., et al., 2022, The LSST Era of Supermassive Black Hole Accretion Disk Reverberation Mapping (arXiv:2208.06203), doi:10.3847/1538-4365/ac88ce

Kumar D., Jain D., Mahajan S., Mukherjee A., Rani N., 2021, Phys. Rev. D., 103, 063511

Kunz M., Trotta R., Parkinson D. R., 2006, Phys. Rev. D., 74, 023503

Lamb D. Q., Reichart D. E., 2000, Astrophys. J., 536, 1

Lamb D. Q., Reichart D. E., 2001, in Costa E., Frontera F., Hjorth J., eds, Gamma-ray Bursts in the Afterglow Era. p. 226 (arXiv:astro-ph/0108099), doi:10.1007/10853853_61

Leizerovich M., Kraiselburd L., Landau S., Scóccola C. G., 2022, Phys. Rev. D., 105, 103526

Lesgourgues J., Tram T., 2014, J. Cosmol. Astropart. Phys., 2014, 032

Lewis A., 2019, preprint, (arXiv:1910.13970)

Li E.-K., Du M., Xu L., 2020, Mon. Not. R. Astron. Soc., 491, 4960

Li X., Keeley R. E., Shafieloo A., Zheng X., Cao S., Biesiada M., Zhu Z.-H., 2021, Mon. Not. R. Astron. Soc., 507, 919

Lian Y., Cao S., Biesiada M., Chen Y., Zhang Y., Guo W., 2021, Mon. Not. R. Astron. Soc., 505, 2111

Liang E., Zhang B., 2005, Astrophys. J., 633, 611

Liddle A. R., 2007, Mon. Not. R. Astron. Soc., 377, L74

Lien A., et al., 2016, Astrophys. J., 829, 7

Lima J. A. S., Alcaniz J. S., 2002, Astrophys. J., 566, 15

Lin W., Ishak M., 2021, J. Cosmol. Astropart. Phys., 2021, 009

Lira P., et al., 2018, Astrophys. J., 865, 56

Liu J., Wei H., 2015, General Relativity and Gravitation, 47, 141

Liu Y., Chen F., Liang N., Yuan Z., Yu H., Wu P., 2022, Astrophys. J., 931, 50

Lucchin F., Matarrese S., 1985, Phys. Rev. D., 32, 1316

Luongo O., Muccino M., 2021, Galaxies, 9, 77

Luongo O., Muccino M., Colgáin E. Ó., Sheikh-Jabbari M. M., Yin L., 2022, Phys. Rev. D., 105, 103510

Lusso E., et al., 2020, Astron. Astrophys., 642, A150

Lyu M.-Z., Haridasu B. S., Viel M., Xia J.-Q., 2020, Astrophys. J., 900, 160

Mania D., Ratra B., 2012, Physics Letters B, 715, 9

Martin J., 2012, Comptes Rendus Physique, 13, 566

Martinelli M., Tutusaus I., 2019, Symmetry, 11, 986

Martínez-Aldama M. L., del Olmo A., Marziani P., Sulentic J. W., Negrete C. A., Dultzin D., D'Onofrio M., Perea J., 2018, Astron. Astrophys., 618, A179

Martínez-Aldama M. L., Czerny B., Kawka D., Karas V., Panda S., Zajaček M., Życki P. T., 2019, Astrophys. J., 883, 170

Martinez Aldama M. L., Panda S., Czerny B., Zajacek M., LSST AGN SC Collaboration 2020a, in Multifrequency Behaviour of High Energy Cosmic Sources - XIII. 3-8 June 2019. Palermo. p. 10 (arXiv:1910.02725)

Martínez-Aldama M. L., Zajaček M., Czerny B., Panda S., 2020b, Astrophys. J., 903, 86

Maseda M. V., et al., 2014, Astrophys. J., 791, 17

Masters D., et al., 2014, Astrophys. J., 785, 153

Mehrabi A., et al., 2022, Mon. Not. R. Astron. Soc., 509, 224

Mejía-Restrepo J. E., Lira P., Netzer H., Trakhtenbrot B., Capellupo D. M., 2018, Nature Astronomy, 2, 63

Melnick J., Terlevich R., Terlevich E., 2000, Mon. Not. R. Astron. Soc., 311, 629

Melnick J., et al., 2017, Astron. Astrophys., 599, A76

Metzroth K. G., Onken C. A., Peterson B. M., 2006, Astrophys. J., 647, 901

Moresco M., 2015, Mon. Not. R. Astron. Soc., 450, L16

Moresco M., et al., 2012, J. Cosmol. Astropart. Phys., 8, 006

Moresco M., et al., 2016, J. Cosmol. Astropart. Phys., 5, 014

Moresco M., Jimenez R., Verde L., Pozzetti L., Cimatti A., Citro A., 2018, Astrophys. J., 868, 84

Moresco M., Jimenez R., Verde L., Cimatti A., Pozzetti L., 2020, Astrophys. J., 898, 82

Moresco M., et al., 2022, Living Reviews in Relativity, 25, 6

Muccino M., 2020, Symmetry, 12, 1118

Müller A. L., Naddaf M.-H., Zajaček M., Czerny B., Araudo A., Karas V., 2022, Astrophys. J., 931, 39

Naddaf M. H., Czerny B., 2022, Astron. Astrophys., 663, A77

Naddaf M.-H., Czerny B., Szczerba R., 2021, Astrophys. J., 920, 30

Netzer H., 2019, Mon. Not. R. Astron. Soc., 488, 5185

Neveux R., et al., 2020, Mon. Not. R. Astron. Soc., 499, 210

Ooba J., Ratra B., Sugiyama N., 2018a, Astrophys. J., 864, 80

Ooba J., Ratra B., Sugiyama N., 2018b, Astrophys. J., 866, 68

Ooba J., Ratra B., Sugiyama N., 2018c, Astrophys. J., 869, 34

Ooba J., Ratra B., Sugiyama N., 2019, Astrophys. Space Sci., 364, 176

Panda S., 2022, Frontiers in Astronomy and Space Sciences, 9, 850409

Panda S., Martínez-Aldama M. L., Zajaček M., 2019a, Frontiers in Astronomy and Space Sciences, 6, 75

Panda S., Marziani P., Czerny B., 2019b, Astrophys. J., 882, 79

Park C.-G., Ratra B., 2018, Astrophys. J., 868, 83

Park C.-G., Ratra B., 2019a, Astrophys. Space Sci., 364, 82

Park C.-G., Ratra B., 2019b, Astrophys. Space Sci., 364, 134

Park C.-G., Ratra B., 2019c, Astrophys. J., 882, 158

Park C.-G., Ratra B., 2020, Phys. Rev. D., 101, 083508

Pavlov A., Westmoreland S., Saaidi K., Ratra B., 2013, Phys. Rev. D., 88, 123513

Peebles P. J. E., 1984, Astrophys. J., 284, 439

Peebles P. J. E., Ratra B., 1988, Astrophys. J. Lett., 325, L17

Penton A., et al., 2022, Mon. Not. R. Astron. Soc., 509, 4008

Perivolaropoulos L., Skara F., 2022, New Astronomy Reviews, 95, 101659

Peterson B. M., et al., 2005, Astrophys. J., 632, 799

Peterson B. M., et al., 2006, Astrophys. J., 641, 638

Philcox O. H. E., Ivanov M. M., Simonović M., Zaldarriaga M., 2020, J. Cosmol. Astropart. Phys., 2020, 032

Planck Collaboration 2020, Astron. Astrophys., 641, A6

Plionis M., Terlevich R., Basilakos S., Bresolin F., Terlevich E., Melnick J., Georgantopoulos I., 2009, in Journal of Physics Conference Series. p. 012032 (arXiv:0903.0131), doi:10.1088/1742-6596/189/1/012032

Plionis M., Terlevich R., Basilakos S., Bresolin F., Terlevich E., Melnick J., Chavez R., 2010, in Alimi J.-M., Fuözfa A., eds, American Institute of Physics Conference Series Vol. 1241, American Institute of Physics Conference Series. pp 267–276 (arXiv:0911.3198)

Plionis M., Terlevich R., Basilakos S., Bresolin F., Terlevich E., Melnick J., Chavez R., 2011, Mon. Not. R. Astron. Soc., 416, 2981

Pogosian L., Zhao G.-B., Jedamzik K., 2020, Astrophys. J. Lett., 904, L17

Postnikov S., Dainotti M. G., Hernandez X., Capozziello S., 2014, Astrophys. J., 783, 126

Prince R., et al., 2022, Astron. Astrophys., 667, A42

Rakshit S., 2020, Astron. Astrophys., 642, A59

Rameez M., Sarkar S., 2019, preprint, (arXiv:1911.06456)

Rameez M., Sarkar S., 2021, Classical and Quantum Gravity, 38, 154005

Rana A., Jain D., Mahajan S., Mukherjee A., 2017, J. Cosmol. Astropart. Phys., 3, 028

Ratra B., 1989, Phys. Rev. D., 40, 3939

Ratra B., 2017, Phys. Rev. D., 96, 103534

Ratra B., Peebles P. J. E., 1988, Phys. Rev. D., 37, 3406

Ratra B., Peebles P. J. E., 1995, Phys. Rev. D., 52, 1837

Ratra B., Vogeley M. S., 2008, PASP, 120, 235

Ratsimbazafy A. L., Loubser S. I., Crawford S. M., Cress C. M., Bassett B. A., Nichol R. C., Väisänen P., 2017, Mon. Not. R. Astron. Soc., 467, 3239

Rezaei M., Solà Peracaula J., Malekjani M., 2022, Mon. Not. R. Astron. Soc., 509, 2593

Riess A. G., 2019, Nature Reviews Physics, 2, 10

Riess A. G., Casertano S., Yuan W., Macri L. M., Scolnic D., 2019, Astrophys. J., 876, 85

Riess A. G., Casertano S., Yuan W., Bowers J. B., Macri L., Zinn J. C., Scolnic D., 2021, Astrophys. J. Lett., 908, L6

Rigault M., et al., 2015, Astrophys. J., 802, 20

Risaliti G., Lusso E., 2015, Astrophys. J., 815, 33

Risaliti G., Lusso E., 2019, Nature Astronomy, 3, 272

Ross A. J., Samushia L., Howlett C., Percival W. J., Burden A., Manera M., 2015, Mon. Not. R. Astron. Soc., 449, 835

Ruan C.-Z., Melia F., Chen Y., Zhang T.-J., 2019, Astrophys. J., 881, 137

Ryan J., 2021a, PhD thesis, Kansas State U. (arXiv:2104.10354)

Ryan J., 2021b, J. Cosmol. Astropart. Phys., 2021, 051

Ryan J., Doshi S., Ratra B., 2018, Mon. Not. R. Astron. Soc., 480, 759

Ryan J., Chen Y., Ratra B., 2019, Mon. Not. R. Astron. Soc., 488, 3844

Sakamoto T., et al., 2011, Astrophys. J. Suppl., 195, 2

Salvaterra R., et al., 2009, Nature, 461, 1258

Samushia L., Ratra B., 2010, Astrophys. J., 714, 1347

Samushia L., Dev A., Jain D., Ratra B., 2010, Physics Letters B, 693, 509

Sangwan A., Tripathi A., Jassal H. K., 2018, preprint, (arXiv:1804.09350)

Schöneberg N., Lesgourgues J., Hooper D. C., 2019, J. Cosmol. Astropart. Phys., 2019, 029

Scolnic D. M., et al., 2018, Astrophys. J., 859, 101

Seikel M., Clarkson C., Smith M., 2012, J. Cosmol. Astropart. Phys., 2012, 036

Shen Y., et al., 2019, Astrophys. J. Lett., 883, L14

Shirokov S. I., Sokolov I. V., Lovyagin N. Y., Amati L., Baryshev Y. V., Sokolov V. V., Gorokhov V. L., 2020, Mon. Not. R. Astron. Soc., 496, 1530

Siegel E. R., Guzmán R., Gallego J. P., Orduña López M., Rodríguez Hidalgo P., 2005, Mon. Not. R. Astron. Soc., 356, 1117

Simon J., Verde L., Jimenez R., 2005, Phys. Rev. D., 71, 123001

Singh A., Sangwan A., Jassal H. K., 2019, J. Cosmol. Astropart. Phys., 2019, 047

Sinha S., Banerjee N., 2021, J. Cosmol. Astropart. Phys., 2021, 060

Solà Peracaula J., de Cruz Pérez J., Gómez-Valent A., 2018, Mon. Not. R. Astron. Soc., 478, 4357

Solà Peracaula J., Gómez-Valent A., de Cruz Pérez J., 2019, Physics of the Dark Universe, 25, 100311

Solà J., Gómez-Valent A., de Cruz Pérez J., 2017, Modern Physics Letters A, 32, 1750054

Spiegelhalter D., Best N., Carlin B., Van Der Linde A., 2002, Journal of the Royal Statistical Society. Series B: Statistical Methodology, 64, 583

Srinivasaragavan G. P., Dainotti M. G., Fraija N., Hernandez X., Nagataki S., Lenart A., Bowden L., Wagner R., 2020, Astrophys. J., 903, 18

Starkey D. A., Horne K., Villforth C., 2016, Mon. Not. R. Astron. Soc., 456, 1960

Stern D., Jimenez R., Verde L., Kamionkowski M., Stanford S. A., 2010, J. Cosmol. Astropart. Phys., 2, 008

Tanvir N. R., et al., 2009, Nature, 461, 1254

Terlevich R., Terlevich E., Melnick J., Chávez R., Plionis M., Bresolin F., Basilakos S., 2015, Mon. Not. R. Astron. Soc., 451, 3001

Thavanesan A., Werth D., Handley W., 2021, Phys. Rev. D., 103

Tsiapi P., et al., 2021, Mon. Not. R. Astron. Soc., 506, 5039

Ureña-López L. A., Roy N., 2020, Phys. Rev. D., 102, 063510

Vagnozzi S., Di Valentino E., Gariazzo S., Melchiorri A., Mena O., Silk J., 2021a, Physics of the Dark Universe, 33, 100851

Vagnozzi S., Loeb A., Moresco M., 2021b, Astrophys. J., 908, 84

Velasquez-Toribio A. M., Fabris J. C., 2020, European Physical Journal C, 80, 1210

Vishwakarma R. G., 2001, Classical and Quantum Gravity, 18, 1159

Wald R. M., 1984, General Relativity. Chicago Univ. Pr., Chicago, USA, doi:10.7208/chicago/9780226870373.001.0001

Wan H.-Y., Cao S.-L., Melia F., Zhang T.-J., 2019, Physics of the Dark Universe, 26, 100405

Wang F. Y., Dai Z. G., Liang E. W., 2015, New Astronomy Reviews, 67, 1

Wang J. S., Wang F. Y., Cheng K. S., Dai Z. G., 2016, Astron. Astrophys., 585, A68

Wang F. Y., Hu J. P., Zhang G. Q., Dai Z. G., 2022, Astrophys. J., 924, 97

Wei J.-J., 2018, Astrophys. J., 868, 29

Wei J.-J., Melia F., 2020, Astrophys. J., 888, 99

Wei J.-J., Wu X.-F., Melia F., 2016, Mon. Not. R. Astron. Soc., 463, 1144

Willingale R., et al., 2007, Astrophys. J., 662, 1093

Willingale R., Genet F., Granot J., O'Brien P. T., 2010, Mon. Not. R. Astron. Soc., 403, 1296

Wu Y., Cao S., Zhang J., Liu T., Liu Y., Geng S., Lian Y., 2020, Astrophys. J., 888, 113

Wu Q., Zhang G.-Q., Wang F.-Y., 2022, Mon. Not. R. Astron. Soc., 515, L1

Xu F., Tang C.-H., Geng J.-J., Wang F.-Y., Wang Y.-Y., Kuerban A., Huang Y.-F., 2021, Astrophys. J., 920, 135

Xu T., Chen Y., Xu L., Cao S., 2022, Physics of the Dark Universe, 36, 101023

Yang Y., Gong Y., 2021, Mon. Not. R. Astron. Soc., 504, 3092

Yang T., Banerjee A., Ó Colgáin E., 2020, Phys. Rev. D., 102, 123532

Yashar M., Bozek B., Abrahamse A., Albrecht A., Barnard M., 2009, Phys. Rev. D., 79, 103004

Yennapureddy M. K., Melia F., 2017, J. Cosmol. Astropart. Phys., 2017, 029

Yu H., Ratra B., Wang F.-Y., 2018, Astrophys. J., 856, 3

Yu Z., et al., 2021, Mon. Not. R. Astron. Soc., 507, 3771

Zajaček M., Karas V., Eckart A., 2014, Astron. Astrophys., 565, A17

Zajaček M., Czerny B., Martínez-Aldama M. L., Karas V., 2019, Astronomische Nachrichten, 340, 577

Zajaček M., et al., 2020a, Astrophys. J., 896, 146

Zajaček M., Araudo A., Karas V., Czerny B., Eckart A., 2020b, Astrophys. J., 903, 140

Zajaček M., et al., 2021, Astrophys. J., 912, 10

Zeng H., Yan D., 2019, Astrophys. J., 882, 87

Zhai Z., Blanton M., Slosar A., Tinker J., 2017, Astrophys. J., 850, 183

Zhang J., 2018, PASP, 130, 084502

Zhang X., Huang Q.-G., 2019, preprint, (arXiv:1911.09439)

Zhang X., Huang Q.-G., 2021, Phys. Rev. D., 103, 043513

Zhang C., Zhang H., Yuan S., Liu S., Zhang T.-J., Sun Y.-C., 2014, Research in Astronomy and Astrophysics, 14, 1221

Zhang B. R., Childress M. J., Davis T. M., Karpenka N. V., Lidman C., Schmidt B. P., Smith M., 2017, Mon. Not. R. Astron. Soc., 471, 2254

Zhao D., Xia J.-Q., 2021, European Physical Journal C, 81, 694

Zheng J., Melia F., Zhang T.-J., 2019, preprint, (arXiv:1901.05705)

Zheng X., Liao K., Biesiada M., Cao S., Liu T.-H., Zhu Z.-H., 2020, Astrophys. J., 892, 103

Zheng X., Cao S., Biesiada M., Li X., Liu T., Liu Y., 2021, Science China Physics, Mechanics, and Astronomy, 64, 259511

Zhu Z.-H., Fujimoto M.-K., 2002, Astrophys. J., 581, 1

Zu Y., Kochanek C. S., Peterson B. M., 2011, Astrophys. J., 735, 80

Appendix A

QSO-Flux

QSOs obey a nonlinear relation between their luminosities in the X-ray and UV bands. Using a sample of 808 QSOs in the redshift range $0.061 \leq z \leq 6.280$, Risaliti & Lusso (2015) confirmed that this relation can be written

$$\log L_X = \beta + \gamma \log L_{UV}, \tag{A.1}$$

where L_X and L_{UV} are the X-ray and UV luminosities of the QSOs. To make contact with observations, equation (A.1) must be expressed in terms of the fluxes F_X and F_{UV} measured at fixed rest-frame wavelengths in the X-ray and UV bands, respectively. With this, equation (A.1) becomes

$$\log F_X = \beta + (\gamma - 1) \log 4\pi + \gamma \log F_{UV} + 2(\gamma - 1) \log D_L. \tag{A.2}$$

Here D_L is the luminosity distance, which depends on the parameters of our cosmological models. We also treat the slope γ and intercept β as free parameters in our cosmological model fits.

For QSO-Flux data, the natural log of its likelihood function is

$$\ln \mathscr{L}_{\rm QF} = -\frac{1}{2}\sum_{i=1}^{N}\left[\frac{\left[\log(F_X^{\rm obs})_i - \log(F_X^{\rm th})_i\right]^2}{s_i^2} + \ln(2\pi s_i^2)\right],$$

where $s_i^2 = \sigma_i^2 + \delta^2$. Here σ_i is the uncertainty in $\log\left(F_X^{\rm obs}\right)_i$, and δ is the global intrinsic dispersion in the data (including the systematic uncertainties), which we treat as a free parameter in our cosmological model fits. We use the Risaliti & Lusso (2019) compilation of 1598 QSO-Flux measurements in the range $0.036 \leq z \leq 5.1003$. The flat priors of cosmological parameters and the Amati relation parameters are in Sec. 4.3 and, as in Khadka & Ratra (2020b), the flat priors of the parameters δ, γ, and β are non-zero over $0 \leq \delta \leq e^{10}$, $-2 \leq \gamma \leq 2$, and $0 \leq \beta \leq 11$, respectively.

As discussed in Khadka & Ratra (2020b) the QSO-Flux data alone favors large Ω_{m0} values for the physically-motivated flat and non-flat ΛCDM and ϕCDM models. Risaliti & Lusso (2019) and Khadka & Ratra (2020b) note that this is largely a consequence of the $z \sim 2$–5 QSO data. While these large Ω_{m0} values differ from almost all other measurements of Ω_{m0}, the QSO-Flux data have larger error bars and their cosmological constraint contours are not in conflict with those from other data sets. For these reasons we have used the QSO-Flux data, but in this Section, and we have not computed QSO-Flux data results for the ϕCDM cases (these being computationally demanding). We briefly summarize our constraints, listed in Tables A.1 and A.2 and shown in Figs. A.1–A.4, below.

A.1 QSO-Flux constraints

Except for flat ΛCDM, the constraints on Ω_{m0} in the QSO-Flux only case are 2σ larger than those in the combined HzBHQASQFG case (see Sec. A.2.1). QSO-Flux data cannot constrain α, nor can they constrain H_0 (for the same reason that GRB data cannot constrain this parameter; see Section 4.4.1). QSO-Flux data set upper limits on $w_{\rm X}$ for flat and non-flat XCDM, with $w_{\rm X} = -1$ within the 1σ range.

A.2 H IIG, QSO-AS, QSO-Flux, and GRB (HQASQFG) constraints

When adding QSO-Flux to HQASG data, the joint constraints favor larger Ω_{m0} and lower Ω_{k0}. In non-flat ΛCDM closed geometry is favored at 3.24σ. The H_0 constraints are only mildly affected by the addition of the QSO-Flux data. The constraint on $w_{\rm X}$ changes from $-1.379^{+0.361}_{-0.375}$ in the HQASG case to < -1.100 (2σ limit) in the HQASQFG case for flat XCDM, while for non-flat XCDM, the constraint on $w_{\rm X}$ in the HQASQFG case is 0.40σ lower than that in the HQASG case and is 1.80σ away from $w_{\rm X} = -1$.

A.2.1 $H(z)$, BAO, H IIG, QSO-AS, QSO-Flux, and GRB (HzB-HQASQFG) constraints

When adding QSO-Flux to the HzBHQASG combination, the Ω_{m0} central values are only slightly larger because the $H(z)$ + BAO data dominate this compilation. The joint-constraint central Ω_{k0} values are lower, and consistent with flat geometry, while the constraints on H_0 from this combination are almost unaltered. The constraints on $w_{\rm X}$ are 0.02σ lower and 0.23σ higher for flat and non-flat XCDM, respectively, both being consistent with $w_{\rm X} = -1$ within 1σ.

A.3 Model comparison

From Table A.1, we see that the reduced χ^2 of the QSO-Flux case for all models is near unity (~ 1.01) and that the reduced χ^2 of cases that include QSO-Flux is brought down to ~ 1.24–1.26 for all models. Based on the BIC (see Table A.1), flat ΛCDM is the most favored model, while based on the AIC, non-flat XCDM, flat XCDM, and flat ΛCDM are the most favored models for the QSO-Flux, HQASQFG, and HzBHQASQFG combinations,

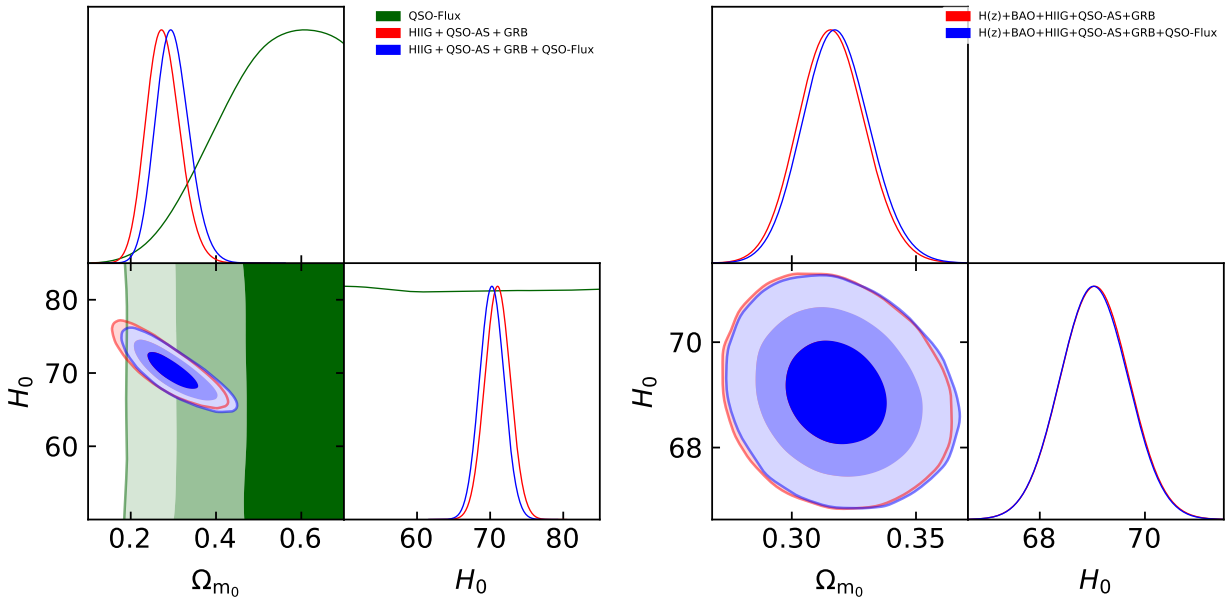

(a) (b)

Figure A.1: Same as Fig. 4.1 (flat ΛCDM) but for different combinations of data and showing only cosmological parameters.

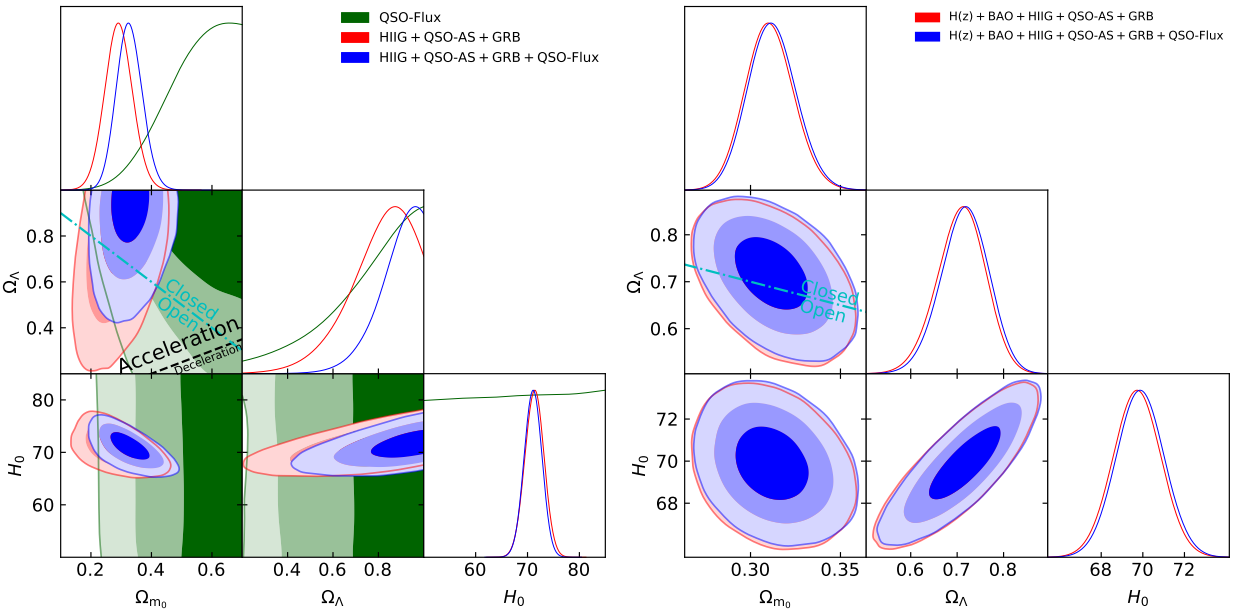

(a) (b)

Figure A.2: Same as Fig. 4.2 (non-flat ΛCDM) but for different combinations of data and showing only cosmological parameters.

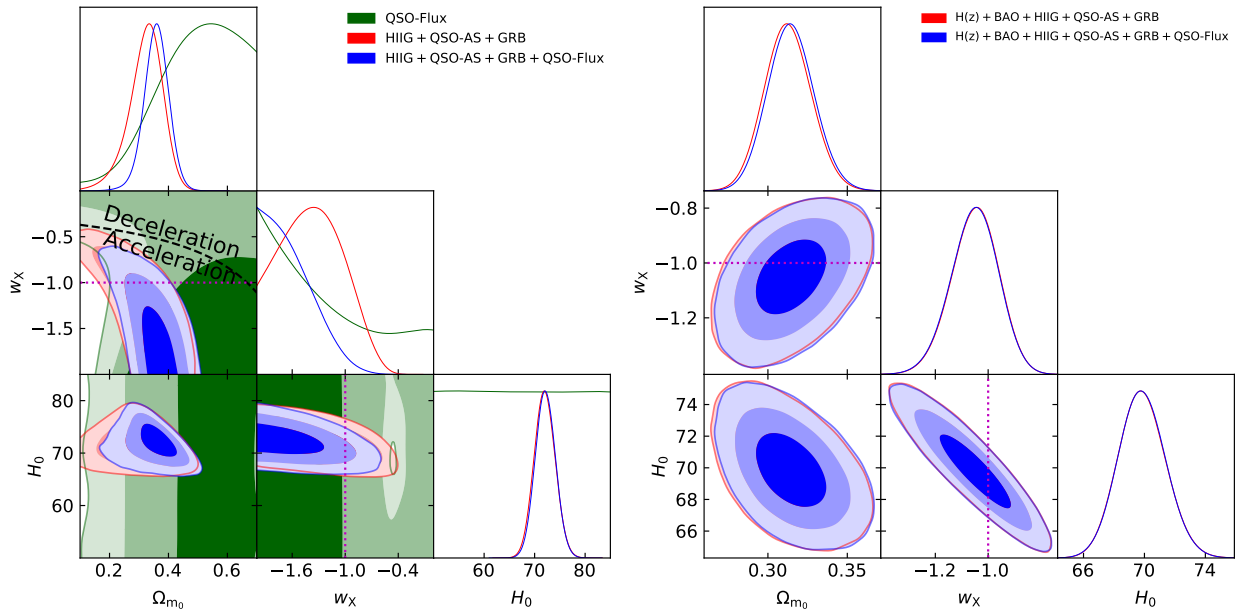

(a) (b)

Figure A.3: Same as Fig. 4.3 (flat XCDM) but for different combinations of data and showing only cosmological parameters.

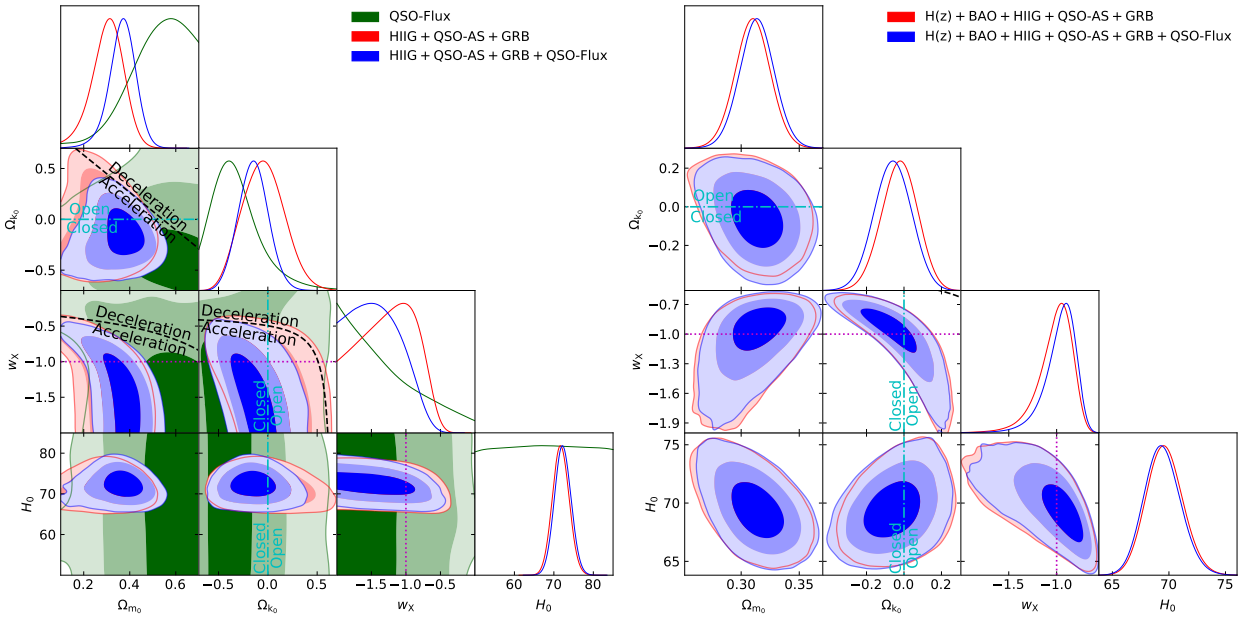

(a) (b)

Figure A.4: Same as Fig. 4.4 (non-flat XCDM) but for different combinations of data and showing only cosmological parameters.

Table A.1: Unmarginalized best-fitting parameter values for all models from various combinations of data.

Model	Data set	Ω_{m_0}	Ω_Λ	Ω_{k_0}	w_X	α	H_0[c]	σ_{ext}	a	b	δ	γ	β	χ^2	ν	$-2\ln\mathscr{L}_{max}$	AIC	BIC	$\Delta\chi^2$	ΔAIC	ΔBIC
Flat ΛCDM	QSO-Flux	0.315	0.685	–	–	–	68.69	–	–	–	–	–	–	1603.28	1593	-50.13	-40.13	-13.24	0.00	1.62	0.00
	HQASG[d]	0.271	0.729	–	–	–	71.13	0.407	50.18	1.138	–	–	–	879.42	387	895.05	905.05	924.91	0.12	0.00	0.00
	HQASQFG[e]	0.305	0.695	–	–	–	70.01	0.399	50.20	1.132	0.231	0.639	7.083	2480.01	1982	848.53	864.53	909.29	0.00	2.58	0.00
	HzBHQASG[f]	0.317	0.683	–	–	–	69.06	0.404	50.19	1.134	–	–	–	903.61	429	917.79	927.79	948.16	1.52	0.00	0.00
	HzBHQASQFG[g]	0.317	0.683	–	–	–	69.06	0.399	50.23	1.119	0.232	0.637	7.144	2499.87	2024	870.31	886.31	931.25	0.00	0.00	0.00
Non-flat ΛCDM	QSO-Flux	0.540	0.985	−0.525	–	–	75.75	–	–	–	0.230	0.611	7.888	1603.83	1592	-53.25	-41.25	-8.99	0.55	0.50	4.25
	HQASG[d]	0.291	0.876	−0.167	–	–	72.00	0.406	50.22	1.120	–	–	–	879.30	386	894.02	906.02	929.85	0.00	0.97	4.94
	HQASQFG[e]	0.325	0.944	−0.269	–	–	71.49	0.404	50.21	1.116	0.230	0.632	7.304	2486.97	1981	844.38	862.38	912.75	6.96	0.43	3.46
	HzBHQASG[f]	0.309	0.716	−0.025	–	–	69.77	0.402	50.17	1.141	–	–	–	904.47	428	917.17	929.17	953.61	2.38	1.38	5.45
	HzBHQASQFG[g]	0.309	0.709	−0.018	–	–	69.59	0.412	50.21	1.128	0.231	0.637	7.151	2503.43	2023	869.71	887.71	938.26	3.56	1.40	7.01
Flat XCDM	QSO-Flux	0.477	–	–	−1.988	–	60.86	–	–	–	0.230	0.625	7.530	1604.18	1592	-52.13	-40.13	-7.88	0.90	1.62	5.36
	HQASG[d]	0.320	–	–	−1.306	–	72.03	0.404	50.20	1.131	–	–	–	880.47	386	894.27	906.27	930.10	1.17	1.22	5.19
	HQASQFG[e]	0.370	–	–	−1.980	–	73.66	0.399	50.18	1.129	0.231	0.632	7.301	2485.59	1981	843.95	861.95	912.31	5.58	0.00	3.02
	HzBHQASG[f]	0.313	–	–	−1.052	–	69.90	0.407	50.19	1.132	–	–	–	902.09	428	917.55	929.55	953.99	0.00	1.76	5.83
	HzBHQASQFG[g]	0.313	–	–	−1.046	–	69.84	0.401	50.18	1.134	0.231	0.635	7.215	2506.25	2023	870.16	888.16	938.71	6.38	1.85	7.46
Non-flat XCDM	QSO-Flux	0.507	–	−0.376	−1.996	–	75.28	–	–	–	0.229	0.611	7.934	1614.59	1591	-55.75	-41.75	-4.12	11.31	0.00	9.12
	HQASG[d]	0.300	–	−0.161	−1.027	–	80.36	0.405	50.21	1.122	–	–	–	879.48	385	894.01	908.01	935.81	0.18	2.96	10.90
	HQASQFG[e]	0.395	–	−0.138	−1.639	–	73.48	0.411	50.21	1.112	0.230	0.627	7.441	2486.77	1980	843.65	863.65	919.61	6.76	1.70	10.32
	HzBHQASG[f]	0.312	–	−0.045	−0.959	–	69.46	0.402	50.23	1.117	–	–	–	904.17	427	917.07	931.07	959.58	2.08	3.28	11.42
	HzBHQASQFG[g]	0.316	–	−0.089	−0.891	–	69.05	0.410	50.23	1.111	0.230	0.633	7.247	2516.49	2022	869.25	889.25	945.41	16.62	2.94	14.16

[c] km s^{-1} Mpc^{-1}.
[d] HIIG + QSO-AS + GRB.
[e] HIIG + QSO-AS + GRB + QSO-Flux.
[f] $H(z)$ + BAO + HIIG + QSO-AS + GRB.
[g] $H(z)$ + BAO + HIIG + QSO-AS + GRB + QSO-Flux.

respectively.[1] From ΔAIC and ΔBIC, we find mostly weak or positive evidence against the models, and only in a few cases do we find strong evidence against our models. According to ΔBIC, the evidence against non-flat XCDM is strong for the QSO-Flux data, and very strong for the HQASQFG and HzBHQASQFG data, and the evidence against non-flat ΛCDM is strong for the HzBHQASQFG data. According to ΔAIC, the evidence against flat XCDM is strong for the HzBHQASQFG data.

[1]Note that based on the $\Delta\chi^2$ results of Table A.1 flat ΛCDM has the minimum χ^2 in the QSO-Flux, HQASQFG, and HzBHQASQFG cases.

Table A.2: One-dimensional marginalized best-fitting parameter values and uncertainties ($\pm1\sigma$ error bars or 2σ limits) for all models from various combinations of data.

Model	Data set	Ω_{m_0}	Ω_Λ	Ω_{k_0}	w_X	α	H_0[c]	σ_{ext}	a	b	δ	γ	β
Flat ΛCDM	QSO-Flux	> 0.313	–	–	–	–	–	–	–	–	0.231 ± 0.004	0.626 ± 0.011	7.469 ± 0.321
	HQASG[d]	$0.277^{+0.034}_{-0.041}$	–	–	–	–	71.03 ± 1.67	$0.413^{+0.026}_{-0.032}$	50.19 ± 0.24	1.138 ± 0.085	–	–	–
	HQASQFG[e]	$0.299^{+0.036}_{-0.043}$	–	–	–	–	$70.25^{+1.60}_{-1.61}$	$0.412^{+0.027}_{-0.032}$	50.18 ± 0.24	1.136 ± 0.085	$0.231^{+0.005}_{-0.004}$	$0.639^{+0.009}_{-0.010}$	$7.091^{+0.281}_{-0.279}$
	HzBHQASG[f]	0.316 ± 0.013	–	–	–	–	$69.05^{+0.62}_{-0.63}$	$0.412^{+0.026}_{-0.032}$	50.19 ± 0.23	1.133 ± 0.085	–	–	–
	HzBHQASQFG[g]	0.318 ± 0.013	–	–	–	–	69.03 ± 0.62	$0.412^{+0.026}_{-0.032}$	50.19 ± 0.23	1.133 ± 0.084	0.231 ± 0.004	0.637 ± 0.009	7.146 ± 0.268
Non-flat ΛCDM	QSO-Flux	> 0.353	> 0.357	$-0.303^{+0.131}_{-0.252}$	–	–	–	–	–	–	$0.231^{+0.004}_{-0.005}$	0.618 ± 0.012	7.709 ± 0.366
	HQASG[d]	0.292 ± 0.044	$0.801^{+0.191}_{-0.055}$	$-0.093^{+0.092}_{-0.190}$	–	–	$71.33^{+1.75}_{-1.77}$	$0.413^{+0.026}_{-0.032}$	50.19 ± 0.24	1.130 ± 0.086	–	–	–
	HQASQFG[e]	$0.327^{+0.039}_{-0.043}$	> 0.691	$-0.204^{+0.063}_{-0.125}$	–	–	71.07 ± 1.64	$0.413^{+0.027}_{-0.032}$	50.20 ± 0.24	1.120 ± 0.086	0.231 ± 0.004	0.632 ± 0.010	$7.291^{+0.306}_{-0.305}$
	HzBHQASG[f]	$0.311^{+0.012}_{-0.014}$	$0.708^{+0.053}_{-0.046}$	$-0.019^{+0.043}_{-0.048}$	–	–	69.72 ± 1.10	$0.412^{+0.026}_{-0.032}$	50.19 ± 0.23	1.132 ± 0.085	–	–	–
	HzBHQASQFG[g]	$0.312^{+0.012}_{-0.013}$	$0.716^{+0.052}_{-0.046}$	-0.028 ± 0.045	–	–	69.88 ± 1.10	$0.412^{+0.025}_{-0.032}$	50.19 ± 0.23	1.131 ± 0.084	0.231 ± 0.004	0.637 ± 0.009	7.144 ± 0.270
Flat XCDM	QSO-Flux	$0.496^{+0.192}_{-0.069}$	–	–	< -1.042[h]	–	–	–	–	–	0.231 ± 0.004	0.624 ± 0.011	7.508 ± 0.326
	HQASG[d]	$0.322^{+0.062}_{-0.044}$	–	–	$-1.379^{+0.361}_{-0.375}$	–	$72.00^{+1.99}_{-1.98}$	$0.412^{+0.026}_{-0.032}$	50.20 ± 0.24	1.130 ± 0.085	–	–	–
	HQASQFG[e]	$0.358^{+0.040}_{-0.038}$	–	–	< -1.100	–	72.14 ± 1.91	$0.411^{+0.026}_{-0.031}$	50.20 ± 0.23	1.125 ± 0.084	0.231 ± 0.004	$0.633^{+0.009}_{-0.010}$	$7.268^{+0.287}_{-0.288}$
	HzBHQASG[f]	$0.313^{+0.014}_{-0.015}$	–	–	$-1.050^{+0.090}_{-0.081}$	–	$69.85^{+1.42}_{-1.55}$	$0.412^{+0.026}_{-0.032}$	50.19 ± 0.24	1.134 ± 0.085	–	–	–
	HzBHQASQFG[g]	$0.315^{+0.013}_{-0.015}$	–	–	$-1.052^{+0.091}_{-0.081}$	–	69.85 ± 1.48	$0.413^{+0.026}_{-0.032}$	50.19 ± 0.24	1.133 ± 0.086	0.231 ± 0.004	0.637 ± 0.009	$7.135^{+0.270}_{-0.271}$
Non-flat XCDM	QSO-Flux	$0.515^{+0.184}_{-0.050}$	–	$-0.310^{+0.137}_{-0.289}$	< -0.294	–	–	–	–	–	$0.231^{+0.004}_{-0.005}$	0.615 ± 0.013	$7.817^{+0.398}_{-0.400}$
	HQASG[d]	$0.303^{+0.073}_{-0.058}$	–	$-0.044^{+0.193}_{-0.217}$	$-1.273^{+0.501}_{-0.321}$	–	71.77 ± 2.02	$0.413^{+0.026}_{-0.031}$	50.20 ± 0.24	1.129 ± 0.085	–	–	–
	HQASQFG[e]	$0.367^{+0.059}_{-0.048}$	–	$-0.146^{+0.143}_{-0.147}$	$-1.433^{+0.241}_{-0.493}$	–	$72.27^{+2.01}_{-1.99}$	$0.413^{+0.026}_{-0.032}$	50.21 ± 0.24	1.116 ± 0.085	0.231 ± 0.004	$0.629^{+0.011}_{-0.010}$	7.382 ± 0.321
	HzBHQASG[f]	0.310 ± 0.014	–	$-0.024^{+0.092}_{-0.093}$	$-1.019^{+0.202}_{-0.099}$	–	$69.63^{+1.45}_{-1.62}$	$0.412^{+0.026}_{-0.031}$	50.19 ± 0.23	1.132 ± 0.085	–	–	–
	HzBHQASQFG[g]	$0.314^{+0.014}_{-0.015}$	–	$-0.060^{+0.096}_{-0.095}$	$-0.968^{+0.184}_{-0.087}$	–	$69.43^{+1.43}_{-1.63}$	$0.412^{+0.026}_{-0.032}$	50.19 ± 0.24	1.130 ± 0.085	0.231 ± 0.004	$0.636^{+0.009}_{-0.010}$	$7.182^{+0.278}_{-0.281}$

[c] km s^{-1} Mpc^{-1}.

[d] HIIG + QSO-AS + GRB.

[e] HIIG + QSO-AS + GRB + QSO-Flux.

[f] $H(z)$ + BAO + HIIG + QSO-AS + GRB.

[g] $H(z)$ + BAO + HIIG + QSO-AS + GRB + QSO-Flux.

[h] This is the 1σ limit. The 2σ limit is set by the prior, and is not shown here.

Appendix B

Corrected GRB data

These data are taken from the appendix of Cao et al. (2022d), where the Platinum data listed in Table B.1 are correct and should be used to do cosmological analysis instead of those reported in Table 8.2 from Cao et al. (2022c).

Table B.1: Updated 50 Platinum GRB samples with 1σ errors, where F_X, $F_{\rm peak}$, $\rm FK_{plateau}$ ($\log \rm FK_{plateau} \equiv \log F_X + \log K_{plateau}$), and $FK_{\rm prompt}$ ($\log \rm FK_{prompt} \equiv \log F_{\rm peak} + \log K_{\rm prompt}$) have units of erg cm^{-2} s^{-1}, and T_X^* and $E_{\rm peak}$ have units of s and keV, respectively. The last Ref. column lists the sources of GRBs, with "C" and "B" representing the third *Swift* GRB Catalog (Lien et al., 2016) and *Swift* BAT burst analyser (Evans et al., 2010), respectively. Central values are estimated to three (or four) significant figures with corresponding non-zero errors matching their decimal places and $\Delta\chi^2 = \chi^2_{\rm PL} - \chi^2_{\rm CPL}$.

GRB	z	$\log T_X^*$	$\log F_X$	$\log F_{\rm peak}$	$\alpha_{\rm plateau}$	$K_{\rm plateau}$	$\log \rm FK_{plateau}$	$\alpha_{\rm prompt}^{\rm PL/CPL}$	$E_{\rm peak}$	$K_{\rm prompt}^{\rm PL/CPL}$	$\log \rm FK_{prompt}$	$\Delta\chi^2$	Ref.
060418	1.49	3.12 ± 0.03	-9.79 ± 0.03	$-6.3^{+0.01}_{-0.02}$	$1.93^{+0.13}_{-0.12}$	$0.938^{+0.118}_{-0.097}$	-9.8 ± 0.1	$-1.5^{+0.06}_{-0.05}$	–	$0.634^{+0.029}_{-0.034}$	$-6.5^{+0.03}_{-0.04}$	0.88	C
060605	3.8	4.04 ± 0.02	-11.26 ± 0.03	$-7.33^{+0.06}_{-0.07}$	$1.98^{+0.07}_{-0.06}$	$0.969^{+0.113}_{-0.087}$	$-11.27^{+0.08}_{-0.07}$	$-0.85^{+0.27}_{-0.25}$	–	$0.165^{+0.079}_{-0.057}$	$-8.11^{+0.23}_{-0.25}$	0.02	C
060708	1.92	3.51 ± 0.04	-10.87 ± 0.04	-6.81 ± 0.02	$2.4^{+0.3}_{-0.24}$	$1.54^{+0.58}_{-0.35}$	$-10.68^{+0.18}_{-0.15}$	-1.33 ± 0.07	–	$0.488^{+0.038}_{-0.036}$	-7.12 ± 0.05	3.14	C
060714	2.71	3.73 ± 0.03	-10.86 ± 0.02	$-7.01^{+0.02}_{-0.03}$	1.93 ± 0.1	$0.912^{+0.128}_{-0.112}$	-10.9 ± 0.08	-1.48 ± 0.1	–	$0.506^{+0.071}_{-0.062}$	$-7.31^{+0.08}_{-0.09}$	4.14	C
060814	0.84	4.22 ± 0.02	-10.91 ± 0.02	-6.22 ± 0.01	$1.96^{+0.07}_{-0.06}$	$0.976^{+0.042}_{-0.035}$	-10.92 ± 0.04	-1.3 ± 0.04	–	0.653 ± 0.016	-6.4 ± 0.02	2.35	C
060906	3.685	4.33 ± 0.04	$-11.88^{+0.05}_{-0.06}$	$-6.91^{+0.03}_{-0.05}$	$2.06^{+0.11}_{-0.1}$	$1.1^{+0.2}_{-0.16}$	$-11.84^{+0.12}_{-0.13}$	-2 ± 0.15	–	$1^{+0.26}_{-0.21}$	$-6.91^{+0.13}_{-0.15}$	0.66	C
061121	1.314	3.79 ± 0.01	-10.03 ± 0.01	$-5.707^{+0.005}_{-0.006}$	$1.87^{+0.08}_{-0.07}$	$0.897^{+0.062}_{-0.051}$	-10.08 ± 0.04	-1.05 ± 0.02	–	$0.451^{+0.007}_{-0.008}$	-6.05 ± 0.01	-0.02	C
061222A	2.088	3.92 ± 0.01	$-9.95^{+0.01}_{-0.02}$	-6.135 ± 0.009	1.8 ± 0.07	$0.798^{+0.066}_{-0.06}$	$-10.05^{+0.04}_{-0.05}$	$-0.487^{+0.132}_{-0.126}$	226^{+103}_{-36}	$0.269^{+0.047}_{-0.056}$	$-6.71^{+0.08}_{-0.11}$	11.27	C
070110	2.352	4.27 ± 0.03	-11.05 ± 0.03	$-7.32^{+0.05}_{-0.07}$	2 ± 0.05	1 ± 0.06	-11.05 ± 0.06	$-1.46^{+0.2}_{-0.21}$	–	$0.52^{+0.151}_{-0.111}$	$-7.6^{+0.16}_{-0.17}$	0.34	C
070306	1.4959	4.87 ± 0.02	-11.27 ± 0.02	$-6.52^{+0.02}_{-0.01}$	1.85 ± 0.05	$0.872^{+0.041}_{-0.039}$	-11.33 ± 0.04	-1.54 ± 0.05	–	0.657 ± 0.03	$-6.7^{+0.04}_{-0.03}$	3.16	C
070508	0.82	3.03 ± 0.01	-9.16 ± 0.01	-5.65 ± 0.01	1.79 ± 0.02	$0.882^{+0.01}_{-0.011}$	-9.22 ± 0.02	$-0.679^{+0.096}_{-0.092}$	213^{+60}_{-26}	$0.571^{+0.036}_{-0.048}$	$-5.89^{+0.04}_{-0.05}$	18.84	C
070521	0.553	3.55 ± 0.03	-10.01 ± 0.03	$-7.06^{+0.05}_{-0.08}$	$1.73^{+0.18}_{-0.16}$	$0.888^{+0.073}_{-0.06}$	-10.06 ± 0.06	$-0.528^{+0.17}_{-0.161}$	184^{+95}_{-29}	$0.662^{+0.05}_{-0.078}$	$-7.24^{+0.08}_{-0.13}$	9.49	C
070529	2.4996	3.09 ± 0.04	$-10.25^{+0.04}_{-0.03}$	$-6.95^{+0.06}_{-0.09}$	$1.71^{+0.13}_{-0.1}$	$0.695^{+0.123}_{-0.081}$	$-10.41^{+0.11}_{-0.08}$	-1.49 ± 0.24	–	$0.528^{+0.185}_{-0.137}$	$-7.23^{+0.19}_{-0.22}$	1.87	C
080310	2.4266	4.33 ± 0.02	$-11.4^{+0.03}_{-0.02}$	$-7.07^{+0.03}_{-0.05}$	1.91 ± 0.06	$0.895^{+0.069}_{-0.064}$	$-11.45^{+0.06}_{-0.05}$	$-1.91^{+0.13}_{-0.15}$	–	$0.895^{+0.182}_{-0.132}$	$-7.12^{+0.11}_{-0.12}$	3.43	C
080430	0.767	4.22 ± 0.02	$-11.17^{+0.01}_{-0.02}$	-6.74 ± 0.02	1.96 ± 0.09	$0.977^{+0.052}_{-0.048}$	$-11.18^{+0.03}_{-0.04}$	-1.75 ± 0.07	–	$0.867^{+0.036}_{-0.034}$	-6.8 ± 0.04	0.15	C
080721	2.6	2.879 ± 0.005	$-8.713^{+0.004}_{-0.005}$	$-5.72^{+0.03}_{-0.02}$	1.72 ± 0.01	0.699 ± 0.009	-8.87 ± 0.01	-0.99 ± 0.09	–	$0.274^{+0.034}_{-0.03}$	$-6.28^{+0.08}_{-0.07}$	-0.01	C
081008	1.967	3.86 ± 0.03	$-10.79^{+0.03}_{-0.04}$	$-6.98^{+0.03}_{-0.04}$	$1.83^{+0.1}_{-0.06}$	$0.831^{+0.096}_{-0.052}$	$-10.87^{+0.08}_{-0.07}$	$-1.34^{+0.12}_{-0.13}$	–	$0.488^{+0.074}_{-0.06}$	$-7.29^{+0.09}_{-0.1}$	0.68	C
081221	2.26	2.93 ± 0.02	$-9.35^{+0.01}_{-0.02}$	-5.823 ± 0.007	2.01 ± 0.04	$1.01^{+0.05}_{-0.04}$	$-9.34^{+0.03}_{-0.04}$	$-1.17^{+0.23}_{-0.22}$	–	$0.375^{+0.111}_{-0.089}$	$-6.25^{+0.12}_{-0.13}$	-25.22	C
090418A	1.608	3.53 ± 0.02	$-10.05^{+0.02}_{-0.01}$	$-6.8^{+0.04}_{-0.05}$	$1.9^{+0.12}_{-0.11}$	$0.909^{+0.07}_{-0.091}$	$-10.09^{+0.07}_{-0.05}$	-1.29 ± 0.17	–	$0.506^{+0.09}_{-0.076}$	$-7.1^{+0.11}_{-0.12}$	-0.03	C
091018	0.971	2.9 ± 0.02	$-9.63^{+0.02}_{-0.01}$	$-6.26^{+0.01}_{-0.02}$	1.73 ± 0.07	$0.833^{+0.04}_{-0.039}$	$-9.71^{+0.04}_{-0.03}$	$-1.3^{+0.2}_{-0.18}$	$35.2^{+2.5}_{-3.7}$	$1.07^{+0.06}_{-0.04}$	-6.23 ± 0.03	30.75	B
091020	1.71	2.95 ± 0.03	-9.71 ± 0.02	-6.44 ± 0.02	$1.95^{+0.13}_{-0.12}$	$0.951^{+0.132}_{-0.107}$	-9.7 ± 0.1	$-1.18^{+0.07}_{-0.08}$	–	$0.442^{+0.036}_{-0.03}$	-6.8 ± 0.05	-0.03	C
091029	2.752	4.3 ± 0.02	$-11.35^{+0.02}_{-0.01}$	$-6.96^{+0.03}_{-0.04}$	2.03 ± 0.07	$1.04^{+0.1}_{-0.09}$	$-11.33^{+0.06}_{-0.05}$	$-0.926^{+0.427}_{-0.362}$	$53.2^{+16.3}_{-6}$	$0.64^{+0.136}_{-0.199}$	$-7.15^{+0.11}_{-0.2}$	6.66	C
100219A	4.7	4.72 ± 0.06	-12.1 ± 0.2	$-7.5^{+0.08}_{-0.12}$	$1.45^{+0.1}_{-0.09}$	$0.384^{+0.073}_{-0.056}$	$-12.52^{+0.28}_{-0.27}$	$-1.43^{+0.39}_{-0.37}$	–	$0.371^{+0.335}_{-0.183}$	$-7.93^{+0.36}_{-0.42}$	0.00	C
110213A	1.46	$3.84^{+0.02}_{-0.01}$	$-9.9^{+0.03}_{-0.02}$	$-7.15^{+0.1}_{-0.14}$	$1.81^{+0.05}_{-0.04}$	$0.843^{+0.039}_{-0.03}$	$-9.97^{+0.05}_{-0.04}$	$-2.82^{+0.37}_{-0.59}$	–	$2.09^{+1.47}_{-0.59}$	$-6.83^{+0.33}_{-0.28}$	1.41	C
110818A	3.36	3.85 ± 0.04	$-11.28^{+0.03}_{-0.04}$	$-6.85^{+0.04}_{-0.05}$	1.84 ± 0.12	$0.79^{+0.153}_{-0.128}$	$-11.38^{+0.11}_{-0.12}$	$-1.11^{+0.2}_{-0.19}$	–	$0.27^{+0.087}_{-0.069}$	$-7.42^{+0.16}_{-0.18}$	-0.04	C
111008A	5	3.99 ± 0.02	$-10.67^{+0.02}_{-0.01}$	-6.27 ± 0.03	1.85 ± 0.05	$0.764^{+0.072}_{-0.065}$	$-10.79^{+0.06}_{-0.05}$	-1.26 ± 0.11	–	$0.266^{+0.057}_{-0.048}$	-6.85 ± 0.12	0.43	C
120118B	2.943	$3.68^{+0.09}_{-0.07}$	$-10.96^{+0.08}_{-0.06}$	-6.86 ± 0.04	$1.99^{+0.17}_{-0.16}$	$0.986^{+0.259}_{-0.194}$	$-10.97^{+0.18}_{-0.15}$	$-1.9^{+0.14}_{-0.15}$	–	$0.872^{+0.199}_{-0.153}$	$-6.92^{+0.13}_{-0.12}$	0.52	C
120404A	2.88	$3.8^{+0.06}_{-0.03}$	$-11.03^{+0.06}_{-0.08}$	$-7.12^{+0.06}_{-0.07}$	$1.68^{+0.08}_{-0.07}$	$0.648^{+0.074}_{-0.059}$	$-11.22^{+0.11}_{-0.12}$	$-1.84^{+0.22}_{-0.24}$	–	$0.805^{+0.31}_{-0.208}$	-7.21 ± 0.2	0.00	C
120811C	2.67	3.16 ± 0.05	$-10.14^{+0.03}_{-0.04}$	$-6.58^{+0.01}_{-0.02}$	$1.62^{+0.09}_{-0.08}$	$0.61^{+0.076}_{-0.06}$	-10.36 ± 0.08	$-1.02^{+0.27}_{-0.24}$	$60.1^{+11}_{-5.1}$	$0.619^{+0.095}_{-0.126}$	$-6.79^{+0.07}_{-0.12}$	11.43	C
120922A	3.1	$3.6^{+0.13}_{-0.03}$	-10.6 ± 0.1	$-6.97^{+0.02}_{-0.04}$	$2.14^{+0.13}_{-0.12}$	$1.22^{+0.24}_{-0.19}$	$-10.51^{+0.18}_{-0.17}$	$-1.95^{+0.11}_{-0.12}$	–	$0.932^{+0.172}_{-0.134}$	$-7^{+0.09}_{-0.11}$	0.02	C
121128A	2.2	3.23 ± 0.02	-9.62 ± 0.02	-5.98 ± 0.01	$1.78^{+0.06}_{-0.04}$	$0.774^{+0.056}_{-0.035}$	$-9.73^{+0.05}_{-0.04}$	$-0.495^{+0.139}_{-0.134}$	108^{+12}_{-8}	$0.373^{+0.048}_{-0.05}$	$-6.41^{+0.06}_{-0.07}$	42.35	C
131030A	1.29	2.85 ± 0.02	$-9.29^{+0.01}_{-0.02}$	$-5.576^{+0.007}_{-0.008}$	$1.68^{+0.03}_{-0.02}$	$0.767^{+0.019}_{-0.013}$	$-9.4^{+0.02}_{-0.03}$	$-0.585^{+0.116}_{-0.111}$	229^{+93}_{-34}	$0.416^{+0.046}_{-0.06}$	$-5.96^{+0.05}_{-0.08}$	12.64	C
131105A	1.686	3.95 ± 0.03	-10.91 ± 0.02	$-6.52^{+0.05}_{-0.04}$	1.92 ± 0.1	$0.924^{+0.096}_{-0.087}$	-10.94 ± 0.06	$-1.15^{+0.18}_{-0.16}$	–	$0.432^{+0.074}_{-0.071}$	-6.89 ± 0.12	1.15	B
140206A	2.7	3.59 ± 0.01	-9.73 ± 0.01	-5.772 ± 0.007	$1.44^{+0.14}_{-0.08}$	$0.481^{+0.096}_{-0.048}$	$-10.05^{+0.09}_{-0.06}$	$-0.536^{+0.11}_{-0.106}$	116^{+11}_{-8}	$0.31^{+0.038}_{-0.028}$	$-6.28^{+0.06}_{-0.07}$	57.56	C
140419A	3.956	3.68 ± 0.01	$-10.01^{+0.02}_{-0.01}$	-6.38 ± 0.01	1.66 ± 0.06	$0.58^{+0.059}_{-0.053}$	$-10.25^{+0.06}_{-0.05}$	-1.03 ± 0.05	–	0.212 ± 0.017	-7.05 ± 0.04	2.37	C
140506A	0.889	3.31 ± 0.04	$-9.9^{+0.03}_{-0.04}$	$-6.06^{+0.02}_{-0.03}$	$1.64^{+0.13}_{-0.12}$	$0.795^{+0.069}_{-0.058}$	-10 ± 0.1	$-0.53^{+0.393}_{-0.341}$	$100.4^{+53.6}_{-13.3}$	$0.664^{+0.087}_{-0.163}$	$-6.24^{+0.07}_{-0.15}$	6.69	C
140509A	2.4	$3.59^{+0.07}_{-0.04}$	$-11.1^{+0.06}_{-0.05}$	$-6.93^{+0.03}_{-0.07}$	$1.81^{+0.14}_{-0.12}$	$0.793^{+0.148}_{-0.109}$	$-11.2^{+0.13}_{-0.11}$	$-1.49^{+0.23}_{-0.24}$	–	$0.536^{+0.163}_{-0.132}$	-7.2 ± 0.19	0.46	C
140629A	2.3	2.86 ± 0.04	$-9.85^{+0.03}_{-0.02}$	$-6.46^{+0.03}_{-0.02}$	1.84 ± 0.1	$0.826^{+0.105}_{-0.093}$	-9.9 ± 0.1	$-1.35^{+0.08}_{-0.09}$	–	$0.46^{+0.052}_{-0.042}$	$-6.8^{+0.08}_{-0.06}$	3.01	C
150314A	1.758	2.49 ± 0.01	-8.61 ± 0.01	-5.42 ± 0.01	1.73 ± 0.02	$0.76^{+0.016}_{-0.015}$	-8.73 ± 0.02	$-0.465^{+0.108}_{-0.105}$	249^{+88}_{-36}	$0.297^{+0.04}_{-0.047}$	$-5.95^{+0.07}_{-0.08}$	15.03	C
150403A	2.06	3.197 ± 0.004	-8.821 ± 0.003	-5.77 ± 0.01	1.675 ± 0.01	0.695 ± 0.007	-8.98 ± 0.01	$-0.92^{+0.04}_{-0.03}$	–	$0.299^{+0.01}_{-0.013}$	-6.3 ± 0.03	1.68	C
150910A	1.36	3.85 ± 0.02	$-9.97^{+0.84}_{-0.02}$	$-7.08^{+0.09}_{-0.15}$	$1.76^{+0.12}_{-0.11}$	$0.814^{+0.088}_{-0.074}$	$-10.06^{+0.88}_{-0.06}$	$-1.46^{+0.54}_{-0.6}$	–	$0.629^{+0.424}_{-0.233}$	$-7.28^{+0.31}_{-0.35}$	-0.05	C
151027A	0.81	4 ± 0.01	$-9.94^{+0.02}_{-0.01}$	$-6.24^{+0.03}_{-0.02}$	1.77 ± 0.06	$0.872^{+0.032}_{-0.03}$	-10 ± 0.03	-1.24 ± 0.08	–	$0.637^{+0.031}_{-0.029}$	$-6.44^{+0.05}_{-0.04}$	0.00	C
160121A	1.96	3.82 ± 0.07	-11.17 ± 0.04	$-7.11^{+0.04}_{-0.05}$	$2.02^{+0.16}_{-0.13}$	$1.02^{+0.2}_{-0.13}$	$-11.16^{+0.12}_{-0.1}$	$-1.82^{+0.15}_{-0.16}$	–	$0.823^{+0.156}_{-0.124}$	-7.2 ± 0.12	2.09	C
160227A	2.38	4.48 ± 0.02	$-11^{+0.02}_{-0.01}$	-7.23 ± 0.05	$1.65^{+0.06}_{-0.05}$	$0.653^{+0.049}_{-0.039}$	$-11.19^{+0.05}_{-0.04}$	$-1.05^{+0.18}_{-0.16}$	–	$0.314^{+0.068}_{-0.061}$	$-7.73^{+0.13}_{-0.15}$	4.74	B
160327A	4.99	3.76 ± 0.04	-11.22 ± 0.04	-6.9 ± 0.03	$1.78^{+0.12}_{-0.09}$	$0.674^{+0.162}_{-0.1}$	$-11.39^{+0.13}_{-0.11}$	-1.57 ± 0.1	–	$0.463^{+0.091}_{-0.076}$	-7.23 ± 0.11	1.95	C
170202A	3.645	3.78 ± 0.04	$-10.65^{+0.02}_{-0.03}$	-6.41 ± 0.02	1.99 ± 0.09	$0.985^{+0.146}_{-0.127}$	$-10.66^{+0.08}_{-0.09}$	$-0.491^{+0.279}_{-0.25}$	$110.4^{+45.8}_{-15}$	$0.235^{+0.084}_{-0.093}$	$-7.04^{+0.15}_{-0.24}$	9.64	C
170705A	2.01	3.64 ± 0.04	$-10.19^{+0.03}_{-0.02}$	-5.95 ± 0.01	1.62 ± 0.1	$0.658^{+0.077}_{-0.069}$	$-10.37^{+0.08}_{-0.07}$	$-0.917^{+0.138}_{-0.132}$	161^{+83}_{-24}	$0.43^{+0.065}_{-0.087}$	$-6.32^{+0.07}_{-0.11}$	9.03	C
180329B	1.998	4.02 ± 0.03	-11.15 ± 0.03	$-7.04^{+0.08}_{-0.12}$	$1.78^{+0.09}_{-0.08}$	$0.785^{+0.082}_{-0.066}$	-11.26 ± 0.07	$-1.91^{+0.32}_{-0.39}$	–	$0.906^{+0.484}_{-0.268}$	-7.08 ± 0.27	-0.01	C
190106A	1.86	4.19 ± 0.02	$-10.43^{+0.01}_{-0.02}$	$-6.47^{+0.01}_{-0.02}$	$1.88^{+0.09}_{-0.04}$	$0.882^{+0.087}_{-0.037}$	$-10.49^{+0.05}_{-0.04}$	$-0.893^{+0.237}_{-0.216}$	$74.8^{+17.1}_{-7.3}$	$0.614^{+0.082}_{-0.115}$	$-6.68^{+0.06}_{-0.11}$	12.68	C
190114A	3.37	3.75 ± 0.03	-10.75 ± 0.02	$-7.39^{+0.09}_{-0.12}$	$1.85^{+0.08}_{-0.07}$	$0.802^{+0.1}_{-0.079}$	$-10.85^{+0.07}_{-0.06}$	$-1.51^{+0.4}_{-0.41}$	–	$0.485^{+0.404}_{-0.216}$	$-7.7^{+0.35}_{-0.38}$	-0.01	C

Table B.2: Same as Table B.1, but for 95 long GRB samples. Note that PL photon indices of GRBs 151215A and 170405A are taken from the time-averaged BAT spectral analysis and PL peak energy flux of the latter is also time-averaged, since their 1 s peak analysis results are either unreasonable or out of range.

GRB	z	$\log T_X^*$	$\log F_X$	$\log F_{\rm peak}$	$\alpha_{\rm plateau}$	$K_{\rm plateau}$	$\log {\rm FK}_{\rm plateau}$	$\alpha_{\rm prompt}^{\rm PL/CPL}$	$E_{\rm peak}$	$K_{\rm prompt}^{\rm PL/CPL}$	$\log {\rm FK}_{\rm prompt}$	$\Delta\chi^2$	Ref.
050315	1.949	4.86 ± 0.03	-11.38 ± 0.02	-6.95 ± 0.03	1.86 ± 0.05	$0.859^{+0.048}_{-0.045}$	-11.45 ± 0.04	$-2.08^{+0.11}_{-0.12}$	–	$1.09^{+0.15}_{-0.12}$	$-6.91^{+0.09}_{-0.08}$	2.84	C
050318	1.44	4.13 ± 0.03	$-11.15^{+0.03}_{-0.04}$	-6.67 ± 0.02	1.97 ± 0.07	$0.974^{+0.062}_{-0.059}$	$-11.16^{+0.06}_{-0.07}$	$-0.806^{+0.281}_{-0.254}$	$67.2^{+13.7}_{-6.1}$	$0.708^{+0.075}_{-0.112}$	$-6.82^{+0.06}_{-0.09}$	12.75	C
050401	2.9	3.12 ± 0.02	$-9.65^{+0.01}_{-0.02}$	-5.96 ± 0.02	$2.1^{+0.36}_{-0.3}$	$1.15^{+0.72}_{-0.39}$	-9.6 ± 0.2	$-0.067^{+0.422}_{-0.363}$	$108^{+36.1}_{-12.9}$	$0.224^{+0.089}_{-0.097}$	$-6.61^{+0.16}_{-0.27}$	10.33	C
050505	4.27	4.27 ± 0.02	-11.05 ± 0.02	-6.78 ± 0.04	1.98 ± 0.05	$0.967^{+0.084}_{-0.077}$	-11.06 ± 0.06	-1.08 ± 0.15	–	$0.217^{+0.061}_{-0.048}$	-7.44 ± 0.15	1.91	C
050730	3.97	4.05 ± 0.01	$-10.1^{+0.02}_{-0.01}$	$-7.34^{+0.07}_{-0.08}$	1.47 ± 0.03	$0.427^{+0.022}_{-0.02}$	$-10.47^{+0.04}_{-0.03}$	$-1.32^{+0.28}_{-0.27}$	–	$0.336^{+0.182}_{-0.121}$	$-7.81^{+0.26}_{-0.28}$	0.00	C
050803	3.5	4.22 ± 0.03	-10.86 ± 0.03	$-7.09^{+0.03}_{-0.04}$	1.78 ± 0.05	$0.718^{+0.056}_{-0.052}$	-11 ± 0.06	$-1.23^{+0.12}_{-0.13}$	–	$0.314^{+0.068}_{-0.052}$	-7.59 ± 0.12	-0.02	C
050826	0.297	4.76 ± 0.08	$-12.3^{+0.1}_{-0.2}$	$-7.5^{+0.08}_{-0.12}$	$2.1^{+0.3}_{-0.24}$	$1.03^{+0.08}_{-0.07}$	$-12.29^{+0.13}_{-0.23}$	$-1.25^{+0.42}_{-0.41}$	–	$0.823^{+0.092}_{-0.085}$	$-7.59^{+0.13}_{-0.17}$	-0.02	C
050904	6.29	4.68 ± 0.06	$-11.5^{+0.2}_{-0.1}$	$-7.27^{+0.07}_{-0.09}$	1.83 ± 0.04	$0.713^{+0.059}_{-0.054}$	$-11.65^{+0.23}_{-0.13}$	$-1.24^{+0.27}_{-0.26}$	–	$0.221^{+0.149}_{-0.092}$	$-7.93^{+0.29}_{-0.32}$	1.24	C
051016B	0.9364	4.26 ± 0.04	-11.59 ± 0.03	$-7.08^{+0.03}_{-0.04}$	1.72 ± 0.1	$0.831^{+0.057}_{-0.053}$	-11.67 ± 0.06	-1.91 ± 0.13	–	$0.942^{+0.085}_{-0.077}$	$-7.11^{+0.07}_{-0.08}$	4.54	C
051109A	2.346	3.91 ± 0.03	-10.52 ± 0.03	$-6.52^{+0.04}_{-0.05}$	2.01 ± 0.09	$1.01^{+0.12}_{-0.1}$	-10.51 ± 0.08	-1.45 ± 0.15	–	$0.515^{+0.102}_{-0.086}$	$-6.81^{+0.12}_{-0.13}$	1.72	C
060115	3.53	3.7 ± 0.07	$-11.3^{+0.05}_{-0.04}$	$-7.14^{+0.04}_{-0.05}$	$2.01^{+0.22}_{-0.11}$	$1.02^{+0.4}_{-0.16}$	$-11.29^{+0.19}_{-0.11}$	-1.27 ± 0.15	–	$0.332^{+0.084}_{-0.067}$	$-7.62^{+0.14}_{-0.15}$	-0.01	C
060223A	4.41	2.79 ± 0.14	$-11^{+0.2}_{-0.1}$	$-7^{+0.03}_{-0.04}$	$1.84^{+0.16}_{-0.1}$	$0.763^{+0.237}_{-0.118}$	$-11.12^{+0.32}_{-0.17}$	-1.58 ± 0.13	–	$0.492^{+0.121}_{-0.097}$	-7.31 ± 0.13	0.45	C
060604	2.1357	4.46 ± 0.03	$-11.77^{+0.03}_{-0.02}$	$-7.63^{+0.11}_{-0.15}$	2.03 ± 0.09	$1.03^{+0.12}_{-0.1}$	$-11.76^{+0.07}_{-0.06}$	$-1.75^{+0.46}_{-0.56}$	–	$0.751^{+0.674}_{-0.307}$	$-7.75^{+0.39}_{-0.38}$	-0.03	B
060607A	3.082	4.37 ± 0.02	$-11.02^{+0.04}_{-0.05}$	$-6.89^{+0.02}_{-0.03}$	1.51 ± 0.04	$0.502^{+0.029}_{-0.027}$	$-11.32^{+0.06}_{-0.08}$	$-1.08^{+0.1}_{-0.09}$	–	$0.274^{+0.037}_{-0.036}$	$-7.45^{+0.08}_{-0.09}$	-0.02	C
060908	1.8836	2.82 ± 0.04	$-9.63^{+0.03}_{-0.02}$	$-6.57^{+0.03}_{-0.02}$	$2.02^{+0.18}_{-0.17}$	$1.02^{+0.22}_{-0.17}$	-9.6 ± 0.1	$-0.274^{+0.388}_{-0.338}$	123^{+88}_{-19}	$0.347^{+0.106}_{-0.149}$	$-7.03^{+0.15}_{-0.26}$	6.25	C
060927	5.6	3.15 ± 0.07	-10.78 ± 0.05	-6.61 ± 0.02	$1.65^{+0.17}_{-0.08}$	$0.517^{+0.195}_{-0.073}$	$-11.07^{+0.19}_{-0.12}$	$-0.286^{+0.273}_{-0.247}$	130^{+56}_{-18}	$0.103^{+0.052}_{-0.048}$	$-7.6^{+0.2}_{-0.3}$	10.04	C
061021	0.3463	3.24 ± 0.02	-10.04 ± 0.02	$-6.26^{+0.01}_{-0.02}$	$1.49^{+0.16}_{-0.09}$	$0.859^{+0.042}_{-0.022}$	$-10.11^{+0.04}_{-0.03}$	$-1.13^{+0.04}_{-0.05}$	–	$0.772^{+0.012}_{-0.009}$	$-6.37^{+0.02}_{-0.03}$	-0.12	C
061110A	0.758	2.25 ± 0.02	-8.33 ± 0.13	$-7.55^{+0.09}_{-0.1}$	2.97 ± 0.04	1.73 ± 0.04	-8.1 ± 0.1	$-2.04^{+0.31}_{-0.36}$	–	$1.02^{+0.23}_{-0.16}$	-7.54 ± 0.18	0.20	C
070208	1.165	3.44 ± 0.09	-10.9 ± 0.1	$-7.47^{+0.1}_{-0.16}$	2 ± 0.24	$1^{+0.2}_{-0.17}$	-10.9 ± 0.18	$-1.09^{+0.61}_{-0.5}$	–	$0.495^{+0.234}_{-0.186}$	$-7.78^{+0.27}_{-0.37}$	0.00	C
070721B	3.626	$3.95^{+0.08}_{-0.04}$	-10.5 ± 0.2	$-6.8^{+0.03}_{-0.05}$	1.52 ± 0.07	$0.479^{+0.055}_{-0.048}$	-10.82 ± 0.25	-0.83 ± 0.17	–	$0.167^{+0.049}_{-0.039}$	$-7.58^{+0.14}_{-0.16}$	0.46	C
070802	2.45	3.92 ± 0.14	-11.7 ± 0.1	$-7.64^{+0.11}_{-0.17}$	$1.78^{+0.2}_{-0.15}$	$0.762^{+0.214}_{-0.13}$	$-11.82^{+0.21}_{-0.18}$	$-2.48^{+0.45}_{-0.9}$	–	$1.81^{+3.71}_{-0.77}$	$-7.38^{+0.59}_{-0.41}$	-0.74	C
071003	1.60435	4.78 ± 0.06	-11.7 ± 0.1	$-6.2^{+0.02}_{-0.01}$	$1.83^{+0.08}_{-0.04}$	$0.85^{+0.067}_{-0.032}$	$-11.77^{+0.13}_{-0.12}$	$-0.84^{+0.06}_{-0.07}$	–	$0.329^{+0.023}_{-0.018}$	$-6.68^{+0.05}_{-0.03}$	-0.02	C
071117	1.3331	3.9 ± 0.07	$-11.24^{+0.07}_{-0.06}$	-5.98 ± 0.01	1.9 ± 0.18	$0.919^{+0.151}_{-0.13}$	$-11.28^{+0.14}_{-0.13}$	$-0.314^{+0.148}_{-0.139}$	143^{+26}_{-13}	$0.424^{+0.046}_{-0.059}$	$-6.35^{+0.06}_{-0.07}$	28.95	C
080319C	1.95	$3.19^{+0.03}_{-0.02}$	$-8.92^{+0.04}_{-0.03}$	-6.33 ± 0.02	$1.49^{+0.06}_{-0.05}$	$0.576^{+0.039}_{-0.03}$	-9.2 ± 0.1	$-1.07^{+0.07}_{-0.06}$	–	$0.366^{+0.024}_{-0.027}$	-6.77 ± 0.05	0.45	C

Table B.2: – *Continued from previous page*

GRB	z	$\log T_X^*$	$\log F_X$	$\log F_{\rm peak}$	$\alpha_{\rm plateau}$	$K_{\rm plateau}$	$\log {\rm FK}_{\rm plateau}$	$\alpha_{\rm prompt}^{\rm PL/CPL}$	$E_{\rm peak}$	$K_{\rm prompt}^{\rm PL/CPL}$	$\log {\rm FK}_{\rm prompt}$	$\Delta\chi^2$	Ref.
080411	1.03	4.21 ± 0.03	$-10.11^{+0.03}_{-0.04}$	-5.523 ± 0.005	$1.86^{+0.09}_{-0.08}$	$0.906^{+0.059}_{-0.05}$	$-10.15^{+0.06}_{-0.07}$	-1.13 ± 0.09	$101.9^{+9.8}_{-6}$	$0.696^{+0.038}_{-0.043}$	-5.68 ± 0.03	41.12	B
080607	3.036	3.46 ± 0.04	$-10.05^{+0.06}_{-0.07}$	$-5.63^{+0.02}_{-0.01}$	1.9 ± 0.3	$0.87^{+0.452}_{-0.298}$	$-10.11^{+0.24}_{-0.25}$	$-0.8^{+0.04}_{-0.05}$	–	$0.187^{+0.014}_{-0.01}$	$-6.36^{+0.05}_{-0.03}$	0.72	C
080710	0.845	4.09 ± 0.03	-11.23 ± 0.04	$-7.22^{+0.06}_{-0.08}$	$1.72^{+0.09}_{-0.06}$	$0.842^{+0.048}_{-0.03}$	-11.3 ± 0.06	$-1.84^{+0.21}_{-0.24}$	–	$0.907^{+0.143}_{-0.11}$	$-7.26^{+0.12}_{-0.13}$	1.78	C
080810	3.35	3.27 ± 0.02	-9.93 ± 0.02	$-6.77^{+0.02}_{-0.03}$	$2.07^{+0.05}_{-0.04}$	$1.11^{+0.08}_{-0.06}$	-9.89 ± 0.05	$-1.24^{+0.11}_{-0.1}$	–	$0.327^{+0.052}_{-0.049}$	$-7.26^{+0.08}_{-0.1}$	-0.02	C
080928	1.69	4.08 ± 0.03	-11.13 ± 0.04	-6.8 ± 0.02	2 ± 0.07	1 ± 0.07	-11.13 ± 0.07	$-1.5^{+0.07}_{-0.08}$	–	$0.61^{+0.05}_{-0.041}$	-7.02 ± 0.05	0.99	C
081028A	3.038	$4.75^{+0.02}_{-0.01}$	$-11.4^{+0.04}_{-0.03}$	$-7.39^{+0.06}_{-0.08}$	1.95 ± 0.04	$0.933^{+0.053}_{-0.051}$	$-11.43^{+0.06}_{-0.05}$	$-1.64^{+0.23}_{-0.24}$	–	$0.605^{+0.241}_{-0.166}$	$-7.61^{+0.2}_{-0.22}$	0.58	C
081029	3.847	4.48 ± 0.03	-11.86 ± 0.05	$-7.51^{+0.09}_{-0.15}$	$1.88^{+0.06}_{-0.05}$	$0.827^{+0.083}_{-0.062}$	-11.94 ± 0.09	$-1.74^{+0.39}_{-0.43}$	–	$0.663^{+0.645}_{-0.305}$	$-7.69^{+0.38}_{-0.42}$	0.62	C
081203A	2.1	4.02 ± 0.02	$-10.92^{+0.03}_{-0.04}$	-6.61 ± 0.02	$1.97^{+0.08}_{-0.07}$	$0.967^{+0.091}_{-0.074}$	-10.94 ± 0.07	$-1.17^{+0.07}_{-0.08}$	–	$0.391^{+0.037}_{-0.03}$	$-7.02^{+0.06}_{-0.05}$	1.82	C
090102	1.55	3.15 ± 0.03	$-9.46^{+0.03}_{-0.02}$	-6.27 ± 0.04	1.65 ± 0.09	$0.721^{+0.063}_{-0.059}$	-9.6 ± 0.1	-0.91 ± 0.14	–	$0.36^{+0.051}_{-0.044}$	-6.71 ± 0.1	1.13	C
090205	4.7	$3.71^{+0.08}_{-0.06}$	-11.34 ± 0.08	$-7.53^{+0.08}_{-0.09}$	$2.04^{+0.15}_{-0.12}$	$1.07^{+0.32}_{-0.2}$	$-11.31^{+0.19}_{-0.17}$	$-1.98^{+0.27}_{-0.29}$	–	$0.966^{+0.634}_{-0.362}$	$-7.55^{+0.3}_{-0.29}$	2.21	C
090423	8.2	3.92 ± 0.05	-11.28 ± 0.05	$-6.91^{+0.03}_{-0.02}$	$1.73^{+0.13}_{-0.12}$	$0.549^{+0.184}_{-0.128}$	-11.54 ± 0.17	-1.65 ± 0.09	–	$0.46^{+0.102}_{-0.083}$	$-7.25^{+0.12}_{-0.11}$	1.56	C
090429B	9.4	$3.2^{+0.11}_{-0.08}$	-10.9 ± 0.1	$-6.94^{+0.03}_{-0.04}$	$1.86^{+0.18}_{-0.16}$	$0.72^{+0.378}_{-0.225}$	$-11.04^{+0.28}_{-0.26}$	-1.7 ± 0.1	–	$0.495^{+0.131}_{-0.103}$	$-7.25^{+0.13}_{-0.14}$	5.39	C
090516A	4.1	4.33 ± 0.02	$-11.27^{+0.02}_{-0.03}$	-5.75 ± 0.03	1.94 ± 0.05	$0.907^{+0.077}_{-0.071}$	$-11.31^{+0.05}_{-0.07}$	$-1.68^{+0.11}_{-0.12}$	–	$0.594^{+0.128}_{-0.098}$	-5.98 ± 0.11	2.91	B
090519	3.85	3.45 ± 0.15	$-11.8^{+0.2}_{-0.1}$	$-7.16^{+0.06}_{-0.08}$	$1.62^{+0.2}_{-0.16}$	$0.549^{+0.204}_{-0.123}$	$-12.06^{+0.34}_{-0.21}$	$-0.31^{+0.44}_{-0.34}$	–	$0.069^{+0.05}_{-0.034}$	$-8.32^{+0.29}_{-0.38}$	-0.18	C
090529A	2.625	4.47 ± 0.13	-12.2 ± 0.1	$-7.31^{+0.09}_{-0.12}$	$1.64^{+0.3}_{-0.15}$	$0.629^{+0.297}_{-0.11}$	$-12.4^{+0.27}_{-0.18}$	$-1.67^{+0.33}_{-0.34}$	–	$0.654^{+0.359}_{-0.227}$	$-7.49^{+0.28}_{-0.3}$	2.57	C
090812	2.452	3.53 ± 0.08	$-10.17^{+0.07}_{-0.06}$	$-6.45^{+0.01}_{-0.02}$	$1.64^{+0.16}_{-0.15}$	$0.64^{+0.141}_{-0.108}$	$-10.36^{+0.16}_{-0.14}$	-0.86 ± 0.06	–	0.244 ± 0.018	$-7.06^{+0.04}_{-0.05}$	-0.03	C
091109A	3.076	3.38 ± 0.05	$-11.15^{+0.04}_{-0.03}$	$-7^{+0.07}_{-0.1}$	1.8 ± 0.24	$0.755^{+0.303}_{-0.216}$	$-11.27^{+0.19}_{-0.18}$	$-1.36^{+0.34}_{-0.32}$	–	$0.407^{+0.231}_{-0.155}$	$-7.39^{+0.27}_{-0.31}$	-0.02	C
091208B	1.063	3.31 ± 0.03	-10.18 ± 0.02	-5.95 ± 0.02	$1.97^{+0.12}_{-0.11}$	$0.979^{+0.088}_{-0.075}$	$-10.19^{+0.06}_{-0.05}$	-1.49 ± 0.07	–	$0.691^{+0.036}_{-0.034}$	-6.11 ± 0.04	-0.05	C
100425A	1.755	3.6 ± 0.07	-11.5 ± 0.04	$-7.13^{+0.05}_{-0.06}$	$2.5^{+0.43}_{-0.36}$	$1.66^{+0.91}_{-0.51}$	$-11.28^{+0.23}_{-0.2}$	$-2.36^{+0.19}_{-0.21}$	–	$1.44^{+0.34}_{-0.25}$	-6.97 ± 0.14	4.85	C
100513A	4.772	3.75 ± 0.08	-11.57 ± 0.06	$-7.32^{+0.06}_{-0.08}$	2.3 ± 0.24	$1.69^{+0.89}_{-0.58}$	-11.34 ± 0.24	$-1.29^{+0.27}_{-0.25}$	–	$0.288^{+0.158}_{-0.109}$	$-7.86^{+0.25}_{-0.29}$	0.00	C
100728A	1.567	4.03 ± 0.03	$-10.18^{+0.05}_{-0.04}$	-6.28 ± 0.01	$1.93^{+0.12}_{-0.11}$	$0.936^{+0.112}_{-0.092}$	$-10.21^{+0.1}_{-0.09}$	-0.7 ± 0.05	–	0.294 ± 0.014	-6.81 ± 0.03	-0.07	C
100901A	1.408	$4.91^{+0.02}_{-0.01}$	-11.34 ± 0.02	$-7.28^{+0.07}_{-0.11}$	2.07 ± 0.04	$1.06^{+0.04}_{-0.03}$	-11.31 ± 0.04	$-1.84^{+0.35}_{-0.4}$	–	$0.869^{+0.366}_{-0.23}$	$-7.34^{+0.22}_{-0.24}$	0.00	C
110106B	0.618	3.87 ± 0.04	$-10.81^{+0.02}_{-0.03}$	$-6.81^{+0.03}_{-0.05}$	1.96 ± 0.13	$0.981^{+0.063}_{-0.06}$	$-10.82^{+0.05}_{-0.06}$	$-1.54^{+0.13}_{-0.14}$	–	$0.801^{+0.056}_{-0.048}$	$-6.91^{+0.06}_{-0.08}$	2.94	C
110422A	1.77	3.5 ± 0.02	$-9.68^{+0.01}_{-0.02}$	-5.56 ± 0.01	1.74 ± 0.06	$0.767^{+0.049}_{-0.045}$	$-9.8^{+0.04}_{-0.05}$	-0.97 ± 0.03	–	$0.35^{+0.011}_{-0.01}$	-6.02 ± 0.02	4.95	C
110503A	1.61	2.54 ± 0.02	-9.08 ± 0.02	$-5.55^{+0.01}_{-0.02}$	1.69 ± 0.04	$0.743^{+0.029}_{-0.028}$	-9.21 ± 0.04	$-0.163^{+0.21}_{-0.194}$	130^{+26}_{-13}	$0.362^{+0.058}_{-0.071}$	$-5.99^{+0.07}_{-0.11}$	22.68	C
110715A	0.82	2.61 ± 0.02	$-9.08^{+0.02}_{-0.01}$	-5.372 ± 0.005	1.75 ± 0.04	$0.861^{+0.021}_{-0.02}$	$-9.15^{+0.03}_{-0.02}$	$-0.985^{+0.081}_{-0.078}$	152^{+26}_{-14}	$0.682^{+0.032}_{-0.039}$	-5.54 ± 0.03	29.78	C

Table B.2: – *Continued from previous page*

GRB	z	$\log T_X^*$	$\log F_X$	$\log F_{\rm peak}$	$\alpha_{\rm plateau}$	$K_{\rm plateau}$	$\log {\rm FK}_{\rm plateau}$	$\alpha_{\rm prompt}^{\rm PL/CPL}$	$E_{\rm peak}$	$K_{\rm prompt}^{\rm PL/CPL}$	$\log {\rm FK}_{\rm prompt}$	$\Delta\chi^2$	Ref.
110731A	2.83	5.09 ± 0.06	$-12.09^{+0.06}_{-0.05}$	-6.05 ± 0.01	$1.43^{+0.26}_{-0.15}$	$0.465^{+0.194}_{-0.085}$	$-12.42^{+0.21}_{-0.14}$	$-0.774^{+0.136}_{-0.131}$	135^{+33}_{-15}	$0.327^{+0.057}_{-0.064}$	$-6.54^{+0.08}_{-0.1}$	17.81	C
111123A	3.1516	4.42 ± 0.04	$-11.61^{+0.05}_{-0.04}$	$-7.14^{+0.05}_{-0.04}$	$2.28^{+0.15}_{-0.14}$	$1.49^{+0.35}_{-0.27}$	$-11.44^{+0.14}_{-0.13}$	$-1.33^{+0.17}_{-0.16}$	–	$0.385^{+0.099}_{-0.083}$	-7.55 ± 0.15	-0.01	C
120327A	2.813	3.49 ± 0.03	$-10.15^{+0.02}_{-0.03}$	$-6.48^{+0.01}_{-0.02}$	$1.65^{+0.08}_{-0.05}$	$0.626^{+0.071}_{-0.041}$	$-10.35^{+0.07}_{-0.06}$	$-1.25^{+0.05}_{-0.06}$	–	$0.366^{+0.031}_{-0.023}$	-6.92 ± 0.05	0.66	C
120802A	3.796	3.54 ± 0.13	-11.17 ± 0.05	-6.67 ± 0.02	$1.99^{+0.18}_{-0.15}$	$0.984^{+0.321}_{-0.206}$	$-11.18^{+0.17}_{-0.15}$	$-1.66^{+0.08}_{-0.07}$	–	$0.587^{+0.068}_{-0.069}$	$-6.9^{+0.07}_{-0.08}$	2.87	C
120804A	1.3	2.57 ± 0.11	$-9.76^{+0.1}_{-0.11}$	$-6.06^{+0.02}_{-0.01}$	1.9 ± 0.24	$0.92^{+0.204}_{-0.167}$	-9.8 ± 0.2	-1.34 ± 0.05	–	$0.577^{+0.025}_{-0.023}$	$-6.3^{+0.04}_{-0.03}$	3.76	C
120907A	0.97	3.21 ± 0.04	$-10.38^{+0.03}_{-0.02}$	$-6.64^{+0.03}_{-0.04}$	1.76 ± 0.1	$0.85^{+0.059}_{-0.056}$	$-10.45^{+0.06}_{-0.05}$	-1.39 ± 0.13	–	$0.661^{+0.061}_{-0.056}$	$-6.82^{+0.07}_{-0.08}$	-0.04	C
121024A	2.298	4.17 ± 0.04	-11.31 ± 0.04	$-6.9^{+0.04}_{-0.06}$	1.87 ± 0.1	$0.856^{+0.109}_{-0.096}$	-11.38 ± 0.09	$-1.07^{+0.19}_{-0.18}$	–	$0.33^{+0.079}_{-0.067}$	$-7.38^{+0.13}_{-0.16}$	-0.03	C
121229A	2.707	4.71 ± 0.24	$-12.4^{+0.2}_{-0.1}$	$-7.46^{+0.12}_{-0.19}$	$2^{+0.3}_{-0.18}$	$1^{+0.48}_{-0.21}$	$-12.4^{+0.37}_{-0.2}$	$-1.35^{+0.96}_{-0.66}$	–	$0.427^{+0.586}_{-0.306}$	$-7.83^{+0.5}_{-0.74}$	-0.01	C
130408A	3.76	3.58 ± 0.04	-10.33 ± 0.05	$-6.46^{+0.06}_{-0.09}$	$1.75^{+0.08}_{-0.06}$	$0.677^{+0.09}_{-0.06}$	$-10.5^{+0.1}_{-0.09}$	$-1.78^{+0.23}_{-0.24}$	–	$0.709^{+0.323}_{-0.213}$	$-6.61^{+0.22}_{-0.25}$	1.84	C
130418A	1.218	2.59 ± 0.04	$-9.25^{+0.04}_{-0.03}$	$-7.47^{+0.09}_{-0.13}$	$1.17^{+0.03}_{-0.02}$	$0.516^{+0.013}_{-0.008}$	$-9.54^{+0.05}_{-0.04}$	$-2.57^{+0.34}_{-0.45}$	–	$1.57^{+0.68}_{-0.37}$	-7.27 ± 0.25	4.70	C
130420A	1.297	3.57 ± 0.05	$-10.87^{+0.03}_{-0.04}$	$-6.66^{+0.02}_{-0.03}$	2.2 ± 0.09	$1.18^{+0.09}_{-0.08}$	$-10.8^{+0.06}_{-0.07}$	$-1.03^{+0.31}_{-0.28}$	$58^{+13.4}_{-5.5}$	$0.821^{+0.07}_{-0.121}$	$-6.75^{+0.06}_{-0.1}$	8.72	C
130505A	2.27	3.25 ± 0.01	-8.92 ± 0.01	-5.52 ± 0.03	1.71 ± 0.02	$0.709^{+0.017}_{-0.016}$	-9.07 ± 0.02	-0.82 ± 0.1	–	$0.247^{+0.031}_{-0.028}$	-6.13 ± 0.08	1.31	B
130511A	1.3033	2.66 ± 0.05	-10.52 ± 0.05	-7.01 ± 0.05	$1.54^{+0.17}_{-0.16}$	$0.681^{+0.104}_{-0.085}$	-10.69 ± 0.11	-1.44 ± 0.17	–	$0.627^{+0.095}_{-0.083}$	-7.21 ± 0.11	0.08	C
130514A	3.6	3.69 ± 0.05	-10.72 ± 0.05	$-6.65^{+0.02}_{-0.03}$	$1.7^{+0.24}_{-0.18}$	$0.633^{+0.28}_{-0.152}$	$-10.92^{+0.21}_{-0.17}$	-1.5 ± 0.09	–	$0.466^{+0.069}_{-0.06}$	$-6.98^{+0.08}_{-0.09}$	2.35	C
130604A	1.06	2.07 ± 0.06	$-8.32^{+0.11}_{-0.1}$	$-7.2^{+0.06}_{-0.08}$	$2.05^{+0.19}_{-0.17}$	$1.04^{+0.15}_{-0.12}$	-8.3 ± 0.2	$-1.32^{+0.26}_{-0.25}$	–	$0.612^{+0.121}_{-0.105}$	$-7.41^{+0.14}_{-0.16}$	-0.01	C
130606A	5.913	3.3 ± 0.05	-10.18 ± 0.04	-6.63 ± 0.02	$1.43^{+0.12}_{-0.06}$	$0.332^{+0.087}_{-0.036}$	$-10.66^{+0.14}_{-0.09}$	$-1.01^{+0.07}_{-0.08}$	–	$0.147^{+0.025}_{-0.018}$	$-7.46^{+0.09}_{-0.08}$	0.14	C
131117A	4.042	2.87 ± 0.08	-10.84 ± 0.05	-7.33 ± 0.06	$1.73^{+0.18}_{-0.12}$	$0.646^{+0.219}_{-0.114}$	$-11.03^{+0.18}_{-0.13}$	$-1.68^{+0.19}_{-0.21}$	–	$0.596^{+0.241}_{-0.158}$	$-7.56^{+0.21}_{-0.19}$	4.82	B
140213A	1.208	3.83 ± 0.04	$-10.13^{+0.04}_{-0.03}$	-5.79 ± 0.01	$1.77^{+0.08}_{-0.07}$	$0.833^{+0.055}_{-0.045}$	$-10.21^{+0.07}_{-0.05}$	-1.71 ± 0.03	–	0.795 ± 0.019	-5.89 ± 0.02	4.64	C
140423A	3.26	3.91 ± 0.03	-10.85 ± 0.03	$-6.73^{+0.03}_{-0.04}$	2 ± 0.08	$1^{+0.12}_{-0.11}$	-10.85 ± 0.08	$-1.19^{+0.11}_{-0.12}$	–	$0.309^{+0.059}_{-0.045}$	-7.24 ± 0.11	0.23	C
140430A	1.6	4.14 ± 0.08	-11.36 ± 0.05	-6.7 ± 0.02	$2.02^{+0.17}_{-0.13}$	$1.02^{+0.18}_{-0.12}$	$-11.35^{+0.12}_{-0.1}$	$-1.39^{+0.07}_{-0.08}$	–	$0.558^{+0.045}_{-0.036}$	-6.95 ± 0.05	4.11	C
140512A	0.725	3.54 ± 0.01	$-9.504^{+0.009}_{-0.01}$	-6.29 ± 0.01	1.73 ± 0.1	$0.863^{+0.048}_{-0.046}$	-9.57 ± 0.03	$-1.24^{+0.04}_{-0.05}$	–	$0.661^{+0.018}_{-0.014}$	-6.47 ± 0.02	2.12	C
140614A	4.233	3.7 ± 0.06	-10.96 ± 0.07	$-7.48^{+0.09}_{-0.14}$	$1.8^{+0.36}_{-0.3}$	$0.718^{+0.585}_{-0.281}$	$-11.1^{+0.33}_{-0.28}$	$-0.78^{+0.83}_{-0.57}$	–	$0.133^{+0.208}_{-0.099}$	$-8.36^{+0.5}_{-0.74}$	-0.05	C
141220A	1.3195	2.78 ± 0.03	$-9.87^{+0.02}_{-0.03}$	-6.09 ± 0.02	$2.1^{+0.15}_{-0.13}$	$1.09^{+0.14}_{-0.11}$	-9.8 ± 0.1	$-0.249^{+0.372}_{-0.326}$	129^{+81}_{-20}	$0.438^{+0.1}_{-0.15}$	$-6.45^{+0.11}_{-0.2}$	6.81	C
150120B	0.46	3.39 ± 0.06	-10.79 ± 0.04	$-7.11^{+0.05}_{-0.07}$	$1.94^{+0.14}_{-0.13}$	$0.978^{+0.053}_{-0.047}$	-10.8 ± 0.06	$-1.94^{+0.21}_{-0.23}$	–	$0.978^{+0.088}_{-0.075}$	$-7.12^{+0.09}_{-0.1}$	0.07	C
151021A	2.33	3.16 ± 0.03	-9.64 ± 0.04	$-6.12^{+0.03}_{-0.02}$	$2.4^{+0.36}_{-0.3}$	$1.62^{+0.87}_{-0.49}$	-9.4 ± 0.2	$-1.42^{+0.09}_{-0.1}$	–	$0.498^{+0.063}_{-0.051}$	$-6.42^{+0.08}_{-0.07}$	-0.02	C
151112A	4.1	4.43 ± 0.04	-11.62 ± 0.03	$-6.88^{+0.03}_{-0.04}$	$2.24^{+0.11}_{-0.1}$	$1.48^{+0.29}_{-0.22}$	$-11.45^{+0.11}_{-0.1}$	$-1.67^{+0.12}_{-0.13}$	–	$0.584^{+0.138}_{-0.104}$	$-7.11^{+0.12}_{-0.13}$	1.98	B

Table B.2: – *Continued from previous page*

GRB	z	$\log T_X^*$	$\log F_X$	$\log F_{\rm peak}$	$\alpha_{\rm plateau}$	$K_{\rm plateau}$	$\log {\rm FK}_{\rm plateau}$	$\alpha_{\rm prompt}^{\rm PL/CPL}$	$E_{\rm peak}$	$K_{\rm prompt}^{\rm PL/CPL}$	$\log {\rm FK}_{\rm prompt}$	$\Delta\chi^2$	Ref.
151215A	2.59	3.06 ± 0.07	-10.73 ± 0.06	$-6.9^{+0.04}_{-0.05}$	$2.2^{+0.16}_{-0.15}$	$1.29^{+0.29}_{-0.22}$	$-10.62^{+0.15}_{-0.14}$	$-1.99^{+0.19}_{-0.21}$	–	$0.987^{+0.304}_{-0.213}$	$-6.91^{+0.16}_{-0.15}$	1.26	B
160117B	0.87	4.1 ± 0.1	-11.75 ± 0.07	-6.98 ± 0.03	$1.65^{+0.12}_{-0.1}$	$0.803^{+0.063}_{-0.048}$	-11.85 ± 0.1	$-2.03^{+0.12}_{-0.11}$	–	1.02 ± 0.07	-6.97 ± 0.06	1.38	C
160203A	3.52	3.66 ± 0.05	-11.37 ± 0.05	$-7.1^{+0.09}_{-0.13}$	$1.9^{+0.43}_{-0.24}$	$0.86^{+0.785}_{-0.261}$	$-11.44^{+0.33}_{-0.21}$	$-2^{+0.34}_{-0.43}$	–	$1^{+0.91}_{-0.4}$	$-7.1^{+0.37}_{-0.35}$	0.00	C
160804A	0.736	4.38 ± 0.06	$-11.52^{+0.03}_{-0.04}$	-6.7 ± 0.03	$1.92^{+0.11}_{-0.1}$	$0.957^{+0.06}_{-0.052}$	-11.54 ± 0.06	$-1.66^{+0.11}_{-0.12}$	–	$0.829^{+0.057}_{-0.049}$	-6.78 ± 0.06	1.60	C
161108A	1.159	4.69 ± 0.11	-11.8 ± 0.1	$-7.44^{+0.06}_{-0.08}$	$1.84^{+0.15}_{-0.14}$	$0.884^{+0.108}_{-0.09}$	-11.85 ± 0.15	$-2.07^{+0.22}_{-0.25}$	–	$1.06^{+0.22}_{-0.17}$	$-7.42^{+0.14}_{-0.15}$	3.11	C
161117A	1.549	4.08 ± 0.02	-10.75 ± 0.02	-6.34 ± 0.01	1.97 ± 0.07	$0.972^{+0.066}_{-0.061}$	-10.76 ± 0.05	$-1.12^{+0.18}_{-0.17}$	$74.4^{+13.8}_{-6.3}$	$0.76^{+0.069}_{-0.106}$	$-6.46^{+0.05}_{-0.08}$	14.08	B
170405A	3.51	3.63 ± 0.02	-10.31 ± 0.03	$-7.81^{+0.01}_{-0.02}$	$1.61^{+0.11}_{-0.06}$	$0.556^{+0.1}_{-0.048}$	$-10.57^{+0.1}_{-0.07}$	-1.59 ± 0.07	–	$0.539^{+0.06}_{-0.054}$	$-8.08^{+0.06}_{-0.07}$	-0.03	B
170519A	0.818	4.15 ± 0.03	$-11.06^{+0.03}_{-0.04}$	$-7.27^{+0.06}_{-0.07}$	1.95 ± 0.08	$0.971^{+0.047}_{-0.046}$	$-11.07^{+0.05}_{-0.06}$	$-1.4^{+0.22}_{-0.21}$	–	$0.699^{+0.093}_{-0.086}$	$-7.43^{+0.11}_{-0.13}$	0.00	C
170531B	2.366	3.8 ± 0.07	-11.4 ± 0.05	$-7.29^{+0.07}_{-0.08}$	$2.01^{+0.21}_{-0.18}$	$1.01^{+0.3}_{-0.2}$	$-11.4^{+0.16}_{-0.14}$	$-1.72^{+0.27}_{-0.29}$	–	$0.712^{+0.3}_{-0.199}$	-7.44 ± 0.22	0.00	C
170903A	0.886	4.41 ± 0.04	$-11.26^{+0.02}_{-0.03}$	$-6.59^{+0.03}_{-0.04}$	2.16 ± 0.12	1.11 ± 0.08	$-11.22^{+0.05}_{-0.06}$	$-1.85^{+0.12}_{-0.13}$	–	$0.909^{+0.078}_{-0.066}$	-6.63 ± 0.07	0.00	C
171222A	2.409	4.78 ± 0.23	-12.1 ± 0.1	$-7.41^{+0.09}_{-0.13}$	2.3 ± 0.24	$1.44^{+0.5}_{-0.36}$	-11.94 ± 0.23	$-2.13^{+0.36}_{-0.45}$	–	$1.17^{+0.87}_{-0.42}$	$-7.34^{+0.33}_{-0.32}$	0.04	C
180205A	1.409	3.21 ± 0.05	-10.31 ± 0.04	$-6.63^{+0.02}_{-0.03}$	$2.04^{+0.13}_{-0.12}$	$1.04^{+0.12}_{-0.11}$	-10.3 ± 0.09	$-1.72^{+0.08}_{-0.09}$	–	$0.782^{+0.064}_{-0.053}$	$-6.74^{+0.05}_{-0.06}$	4.10	C
180404A	1	4.2 ± 0.08	-11.62 ± 0.04	-7.03 ± 0.04	$1.7^{+0.3}_{-0.18}$	$0.812^{+0.188}_{-0.095}$	$-11.71^{+0.13}_{-0.09}$	$-1.67^{+0.13}_{-0.14}$	–	$0.796^{+0.081}_{-0.069}$	-7.13 ± 0.08	-0.04	C
180620B	1.1175	4.67 ± 0.04	$-10.98^{+0.02}_{-0.03}$	$-6.48^{+0.01}_{-0.02}$	1.93 ± 0.07	$0.949^{+0.051}_{-0.049}$	$-11^{+0.04}_{-0.05}$	-1.1 ± 0.06	–	$0.509^{+0.023}_{-0.022}$	$-6.77^{+0.03}_{-0.04}$	1.68	C
180624A	2.855	4.17 ± 0.06	$-11.54^{+0.05}_{-0.06}$	$-7.05^{+0.05}_{-0.06}$	$1.96^{+0.11}_{-0.1}$	$0.947^{+0.152}_{-0.119}$	$-11.56^{+0.11}_{-0.12}$	$-1.87^{+0.18}_{-0.2}$	–	$0.839^{+0.26}_{-0.181}$	-7.13 ± 0.17	0.00	C
180720B	0.654	3.62 ± 0.004	-8.849 ± 0.003	$-6.2^{+0.06}_{-0.08}$	1.7 ± 0.01	0.86 ± 0.004	$-8.915^{+0.006}_{-0.005}$	$-0.664^{+0.162}_{-0.152}$	215^{+195}_{-41}	$0.625^{+0.056}_{-0.09}$	$-6.4^{+0.1}_{-0.15}$	6.20	C
181010A	1.39	3.16 ± 0.04	-9.93 ± 0.02	$-6.9^{+0.03}_{-0.05}$	$2.04^{+0.13}_{-0.12}$	$1.04^{+0.12}_{-0.11}$	-9.9 ± 0.1	-1.18 ± 0.14	–	$0.489^{+0.064}_{-0.056}$	$-7.21^{+0.08}_{-0.1}$	0.40	C
181020A	2.938	4.29 ± 0.03	$-10.42^{+0.06}_{-0.11}$	-6.12 ± 0.01	1.97 ± 0.05	$0.96^{+0.068}_{-0.064}$	$-10.44^{+0.09}_{-0.14}$	$-0.86^{+0.04}_{-0.05}$	–	$0.21^{+0.014}_{-0.012}$	$-6.8^{+0.04}_{-0.03}$	1.09	C
181110A	1.505	3.77 ± 0.03	-10.4 ± 0.1	-6.62 ± 0.02	$1.73^{+0.07}_{-0.04}$	$0.78^{+0.052}_{-0.028}$	$-10.51^{+0.13}_{-0.12}$	$-1.85^{+0.07}_{-0.08}$	–	$0.871^{+0.067}_{-0.054}$	-6.68 ± 0.05	1.75	C

Appendix C

Golden sample of C IV QSO data

Table C.1: Sample of QSOs with a high-quality detection of the C IV time-delay. The sample is based on 38 sources compiled by Kaspi et al. (2021). In the table, we list from the left to the right column: object name, redshift, flux density at 1350 Å, monochromatic luminosity at 1350 Å for the flat ΛCDM model ($H_0 = 70\,\mathrm{km\,s^{-1}\,Mpc^{-1}}$, $\Omega_{m0} = 0.3$, $\Omega_\Lambda = 0.7$), the rest-frame C IV time-lag (in days) determined for all the sources using either the ICCF or the zDCF method (or their combination), and the original reference.

Object	z	$\log\left(F_{1350}/\mathrm{erg\,s^{-1}cm^{-2}}\right)$	$\log\left(L_{1350}/\mathrm{erg\,s^{-1}}\right)$	τ (days)	Reference
NGC 4395	0.001064	-11.4848 ± 0.0272	39.9112 ± 0.0272	$0.040^{+0.024}_{-0.018}$	Peterson et al. (2005, 2006)
NGC 3783	0.00973	-9.7341 ± 0.0918	43.5899 ± 0.0918	$3.80^{+1.0}_{-0.9}$	Peterson et al. (2005, 2006)
NGC 7469	0.01632	-9.9973 ± 0.0712	43.7803 ± 0.0712	$2.5^{+0.3}_{-0.2}$	Peterson et al. (2005, 2006)
3C 390.3	0.0561	-10.8036 ± 0.2386	44.0719 ± 0.2386	$35.7^{+11.4}_{-14.6}$	Peterson et al. (2005, 2006)
NGC 4151	0.00332	-9.7544 ± 0.1329	42.6314 ± 0.1329	$3.34^{+0.82}_{-0.77}$	Metzroth et al. (2006)
NGC 5548	0.01676	-10.2111 ± 0.0894	43.5899 ± 0.0894	$4.53^{+0.35}_{-0.34}$	De Rosa et al. (2015)
CTS 286	2.551	-11.6705 ± 0.0719	47.0477 ± 0.0719	459^{+71}_{-92}	Lira et al. (2018)
CTS 406	3.178	-12.0382 ± 0.0402	46.9101 ± 0.0402	98^{+55}_{-74}	Lira et al. (2018)
CTS 564	2.653	-11.7615 ± 0.0664	46.9978 ± 0.0664	115^{+184}_{-29}	Lira et al. (2018)
CTS 650	2.659	-11.8815 ± 0.1068	46.8802 ± 0.1068	162^{+33}_{-10}	Lira et al. (2018)
CTS 953	2.526	-11.7082 ± 0.0868	46.9996 ± 0.0868	73^{+115}_{-58}	Lira et al. (2018)
CTS 1061	3.368	-11.4788 ± 0.0405	47.5299 ± 0.0405	91^{+111}_{-24}	Lira et al. (2018)
J 214355	2.607	-11.7786 ± 0.0485	46.9624 ± 0.0485	136^{+100}_{-90}	Lira et al. (2018)
J 221516	2.709	-11.6263 ± 0.0569	47.1550 ± 0.0569	153^{+91}_{-12}	Lira et al. (2018)

DES J0228-04	1.905	-11.9791 ± 0.0405	46.4298 ± 0.0405	123^{+43}_{-42}	Hoormann et al. (2019)
DES J0033-42	2.593	-12.2248 ± 0.0201	46.5105 ± 0.0201	95^{+16}_{-23}	Hoormann et al. (2019)
RMID 032	1.715	-13.8040 ± 0.0210	44.4928 ± 0.0210	$21.1^{+22.7}_{-8.3}$	Grier et al. (2019)
RMID 052	2.305	-13.1121 ± 0.0021	45.4990 ± 0.0021	$32.6^{+6.9}_{-2.1}$	Grier et al. (2019)
RMID 181	1.675	-13.7265 ± 0.0149	44.5451 ± 0.0149	$102.1^{+26.8}_{-10.0}$	Grier et al. (2019)
RMID 249	1.717	-13.3140 ± 0.0099	44.9841 ± 0.0099	$22.8^{+31.3}_{-11.5}$	Grier et al. (2019)
RMID 256	2.244	-13.4939 ± 0.0030	45.0888 ± 0.0030	$43.1^{+49.0}_{-15.1}$	Grier et al. (2019)
RMID 275	1.577	-12.5961 ± 0.0010	45.6110 ± 0.0010	$76.7^{+10.0}_{-3.9}$	Grier et al. (2019)
RMID 298	1.635	-12.6497 ± 0.0010	45.5960 ± 0.0010	$82.3^{+64.5}_{-24.5}$	Grier et al. (2019)
RMID 312	1.924	-13.3424 ± 0.0040	45.0770 ± 0.0040	$70.9^{+9.6}_{-3.3}$	Grier et al. (2019)
RMID 332	2.581	-13.1795 ± 0.0020	45.5510 ± 0.0020	$83.8^{+23.3}_{-6.5}$	Grier et al. (2019)
RMID 387	2.426	-12.9782 ± 0.0010	45.6870 ± 0.0010	$48.4^{+34.7}_{-10.1}$	Grier et al. (2019)
RMID 401	1.822	-12.8714 ± 0.0030	45.4900 ± 0.0030	$60.6^{+36.7}_{-13.0}$	Grier et al. (2019)
RMID 418	1.418	-13.0533 ± 0.0030	45.0398 ± 0.0030	$58.6^{+51.6}_{-21.3}$	Grier et al. (2019)
RMID 470	1.879	-13.5732 ± 0.0060	44.8210 ± 0.0060	$27.4^{+63.5}_{-22.0}$	Grier et al. (2019)
RMID 527	1.647	-13.4655 ± 0.0030	44.7880 ± 0.0030	$47.3^{+13.3}_{-5.0}$	Grier et al. (2019)
RMID 549	2.275	-13.2283 ± 0.0020	45.3690 ± 0.0020	$68.9^{+31.6}_{-9.6}$	Grier et al. (2019)
RMID 734	2.332	-13.0935 ± 0.0010	45.5299 ± 0.0010	$68.0^{+38.2}_{-11.5}$	Grier et al. (2019)
RMID 363	2.635	-12.2525 ± 0.0206	46.4997 ± 0.0206	$300.4^{+17.1}_{-4.7}$	Shen et al. (2019)
RMID 372	1.745	-12.6952 ± 0.0198	45.6201 ± 0.0198	$67.0^{+20.4}_{-7.4}$	Shen et al. (2019)
RMID 651	1.486	-12.7234 ± 0.0198	45.4200 ± 0.0198	$91.7^{+56.3}_{-22.7}$	Shen et al. (2019)
S5 0836+71	2.172	-11.5354 ± 0.0680	47.0128 ± 0.0680	230^{+91}_{-59}	Kaspi et al. (2021)
SBS 1116+603	2.646	-11.5013 ± 0.0485	47.2553 ± 0.0485	65^{+17}_{-37}	Kaspi et al. (2021)
SBS 1425+606	3.192	-11.2978 ± 0.0356	47.6551 ± 0.0356	285^{+30}_{-53}	Kaspi et al. (2021)